Fluid Power and Motion Control

Fluid Power and Motion Control

(FPMC 2008)

Edited by

Dr D N Johnston
Symposium Organiser

Professor A R Plummer
Director

Centre for Power Transmission and Motion Control
University of Bath, UK

British Library Cataloguing Publication Data

A catalogue record for this book is available from the British Library

Printed by:
Hadleys Ltd
13 Winstanley Way, Basildon, Essex SS14 3BP, United Kingdom
Tel: +44 (0) 1268 533121
Fax: +44 (0) 1268 286879
www.hadleyprint.com
e-mail: enquiries@hadleyprint.com

ISBN 9780861971503

Printed in Great Britain

Front cover picture: the Roman Baths at Bath
Back cover picture: CFD model of flow through a ball valve

Contents

Session 5 Pneumatics

Session 6 Efficient and intelligent systems

Session 7 Pumps and noise

Session 8 Control II

Session 9 Systems, modelling and design

Session 10 High performance valves II

Session 11 Control III

Preface

The Fluid Power and Motion Control Symposium took place on 10-12 September 2008. It was the 21st in the series of Symposia held annually at the University of Bath, and was the first to be co-organised by the American Society of Mechanical Engineers (ASME). It was co-sponsored by the Network of Fluid Power Centres in Europe (FPCE). It was a truly international event, with authors from eleven countries. Thirty-six fully refereed papers were presented with particular emphasis on advances in hydraulic and pneumatic systems and components. The event included a visit to the Roman Baths.

A change for the future is that the FPMC Symposia are planned to alternate each year between Bath and the USA. We are delighted that ASME has agreed to collaborate with us in this venture, and look forward to a long and fruitful partnership.

Without the continued support and enthusiasm of authors, reviewers, delegates and staff, it would not be possible to sustain such a long-running and successful series of events. Heartfelt thanks are due to all who have contributed. Special thanks are due to Gillian Elsworth for her considerable effort in compiling the material for this book, and for organizing and ensuring the smooth running of the event. We are also grateful for the support from Hadleys Ltd.

Professor A R Plummer, Director
Dr D N Johnston, Symposium Organiser
Centre for Power Transmission and Motion Control
Bath, September 2008

Session 1

Condition monitoring, sensors and automation

A novel system layout for extended functionality of mobile machines

Dipl.-Ing. Thorsten Stamm von Baumgarten
Institute of Agricultural Machinery and Fluid Power
Technische Universität Braunschweig
Dipl.-Ing. Björn Grösbrink
Institute of Agricultural Machinery and Fluid Power
Technische Universität Braunschweig
Dr.-Ing. Thorsten Lang
Institute of Agricultural Machinery and Fluid Power
Technische Universität Braunschweig
Prof. Dr.-Ing. Dr. h.c. Hans-Heinrich Harms
Institute of Agricultural Machinery and Fluid Power
Technische Universität Braunschweig

ABSTRACT

Since the introduction of electronic actuated valves, the demands for application-oriented machine functions in the field of agricultural and construction machinery has continuously grown. As a result of this, the automation of mobile hydraulic systems has gained relevancy. This paper presents steps towards automation of mobile machines such as closed-loop velocity control, adjustable end position damping and flexible workspace zoning with help of integrated position and velocity sensors as well as software-based control. The performance of automation functions such as velocity control depends amongst other things on the dynamic behaviour of the hydraulic power supply. For this reason, this paper will present a hydraulic system which had been developed and implemented at the Institute of Agricultural Machinery and Fluid Power. Consecutively, a new approach for a hydraulic system which is part of a current follow-up project will be presented und discussed.

1. INTRODUCTION

Presently, mobile hydraulic driven machines are mainly controlled open – loop that means that the system normally consists of input devices (e.g. joysticks), power supply (e.g. hydraulic pumps), control devices (e.g. hydraulic valves) and actuators (e.g. hydraulic differential cylinders). The human operator only gets feedback of the actuators (e.g. position and velocity which can only be estimated) by eyesight. In some cases this may not even be possible due to obstructions in the line of sight. In case of simple serial kinematics such as front-end loaders which consist of a swing and implement, the human operator is unable to control the position and velocity of the implement in such manner to achieve

Fluid Power and Motion Control 2008 Edited by Dr D N Johnston and Professor A R Plummer

reproducible movement sequences. Due to this the open-loop controlled system generally has inadequate dynamic behaviour (e.g. accuracy). The behaviour of actuators such as differential cylinders strongly depends on the parameters oil-temperature, load pressure etc. The objective of this project is to improve the situation as mentioned above by developing and implementing a robust closed-loop controller concept with the help of position and velocity sensors, which are integrated in the cylinder drives. A system with closed-loop controller will allow the implementation e.g. automated movements at predefined speeds.

With regard to safety and strain for the machine operator further possibilities yield the implementation of additional assistance functions because of information feedback of the cylinder position and velocity, such as end position damping and flexible workspace zoning which support the human operator. Due to these measures the efficiency and safety of the mobile working machine can be increased and the strain for the machine operator can be reduced.

Figure 1: Stationary front-end loader test rig (left) and tractor with mounted front-end loader (right)

The measures as mentioned above were developed and implemented on two systems separately, as shown in Figure 1. The stationary front-end loader test rig consists of a load-sensing hydraulic system (LS) with electro-hydraulic controlled valves and a front-end loader. The measuring and control system is made up of a PC, dSPACE Autobox and additional sensors. The cylinder drives are equipped with sensors which measure position and velocity of the piston relative to the cylinder housing. A rocker can be used to induce pushing and pulling loads on the implement of the front-end loader. The tractor depicted is a series tractor equipped with a conventional front-end loader. The cylinder drives are similar to those of the test facility and are equipped with the same sensors.

2. CLOSED-LOOP VELOCITY CONTROL

In this section the development and implementation of a closed-loop controller for the cylinder drives of the front-end loader depicted in Figure 1, will be discussed. A brief insight will be given into the setup of the controlled system. Further on, the properties of the open-loop system with respect to velocity control will be discussed. To sum up, the advantages of the closed-loop control compared to the open-loop control for this application will be shown.

The implements of mobile machines are often driven by open-loop controlled load sensing hydraulic systems. As already mentioned above, the input signal can be given by a joystick or similar device. The system consists of power supply, valves and actuators as shown in Figure 2. The output signal in this case is the velocity of the cylinder drives. The velocity is measured by sensors integrated in the cylinder drives. The cylinder piston velocity is calculated within the sensor which has the benefit that the velocity signal only has a negligible superimposed noise signal. Another benefit of the internally integrated sensors compared to externally mounted sensors such as angle encoders is increased robustness regarding rough working environments of mobile machines.

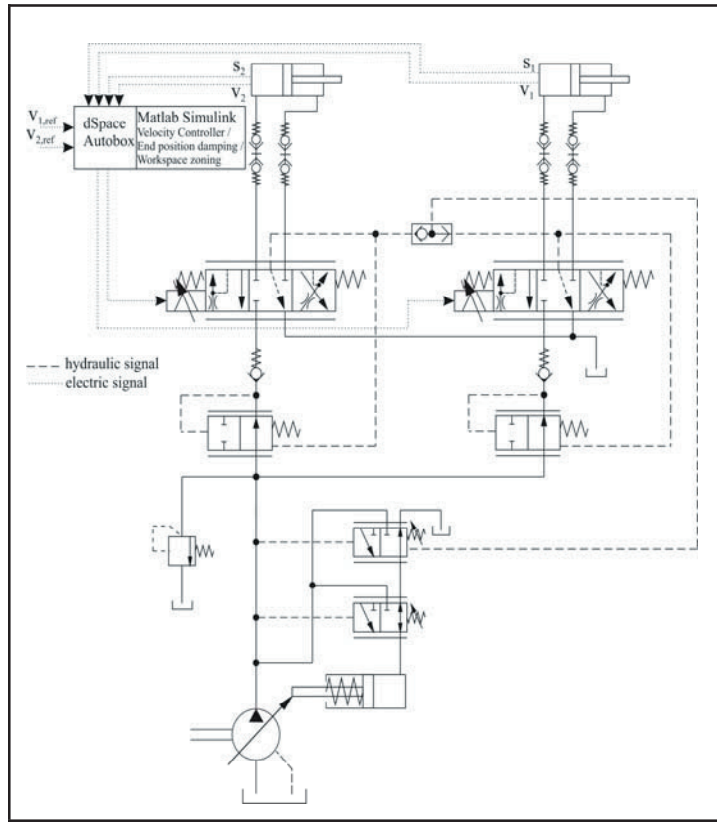

Figure 2: Hydraulic system with measuring and control unit dSPACE Autobox

The velocity of the cylinder drive is proportional to the volume flow. The volume flow on the other hand is amongst others dependent of the parameters temperature, load pressure (taking into account that the pressure compensators have the task to maintain a volume flow independent of the load pressure) and pulling/pushing loads etc.

To determine the effects the parameters have on the behaviour of the system, measurements were done using the open-loop controlled system. To examine the behaviour of the system, a specific run for the reference velocity has been chosen as can be seen in Figure 3. The

step at time 0 s is used to determine the response (agility) of the system. The areas, where the reference velocity is constant, are used to determine the stationary accuracy at various velocities and parameter settings.

In the next step, measurements were made at constant temperature but with varying load pressure. By adding mass to the implement of the front-end loader, in this case a shovel, the load pressure was increased from about 30 bar to 60 bar and then up to 120 bar. As seen in Figure 3, with increasing load pressure the deviation of the actual velocity to the reference velocity of the cylinder drives increases especially at small velocity values.

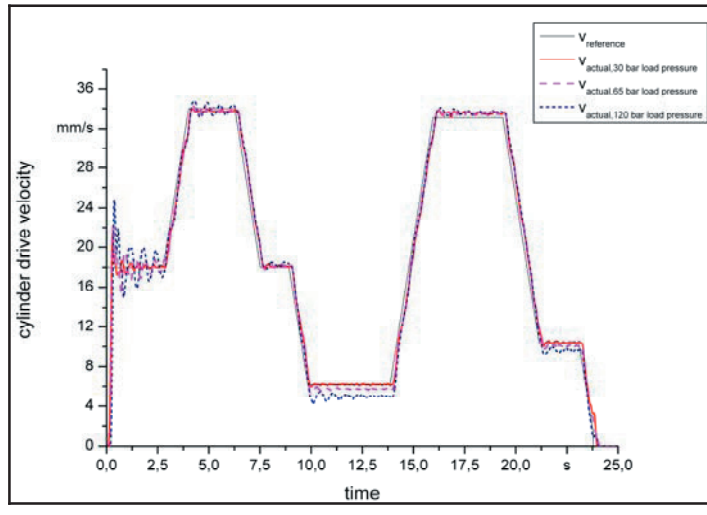

Figure 3: Cylinder drive velocity dependency of load pressure

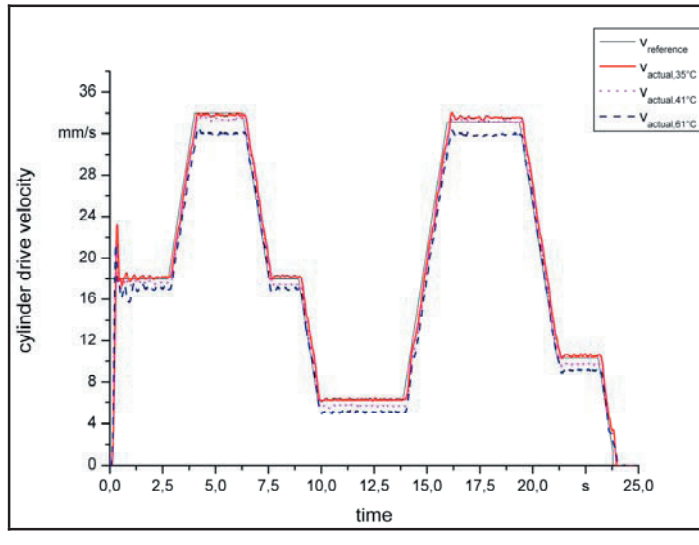

Figure 4: Cylinder drive velocity dependency of oil temperature

Figure 4 shows the cylinder drive velocity over time. To demonstrate the effect the temperature of oil has, measurements were done at 35°C, 41°C and 61°C. With increasing temperature the deviation of the actual velocity to the reference velocity increases. The deviation is up to 20% at low velocities.

To sum up, it is fairly clear that the parameters temperature, load pressure have a negative effect on the system behaviour. By taking more parameters into account it is predictable, that the system behaviour can be influenced even greater. To compensate the mentioned effects, a closed-loop controller has been developed and implemented.

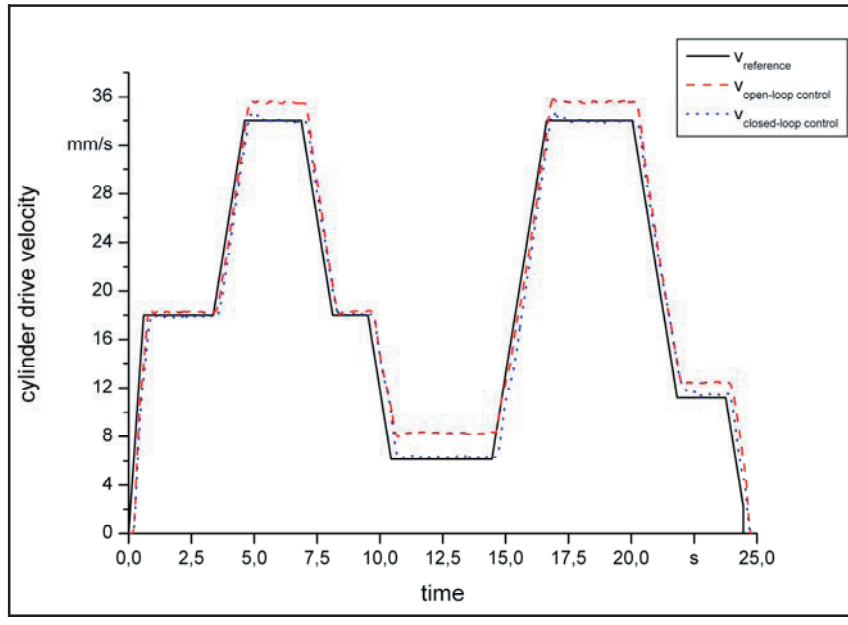

Figure 5: Comparison of open-loop and closed-loop velocity controlled system

After the closed-loop controller was installed, the same reference velocity run was given as input signal. The experiments were held under the same conditions, i.e. temperature and load pressure. In Figure 5, the results of the cylinder piston velocity controlled open- and closed-loop are presented and can be compared. The actual velocity of both control methods has an almost identical gradient at time 0-1 s. The reason for this is that the closed-loop controller possesses a feed - forward of the reference velocity, which is identical to input of the reference velocity at the open – loop controller. By focusing on the stationary accuracy of both controllers, it is noticeable that the closed-loop controller has a higher accuracy due to the use of an integrator.

The tractor which was used in this project is equipped with conventional proportional valves. Because the cylinder drives of the implements of rugged mobile machines normally only have to exert great forces and don't have to be precise in position, the implemented control valves for the cylinder drives of the tractor have a relatively low volume flow resolution, to which the cylinder velocity is proportional. A minimal control deviation of

about 1 % maximum still may exist, because the resolution of the valve control spool position is fixed to 8 bit resulting from the implemented CAN-Bus protocol. For this reason, the control value of the closed-loop controller is kept constant as soon as the deviation of the actual velocity to the reference velocity reaches a set minimum boundary, to prevent unwanted oscillations of the cylinder drives due to the velocity controller behaviour.

The spectrum of application areas of mobile working machines has increased over the years and thus requires versatility. Due to the fact that the metering edge geometry of the valve control spool is fixed, the relationship between the input signals i.e. joystick and the output, in this case the cylinder drive velocity, is defined by a fixed relation. To expand the functionality of a mobile working machine, a software-based variable velocity gain function has been implemented into the cylinder velocity controller. The advantage is that the movement behaviour of the front-end loader can be varied from delicate (progressive) to coarse (linear) depending on the requirements of the work task.

3. END POSITION DAMPING

Focusing on cylinder drives, damping has the task to reduce the "slam-effect" when the cylinder piston reaches either ends of the cylinder housing. Most common are mechanical and hydraulic dampers with control throttles. The implementation of an end position damping has several benefits. The strain of joints is reduced and the total lifespan of the components is increased. The physical and mental strain of the operator of a mobile machine is reduced which allows the operator to concentrate over a longer period of operation time. Besides the mentioned benefits, the use of mechanical or hydraulic dampers has disadvantages. Additional mechanical damper components have to be installed into the cylinder drive housing. The damping ratio of mechanical and hydraulic dampers cannot be changed continuously. Due to the use of position and velocity sensors it is possible to develop and implement a software-based end position damping task (Figure 6) for the front-end loader.

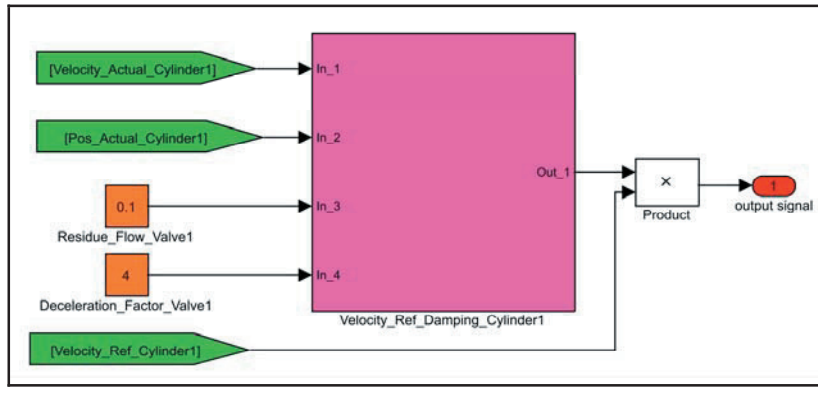

Figure 6: Simulink model of end position damping

The damping task is a function of the measured position and velocity of the cylinder piston, a residue oil flow through the controlled valve and the set deceleration factor. It is

important to set a minimum residue oil flow through the valve to allow the cylinder piston to reach the ends of the cylinder housing. The deceleration factor sets the damping rate. The output signal "Out_1" of the "Velocity_Ref_Damping_Cylinder1" block resembles a proportional transfer function with second order delay. The gradient of the function is defined by the deceleration factor as well as the measured velocity and position of the cylinder. The stationary value of the function is influenced by the minimum residue oil flow. Figure 7 depicts the measured velocities of the swing cylinders of the front-end loader with varied damping rates.

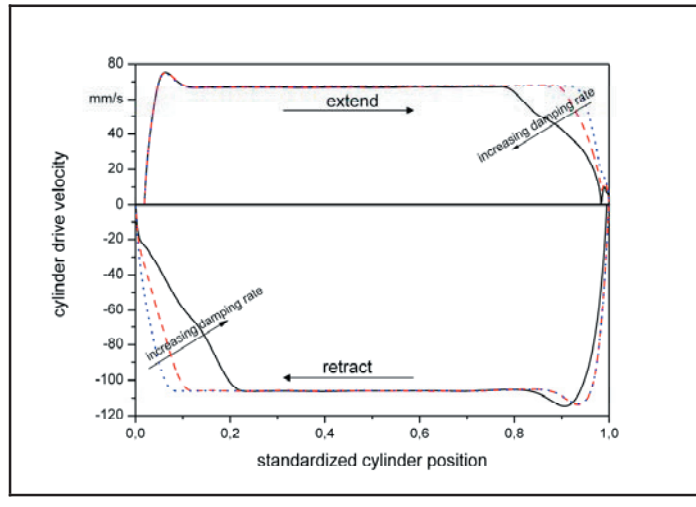

Figure 7: Cylinder velocity run with activated end position damping

The software-based damping has several advantages to the mechanical-based damping. The damping ratio can be continuously adapted via software to the operation requirements. A delay-free acceleration out of the end positions is possible. No additional components except for the already integrated sensors have to be installed and it is easily transferable to other systems with integrated position and velocity sensors.

4. WORKSPACE ZONING

Loaders and similar mobile machines are often used in areas, in which the operator has to pay attention to the movements of the mobile machine relating to the operational area to prevent accidents. For example, mobile excavators are used to maintain railway tracks. The operator of the machine continuously has to pay attention that the boom or other parts of the mobile excavator do not run into the catenaries to prevent a short circuit between the catenaries and the railway track. Over a longer period of operation, fatigue sets in and the alertness of the operator starts to deteriorate. It is clear that the likelihood of an accident grows continuously. For this reason, a method to limit the workspace of the front-end loader has been developed and implemented. The aim of this project is to limit the movement of the front-end loader in horizontal and vertical direction (Figure 8). Following, a short insight will be given into the procedures used for the workspace zoning.

The front-end loader can be considered as a multi-body system. The implement, in this case a shovel, is defined by a set of four points P1,…,P4. Any other implement may also be used. The area that is defined by the relative points must only be arranged accordingly. In the next step coordinate systems are introduced.

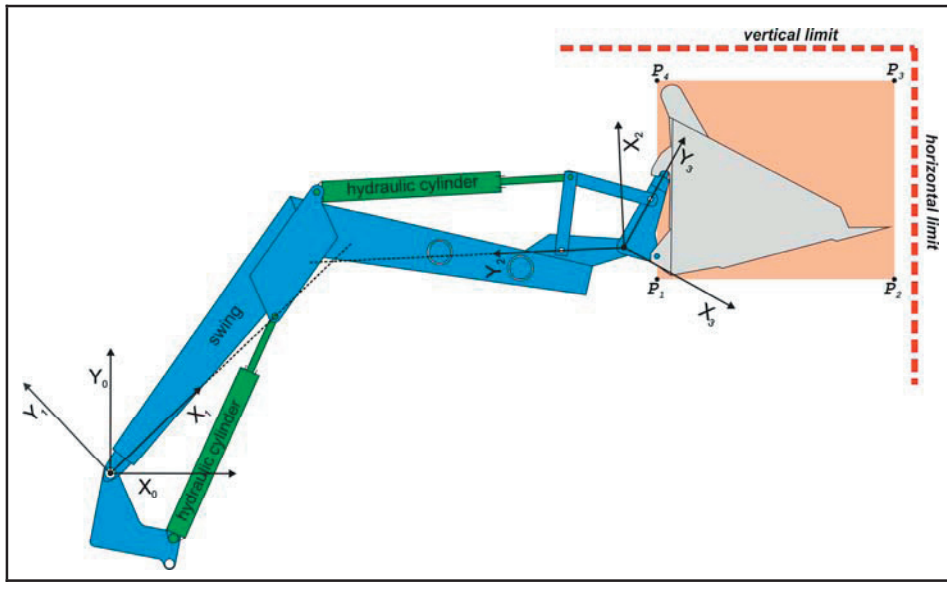

Figure 8: Front-end loader

Transformation matrices are used to transform relative points from one coordinate system to another with help of the equations (1) and (2) [1].

$$\underline{r_{p1}^{(0)}} = \underline{T_3^2} \cdot \underline{T_2^1} \cdot \underline{T_1^0} \cdot \underline{r_{p1}^{(3)}} \tag{1}$$

$$\underline{r_{p1}^{(3)}} = \begin{bmatrix} x_{p1}^3 \\ y_{p1}^3 \\ 0 \end{bmatrix}, \quad \underline{T_i^{i-1}} = \begin{bmatrix} \cos\varphi_i & -\sin\varphi_i & 0 & x_i \\ \sin\varphi_i & \cos\varphi_i & 0 & y_i \\ 0 & 0 & 1 & 0 \\ 0 & 0 & 0 & 1 \end{bmatrix} \tag{2}$$

With the help of direct kinematics, the positions of the points Pn relative to the base coordinate system of the mobile working machine are calculated. This allows the operator to continuously observe and control the horizontal and vertical distance of the implement to the base coordinate system. If for instance, the operator wants to limit the height of the implement, the front-end loader is driven to a specific height which should not be exceeded i.e. height of catenaries. Next, the operator sets the measured y-coordinate as maximum height allowed. This value is stored in a database of the workspace limitation function. The procedure can be done in both directions of the x- and y-coordinate system. After the value is stored, the operator activates the workspace limitation function. As soon as the operator

moves the front-end loader towards the vertical or horizontal limit with a specific reference velocity, the workspace limitation function intervenes and adjusts the reference velocity signal appropriately. The adjustment depends on the distance to the limit and the reference velocity value and is similar to the end position damping function. The workspace limitation function switches off automatically as soon as the front-end loader is moved in opposite direction to the limit. With this function established, the operator does not have to keep an eye on the position of the implement during operation constantly. The function reduces the strain of the operator tremendously.

5. ADAPTIVE HYDRAULIC SYSTEM

Currently a large number of mobile machines such as the tractor depicted in Figure 1, are equipped with hydraulic-mechanical LS systems. Compared to other hydraulic systems such as constant pressure and constant flow systems, the LS system achieves a high power efficiency considering the whole operating range. As already mentioned above, the degree of automation of mobile machines has increased, resulting in increased demands for dynamic behaviour and greater efficiency at the same time. For example, the dynamic performance of the closed-loop velocity control of the actuators of the front-end loader discussed in chapter 3 greatly depends on the dynamic performance of the hydraulic system which supplies the actuators with power. It is possible to increase the dynamic performance of the conventional LS system, but it has to be kept in mind that the stability and efficiency of the system will be decreased.

To deal with this problem, LS systems have been equipped with an electric actuated pump and pressure sensors, e.g. in [2], [3]. Although these systems, also known as electro-hydraulic LS systems (ELS), are fully functional they have not been implemented in the field of mobile hydraulic applications up to now. The reason for are the relatively high costs for additional sensors and the demand for robustness and reliability of the sensors. Hence current research has the focus to simplify the system complexity and to reduce the functional requirements to components and sensors e.g. [4], [5].

To increase the robustness and reduce the complexity of the system, a different approach for an adaptive hydraulic system had been developed and implemented at the Institute of Agricultural Machinery and Fluid Power. The system mainly consists of a variable displacement pump with an integrated electro-proportional swash-plate angle a controller and output flow controller, electronic actuated valves and an open-center pressure compensator which acts as a bypass and regulates the pump pressure according to the LS principle. In contrast to the conventional LS as depicted in Figure 2, there is no hydraulic signal transfer between the valve group and the pump displacement actuator. The system allows several possibilities for the control system of the pump flow and the valve opening. The control strategy of the flow demand system (Figure 9) relies on the information of the motion commands given by input-devices such as joysticks. With the motion commands and additional information such as pilot volume flow the necessary pump flow to the actuators is calculated and in consideration of the pump speed the delivery volume of the pump is set.

To counter the occurrence of pressure peaks in the system in case of a fast reduction of oil flow to the consumers, a bypass is needed to allow the surplus oil to flow back into the tank, due to the limited accuracy of the electro-hydraulic displacement volume adjustment

of displacement pumps in open circuits suitable for mobile application areas Due to the fact that the inaccuracy of the swash plate angle controller as well as the impact of this inaccuracy on the pump pressure increases with decreasing delivery volume, a pressure compensator is essential for small volume flows. The pressure compensator or bypass can be used to produce a controlled flow rate excess, which benefits the system dynamics. If high oil flow accelerations are needed, the bypass temporarily closes resulting in a higher flow rate to the consumers. This happens much faster as the pump is able to increase the displacement volume.

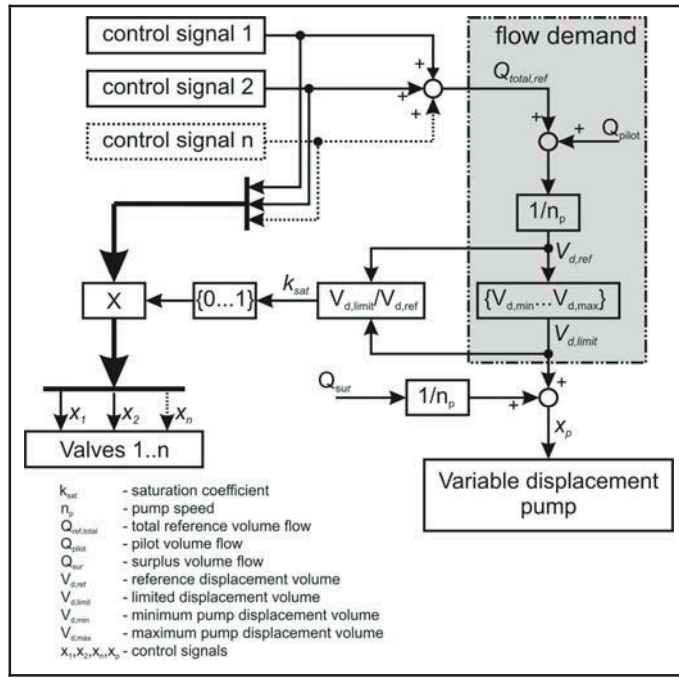

Figure 9: Signal diagram of the open-loop controlled flow demand system [6]

An optimisation of the presented flow demand system is possible, if a heterodyne closed-loop controller for the pump delivery flow volume is implemented. With this step the deviations, such as hysteresis errors of components, leakages etc., can be compensated. For this reason a follow-up project for the adaptive flow demand system has been initiated at the Institute of Agricultural Machinery and Fluid Power. The aim of the research project is the development and analysis of a novel alternating control scheme for hydro-mechanical and electro-mechanical LS systems, with which an optimal energy transfer should be achieved in the entire operation range of mobile machines.

The function of the new hydraulic system is based, like the conventional hydro-mechanical LS system, on controlling the pressure difference of the pump and highest load pressure of the consumers. Figure 10 depicts the hydraulic circuit diagram of the system.

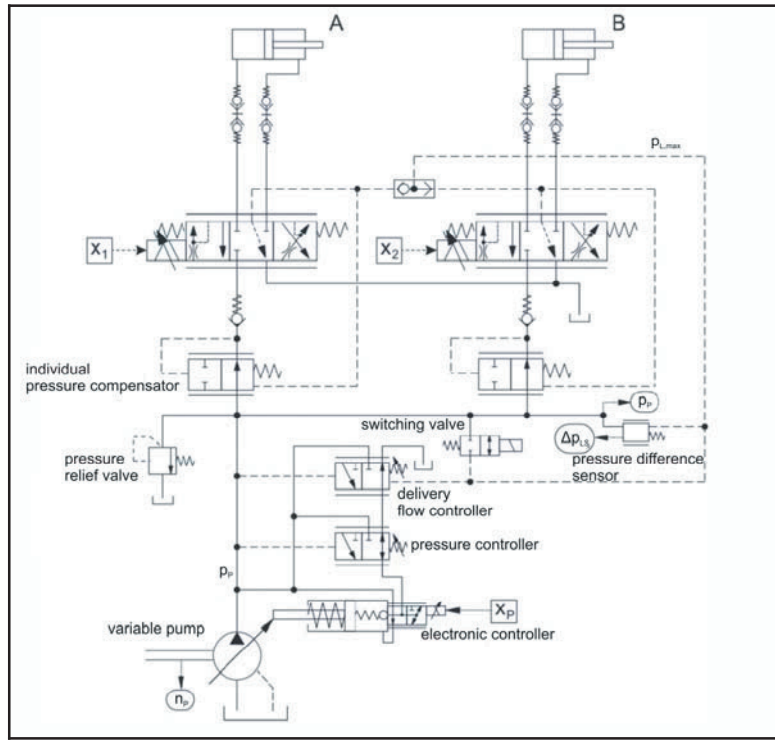

Figure 10: Hydraulic circuit diagram of the novel system

The system combines an open-loop and a closed-loop control mechanism. To achieve a sufficient accuracy of the pump displacement at small swash plate angles with the help of conventional mobile components, the swash plate angle adjustment is done up to a specified boundary by the hydro-mechanical volume flow controller. This results the pressure drop and energy loss which is also known from conventional hydro-mechanical LS systems, but only at small swash plate angles and thus considerably small scale power transfer.

Due to the fact, that the hydraulic systems of some mobile machines, such as tractors, spend a great amount of time in stand-by, it is especially important to reduce the power dissipation in this operation area. An electro proportional adjustment of the pump with sufficient precision would, due to the low pump pressure in this operation area, require an additional pilot pressure supply and thus increase the power dissipation. If the consumers require higher volume flow, the electro-hydraulic controller takes over the displacement of the pump. This method provides the possibility to reduce the pressure difference and thus the reduction of the power loss compared to the conventional control method. The transition between the two control methods depends on several parameters as can be seen in Figure 10. Both displacement volume controllers are combined in such a way with one another, that the swash plate angle is always controlled to the minimal value as depicted in Figure 11. Additional, a maximum pressure controller is depicted which is used to limit the pressure and thus maintains its normal function.

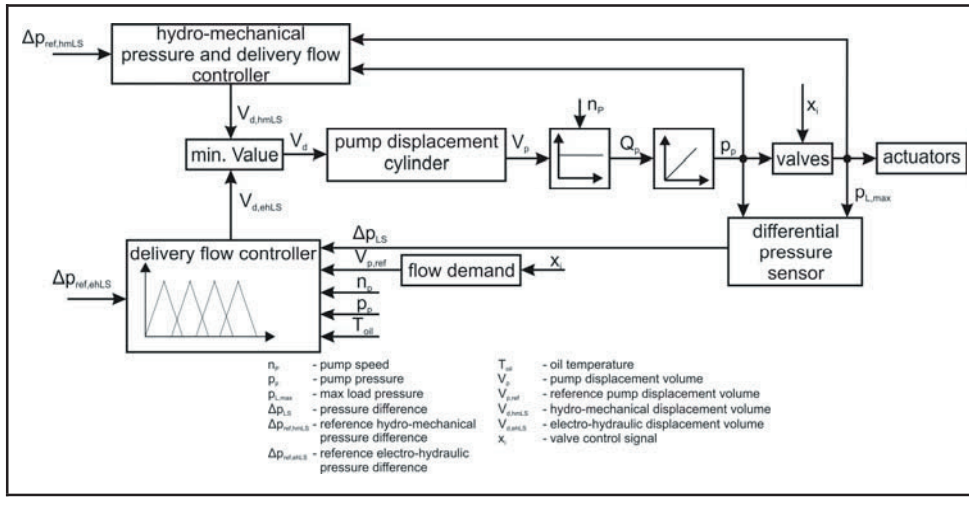

Figure 11: Signal diagram of the adaptive flow demand system

In order that the load volume flow which can be seen as a disturbance does not have to be compensated by the closed-loop controller, the information from the operator input signals to the valves can be used as a disturbance feed forward to relieve the pressure difference controller. The previously described flow demand controller (grey box Figure 9) is overlaid by the electro-hydraulic pressure difference controller to increase the precision of the system. A further advantage of the disturbance feed forward in the main working range is, that the variation of the volume flow demand is known directly and the signal to the swash plate angle controller of the pump is given at the same time as the signals to the valves, thus compensating a portion of the delay time which results from inertia of the pump controller.

To use the presented system, the pressure difference of the load and pump pressure must be available as an electronic signal. To avoid the mentioned problems of pressure sensors in mobile applications, the pressure difference is identified by determining the spool position of a pressure compensator on which the pump and load pressure as well as a spring acts. Since the pressure compensator does not control any volume flow, it has no direct impact on the dynamic stability of the system. Furthermore, the system possesses some of the features which are already known from former presented electro-hydraulic systems such as the timely recognition of pump saturation and the possibility to operate the system in such a manner, that the primary pressure compensator of the consumer with the highest load can be opened fully and thus reducing the pressure drop extensively.

The main difference of the described system to classically known electro-hydraulic LS systems is the considerably simple setup and thus less sensitive to harsh working conditions of mobile machines which allows the implementation of the system into these machines. Compared to currently researched flow demand open-loop and closed-loop systems, the system has an advantage by dispensing with a bypass pressure compensator. This is possible due the increased precision of the system because of the flow demand control with heterodyne pressure difference closed-loop control. The reason to do without a bypass is the fact, that the regarded absolute energy saving potential in comparison to the

conventional LS system depending on the operation point is relatively small, because with greater volume flow demand an increased pressure surplus is needed to overcome the flow losses, independent of the pump control system. In comparison to the previous project, the system has the advantage that it makes use of a closed-loop rather than just an open-loop controller which allows the system to "recognise" unknown consumers, such as the power-beyond link of a tractor, and is able to adjust accordingly.

6. CONCLUSION

The implementation of a closed-loop controller for velocity controlled cylinder drives shows a significant improvement regarding stationary accuracy and effects regarding parameter such as temperature and load pressure. With respect to mobile working machines, the introduced system can aid the development of automated movement procedures of frequently repeating processes.

With respect to assistance systems, the end position damping function and workspace limitation function increase the durability and safety of mobile machines. Due to the fact that the developed assistance functions are software based, the functions are easily portable from one mobile machine to another. A further step with regard to workspace limitation may be the introduction of sensors which measure tilt of the mobile machinery. With this additional information, the accuracy of the workspace limitation can be increased.

The flow demand system, presented in this paper, shows on the one hand an increased system efficiency and stable behaviour in comparison to the conventional LS system. On the other hand, the system has the disadvantage that it cannot sense disturbances such as the power-beyond line of a tractor. It is expected that novel system presented will show an improvement by a heterodyne closed-loop control method of efficiency due to the fact that no bypass valve is used and the disturbances can be accounted for. A further advantage is that the use of conventional components and the relatively simple setup should fulfil the requirements for an application in mobile machines.

REFERENCE

[1] **Heimann, B., Gerth, W., Popp, K.** *Mechatronik, Komponenten – Methoden – Beispiele*. Fachbuchverlag Leibzig im Carl Hanser Verlag, 2001

[2] **Zähe, B.** *Energiesparende Schaltungen hydraulischer Antriebe mit veränderlichem Versorgungsdruck und ihre Regelung*. Dissertation, RWTH Aachen, 1993.

[3] **Esders, H.** *Elektrohydraulisches Load Sensing für mobile Anwendungen*. Fortschrittberichte VDI, Reihe 14, Nr. 75, VDI Verlag, 1996

[4] **Djurovic, M.; Helduser, S.:** *New control strategies for electrohydraulic Load-Sensing.* Bath Workshop on Power Transmission and Motion Control – PTMC,2004

[5] **Finzel, R.; Helduser, S.** *Energy-Efficient Electro-Hydraulic Control Systems for Mobile Machinery / Flow Matching*. 6th International Fluid Power Conference Dresden, Vol. 1, pp. 89-102, 2008

[6] **Fedde, T.; Harms, H.-H.** *An adaptable hydraulic system for tractors,* Bath Workshop on Power Transmission and Motion Control – PTMC, 2005

Utilization of RFID and pressure sensor for intelligent hose condition monitoring

Antti Aarnio, Lauri Elo, Esa Mäkinen, Leena Ukkonen, Mikael Soini, Lauri Sydänheimo, Matti Vilenius, Markku Kivikoski
Tampere University of Technology
Department of Electronics, Rauma Research Unit
Department of Intelligent Hydraulics and Automation, Rauma Research Unit

ABSTRACT

Hose malfunctions are a common source of failure in hydraulic systems. Usually a hydraulic hose is replaced to a new hose when it starts leaking – sometimes it breaks completely before the replacement. Replacing hoses before they break could prevent dangerous situations and financial losses. An intelligent hose may itself indicate its condition using integrated sensors for measuring the hose loading condition and RFID-tag for the identification. Maintenance can use this information for replacing hoses before they break.

1. INTRODUCTION

Current the replacement of hydraulic hoses is normally not based on the real knowledge on the condition or estimated life time of existing hoses. Making the intelligent hose aims to financial savings and to prevent hazardous situations in the hydraulic systems. This is a research which started because of the need of intelligent hose in hydraulic systems. In this paper, possibilities to solve this problem utilizing an intelligent hose are discussed and some proposed features are experimentally tested with two prototypes. Active measurement and passive identification are discussed in this paper. In the larger picture they also need some kind of data acquisition system to collect and storage data, but in this paper that is not yet considered.

There are different kinds of hydraulic hoses. Different hoses are chosen to different applications and environments. The most common hydraulic hoses are rubber hoses. Other kinds are thermoplastic hoses, Teflon (PTFE) hoses and full-metal hoses. This paper concerns rubber hoses. Structure of the rubber hose is in figure 1. The rubber hose has an inner layer, a reinforcement layer or layers and a surface layer.

Fluid Power and Motion Control 2008 Edited by Dr D N Johnston and Professor A R Plummer

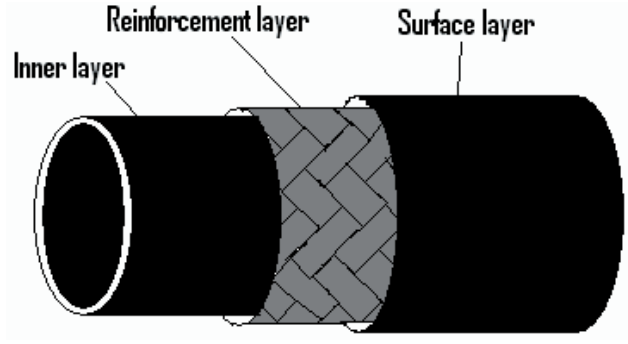

Figure 1. Structure of the rubber hose.

The reinforcement layer is around the inner layer and it is the support tissue of the hose and it defines the pressure endurance of the hose. The reinforcement layer consists usually of steel fibers that are weaved crosswise so that they form so called steel braid. Other way to make the reinforcement layer is to set steel fibers to form spiral so that they don't cross each other. The spiral hose has better endurance to dynamic pressure but its manufacturing costs more than manufacturing of the steel braid hose. The steel braid hoses that have one or two reinforcement layers are the most common hoses in hydraulics.

The inner layer is usually made of nitrile rubber. Nitrile rubber stands mineral-oil based hydraulic oils and about 100ºC of continuous temperature. The surface layer must stand external stress such as friction, hit and cut. The surface layer is usually made of neoprene, but sometimes above the surface layer is yet a special protection layer such as polyethylene layer. Neoprene has good endurance to mechanical stress, weather and ozone.

1.1 Failure mechanisms of the hydraulic hoses

Information about the failure mechanisms of the hoses is important, when an intelligent hose is designed. Known failure reasons are friction, hit, cut, too much bent hose, wound hose, coupling unfastening from hose, UV-radiation, ozone, chemical liquids, too high static pressure, pressure shocks, pulsating pressure, cold or hot temperature, aggressive fluid, too fast flow of fluid and stretched hose. Different kinds of hoses fail because of different reasons. Rubber hoses failure usually from pressure shocks and hot temperature in hydraulic systems. Figure 2 shows the failure mechanisms of rubber hoses.

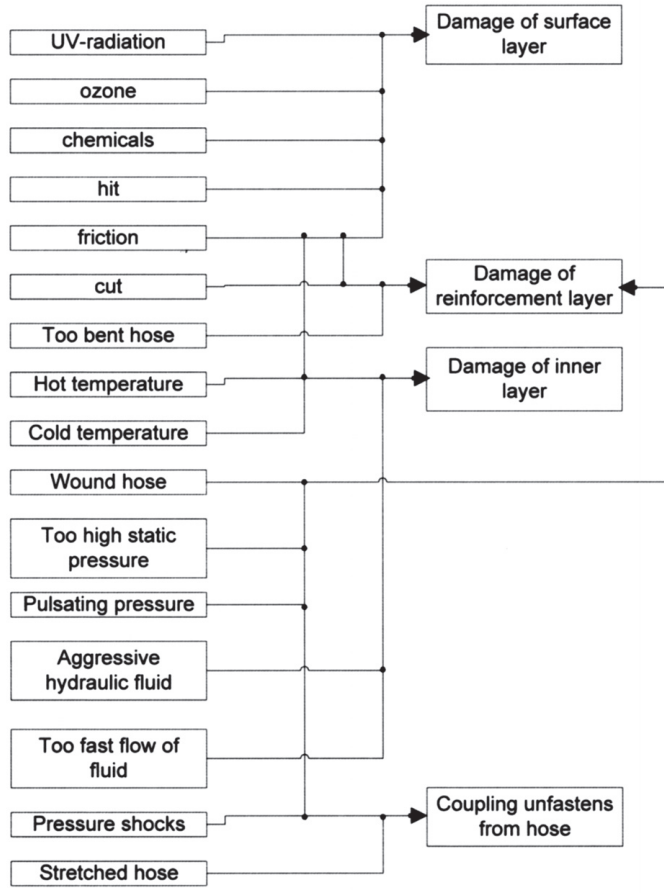

Figure 2. Failure mechanisms of rubber hoses.

Pressure inside the hose causes force against the inner layer and thus force against the reinforcement layer. Force against the reinforcement layer makes the hose shorten or lengthen. Usually hoses shorten with pressure increase and this means also growth in the outer diameter of hoses. When the length of the hose changes, its steel fibers move against each other and so they weaken. Changes of pressure fatigue and break steel fibers of the reinforcement layer of the hose. In some cases pressure information might be available from the system data, but not always. That's why the prototype of the intelligent hose is made in this paper. Results using strain gauges are promising but current consumption is the main disadvantage.

Age of the hose is one thing that in general affect to the condition of the hose. Knowing age of the hose helps to estimate the condition of the hose. Other thing that is important is time that hose have been in use under stress. But using this information, only an estimate of the condition of the hose is known, not the real condition of the hose. RFID-tag based prototype of the intelligent hose gives good results to passive identification of the hose and

thus knowing age of the hose. The main problem is the steel reinforcement layer of the hose.

2. CONCEPT OF THE INTELLIGENT HOSE

Purpose of the intelligent hose is to monitoring its condition using electronics on the surface on the hose. Condition monitoring of the hose needs some active sensor, which measures something from the hose. From this measurement, condition of the hose can be solved with the microprocessor of the sensor. In addition to that, RFID-tag can give passive information about the hose. Naturally, some kind of data acquisition system is needed. The data acquisition system is used to collect measurement and status information from industrial environment for preventive maintenance.

2.1 Active measurement

Active measurement can be for example temperature, pressure, moisture measurements etc. In this paper, active measurement is done using steel strain gauges and microcontroller for pressure measurement. Two strain gauges were attached on the surface of metal clamp, which was attached around the hose. One strain gauge is the measuring gauge and other is for temperature compensation. The clamp is needed, because strain gauges are easier to glue on metal than on rubber. Strain gauge bridge needs also an instrumentation amplifier, because its measurement signal without amplification is too low for the microcontroller.

Strain gauges were HBM 120Ω steel strain gauges. Strain gauges were part of Wheatstone bridge. Bridge output voltage was amplified and connected to input pin of the microcontroller. Low power microcontroller was MSP430F2274 manufactured by Texas Instruments. It has peripherals such as A/D-converter, timers and two operational amplifiers which can be programmed to different modes (1).

The microcontroller can be programmed to real-time pressure gauge or it can be programmed to indicating peak value of pressure. The microcontroller can be also programmed to count the amount of the pressure shocks. An operational amplifier in the microcontroller is programmed to comparator mode and a timer counts output pulses of the comparator which are also pressure shocks.

Active measurement using strain gauges was tested in the testing system. Used hose was a rubber hose which has 1'' inner diameter and one steel braid reinforcement layer. Working pressure for the hose is 88bar and breaking pressure is 350bar. EN 857 standard says that this kind of hose has endurance for 150000 pressure shocks, that are 1,25 times higher than the working pressure of the hose (2).

Pressure and pressure shocks were made with the hydraulic circuit which has a servo valve for changing pressure. The servo valve was used for throttle the flow of hydraulic oil. It was controlled with Labview. In the end of the hose, was installed normal pressure gauge for real pressure information to Labview. With this pressure information, calibration of the strain gauge sensor is possible. Strain gauge bridge output voltage was also input to Labview. Figure 3 shows the testing system.

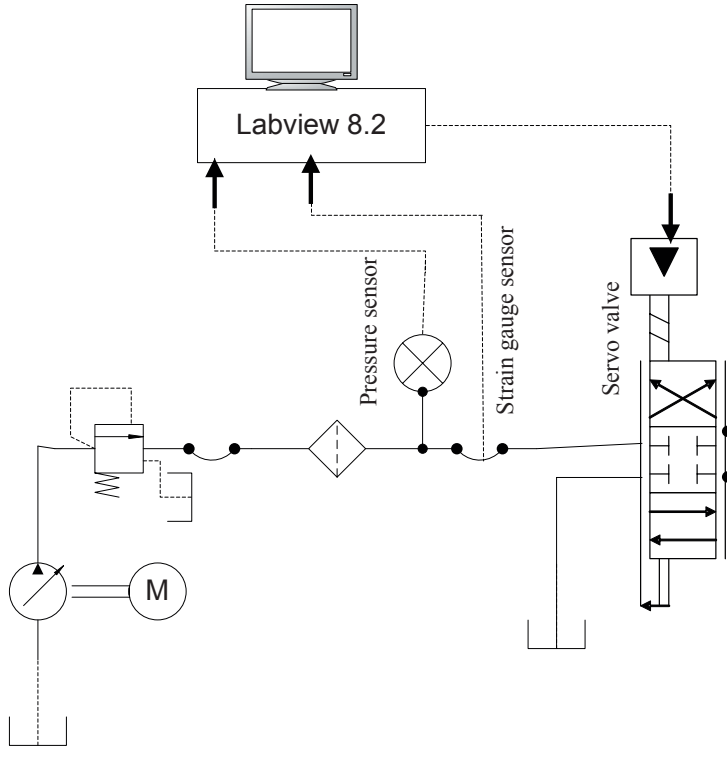

Figure 3. Testing system.

2.2 Passive identification

Condition monitoring of individual hoses is important to prevent hose malfunctions. Previous sections presented a method where hose condition was monitored actively with strain gauges which can report about upcoming malfunction and the hose can be replaced before a break down. The identification of individual hoses can be used in preventive condition monitoring. The identification of the hose and hose information such as manufacturing or installation dates can be used to enable in-time hose replacements. Identification can be performed with handheld mobile reader, for example, during maintenance check-ups.

In this paper the identification of the steel enforced rubber hydraulic hose is performed with passive UHF RFID technology. Tags are EPC (Electronic Product Code) gen2 compliant (3). Coarsely, RFID systems consist of a reader, a tag and a data processing system. Communication in passive UHF RFID systems is based on backscattering of modulated electromagnetic waves: the reader transmits energy and commands to the tag which responds by backscattering its identification data back to the reader. Passive tags consist of a microchip and an antenna. There is no internal source of energy and therefore all the energy for the tag to function originates from the electromagnetic waves radiated by the reader. (4)

3. RESULTS OF THE ACTIVE MEASUREMENT

Results show, that using strain gauges, pressure inside the hose can be calculated and the amount of pressure shocks can be counted. Current consumption of the strain gauge bridge (about 32mA) is the main disadvantage of the measurement system. Current consumption should be so low that device could be battery operated and still long-life device. In addition to that strain gauge bridge output voltage has some oscillation and is different between measurement times.

3.1 Pressure measurement

Using microcontroller, it is possible to scale strain gauge bridge output voltage close to real pressure that influences inside the hose. 10-bit SAR-type A/D-converter of microcontroller is used in pressure measurement program. Measurement result appears in the register of A/D-converter. Figure 4 shows an average of ADC-register values in function of pressure.

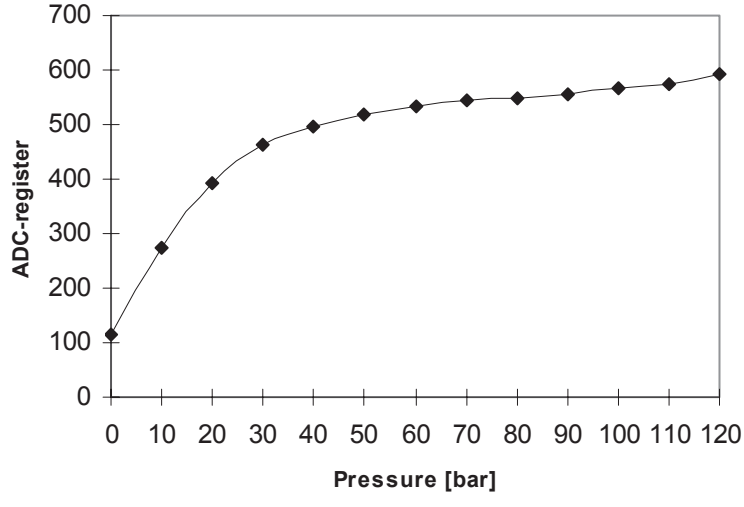

Figure 4. ADC-register values in function of pressure.

Figure 4 shows that strain gauge output voltage is near to a logarithmic curve. So ADC-register value can be scaled and placed to exponent function. This is done in figure 5.

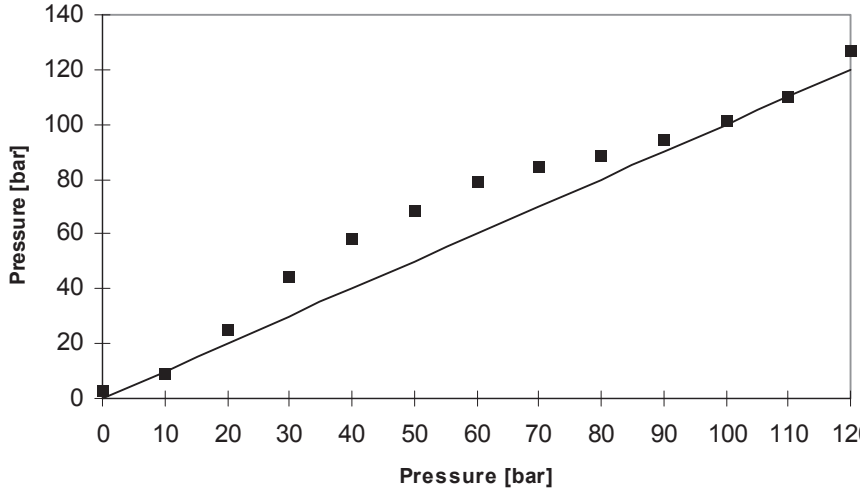

Figure 5. Scaled value of ADC-register with the real pressure value.

3.2 Counting of pressure shocks

When the microcontroller counts pressure shocks, its embedded operational amplifier is programmed to a comparator mode. The comparator has programmable reference voltage and every time when amplified measurement voltage exceeds reference voltage, the comparator generates a pulse. These pulses are counted by the timer of the microcontroller. The comparator needs some hysteresis because of the oscillation of the bridge output voltage. Otherwise the comparator generates too many pulses. Appropriate hysteresis is difficult to set, but it is clear that some hysteresis is needed. Hysteresis is achieved with two external resistors. Hysteresis was made so that lower threshold voltage is 0,764V and upper threshold voltage is 0,812V. If measurement signal fluctuates between these threshold voltages, comparator output doesn't change.

Measurement system was tested with different frequency pressure pulses. 0,5s long pressure pulse and 1s long pressure pulse cause on average about 12 pulses to the register of the timer. Figure 6 shows pressure inside the hose when 1s lasting pressure pulses were generated. Figure 7 shows amplified measurement voltage with same pulses.

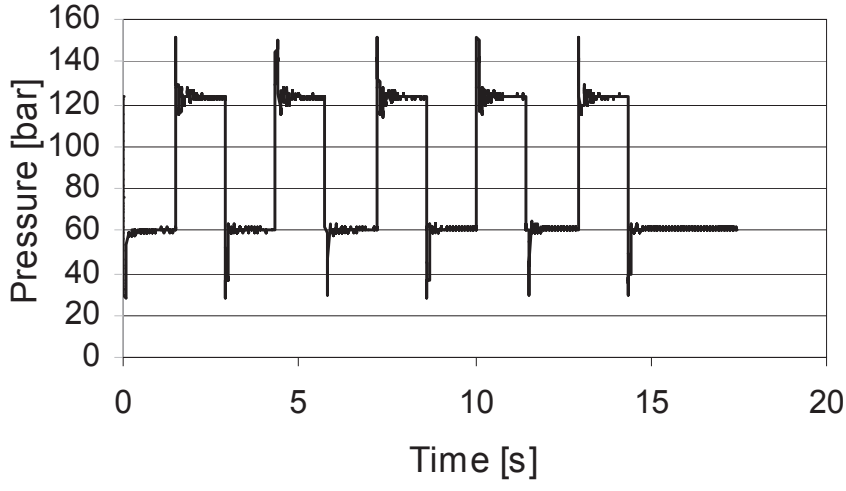

Figure 6. 1s lasting pressure pulses inside the hose.

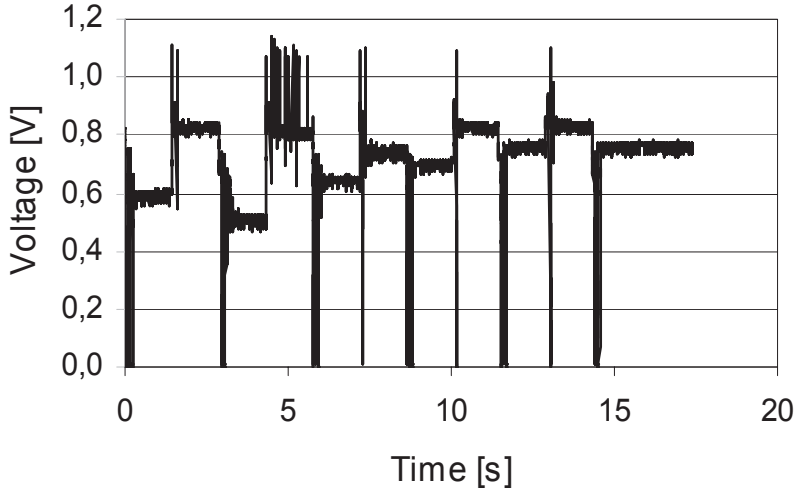

Figure 7. Amplified measurement voltage when the hose is pressurized with 1s lasting pressure pulses.

The hose was also pressurized with faster pressure pulses. 0,1s and 0,01s lasting pressure pulses were generated. It was noticed, that with 0,1s lasting pulse, timer counts 24 pulses on average. With 0,01s lasting pulse, timer counts only 1,33 pulses on average. 0,01s lasting pulse is so fast that signal has no time to fluctuate near to threshold voltage and timer counts almost right. Figure 8 shows the time transient of pressure inside the hose, when the servo valve is closed for 0,01s. Figure 9 shows amplified measurement voltage with the same time transient.

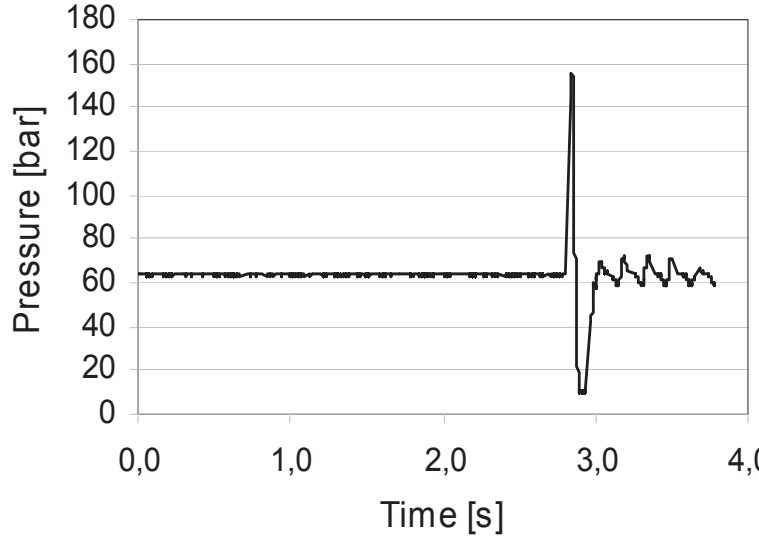

Figure 8. Pressure inside the hose when pressure pulse lasts 0,01s.

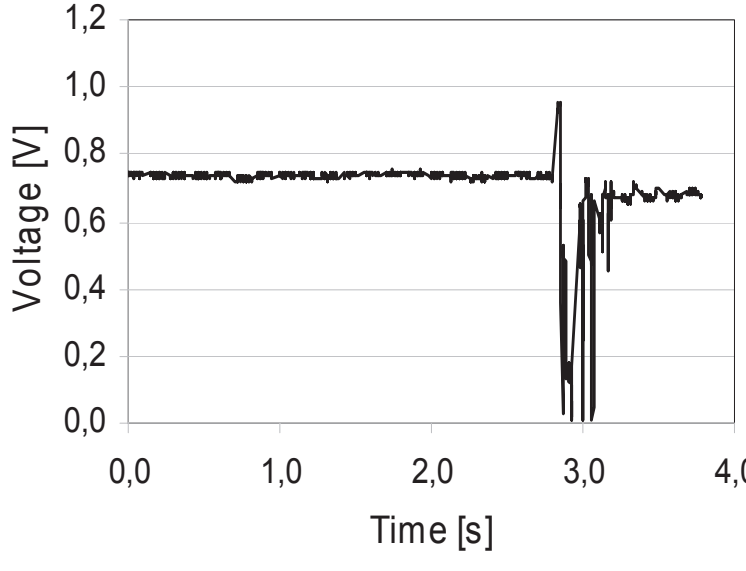

Figure 9. Amplified measurement voltage when pressure pulse lasts 0,01s.

4. RESULTS OF THE PASSIVE IDENTIFICATION

The reinforcement layer of a hose made from steel causes challenges for RFID based identification (5, 6, and 7). Therefore, a thin insulation layer is needed to enable the identification of the hose. Without this insulation layer, identification is very unreliable and the range is restricted to very short distances. This paper studies the suitability of different UHF RFID tags to steel enforced rubber hose identification. The parameters measured are identification distance and effect of identification direction.

In the test procedure 19 different UHF tags were tested. After the initial studies, the most functional tags, shown in figure 10, were selected to primary tests. The test configuration, also shown in figure 10, includes hydraulic hose, RFID tags attached to the hose and circularly polarized reader antenna.

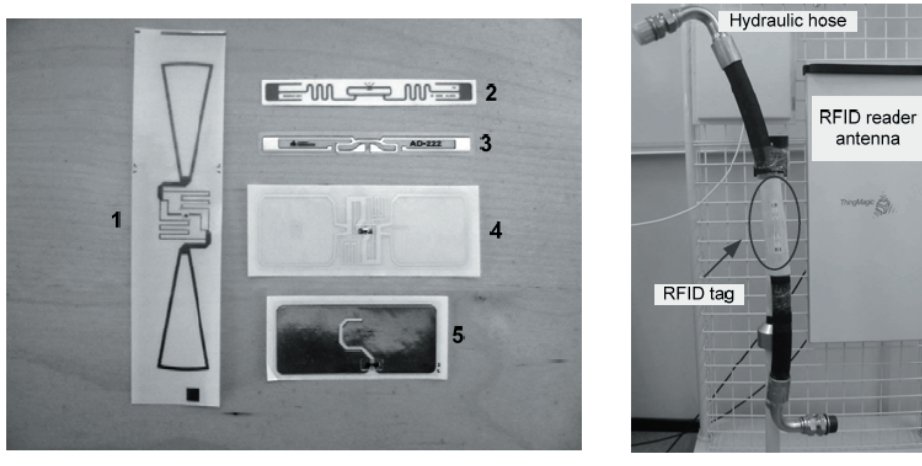

Figure 10. Tags for hose identification and test equipment.

Insulation materials used were rubber mat, foamed plastic and carton. The thickness of the insulation layer was 1 mm. Insulation layer effect to identification distance is shown in table 1 with tags (1-5) presented in figure 10.

Table 1. Identification distances with different tags and insulation materials.

Tag	Rubber mat	Carton	Foamed plastic
1	no result	181 cm	>500 cm
2	no result	23 cm	87 cm
3	no result	30 cm	76 cm
4	no result	40 cm	95 cm
5	no result	no result	53 cm

Rubber matting insulation does not provide reliable continuous identification of hydraulic hose. Carton layer provides the successful identification with tags 1-4. Tag 1 enable clearly the longest identification distance and tags 2-4 make short range identification possible. Foamed plastic insulation enable the identification of all of these 5 tags with identification distance over 50 cm. Tag 1 with large size dipole antenna and foam plastic insulation enable the farthest identification range.

Further, the effect of identification direction was tested with tags 1 and 4 which enabled the longest identification ranges. Results are shown in figure 11 (0º indicates that the reader and the tag are orthogonal against each other). It can be seen that tag 1 enables the identification angle of 150º when identification distance is 1m; 50º when distance is 2m; and 30º when distance is 3m. Tag 4 provides identification angle of 50º when identification distance is 0,5m. From the results it can be seen that omnidirectional identification of tags attached to hydraulic hoses is very challenging task.

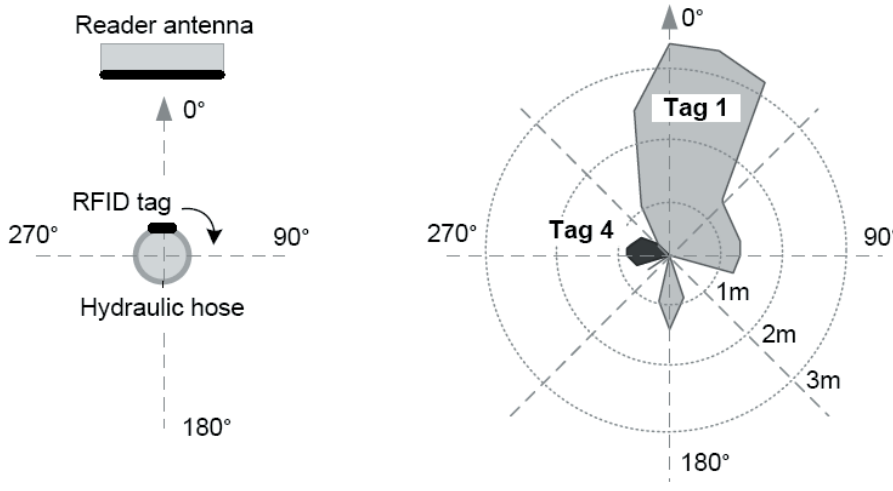

Figure 11. The effect of direction to identification: measurement configuration and results.

5. FUTURE WORK

In this paper, the amount of pressure shocks is counted using steel strain gauges. There may be other sensors, which are better alternatives to this application. It is clear, that steel strain gauges aren't the best sensors for low current consumption. In addition to that steel strain gauges need a metal clamp around the hose that causes problems to the measurements.

Other sensors could be for example semiconductor strain gauges, piezoelectric films or accelerometers. Semiconductor strain gauges are based on resistance change, same way as metal strain gauges. They suit for static and dynamic measurements, so they could be real-time pressure sensors or pressure shock sensors. Semiconductor strain gauges can also have over 10kΩ resistances and higher sensitivity for strain than metal strain gauges. This means that they don't consume much current, which is important in battery operated and wireless sensors. Disadvantage for these sensors is high price and temperature sensitivity.

Piezoelectric films are based on the piezoelectric phenomenon. When they are under mechanical stress, they generate voltage between two electrodes. This voltage is not durable and will decay with a time constant of the measurement circuit. This means that piezoelectric films could suit for counting of pressure shocks but not for static real-time pressure measurement. Great advantage for piezoelectric films is that they don't itself consume power, only possibly needed amplifier consumes power (8). In addition to that they are cheap. Measurements with FLDT-028K piezo film shows that it generates about 0,8V voltage peak when the hose receives pressure shock. This means that piezo film doesn't need any amplifier. Therefore, only the microcontroller consumes power in this kind of application.

Accelerometer notices vibration and shocks. They can be based in many different principles. One principle is change in capacitance due to acceleration. ADXL330-accelerometer is based on this principle. ADXL330 has proportional voltage output to acceleration (9). It is easy to attach above the hose, current consumption is low and it is very small in size. It was generated 10 pressure pulses to the hose and microcontroller counted 9 pulses from voltage output of accelerometer. So preliminary, accelerometer seems to be good solution for counting pressure shocks of the hose.

6. CONCLUSIONS

Active measurements gave good results, but there are some challenges left. It is difficult to make a very precise sensor, which shows exactly the condition of the hose but sensor with some uncertainty can be done. Metal strain gauges seem to consume too much current for battery operated device, but accelerometers and piezoelectric films have potential to be low current sensors for this application.

It can be concluded that with a thin insulation layer, the identification of tags attached to hydraulic hose is feasible. The insulation layer material has a remarkable effect to the reading distance. UHF tags studied in this paper enable long operation distance, which can be important in industrial maintenance operations. However, identification is very direction dependent that may cause challenges to condition monitoring system implementation.

REFERENCES

1. MSP430F22x2, MSP430F22x4 Mixed Signal Microcontroller. 2007, Texas Instruments. 85p.
2. SFS-EN 857. Rubber hoses and hose assemblies. Wire braid reinforced compact type for hydraulic applications. Specifications, 1997, 12p.
3. Alien Technology (2005a) 'EPCGlobal class 1 Gen 2 RFID specification', White Paper, Available at: http://www.alientechnology.com/docs/AT_wp_EPCGlobal_WEB.pdf. Accessed on April 2006.
4. Finkenzeller, K. (2003) RFID Handbook, 2nd edition, West Sussex, UK: John Wiley & Sons, pp.7-59.
5. Ukkonen, L., Raumonen, P., Keskilammi, M., Sydänheimo, L., Kivikoski, M. Challenges in the Development of Tag Antennas for Passive RFID of Metallic Objects, Proceedings of 28th Convention on Radio Science & 6th Finnish Wireless Communication Workshop, Oulu, Finland, pp. 267-270, 2003.
6. Ukkonen, L., Sydänheimo, L., Keskilammi, M., Kivikoski, M. Development of Novel RFID Tags for Identification of Metallic Objects.

Proceedings of 11th IFAC Symposium on Information Control Problems in Manufacturing, Salvador da Bahia, Brasilia, 2004.
7. Sykkö, T., Ukkonen, L., Sydänheimo, L., Kivikoski, M. Performance Comparison of Four Basic Antenna Types near Two Differently Sized Metallic Surfaces. Proceedings of International Conference on Antennas, Radar, and Wave Propagation, Banff, Canada, 2005.
8. Piezo Film Sensors, Technical Manual. Images SI inc, Sensor products division. 73p.
9. ADXL330, Small Low Power 3-axis ±3g Accelerometer, datasheet. 2007, Analog devices. 16p.

Condition monitoring and fault diagnosis for vane pumps using flow ripple measurement

M Yang, K A Edge, D N Johnston
Department of Mechanical Engineering
University of Bath

ABSTRACT

Vane pumps are simple in principle and can be mass produced inexpensively, making them well suited to the automotive industry. They also have many other applications, such as in the chemical industry and food industry. A common type of damage to a vane pump is cavitation erosion on the side plates. If this damage is not detected in time, it could cause failure of the pump, which depending on the type of system may have safety implications, and in some cases a high cost from lost production whilst the system is shut down. This kind of damage is common on other types of pumps such as gear pumps and piston pumps. So a practical method for fault diagnosis of hydraulic pumps is required which does not necessitate removal of a pump from the working system.

This paper presents a method of detecting and identifying cavitation damage on pump side plates via pump flow ripple. Power steering vane pumps are used for this study, although the principles may also be applicable to other types of vane pump, and indeed to piston and gear pumps. The investigation has been done through measurement and simulation. A numerical model of a vane pump is described, and simulated cavitation damage is introduced into the model. This damage is shown to have a clear effect on the simulated flow ripple. The pump flow ripple has also been measured experimentally using the Secondary Source Method, and artificial damage has been introduced into the pump. The damage is shown to have a clear effect on the measured flow ripple, consistent with the simulation results.

Whilst the secondary source enables the measurement of flow ripple in laboratory conditions, it is generally impracticable for in-situ measurement for condition monitoring. A simplified method for calculation of pump flow ripple from in-situ pump pressure ripple measurements and system impedance is discussed.

Fluid Power and Motion Control 2008 Edited by Dr D N Johnston and Professor A R Plummer

1. INTRODUCTION

Condition monitoring for hydraulic pumps has been developed over the last couple of decades. Some of the present methods have been simply transformed from those for mechanical systems. Parameters such as vibration of the pump casing, acoustic noise, temperature and leakage flow have been selected for monitoring purposes [1]. However most of these parameters do not have a direct relation with the pump's condition and cannot necessarily provide an indication of potential damage at an early stage. Some studies have been carried out by researchers on the use of pump pressure ripple for diagnostic purposes [2]. Other researchers [3] used not only pump pressure ripple but also temperature and cylinder motion for condition monitoring. They did identify serious internal leakage and insufficient suction flow of the pumps. However their methods did not have good sensitivity and could not indicate potential damage at an early stage. In addition, the type and location of damage could not be established.

System pressure ripple is very strongly dependent on the system impedance characteristics and on the location of the measurement, as reflections, standing waves and resonances occur. A simple pressure ripple measurement is unlikely to provide clear information about the state of the pump. However pump flow ripple is relatively independent of the system impedance and can be a far clearer indicator of the state of the pump [4]. Unfortunately however, flow ripple is far more difficult to determine and cannot be measured directly. Indirect methods based on pressure ripple measurements, such as the Secondary Source Method (SSM) [4][5][6] need to be used instead.

The main aim of the project was to investigate whether pressure ripple measurements can form a useful indicator for pump fault diagnosis, and to develop suitable, practical, analysis techniques. Tests were performed on a group of balanced vane pumps. The SSM was employed for determining the pumps' flow ripple and source impedance. A simulation model of the pump was also developed. Simulated results were compared with those from the SSM to investigate the validity of the simulation model and to adjust the unknown parameters in the model to get the best match. One of the pumps was then damaged artificially and the same experiments performed on it. This damage was also simulated in the model for comparison.

As the SSM is not suitable for in-situ testing on a real system, another aim of the work was to develop a simplified method that would require minimal instrumentation whilst providing similar information. This project focused on vane pumps, though the technique may be relevant to other types of pump.

2. EXPERIMENTAL RESULTS AND VALIDATION OF SIMULATION MODEL

Flow ripple tests were done on a group of identical pumps using the SSM. The pumps were of the balanced vane type for use in automobile power-assisted steering systems. A simulation model was also developed. This model will be described in more detail in future publications.

The SSM is a precise and efficient method for measuring the source flow ripple and the source impedance of a pump in terms of harmonic spectra. Given these two quantities, the fluid pulsation characteristics of the pump can be described completely [4] [5].

The method is based on the measurement of harmonics of pressure ripple at a series of points along the length of a rigid pipe connected to either the delivery or suction port of the test pump. The pressure ripple that occurs at two or three positions is analyzed to establish the flow ripple. The hydraulic circuit is shown in figure 1. In this work the 'secondary source' was a rotary valve, designed to produce four short-duration flow pulses per revolution [6]. The frequency of the pulses was controlled by the speed of rotation.

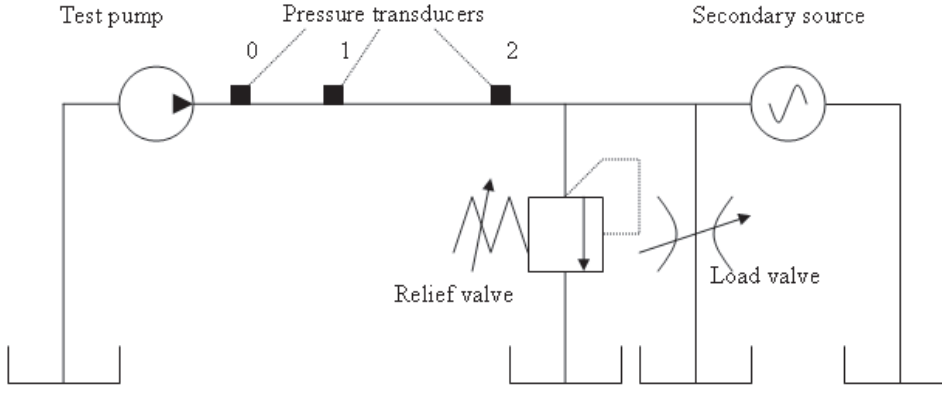

Figure 1 Hydraulic circuit for secondary source method

Tests were performed at speeds of 1000rpm, 1500rpm, and 2000rpm, and pressures of 20bar, 40bar and 60bar. Two examples of experimental flow ripples of one pump and the flow ripple from the simulation model are plotted in Figure 2 and Figure 3. Figure 2 shows excellent agreement between experiment and simulation. The best agreement between experiment and simulation was generally found to occur at lower speeds and pressures. Differences at higher speed and higher delivery pressure might be attributed to limitations in the simulation model, such as in modelling of the leakage transients, or to errors in the analysis for the SSM. To determine the flow ripple in the pump using the SSM, it is necessary to apply a model to the measured source impedance and to make certain assumptions about the nature of the pump's internal passageways, and this can incur errors. In addition the SSM analysis is performed on harmonic measurements up to a certain frequency, and the waveform is reconstructed from this, so the effect of higher frequency components is neglected. The simulated flow ripples are also reconstructed from harmonic frequencies to match the experimental flow ripples.

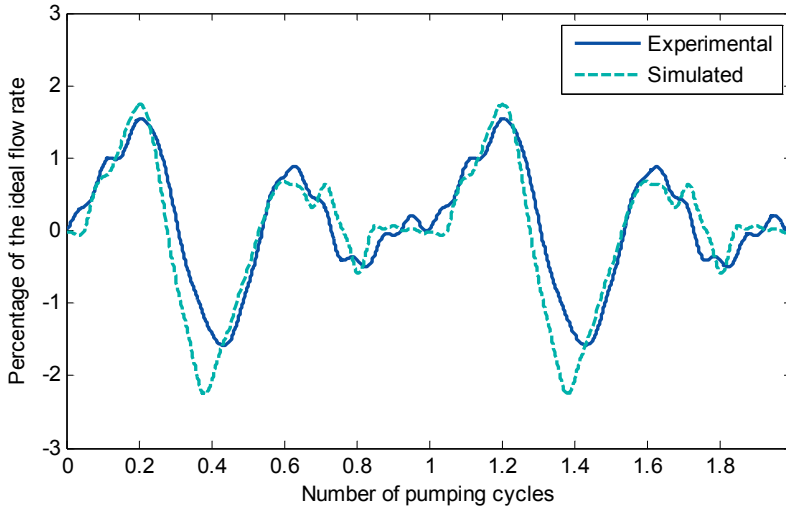

Figure 2 Comparison of simulated and experimental flow ripple at 1000rpm 20bar

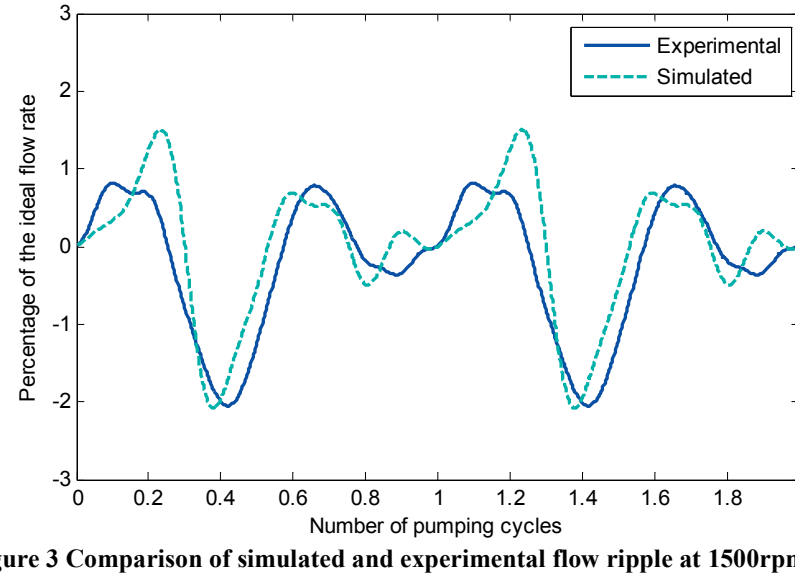

Figure 3 Comparison of simulated and experimental flow ripple at 1500rpm 20bar

3. PUMP DAMAGE

Cavitation is one of the most common causes of damage in a pump. As it was difficult to obtain pumps that had been damaged by real use, artificial damage was introduced in one of the pumps. The damage was intended to imitate that which occurs in a region of the pump side plate which is likely to be subject to cavitation in real machine. Whilst it would be desirable to test a pump with real damage, this artificial damage has the advantage of being more predictable and easier to simulate.

As Figure 4 shows, the damage is a circular indentation drilled on the plate close to one of the relief grooves. The diameter of this indentation was 1.5mm and it was subsequently enlarged to 1.8mm. The depth of the indentation was about 0.5mm. The thickness of the vane was 1.25 mm, so the damage provides a short-duration leakage path as the vane passes over it.

Figure 4 Photograph of the side plate with artificial cavitation damage

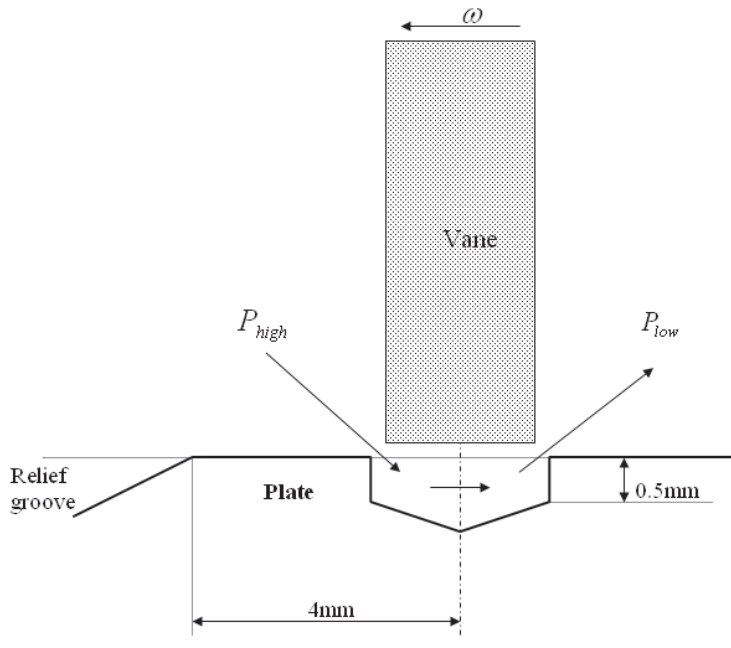

Figure 5 Illustration of the artificial damage

Theoretically when the vane passes across the artificial damage, fluid flows from the high pressure chamber (to the left of the vane in figure 5) into the indentation and then to the low pressure chamber (to the right of the vane). This causes a transient drop in delivery flow which would be expected to appear as a negative spike in the flow ripple. Experiments to determine the flow ripple were performed at the same range of speeds and pressures as for the undamaged pumps. The steady flow rate was also measured and showed no noticeable difference after the pump was damaged. Here only flow ripples at two conditions are plotted as results in other conditions show similar trends. Figure 6 shows the measured flow ripples of the undamaged pump and damaged pump at 1000rpm, 20bar and 60bar. Figure 7 shows the simulated flow ripples of the undamaged pump and damaged pump at 1000rpm, 20bar. The *x* axis on the graphs represents the angular position of the pump rotor relative to a datum angle; one pumping cycle represents one tenth of one complete revolution (the pump has ten vanes). A vane passes across the hole between 0.74 and 0.78 on the *x* axis, and the next vane passes between 1.74 and 1.78. As only harmonics of pumping frequency were measured, the waveforms for each pumping cycle are identical.

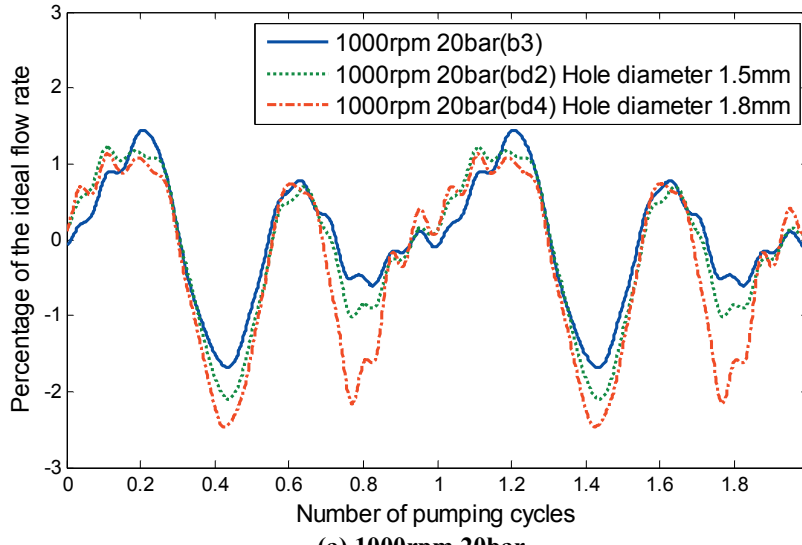

(a) 1000rpm 20bar

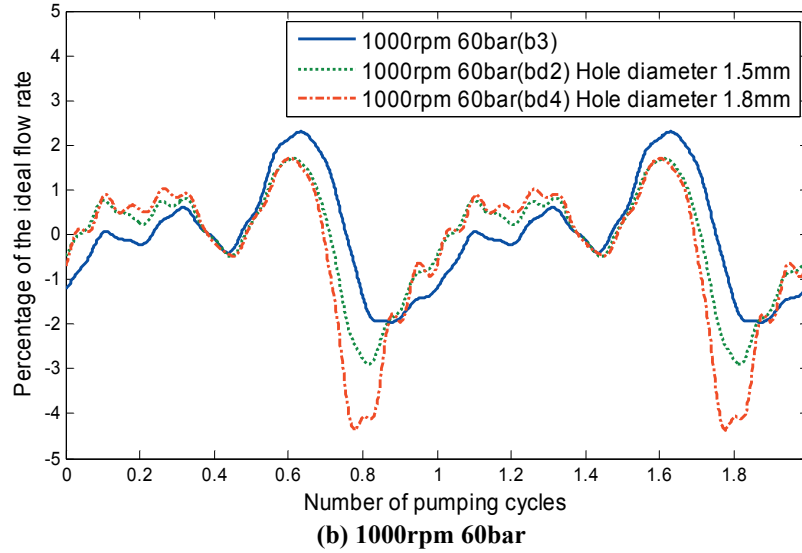

(b) 1000rpm 60bar

Figure 6 Comparison of measured flow ripples of undamaged and damaged pumps

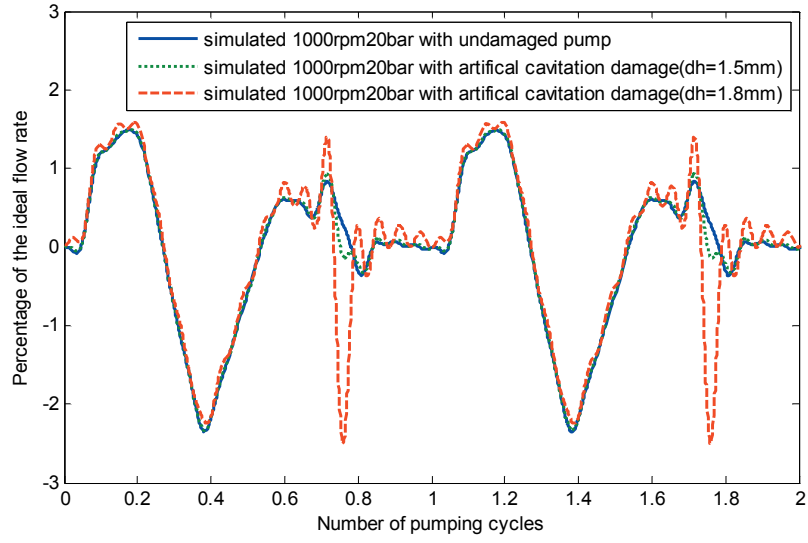

Figure 7 Comparison of simulated flow ripples of undamaged and damaged pumps

To have a clear view of the change of flow ripple caused by the artificial damage, the flow ripple of the undamaged pump was subtracted from the flow ripple of the damaged pump. This was done for both experimental results and simulation results. Here only results at 1000rpm (Figure 8 and Figure 9) are shown as at higher speed the results are not as clear as those at 1000rpm. Figure 8 shows that the effect of the damage is to produce a relatively clear drop in the flow when a vane passes the location of the damage. The size of this drop in flow increases with pressure. This is as would be expected, and shows that the measured flow ripple gives a clear indication of the detailed dynamic behaviour of the pump. There is also a small effect on the flow at other points in the cycle. This may be a real effect but is more likely to be due to limitations in the measurement technique, such as source impedance modelling errors.

Figure 9 shows the difference in the simulated flow ripple between the undamaged and damaged pump. Here the damage gives a very clear pulse in the flow. For a more direct comparison between simulation and experiment, the simulation results were Fourier transformed and the spectrum truncated to the same number of harmonics as the measurements. The ripple in the results is entirely due to this truncation.

These results indicate pump fault diagnosis might best be done at relatively low speeds and higher pressures, as the clearest variations were apparent at these conditions.

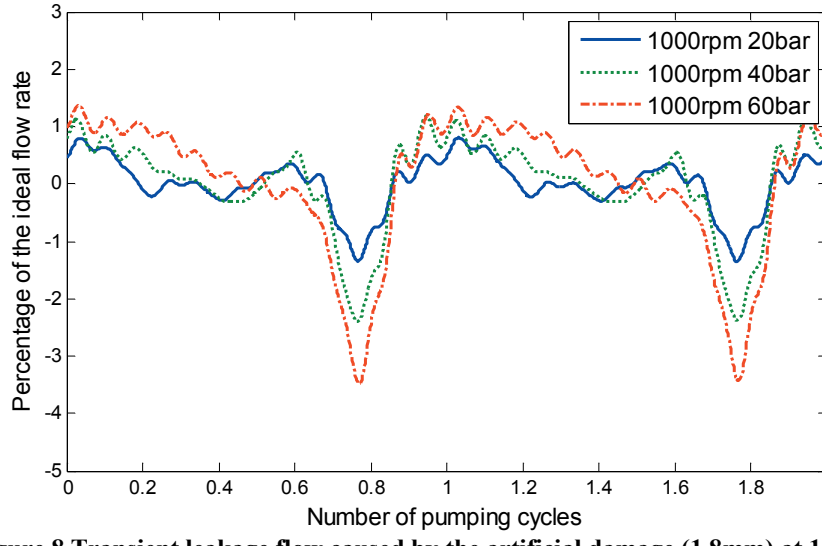

Figure 8 Transient leakage flow caused by the artificial damage (1.8mm) at 1000rpm

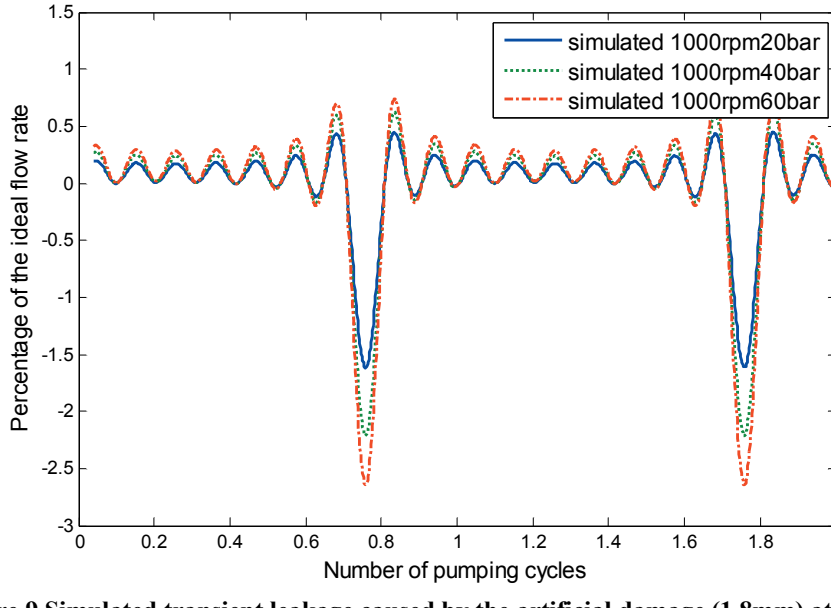

Figure 9 Simulated transient leakage caused by the artificial damage (1.8mm) at 1000rpm

4. FAULT DIAGNOSIS

So far, cavitation damage could be distinguished 'intuitively' from the flow ripple of a damaged pump. However, the Secondary Source Method for measuring pump source flow ripple is rather complicated, time consuming and expensive from the average customers' points of view, and not practicable as an in-situ method for production pumps in real use. Also it is necessary for an experienced person to analyse the results and interpret them to identify faults. Therefore a method is desired which makes pump fault diagnosis economical, easy to operate, and which interprets the results automatically to give a clear indication of the existence and type of faults.

The idea to be considered here is to use the pressure ripple and overall system impedance (including pump source impedance) to determine the source flow ripple of the damaged pump. This will be called the 'deduced flow' method (DFM). The flow chart is shown in Figure 10.

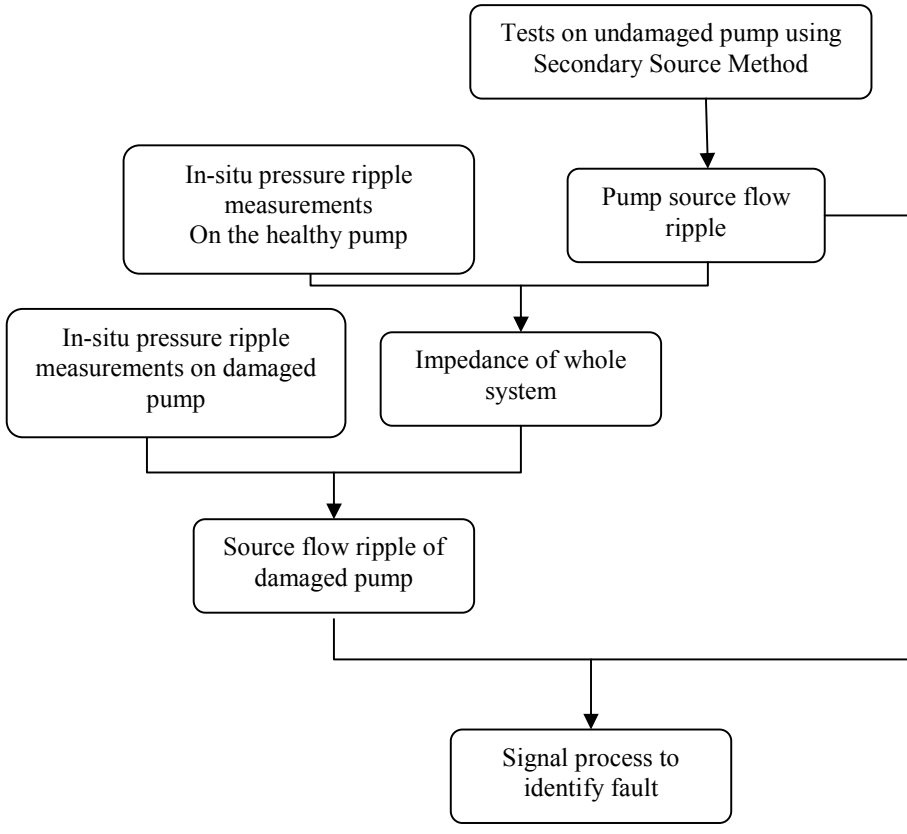

Figure 10 Flow chart of vane pump fault diagnosis with the Deduced Flow Method

The technique would first require the flow ripple to be measured using the SSM. The pump would then be installed where it is needed to be used. The only modifications required to its working system are that a pressure transducer needs to be fitted near the pump delivery, and a shaft position measurement is needed (a single pulse per revolution is sufficient). The shaft position measurement is needed to determine the shaft speed accurately and to establish a timing reference point for the waveform so that one waveform can be subtracted from another. The pressure ripple measured using this transducer needs to be Fourier transformed and the amplitudes and phases of the harmonics of pumping frequency determined. The system impedance at a particular frequency can then be determined from a measurement from this transducer and from the previously measured source flow ripple using equation 1. The source impedance of the damaged pump is assumed to be the same as that of the undamaged pump, since experiments show that there is very little difference in source impedance after the pump is damaged.

$$\text{System impedance} = \frac{\text{Pump out let pressure ripple}}{\text{Pump source flow ripple}} \tag{1}$$

For an initial study in laboratory conditions, all the in-situ measurements were done in the same SSM circuit using one of the SSM pressure transducers. In practice, they would be done in a different circuit.

First, a test was run on an undamaged pump using the SSM at 1000rpm and 60bar to determine the pump flow ripple. The harmonic amplitudes and phases of the pump outlet pressure ripple were determined, using the pressure transducer closest to the pump. The impedance of the whole system including the pump source impedance was then calculated in the frequency domain using equation 1.

Subsequently, the undamaged pump was removed and replaced with the damaged pump (with 1.5mm indentation diameter). The damaged pump was also run at 1000rpm, 60bar. The harmonic components of the pressure ripple of this damaged pump were again measured by the transducer closest to the pump. The flow ripple of this damaged pump was then calculated by equation (1). The result is shown in Figure 11, comparing the flow ripple determined using the DFM in this way with that determined using the SSM directly on the damaged pump. It can be seen that there are only minor differences between the two flow ripples. However, at the lower pressures of 20bar and 40bar, there was more difference in the flow ripples determined by the SSM and the DFM, perhaps due to different fluid air content and temperatures in the different tests. Regardless of this experimental error the calculated flow ripple is acceptably close to the one given by the SSM.

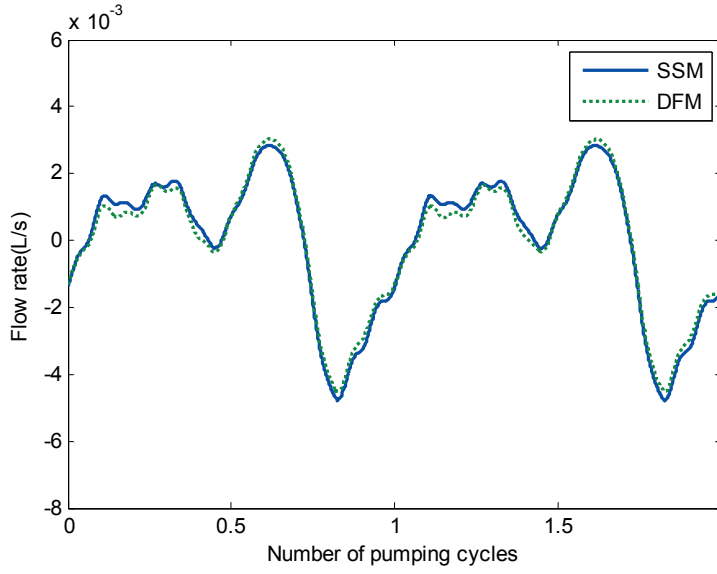

Figure 11 Comparison of flow ripples from the SSM and the Deduced Method at 1000rpm, 60bar (damaged pump with 1.5mm indentation diameter)

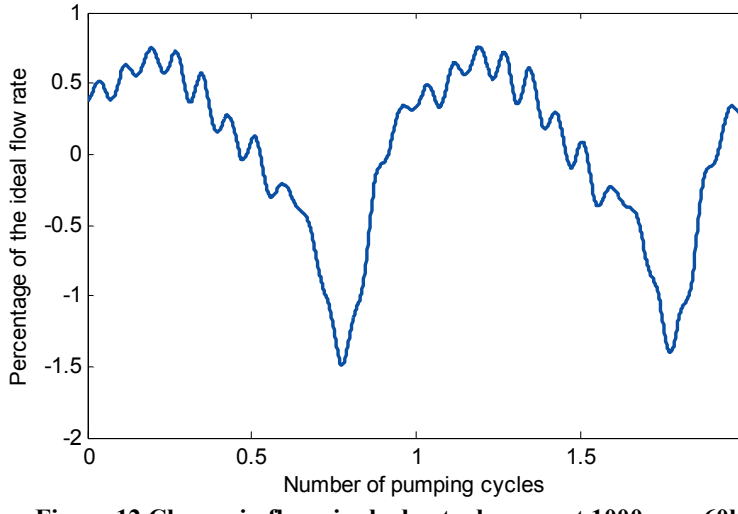

Figure 12 Change in flow ripple due to damage at 1000rpm, 60bar

The flow ripple of the damaged pump established by the DFM was subtracted from the flow ripple of the undamaged pump measured by the SSM. The result is shown in Figure 12.

The cyclic increase in the leakage flow due to the damage is clearly apparent in Figure 12. However for automated condition monitoring, it is desirable that the signal should be monitored automatically, and a warning produced when the signal exceeds a certain threshold. This should be sufficiently tolerant of normal variations to avoid 'false alarms'.

A simple fault detection algorithm was tried, based on the peak value of the difference between the flow ripple at the current time (determined using the DFM) and the original flow ripple of the undamaged pump (determined using the SSM). The average value of this difference in the period between one tenth of a pumping cycle before and after the peak was determined. If this was greater than a certain threshold this was taken to be an indication of side-plate damage. The threshold was taken to be 0.7% of the ideal mean flow rate.

This algorithm was found to give a positive indication of wear for the results shown in figure 12. It was also tested on measurements on an undamaged pump, and correctly gave a negative indication. However, individual pumps, even of the same type, may have different flow ripple characteristics due to manufacturing variation. To improve the method and to establish its robustness, more tests on other pumps of the same type are required.

5. DISCUSSION AND CONCLUSION

The simulation of vane pump flow ripple shows good correlation with experimental results at low speed and low pressure such as 1000rpm, 20bar and 1500rpm, 20bar. At these two conditions, the simulated flow ripples are nearly identical to the flow ripples produced by the SSM. However the simulation model does not show good accuracy at high speed and high pressure. There might be some additional leakage flow effects not properly modelled in the simulation. Further enhancement of the model is required to achieve more accurate flow ripple predictions.

The Deduced Flow Method (DFM) provides a means of obtaining the pump flow ripple in-situ under normal operating conditions whilst the pump is in service. It relies on the system impedance not changing appreciably between the calibration phase and the in-service monitoring. This may be difficult to achieve in practice. It also depends on a flow ripple measurement having been taken using the SSM or a similar measurement technique. In practice it is likely that the flow ripple measurement using the SSM would only be performed on a small number of pumps of a particular type, rather than every single pump. This could cause significant errors on the test results if pumps vary appreciably due to manufacturing factors.

The method is likely to be sensitive to variations in test conditions. The temperature and air content of the fluid may have an important influence. Significant variations in the results were observed at lower pressures, at which entrained air is likely to have a significant effect on the system impedance as well as the pump flow ripple.

Another drawback of this method is the uncertainty of the type of damage. If cavitation damage occurs, this method can detect it. Other types of damage may have different effects on the flow ripple, or may have effects that are indistinguishable from cavitation damage. Also other system faults, such as reduced pump inlet pressure, may affect the flow ripple. A good detection algorithm should be able to distinguish, with reasonable probability, between different types of damage and faults.

Further work is needed to test the DFM method under more realistic conditions, that is, using a more practical and realistic working system rather than the SSM system, with real pump damage, and with a wider range of pumps. Whilst only initial results are shown here, they look promising. Compared to this method, it is unlikely that a simple and direct pressure ripple measurement would provide sufficiently clear information for meaningful diagnosis.

Whilst the method has been applied to a vane pump for power assisted steering system, it may not be suited to such pumps because of their low cost. The added expense of a pressure transducer and signal processing is unlikely to be cost effective for a production vehicle. However the method may be more suited to higher cost pumps such as aerospace pumps or industrial pumps.

REFERENCES

1. Liu S. and Hung J., 1991. *Pulsating parameter method for fault diagnosis for a hydraulic pump*. Industrial Electronics, Control and Instrumentation, 1991. Proceedings. IECON '91., 1991 International Conference on,1991. 2145-2150 vol.3

2. Li, Z, 2005. *Condition monitoring of axial piston pump.* Thesis (Master of Science). University of Saskatchewan, Saskatoon.

3. Zhou, R., Lin, T., Han, J., Yan, D., 2001. *Fault diagnosis of airplane hydraulic pump*. Proceedings of the 4th world congress on intelligent control and automation, June 10-14, Shanghai, China.

4. Johnston D.N., 1987. *Measurement and prediction of the fluid borne noise characteristics of hydraulic components and systems.* Thesis (Ph.D.). University of Bath.

5. Edge K.A., and Johnston D.N., 1990. *The secondary source method for the measurement of pump pressure ripple characteristics, Part 1: description of method.* Proc IMechE, part A, vol. 204, pp33-40

6. Johnston, D. N. and Drew, J. E., 1996, *Measurement of positive displacement pump flow ripple and impedance*, Proc IMechE pt I, Vol 210, pp65-74

Session 2
System modelling

Recursive Generalized Neural Networks (RGNN) for the Modeling of a Load Sensing Pump

TRAVIS WIENS, RICHARD BURTON, GREG SCHOENAU, DOUG BITNER
Department of Mechanical Engineering, University of Saskatchewan
Saskatoon, Saskatchewan, Canada
Contact: richard.burton@usask.ca

ABSTRACT
Modeling of fluid power components and systems is a challenge at the best of times. As knowledge of physical components becomes more focused on micro-properties, the describing equations become more comprehensive and reflect dynamic performance that in the past has not been possible to accurately model. Usually the equations are very nonlinear which make the resulting describing differential equations difficult to solve. But perhaps a more substantial problem in modeling is being able to assign values to a large number of parameters which are used to describe the system. A further complication arises in that the parameters are functions of operating conditions.

An alternate approach to modeling is to use a "black box" in which equations which reflect physical properties are replaced by input/output data relationships. Neural networks are common forms of the mechanism which govern the foundation of the black box in which neurons are trained to "learn" the input/output relationships of a physical system through training and testing processes. The authors have examined various types of neural network morphologies in an attempt to model a load sensing pump using this approach. In a paper submitted at the Bath workshop last year, some success was reported in capturing the dynamics of an experiential load sensing pump but it was concluded that a different network morphology was necessary to make the approach practical and more efficient. In this paper the authors introduce a recursive generalized neural network (RGNN) form that appears to overcome some of the difficulties that were encountered in earlier studies. In addition, the network was trained using a non gradient technique (the complex method) which runs counter to the gradient-based foundation of most back-propagation techniques.

Experimental data used in these previous studies were used to train the recursive generalized neural network and under testing, accurately reflected both the static and the dynamic characteristics of the pump. The key to the successful training of the network was the setting up of experimental test procedures which would capture the dynamic performance of the unit at expected operating conditions.

The result of this study is significant because the designed neural network is very efficient and lends itself to integration to other conventional simulation packages.

Fluid Power and Motion Control 2008 Edited by Dr D N Johnston and Professor A R Plummer

Keywords: Recursive Generalized neural networks, load sensing pumps, black box modeling

1. INTRODUCTION

Load sensing pumps are designed to maintain the pump pressure to be a pre-selected value higher than the load pressure for single load applications and higher than the highest load for multiple load systems. This pump configuration can be used to implement flow control and/or reduce energy losses in the system. Load sensing systems are feedback systems and as such stability and load interaction can be an issue. A great deal of research has been focused on the modeling and behavior of load sensing systems, Krus, [1], Erkkila [2], Kim and Cho, [3] and Wu et al [4] just to name a few. Many of these models are based on linearizing techniques and as such are valid only at specified operating conditions. The use of describing equations that are not linearized is becoming much more popular because of the ability to integrate nonlinear properties into the models. However, such models do require knowledge of the physical relationships between variables and the measurement of certain parameters which can be extremely difficult to accomplish. Such is the case with load sensing systems.

An alternate to conventional equation based modeling is to use a "black box" approach in which input/output behavior is captured without trying to define the internal physical relationships and parameter values. One of the more common forms of this black box involves neural networks (NN) and has been used successfully to model steady state characteristics of swash plate torques in pumps, (McNamara et al, [5]) and of the nonlinear flow pressure characteristics of orifices (Xu et al, [6]). Neural networks are a known entity in fluid power systems and have been successfully applied in control, fault detection and indirect measurement applications (Watton and Xue [7], Chen et al, [8]).

The authors have been studying the use of neural networks as a tool for black box modeling for many years. Some the original work involved identification of steady state characteristics of orifices (Xu et al, [6]) and has been expanded to that of dynamic systems (Xu et al, [9], Lamontagne et al, [10] and most recently, Li et al, [11,12]). Of these three studies, the work of Li is most applicable here.

Xu et al [6] attempted to model the dynamics of a load sensing pump using a feedforward neural network with time delays placed from the output of the network to the input of the network. Problems associated with accumulation of error due to the recursive nature of the network morphology limited the success of this approach. Lamontagne [10] considered the same problem but placed the time delays in the input of the network. Although the error accumulation problem was solved, the new configuration captured the dynamics of the load sensing pump in a very narrow operating region. However, Lamontagne did establish that care had to be taken in the choice of inputs and outputs for the load sensing pump. In Li's work [11,12], a dynamic neural unit (DNU) was used to replace the static neuron in a feedforward network which when used in conjunction with a second static neural network (SNN), was able to capture the dynamic behavior of a load sensing pump over a large operating range. Although this research did provide a dynamic black box model of a load

sensing pump, the fact that two neural networks had to be used was viewed as problematic when being implemented in a practical situation. This study concluded that a different morphology for the neural network was necessary to reduce the computational overhead of the proposed network and it was this conclusion that motivated this follow up study.

In a separate study, the authors have been involved with the design of a neural controller for a natural gas vehicle (Wiens et al, [13]). In the study, Wiens used a generalized neural network GNN [14] from which the networks used by Li, Lamontagne and Xu could all be considered a subset. This generalized network was made dynamic by integrating time delays between and around the neurons themselves and hence formed the recursive generalized neural network (RGNN). It was proposed that this more general form might capture the dynamics and steady state properties of the pump in a more efficient fashion than that experienced by Li. Thus the objective of this research and hence paper, is to introduce the recursive generalized neural network morphology and to demonstrate its ability to model in a black box form, the load sensing pump.

The first section will consider the basic operation of the load sensing pump and the importance of choosing the inputs and outputs to the network. The second section will briefly review Li's work. The third section will consider the RGNN and it relationship to Li's model. Section 4 will introduce the RGNN and the non-gradient approach to training using the Complex method. Section 5 will discuss the results, draw conclusion from the results and will lay out plans for future work.

It should be noted that discussion in the first two sections is abbreviated as the material has been provided in more depth in the cited references. In addition discussion of neural networks is also limited to that which will be necessary to explain the RGNN. Details can be found in the many manuscripts that have been published. Permission to use figures from these references has been obtained.

2. LOAD SENSING PUMP MODEL INPUTS AND OUTPUTS

A schematic of a load sensing pump is shown in Figure 1. The objective of load sensing systems is to maintain the pressure drop $P_s - P_L$ across the controlling orifice constant. Thus P_s is controlled to follow P_L via the load sensing pump compensator. The desired pressure drop is dictated by the load sensing compensator spring. Any deviation from the set point will result in the compensator spool porting fluid to or from the pump controlling spool passageway. This in turn will result in the pump stroking or destroking in an attempt to reduce the deviation form the set point to zero.

Lamontagne et al [10] demonstrated the importance of taking great care in choosing the inputs and outputs to the neural based model. If P_s and P_L were chosen as inputs and Q_s the output, the model would then simulate the pump and the compensator. This is desirable because in most applications, the compensator spool is integral to the pump.

However, for a fixed controlling orifice opening, and any load pressure, P_L, the output flow would be the same in the steady state. Thus a multitude of input values of P_L and P_s would result in the same output. This situation "confuses" the neural network and its performance deteriorates rapidly. Thus using a neural network to capture the dynamics of a system with feedback internal to its operation (and which dominates the behaviour) is not tenable. As a result, the inputs to the load sensing pump were chosen to be P_s and P_c; thus, the compensator could not be included in the model and would have to be modeled separately either in a conventional form or with a second neural network.. This is a limitation of the black box neural network approach. It should be noted that hence forth, the term load sensing pump refers to the pump only.

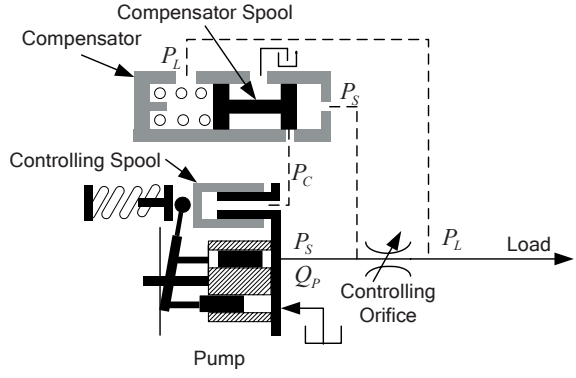

Figure 1 Schematic of the load sensing pump (reproduced by permission)

3. THE DYNAMIC NEURAL UNIT (DNU) AND THE DYNAMIC NEURAL NETWORK (DNN)

Li et al [11,12] approached the modeling of the load sensing pump using a basic Dynamic Neural Unit (DNU) introduced by Gupta and Rao [15]. This morphology is shown in Figure 2(a). Each neuron (unit) is dynamic and the dynamic network is formed by combining several of the units in some appropriate form to yield a Dynamic Neural Network (DNN). The particular combination used by Li is shown in Figure 2. The neural network used P_s and P_c as the inputs and Q_s as the output. A special experimental test system was developed which allowed data to be collected for a large variation of operating conditions (Li et al, [11,12]). In the first study [11], the DNN was successful in capturing the dynamics of the pump, but the steady state error was quite substantial. The results were analyzed and a look-up postprocessor table was developed which would compensate the output of the DNN. The compensated model performed in an adequate fashion but concern was expressed about having to use a "grey box" approach (one in which a-priori knowledge

is used in conjunction with the DNN) versus a "black box approach (in which only input output information is required).

In the second study by Li et al [12], the look-up table postprocessor was replaced by a static neural network which was trained to compensate for the steady state error. The modified network and training scheme is illustrated in Figure 3. The DNN was first trained to capture the dynamics and then the steady-state NN (SNN) added and trained to compensate for steady state errors. A typical result is shown in Figure 4. In this figure, the DNN did capture the dynamics of the pump, but by itself shows considerable magnitude error; the addition of the SNN to the overall model shows very acceptable agreement. However, the need to train a separate SNN to compensate the DNN was deemed unacceptable in terms of the computational hardware needed to implement the two for a practical application.

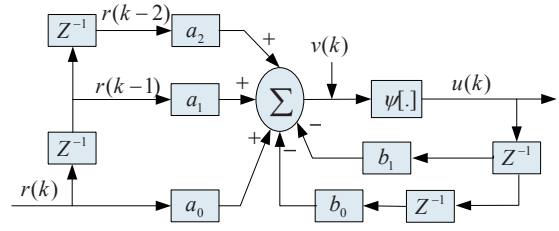

(a) Basic Dynamic Neural Unit (DNU) based on Gupta et al [15]

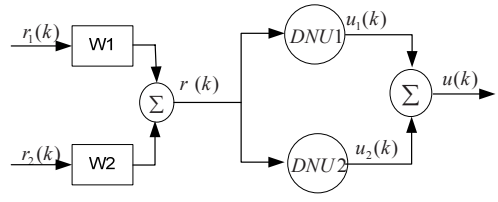

(b) DNN form

Figure 2 Basic Dynamic Neural Unit (DNU) and DNN adopted in this study (reproduced with permission) [12]

4. RECURSIVE GENERALIZED NEURAL NETWORKS (RGNN) AND TRAINING SCHEME

4.1 The recursive generalized neural network

As discussed in the introduction, it was decided to implement a recursive generalized neural network (RGNN) to replace the DNN used by Li et al. Since the form is not common in the fluid power literature, it is useful to show how the RGNN relates to the more standard neural unit and multilayered perceptron (MLP) morphology. Consider Figure 5 which demonstrates a basic neuron and represents the darkened nodes shown in Figure 5(b). With

reference` to Figure 5(a), the inputs u_1, u_2 ….u_i and a "bais" of 1 are modulated by "trainable" weights $w_1, w_2, w_3 \ldots\ldots w_i$ respectively, summed and then passed through a "squashing" function (which gives the neuron the capability of learning nonlinear relationships when used in a MLP). By adjusting the weights w_i, the output of the neuron can be forced to perform in some desired manner. When many of these neurons are assembled as shown in Figure 5(b), a MLP [16] is formed (in this case shown with one "hidden" layer).

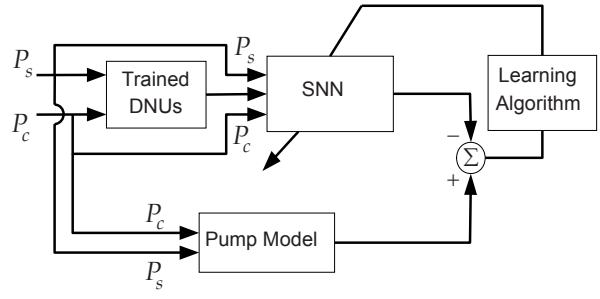

Figure 3 Modified DNN using a SNN as a postprocessor (reproduced with permission) [12]

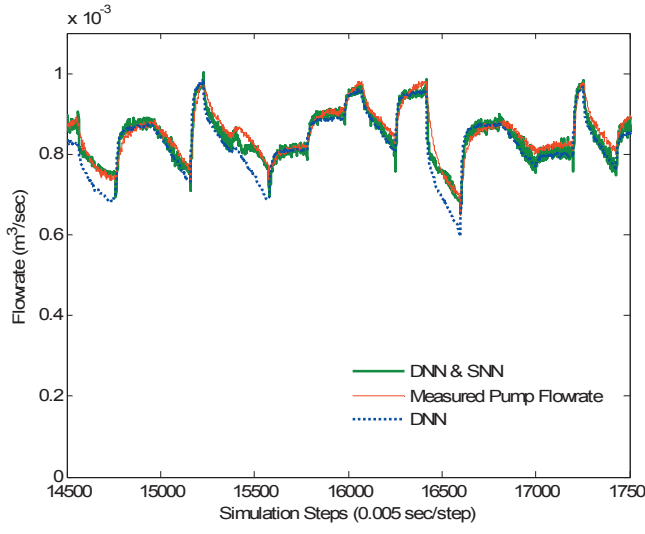

Figure 4 Typical test output flow rates (predicted and actual) (reproduced with permission) [12]

It is necessary now to introduce first the generalized neural network (Werbos, [14]) shown schematically in Figure 6. This network is based on feed-forward paths only. Each "node" or neuron represents the basic neuron structure that was shown in Figure 5(a). The first set of nodes is fed by the input signals. The second set of nodes corresponds to hidden layer neurons. Each of these neurons or nodes receives a signal from each input and from each of the neurons to the left of it. The output neurons receive signals from all the neurons to the left including the inputs. This makes the network totally "connected" in the feed-forward sense.

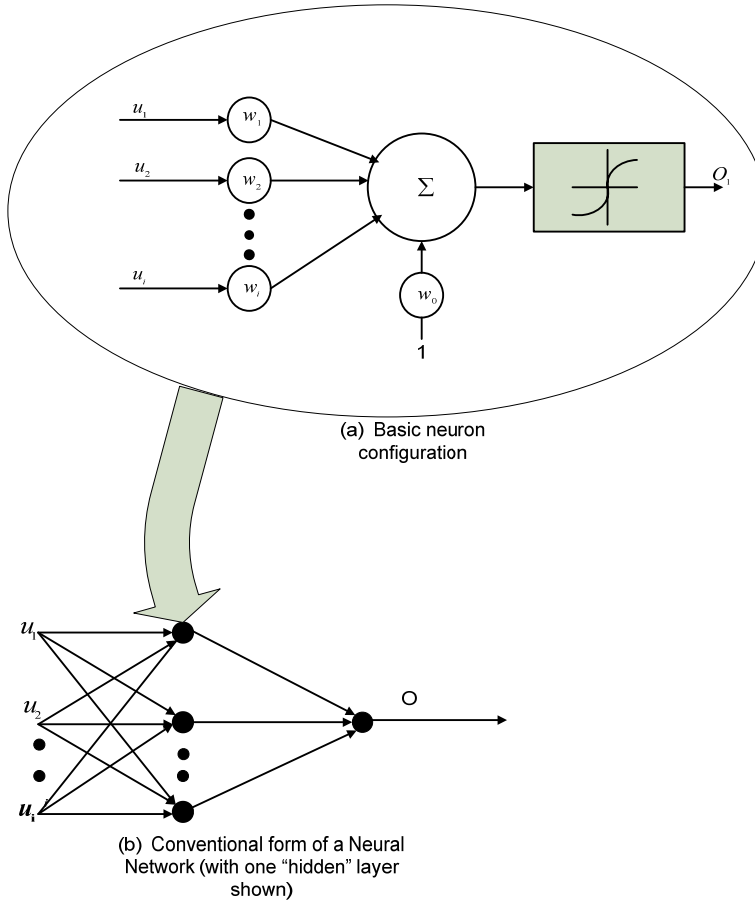

Figure 5. Conventional form of the multilayered perceptron (MLP) with one hidden layer. The bias for each neuron is assumed to be part of each node.

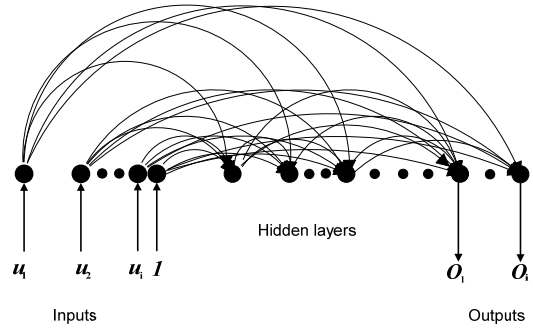

Figure 6, Generalized neural network morphology

As an example, the generalized form of the multilayered perceptron (MLP) shown in Figure 5(b) is shown in Figure 7. The input "1" is the bias that is shown in Figure 5(a) and is fed into all nodes to its right.

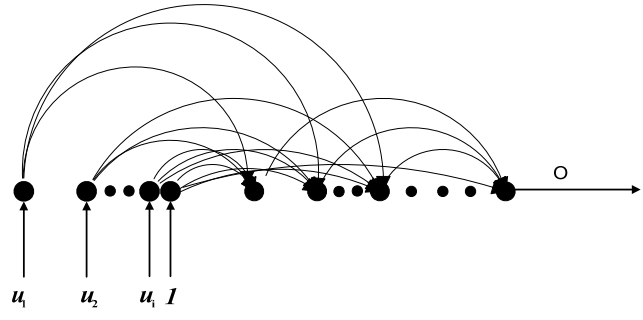

Figure 7. Generalized Neural Network for the MLP shown in Figure 5(b) The bias of each neuron is provided by the last input set at 1

The GNN illustrated in Figure 6 is a feed-forward network and is considered "static" in nature in that no dynamics can be captured in the network itself. It is well known that if any node contains time delayed inputs and/or time delays in feedback loops around the neuron (recursive mode), then the GNN becomes a dynamic network. In this study, it is labeled a recursive generalized neural network, RGNN, and hence can be trained to capture dynamic relationships between the input and output training data. The most general form of the RGNN is shown in Figure 8. In this study, any line that is fed back within the node (self recursive) or to any of the nodes to its left is assumed to have one time delay in the path. Many other configurations could be adopted but this was deemed to be the simplest.

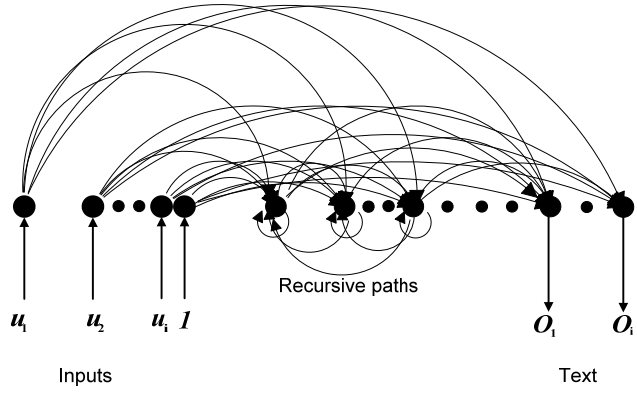

Figure 8. Recursive generalized neural networks. Each feedback path contains one time delay. Feed-forward paths do not.

It is also of interest to illustrate that the DNU and DNN used by Li is in fact a subset of the RGNN. The DNU and its RGNN form are shown in Figure 9 and the DNN and RGNN in Figure 10. It is evident that the form used by Li et al is indeed a subset of the RGNN. What is very important here is that the DNN is not fully connected and contains neurons that are in fact linear. Indeed, only two of the neurons contain nonlinear squashing functions. It was believed that this lack of total connectivity was one factor in limiting the success if Li's DNU's to capture both the steady state and dynamic characteristics of the pump. Thus the RGNN shown in Figure 8 was adopted for this study.

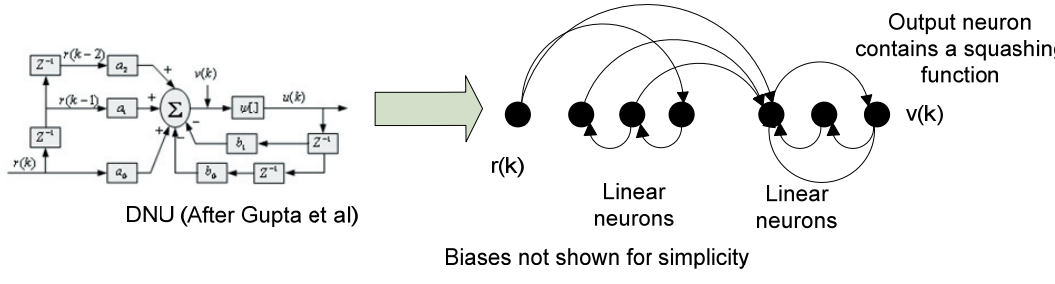

Figure 9 Representation of the DNU (after Gupta et al) to the RGNN. All neurons except the output neuron do not contain squashing functions and hence are linear.

The approach of training the RGNN was to subject the system to a series of inputs that would represent the magnitude and frequency of information that the system would be exposed to and then adjust the weights to force the output of the network to some desired waveform. This training continued until some error criteria had been satisfied. At that point the network was tested using a data set not used in training. If the network performance was acceptable to some specified measure, then it was assumed trained.

The challenge became one of deciding a method of training the network to "learn" a set of input/output data and this is now considered.

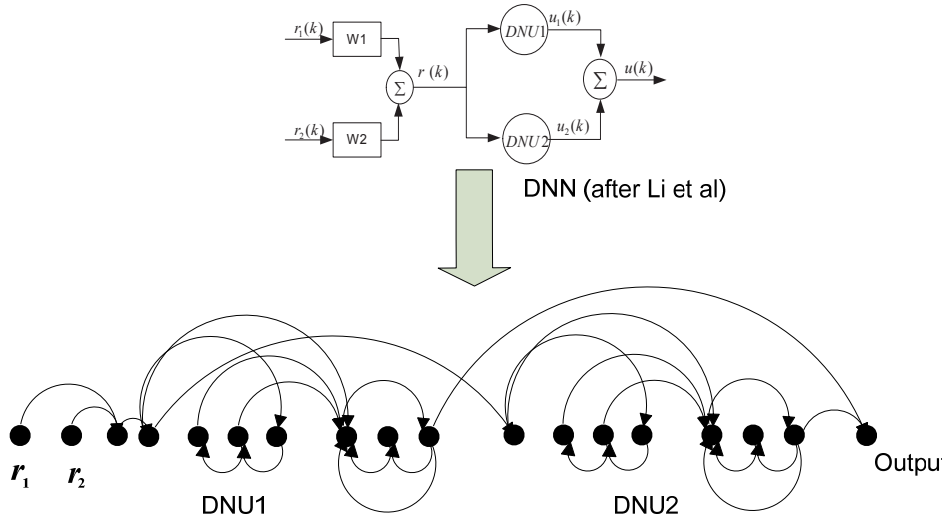

Figure 10. Representation of the DNN (after Li) to a generalized form. Biases are not shown for simplicity.

4.2 Training of the RGNN

Training of a neural network is usually accomplished using back-propagation (the error is propagated back through the network to upgrade each weight, Narendra and Parthasarthy [17]) or using genetic algorithms [18]. Back-propagation requires a calculation of a gradient which can add a substantial amount of computational overhead to the training process. Because the RGNN involves recursive iterations, one would expect the training approach to be recursive as well. However, in most studies including that of Lamontagne and Li, a non recursive algorithm appeared to work quite well. A non gradient technique called the Complex Method (Andersson, [18]) was applied to the training of a static neural network by Xu et al [9]. They were successful in training a static neural network to model the nonlinear static characteristics of a hydraulic orifice. Because the technique does not involve the calculation of a gradient, this same approach was applied to the training of the RGNN. Since this technique has not been applied to a RGNN, it is of benefit to outline in detail the steps used to implement the Complex method to this situation.

It is the objective of training to find a set of weights $\boldsymbol{W}$ which will reduce the root mean square error between the actual and model flow rates over a specified sampling period, to some acceptable value. W would appear as a matrix of the individual RGNN weights where all the matrix elements below the diagonal represent the feedback recursive weights, the

elements on the diagonal represent the weights of the individual neuron recursive paths and the elements above the diagonal represent weights of the feed-forward paths.

The following steps were followed in implementing the Complex method to the RGNN.

Step 1. The elements of the matrix $\boldsymbol{W_1}$ were set in a random fashion. Bounds were established for each of the weight elements such that in the feed-forward paths, weights could not exceed ± 5 and in the recursive loops, ± 1. An "epoch" of data which represented expected operating ranges (magnitude and frequency), for P_c and P_s were input into the RGNN. The same epoch of information was also used as inputs to the actual pump. The measured flow and model output flow were compared every .005 secs (200 hz sampling rate) for 12000 points and the difference (error) summed and square rooted. This gave rise to the RMS of the error for the first set, and was denoted as E_1. The weight matrix and error were recorded.

Step 2. The weight elements in the Matrix were again set in a random fashion to form a second matrix, $\boldsymbol{W_2}$. Using the same epoch of data and procedure presented in step 1, a new error was determined E_2. The second weight matrix and error were recorded.

Step 3. This procedure was repeated N times (in this study, N= 1216) to produce a table of matrices and their corresponding errors as shown in Table 1.

Table 1 The weight matrix and corresponding error values

$\boldsymbol{W_1}$	$\boldsymbol{W_2}$	$\boldsymbol{W_3}$	.....	$\boldsymbol{W_{1216}}$
E_1	E_2	E_3	.....	E_{1216}

In this table, $\boldsymbol{W_i}$ are matrices consisting of 810 elements. This set of weights form a "Complex" for the next step.

Step 4. In the above table, the set of weights which yielded the greatest error (labeled as $\boldsymbol{W_{gerror}}$ and E_{gerror}) were identified. This set of weights $\boldsymbol{W_{gerror}}$ was then removed from the table.

Step 5. Since the remaining weight matrices (1215), all have the same number of rows and columns they can be numerically added to form a new matrix called $\boldsymbol{W_{sum}}$. From $\boldsymbol{W_{sum}}$, $\boldsymbol{W_{gerror}}$ is subtracted. The center of gravity of the complex was thus determined as:

$$\boldsymbol{W_{cg}} = (\boldsymbol{W_{sum}} - \boldsymbol{W_{gerror}})/(N-1) \quad (1)$$

Note that in many cases, the elements of $\boldsymbol{W_{gerror}}$ are very small compared to the elements of $\boldsymbol{W_{sum}}$ and thus:

$$\boldsymbol{W_{cg}} \approx (\boldsymbol{W_{sum}})/(N-1) \quad (2)$$

Step 6. In this step, the worst set of weights $\boldsymbol{W_{gerror}}$ was changed according to the procedure outlined by Box [19]. This was done by taking the "distance" between the worst set of

weights W_{gerror} and W_{cg} and extending the distance beyond the center of gravity by an amount 1.3 times the distance. This is shown in Figure 11.

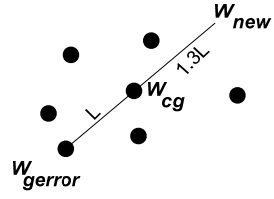

Figure 11. The determination of a new set of weights using the worst set of weights and the weights at the center of gravity.

Thus, $W_{new} = W_{cg} + 1.3 * | W_{gerror} - W_{cg} |$, (3)

and is called the mirror equation. This meant that each distance between each element in W_{gerror} and W_{cg} was multiplied by a factor of 1.3 and added to each element in W_{cg} to yield W_{new}. This W_{new} replaced the W_{gerror} in Table 1.

Step 7. As a check, the W_{new} was subjected to the same epoch of information as in step 1. A new error E_{new} was calculated and if it was less than the old E_{gerror}, the W_{new} did indeed, replace W_{gerror} to form a new complex. In addition, the elements of W_{new} were checked to ensure that they did not exceed the bounds. If any did, they were set equal to the bounds and the procedure continued. If for the new W_{new}, E_{new} was greater than E_{gerror}, then the elements of W_{new} were not acceptable and had to be adjusted in some other fashion. This adjustment was such that the weights would move toward the weights of the "best" error W_{best} in the manner defined by Andersson [18]. In this procedure, a new factor β was defined such that

$$\beta = \left(\frac{n_r}{n_r + k_r - 1}\right)^{\frac{n_r + k_r - 1}{n_r}} \quad (4)$$

Anderson recommended n_r to be 4, and k_r was a variable.

Hence

$$W_{new,new} = \frac{W_{gerror} + W_{cg} + (1-\beta)W_{best}}{(W_{cg} - W_{best})(1-\beta)(2R-1)}, \; R \text{ being a random variable.} \quad (5)$$

If the error associated with $W_{new,new}$ was still not better than E_{gerror}, the k_r was adjusted until the error did become better. Once this happened, $W_{new,new}$ replaced W_{gerror} in Table 1 and the procedure returned to step 3.

Step 8. The process continued until the number of iterations exceeded a preset value or the error of all weight matrices decreased to an acceptable value.

Once the stopping criteria was reached, W_{best} was found from Table 1 and used in the RGNN for final testing.

5. EXPERIMENTAL RESULTS

The experimental system used to obtain the data for training the RGNN was discussed in Li [12] and details will not be repeated here. Suffice to say that the inputs P_S and P_C were varied dynamically over a range in which the pump was expected to operate. The output flow was recorded as a function of these inputs. The data was input into the RGNN and the predicted model flow compared to its experimental counterpart. The model was first trained using this epoch of information which contained some 12000 data points spaced at .005 sec (200 Hz sampling rate). Figure 12 shows the predicted flow from both Li's model and the RGNN and the actual flow meter at the end of the training sequence. It is observed that the RGNN can reproduce the pump flow very closely. It is also observed that Li's model tends to show magnitude errors at the peaks compared to the RGNN model.

The true test of a neural network is to subject the network to data that did not appear directly in the training epoch. This was done for both Li's model and the RGNN model and the results shown in Figure 14. Figure 15 shows an expanded scale and it is visually evident that for this part of the epoch, the RGNN is superior to that of Li's model. It is evident that both models do predict the pump flow, but not with the same accuracy that the testing data illustrated. With the exception of one or two points in the lower flow rate region, the RGNN performs better than the Li's model; these results are consistent with many other tests performed on both models. Table 2 summarizes some of the RMS errors for the two models and the visual evidence is further verified.

It is important to note that the training time of the RGNN was approximately 2 1/2 hours compared to 10-12 hours for the DNN based model for the same epoch of information. The RGNN contained 30 neurons and 810 weights. No attempt was made to optimize the number of neurons in the RGNN. In the complex method, the mirror equation was enacted 60144 times, the more complex weight adjustment initiated 38641 times and the bounds reached 6019 times.

6. DISCUSSION AND CONCLUSIONS

This paper has presented the use of a recursive generalized neural network to model a load sensing pump. As with Li's model, the results and hence the models were considered to be quite acceptable for simulation purposes. However, the actual process to train Li's model required several procedures (training first a DNN and then compensating steady state errors using a static neural network). The RGNN required only one procedure to train and was shown to be computationally more efficient than Li's approach. The use of the non gradient based Complex method to train the network was a contributing factor. The actual form of the RGNN required no special constraints on the individual neurons whereas the DNN did require having several of the nodes made linear (viewing the DNN in the RGNN sense). In addition, the RGNN did produce results that were consistently better than the DNN approach

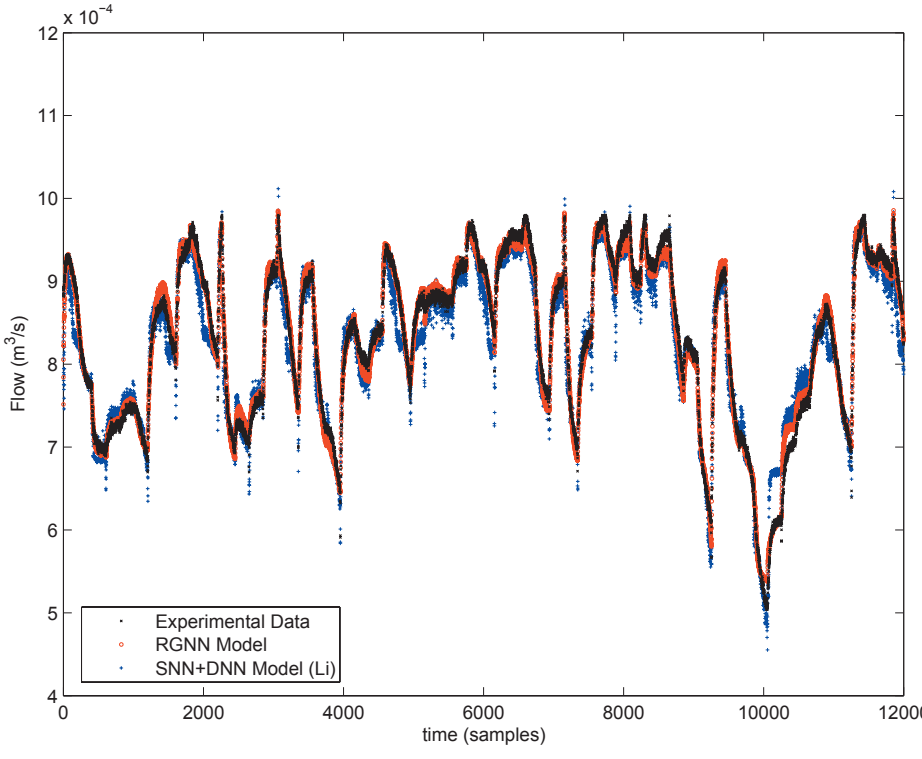

Figure 13 A comparison of the RGNN and Li's models output flow to the actual measured flow from the pump for a training set.

Table 2 A summary of typical RMS errors for the two models.

	Training RMS over total epoch	**Testing RMS over total epoch**
Li's model	.406	.363
RGNN model	.187	.242

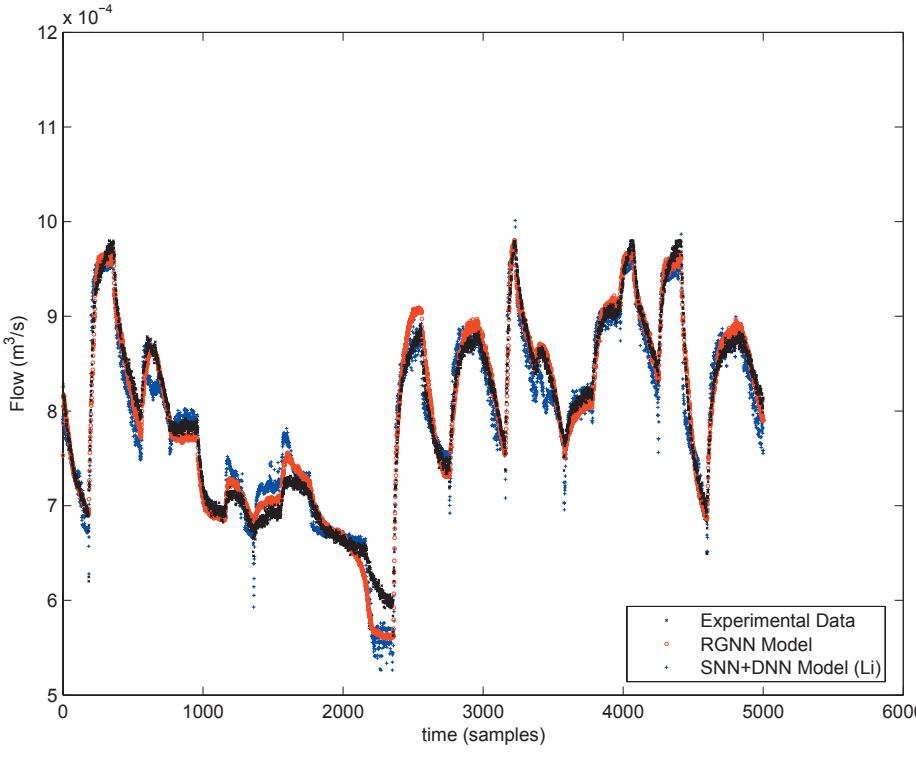

Figure 14 A comparison of the RGNN and Li's models output flow to the actual measured flow from the pump for a testing set.

It was concluded that the approach of using a RGNN to model a hydraulic pump was feasible. However, the model was verified using random variations in the input signals. The model now needs to be subjected to frequency type inputs to establish is validity in both the time and frequency domains to ensure that all the important dynamic properties have indeed been identified by the model. It was believed that for the approach to be truly practical, the RGNN must be integrated with models developed using more traditional modeling approaches. This is now the task at hand.

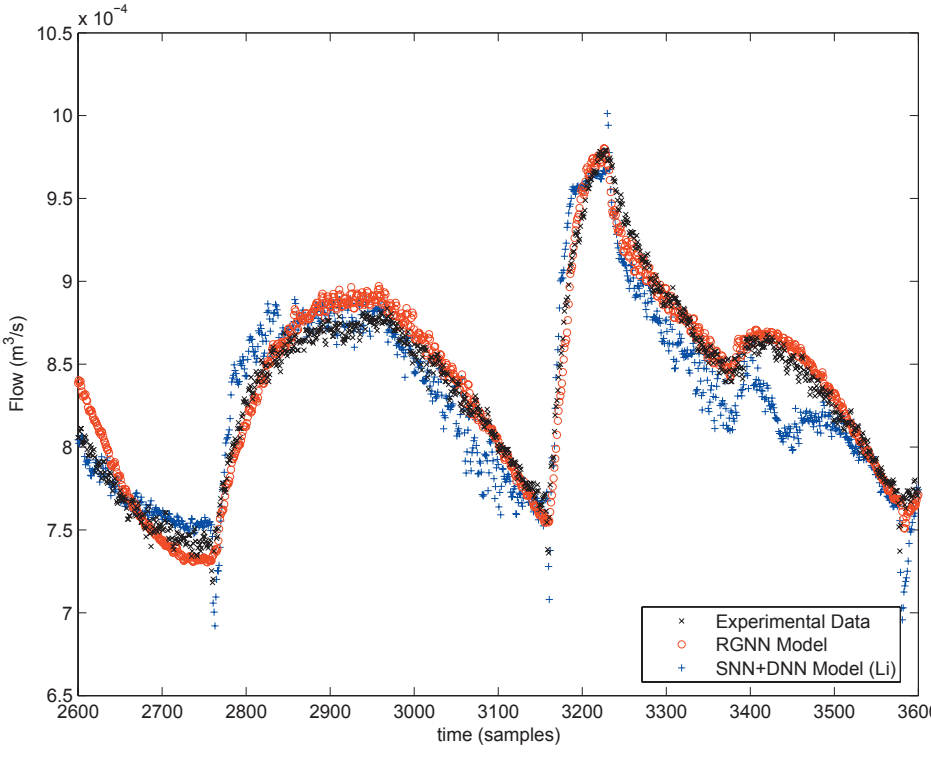

Figure 15. A comparison of the RGNN and Li's models output flow to the actual measured flow from the pump for a testing set, expanded scale.

ACKNOWLEDGMENTS

The financial support from National Science Engineering Research Council of Canada

REFERENCES

(1) Krus, P. 1988. On Load Sensing Fluid Power Systems with Special Reference to Dynamic Properties and Control Aspects, PhD thesis, No 198, Department of Mechanical Engineering, Linkoping, Sweden, (ISBN 91-7870-402-2).

(2) Erkkila, M. 1999. Practical Modelling of Load Sensing Systems, Proceedings of the Sixth Scandinavian International Conference on Fluid Power, SICFP'99, Tampere, Finland, pp 445.

(3) Kim, S.D. and Cho, H.S. 1988. Stability Analysis of a Load-Sensing Hydraulic System, Proceedings of the Institute of Mechanical Engineering, Part A, Vol. 202, pp. 79-88.

(4) Wu, D., Burton, R. Schoenau, G. and Bitner, D., 2002. Establishing Operating Points of a Linearized Model of a Load Sensing System, International Journal of Fluid Power, Vol. 3, No. 2. pp 47 – 54.

(5) McNamara, J., Edge, K., and Vaughan, N., 1997. Hybrid Analytical/Neural Network Model of Variable Displacement Pump Dynamics, American Society of Mechanical Engineers, The Fluid Power and Systems Technology Division (Publication) FPST, v4, Fluid Power Systems and Technology, p 71-76.
(6) Xu,X.P, Sargent,C.M, and Burton, R.T., 1994. Experimental Identification of Flow Orifice Using Neural Network and the Conjugate Gradient Method, Transactions of the ASME, Journal of Dynamic Systems, Measurement and Control, Vol. 118, No. 2, June, pp. 272-277.
(7) Watton, J. and Xue, Y., 1997. Simulation of Fluid Power Circuits Using Artificial Network Models (Part 1 and 2), Proc, Instn. Mech. Engrs.- Part I, Vol. 211, pp.417-438.
(8) Y. Chen, R.T. Burton, and G.J. Schoenau, 1997. Indirect Measurement of Actuator Position using a Network Based Predictor. Proceedings of the Fifth Scandinavian International Conference on Fluid Power, Linkoping, Sweden, May.
(9) Xu, X.P., Ramden, T., Burton, R.T, Krus, P., and Sargent, C.M., 1994. Feasibility of Training a Neural Network Based Hydraulic Component Simulator using the Complex Method. Innovations in Fluid Power, Seventh Bath International Fluid Power Workshop, RSP Research Studies Press Ltd. Publishers, Bath, England, Sept.
(10) Lamontagne, D., Burton, R., Ukrainetz P., and Ruan, J. 2003. Investigations in Modeling a Load Sensing Pump using Neural Networks, Proceedings of the Fourth International Symposium on Fluid Power Transmission and Control (ISFP'2003), Wuhan, PRC, pp 151-158.
(11) Li, L., Burton, R and Schoenau, G. 2006. Feasibility Study on the use of dynamic Neural networks (DNN's) for modeling a variable displacement load sensing pump, Proceeding of the MINEC 2006 ASME International Mechanical Congress and Exposition, Nov., Chicago, paper number 15588.
(12) Li L. Bitner, D, Burton, R. and Schoenau, G. 2007. Experimental study on the use of a Dynamic Neural Network for Modeling a Variable load sensing pump, Proceedings of PTMC, 2007, Bath, UK.
(13) Wiens, T., Schoenau, G., Burton, R. 2007. Limit Cycle Behaviour of a Neural Controller with Delayed Bang-Bang Feedback, International Journal of Intelligent Technology, Vol 2, n 2.
(14) Werbos, P.1990, Backpropagation Through Time: What It Does and How to Do it, Proceedings of the IEEE, Vol 78, pages 1550–1560.
(15) Gupta M. and Rao, D.,1993. Dynamic neural Units and Function Approximation, IEEE Conf. On Neural Networks, San Francisco, pp. 743-748, March 18- April 1.
(16) Haykin, S., 1998. Neural Networks: A Comprehensive Foundation, Prentice Hall
(17) Narendra, K.S, and Parthasarthy K. 1990. Identification and Control of Dynamical Systems Using Neural Networks, IEEE Trans. Neural Networks, Vol. 1, pp. 4-27.
(18) Andersson, J,2001. Multiobjective Optimization in Engineering Design - Application to fluid Power Systems, Doctoral thesis, Division of Fluid and Mechanical Engineering Systems, Department of Mechanical Engineering, Linkoping University.
[19] Box, M.J., 1965. A new method of constrained optimization and a comparison with other method, Computer Journal, Vol. 8, No. 1, pp. 42-52, 1965.

An Open-Source Modelica Library of Fluid Power Models

Christiaan J. J. Paredis
Center for Compact and Efficient Fluid Power
Systems Realization Laboratory
G.W. Woodruff School of Mechanical Engineering
Georgia Institute of Technology
Atlanta, GA 30332, USA
chris.paredis@me.gatech.edu

ABSTRACT

In this paper, a new open-source library of fluid power models is introduced. The intent of the library is to formally collect knowledge about fluid power components and systems, and to share and communicate this knowledge openly among the members of the fluid power community. The library takes advantage of the object-oriented features of the Modelica language to formulate the models in a formal, modular and reusable fashion. The models range from low-level fluid models and models for physical flow phenomena to models for specific fluid power components and systems. In this paper, the key features of the library are highlighted and illustrated with examples.

1. WHY ANOTHER FLUID POWER MODELING TOOL?

Over the last several decades, system designers have recognized that the use of modeling and simulation can significantly reduce the resources necessary for exploring and analyzing the space of system alternatives. As a result, modeling and simulation of fluid power systems also has grown significantly in popularity and capability. Several dynamic simulation tools for fluid power systems have been developed both in academia (10, 17) and commercially (4, 9, 11, 13) (see http://fluid.power.net/fpn/docs/software.php3 for a comprehensive list of fluid power simulation tools).

Although these tools provide more than adequate support for the analysis of simple hydraulic circuits, they often come up short when a higher level of accuracy is required or when applications outside the traditional scope of fluid power systems are explored. For instance, in very high pressure applications, the fluid viscosity depends strongly on the pressure, requiring the use of more detailed fluid models; or in electro-hydraulics, the band-width of the dynamic response of components often needs to be considered. Rather than developing a completely new set of models and a corresponding simulation tool for each of these application domains, it is desirable to have a library of simulation models that is modular and extensible so that it can be easily adapted to new needs.

In this paper, such a library of fluid power models is introduced. The library has been designed with the following five primary goals in mind:

Fluid Power and Motion Control 2008 Edited by Dr D N Johnston and Professor A R Plummer

1. Integration with other disciplinary domains. The main purpose of fluid power systems is to transfer energy in a compact fashion. But this energy transfer is more and more often controlled using electronic interfaces, and, ultimately, this transferred energy is converted into mechanical energy so that the dynamics of the electronic, the control and the mechanical system also need to be considered. When analyzing fluid power systems, it is therefore crucial that fluid power models be seamlessly integrated with models for these other disciplinary domains.

2. Modular model architecture. Fluid power systems are almost always designed as a configuration of commercial-off-the-shelf components. This modularity in the physical system should also be reflected in the fluid power model library. Modularity in the models allows the user to model an almost infinite number of system configurations from a small number of basic models, and can drastically reduce the effort needed to extend, improve and maintain the library.

3. Efficient simulation. Although modularity in the models reduces the modeling effort, it may also increase the computational cost of the resulting simulations. When using simulations to support design, repeated analyses of fluid power systems are typically required with different parameter values or circuit topologies. A good balance must be established between ease of modeling and efficiency of simulation.

4. Expressive model semantics. The dynamic modeling of fluid power systems requires that the modeling language be able to capture both differential and algebraic equations. In addition, the structure of the model equations often changes at discrete moments in time (e.g., when a valve opens or a cylinder reaches its end of travel). For fluid power systems, it is therefore desirable to use a modeling language that can express differential algebraic equations combined with discrete events.

5. Open and sharable. Models are formal expressions of our knowledge about a particular domain or phenomenon. To promote the exchange of knowledge about fluid power systems, it is important that the models be fully accessible to all stakeholders in the community. This means that the models are expressed formally without ambiguity, and that the full model equations can be viewed, critiqued and, if necessary, updated by the members of the community.

Currently, there is not a single model library or simulation tool that excels at all of these criteria. In the remainder of this paper, the basic structure and philosophy of a new library is described which provides a better trade-off between these sometimes conflicting criteria. The library accomplishes this by taking advantage of the Modelica language with its formal, equation-based semantics that enable symbolic manipulation during compilation and efficient solving of the resulting differential algebraic equations.

2. SCOPE AND ARCHITECTURE OF THE MODEL LIBRARY

2.1 Scope of the model library

The scope of the library is the dynamic behavior of fluid power systems. It is assumed that the components and physical phenomena can be adequately approximated using lumped parameter models described in Differential Algebraic Equations systems or DAEs (as

opposed to distributed parameter models described in Partial Differential Equations). DAEs are commonly used for system-level modeling where the system dynamics result from the exchange of energy or signals between subsystems or components. This is an appropriate modeling paradigm when these interactions occur at well-defined interfaces or ports. Similar to the electrical and, to some extent, the mechanical and thermal domains, the fluid-power domain shares this systems-oriented approach: fluid power systems are composed from modular components connected to each other through standardized ports.

At this point, the library is limited to hydraulic components, but it is the intent to expand the library in the future to include pneumatic components also. Even in the hydraulic domain, the library does not include models for all commercially available components. However, it does include most of the key building blocks from which these additional models can be defined. The intent has been to provide a well thought-out structure that can then be further developed in an open-source effort.

2.2 The Modelica modeling language

Modelica (12) is a formal, object-oriented language geared towards the lumped-parameter modeling of system behavior resulting from the exchange of energy and signals between subsystems or components. The language provides an ideal platform for addressing all five criteria listed in Section 1:

1) The new fluid power library is seamlessly integrated with the open-source Modelica Standard Library which includes several domains: electrical (analog, digital, and multiphase), signals and controls (continuous, discrete, and state graphs), mechanical (translational, rotational, and 3D rigid-body dynamics), thermal and fluids.

2) Modelica is an object-oriented, noncausal, equation-based language that supports the development of modular, reusable models. The models have a well-defined, port-based interface so that they can be composed into larger systems using a graphical editor.

3) By taking advantage of the equation-based nature of Modelica, a solver can symbolically manipulate the equations and compile them into an executable that is commonly an order of magnitude faster than comparable procedural solvers (3). In addition, symbolic manipulation allows for the solution of structurally singular systems, i.e., with a DAE perturbation index larger than one (1).

4) Modelica has a broad, flexible set of modeling constructs for defining differential equations, algebraic equations, conditional equations, and discrete event handling.

5) Modelica is quickly becoming a de-facto standard for differential algebraic equation modeling. Modelica is supported by several simulation solvers including an open-source solver developed as part of the OpenModelica Project (16) (See http://www.modelica.org for a complete list of solvers).

2.3 Over view and general characteristics

The fluid power library is developed in a modular fashion, in three layers. First, there is a layer (the package `BasicModels`) with models of basic physical phenomena such as the flow through an orifice, or an ideal lossless exchange between hydraulic and mechanical translational energy. In the second layer (the package `Components`), these basic models are combined into models for generic fluid-power components, such as servo valves, cylinders, or pumps. The third layer is strictly speaking not part of the library; it contains models for very specific components, such as pump ABC from company XYZ. In this layer, the generic models from the second layer are instantiated with specific values for all the model

parameters reflecting the particular flow characteristics of a specific component. This layer should be structured by component vendor (e.g., a separate library, called `XYZComponents`, for components produced by vendor XYZ).

The fluid power library also contains a package with models for fluids. The fluid models are completely separate from the component models so that a component can be modeled once and then used with a variety of fluids. The interface to the fluid model only assumes that the fluid properties depend on the local state: the pressure and temperature. Since the library deals with fluids, it has been based on the `Modelica.Fluids` library developed by Casella *et al.* (2) and on the `Modelica.Media` library developed by Elmqvist *et al.* (6). The fluid power library further extends these libraries by including phenomena, technologies and components that are specific to the fluid-power domain.

3. THE FLUID MODEL

The behavior of a fluid power system is determined to a large extent by the properties of the fluid. Throughout the system, the relationships that define this fluid behavior need to be considered. In the fluid power library, these relationships are grouped together in a separate fluid model. The model is based on the models developed in the `Modelica.Media` package of the Modelica Standard Library (6). However, the structure of the model has been simplified so that only the relationships relevant to the fluid power domain (i.e., only hydraulic fluids at this point in time) have been retained.

Even with this simplification, the model is still quite expressive compared to most other fluid power simulation tools. The model is structured as a `replaceable package`, meaning that the user can not only specify certain constant fluid properties, but has the total freedom to define how these properties depend on the fluid state, that is, the pressure and the temperature. The most common properties of the fluid are defined in a model called `BaseProperties`, which includes pressure, temperature, density, specific enthalpy, and specific internal energy. Stubs have been provided for the functions in which the relationships between these variables can be defined. For instance, if the user wants to evaluate the performance of the fluid power system under very high pressures, `d_pT` can be redeclared to consider the Tait equation rather than a constant bulk modulus:

```
redeclare final function extends d_pT
 "Return density as a function of p and T (Tait equation)"
 import SI = Modelica.SIunits;
protected
 SI.BulkModulus K0 "Temperature-dependent bulk modulus";
 constant SI.BulkModulus K00 = 8.4e9 "Bulk modulus at 0K";
 constant Real K0prime = 10.9 "Constant in Tait equation";
 constant Real betaK(final unit="1/K")=0.0058 "Temp coefficient";
 constant Real aV(final unit="1/K")=7.7e-4 "Therm. exp. coef.";
 constant Density d0 = 870 "Reference density at p0 and T0";
algorithm
 K0 := K00*Modelica.Math.exp(-betaK*T);
 d  := d0/(1+aV*(T-T0))/
       (1-Modelica.Math.log(1+p*(1+K0prime)/K0)/(1+K0prime));
end d_pT;
```

Other quantities that are not part of the `BaseProperties` model are also pre-defined as function stubs that need to be redeclared by the user when creating a new fluid model; the most commonly used functions are `dynamicViscosity` and `thermalConductivity`.

To make sure that the fluid model is used within its range of applicability, it is good practice to include `assert` statements, for instance, to assert that the absolute pressure be positive. If the assert statement fails, the simulation stops and an error message is displayed.

4. THE PACKAGE OF BASIC MODELS

The `BasicModels` package contains all the basic building blocks from which component-level models can be constructed. These models include flow models through pipes and orifices, boundary condition models (sources and sinks), energy conversion models (to and from rotational and rotational mechanical energy), and models for fluid volumes. The models in this package are usually idealized models that need to be combined with other basic models to capture all the physical phenomena occurring in fluid power components. For instance, a `WallFriction` model for laminar-turbulent flow through a line needs to be combined with a `Volume` model to capture also the compliance of the line or hose.

The `BasicModels` package is further divided into two: `Thermal` and `NonThermal`. In fluid power analyses, it is common to assume that the temperature has reached steady state and does not vary throughout the system. Taking this into account explicitly can result in a significant reduction in the size of the state of the system (and therefore in the computational cost of the simulation); therefore, the fluid power library has two sets of basic models — with and without a thermal state. The difference between the two types of models is minor and can usually be modeled through the inheritance mechanism: each model in the `NonThermal` package has an associated model in the `Thermal` package which extends the `NonThermal` model by adding the thermal balance equations.

4.1 The Energy Transfer Model

To model the flow of energy, Modelica includes a restricted class called `connector`. A connector is defined by one or more across and through variables (or effort and flow variables in bond graph terminology (15)). When connecting two components by their matching connectors, Modelica automatically imposes the equivalents of Kirchhoff's laws: the across variables are equal and the through variables add up to zero. In the fluid domain, a connector includes the variable pairs pressure / mass-flow rate and specific enthalpy / enthalpy-flow rate (2). The equivalent model in the `NonThermal` package omits the specific enthalpy and the enthalpy-flow rate.

At first glance, it seems as though the enthalpy flow rate variable is redundant — given the mass flow rate and the specific enthalpy, the enthalpy flow rate can be determined. However, as is explained in detail in (6), the enthalpy flow rate is important to enable the modeling of splitting, joining and reverse fluid flow. For instance, fluid flowing from component A to component B is characterized by the specific enthalpy of component A. When the flow reverses, the specific enthalpy in the connector may change discontinuously because it is now determined by the fluid flowing from component B to component A. The causality for the assignment of the specific enthalpy in the connector needs to be reversed

accordingly. The Modelica language includes the `semiLinear` construct to support this modeling approach (6).

4.2 The Flow Models

The package `BasicModels` also contains models describing the flow of fluid through pipes and orifices: `GenericPressureLoss`, `LaminarRestriction`, `SharpEdgedOrifice`, `SuddenExpansion`, `VariableRestriction`, and `WallFriction`. These models have been derived from the `Modelica.Fluid` library (2). They have been simplified by explicitly taking into account the most common operating conditions for fluid power systems. Since flow rates in fluid power systems can change significantly over time (e.g., depending on the control signal of a servo valve), all the flow models (except `LaminarRestriction` account for both laminar and turbulent flow with cubic-spline interpolation in the transitional region, as is illustrated in Figure 1. At a pressure drop of zero, the two cubic polynomials meet and transition smoothly with matching first derivatives; the second derivatives are also matched as long as this does not result in a non-monotonic function.

The most commonly used flow model is the `VariableRestriction` model. It is the foundation for all the valves in the `Components` package. The flow characteristic of the variable restriction is defined by a tabular metering curve that relates a control input to the flow rate for a specified nominal pressure drop, nominal density, and nominal viscosity. Rather than imposing this flow rate under all flow and fluid conditions, the metering curve is used only to approximate a relationship between the control input and a corresponding diameter and loss factor. Based on this relationship, the flow rate is computed for current pressures, densities and viscosities, so that a reasonable approximation is obtained even when the flow and fluid conditions deviate from nominal.

A second important flow model is the `WallFriction` model. This model represents the pressure loss in a straight pipe defined by its length, inner (hydraulic) diameter, and surface roughness. The flow characteristic is based on an implementation of a Moody chart and accounts for both laminar and turbulent flow (7).

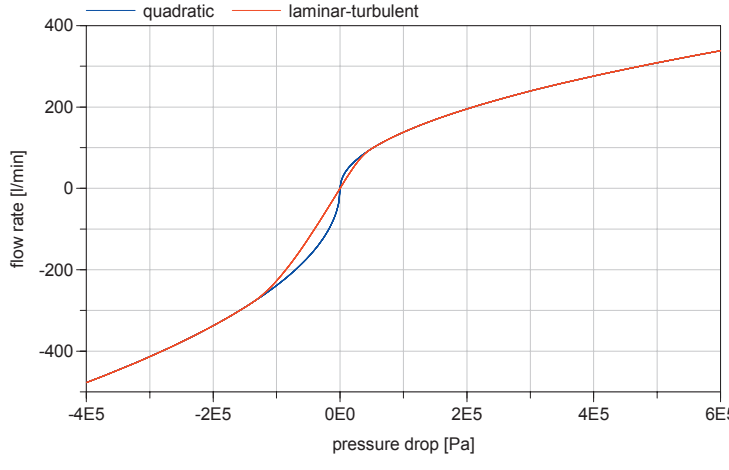

Figure 1: The flow characteristic for an asymmetric, sharp-edged orifice.

Note that, as for all models in the fluid power library, the flow models are noncausal. Their causality will be automatically determined by the Modelica compiler. As a result, the models could be connected to an ideal flow source (imposing a given mass flow rate) or to an ideal pressure source (imposing a given pressure drop) without any need for changes to the model. It is, however, possible for the user to specify a preferred causality so that costly root-finding can be avoided during simulation.

It is also important to recognize that the models in the `FluidPower` library are *lumped parameter* models. Sometimes (e.g., for long lines) it may be desirable to include distributed parameter models. This can be achieved within the scope of the current library by discretizing the distributed component. For instance, a finite volume approach can be used to discretize a long line into a sequence of short segments each of which is characterized by a model from the `BasicModels` package. Modelica provides convenient constructs from defining such components in which the structure of the equations is parameterized.

3.4 Energy Conversion Models

Since it is typically the purpose of fluid power systems to transfer energy in a compact fashion from a prime mover to a mechanical load, it is crucial to include models that convert the energy between the fluid power and mechanical domains. In the package `BasicModels`, the models are defined for such energy conversion under idealized, lossless conditions: `FluidPower2MechTrans`, `FluidPower2MechRotConst` and `FluidPower2MechRotVar`. In practical energy conversion components, there will of course always be losses due to mechanical friction or leakage, but these should be modeled in models of the actual components, as shown in Figure 2 for a hydraulic cylinder. The mechanical interfaces for the models are defined in `Modelica.Mechanics.Translational` and `Rotational` in the Modelica Standard Library.

4. THE PACKAGE OF COMPONENT MODELS

Whereas the `BasicModels` package described the physical phenomena that occur in fluid power systems, the `Components` package describes how these physical phenomena interact with each other to achieve the functions of actual fluid power components. To maintain this clear distinction and to facilitate modularity and model reuse, all the component models are purely compositions or extensions of basic models or other component models. The models in the `Components` package are divided into sub-packages for `Cylinders`, `Lines`, `MotorsPumps`, `Sensors`, `Valves`, and `Volumes`. Rather than describing every model in every package in this paper, only a few representative models are described to illustrate the modeling approach.

4.1 Maintaining consistent fluid models

The component models all extend the partial model `PartialFluidComponent`. This partial model simply states which fluid model should be used and whether thermal energy exchange is to be considered in the fluid flow. By default, the fluid model is `GenericOil`, but the user can replace it with any model from the `Fluids` package. Similarly, by default, no thermal energy exchange is considered (i.e., only pressure and mass flow rate are

included in the fluid connectors). To maintain consistency of the fluid properties throughout the system, this medium model and basic package are passed on to all the subcomponents or basic models used to describe the component. Using a redeclaration for every sub-component, the consistency of the `Basic` and `Medium` models is maintained throughout the component model and, at a higher level, throughout the model of the entire fluid power circuit.

4.2 A Simple Model: A Double Acting Cylinder

As an example of how basic models can be combined into realistic component models, consider the `DoubleActingCylinder` model depicted in Figure 2. The cylinder model combines models from `FluidPower.BasicModels` with models from `Modelica.Mechanics.Translational` and `Modelica.Thermal.HeatTransfer` to describe the hydraulic, mechanical and thermal behavior of the component. Hydraulically, the cylinder is described by two fluid chambers that are rigidly connected to each other by a piston. There is leakage between the two chambers, across the piston seal, as well as between each chamber and the environment. The environment is modeled as a constant pressure sink.

Each cylinder chamber also includes equations that describe the large mechanical stiffness and damping that occur when the chamber empties and the piston touches the cylinder end cap. The mechanical aspect of the model further includes an inertia representing the piston, a damper representing the friction between the piston and the cylinder, and two rigid connections representing the constant lengths of the cylinder and the rod.

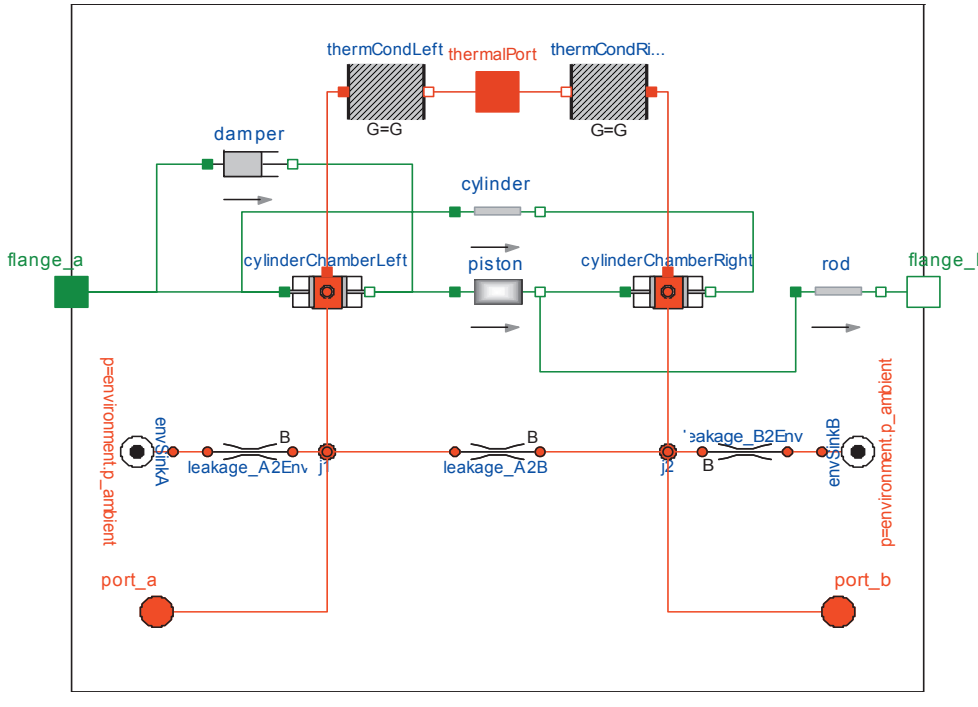

Figure 2: A `DoubleActingCylinder` defined as a configuration of basic models.

The thermal aspect of the cylinder is represented by the internal energy stored in the volume of each cylinder chamber (assuming `BasicModels.Thermal` is selected), and thermal conductors from the cylinder chamber to the outside thermal port of the cylinder.

The parameters for each of these modeling elements are derived from a limited set of parameters for the `DoubleActingCylinder`. For instance, the cross section of `cylinderChamberRight` is defined as: `pi/4*(boreDiameter^2 - rodDiameter^2)`. By taking advantage of Modelica's annotation constructs, the parameters for the component models are neatly organized and presented to the user in categories, as shown in Figure 3.

Although this model captures the main characteristics of a double-acting cylinder, it could definitely be further refined. For instance, one could include more detailed friction models that capture the dependence of the friction force on the pressure drop across the seal. However, when making such refinements, one must maintain a good balance between model accuracy and model complexity. To accommodate a variety of levels of detail in the models, while still maintaining fast simulation execution, the models in the library often take advantage of the `replaceable` and `redeclare` construct of the Modelica language. This approach is described in more detail in the next section.

4.3 Reconfigurable Models: A Directional Control Valve

Often fluid power components have been designed as configurable product platforms. That means that the customer can freely choose not only certain parameters values (e.g., the stroke length), but also certain configuration features. For instance, a pump can be purchased with or without a built-in relieve valve, or a cylinder can be purchased with a variety of cushioning options. Often multiple features can be combined in any combination. If one were to develop a separate model for each resulting combination of features, the number of models would quickly grow very large. To avoid this explosion of models, the fluid power library takes advantage of the reconfiguration capability of Modelica models.

This is best illustrated with an example. As shown in Figure 4, consider a directional control valve that can be configured with optional relief and check valves. By declaring these valves as `replaceable` in the Modelica model, they can be reconfigured as needed whenever a usage of the model is created. For instance, in the usage shown in Figure 4, the

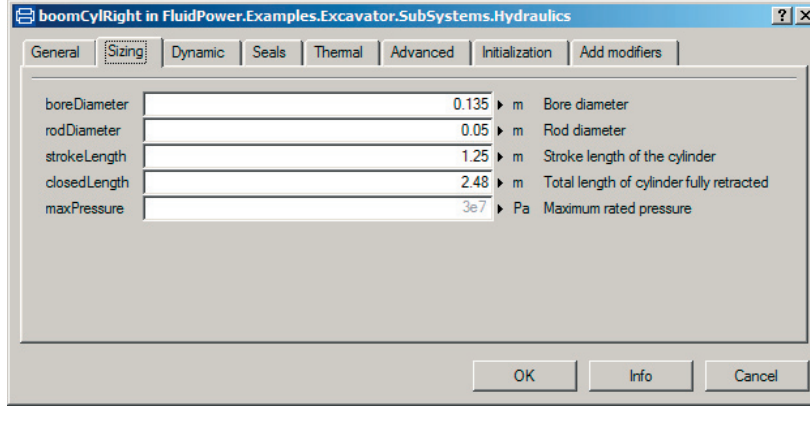

Figure 3: The parameter popup for a `DoubleActingCylinder`.

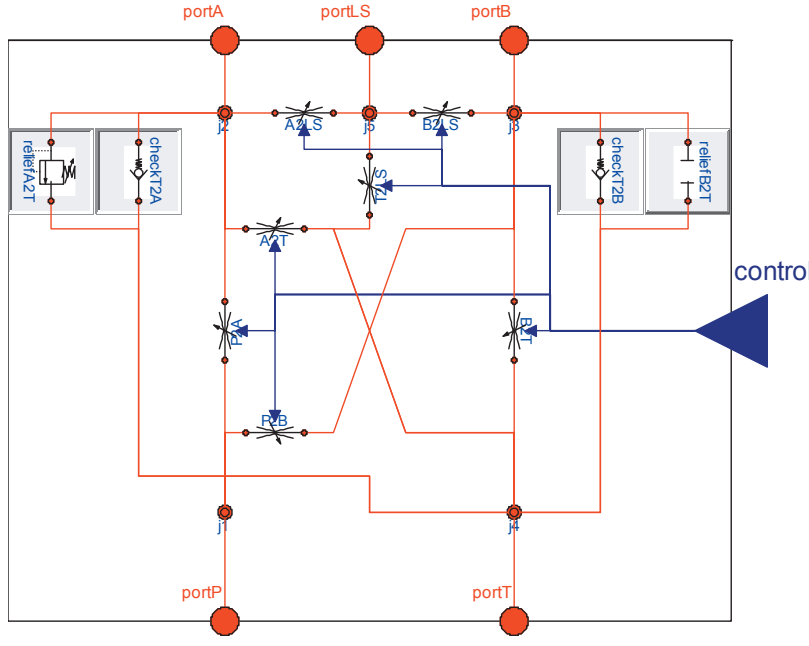

Figure 4: A usage of the reconfigurable directional valve, `Valve4_3LS`. The check and relief valves can be reconfigured; e.g., `reliefB2T` has been replaced by an open circuit.

relief valve from port B to port T has been replaced by an open circuit. Even for this simple example, one would have needed 2^4=16 non-reconfigurable models to account for all possible combinations of open circuits, relief and check valves.

Notice also the use of four `VariableRestriction` models in a Wheatstone bridge configuration to model the spool. By specifying an appropriate metering curve for each of the `VariableRestriction` models, almost any valve can be adequately approximated. In the future, we plan to include in the library a set of higher-fidelity models that also account for flow forces acting on the spool.

Finally, as one can see in this and the following figures, the Modelica models include graphical representations that reflect the symbols defined in the ISO 1219 standard (8). However, since Modelica is a general-purpose modeling language the Modelica we do not have the freedom to comply fully with the fluid power standard. One could consider this a short-coming, but one could also look at this as a way to distinguish clearly between the circuit schematic and the corresponding behavioral model — these two, though similar, are not to be confused.

5. SOLVING THE MODELS

So far, the focus has been on the Modelica models in the library, their organization, expressiveness and flexibility. However, one of the most important benefits of the Modelica

language manifests itself when simulating these models. Because the Modelica language is declarative, equation-based and noncausal, the models can be symbolically manipulated by a compiler to greatly simplify the system of differential algebraic equations that is ultimately integrated. Modelica's object-oriented modeling approach typically results in a large implicit DAE system consisting of models describing the behavior of all the components combined with connection constraints (Kirchhoff's laws). A Modelica compiler applies graph-based algorithms (e.g., the Tarjan algorithm (3)) and symbolic differentiation to these equations to convert this implicit DAE system into a semi-explicit DAE of the form:

$$\begin{cases} \dot{y} = f(y,z,t) \\ g(y,z,t) = 0 \end{cases} \qquad \text{(Equation 1)}$$

which can be solved using a combination of a traditional ODE solver with a root-finding algorithm (to solve for z in the implicit algebraic constraints, $g(y,z,t) = 0$). Even when structural singularities occur, the compiler automatically reduces the perturbation index by using symbolic differentiation and the Pantelides algorithm (14). In addition, the solution of the systems of algebraic constraints is greatly simplified through the use of tearing algorithms (5, 18). An excellent, very detailed discussion of these algorithms is provided in (3).

Although an end-user of the model library does typically not need to have detailed knowledge of these mathematical algorithms, it is important to point out the impact of these algorithms on the expressivity of the models. For instance, a common physical phenomenon in hydraulic systems is friction, including stiction. An ideal stiction model requires a change in causality at zero velocity, which in turn may result in the need for dynamic state selection. Rather than having to worry about these algorithmic details, a user can rely on the Modelica compiler to handle dynamic state selection, so that the focus can remain on the (declarative, equation-based) modeling of the physical phenomena. In addition, as compared to procedural approaches used in Simulink (19) or Easy5 (13), the symbolic manipulation—made possible through the use of declarative equations in Modelica—can result in a significant speed-up of the simulation. The example in the next section provides some further statistics about this symbolic manipulation process.

6. EXAMPLE

To illustrate the use and capabilities of the fluid power library, an excavator example is included in the `Examples` package. As shown in Figure 5, the model consists of a load sensing circuit for the swing, boom, arm, and bucket degrees of freedom of the excavator. In addition to the hydraulic circuit, the model includes the full 3-dimensional rigid body dynamics model for the excavator. The control for this example consists of open-loop time signals for the control valves of each of the degrees of freedom. From the diagnostics provided by the Dymola compiler (4), the model contains 3154 scalar time-dependent variables of which 523 appear in differentiated form in the equations. From this set of 523 potential states, the compiler selects 46 scalars as the minimal state for the nonlinear state-space representation (Equation 1). In addition, there are 17 algebraic loops; one loop contains 4 simultaneous iteration variables, while the remaining loops each contain only one

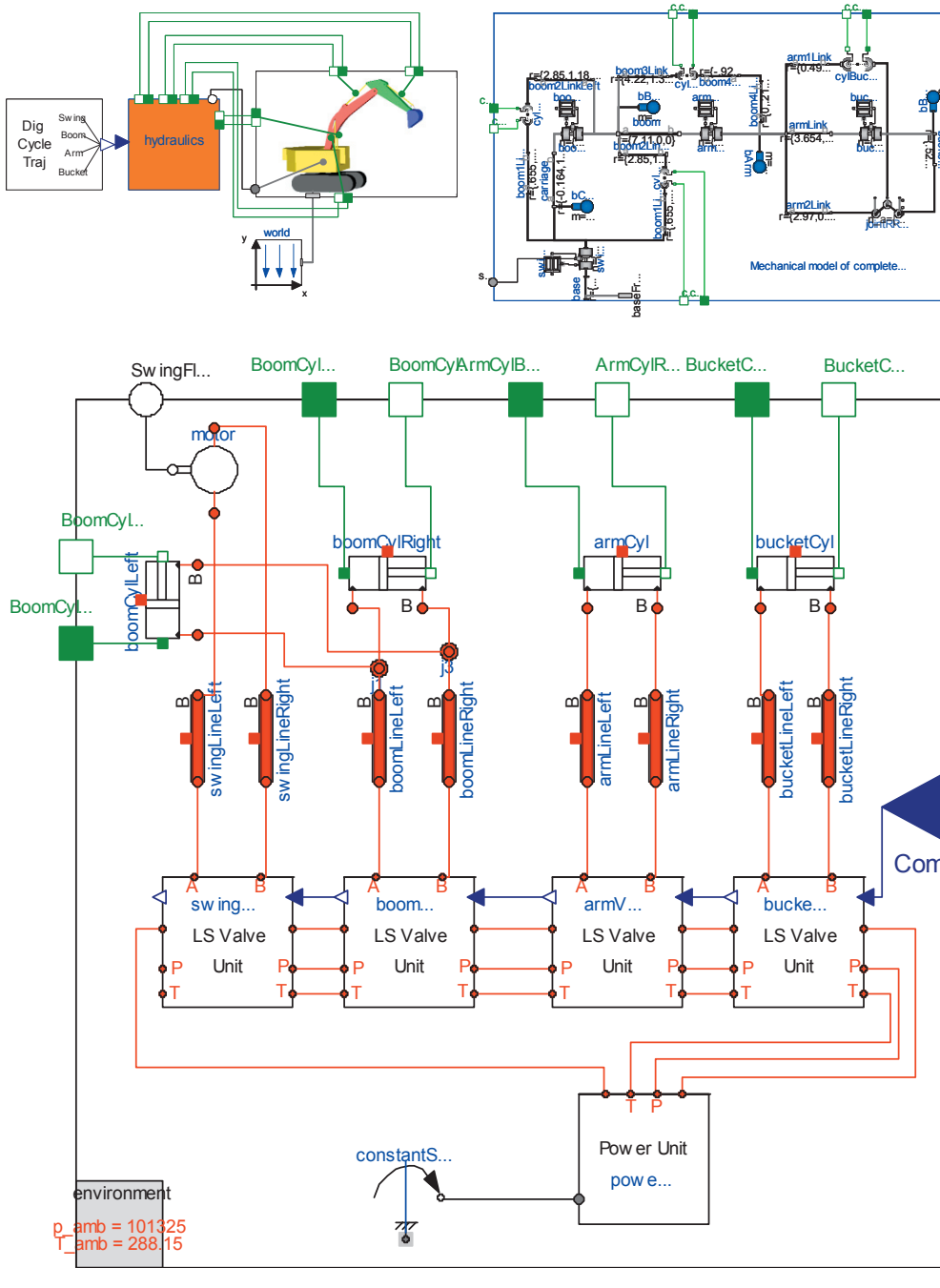

Figure 5: An excavator example, included in the fluid power library; bottom: hydraulic circuit; right-top: 3D rigid-body model; left-top: combined, total system model.

iteration variable. Although this is still a relatively small problem, it would have been almost impossible to resolve all the structural singularities and set up solvers for the algebraic loops by hand. Thanks to the symbolic manipulation of the equations, the resulting simulation for a 20-second dig-cycle is quite fast, requiring 24 seconds of CPU time on an Intel 6400 Duo-Core processor, running on only one of two cores at 2.13GHz.

7. DISCUSSION AND SUMMARY

In this paper, the key features of a new Modelica library for the fluid power domain have been presented. The development of this library was motivated by the need for an open, sharable source of fluid power knowledge. In addition, to support simulation-based design optimization, there is a need for more computationally efficient fluid-power simulation tools. The author believes that the library presented in this paper addresses many of these needs, and that it provides advantages over other fluid power modeling and simulation tools in terms of modularity, fidelity, speed and ease of use. Even when many researchers in the fluid power community rely on Matlab and Simulink to model their systems, they could still benefit from the increased simulation speed and model fidelity of the new Modelica library. They can export the models for their fluid power systems as Simulink S-functions, which can then be used in Simulink to design and test the corresponding controllers (although these controllers can often be modeled well in Modelica also).

Although the library is currently not complete, the basic structure of the library has been developed and thoroughly vetted, and the most commonly used hydraulic components have been modeled, tested, and demonstrated for an excavator model with a pressure-compensated load-sensing circuit. By making the library available through an open source licensing agreement, we hope that fluid-power researchers and practitioners will take advantage of the library and contribute to its further development. In this way, it could serve as a powerful tool to facilitate the further dissemination of knowledge about fluid-power systems.

8. ACKNOWLEDGEMENTS

This work has been funded in part by Deere & Company and by the ERC for Compact and Efficient Fluid Power, supported by the National Science Foundation under Grant No. EEC-0540834. The author would also like to thank Roger Burkhart, Aaron Enes, Jonathan Jobe, Tommy Johnson, Alek Kerzhner, and Roxanne Moore for their contributions to the development or testing of the fluid power library.

9. BIBLIOGRAPHY

(1) Ascher, U. M., and Petzold, L. R., 1998, *Computer Methods for Ordinary Differential Equations and Differential-Algebraic Equations*, SIAM, Philadelphia, Pennsylvania.

(2) Casella, F., Otter, M., Proelss, K., Richter, C., and Tummescheit, H., 2006, "The Modelica Fluid and Media Library for Modeling of Incompressible and Compressible Thermo-Fluid Pipe Networks," *Proceedings of the 5th International Modelica*

Conference, The Modelica Association and Arsenal Research, Vienna, Austria, pp. 631-640.
(3) Cellier, F. E., 2006, *Continuous Systems Simulation*, Springer-Verlag, New York.
(4) Dynasim AB, 2008, Dymola, Dynasim AB, http://www.dynasim.se.
(5) Elmqvist, H., and Otter, M., 1994, "Methods for Tearing Systems of Equations in Object-Oriented Modeling," *ESM 94 European simulation multiconference*, Barcelona, Spain.
(6) Elmqvist, H., Tummescheit, H., and Otter, M., 2003, "Object-Oriented Modeling of Thermo-Fluid Systems," in *Proceedings of the 3rd International Modelica Conference*, Modelica Association, Linköping, pp. 269-286.
(7) Idelchik, I. E., 1994, *Handbook of Hydraulic Resistance, Third Edition*, CRC Press, Boca Raton, Florida.
(8) ISO, 2006, "ISO 1219-1:2006: Fluid Power Systems and Components — Graphic Symbols and Circuit Diagrams — Part 1: Graphic Symbols for Conventional Use and Data-Processing Applications," International Organization for Standardization, Geneva, Switzerland.
(9) ITI GmbH, 2008, *SimulationX 2.0*, ITI GmbH, http://www.simulationx.com/.
(10) Larsson, J., 2002, "User's Guide to HOPSAN," Linköping University, Linköping, http://hydra.ikp.liu.se/Users_Guide.pdf.
(11) LMS International, 2008, *LMS Imagine.Lab Fluid Systems*, LMS International, http://www.lmsintl.com.
(12) Mattsson, S. E., Elmqvist, H., and Otter, M., 1998, "Physical System Modeling with Modelica," *Control Engineering Practice*, **6**, pp. 501-510.
(13) MSC.Software Corporation, 2008, *MSC.Easy5*, MSC.Software Corporation, http://www.mscsoftware.com.
(14) Pantelides, C. C., 1988, "The Consistent Initialization of Differential-Algebraic Systems," *SIAM Journal of Scientific and Statistical Computing*, **9**(2), pp. 213-231.
(15) Paynter, H. M., 1961, *Analysis and Design of Engineering Systems*, MIT Press, Cambridge, MA.
(16) Pop, A., Fritzson, P., Remar, A., Jagudin, E., and Akhvlediani, D., 2006, "OpenModelica Development Environment with Eclipse Integration for Browsing, Modeling, and Debugging," *Proceedings of the 5th International Modelica Conference*, The Modelica Association and Arsenal Research, Vienna, Austria, pp. 459-465.
(17) Richards, C. W., Tilley, D. G., Tomlinson, S. P., and Burrows, C. R., 1990, "BATHfp—a Second Generation Simulation Package for Fluid Power Systems," *Proceedings of BHRA International Fluid Power Symposium, Cambridge, UK*.
(18) Steward, D. V., 1965, "Partitioning and Tearing Systems of Equations," *SIAM Journal of Numerical Analysis*, **2**(2), pp. 345-365.
(19) The Mathworks Inc., 2005, *Matlab/Simulink*, The Mathworks Inc., http://www.mathworks.com/products/simulink/.

Modelling pipeline dynamics using optimized finite element model

Kazushi SANADA
Professor, Dr. Eng., Yokohama National University
Graduate School of Engineering, Department of Mechanical Engineering

ABSTRACT

An optimized finite element model of pipeline dynamics has been proposed by the authors. The model is based on a non-uniform interlacing grid system. The grid spacing is optimized to make natural frequencies of the model as close as possible to theoretical ones for extreme boundary conditions. Adjusting the non-uniform grid spacing, the model can be optimized to minimize errors in natural frequencies. Finite element approximation of the equation of motion and the continuity equation leads to a set of ordinary differential equations. It can be represented in state space form. The state-variable vector consists of state variables representing pressure and flow rate at the grid points. The model can be used in adaptive time step integrators, such as Simulink. In this paper, experimental verification of the optimized finite element model is focused. The model is applied to simulation of fluid transients in a test rig made of a stainless-steel pipe having 10 mm in diameter and 36 m in length. The working fluid is water. Fluid transients are caused by quick valve operation. Finally, the optimized finite element model is applied to modelling of a fuel injection valve used for gasoline direct injection systems.

Keywords: Modeling, Simulation, Pipeline dynamics, Optimized finite element model

1. INTRODUCTION

Models of pipeline dynamics have been well investigated in frequency domain. In a two-port model [(4)], input and output variables are related to each other by a transfer matrix or an impedance matrix that contains hyperbolic functions. Both steady laminar friction and unsteady laminar friction can be considered in the models. For time domain analysis, the method of characteristics [(5)(6)] has been widely used. Various forms of friction can be used. Accurate approximations of unsteady laminar friction have been studied by many researchers [(7)(8)]. Another technique to simulate fluid transients in pipelines is the transmission line method [(9)(10)]. The method of characteristics and the transmission line method assume a fixed time step for the numerical integration. However, adaptive time-step integrators are necessary for simulation of hydraulic systems [(11)]. A modal approximation technique was proposed [(12)-(14)]. It was pointed out that the modal approximation model can preserve the poles and the zeros of an original impedance matrix [(15)]. However the model assumes linear friction term. The other two standard methods are

Fluid Power and Motion Control 2008 Edited by Dr D N Johnston and Professor A R Plummer

the finite difference method [16] and the finite element method [17]. There is no difficulty in using adaptive time step in numerical integration. However the finite difference method produces oscillatory results and it is poor in accuracy of time delay of pipeline. The inaccuracy is caused by error in model's natural frequencies. The finite element method has a similar problem. However, in order to reduce the error, an optimized finite element model was proposed by the authors [1]. The model can reproduce natural frequencies very accurately. By adjusting non-uniform grid system, the model has been optimized to minimize the error in natural frequencies. The finite element approximation to the basic equations in space domain leads to a set of ordinary differential equations, which can be written in state space form. Soumelidis et. al. published a paper in which evaluation was made in terms of accuracy, computational efficiency and flexibility about the four most established modeling methods, the method of characteristics[6], the transmission line method[10], the modal approximation method [13], and the finite element method[1]. In this paper, the optimized finite element model is focused and the model is evaluated by experiments. And as an application of the model, modelling of a fuel injection valve used for gasoline direct injection systems is explained.

2. OPTIMIZED FINITE ELEMENT MODEL OF PIPELINE DYNAMICS

According to the reference [1], outline of the optimized finite element model is explained. Defining variables as shown in Fig.1, assuming one-dimensional flow, and neglecting a convection term, the equation of motion of fluid flow in a circular pipe is written as

$$\frac{\partial q}{\partial t}+\frac{A}{\rho}\frac{\partial p}{\partial x}+p_f(q)=0\,, \tag{1}$$

the continuity equation is written as

$$\frac{\partial p}{\partial t}+\frac{\rho c^2}{A}\frac{\partial q}{\partial x}=0\,. \tag{2}$$

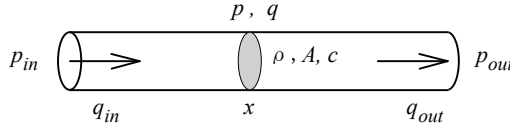

Fig. 1 A pipe

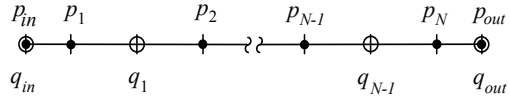

Fig. 2 Interlacing grid system

Based on an interlacing grid system as shown in Fig.2, finite element approximation of the basic equations leads to ordinary differential equations, Eq.(3) and Eq.(4):

$$\frac{\mathrm{d}\boldsymbol{q}}{\mathrm{d}t} + \frac{A}{\rho}\boldsymbol{B}\boldsymbol{p} + \frac{A}{\rho}\boldsymbol{F}\bar{\boldsymbol{p}} + \boldsymbol{p}_f(\boldsymbol{q}) = \boldsymbol{0}, \text{ and} \tag{3}$$

$$\frac{\mathrm{d}\boldsymbol{p}}{\mathrm{d}t} + \frac{\rho c^2}{A}\boldsymbol{E}\boldsymbol{q} = \boldsymbol{0}. \tag{4}$$

Elements of the vectors $\boldsymbol{q}$ and $\boldsymbol{p}$ are flow rate variables and pressure variables at the grid points:

$$\boldsymbol{q} = [q_{in}, q_1 \cdots q_{N-1}, q_{out}]^T, \text{ and} \tag{5}$$

$$\boldsymbol{p} = [p_1, p_2 \cdots p_N]^T. \tag{6}$$

The input vector $\bar{\boldsymbol{p}}$ represents pressure variables defined at the inlet and the outlet of a pipe:

$$\bar{\boldsymbol{p}} = [p_{in}, p_{out}]^T. \tag{7}$$

The friction term $\boldsymbol{p}_f$ is a function of flow rate at grid points. Various types of friction can be formulated, such as steady laminar friction, unsteady laminar friction and steady turbulent friction.

$$\boldsymbol{p}_f = [p_f(q_{in}), p_f(q_1) \cdots p_f(q_{N-1}), p_f(q_{out})]^T. \tag{8}$$

The matrices $\boldsymbol{B}$, $\boldsymbol{E}$ and $\boldsymbol{F}$ are calculated from the finite element approximation. Eq.(3) and Eq.(4) can be written as follows.

$$\frac{\mathrm{d}}{\mathrm{d}t}\begin{bmatrix}\boldsymbol{q}\\ \boldsymbol{p}\end{bmatrix} = \begin{bmatrix}\boldsymbol{0} & -\frac{A}{\rho}\boldsymbol{B}\\ -\frac{\rho c^2}{A}\boldsymbol{E} & \boldsymbol{0}\end{bmatrix}\begin{bmatrix}\boldsymbol{q}\\ \boldsymbol{p}\end{bmatrix} + \begin{bmatrix}-\frac{A}{\rho}\boldsymbol{F}\\ \boldsymbol{0}\end{bmatrix}\bar{\boldsymbol{p}} - \begin{bmatrix}\boldsymbol{p}_f\\ \boldsymbol{0}\end{bmatrix} \tag{9}$$

This is simply represented by a state space equation:

$$\frac{\mathrm{d}\boldsymbol{x}}{\mathrm{d}t} = \boldsymbol{A}_{p0}\boldsymbol{x} + \boldsymbol{B}_p\bar{\boldsymbol{p}} - \begin{bmatrix}\boldsymbol{p}_f\\ \boldsymbol{0}\end{bmatrix}, \tag{10}$$

where the state variable vector is

$$\boldsymbol{x} = \left[\boldsymbol{q}^T, \boldsymbol{p}^T \right]^T, \tag{11}$$

and the coefficient matrices are:

$$\boldsymbol{A}_{\boldsymbol{p}0} = \begin{bmatrix} \mathbf{0} & -\frac{A}{\rho}\boldsymbol{B} \\ -\frac{\rho c^2}{A}\boldsymbol{E} & \mathbf{0} \end{bmatrix}, \quad \boldsymbol{B}_{\boldsymbol{p}} = \begin{bmatrix} -\frac{A}{\rho}\boldsymbol{F} \\ \mathbf{0} \end{bmatrix}. \tag{12}$$

By setting extreme boundary conditions, (a) closed-closed, (b) closed-opened, and (c) opened-opened, eigen values of the model can be calculated from the coefficient matrix $\boldsymbol{A}_{p0}$. Theoretical un-damped natural angular frequencies can be given as (a) $2(i-1)\omega_n$, (b) $(2i-1)\omega_n$, and (c) $2i\omega_n$, where i is integer of 1,2,3..., where $\omega_n = \pi c/(2L)$, c is wave speed and L is pipe length. By adjusting the grid spacing, errors in the un-damped natural frequencies of the model can be minimized.

3. EXPERIMENTAL STUDY

The optimized finite element model was examined by comparisons with experimental results. A test rig was used for experiment and it is shown in Fig. 3. Test parameters are listed in Table 1. The pipe (1) was made of a stainless pipe of 10 mm in inner-diameter and 1 mm in thickness. The total length was 36 m. Working fluid was tap water of 16 degree Celsius. The upstream of the pipe was connected with a spool valve (2), a ball valve (3), and an air-compressed tank (4). The ball valve (3) had the same inner-diameter as the pipe and it was opened during experiments. The spool valve was switched by manually hitting the spool by a hammer. The downstream end of the pipe (1) was connected to a ball valve (5) and a reservoir (6). The ball valve (5) was closed during the experiment. Three pressure sensors (7), (8) and (9) were attached at the pipe to pick up transient pressures at the upstream-end p_U, the mid-point p_M, and the downstream-end p_D. The transient pressure signals were sent to an AD converter and recorded in a personal computer (10). Sampling period for data acquisition was 2 ms.

An example of experimental results is shown in Fig. 4 by broken lines. Pressure of the tank (4) was set as 0.2MPa. By switching the spool valve (2), the upstream pressure p_U was increased quickly. Because of pressure wave travelling along the pipe, the mid-point pressures p_M and the downstream-end pressure p_D showed oscillations. The pressure fluctuations were damped and the pressures converged to the tank pressure. Wave speed was about 1310m/s. Because of friction loss of the pipe, the fluctuation was damped in a short time. In order to estimate Reynolds number, applying the Joukowsky's equation of water hammer, assuming pressure surge of 0.2MPa at the pressure of the tank (4), the flow velocity occurred at the spool valve (2) is estimated as:

$$\Delta V = \frac{\Delta p}{\rho c} = \frac{0.2 \times 10^6}{999 \times 1310} \approx 0.153 \text{ m/s} . \quad (13)$$

Corresponding Reynolds number is about 1500. Therefore the flow was laminar and unsteady laminar friction was used for simulation.

A block diagram for simulation is illustrated in Fig. 5. A block named "OFEM" represents the optimized finite element model which has pressures as the input variables. One of the input variables p_{in} is given by the measured results of the upstream-end pressure p_U. Another input p_{out} is given by measured results of the downstream-end pressure p_D. These input signals are updated every 2 ms. The downstream end of the experimental pipe is a blocked end. The boundary condition is modelled using an impedance Z which is enough high to ignore flow rate at the downstream end q_{out}. Typical value of the impedance Z is 1013 Pa/(m^3/s). Mid-point pressure p_M and downstream-end pressure p_D are obtained as simulation results. Parameters for the simulation are listed in Table 1. Simulink was used for the simulation. Simulated results are plotted in Fig. 4 by broken lines. Simulated results of the mid-point pressure p_M and the downstream pressure p_D are plotted by solid lines. They show a good agreement with experimental results.

In the Simulink model of Fig. 5, the optimized finite element model is installed in a state space block named "OFEM". Coefficient matrices of the optimized finite element model are set as the ABCD matrices. The matrices are calculated according to the finite element approximation. The calculation procedure is complicated. A program was made so that the matrices of the OFEM can be automatically calculated. It was programmed using Visual C++ on Windows XP SP2. The program has a graphical user interface as shown in Fig. 7. Input signals, the number of elements N, inner diameter and other parameters can be specified. Friction type can be selected among lossless, steady laminar friction, and unsteady laminar friction. Name of the coefficient matrices can be specified by a text in a box "name". Pushing a "RUN" button, the matrices of the OFEM is automatically calculated. Finally, the "SAVE" button can store the matrices as an M-file which can be used for MATLAB/Simulink. The output matrix $\boldsymbol{C}$ was modified in order to detect the midpoint pressure from the state space vector $\boldsymbol{x}$ of the OFEM. Also a matrix $\boldsymbol{D}$ of the state space block was modified to have the same column width as that of the output vector $\boldsymbol{y}$.

Table 1 Parameters for experiment and simulation

c	1310	m/s
L	36.0	m
N	10	
R	5.0	mm
ν	1.05×10^{-6}	m^2/s
ρ	999.0	kg/m^3

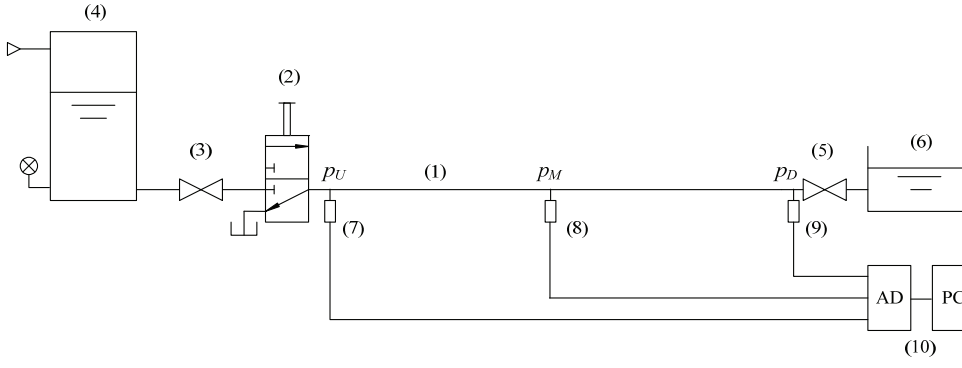

Fig. 3 Experimental pipeline and measurement system

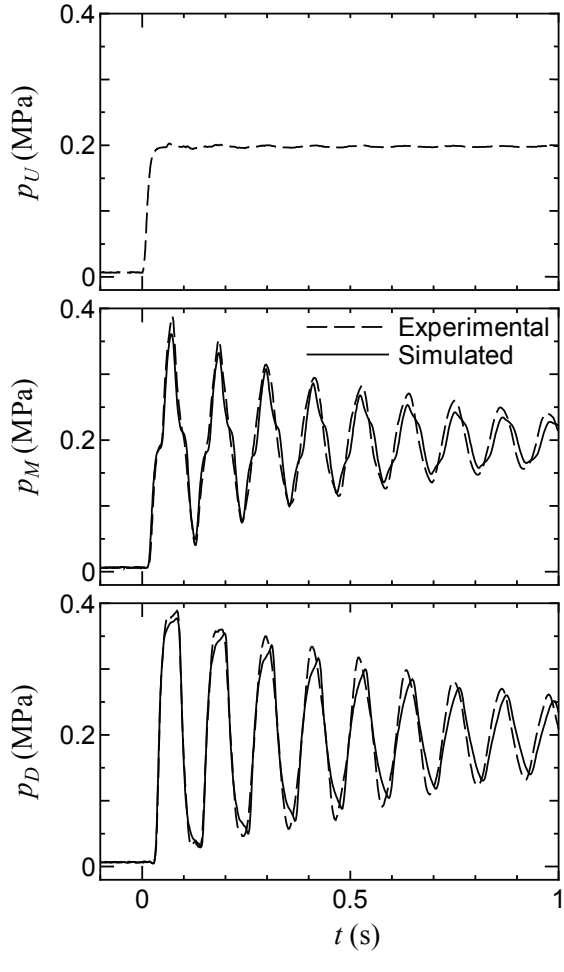

Fig. 4 Comparison of experimental and simulated transient pressures

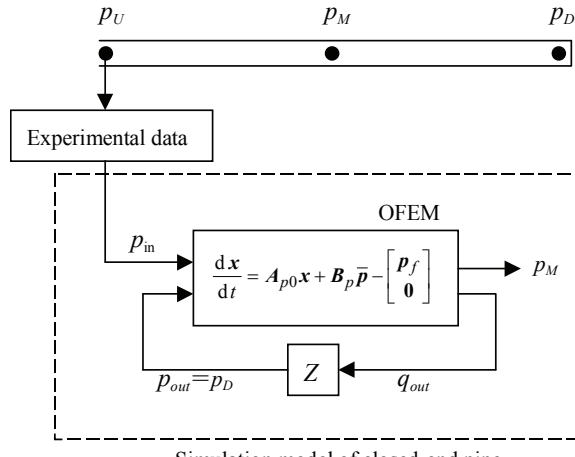

Fig. 5 A schematic diagram of simulation

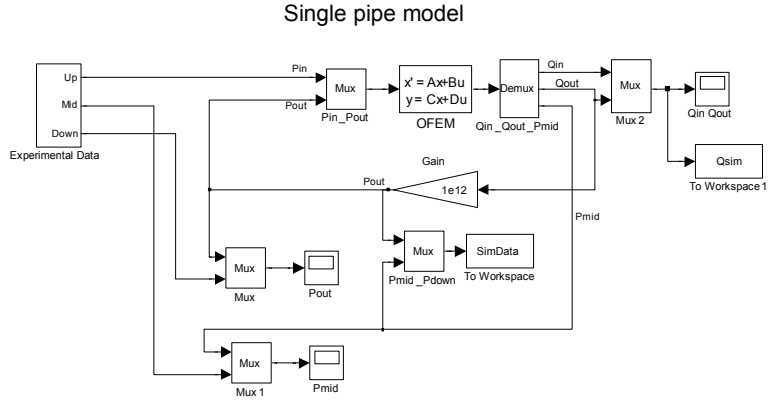

Fig. 6 Simulink model of the single pipe model

An alternative modelling technique is to connect two optimized finite element models in series at the mid-point. The block diagram of the series connection is shown in **Fig. 8**. The boundary condition of blocked end can be represented only by setting null to the downstream-end flow rate port of the downstream-side OFEM block. The modelling could be more simplified. A pressure-input type OFEM is used as the upstream-side OFEM block. The upstream pressure signal is given to the p_{in} port of the OFEM. The Simulink model is shown in **Fig. 9**. The simulated results are plotted in **Fig. 10** by solid lines. Simulation results show a good agreement with experimental results.

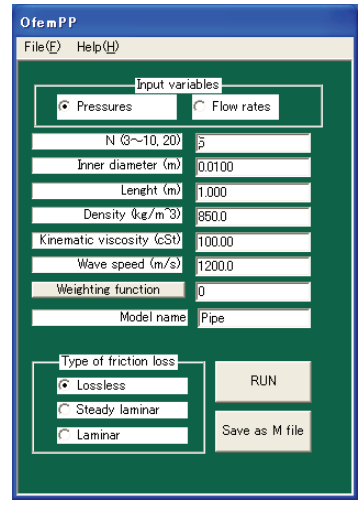

Fig. 7 GUI Interface of Optimized Finite Element Model (Copyright Yokohama National University, made by Kazushi SANADA)

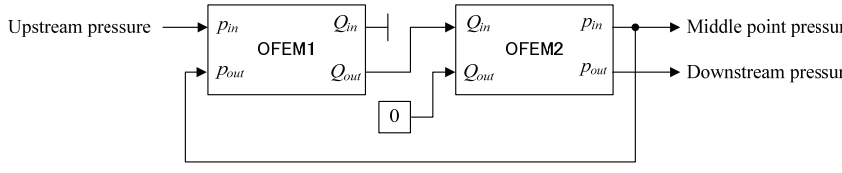

Fig. 8 Block diagram of the series connection model

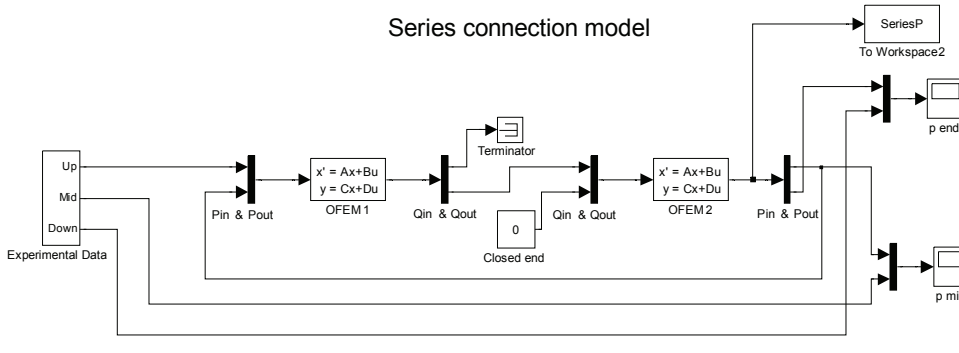

Fig. 9 Simulink model of the series connection model

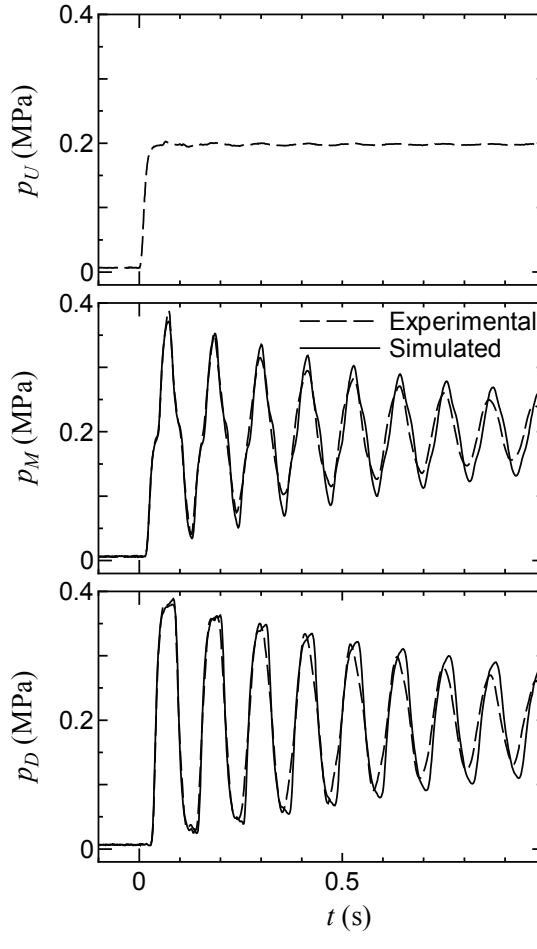

Fig. 10 Simulated results based on the series connection model

4. MODELING A FUEL INJECTION VALVE

In this section, the optimized finite element model is applied to modelling of a fuel injection valve used for gasoline direct injection systems. A schematic diagram is shown in Fig. 11. The solenoid is activated by drive current, a valve body moves upwards and a nozzle is opened. An anchor is connected to the valve body. A mass-pipe is a device to reduce rebound action of the valve body. Fuel is delivered through a fuel pipe from a fuel pump.

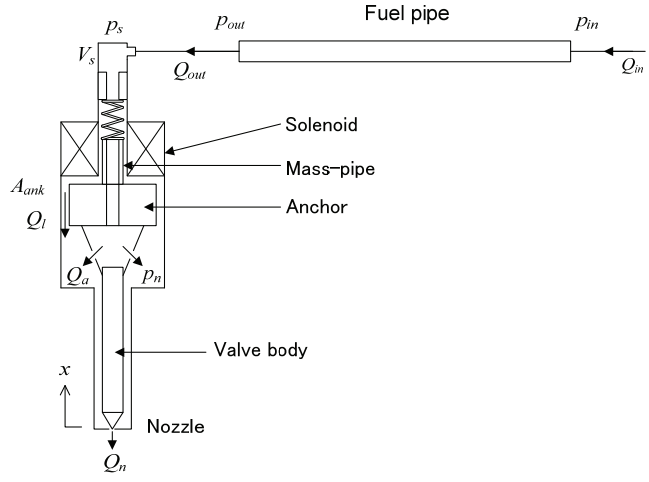

Fig. 11 A model of a fuel injection valve and a flexible line

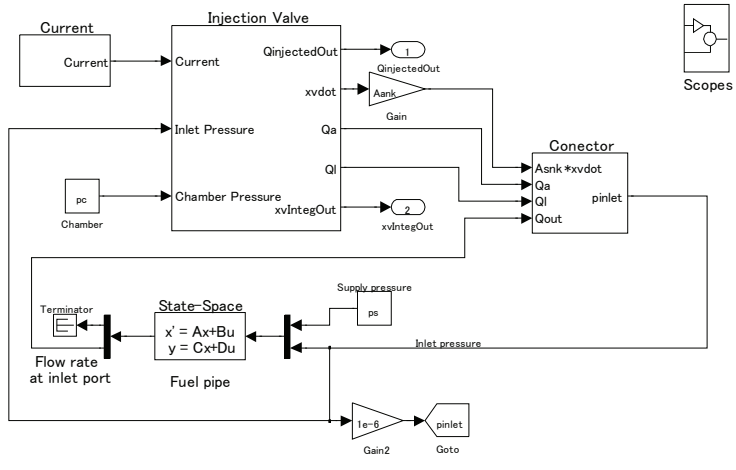

Fig. 12 Simulation model of fuel injection valve

The equation of motion of the valve body is

$$M_v \ddot{x}_v = A_s p_n + F_{sol} - A_s p_s - F_v - F_{ank} + F_{core}, \tag{14}$$

where x_v is valve displacement and M_v is mass of the valve body. The first term in the right hand side represents force caused by nozzle pressure p_n acting on the anchor area A_s. The second term is solenoid force. The third term is force caused by supply pressure p_s. The fourth term is contact force F_v between the mass-pipe and the anchor. The fifth term F_{ank} is viscous friction at annular clearance of the anchor. The sixth term F_{core} is

contact force that causes rebound motion of the valve body. The rebound force was modelled by a combination of a spring and a damper. The damper coefficient c_{pen} is in proportional to penetration depth x_{pen}.

The equation of motion of the mass-pipe is

$$M_{mp}\ddot{x}_{mp} = -F_s + F_v - F_{mp}, \tag{15}$$

where M_{mp} is the mass of the mass pipe, and x_{mp} is its displacement. The term F_s is spring force and F_v is contact force between the mass-pipe and the anchor. The third term F_{mp} is viscous friction.

Compressibility of fuel in a nozzle chamber is written as:

$$\frac{d}{dt}p_n = \frac{K}{V_n}\left(Q_a - Q_n + Q_l - A_s\dot{x}_v\right) \tag{16}$$

where p_n is nozzle pressure. The volume V_n can vary according to valve body displacement x_v. Flow rates Q_a, Q_n and Q_l represent fuel flow through holes of the anchor, fuel flow rate injected through the nozzle, and leak flow through annular clearance of the anchor, respectively. Injection flow rate Q_n is written as:

$$Q_n = c_n A_n(x_v)\sqrt{\frac{2}{\rho}\left|p_n - p_c\right|}\,\mathrm{sgn}\left(p_n - p_c\right) \tag{17}$$

where A_n is valve opening area, c_n is discharge coefficient, and p_c is pressure in combustion chamber.

Integrating the component sub-models, a Simulink model was built as shown in Fig. 12. A fuel pipe model is the ABCD block in which the optimized finite element model was set. An example of simulation results is shown in Fig. 13. Current, inlet pressure, nozzle pressure, needle valve displacement are plotted. Rebound phenomena can be seen in the valve displacement. Inlet pressure shows fluctuation caused by pipeline dynamics of the fuel pipe. The optimized finite element model enables us to study such pressure fluctuations occurred in fuel lines.

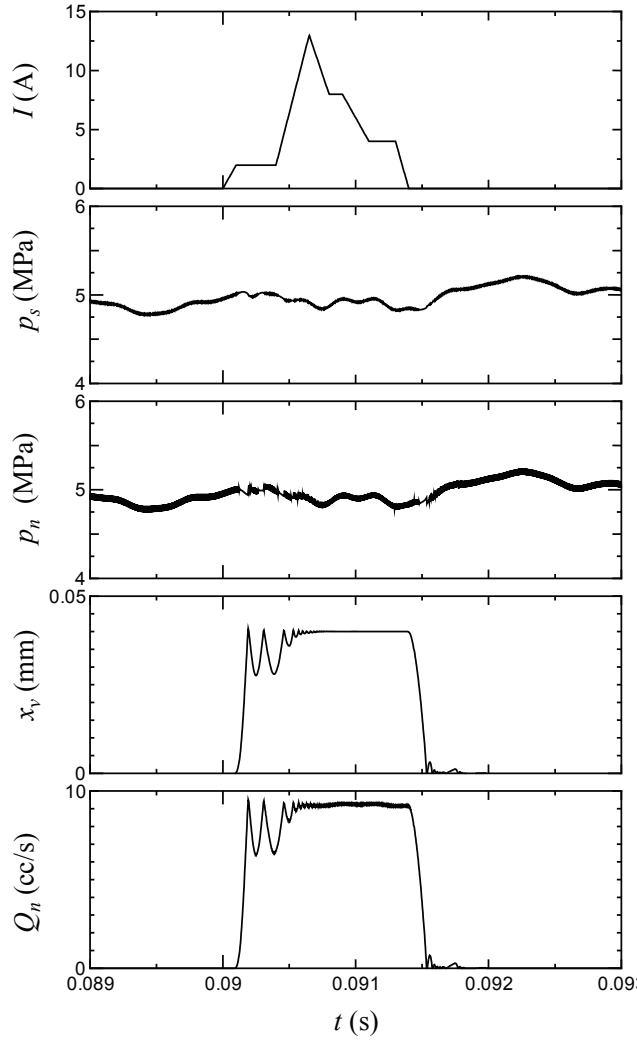

Fig. 13 An example of simulation results

5. CONCLUSIONS

The optimized finite element model of pipeline dynamics was verified by experiments using a test rig. Two simulation schemes were tested. The first scheme is to use one OFEM model of pressure input type. The second scheme was to connect two OFEM blocks in series. Simulation results showed a good agreement with experimental results. A GUI program for calculation of OFEM's coefficient matrices was made by the author. An application of modelling a fuel injection valve is explained. The finite element model of pipeline dynamics is useful for simulation study of transient phenomena occurred in fluid lines such as fuel injection systems.

NOMENCLATURES

A	cross-sectional area
$\boldsymbol{A_p}$	system matrix of the optimized finite element model
$\boldsymbol{B_p}$	input matrix of the optimized finite element model
c	wave speed
N	the number of elements
p	pressure
p_D	downstream pressure
p_i	pressure at a grid point
p_f	pressure loss per unit length
p_{in}	inlet pressure of a pipe
p_M	mid point pressure
p_{out}	outlet pressure of a pipe
p_U	upstream pressure
q	flow rate
q_i	flow rate at a grid point
q_{in}	inlet flow rate of a pipe
q_{out}	outlet flow rate of a pipe
R	radius of a pipe
t	time
x	position along pipe axis
$\boldsymbol{x}$	state variable vector
ρ	density

REFERENCES

(1) Sanada, K., Richards, C. W., Longmore, D. K., and Johnston, D. N. (1993), "A finite element model of hydraulic pipelines using an optimized interlacing grid system", Proc Instn Mech Engrs, Part I: Journal of Systems and Control Engineering, **207**, p.213-222.

(2) Sanada, K., Richards, C.W., Longmore, D. K., Johnston, D. N. and Burrows, C. W. (1993), "Practical Requirements for Modelling the Dynamics of Hydraulic Pipelines", Proc. Second JHPS International Symposium on Fluid Power, p.657-664.

(3) Sanada, K. (1999), "Simulation of Pipeline Dynamics Using an Optimized Finite Element Model", Journal of Robotics and Mechatronics, **11**(4), p.283-287.

(4) Goodson, R. E. and Leonard, R. G. (1972), "A survey of modeling techniques of fluid line transients", Trans. ASME, J. Basic Engng, **94**(2), p.474-482.

(5) Wylie, E. B. and Streeter, V. L. (1978), Fluid Transients, McGraw-Hill.

(6) Fox J.A., Hydraulic Analysis of Unsteady Flow in Pipe Networks, The Macmillan Press Ltd., 1977.

(7) Zielke, W. (1968), "Frequency-dependent friction in transient pipe flow", Trans. ASME, J. Basic Engng, **90**(1), p.109-115.

(8) Kagawa, T., Lee, I., Kitagawa A. (1983), "High speed and accurate computing method of frequency-dependent friction in laminar pipe flow for characteristics method", Bull. JSME, Ser.B, **49**(447), p.2638-2644 (in Japanese).

(9) Kitsios, E. E., and Boucher, R. F. (1986), "Transmission line modelling of a hydraulic position control system", Proc. Instn Mech. Engrs, Part B, **200**(B4), p.29-36.

(10) Krus P., Weddfelt K., Palmberg J.O. (1994), "Fast Pipeline Models for Simulation of Hydraulic Systems", Transactions of the ASME, Journal of Dynamic Systems, Measurements, and Control, **116**(1), pp. 132-136.

(11) Richards, C. W., Tilley, C. R., Tomlinson, S. P. and Burrows, C. R. (1990), "Type insensitive integration codes for the simulation of fluid power systems", Proceedings ASME Winter Annual Meeting, Texas, USA, November 1990, 90WA FSPT6, ASME, New York.

(12) Hullender, D. A. and Healey, A. J. (1981), "Rational polynomial approximations for fluid transmission line models", Fluid transmission line dynamics, ASME, New York.

(13) Wongputorn P., Hullender D.A., Woods R.L., Rational Polynomial Transfer Function Approximations for Fluid Transients in Lines,Proceedings of ASME FEDSM 2003, 4th ASME_JSME Joint Fluids Engineering Conference, Honolulu, Hawaii, July 2004, pp. 2797-2804.

(14) Hullender, D. A. and Hsue, C. Y. (1983), "Modal approximations for the fluid transmission line dynamics", Fluid transmission line dynamics, ASME, New York.

(15) Watton, J. (1988), "Modelling of electrohydraulic systems with transmission lines using modal approximations", Proc. Instn Mech. Engrs, Part B, **202**(B3), p.153-163.

(16) Watton, J. (1989), Fluid power system, modelling, simulation, analog and microcomputer control, p.262-265, Prentice Hall, Englewood Cliffs, NJ.

(17) Paygude, D. G., Vasudeva Rao, B. and Joshi, S. G. (1985), "Fluid transients following a valve closure by FEM", Proceedings of International Conference on Finite elements in computational mechanics, Bombay, India, 2-6 Dec., p.615-624, Pergamon Press, Oxford.

(18) Michail I. Soumelidis, D. Nigel Johnston, Kevin A. Edge, Derek G. Tilley, A Comparative Study of Modelling Techniques for Laminar Flow Transients in Hydraulic Pipelines, Proceedings of the 6th JFPS International Symposium on Fluid Power, TSUKUBA 2005, November 7-10, 2005, p.100/105.

Modelling of Hydraulics and Mechanics of a Mobile Machine

Antti Vuohijoki, Mika Hyvönen, Kalevi Huhtala and Matti Vilenius
Tampere University of Technology, Department of Intelligent Hydraulics and Automation (IHA), Finland

ABSTRACT

The effects of the control system flaws in a mobile machine are difficult, and even dangerous, to identify. The use of simulation offers a safe way to find these flaws. In this paper the behaviour of a small mobile machine, has been analysed in two driving situations. The analysis was based on the verified simulation model.

Analysis revealed few problems. Five simple improvements were proposed to correct problems. These proposals were simulated and analysed. Also distributed restriction edge control was tested and the preliminary results were promising.

1. INTRODUCTION

The research subject of this study is a prototype of a small skid steered mobile machine. The weight of the machine is 610 kg and the power of its diesel engine is 15 kW. The machine is electrically controlled and it can be teleoperated via radio modems (1). The hydraulic system is made with common mobile hydraulic components. The hydraulic diagram of the machine is presented in Figure 1.

Skid steering is friction dependent, which causes problems when the machine is driven on different surfaces. Also the load and weight distribution have an impact on the behaviour of skid steered machine (2). Demands for controllability and predictability of the behaviour are especially high, if the machine is teleoperated, then the operator might not have exact knowledge of the driving conditions of the machine.

The simulation model used in this study is earlier presented in reference (3). Only the model of the diesel engine is different. It is based on the model presented by Tsal and Goyal (4)(5). By using this model it is possible to approximate the amount of the used diesel-fuel. This feature is not utilized in this study.

Fluid Power and Motion Control 2008 Edited by Dr D N Johnston and Professor A R Plummer

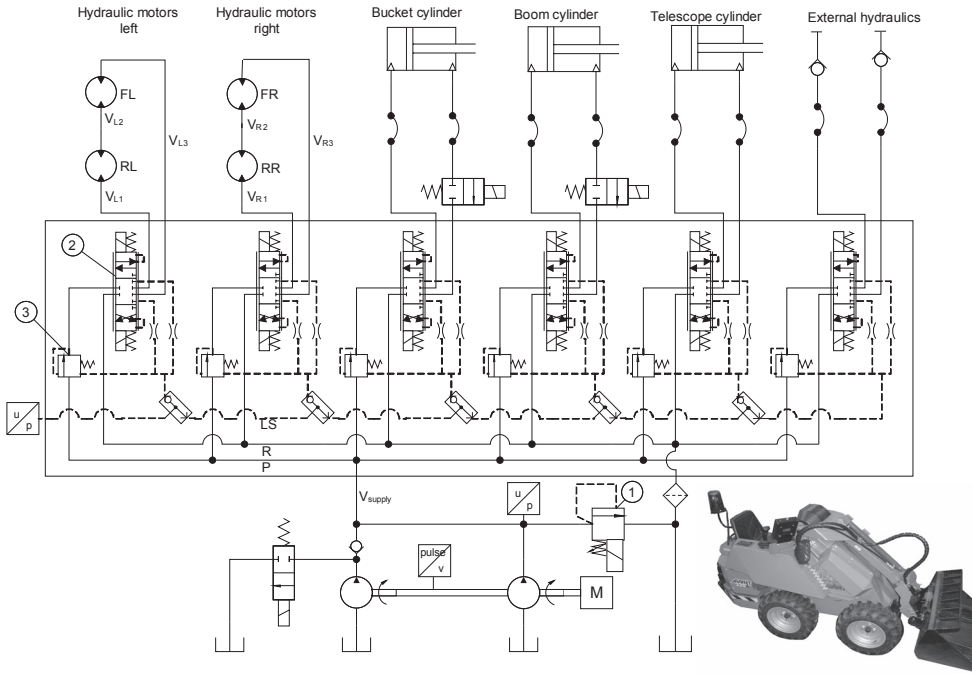

Figure 1: The original hydraulic diagram of the prototype and a picture of the prototype. Key components of the study are numbered: 1 pressure relief valve, 2 main valve, 3 pressure compensator.

2. ANALYSIS OF THE BEHAVIOUR OF THE MACHINE

In this chapter the behaviour of the vehicle will be studied in two different situations. These situations are the take off and the stopping of the machine in straight forward translation. The study is based on the simulation and on measurements. The model used in this study is verified. The verification results are published before (3). In this analysis only the left side of the machine is considered.

2.1 The Analysis of the Situation when the Machine takes off

The following paragraphs will describe the phenomena of the take off as thoroughly as possible. The main point of view in this study is on the hydraulic system which defines the behaviour of the whole vehicle hand in hand with the mechanics of the system.

The command signal of the pressure relief valve, number one in Figure 1, is adjusted to 35 bars. At 1.5 seconds the command value of the main valve, number two in Figure 1, begins one second ramp to its maximum value. At 1.7 seconds the command signal of the main valve reaches the level of 0.2, which changes the control mode of the pressure relief valve. In this mode it starts to follow the highest working pressure of volumes V_{L1}, or V_{L3} added with 20 bars. The control system of the pressure relief valve is described in Figure 3. At

this point the supply pressure is still 35 bars and the highest working pressure is only 2 bars. The highest working pressure is small at this point because, the leakage through the main valve is smaller than the external leakage of the hydraulic motors. The pressure difference of 33 bars is higher than the command value, which causes the pressure relief valve to open. Relative position of the spool of the pressure relief valve is described in Figure 4.

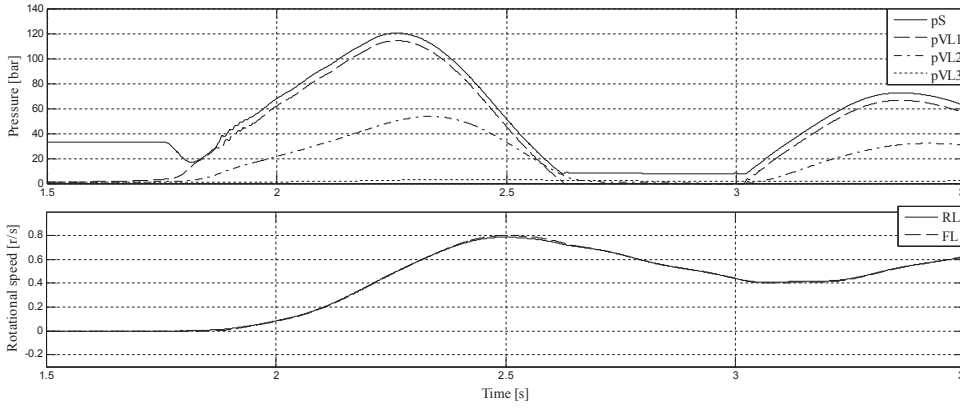

Figure 2: Pressures and rotational speeds at the take off

At 1.75 seconds the pressure relief valve starts to open, which causes a drop in the supply pressure. At the beginning of the drop the supply pressure is 35 bars. At the same time the highest working pressure is 4 bars. The supply pressure presses the compensator spool, number three in Figure 1, against the springs in the LS-chamber and the force equilibrium of the spool is at position 7.3mm. As a result of the drop in the supply pressure the spool of the pressure compensator starts to move in to negative direction. At the same time the pressure in LS-chamber starts to rise, due to the opening of the main valve. This accelerates the movement of the compensator.

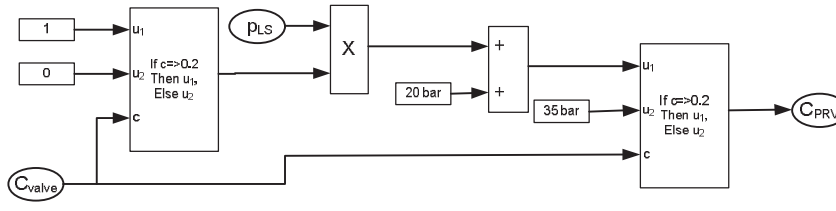

Figure 3: Schematic of the original control system of the pressure relief valve.

The inputs of the control system of the pressure relief valve, described in Figure 3, are command value of the main spool, which is C_{valve} in Figure 3, and the highest working pressure, which is p_{ls} in Figure 3. The output is the command signal of the pressure relief valve, which is C_{prv} in Figure 3. When the command signal of the main valve is less than 0.2, the command signal of pressure relief valve is constant value of 35 bars. If the command signal of main valve is higher than 0.2, the system adds 20 bars to the highest working pressure and uses this value as a command signal of the pressure relief valve.

When the main valve leaves the dead zone and the flow raises the pressure in volume V_{L1}. The rising pressure in the V_{L1} builds up a pressure difference over the motor RL, which creates torque on the output shaft of the motor. At 1.78 seconds the torque exceeds the opposing static friction force and the shaft of the motor RL starts to revolve.(6) The acceleration of hydraulic motor causes the body of the vehicle to tilt backwards. The push from the motor RL helps the motor FL to start to revolute. This takes place at 1.83 seconds.

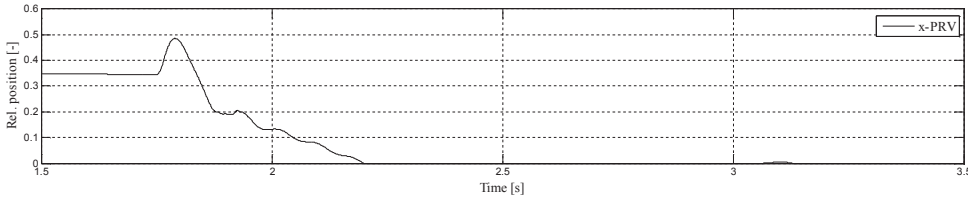

Figure 4: Relative opening of the pressure relief valve

At the time of 1.81 seconds the supply pressure reaches the minimum value. At this point the pressure difference over the main spool is 4 bars. The smallest pressure difference, 0.42 bars, takes place at 1.835 seconds. At this point the pressure related net force acting on the spool of the pressure compensator is negligible and the spring force is dominant. This causes the compensator spool to move rapidly into negative direction. The position of the compensator is described in Figure 5. At 1.87 seconds the rapid movement ends and the compensator spool starts to oscillate. The oscillation of the compensator spool is reflected on the supply pressure and on the pressure in V_{L1}. At 2.03 seconds the compensator spool reaches the new equilibrium, this is at 0.5 mm. At this point the edge 2 of compensator restricts the flow. This edge usually works as a shuttle valve of compensator, which means that the compensator is not working properly.

The control system of the pressure relief valve is still trying to maintain the pressure difference of 20 bars over the main valve. At 2.1 seconds the pressure difference over the orifice of the main valve is 6 bars, which is still insufficient for the pressure compensator to work correctly. The pressure relief valve is closed at 2.2 seconds, which leads to a situation, where the main valve is transmitting all the flow produced by the pump to the motors. In this situation the supply pressure and the pressure in the V_{L1} are still climbing, and the motors are still accelerating. At 2.25 seconds the pressure in V_{L1} reaches its maximum, in this point motors RL and FL are consuming more flow than the pump produces. The inertia of the vehicle forces the motors to run fast, even tough the feed flow trough main spool is insufficient. This causes sudden drop in the supply pressure and in the pressure of V_{L1}. Because of this motors RL and FL start to decelerate. At 2.58 seconds the pressure difference over the motor RL switches direction. This means that motor starts to work as a pump. At 2.63 seconds the motor RL starts to cavitate. At the same time with the cavitation of the RL fast pressure transient causes pressure compensator to oscillate. The motor FL starts to work as a pump at the time of 2.65 seconds and it starts to cavitate at 2.71 seconds. At this time the vehicle is in uniformly decelerating and the hydraulic system is sucking air in trough the gaps of hydraulic motors.

After the rotational speed of the motor is decreased enough and the demanded flow is again smaller than the flow produced by the pump, the pressure in V_{L1} starts to rise and the

cavitation ends. This takes place at 2.97 seconds. Again a fast pressure transient leads into oscillations of the pressure compensator.

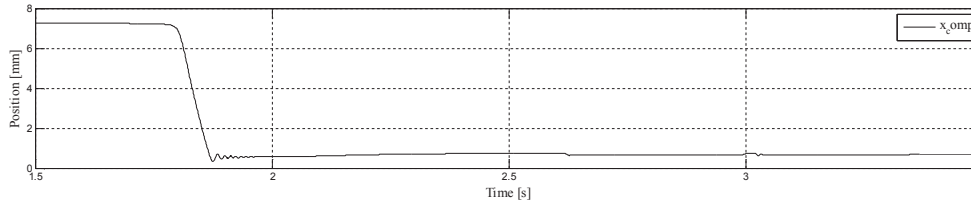

Figure 5: Position of the compensator spool

2.2 The Analysis of the Situation when the Machine stops

The closing ramp of the main valve begins at 16 seconds; the duration of the ramp is 1 second. At 16.19 seconds the pressure compensator starts to move into positive direction, which indicates that the pressure difference over the orifice of the main valve starts to change and the orifice starts to restrict the flow. At this time the spool of the main valve has reached relative position of 0.93. Also the rotational speed of the hydraulic motors start to slow down, but the rate of deceleration is still very small.

At 16.63 seconds the pressure difference over the orifice of the main valve starts to build up due to the rising supply pressure. The pressure relief valve stays closed, because the pressure difference over the main valve is still under 20 bars.

At 16.8 seconds, the command signal of the main valve decreases below 0.2, and the command signal of the pressure relief valve changes in to a constant value of 35 bars. At this point the supply pressure is approximately 45 bars, which causes pressure relief valve to open. This takes place at 16.83 seconds. The opening of pressure relief valve makes the pressure fall faster in the volume V_{L1}. The pressure difference over the motor RL is still positive. But at 16.86 seconds the pressure difference over the motor RL becomes negative causing the motor to work as a pump. As a result the hydraulic motor decelerates faster. The main spool is still slightly open, and the supply pressure squeeze oil through it.

At the time 16.87 the pressure in the volume V_{L3} rises higher than pressure in the volume V_{L1}. This changes the source of the highest working pressure, and the compensated pressure difference over the orifice of the main valve starts to decrease instead of increase, due to the still rising pressure in volume V_{L3}. As a result the compensator spool starts to open.

At 16.88 seconds the pressure difference over the motor FL turns negative and it starts to work as a pump.

The main valve enters in to the dead zone at 16.91 seconds, and closes the main flow passage from pump to hydraulic motors. The motors are supplied only by the leakage flow. At this point the remaining rotational speed is 0.42 r/s and the inertia of the vehicle forces the motor RL to revolute. As a result the motor starts to cavitate at 16.92 seconds.

Due to the pumping motors RL and FL the pressure in V_{L3} is still rising. This builds up the negative pressure difference over the FL, causing also the breaking torque to increase. This makes the vehicle tilt forward, which builds up the friction force. Tilting of the machine also decreases the friction force of the rear tire. At 17.04 seconds the pressure difference over the motor FL is approximately 60 bars and the pressure difference over the motor RL is only 6 bars. Due to the reduction of friction based torque affecting the rear tire the motor RL stops and the tire connected to it starts to slide. The front tyre starts to slide at 17.05 seconds. The velocity decreases and it tilts backwards, this increases the friction force on the rear tire and causes it to rotate, at 17.07 seconds. At the same time, the friction force on front tires reduces which causes the volume V_{L3} to discharge its pressure through the motor FL. The motor FL starts to work as a motor in negative rotation direction at 17.10 seconds. The negative flow through the motor FL pressurises the volume V_{L2}. The raise of the pressure in the volume V_{L2} increases the negative pressure difference over the motor RL. It starts to work as a motor into negative direction at 17.12 seconds. At this moment the machine is in backward motion.

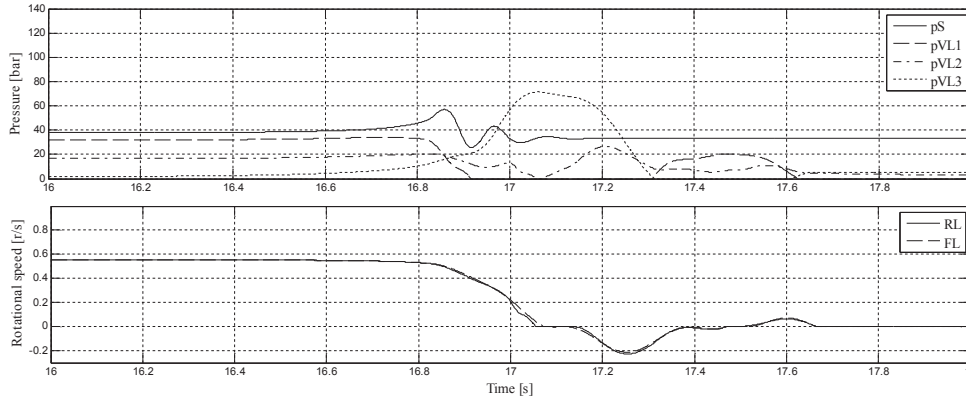

Figure 6: Pressures and rotational speeds when the vehicle is stopping

At 17.28 seconds the direction of the pressure difference over the motor FL changes and the motor starts to work as a pump. The volume V_{L1} starts to pressurise at 17.35 seconds. After 0.03 seconds the direction of pressure difference over the motor RL changes and pump works as a pump. At this point both motor RL and motor FL are working as pumps. The negative speed of the machine is decelerating until the tires start to slip again and the direction of movement changes. This time the kinetic energy too small to cause any disturbances and the vehicle stops.

2.3 The Results of the Analysis

The analysis enlightened few key points that affect the behaviour of the machine. First of all, the pressure difference over the first motor rises too rapidly. This forces the machine into pitching motion. The reasons for the steep pressure rise are the high static friction, the uncontrolled pressure difference over the main spool, and too big opening of the orifice. The pressure difference over the main spool should be controlled by pressure compensator. The problem with pressure compensator is that it needs a minimum pressure difference to

work correctly. The simulation of the system shows that it restricts the flow with the edge that is designed to work as a check valve.

The reasons for insufficient pressure difference, in the situation when the machine takes off are the control system of the pressure relief valve, and the dead zone of the main valve. The control system of the pressure relief valve causes the pressure to drop, while it is trying to add 20 bars on the undeveloped working pressure. The reason for undeveloped working pressure is too small positive net flow in the volume V_{L1}. This is caused by the dead zone of the valve.

When the machine is already moving and the supply pressure is stabilized, the pressure compensator is still not working correctly. This is caused by too big main valve. The reason for such a big valve is the virtual gearbox function, which adds the flow of the second pump into the system (7).

3. PROPOSALS TO IMPROVE THE BEHAVIOUR

The control system and the hydraulic system of the simulation model were modified in five ways. The common objective for these modifications was the improvement of the behaviour of the vehicle at the take off. Modifications are presented shortly in following sub-chapters. Results of these modifications will be compared, and the original system is used as a reference.

3.1 Modifications of the Control System

The command signal of the main valve was modified. This was made to clarify start of the opening and to reduce the over opening of the valve. The secondary objective was the reduction of the drop in the supply pressure.

The modified command signal begins with a step from 0 to 0.12. The step is followed by a one second ramp from 0.12 to 0.35. The dead zone is compensated by the step and the over opening is saturated by the end value of the ramp. In the simulation model the modification was made to the control signal. If this would utilized in real system the control signal would be computed by the control system of the machine. The command signal described in this chapter was used in following modifications.

The control system of the pressure relief valve is modified in two ways. First, the control strategy was changed in the following way: If the command signal of the main valve is less than 0.2 the output of the pressure relief valve is 35 bars. When the command signal of the main valve is more than 0.2, and the highest working pressure added with 20 bars is more than 35 bars, the output of control system is this value. Otherwise the output of the control systems stays at 35 bars. The modified control strategy is presented in Figure 7. Second, the rising- and falling rate of the output signal of the control system was changed from 810 to 100 bar/seconds. The aim of the first modification was the minimization of the drop in supply pressure when the main valve is opened. The aim of the second modification was to slower the pressure rise after the valve is opened.

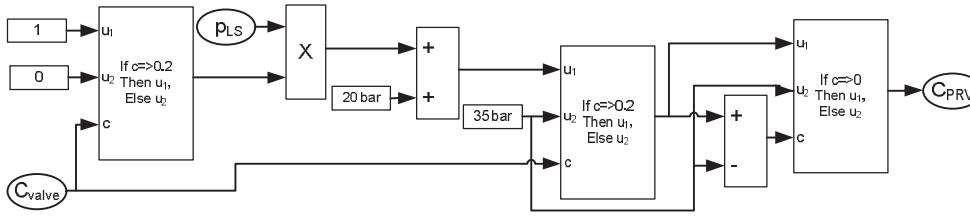

Figure 7: Schematic of the modified control system of the pressure relief valve.

In Figure 8, the simulation results with modified opening of the valve and with modified control system of the PRV are presented.

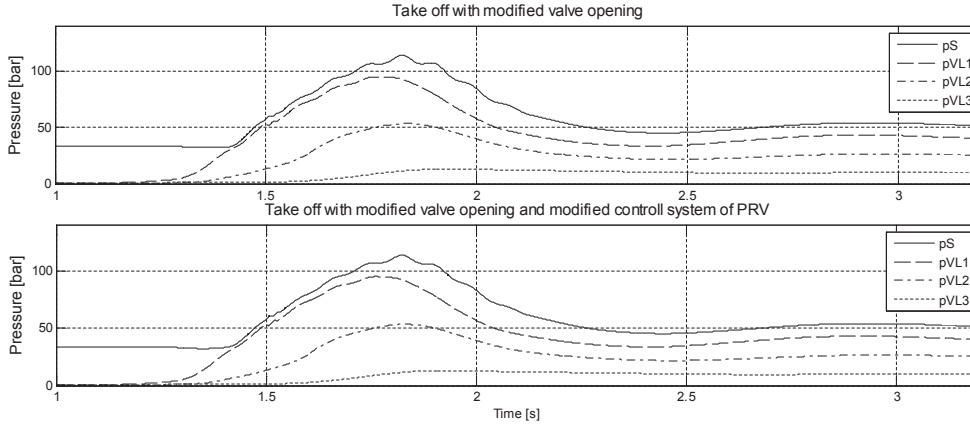

Figure 8: Simulated pressures with modified command signal of the main valve and modified PRV control

The Figure 8 shows that the opening of the valve has bigger effect on the pressure drop, than expected. Compared to the original system, described in Figure 2, the reduction of the pressure drop is significant. In both cases the pressure difference over the main valve is still insufficient for the pressure compensator to work correctly. The next modification is a constant command signal of the PRV. This modification was made to ensure sufficient pressure difference over main valve.

As it could be seen from the Figure 9, the system with constant supply pressure setting holds the pressure difference over the main valve sufficient. This ensures that the pressure compensator works correctly. The behavior of the pressure compensator with constant supply pressure setting, and with modified valve opening ramp are presented in Figure 10.

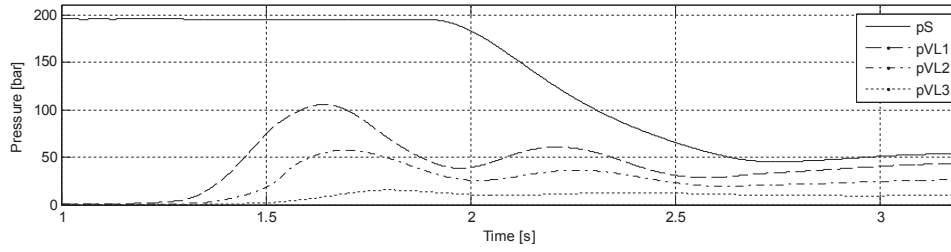

Figure 9: Simulation results with constant setting of the supply pressure

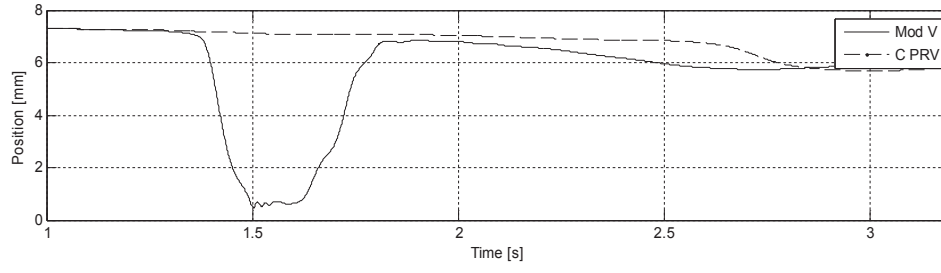

Figure 10: Position of the compensator with constant pressure setting and with modified valve opening.

In Figure 10, the position of the compensator with constant pressure setting is referred as C.PRV. With constant pressure setting the pressure compensator holds its position steadily. The modified valve opening is referred as Mod.V., in Figure 10. As it can be seen from the Figure 10, the pressure compensator, in the system with modified valve opening, first dives fast, but recovers at 1.8 seconds. After that, the pressure difference over the main valve is nearly constant.

3.2 Modifications of the Hydraulic Circuit

The torque created by the hydraulic motors rises too fast. This could be reduced by offering an auxiliary flow bath in parallel with motors. In to the simulation model by-pass valves were added in parallel with hydraulic motors. The schematic of the installation of by-pass valves is described in Figure 11.

The opening of by-pass valves is depends on the command signal of the main valve in following way: When the relative command signal of the main valve is more than 0.1 or when the derivative of the command signal of the main valve is zero, the command of the by-pass valve is 0. Otherwise the command signal of the by-pass valve is 1.

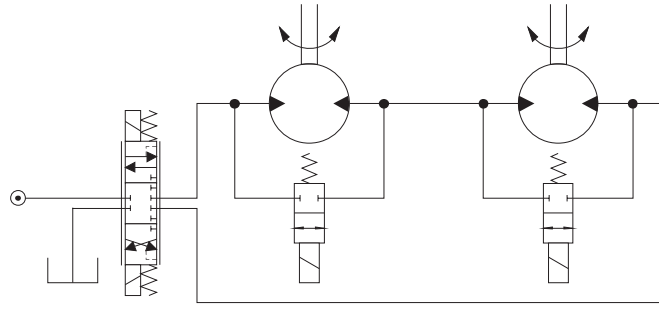

Figure 11: Motors with by-pass valves

The Figure 12 shows a schematic of the control system of by-pass valves, where C_{valve} is the command signal of the main valve, C_{bypass} is the command signal of by-pass valves.

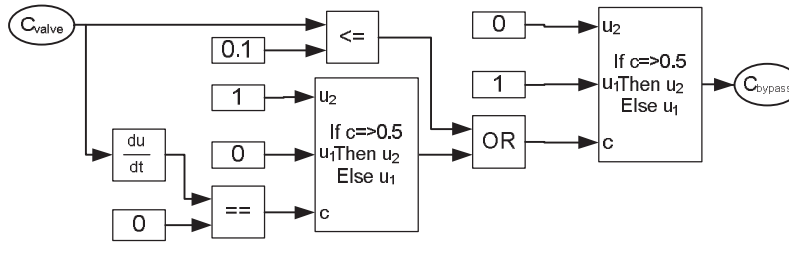

Figure 12: Control system of the by-pass valves

The effect of the by-pass valves are tested with two different nominal sizes. The simulated pressures in volumes are presented in Figure 13. In upper Figure the size of the by-pass valve is 1 liter/minute at 10 bars pressure difference, and in lower Figure the size is 2 L/min at 10 bars.

As it can be seen from the simulations results in Figure 13, the by-pass valve reduces the maximum pressure level. It also reduces the pressure difference over hydraulic motors. The controls system of the by-pass valves causes a pressure transient at the time of 2 seconds. With enhanced control system these results could be even better. It can be also seen, that the pressure differences over the main valve is bigger than original system, which means that the pressure compensator is working better.

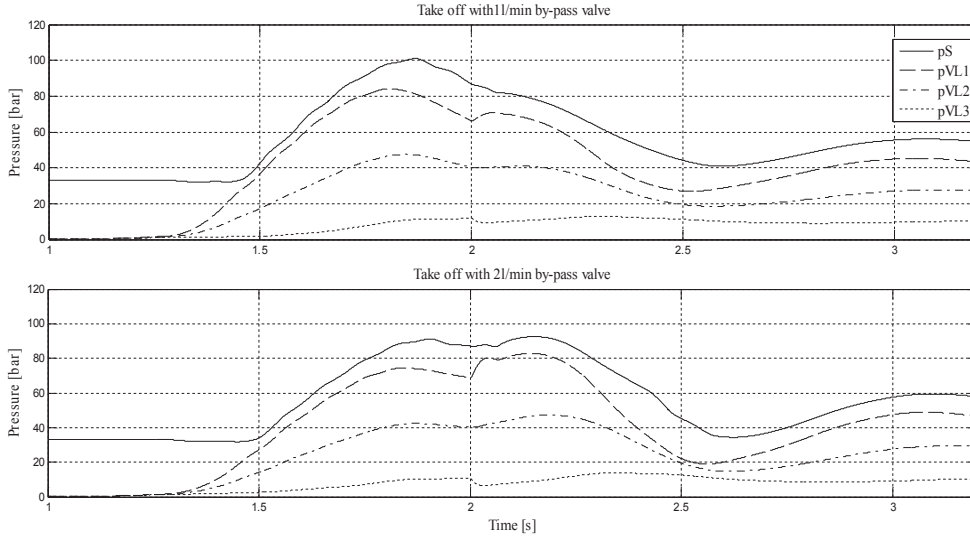

Figure 13: Pressures simulated with by-pass valve

3.3 Results of the Modifications

Acceleration is used as an indicator in this comparison. It is used because; it represents the effect of the traction force of the vehicle. The rotational speed of the hydraulic motor, which was used earlier, could be affected by the pitching motion.

As the Figure 14 shows modified systems work better than the original system. The smallest peak value of the acceleration is achieved with 2l/min by-pass valve. The acceleration difference between the original system and the best modified system is 1.32m/s^2, which means that the reduction is 41 percents.

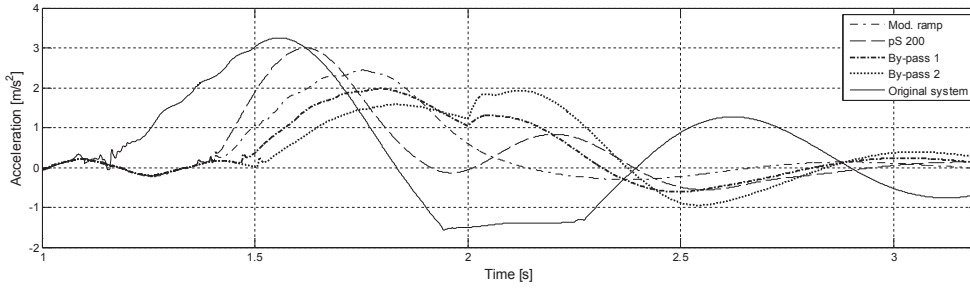

Figure 14: Accelerations of the original system, and of modified systems

Another important improvement of these modifications is the cavitation free operation of hydraulic motors. In this case cavitation includes two remarkable problems. First of all it ruins the motors and the rest of the system. Secondly it increases oscillations of the vehicle.

4. FUTURE WORK: TOWARDS DISTRIBUTED RESTRICTION EDGE CONTROL

The distributed restriction edge control was tested to fulfil the academic desire for knowledge. Tests were made with the simulation model used in this study. The model of the main valve, without compensator model, was modified in the way that it is possible to control its edges separately. Also the by-pass valves were included to the system. Command signals for restriction edges were produced by signal generators. Figure 15 presents simulation results of these introductory tests.

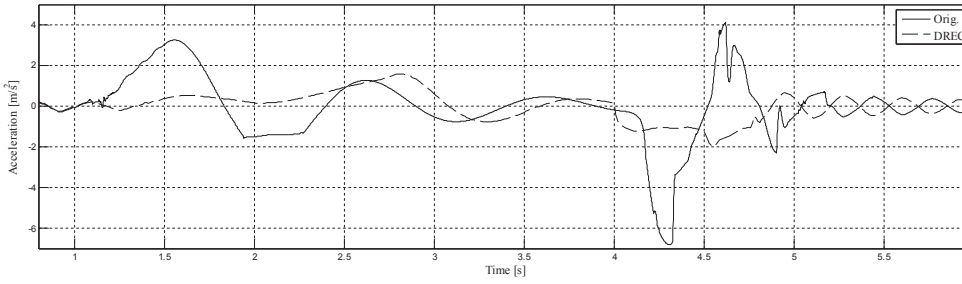

Figure 15: Simulated acceleration of the system with distributed restriction edge control vs. the original system

In Figure 15 Orig. refers to the simulation data of the original system, DREC refers to distributed restriction control. In this paper DREC is used as distributed restriction edge control.

As it can be seen from the Figure, the DREC is working quite well compared to the original system. Especially the stopping of the vehicle has improved. Even though, the development of the control system of the DREC is still in its initial phase.

In near future the control system of the DREC will be developed further. Also the hydraulic circuit will be developed more suitable for the use of DREC. In previous test, only volumes VL1 and VL3 were controlled. But in following studies also the volume VL2 will be controlled. This could give a possibility to control the pressure difference over each motor.

5. CONCLUSIONS

Verified simulation model gives a good way to understand the behaviour of a mobile machine. The simulation model produces broad variety of data that is not available through measurements of the real machine. Through careful analysis of simulation data, it is possible to point out the features, e.g. flaws in control system, which have negative impact on the behaviour of the vehicle.

The use of simulation model makes it easier and more reliable to test new control systems and hydraulic systems. In this study the control system of the pressure relief valve and the

opening of the main valve were modified. Also the hydraulic system was modified by adding by-pass in parallel with hydraulic motors. These modifications were made to achieve better controllability when the machine takes off. Simulation results of these modifications show that, by reducing the flaws of control system, and by modifying the hydraulic system it is quite easy to improve the operation of skid steered mobile machine.

Simulations of the original system and modified system show that the necessity of the pressure compensator could be questioned in this kind of solution. After all it worked properly only with constant pressure setting, and the results were not too encouraging.

Reduction of torque created by the motors had promising results. In this case the reduction was made with simple by-pass valves. Due to these results, the distributed restriction edge control could be an answer, when the torque of the motors needs to be reduced. Also the results shown in the future work chapter support this concept.

NOTATION

C_{valve}	Command signal of the main valve	[-]
C_{PRV}	Command signal of the pressure relief valve	[bar]
$C_{by\text{-}pass}$	Command signal of the by-pass valve	[-]
DREC	Distributed Restriction Edge Control	
FL, FR	Front motors Left and Right	
LS	Load-Sensing-signal line	
p_{LS}	Load-Sensing pressure	[bar]
P	Supply pressure line	
PRV	Pressure Relief Valve	
RL, RR	Rear motors Left and Right	
T	Tank line	
V_{L1}, V_{R1}	Volume of the hose, from port A to rear motor.	[m^3]
V_{L2}, V_{R2}	Volume of the hose that connects front and rear motors	[m^3]
V_{L3}, V_{R3}	Volume of the hose, from port B to front motor.	[m^3]

REFERENCES

(1) Uusisalo, J. et al., 2007, Portable Remote Control for Teleoperated Hydraulic Mobile Machine, Proc. of SICFP'07, Finland, 2007

(2) Vilenius, J., 2007, Characteristics of Valve Controlled Hydraulic Power Transmission in Teleoperated Skid Steered Mobile Machine, Dissertation NO 654, Tampere University of Technology, 2007

(3) Hyvönen, M. et al., 2006, Mathematical Model of the Valve Controlled Skid Steered Mobile Machine, Proc of FPNI'06, Denmark, 2006.

(4) Tsal,C-S. and Goyal, M.R., 1986, Dynamic Turbocharged Diesel Engine Model for Control Analysis and Design, SAE paper no.860455.

(5) Erkkilä, M., Dynamic Model of CVT Power Train, Proc of SICFP'07, Finland, 2007

(6) Canudas de Wit. el al, 1995, A New Model for Control of Systems with Friction, IEEE Transactions on Automatic Control, vol 40, pp. 419-425.

(7) Raneda, A. et al., 2003 Development of A Teleoperated Hydraulic Mobile Machine, Proc. of SICFP'03, Finland, 2003

Session 3
Control I

Synchronous motion control of thrust system of pipe jacking shield machine

Hu Shi, Guofang Gong, Huayong Yang
State key laboratory of fluid power transmission and control, China

ABSTRACT

This paper deals with the motion synchronization of the thrust jacks for pipe jacking shield tunneling machine. The thrust hydraulic system of the experimental shield machine is introduced. The system modeling together with synchronization motion control analysis of the thrust jacks is performed by means of computer simulations, investigating the factors impacting the thrust motion and the advance track of the machine. The experiment is conducted with the use of master-slave PID strategy with dead-band compensating control. The experimental results as well as the comparison of jacking motion with and without designed control practice show that the proposed thrust hydraulic system and its control strategy can meet the requirements of tunneling and achieve a satisfying performance.

1. INTRODUCTION

Pipe jacking shield machine, widely used in pipeline construction project such as underground drainage of city and gas transportation, is a kind of modern and popular construction machinery for tunneling.

The jacking system, driven by hydraulic power, is a key part of shield machine. The actuators are composed of several cylinders distributed rectangularly in the section of shield. The thrust system usually performs the basic task of jacking shield ahead while tunneling, and for more advanced operation, it is also responsible for controlling the attitude and position of shield ensuring that the shield can advance along the expected route. During excavating, the thrust hydraulic cylinders push shield forward while the cutter head located at the front of shield is revolving and cutting the earth.

Working under varying nonlinear loads, the shield tunneling machine has a high installed power. The advancement of the machine tracking the designed line is dependent on the thrust forces of the hydraulic cylinders, and the shield sometimes deviates from the alignment during excavation due to the complicated geological conditions and other unpredictable factors. Thus, the hydraulic jacking control system plays a very important role in shield machine tunneling[1][2].

The system with multi-actuator is always accompanied with the synchronization problem, the thrust system described in this paper is no exception. For the thrust control itself of the hydraulic system, it has been investigated in the term of speed and pressure control[3][4]. This paper firstly presents an experimental test station involved in this study and the jacking hydraulic system with pressure and flow compound control technique which is divided into six groups. In each group, it typically consists of a flow control proportional

Fluid Power and Motion Control 2008 Edited by Dr D N Johnston and Professor A R Plummer

valve and a pressure relief proportional valve. A major issue being considered in the study is synchronous motions of the thrust cylinders for straight line excavating, which are affected by uneven load acting on the cutter under the complex and bad excavating conditions. Motion analysis and modeling of jacking shield machine are also given. The simulation and experimental results demonstrate that the master-slave synchronous motion control adopting PID controller with dead band can guarantee a preferable non-synchronous error among the motions of the cylinders.

2. EXPERIMENTAL SYSTEM TEST STATION

2.1 Experimental test station

Figure 1 shows the experimental system of the pipe jacking shield machine. The test station consists of a cylindrical soil container for geoenvironment simulation, the jacking machine and the condition monitoring system. The soil container, with an inner diameter of 4000mm and an axial length of 6000mm, can be stuffed with a variety of soils which will be pressurized by the bag filled with high pressure water. The water bag loading system can assure the soil of the pressure up to 0.4MPa so that the jacking machine will be able to go through this artificial underground condition.

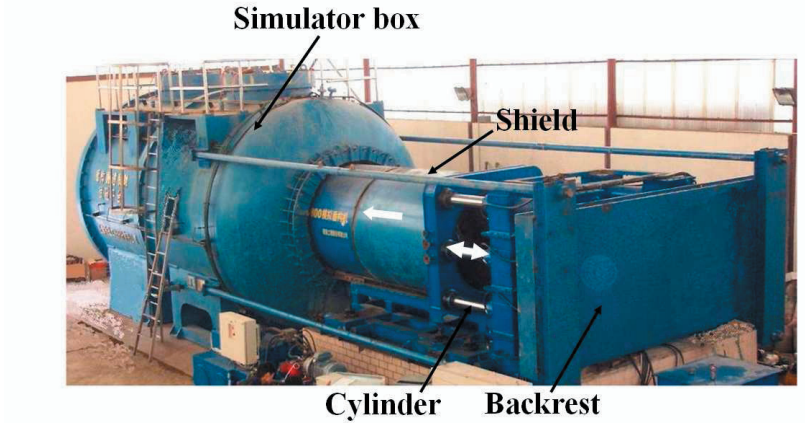

Figure 1 Experimental system

Figure 2 shows the schematic of the jacking machine. It is a EPB (earth pressure balance) jacking machine with a screw conveyor discharging the muck cut down by rotating cutterhead with a diameter of 1800mm. The jacking system is composed of six hydraulic cylinders which have the same stroke of 1500mm. The cylinder body is fixed with a backrest while the piston rod is movable to push the machine forward as shown in Figure 1. When the driving distance is beyond the stoke of the cylinder, the additional blocks are needed to be set between the machine and the hydraulic cylinder to relay the jacking process.

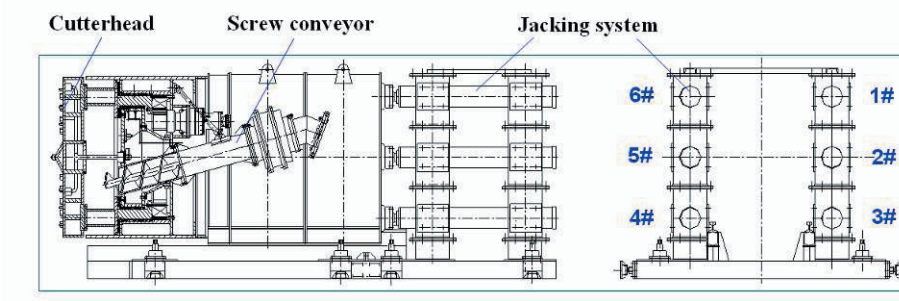

Figure 2 Experimental jacking machine

2.2 Hydraulic jacking system

The hydraulic system employed in the experiment for jacking shield thrust works according to the proportional pressure and flow regulation principle, as shown in Figure 3. The thrust hydraulic cylinders are divided into six identical groups to implement control task, and Figure 3 shows one group. The fluid flowing into each group is controlled by appropriate input signal of the flow control valve 2 while the working pressure is set by the pressure relief valve 3.

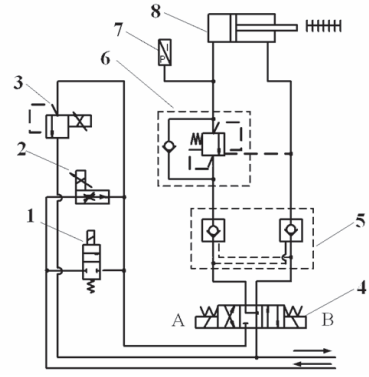

Figure 3 Hydraulic system of jacking machine

As shown in Figure 3, each group comprises a flow control proportional valve 2 and a pressure relief proportional valve 3 to achieve the flow and pressure compound control. The flow rate through flow control valve remains almost invariable as a combination hydrostat maintains a constant level of pressure difference across the proportional valve, irrespective of system or load pressure changes. Besides, the distributed fluid flow also partly passes through the pressure valve to ensure that the system pressure stays at a constant level. By adjusting the electric current through the coils of the valves, the pressure and flow rate of the system can be regulated to meet the thrust requirements. When tunneling, the solenoid B of 4-way directional valve 4 is energized, shifting the valve to its right position thus making cylinder piston rod move forward. Pressure sensor and the displacement sensor real-timely measure the pressure and the displacement of hydraulic cylinder which are subjected to online data transmission to the central control system so as to be compared with reference input signals to implement pressure and flow control respectively.

When the shield machine stops for adding the blocks, the hydraulic cylinders must be able to perform the retraction action separately with the 4-way valve 4 working at left position. Meanwhile, the flow valve is shorted by 2-way directional valve 1 to make a high flow rate running condition thereby high speed of the rod. There also exist a counterbalance valve 6 and a hydraulic lock 5 for each thrust group, the former assures a stable return movement while the latter locks the circuit to prevent leakage for safety protection when the cylinder thrust is released.

3. MOTION ANALYSIS AND MODELING

The problem of synchronizing multiple linear hydraulic actuators arises in hydraulic operated heavy-duty applications, where the synchronous operation of multiple hydraulic actuators under load has important performance implications[5]. This issue is most pronounced in hydraulically operated shield jacking machine thrust system under varying heavy loads when tunneling in straight line. Usually, there are three approaches to address the issue. The first is to design a flow divider circuit, the performance of which is restricted by flow divider itself and the compressibility of the working fluid. The second is to make actuators connected mechanically, which increases the system complexity in turn. The third is electro-hydraulic synchronization adopted in this paper, which is a closed loop system. Moreover, the last method can provide a much higher accuracy with simple operation.

Consider a hydraulic thrust system with n (here in this system n=6) ram-type cylinders acting to counter the excavating load, as shown in Figure 4. In view of the long installed distance between cylinders comparing with the trivial synchronization error as well as the issue of the synchronization motions in horizontal direction being addressed, it is assumed that the thrust system has 3 degrees of freedom of moving along the horizontal direction, pitch motion and rotation. The roll axis r is defined to be parallel to the line connecting cylinder 1 to cylinder 3 and the pitch axis p is defined be perpendicular to the line connecting the cylinder 1 to cylinder 3.

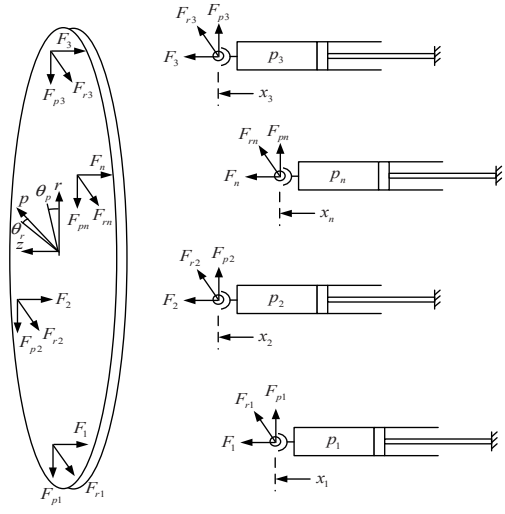

Figure 4 Diagram of acting forces in *n*-cylinder hydraulic thrust system

Figure 4 shows the forces acting on the hydraulic cylinders, The contact action between the cylinder and the load is equivalent to spherical contact surfaces. From Newton's second law and the conservation of angular momentum, the following equations can be obtained to represent the motion of the shield along horizontal direction and rotations about axes *r* and *p*:

$$\begin{cases} -\sum_{i=1}^{n} F_i - \sum_{i=1}^{n} F_{ri}\sin\theta_r - \sum_{i=1}^{n} F_{pi}\sin\theta_p = m\ddot{x}_p \\ \sum_{i=1}^{n}(F_i + F_{ri}\sin\theta_r)(-1)^{\sigma ri} l_{ri} = J_r\ddot{\theta}_r \\ \sum_{i=1}^{n}(F_i + F_{pi}\sin\theta_p)(-1)^{\sigma pi} l_{pi} = J_p\ddot{\theta}_p \end{cases} \quad (1)$$

where x_p represents the position of the center of the load (x_p=0 when the hydraulic cylinder extension is zero). m is the total mass of the load. In Eq. (1), F_i represents the reaction force acting on the cylinder i (i=1,2, ⋯ n) and l_{ri} (or l_{pi}) is the moment arm for F_i (i=1,2, ⋯ n) with respect to rotational axis r (or axis p). σ_{ri} (or σ_{ri}) represents the moment factor (σ_{ri} =0 when F_{ri}), J_r (or J_p) represents the rotational moment of inertia of the load about the axis r (or axis p) and θ_r (or θ_p) represents the rotation angle about the axis r (or axis p). F_{ri} (or F_{pi}) represents the friction force between the load and the cylinder along the direction of the axis r (or axis p).

Consider the forces F_i (i=1,2, ⋯ n) acting on the cylinders, the equations of motion for the cylinders can be represented by:

$$p_i A_i - F_i - F_{fi} - B_{pi}\dot{x}_i - \sum_{i=1}^{n} F_{ri}\sin\theta_r - \sum_{i=1}^{n} F_{pi}\sin\theta_p = m_i\ddot{x}_i \quad i=1,2,\ldots n, \quad (2)$$

where p_i represents the pressure in the chamber of cylinder i and A_i represents the effective piston area. m_i represents the piston mass of cylinder i. F_{fi} represents stiction and B_{pi} represents the viscous friction and coeffecient.

If the soils ahead of the jacking machine when thrusting are equivalently taken as a mass-spring-damper system with stiffness k_i and damping ratio b_i, then the contacting effect can be modeled by the following equation:

$$F_i = F_{si} + k_i x_i + b_i\dot{x}_i \text{ , } i=1,2,\ldots n, \quad (3)$$

where F_{si} represents the earth pressure at rest in the neighborhood of the acting point i. x_i represents the position of the cylinder group i relative to the tunnel lining ring.

The fluid that flows into each cylinder is controlled by a flow control valve. Consider the compressibility of the fluid in the cylinders and ignore the valve dynamics as well as leakages in the cylinders, the pressure dynamics in each cylinder can be represented by the following equation:

$$\dot{p}_i = \frac{\beta}{V(x_i)}[-A_i\dot{x}_i - K_{cei}p_i - K_{pqi}x_{pi} + K_{fqi}u_{qi}], \quad i=1,2,\cdots n \quad (4)$$

where $K_{cei} = K_{ci} + C_{ti}$

$$x_{pi} = \frac{K_{ui}u_{pi}}{s^2 + 2\xi_i\omega_{ni}s + \omega_{ni}^2}$$

In Eq. (4), β is the bulk modulus of the working fluid, V_i represents the total fluid volume to the respective cylinder chamber and C_{ti} is the leakage coefficient. K_{ci} and K_{pqi} are the flow-

pressure coefficient and the flow coefficient of the pressure relief valve in group *i*. K_{fqi} is the flow coefficient of the flow control valve in group *i*. u_{pi} and u_{qi} are the control input signals of the pressure and the flow valves. x_{pi} is the poppet displacement of the pressure valve in group *i*.

4. CONTROL STRATEGY

Considering variations in loads, fluid volume in cylinders and fluid viscosity, a closed-loop control system with master/slave strategy is adopted in the electro-hydraulic thrust system of the shield jacking machine. It means that one group of cylinders track another group's displacement and keep error within a specified range. As shown in Figure 5 which represents the control model of two opposite cylinders, synchronization control is attained by a speed error feedback correction. Because the variation of load leads to discontinuous push velocity, the goal of outer-loop control is to compensate discontinuous push velocity by means of regulating input voltage of the proportional pressure valve while the inner-loop control takes charge of the flow rate regulation with the flow control proportional valves. There are cylinder 1 as a master, cylinder 2 as a slave, and controller 3 as a displacement compensator for synchronization control. Cylinder 1 is taken as the reference cylinder, whose movement has to be followed by cylinder 2.

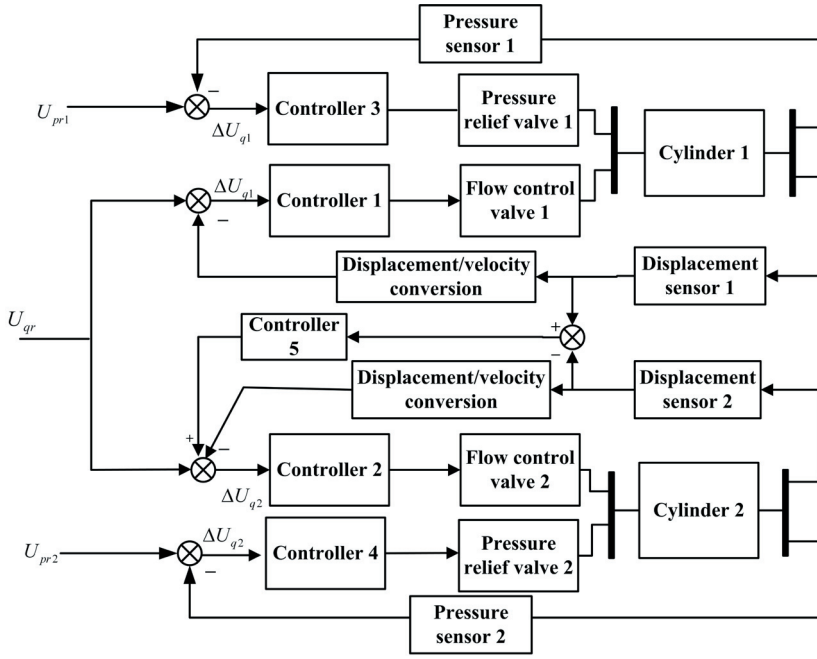

Figure 5 Block diagram of the motion synchronization

In this work, taking into account of the practicability as well as the engineering application requirements, controller 5 is a proportional integral derivative controller with dead band to prevent the oscillation as a result of highly frequent adjustments. As shown in Figure 6, the control parameters can be described by

$$p(t)=\begin{cases} e(t), & \text{when } |e(t)|=|y(t)-r(t)|>\varepsilon \\ 0, & \text{when } |e(t)|=|y(t)-r(t)|\le\varepsilon \end{cases}$$

where *r(t)* is input, *y(t)* output, *e(t)* error signal, ε a variable band parameter. It is equal to a nonlinear control method in essence. Two displacement sensors measure the displacement of two cylinders which will be subject to subtraction. The displacement error delivered to controller 5 will be checked whether it falls in the acceptable limit of error namely dead band. If yes, the output of controller 5 will be zero. Otherwise, controller 5 functions combining with embedded proportional integral derivative control algorithm, adding its output value to the reference input of cylinder 2 flow regulation so as to accompany cylinder 1 in displacement.

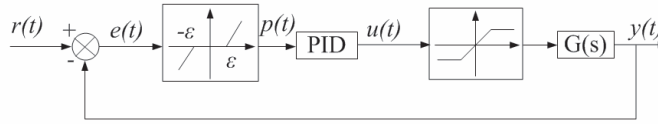

Figure 6 Block diagram of the PID control system with dead band

5. SIMULATION

The simulation is carried out in Matlab/Simulink environment which is also in the charge of control model creating. The two figures in Figure 7 present the influence of the hydraulic valves and the working load on the cylinder motion. As we all know, any two different hydraulic flow control valves can not have the identical parameters, so changing coefficient will definitely disturb the steady motion. That case is also the same to the uncertain and unknown loads caused by excavating the soils. Figure 7 (a) and (b) show the speed responses under the different flow control valve parameters and different viscous damping coefficients of load. It can be seen that the latter is more crucial to the motion synchronization than the former.

The two figures in Figure 8 illustrate the simulation results of synchronous motion control with the above described control method. Incorporating the disturbances of valve and load in simulation, the two cylinders being considered have a striking difference in working condition, but the moving velocity is in agreement with each other after the shaking response for compensation at the starting point. As a result of the same running speed, the displacement of the following cylinder follows the reference one precisely. From Figure 8(b) it can be noted that the displacement error between two cylinders is approximately 0.35mm, which definitely satisfies the requirements in engineering applications.

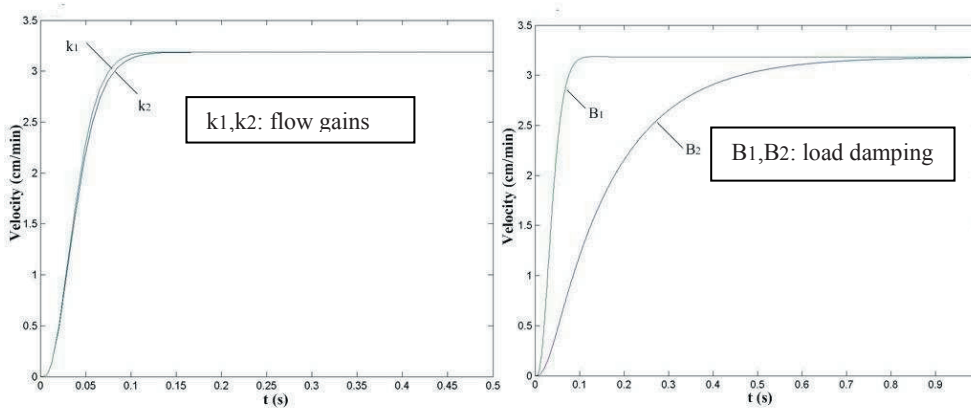

(a) **(b)**

Figure 7 Influence of hydraulic system and load on jacking speed

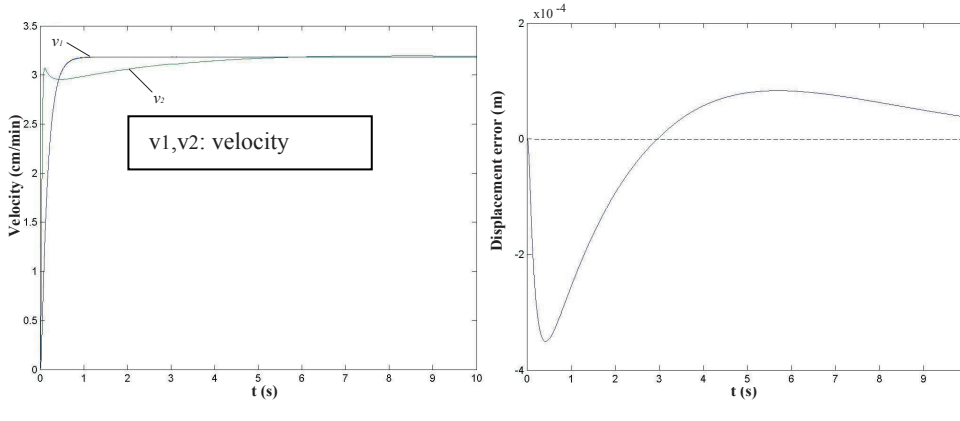

(a) **(b)**

Figure 8 Simulation results of synchronous motion control of two cylinders

6. EXPERIMENT

In this project, experiments are conducted with a test rig mentioned in the earlier part of this paper. For synchronous motion control, unequal load is applied on the hydraulic cylinders installed in symmetric position.

Figure 9 shows the experimental results of the synchronous motion control in the case of simulating the tunneling through soft clay layer in the test soil box. It can be seen from Figure 9(a) that the velocity curve of the following cylinder is much smoother than the reference one, but both are kept at the level of 36 mm/min. This control scheme has proven to be effective in obtaining good motion synchronization performance as shown in Figure

9(b) and Figure 9(c), achieving a high displacement agreement through the whole thrust course with the displacement error being limited within ±3mm, under large pressure difference of two thrust cylinders caused by uneven and varying load applied on the excavated soil as shown in Figure 9(d). Furthermore, to demonstrate the disagreement without employing the synchronous control strategy, Figure 10 gives the displacements and error of two cylinders as well as the machine angle resulted in by non-synchronous motion in a given test distance.

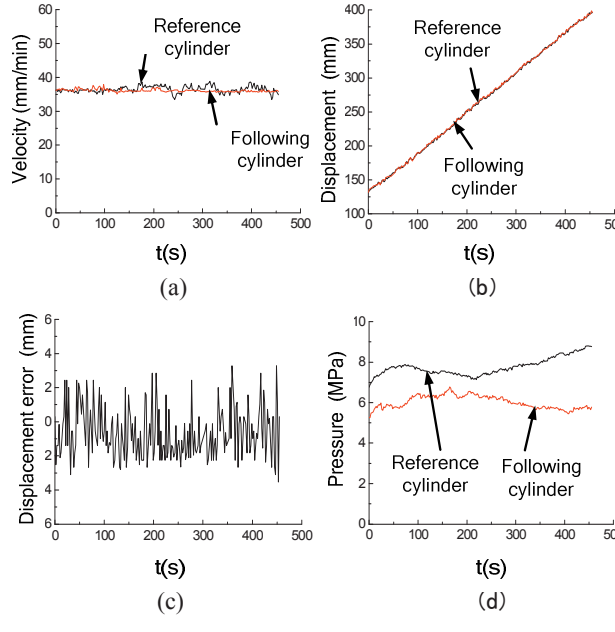

Figure 9 Measured synchronous motion behavior of two symmetric cylinders

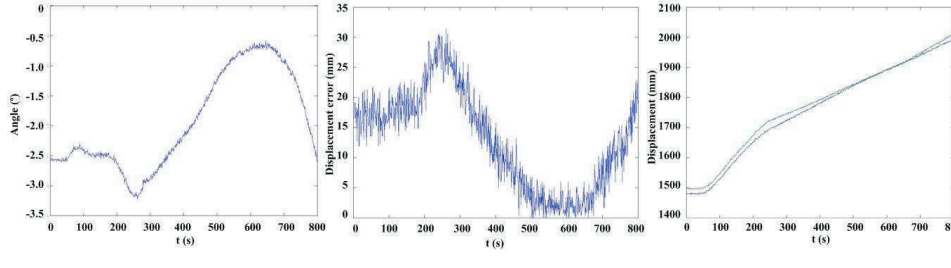

Figure 10 Measured non-synchronous motion behavior of two symmetric cylinders

7.CONCLUSION

This paper proposes an electro-hydraulic jacking system and its motion synchronization control. With the closed-loop master/slave control scheme, this system guarantees low non-synchronous error by applying a controller for compensating the displacement error between the reference and following cylinders. The experimental results show that the non-synchronous error can be kept within ±3mm under large pressure difference.

8.ACKNOWLEDGEMENT

This project is funded by National Outstanding Youth Foundation of China (No.50425518) and National Basic Research Program (973 Program) of China (No.2007CB714004). Their support is gratefully appreciated.

References

.

[1] Walter, W., and Herbert, H., *Hydraulic control system for and methods of controlling the operation of tunnelling apparatus*, United States Patent, 1983, 4391553.

[2] Maidl,B., Herrenknecht,M., and Anheuser,L., *Mechanised shield tunneling*, Ernst & Sohn, VCH, Berlin, 1996.

[3] Hu, G., Gong, G., and Yang H., "Electro-hydraulic control system of shield tunnel boring machine for simulator stand," *Proceedings of the 6th international conference on fluid power transmission and control*, Hangzhou, China, 2005:94-99.

[4] Hu, G., Gong, G., and Yang H., "Thrust hydraulic system of shield tunnel boring machine with pressure and flow compound control," *Chinese Journal of Mechanical Engineering*, 42(6),2006:124-127. (in Chinese)

[5] Hong, S., and George T. C., "Motion synchronization for dual-cylinder electrohydraulic lift systems." *IEEE/ ASME transactions on mechatronics*, 7(2), 2002:171-181

Improvement in Feedback Signal Quality for Water Hydraulic Manipulator

Ali Muhammad*, Jouni Mattila*, Tapio Virvalo* and Matti Vilenius*
*Department of Intelligent Hydraulics and Automation, Tampere University of Technology

ABSTRACT

The performance of hydraulic positioning servo systems is very often limited by the poor dynamics of the valve and the actuator. The use of velocity and acceleration as feedback signals can significantly improve the dynamic response of such system. However, this improvement depends on the quality of the feedback signal. In this paper we investigate the possible improvement in the quality of the feedback signal and its effect on the dynamic performance of the system. A step-by-step approach is followed starting from a single hydraulic cylinder and then extending the findings to a 5-DOF water hydraulic manipulator.

NOMENCLATURE

DOF	:	Degrees of freedom	q_e	:	Joint angle error
K_a	:	Acceleration feedback gain	q_m	:	Measured joint angle
K_f	:	Velocity feed-forward gain	T_s	:	Sampling time
K_h	:	Feedback gain	u	:	Control signal
K_p	:	Proportional gain	ξ_d	:	Desired damping
K_{qa}	:	Velocity gain	ξ_n	:	Natural damping
K_v	:	Velocity feedback gain	ω_d	:	Desired frequency
q_d	:	Desired joint angle	ω_n	:	Natural frequency

1. INTRODUCTION

Hydraulic servo systems can exhibit poor and variable dynamics, limiting the closed loop gains. In addition, the positioning accuracy of hydraulic drives suffers from several nonlinearities which exist in the valve and the actuator. The most dominant of these nonlinearities are the valve offset and hysteresis, the friction in the load and the actuator and the leakage both in the valve and the actuator. Despite their drawbacks, hydraulic servo systems still compete with their electrical counterparts in demanding industrial applications because of their high power to size ratio and reliability (1).

Fluid Power and Motion Control 2008 Edited by Dr D N Johnston and Professor A R Plummer

The most popular controller used in hydraulic position servo systems is the P-controller. Though robust, it gives a very sluggish response when tuned using robustness criteria (2). Another drawback of the P-controller is that it provides a very limited possibility to influence the system dynamics. As a result, a lot of research has been done to investigate and to develop better solutions.

In (3), the traditional PI-controller has been modified to implement a nonlinear PI-controller. However, the testing of the controller was limited only to a single joint of a hydraulic manipulator. On the other hand, Virvalo has suggested avoiding the integral term in controllers for hydraulic position servo systems (4). It has been shown that because of the nonlinearities in the valve, the use of the integrator can lead to a hunting behaviour. Moreover, Virvalo has compared the performance of the P-controller, the filtered P-controller (P-controller with the first order lag) and the state-feedback controller with varying loads (5). The results show that the performance of the state-feedback controller depends on the load variation. Linjama (2) has analysed the robustness of the same controllers with a focus on the parameter variations and sampling time. He concluded that one has to be careful when state-feedback control is realized in practice. In (6), Torben tests a set of linear controllers on a two joint manipulator driven by linear hydraulic drives. Bonchis has documented the performance of a very wide range of controllers for hydraulic drives in his work (7). But once again all the tests were performed on a single joint of a mining manipulator.

Since hydraulic drives exhibit nonlinear and variable characteristics, many researchers have investigated solutions using nonlinear and adaptive controllers. The use of linearised pressure dynamics as a feedback has been studied in (8). The system was found to be robust against the load and parameter variations, but position tracking results were not remarkable. In the same study, Torben also tests adaptive controllers on a two joint manipulator driven by linear hydraulic drives. In this case, despite attaining better accuracy, the position tracking exhibit chattering due to the noise in the velocity feedback signal. In (9), Tochizawa conducts experiments with a two joint manipulator driven by rotary hydraulic actuators. The controllers have been compared under the condition of varying load on the manipulator. The adaptive controller was found much more complicated to implement but it did not guarantee any more accuracy than the classical controller.

The paragraphs above provide only a glimpse of the developments in the control of hydraulic position servo systems. The majority of the research has been done with oil hydraulic actuators, and more importantly, with systems composed only of one or two actuators. Considering the nonlinearities of hydraulic components, the situation actually gets worse with water hydraulic actuators. The choice for water hydraulic components is much more limited and the quality of the water hydraulic servo valves is not as high as that of the oil hydraulic servo valves. The leakage is normally higher due to low viscosity, and so is the friction in the actuator. Despite these limitations, the characteristic advantages of hydraulics together with water as the pressure medium (fire and environmentally safe, chemically neutral, not activated, not affected by radiation) are highlighted in critical applications such as remote handling operations in the International Thermonuclear Experimental Reactor (ITER) (10).

With these developments in water hydraulic applications, it is clear that an investigation in the control techniques is required to improve the position control of these systems. The positioning response is important not only to move such water hydraulic manipulators from point to point in space, but also to employ the force control techniques, such as the position-based impedance control (PBIC), where the performance of the scheme heavily depends on the performance of the internal position control loop (11).

In the following section, we will briefly discuss the background and the choice for state-feedback controller in our study. Section 3 presents the experimental setups of 1-DOF and 5-DOF manipulators. We will develop the state-feedback controller for 1-DOF setup and analyse the effect of the quality of the feedback signals on the performance of the system in section 4. The results from section 4 will be used to implement and test the controller for 5-DOF manipulator in section 5. In the last section, we will draw the conclusions on the basis of our results and describe the future goals.

2. STATE-FEEDBACK CONTROLLER AND HYDRAULIC MANIPULATORS

A dexterous manipulator composed of water hydraulic actuators is a requirement for carrying out remote handling operations in the diverter region of ITER. The application is demanding in terms of compactness, reliability, dexterity and accuracy. The manipulator should be operable remotely and include the master-slave scheme. The positioning response and accuracy are important not only for point-to-point motion of the manipulator in space but also for the employment of the force control schemes, such as position based impedance control (PBIC) or hybrid position and force control (11). Since hydraulic components (both water and oil) exhibit poor dynamics, the performance can only be improved by using control techniques that can improve the dynamics of the system.

It is well known that the use of states such as velocity and acceleration as feedback can considerably improve the dynamics of fluid power (hydraulic) servo systems. As a result, higher closed loop gains can be used for improved dynamic response and reduced steady state error. Controllers employing such technique are widely termed as state-feedback controllers. The characteristics of the state-feedback controller can be useful in hydraulic manipulators, where the dynamic response of each drive propagates further, to strongly diminish the end-effecter positioning response.

The design of the state-feedback controller is based on the principal of selecting new pole locations. Figure 1 shows the state-feedback controller with ideal feedback signals. Mathematically the modified linear model of the system can be written as in equation 1.

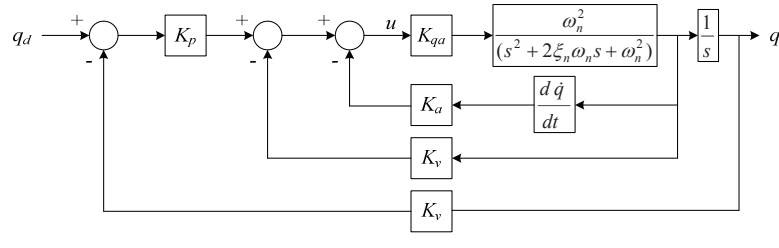

Figure 1: State-feedback controller with ideal feedbacks

$$\frac{Q(s)}{U(s)} = \frac{K_p K_{qa} \omega_n^{\ 2}}{s^3 + (2\xi_n \omega_n + K_a K_{qa} \omega_n^{\ 2}) s^2 + (\omega_n^{\ 2} + K_v K_{qa} \omega_n^{\ 2}) s + K_p K_{qa} \omega_n^{\ 2}} \tag{1}$$

Assuming ideal feedback of the states (velocity and acceleration), the poles of the above system can be selected as desired, by modifying the feedback gains. In practice this means using both velocity and acceleration sensors, which will result in additional cost and complicated instrumentation, especially in the systems with several hydraulic actuators. If the velocity sensor will be used alone, the quality of the acceleration signal will depend on the resolution of the velocity sensor, and if the acceleration sensor will be used alone, the integration will result in an offset in the velocity signal.

In practice, velocity and acceleration signals are obtained by numerical differentiation of the position signal. This results in poor quality velocity and acceleration signals. The reason is the quantisation noise, which is inversely proportional to the resolution of encoder/resolver and directly proportional to the sampling period. Increasing the resolution of the encoder/resolver may improve the performance, but this will result in increased instrumentation cost. Also, it does not provide the complete answer, because the quantisation noise may still appear at small velocities. In figure 2, the realisation of the state-feedback controller is shown where only position feedback signal is available.

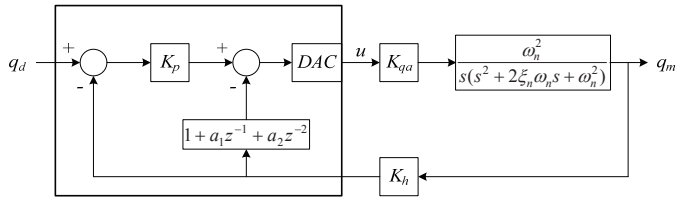

Figure 2: Realisation of state controller

To fully utilize the capabilities of the state-feedback controller, velocity and acceleration signals of a relatively good quality are required. This requirement reduces its practical application in several cases (2). In (12) Mäkinen evaluates the effects of the feedback signal quality on the position servo control of a pneumatic drive. The best results were achieved by using an observer to calculate the velocity and the acceleration feedback signals. Mäkinen also shows that the use of a filter results either in too much delay or in a failure to eliminate the quantisation noise completely. In (13), Virvalo concludes that a high resolution of the position encoder is required to implement the state-feedback controller for the hydraulic drives. The study showed that good results can be obtained when an n-sample estimator is used to calculate the velocity and acceleration signals. Implementation of an n-sample estimator is shown in equation 2. The principle of the observer and its implementation is shown in figure 3.

$$\dot{q}(k) = \frac{q(k) - q(k-n)}{n \cdot T_s} \tag{2}$$

By using the approach in (2) and (5) we implemented the state-feedback controllers for the 1-DOF hydraulic test setup presented in the next section. Figure 4 shows the step response of the system for different implementations of the state-feedback controller. In figure 4a the

velocity and the acceleration signals have been obtained using 4-sample and 2-sample estimators respectively. In figure 4b the velocity and acceleration signals have been obtained using 8-sample and 4-sample estimators respectively. In figure 4c both states have been obtained using the observer.

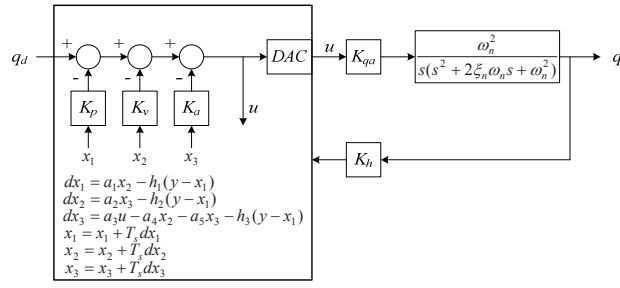

Figure 3: Realisation of states' observer

All the controllers have been tuned in such a way to obtain the fastest dynamic response without any overshoot. It has to be mentioned here that the offset of the valve has been adjusted to obtain a steady state positioning accuracy better than $\pm 0.005^o$. The dynamic response is reasonable in all three cases. The settling time is much longer for the first case, since much lower gains were possible because of larger amounts of quantisation noise in the feedback signals. When the observer is used to obtain the feedback signals (figure 4c) the highest gains were possible and the dynamic response is the smoothest.

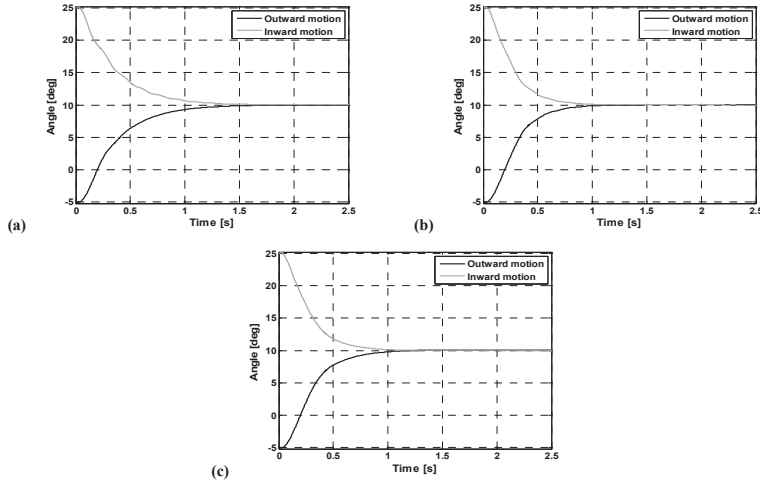

Figure 4: System response for a large step input

However, a large step is never a realistic input for a manipulator. Most of the time manipulators are required to follow smooth position profiles in space. These profiles are designed according to the dynamic limitations of the manipulator and the task at hand. In most hydraulic manipulators, the driving velocity is limited because of large manipulator size and supply pressure. These lower velocities and accelerations result in a much higher quantisation noise and thus strongly restrict the servo loop gains.

Another realistic input for a manipulator is a small position step. When a force controlled manipulator comes in contact with the environment, it should react to the forces to avoid damage to the environment and to itself. In such cases small deflections in the position of the manipulator are required. These small changes in position result in higher quantisation noise distorting the dynamic response, which may lead to undesirable results.

3. EXPERIMENTAL SETUP

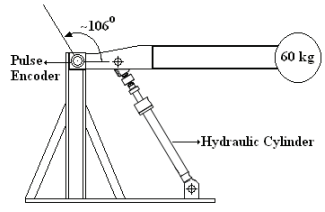

Figure 5: 1-DOF test bench

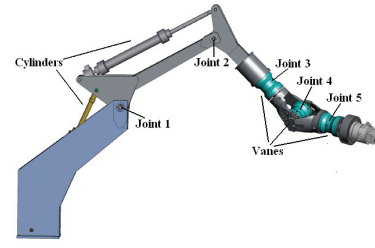

Figure 6: 5-DOF manipulator

Initial experiments were performed using the 1-DOF hydraulic test bench sketched in Figure 5. Cylinder dimensions are 35/25-300 mm and the arm can be driven up to 106°. A load of 60 kg is attached at the end of the arm to give it a realistic behaviour of a manipulator link. The inertia load on the piston is around 4000 kgm^{2}at the nominal position. The cylinder is driven by a flow control servo valve with a flow rate of 4 l/min at a nominal pressure of 3.5 MPa (35 bar) per control notch. The position of the arm is measured by using a pulse encoder with a resolution of 5000×50×4 pulses/revolution. The sampling frequency of the system is 1 kHz. A supply pressure of 12 MPa (120 bar) is used in this case.

The final implementation and testing is done using the 5-DOF water hydraulic manipulator shown in Figure 6. The manipulator consists of a 2-link planar arm with shoulder and elbow rotational joints, powered by the water hydraulic cylinders. The end of the planar arm is fitted with a robotic wrist, with three rotational joints powered by the water hydraulic vane actuators. The dimensions of the cylinders for the first and the second joint are 63/32-350 mm and 50/28-350 mm respectively. The cylinders and vanes are driven by flow control servo valves with a flow rate of 6 l/min and 4 l/min at a nominal pressure of 3.5 MPa (35 bar) per control notch respectively. The joint angles are measured using pulse encoders with a resolution of 5000×25 pulses/revolution. The sampling frequency of the system is 1 kHz. A supply pressure of 20 MPa (200 bar) is used.

4. EXPERIMENTAL RESULTS WITH 1-DOF SETUP

In this section we will consider the performance of the state-feedback controller when the position input is either a profile with a small velocity or a small step. The tuning parameters of the controllers and the valve offset adjustment are kept the same as for a large step input of figure 4. Figure 7 shows two realistic position profiles which can be used as an input to a

manipulator. With these profiles, the response of the system can be tested for both inward and outward motion of the cylinder.

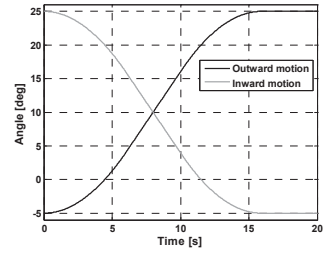

Figure 7: Position input profile (maximum velocity 3 deg/s)

During the motion of the arm, velocity and acceleration feedback signals were recorded and are shown here in figure 8 and 9 respectively. In figures 8b, 8c and 8d, the velocity feedback signal has been obtained using the 4-sample estimator, the 8-sample estimator and the observer respectively. For comparison, in figure 8a we also have a plot of the velocity signal obtained by direct differentiation (Euler's method) of the position feedback signal. It is clear from these plots that the multi-sample estimator reduces a considerable amount of the quantisation noise, but at the same time the feedback is delayed, depending on the number of samples used. Although there is some delay (approximately 4 samples) in the feedback signal obtained from the observer, the signal is far smoother than in all other cases. In section 5 we will discuss a possible approach to reduce this delay.

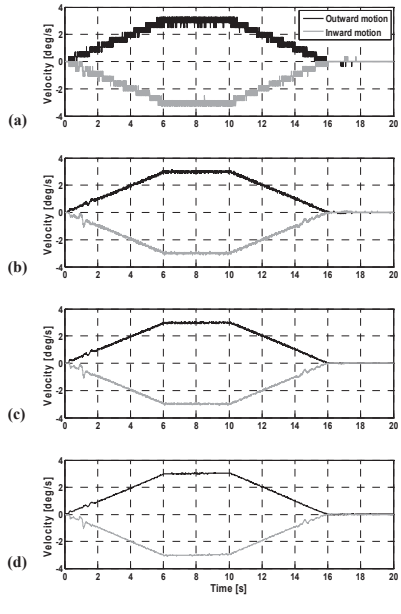

Figure 8: Velocity feedback signal

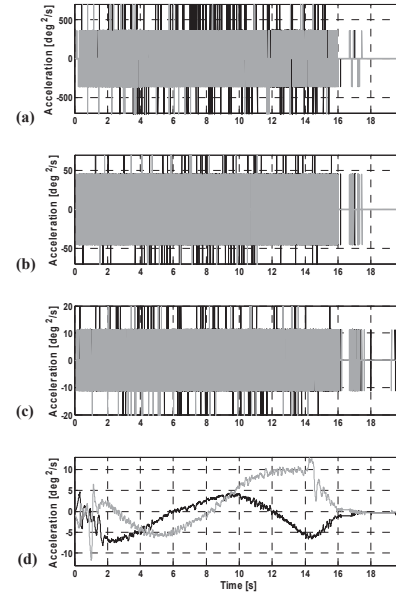

Figure 9: Acceleration feedback signal

In figures 9b, 9c and 9d, the acceleration feedback signal has been obtained using the 2-sample estimator, the 4-sample estimator and the observer respectively. A striking difference between the qualities of the acceleration feedback signals can be observed from these plots. The acceleration feedback obtained from the observer is a meaningful signal and can be utilized effectively for the control purpose (in this case to improve the damping of the system). The acceleration feedback signal in the other cases is far too noisy. The signal-to-noise ratio is quite high and can seriously restrict the possible effectiveness of the state-feedback controller.

The tracking error for each controller is shown in figure 10 in the same sequence as above, and figure 11 shows the controller output for each response respectively. As the noise level in the feedback signal is reduced, much higher gains can be used, resulting in smaller tracking errors. The tracking error has been reduced by more than half when the observer has been used to obtain the states.

Another observed behaviour was the quite audible and the noticeable vibrations during the tracking response in figure 10a. The reason becomes very clear from the controller output plot in figure 11a. Not only did the use of the observer result in reduced tracking error but the response is also far smoother. This is a very important characteristic when the controller is used in the multi-DOF case, as these minor vibrations can lead to a completely unstable system.

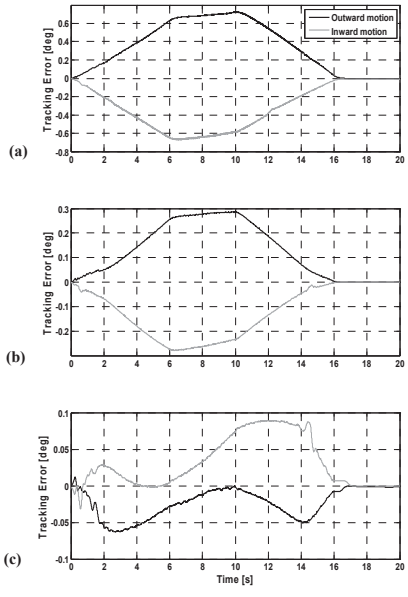

Figure 10: Tracking error

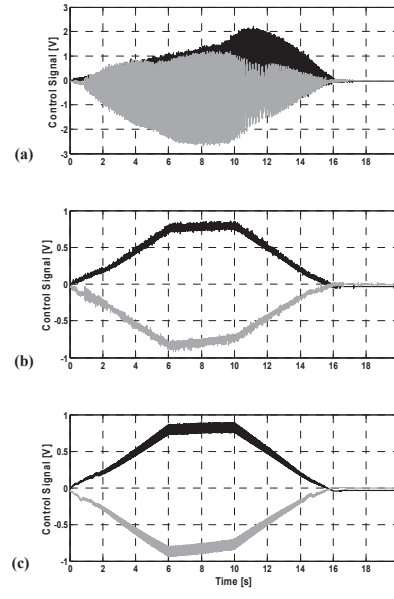

Figure 11: Controller output

In figure 12, the plots show the response of the system for the same controllers when a small step input is used. Although the system remains stable and no overshoot occurs, the dynamic response of the controller is far less smooth when the velocity and acceleration

feedbacks are obtained using the n-sample estimators (figures 12a and 12b). Because of the manipulator's chain like structure, these small vibrations can propagate from joint to joint and lead to undesired behaviour of the manipulator's end-effecter. The reason for this is fewer samples for the n-sample estimator during a small motion. The dynamic response of the system remains smooth when the observer is used to obtain the states (figure 12c), which makes it a good candidate for further study and applications for multi-DOF hydraulic manipulators.

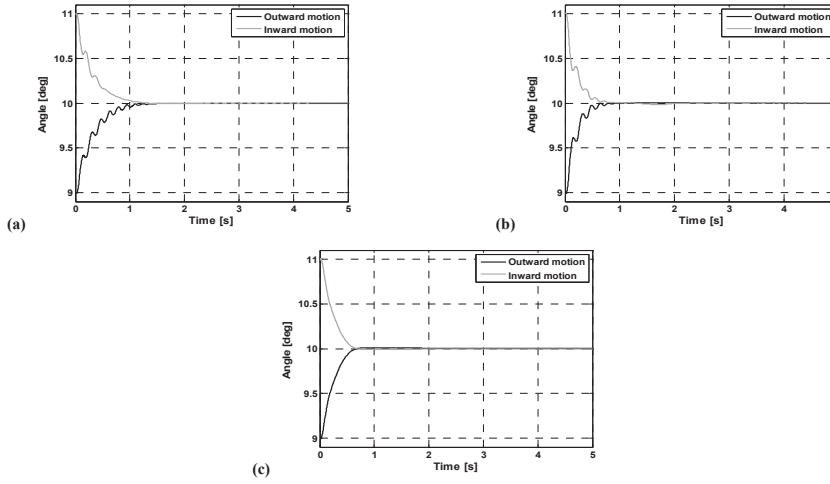

Figure 12: System response for a small step input

5. EXPERIMENTAL RESULTS WITH 5-DOF MANIPULATOR

On the basis of the results in the last section, it can be concluded that if the states are obtained from the observer, state-feedback controller can be used for improved dynamic response of hydraulic manipulators. However, before the application of this approach, we made some further improvement in the observer outputs. The goal of the observer is to keep a minimum error between the actual and the calculated states of the system. Normally, the observer is designed with the same sampling time as the controller and solved once per sampling period. For this case, the position error of the observer is shown in figure 13a. Large deviations can be noticed at the beginning, and an oscillatory behaviour at the end.

The observer calculates the states of the system using the difference equations shown in figure 3. The calculations will produce a better result if a smaller sampling time is used for the integrators and the observer can be solved more than once during the sampling period of the controller. We used a sampling time that is half of the controller's sampling time and solved the observer five times faster than the controller. Figure 13b shows the position error between the calculated and the measured position of the system. The deviations are much smaller, and more importantly, no vibrations are observed in the response. Also, in this case the output of the observer matches with the system output in much less time (approximately 50 milliseconds). This again can be a useful approach in hydraulic manipulators, since the dynamics of the actuators varies considerably, depending on the posture of the manipulator.

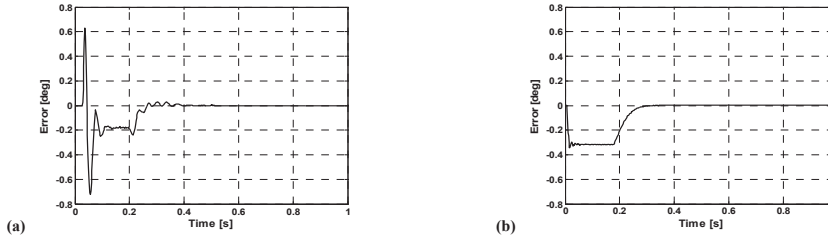

Figure 13: Observer position error

The state-feedback controller was designed using feedbacks obtained from the observer, for each joint of the 5-DOF water hydraulic manipulator. The tracking response and the error for four different profiles are shown in figures 14 and 15. The manipulator remains stable in its entire workspace. The tracking and the steady state error is still relatively large at the end-effecter. This can be improved considerably if the non-linearities, such as the valves' offsets and leakages are adjusted, which is beyond the scope of our current work.

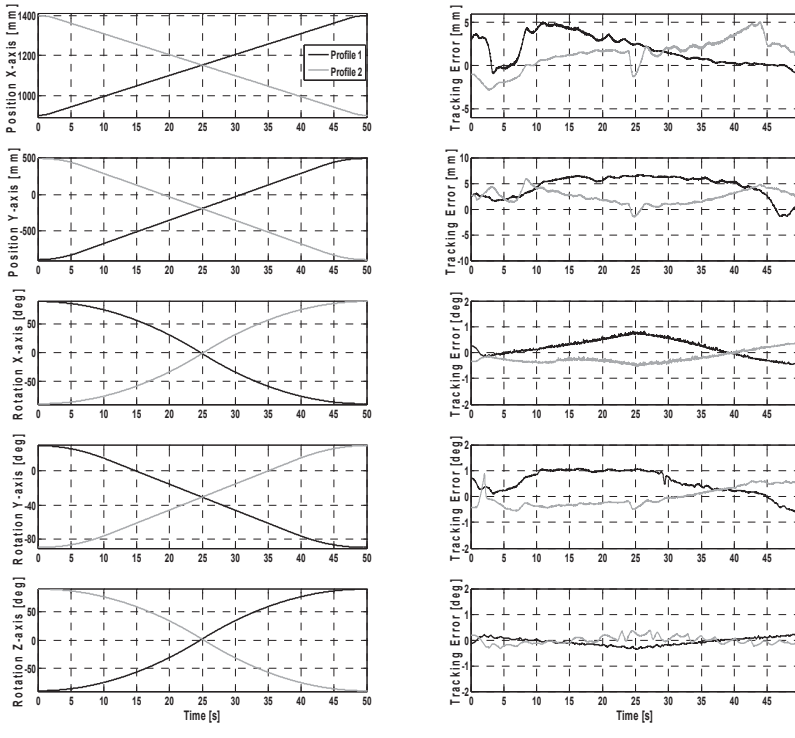

Figure 14: Position response and tracking error

During our study we also developed state-feedback controllers using the n-sample estimators for the calculation of the states as mentioned in the last section. The results are not shown here, but it was found that the stability of the manipulator was not guaranteed in the entire work space. The robustness was severely compromised and the manipulator repeatedly went unstable.

Figures 16 and 17 show the response of the manipulator's end-effecter for a small step input. The response is acceptable and the manipulator moves from one position to another in a swift manner. The noticeable overshoot is due to the presence of a relatively large hysteresis in the servo valve of the second joint of the manipulator. In fact, the manipulator starts to drift again after reaching to steady state, which is again due to the hysteresis in the servo valve.

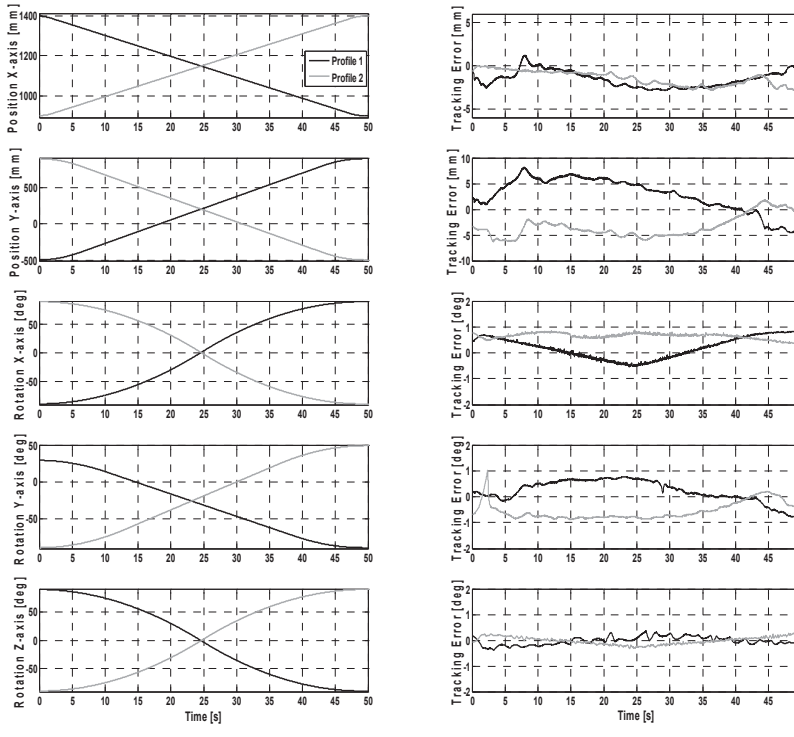

Figure 15: Position response and tracking error

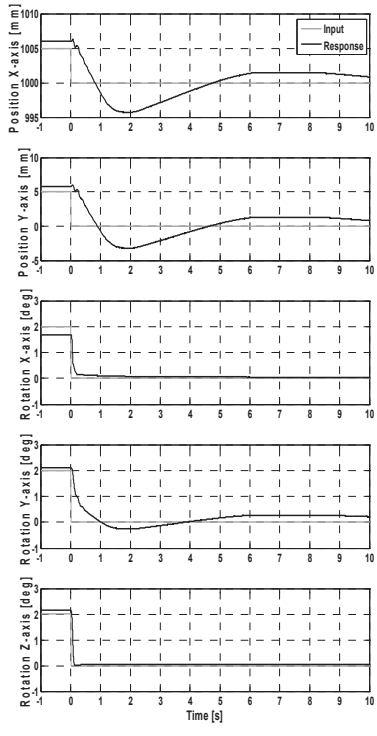

Figure 16: Step response

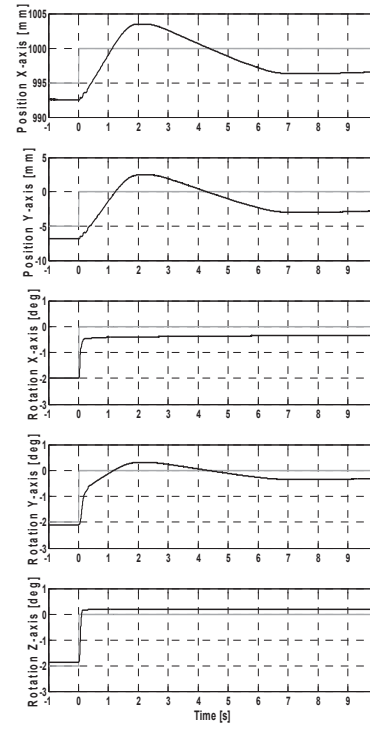

Figure 17: Step response

6. CONCLUSIONS

In this study we analysed the effects of the feedback signal quality on the performance of the state-feedback controller for water hydraulic manipulators. The results show that the dynamic response of the system depends on the feedback signal quality. The presence of noise degrades the dynamic response of the system. The use of the observer to obtain feedback signals results in a smoother dynamic response. Initial experiments were performed on a 1-DOF hydraulic linear drive.

Calculation of the states by the observer can be enhanced if a smaller sampling time for the integrators is used and the observer is solved several times faster than the controller. In modern control systems this is relatively easy to achieve because of the ease of the multi-loop programming and the availability of the high computational power.

The results were used for implementing the state-feedback controller for a 5-DOF water hydraulic manipulator. The response of the system was found to be improved and stable as compared to the case, where the states were obtained using the n-sample estimator. However, further enhancements needs to be done to improve the tracking and the steady

state accuracy of the manipulator. The offsets of the valves and the leakage need to be compensated, which is a function of the manipulator's position in space. The performance of the system needs to be tested with varying conditions of the load. Once the dynamic performance and positioning accuracy are satisfactory, force control needs to be included to make the manipulator practically applicable for remote handling operations.

ACKNOWLEDGEMENTS

This work, supported by the European Communities under the contract of Association between EURATOM/TEKES, was carried out within the framework of the European Fusion Development Agreement. The views and opinions expressed herein do not necessarily reflect those of the European Commission.

REFERENCES

(1) Measson Y., David O., Louveau F., Friconneau J.P., "Technology and control for hydraulic manipulators", Symposium On Fusion Technology (SOFT 2002), Helsinki, Finland, 2002.

(2) Linjama M., Virvalo T., "Robustness of some low-order controllers in an electrohydraulic position servo drive", Bath Workshop on Power Transmission and Motion Control (PTMC 2001), Bath, United Kingdom, 2001.

(3) Sepehri N., Khayyat A.A., Heinrichs B., "Development of nonlinear PI controller for accurate positioning of an industrial hydraulic manipulator", Journal of Mechatronics, Vol. 7, No. 8, pp. 683-700, 1997.

(4) Virvalo T., "PI and PID-controllers in a hydraulic position servo system - What it is all about", Proceedings of the Fifth International Conference on Fluid Power Transmission and Control (ICFP 2001) April 3-5, 2001, Hangzhou, China, 2001.

(5) Virvalo T., Linjama M., Experimental study of robustness of some controllers in a hydraulic position servo drive", Hydraulika a Pneumatika, June 5-6, 2001, Ostrava, Czech Republic, 2001.

(6) Andersen T.O, Hansen M.R., Pedersen. H.C., Conrad F., "Comparison of linear controllers for a hydraulic servo system", Proceedings of the 6th JFPS International, Symposium on Fluid Power, Tsukuba, November 7-10, 2005.

(7) Bonchis A., Corke P.I., Rye D.C., "Experimental evaluation of position control methods for hydraulic systems", IEEE Transactions on Control Systems Technology, Vol. 10, No. 6, November 2002.

(8) Andersen T.O, Hansen M.R., Pedersen. H.C., Conrad F., "Feedback linearization applied on a hydraulic servo system", Proceedings of the 6th JFPS International, Symposium on Fluid Power, Tsukuba, November 7-10, 2005.

(9) Tochizawa M., Edge K.A., “A comparison of some control strategies for a hydraulic manipulator”, Proceedings of the American Control Conference, San Diego, California, June 1999.

(10) Siuko, M., Pitkääho, M., Raneda, A., J. Poutanen, J., Tammisto, J., Palmer, J. and Vilenius, M., “Water hydraulic actuators for ITER maintenance devices”, Fusion Engineering and Design 69 (2003) pp. 141-145.

(11) Tafazoli S., Salcudean S.E., Hashtrudi-Zaad K., Lawrence P.D., “Impedance control of a teleoperated excavator”, IEEE Transactions on Control Systems Technology, Vol. 10, No.3, May 2002.

(12) Mäkinen E. Virvalo T., “Influence of Position Feedback Signal Quality on Behaviour of a State Controlled Pneumatic Position Servo”, Proceedings of the ICMA 02, The Fourth International Conference on Machine Automation human-Friendly Reliable Mechatronics, Tampere, Finland, September 11-13, 2002.

(13) Virvalo T., Linjama M., Mattila J., “Comparing different controllers of an electrohydraulic position servo”, Proceedings of the 4th International Conference on Fluid Power Transmission and Control, '97 ICFP, September 9-11, Hangzhou, China, 1997

Robust Control Performance Comparison for a Water Hydraulic Servo Motor System

Kazuhisa ITO [1], Shigeru IKEO [2], Hidekazu TAKAHASHI [3] and Naoki KANAMORI [1]

[1] Dept. of Mechanical Eng., Tottori University JAPAN
[2] Dept. of Mechanical Eng., SOPHIA University JAPAN
[3] Yamatake Corporation, JAPAN

ABSTRACT

The water hydraulic technique has become a new drive source comparable to electric, oil hydraulic and pneumatic drive systems. In this research, the rotational angle and speed control of a water hydraulic servo motor were considered with H_∞ optimized control, sliding mode control with disturbance observer and adaptive control methods. We examined the motor control performance for load fluctuations. Finally in this paper, all control results were compared from the viewpoint of the steady state error, the percent overshoot and the settling time as performance indices.

Keywords: Water hydraulic system, motor control, robust control, performance comparison

1. INTRODUCTION

Water hydraulic drive systems developed in late 80's used pure tap water as a pressure medium and is environment-friendly power source system compared with other drive sources. At first a water hydraulic system was used as a complementary system for oil hydraulics, but recently manufacturers have to take much care of the industrial wastes as a social demand. This situation is pushing the water hydraulic techniques as a fourth power source. For the water hydraulic cylinder control performance with this drive system, many experimental results have been already reported, *e.g.* (1), (2), etc. On the other hand, very few results on water hydraulic motor control are available (3)-(7). This actuator shows large friction in the lower speed region and much leakage flow compared with water hydraulic cylinder case as reported in (3). Laamanen *et al.* (4),(5) challenged the motor speed control with PCM control approach, but high control accuracy could not obtain and the rotational angle control was still an open problem. For the uncertainties in the system, robust control theory seems to be a powerful design tool compared with the PID control method, which takes much time to tune their control parameters (7).

In this paper, the robust controller designs for rotational angle and speed of water hydraulic servo motor with various strategies will be discussed and their control performances will be compared quantitatively. Considering the feasibility and simplicity, three strategies are selected: H_∞ control, sliding mode control with disturbance observer, and adaptive control. These control results will be examined with control performance indices: steady state error, settling time and percent overshoot. As a result, the best angle control performances were obtained with sliding mode control strategy combined with disturbance observer, and for speed control, adaptive control was the best solution.

2. EXPERIMENTAL SETUP

The experimental system for water hydraulic servo motor control and the specifications of key devices are shown in Figure 1 and Table 1. The axial piston type water hydraulic motor is used

Fluid Power and Motion Control 2008 Edited by Dr D N Johnston and Professor A R Plummer

in the experiments and the rotational angle of motor shaft is detected by the rotary encoder. The motor shaft is connected to the removable inertial load, which can be changed in three level from 0.10 to 0.31kg·m^2. The water hydraulic servo valve adopts the nozzle-flapper structure and its bandwidth is about 100Hz. The designed controllers are installed on a dSPACE board and generate the control signals based on the proposed algorithm. Note that rotational speed of motor is obtained from the difference of rotational angle at each sample timing. In this research, the sampling time is 1ms in both rotational angle control and rotational speed control.

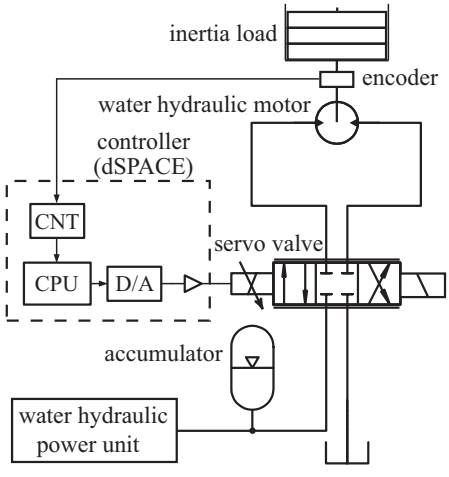

Figure 1 Schematic diagram of water hydraulic servo motor control system

Table 1 Specification of the experimental set-up

module	specification
power unit	14MPa, max 21×10^{-3} m^3/min
servo valve (nozzle-flapper type)	1.7×10^{-4} m^3/s @7MPa bandwidth 100Hz
motor	15×10^{-6} m^3/rev (axial piston type)
rotary encoder	5400 pulse per revolution
water temperature	30±1 deg (tap water)

3. SYSTEM MODEL

Introducing the load pressure $P_L = P_1 - P_2$ and the load flow $Q_L = (Q_1 + Q_2)/2$, the system can be described as

$$\begin{bmatrix} \dot{\theta} \\ \dot{\omega} \\ \dot{P}_L \end{bmatrix} = \begin{bmatrix} 0 & 1 & 0 \\ 0 & -c_e\frac{D\mu}{2\pi I} & \frac{D}{2\pi I}(1-c_f) \\ 0 & -\frac{KD}{\pi V_0} & -\left(c_s + \frac{2Kk_P}{V_0}\right) \end{bmatrix} \begin{bmatrix} \theta \\ \omega \\ P_L \end{bmatrix} + \begin{bmatrix} 0 & \frac{f_0}{I} & \frac{2Kk_X}{V_0} \end{bmatrix}^T u \tag{1}$$

where θ is the rotational angle, ω rotational speed, and D motor displacement, I inertial load, μ viscosity of water, K bulk modulus of water, V_0 piping volume. Parameters c_e, c_f, c_s and f_0 are the uncertain coefficients of viscous friction, Coulomb friction and leakage, and the direction depending static friction force respectively. Moreover k_X, k_P are linearized flow gain of servo valve around driving point. A nominal system for rotational angle control is obtained by neglecting these uncertain parameters and nonlinear functions. Since the dynamics of P_L is enough quick to take no account, the system is then reduced to

$$\begin{bmatrix} \dot{\theta} \\ \dot{\omega} \end{bmatrix} = \begin{bmatrix} 0 & 1 \\ -\omega_n^2 & -2\zeta_n\omega_n \end{bmatrix} \begin{bmatrix} \theta \\ \omega \end{bmatrix} + \begin{bmatrix} 0 \\ \omega_n^2 \end{bmatrix} u := A \begin{bmatrix} \theta \\ \omega \end{bmatrix} + bu \tag{2}$$

where $\omega_n = \sqrt{Dk_X/2\pi Ik_P}$, $\zeta_n = \sqrt{D^3/8\pi^3 Ik_P k_X}/2$ are natural angular frequency and damping coefficient, respectively, and (A, b) is a controllable pair. In the frequency domain,

the nominal system $P_n(s)$ is described as

$$P_n(s) = \frac{\omega_n^2}{s^2 + 2\zeta_n\omega_n s + \omega_n^2} \tag{3}$$

In this research, physical parameters for nominal system are obtained at supply pressure $P_S = 5$MPa and $I = 0.20$kg·m^2, and $k_X = 4.230 \times 10^{-6}$m^3/(s·V), $k_P = 4.175 \times 10^{-12}$m^3/(Pa·V), $D = 15 \times 10^{-6}$m^3/rev, $V_0 = 1.272$m^3, $K = 2.25$GPa. In this case, $\omega_n = 1.537$ rad/s and $\zeta_n = 2.169$. A nominal system for rotational speed control is similarly estimated.

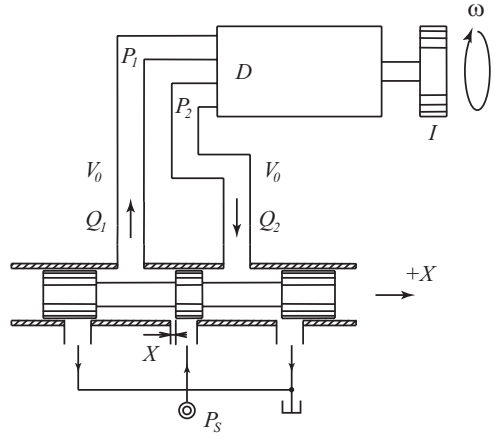

Figure 2 Water hydraulic servo motor system

4. CONTROLLER DESIGN

In this section, three robust controllers are proposed: a 2-DOF H_∞ controller, a sliding mode controller with disturbance observer, and an adaptive controller.

4.1 2-DOF H_∞ controller

For the H_∞ controller, design specifications are: 1) closed loop system is robust stable for unmodeled dynamics caused by load and or supply pressure change, 2) sensitivity from input disturbance to the system should be attenuated in lower frequency domain, and 3) steady state error for step reference signal is zero. To satisfy both first and second specifications, the solution of the mixed sensitivity problem is applied to the controller design. On the other hand, for the last specification, the internal model principle implies that the resulting controller should contain an integrator, but at the same time, this means that the solvable condition for the H_∞ standard problem fails to be satisfied. Therefore a sufficiently small positive constant ε will be introduced in input-side weighting function to avoid this situation (8).

In controlling a water hydraulic motor, strong nonlinear friction exists in the lower rotational speed region, so that stick-slip phenomena may happen. In general, direct performance improvements with H_∞ controller in time domain is difficult because performance would be evaluated with sensitivity function via weighting function in frequency domain. To solve the problem, two degree-of-freedom (2-DOF) control is introduced as shown in Figure 3 combining an H_∞ feedback controller with a feedforward compensator which acts to improve the tracking performance. In Figure 3, $P_n(s)$ stands for nominal system and $G_M(s)$ is selected such that $P_n^{-1}(s)G_M(s)$ is stable and proper. In this case, the transfer function from a given

reference signal r to rotational angle θ coincides with $G_M(s)$ for any proper $K(s)$. This implies that tracking performance and robust performance can be designed separately. If there exists uncertainties in real system $P(s)$, feedback controller $K(s)$ compensates their effects. For rotational speed control, this 2-DOF controller is introduced. The reference model transfer function is designed as

$$G_M(s) = \frac{\omega_r^2}{s^2 + 2\zeta_r\omega_r s + \omega_r^2} \tag{4}$$

where ω_r, ζ_r are its natural angular frequency and damping coefficient.

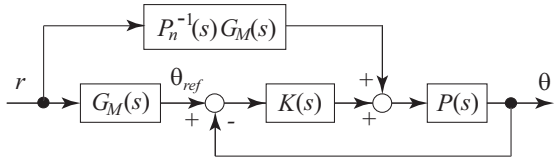

Figure 3 2-DOF H_∞ water hydraulic rotational angle control system

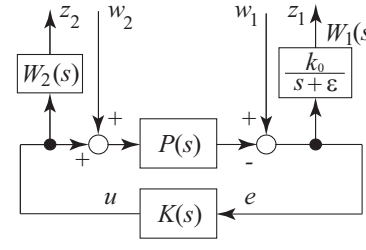

Figure 4 Generalized plant for H_∞ controller design

H_∞ feedback controller is designed as follows. The generalized plant of both rotational angle and speed control problems are shown in Figure 4. In this figure, weighting functions $W_1(s)$ and $W_2(s)$ are for tracking performance and robust stability index, respectively, and $K(s)$ is the controller to be designed. $W_1(s)$ is in the quasi integrator with sufficiently small positive constant ε. In the H_∞ control problem, the controller is designed to minimize the H_∞ norm of transfer function from reference signal $[w_1, w_2]^T$ to performance index signal $[z_1, z_2]^T$. In this paper, this corresponds to 1) sensitivity reduction from reference signal w_1 to rotational angle error z_1, 2) input penalty on w_1 or disturbance w_2, *e.g.* frictions, 3) prevention of performance deterioration by w_2, and 4) robustness improvements for uncertainties. Uncertainties Δ_m in servo motor control system are treated as a multiplicative perturbation, which has easy interpretation on a Bode diagram, and is defined as $\Delta_m(j\omega) = (P(j\omega) - P_n(j\omega))/P_n(j\omega)$. Figure 5 shows the frequency response characteristics of multiplicative uncertainty of rotational angle of water hydraulic servo motor. The controller should attenuate sensitivity around 10Hz since major gain fluctuations can be observed in this figure. Therefore weighting function $W_2(s)$ are

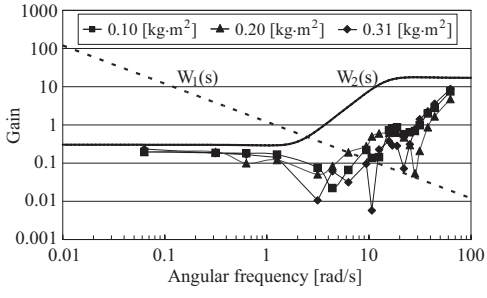

Figure 5 Frequency responses of multiplicative uncertainty $\Delta_m(s)$ and designed weighting functions $W_1(s), W_2(s)$

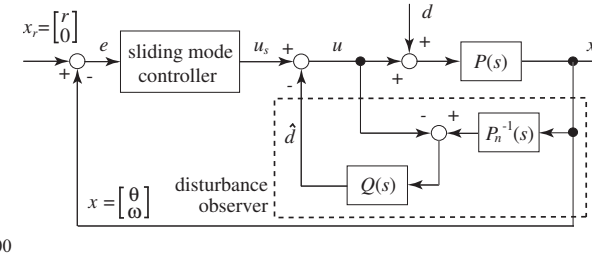

Figure 6 Block diagram of sliding mode controller with disturbance observer

obtained as follows

$$W_2(s) = \frac{17(s^2 + 2.4s + 4)}{s^2 + 18s + 225} \tag{5}$$

As a result, the $W_1(s)$ and H_∞ controller $K(s)$ satisfying all specifications are obtained as eq.(6) via γ-iteration on MATLAB ($\gamma_{\min} = 0.9375$).

$$W_1(s) = \frac{1.2}{s+1\times10^{-6}}, \quad K(s) = \frac{14.03s^4+344.9s^3+6673s^2+5.414\times10^4 s+4.17\times10^5}{s^5+271.2s^4+4528s^3+6.316\times10^4 s^2+2.05\times10^5 s+0.205} \tag{6}$$

For rotational speed case, these functions are obtained similarly.

4.2 Sliding mode controller with disturbance observer (SMC-DO controller)

It is well known that a sliding mode control (SMC) strategy can admit nonlinear uncertainty in the system and is effective in improving the robustness in an oil hydraulic control system (9). But the system should satisfy the matching condition that the uncertainty should exist only in the input channel. In this paper, a disturbance observer (DO) is introduced to cover this assumption indirectly. The disturbance observer is a popular method to cancel the input uncertainty in mechanical system control, but no report can be available so far in water hydraulic motor control system. Figure 6 shows the structure of proposed SMC-DO control system and from this figure, the estimated disturbance can be described using Q-filter as

$$\hat{d} = Q(s)P_n^{-1}(s)x - Q(s)u \tag{7}$$

where

$$Q(s) = \frac{l_2\omega_n^2}{s^2 + (2\zeta\omega_n + l_1)s + l_2\omega_n^2} \tag{8}$$

and l_1, l_2 are design parameters and $P_n(s)$ is the nominal system of water hydraulic servo motor system. From Figure 6, the transfer functions from u_s to x and from disturbance d to x are obtained as

$$\frac{x}{u_s} = \frac{P(s)}{1 - Q(s) + Q(s)P_n^{-1}(s)P(s)}, \quad \frac{x}{d} = \frac{P(s)(1 - Q(s))}{1 - Q(s) + Q(s)P_n^{-1}(s)P(s)} \tag{9}$$

where $P(s)$ is a transfer function of real system. Equation (9) shows that the disturbance has no influence on the output x for lower frequency signal because $Q(s) \approx 1$ under the cut off frequency. Moreover, the transfer function from u_s to x corresponds to a desired dynamics

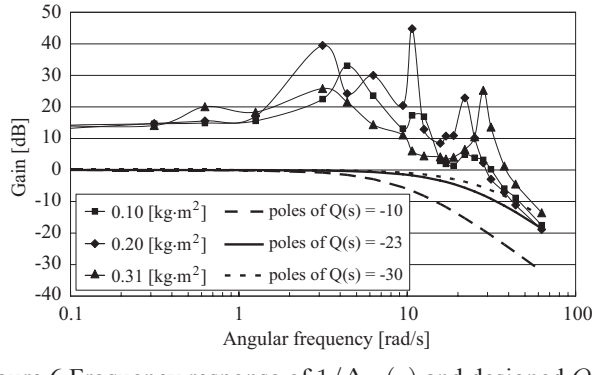

Figure 6 Frequency response of $1/\Delta_m(s)$ and designed $Q(s)$

P_n. After compensating the disturbance, the remaining uncertainties Δ_m from u_s to x are treated as a multiplicative perturbation $P(s) = (1 + \Delta_m(s))P_n(s)$ as in section 4.1. Treating this as a mixed sensitivity problem, we choose the sensitivity function $S(s)$ as a high pass filter and this gives the guide line for selecting a $Q(s)(\approx 1 - S(s) = T(s))$ where $T(s)$ is the complementary sensitivity function. Furthermore, $Q(s)$ should satisfy the condition for robust stability: $\|\Delta_m(s)T(s)\|_\infty < 1$. The response of the system under the supplied pressure $P_S = 5$MPa and the inertial load $I = 0.20$kg·m^2 is treated as the nominal response. Figure 6 shows frequency response of the inverse of uncertainty, $1/\Delta_m(s)$ for inertial load variations. The figure also shows $T(s)$ where the poles of $Q(s)$ are chosen at $\lambda = -23$ (multiple root) with trials and error. From this figure, it is observed that this $T(s)$ satisfies robust stability condition.

Next the sliding mode controller block will be designed. The problem in general sliding mode control is the chattering phenomenon caused by a switching delay. This problem may be harmful in a water hydraulic system because of the high pressure surge. The disturbance observer first cancels the error between the nominal model and plant: the remains are then compensated by the SMC method. The net input to the plant is $u = u_s - \hat{d} + d$ where d, $\hat{d}$ are unknown and estimated disturbance, respectively, and the SMC input u_s is designed as follows:

$$u_s = -(Sb)^{-1}SA(x - x_r) - (Sb)^{-1}\kappa|\sigma|^\alpha \mathrm{sgn}(\sigma) + r, \quad x_r = [r,\, 0]^T \tag{10}$$

where the switching hyperplane S is constructed by $S = b^T P$. The matrix $P > 0$ is the unique solution of Riccati equation for $Q, \gamma > 0$,

$$PA_\gamma + A_\gamma^T P - Pbb^T P + Q = 0, \;\; A_\gamma = A + \gamma I \tag{11}$$

where A, b are defined in eq.(2) and $\sigma = S(x - x_r)$. The constants $\kappa, \alpha (0 < \alpha < 1)$ are design parameters. The first term in eq.(10) makes the state converge to the origin when the state is constrained to the sliding hyperplane. On the other hand, the second term drives the state to hyperplane with the switching input. A block diagram of the SMC-DO method for rotational angle control of the motor is shown in Figure 6 where r is the reference angle. The design step for the rotational speed controller is here omitted.

4.3 Adaptive controller

The rotational angle control system of the water hydraulic servo motor system eq.(2) is written in discrete time domain as

$$(1 + a_1 z^{-1} + a_2 z^{-2})y(k) = z^{-1}(b_0 + b_1 z^{-1})u(k) \tag{12}$$

where $u(k)$, $y(k)$ are input and output signal at step k, coefficient a_1, a_2, b_0, b_1 are unknown, and z is the time shift operator. The output signal y is corresponds to the rotational angle θ or speed ω. The reference model is similarly obtained by discretization of eq.(4) as

$$(1 + a_{m1} z^{-1} + a_{m2} z^{-2})y_{ref}(k) = z^{-1}(b_{m0} + b_{1m} z^{-1})r(k), \;\; b_{m0} \neq 0 \tag{13}$$

where $r(k)$ is a reference input and $y_{ref}(k)$ stands for the output for rotational angle or speed of water hydraulic motor. Defining the output error as

$$e_1(k) = y_{ref}(k) - y(k), \tag{14}$$

the adaptive controller is designed to generate $u(k)$ such that $e_1(k) \rightarrow 0\,(k \rightarrow \infty)$ while all signals in control systems remain in bounded. The derivation of controller is omitted and the designed adaptive controller is given by

$$u(k) = \frac{1}{\hat{\theta}_1(k)} \left[D(z^{-1}) y_{ref}(k+1) - \hat{\bar{\theta}}^T(k) \bar{\phi}(k) \right] \tag{15}$$

where $D(z^{-1})$ is a second-order Hurwitz polynomial, and the estimated parameter $\bar{\theta}(k)$ and regressor vector $\bar{\phi}(k)$ are defined as follows:

$$\hat{\bar{\theta}}(k) = [\hat{\theta}_2(k),\, \hat{\theta}_3(k),\, \hat{\theta}_4(k)]^T, \quad \bar{\phi}(k) = [u(k-1),\, y(k),\, y(k-1)]^T$$

With this adaptive input, error dynamics eq.(14) can be rewritten as $e_1(k) = \tilde{\theta}^T(k)\phi(k-1)$ where $\tilde{\theta}(k) = \hat{\theta}(k) - \theta_0$, $\hat{\theta}(k) = [\hat{\theta}_1(k),\, \hat{\bar{\theta}}^T(k)]^T$, $\phi(k) = [u(k),\, \bar{\phi}^T(k)]^T$ and θ_0 is the true value vector of motor system. Applying the notion of positive realness of function and Kalman-Yakubović Lemma to output error, parameter update law ensuring the global convergence property of e_1 can be obtained as eqs.(16)-(18):

$$\hat{\theta}(k) = \hat{\theta}(k-1) + \Pi(k-1)\phi(k)e_1(k) \tag{16}$$

$$\Pi(k) = \frac{1}{\lambda_1(k)} \left[\Pi(k-1) - \frac{\Pi(k-1)\phi(k)\phi^T(k)\Pi(k-1)}{\sigma + (k)\phi^T(k)\Pi(k-1)\phi(k)} \right] \tag{17}$$

$$\lambda_1(k) = 1 - \frac{\|\Pi(k-1)\phi(k)\|^2}{\sigma + \phi^T(k)\Pi(k-1)\phi(k)} \frac{1}{\mathrm{tr}\Pi(0)} \tag{18}$$

where the initial value of parameter update gain $\Pi(0)$ is given by an arbitrary positive definite matrix and $\sigma > 0$, $\lambda_1(0) > 0$. Note that in this section, the fixed trace method is adopted for robustness because friction, leakage flow and parameter fluctuations exist in the system. This method ensures that the trace of P is kept as a constant therefore some kind of robustness would be expected (10). Moreover the boundedness of the regressor vector ϕ is derived using the Key Technical Lemma (11). The complete control system structure is shown in Figure 7.

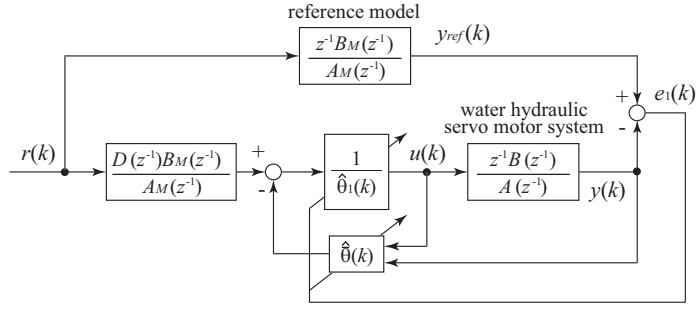

Figure 7 Block diagram of adaptive control system

5. EXPERIMENTAL RESULTS

In this section, experimental results with designed control strategies for various loads, supply pressure and reference set-points are shown. In those, subscript '*ref*' stands for the reference trajectory generated via reference model $G_M(s)$ whose input is reference signal 'r'. The supply pressure was 5MPa in rotational angle control experiments and 7.5MPa in rotational speed control.

5.1 Results with 2-DOF H_∞ controller

Figure 8 shows the experimental results with 2-DOF H_∞ controller. In the experiments, the square wave changing from 0-90 deg was given as the reference angle with inertial load fluctuation: $I = 0.20\text{kg}\cdot\text{m}^2$ from 0 to 5s, $I = 0.10\text{kg}\cdot\text{m}^2$ from 5 to 10s and $I = 0.31\text{kg}\cdot\text{m}^2$ after 10s. These were realized by adding or removing the inertial load. The reference model was chosen as $\zeta_r = 1.2$, $\omega_r = 5$ rad/s in eq.(4) by trial and error. The steady-state error was less than 0.15 deg and the figure shows the robustness of 2-DOF H_∞ rotational angle controller.

For rotational speed control, a similar reference signal was given changing from 20 to 40 rad/s and the control results are shown in Figure 9. The reference model was set as $\zeta_r = 2$, $\omega_r = 5$ rad/s achieving less than 10% overshoot. A small overshoot was observed because controller had generated large input to overcome static friction at the beginning of motion while stationary tracking performance was fairly good. Note that the effects of sensor noise could be observed, because the quasi derivative is used to obtain the rotational speed.

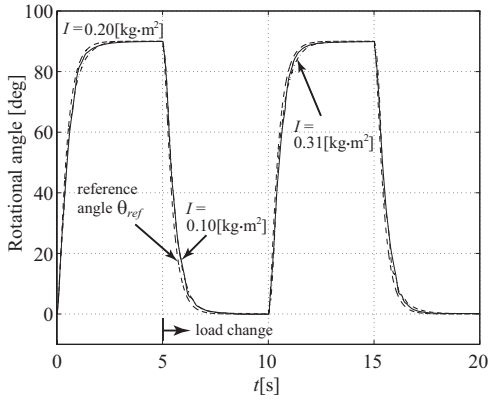

Figure 8 Experimental results of angle control for various inertial load with 2-DOF H_∞ controller (r =0-90 deg)

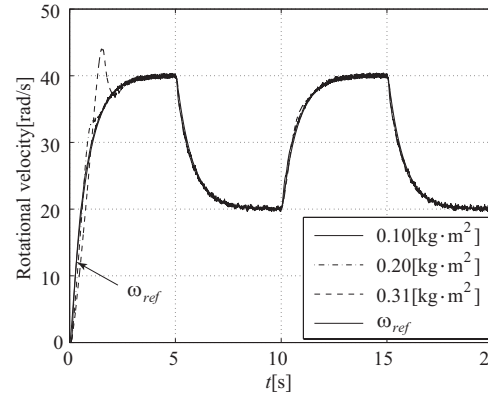

Figure 9 Experimental results of speed control with 2-DOF H_∞ controller (r=20-40 rad/s)

5.2 Results with sliding mode controller with disturbance observer (SMC-DO controller)

Under the same reference model $G_M(s)$, disturbance observer control, sliding mode control and their combination strategy were examined.

For rotational angle control, first, the results with only disturbance observer controller is shown in Figure 10 where the results with 2-DOF H_∞ controller is also plotted for comparison. In this experiments, reference angle is 90 deg. The settling time is about 2s, while one for on H_∞ control was 3s. Therefore the transient response can be improved because disturbance observer cancels modeling error based on input/output signals directly. In case for smaller reference angle r =10 deg, the dead time was also improved to 0.2s from 0.65s with H_∞ control where dead time is almost 0 for r =90 deg in the figure. But, in the response after 8s, oscillating motion can be observed and this occurs for all case independent of inertial load. This is because of the static friction acting around $\omega = 0$. The motor shaft stopped due to static friction for small control input around reference angle, but the controller would generate larger control input after certain time interval, then the shaft rotated with overshoot then stopped again, and this mechanism was repeated. This phenomenon should be avoided in application and implies that the desired control performance can not be obtained with disturbance observer

alone. This shows that water hydraulics have strong nonlinearity compared with oil hydraulics. Secondly, sliding mode control strategy was examined under same condition and the results is shown in Figure 11 with various design parameter κ. In the design, $\gamma = 3.5$ in eq.(11), $\alpha = 0.7$ in eq.(10) were chosen by trial and error, and the inertial load was fixed to 0.2kg·m^2. From this figure, even if larger sliding mode control gain were given, stationary error of 5 deg remained. Therefore rotational angle control could not be achieved, particularly, the result with $\kappa = 40$ showed undesirable chattering and this was a limitation for using sliding mode control alone. The sliding mode control theory originally needs matching condition that modeling errors and/or disturbances can exist in the same channel for control input. In this case, the control input exists only in water pressure dynamics and no inputs in motor dynamics where large frictions exist. Hence this shows similar results with the case of disturbance observer alone.

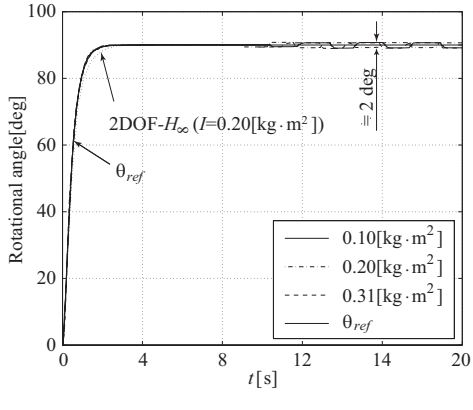

Figure 10 Experimental results of angle control with disturbance observer-based controller ($r = 90$ deg)

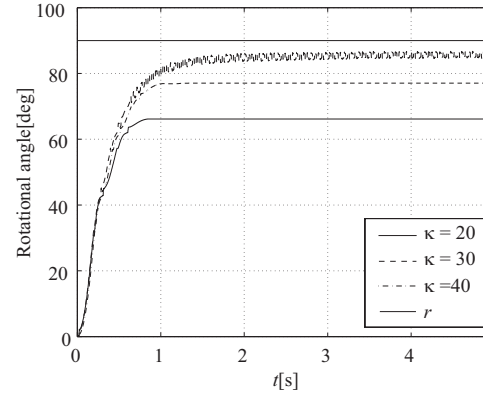

Figure 11 Experimental results of angle control with sliding mode controller ($r = 90$ deg)

Then the SMC-DO control input combined with sliding mode controller and disturbance observer is examined for the same reference trajectory given in section 5.1. The obtained control results are shown in Figure 12 and this shows good tracking performance and higher robustness for inertial load changes. The sliding mode controller and disturbance observer work complementary, and the control input oscillates with small magnitude around reference angle acting like a dither signal. The steady state angle error is less than 0.017 deg and this is almost same as the resolution of encoder.

For rotational speed control, Figure 13 shows the control results with disturbance observer controller alone. The reference angle and model were the same as H_∞ speed control case. Because the motor shaft was at rest first and then began to rotate, almost 25% overshoot could be seen with large control input with disturbance observer, but after that good speed control performance was obtained. However this overshoot can be improved by choosing the observer poles with smaller real parts, on the other hand with too smaller dominant pole, the tracking performance would be lost. In this case, disturbance observer poles were chosen as -5 (multiple root) by trial and error and no hunting response could be observed. For similar conditions, the SMC-DO controller was also examined and control results are shown in Figure 14. The control parameters were $\alpha = 0.7$, $\kappa = 300$. In this case, transient tracking performance showed larger overshoot because control input generated by disturbance observer part was large.

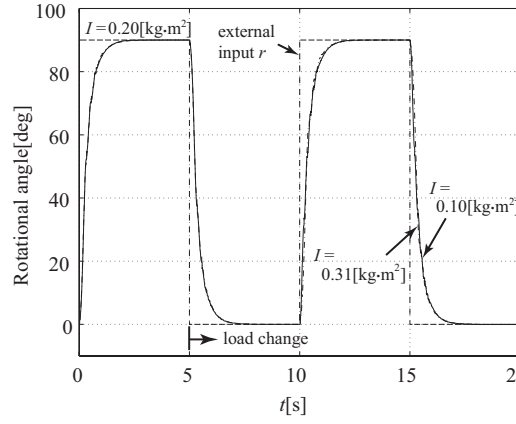

Figure 12 Experimental results of angle control with sliding mode controller with disturbance observer (r =0-90 deg)

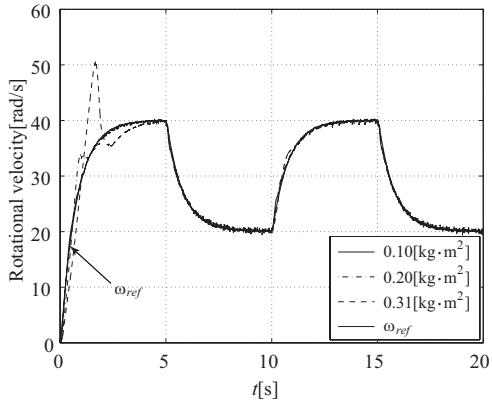

Figure 13 Experimental results of speed control with disturbance observer-based controller (r =20-40 rad/s)

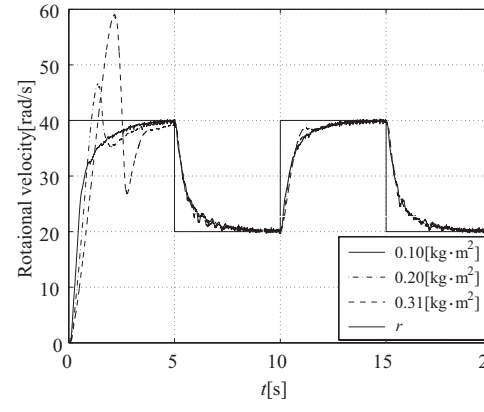

Figure 14 Experimental results of speed control with sliding mode controller with disturbance observer (ω_{ref}=20-40 rad/s)

5.3 Results with adaptive controller

For rotational angle control, the adaptive controller was examined under inertial load 0.20kg·m^2 and reference angle θ_{ref} 30 deg (20s interval). The reference model was same as used in section 5.1, $\zeta_r = 1.2$, $\omega_r = 5$ rad/s, and filter $D(z)$ in eq.(15) was chosen as $(1 - 0.1z^{-1})^2$ and $\sigma = 50$ in eq.(17) by trial and error. The initial condition in adaptive controller was set as $\hat{\theta}(0) = [1, 0, 0, 0]^T$, $\Pi(0) = 10^{-6} I_4$, which does not based on any prior information where I_4 stands for 4th order unit matrix. The control results and adaptive parameters are shown in Figures 15 and 16. Figure 15 contains the results obtained so far in this paper. The adaptive controller shows the best control performance both in transient response and in steady state error. But, after the rotational direction of θ_{ref} is once inverted, the result with the adaptive controller had large tracking error and its adaptive control parameters diverged as shown in Figure 16. The reason for this is as follows: the adaptive controller finished control parameter tuning at around 6s and achieved almost zero tracking error, but this was for the positive

rotational direction only. At 10s, the reference angle was set to be zero deg. The adaptive control parameters started to be retuned, the adaptive control system should compensate nonlinear static friction including the directional reverse of the friction force from negative static friction to positive. Then the nonlinearity surpassed the adaptation capability of control system. In fact, the adaptive controller seemed to cover it for a while but after that all of the control parameters began to deviate. This response occurred in case when θ_{ref} changed to the negative direction and then to the positive direction. This implies that strong nonlinearities existing in the water hydraulic motor system which can not be compensated by the adaptive control strategy which assumes that the nominal system were linear structure. On the other hand, the rotational speed control results for the same reference given so far (20-40 rad/s, 10s interval) are shown in Figures 17 and 18. The reference model $G_M(s)$ for ω_{ref} is also same ($\zeta_r = 2$, $\omega_r = 5$ rad/s), but was implemented in discrete time system with 1ms, and filter $D(z^{-1})$ and initial conditions were also same as previous experiments.

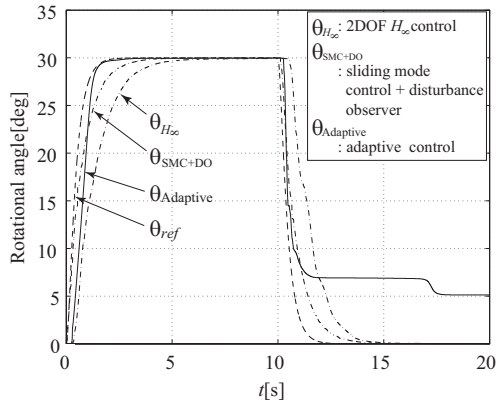

Figure 15 Experimental results of angle control with adaptive controller (r = 0-30 deg, I= 0.20kg·m^2)

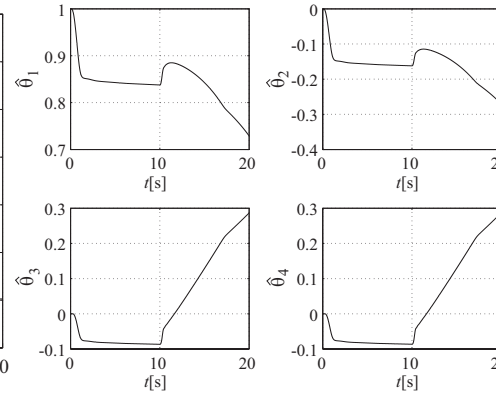

Figure 16 Estimated controller parameters

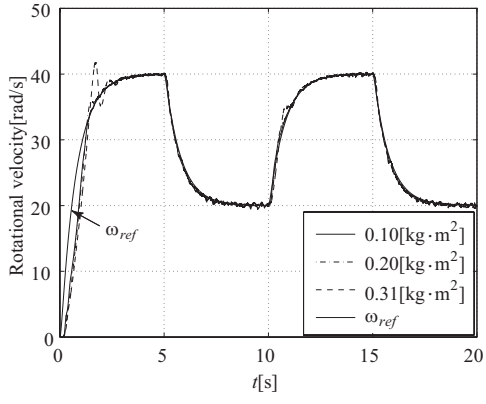

Figure 17 Experimental results of rotational speed control with adaptive controller (r = 20-40 rad/s)

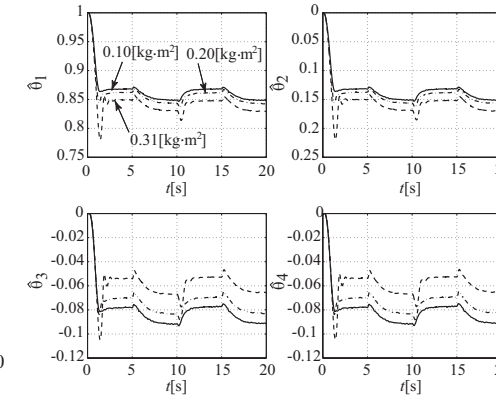

Figure 18 Estimated controller parameters

The obtained control performance was very good and the adaptive control parameters were tuned for each experimental condition properly. These converged to almost constant values and no parameter drifts could be observed. For maximum inertial load, a small overshoot can be seen in the first peak transient response, but subsequently good control performance was realized. In the rotational speed control of water hydraulic motor system, nonlinearities in the system seemed to take almost constant values for given driving point, therefore relatively good control performance could be obtained with adaptive control strategy compared with angle control case.

6. PERFORMANCE COMPARISON WITH VARIOUS ROBUST CONTROLLER

In this section, quantitative evaluations for control performances with proposed three strategies given in last section are discussed. All results are average taken over 3 times experiments.

6.1 Rotational angle controls

For rotational angle control, the steady state error at 5s with 2-DOF H_∞ controller and SMC-DO controller are evaluated. Especially for H_∞ control, the tracking error at 10s is also considered. The results with disturbance observer approach, sliding mode control and adaptive control were excluded for their lower control performances. The evaluation results are shown in Figures 19 and 20 and abbreviations used in figures are as follows:

H_∞@5s : steady state error with 2-DOF H_∞ controller at 5s
H_∞@10s : steady state error with 2-DOF H_∞ controller at 10s
SMC-DO@5s : steady state error with SMC-DO controller at 5s

These figures show that 1) the SMC-DO controller had best control precision and robustness for inertial load fluctuation, 2) the H_∞ controller remained relatively larger error compared with SMC-DO approach. Steady state error seems to be larger for larger reference angle, in spite of the inertial load. This can be interpreted that the controllers tend to compensate nonlinearities such that static/Coulomb frictions and leakage flow which lead to larger error.

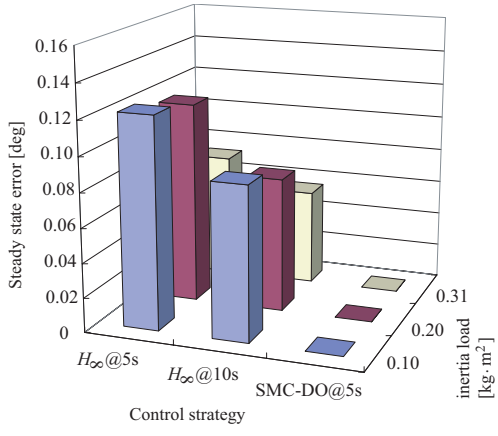

Figure 19 Steady state rotational angle errors with various control strategies ($r = 30$ deg)

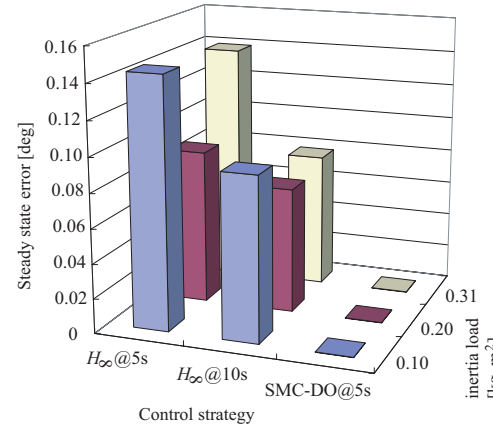

Figure 20 Steady state rotational angle errors with various control strategies ($r = 90$ deg)

6.2 Rotational speed controls

For rotational speed control, the results with 2-DOF H_∞ control, disturbance observer, sliding mode control, SMC-DO control and adaptive control are evaluated on the percent overshoot and the settling time which are:

(a) percent overshoot (PO): $PO = \frac{(\text{peak overshoot}) - (\text{final value})}{(\text{final value})} \times 100$
(b) settling time: the time that rotational speed error converges to within $\pm 2\%$ of reference speed

The evaluated results are shown in Figures 21 and 22. Note that in Figure 21 only the case with 0.31kg·m^2 and reference speed 40 rad/s are shown because POs are almost zero in other cases. The legends in figures are:

2-DOF H_∞	: 2-DOF H_∞ control	SMC-DO	: SMC-DO control
DO	: disturbance observer approach	MARCS	: adaptive control
SMC	: sliding mode control		

With the 2-DOF H_∞ controller, settling time was about 3s considering 10 % overshoot. This is almost the same settling time as the feedforward model transfer function $G_M(s)$ and can be improved further by tuning it. For the disturbance observer approach, the trade-off between suppression of large control input signal and performance of disturbance estimation showed larger overshoot. It can be make smaller by assigning the observer pole near to the origin, but this will lead to a larger settling time. With the sliding mode controller, however, the state variable constraint to the designed hyperplane was influenced by sensor noise, hence the robustness of this controller achieved smaller overshoot and settling time. The SMC-DO controller generated larger control input compared with no disturbance observer case and as a results, both overshoot and settling time got worse because over estimation of disturbance occurred initially. On the other hand, the adaptive controller compensated unmodelled dynamics in the system because these nonlinearities are almost constant under a given fixed driving point. In fact, this strategy showed the smallest overshoot. Note that for lower reference rotational speed, e.g. 30 rad/s or 20 rad/s, that was harder to control, the settling time was a few percent longer in experiments.

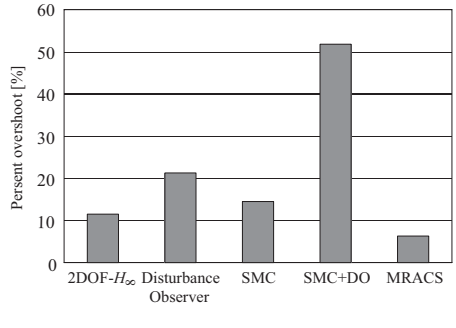

Figure 21 Percent overshoot with various control strategies ($I = 0.31$kg·m^2, $r =$40 rad/s)

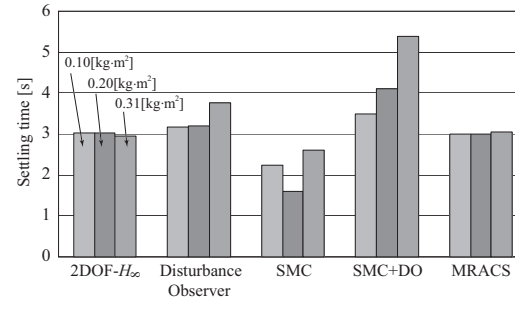

Figure 22 Settling time with various control strategies ($r =$40 rad/s)

7. CONCLUSIONS

In this research, the performance of various robust controller designs applied to a water hydraulic servo motor system were discussed. More specifically, rotational angle controllers and

rotational speed controllers were constructed with 2-DOF H_∞ theory, disturbance observer approach, sliding model control theory, and adaptive control theory. The performance was evaluated quantitatively with steady state error, overshoot and settling time.

For the rotational angle control of motor, particular high nonlinearities such as friction and leakage flow as well as uncertainties such as load fluctuation and flow gain with spool displacement and pressure in servo valve should be considered. These could be compensated by the sliding mode control combined with a disturbance observer to cover unmatched dominant uncertainties, *e.g.* friction. As a result, very high control accuracy was obtained and the steady state error was 0.017 deg for given square wave reference angle. This was the best approach. Moreover, H_∞ control theory was an effective approach, but it should be applied in 2-DOF form to improve the tracking performance with feedforward path.

On the other hand, for the rotational speed control, the effects of friction in motor and flow gain fluctuations in servo valve became relatively small to the one by inertial load change, therefore the control system could be treated almost as linear. This makes the situation to be more simple and adaptive control performance were relatively easy to improved compared with other approaches. H_∞ control could applicable to the system for its small overshoot and settling time while the controllers tend to be higher order. Moreover, the disturbance observer approach seemed to generate larger control input for compensating static friction or noise, so it is not appropriate for speed control.

REFERENCES

(1) K.Sanada: A Method of Designing a Robust Force Controller of a Water-Hydraulic Servo System, IMech. Eng., Part I: Systems and Control Engineering, **216**, pp.135-141, 2002

(2) H.Sairiala, K.Koskinen and M.Vilenius: Trajectory Tracking Control of Low - Pressure Water Hydraulic Cylinder Drive with Proportional Valve, 7th Triennial International Symposium on Fluid Control, Measurement and Visualization, Sorrento, Italy, 2003

(3) Y.Mochizuki and C.Yamashina: Servo Control of a Water Hydraulic Axial Piston Motor, EBARA Engineering Review, **184**, pp.17-23, 1999 (in Japanese)

(4) A.Laamanen, M.Nurmia, M.Linjama, K.Koskinen and M.Vilenius: Two different control methods for digital flow control unit, The proceedings of the 5th Scandinavian Int. Conf. on Fluid Power, SICFP'03, May 7-9, Tampere, Finland, 2003

(5) A.Laamanen, M.Linjama, J.Tammisto, K.Koskinen and M.Vilenius: Velocity control of water hydraulic motor, Proc. of the 5th JFPS Int. Symposium on Fluid Power, Vol.1, pp.167-172, Nara, Japan, 2002

(6) E.Urata and M.Shinoda: Influence of amplifier and feedback on the dynamics of a water hydraulic servo motor, Proc. of the 4th JHPS Int. Symposium, pp.567-572, 1999

(7) D.Terasaka, K.Ito and S.Ikeo: PID-Control of Water Hydraulic Servomotor System, Proc. of the 5th JFPS Int. Symposium on Fluid Power, Vol.**1**, pp.143-148, Nara, Japan, 2002

(8) T.Mita, K.Kuriyama and K.Z.Liu: H_∞ control with weighting functions having purely imaginary poles – Implementing internal models in to H_∞ controllers, Int.J. of Robust and Nonlinear Control, Vol.**6**, pp.537-560, 1996

(9) S.H.Cho and K.A.Edge: Adaptive sliding mode tracking control of hydraulic servosystems with unknown non-linear friction and modelling error, IMech. Eng., Part I: Systems and Control Engineering, **214**, pp.247-257, 2002

(10) Y.Lin and K.S.Narendra: A New Model for Adaptive System, IEEE-AC, **25**-3, pp.585-587, 1980

(11) G.C.Goodwin and K.S.Sin: Adaptive Filtering Prediction and Control, Prentice-Hall, 1984

Session 4
High Performance valves I

Magnetorheological (MR) damper with a fast response time

Jari Kostamo, Esa Kostamo, Jyrki Kajaste, Matti Pietola
Department of Engineering Design and Production
Helsinki University of Technology, Finland

ABSTRACT

It is well known magnetorheological and electrorheological dampers are suitable for semi active vibration control tasks. The fast response time of the MR fluid makes it possible to control vibrations in real time and it has been shown good results in vibration damping can be achieved and the performance of the semi active method is almost comparable to active damping in some cases.

Typically MR dampers have been applied in vibration damping at relatively low frequencies ranging from almost static conditions up to about some 10Hz. Based on recent research results the real time controllable bandwidth of MR technology in semi active vibration control could be much higher than that has been generally reported. In this article a high frequency magnetorheological valve has been combined with a hydraulic cylinder to form a semi active damping device. The main design criteria for this kind of device are given in this article and an experimental device is built to verify the performance. The performance of this combination will be analyzed and the experimental results are compared with theory.

1. INTRODUCTION

The dampers based on active fluids have been researched since the fluids were invented in late 40's and early 50's. The success of this technology began in the beginning of 1990's when the development in material technology and chemistry made the manufacturing of high quality and low cost MR fluids possible. Since the invention of this technology the application of these fluids has also been researched in damping tasks and therefore it is well known idea. (1-3)

The major advantage of the active fluids is that no moving parts are needed to control the fluid flow. This makes the construction of the valve mechanically very simple. There is no need for high precision machined valve parts and reliability is also increased because the valve is tolerant to impurities. There are also many similarities in the manufacturing of the

Fluid Power and Motion Control 2008 Edited by Dr D N Johnston and Professor A R Plummer

MR valve compared with traditional electric machines and therefore the potential for producing MR valves in industrial scale is generally not a problem – the technology already exists.

The application area of MR and ER dampers is wide. They have been applied successfully in automotive industry and today's premium cars can be bought with semi active suspension based on MR fluids (4-6). In addition to passenger cars, MR dampers have been applied in off-road motorcycles (7). Another application area of MR dampers has been the damping of large structures for example buildings and bridges. Lord Corporation has manufactured a large damper for mitigating earthquake shocks from tall buildings and it has been tested in (8, 9).

It has been shown fast response times can be achieved with magnetorheological valves. The MR fluid responds to external magnetic field in less than 0.5ms and valves with a response time of less than one millisecond can be constructed. (10, 11) In this study a high frequency MR valve will be combined with a cylinder to form a compact damping device. The purpose is to evaluate the performance of a semi active damper whose parameters can be changed rapidly. By combining a highly dynamical semi active MR damper with a feedback system the parameters of the damper could be changed several times during a vibration cycle and different damping properties could be defined for example for higher and lower vibration frequencies. The basic idea of the damping device discussed in this study is shown in Figure (1).

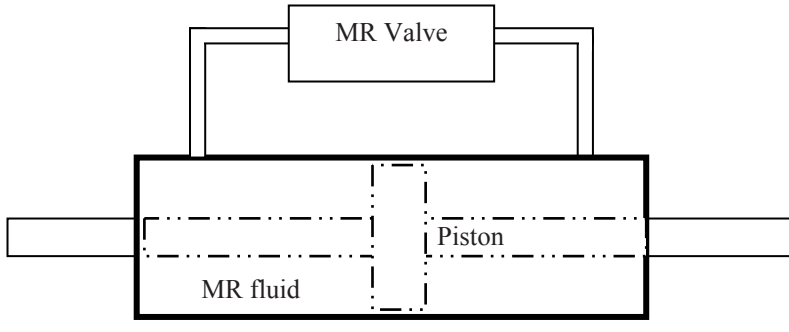

Figure 1: Functional principle of the MR damper

The major problem in designing MR or ER fluid devices is the multidisciplinary nature of these devices. There are many design consideration which have to be taken into account even though the idea of the device is rather simple. The combination of high frequency electromagnetic parts immersed in high pressure fluid with iron particles makes the design of MR valve a challenging task. The design considerations of the valve and the designing a high frequency valve are discussed more closely in (11).

2. MAGNETORHEOLOGICAL DAMPER

Recent study presented by Goncalves (10) suggests that the response time of MR fluids is between 0.4-0.65 milliseconds. The measurement method used by Goncalves (10) is based on measuring the pressure difference over the MR fluid gap with different flow velocities. By increasing the flow velocity the dwell time of the fluid in the valve can be reduced until no MR effect is observed. Using this method the pressure difference developed in the valve can be measured as a function of the dwell time and the response time of the fluid can be estimated. If the results of this research are applicable to dampers, it should be possible to construct MR dampers with a response time of less than a millisecond.

2.1 Magnetorheological Valve

This measurement method used for estimating the response time of the MR fluid in a study done by Goncalves is very close to the functional principle of the valve presented in this paper (10). The research results therefore give an idea of optimal response time which could be achieved with a damper in an ideal case. Motivated by these results an MR valve with a rectangular flow gap was designed and combined with a hydraulic cylinder. The dimensions of the valve are shown in Figure (2) and the numerical values are given in Table (1).

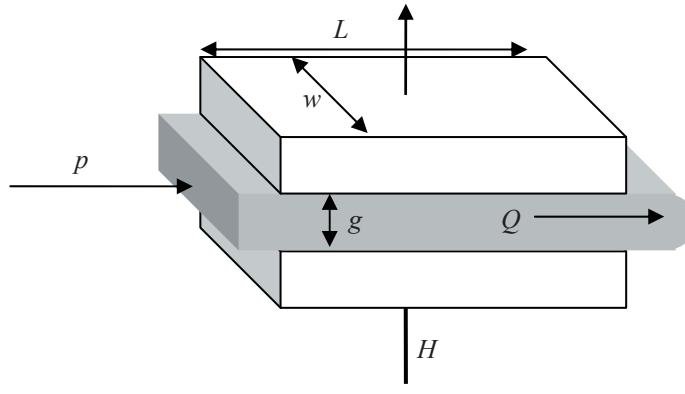

Figure 2: Funtional principle and dimensions of the magnetorheological valve.

Dimension	Value
Height of the MR fluid gap, g	0.61 mm
Length of the MR fluid gap, L	30 mm
Width of the MR fluid gap, w	39 mm
Piston rod diameter	16 mm
Piston diameter	28 mm
Stroke length	55 mm
Number of ampere turns	140

Table 1: Dimensions of the magnetorheological damper

The magnetorheological fluid used in this study was provided by LORD Corporation. The basic properties of the MRF-132AD are given in Table (2). The magnetic field induced yield stress is given by the manufacturer as a graph defining the yield stress as a function of magnetic field strength. The fluid is especially designed for energy dissipative devices and it is therefore well suited for this research (12).

Properties	Value
Base Fluid	Hydrocarbon
Operating Temperature	-40°C to 130°C
Density	3090 kg/m^3
Viscosity (at 40°C)	0.09 (±0.02) Pa-s

Table 2: Properties of the MRF-132AD (12)**.**

2.2 Model of the MR Damper

The magnetic field induced yield stress of the MR fluid is often represented as Bingham plastic having magnetic field dependent yield strength. For stresses τ above the field dependent yield stress τ_0, the flow is governed by Bingham's equation. In the Bingham model the total shear stress is given by

$$\tau = \tau_0(H)\,\mathrm{sgn}(\dot{\gamma}) + \eta\dot{\gamma} \quad |\tau| > |\tau_0| \tag{1}$$

$$\dot{\gamma} = 0 \quad |\tau| < |\tau_0|, \tag{2}$$

where τ_0 is the yield stress caused by the magnetic field H; $\dot{\gamma}$ is the shear rate and η is the field-independent viscosity. (13, 14) .

If the Bingham model is assumed, a simple approximation of the pressure difference over the valve can be calculated using Equation (3). (3).

$$\Delta p = \Delta p_\eta + \Delta p_\tau(H) = \frac{12\eta q L}{g^3 w} + \frac{c\tau_0(H) L}{g} \tag{3}$$

Where Δp is total pressure loss in a rectangular flow channel, Δp_η is viscous pressure loss component $\Delta p_{\tau 0}$ is field dependent induced yield stress component, q is flow rate, c is velocity profile related parameter (value 2 … 3).

Given this equation, it is straight forward to calculate estimates on the force produced by the damper. The total force is the pressure difference in the damper multiplied by the piston area and the friction of the seal must be added to this term. The damping force can be described by Equation (4).

$$F = \Delta p A + F_\mu, \tag{4}$$

where F is damper force, and A is effective piston area of hydraulic cylinder and F_μ is static friction force.

When analyzing the behavior of the MR valve more closely it will turn out the Equation (3) doesn't give good enough results if the valve is operated at high magnetic fields and higher velocities. The problem of the Equation (3) is that it predicts too low value for the apparent viscosity and the error gets bigger as the flow rate increases. A well known and more precise model describing the Bingham flow in a rectangular flow channel is presented e.g. in (15). The equation for the pressure difference can be written in this case as

$$4\left(\frac{L}{g\Delta p}\right)^3 \tau_0{}^3 - 3\left(\frac{L}{g\Delta p}\right)\tau_0 + \left(1 - \frac{12\eta L q}{w g^3 \Delta p}\right) = 0\,. \tag{5}$$

The problem related to this equation is that the analytic solution can not be found easily. However, the solution can be found with numerical methods and it is rather straightforward to use for example Matlab to find an estimate of the solution.

The controllable force and dynamic range are also very important parameters used in evaluating the overall performance of MR dampers. The damper force can be decomposed into a controllable force, $F_\tau = \Delta p_\tau A$, due to controllable yield stress τ_0 and an uncontrollable force F_{uc}. The uncontrollable force includes a viscous force $F_\eta = \Delta p_\eta A$ and a friction force F_μ The dynamic range is defined as the ratio between the damper resisting force F and the uncontrollable force F_{uc} as follows (8)

$$D = \frac{F}{F_{uc}} = 1 + \frac{F_\tau}{F_\eta + F_\mu} \tag{6}$$

The same equation can be applied to describe the dynamical range of the valve itself if the forces are replaced with equivalent pressure quantities. In that case the dynamic range can be written

$$D = \frac{\Delta P}{\Delta P_{uc}} = 1 + \frac{\Delta P_\tau}{\Delta P_\eta + \Delta P_{\tau_0}}\,. \tag{7}$$

2.3 The model proposed for simulations

The main problem related to simulating Bingham model is it predicts an infinite viscosity when the fluid is not flowing. This leads to numerical problems because the controllable force $F_\tau = \Delta p_\tau A$ is not uniquely defined at zero speed but it depends on the excitation force. The same problem is caused by the friction of the cylinder seals also. Therefore a different kind of model is needed for dynamic simulations. The numerical properties of the MR damper model can be improved if a finite viscosity is assumed at low velocities and zero speed.

The friction model proposed in this study is a combined model of Stribeck friction and tanh-function. The advantage of this model is its good numerical properties with the

simulations. The disadvantage is the zero friction force it assumes at zero speed. This might lead to inaccurate results in high quality servo systems because the friction force does not go to zero in real applications with sliding contacts. However, the model is considered feasible for this study because a damper is typically used for reducing vibrations and the final position does not have to be exact. A closer analysis of the properties of this function can be found from the work done by Andersson (16) and Jacobson (17). The combined Stribeck-tanh model can be described for a MR damper as

$$F = ((F_\mu + F_\tau) + (F_S - (F_\mu + F_\tau))e^{-(|v|/v_s)^i}) \tanh(k_{tanh} v) + \frac{12\eta v L}{g^3 w} A^2, \qquad (8)$$

where v is the velocity of the piston, F_s the maximum static friction force, v_s the speed coefficient, k_v the viscous friction coefficient, k_{tanh} is a coefficient that determines how fast the tanh function changes from near -1 to near +1 and i an exponent.

3. EXPERIMENTAL SETUP

The experimental setup consists of an MR damper, a servo hydraulic system for providing the excitation and a real time measurement computer for collecting the data and controlling the process. The devices used for measurements are described more closely in the following chapters.

3.1 MR Damper

The damper consists of a symmetric hydraulic cylinder, an MR valve and control electronics. In addition there exists a valve for pre-pressurizing the device and sensors for measuring the desired data. The load cell for measuring the damper force is attached in between the damper and the driving hydraulic cylinder. The pressure sensors for measuring the pressure difference over the valve are attached directly to the inlets of the MR fluid gap. By doing this the measurement delays can be minimized and the response of the damper can be measured in a reliable way. The pressure sensors used here are manufactured by Dynisco and they are suitable for measuring dynamic pressure fluctuations at a pressure range from 0 to 100bar. The control electronics of the valve is based on a high performance pulse width modulated amplifier and a current control circuit. The instrumentation used for measuring the behavior of the valve is shown in Figure (3).

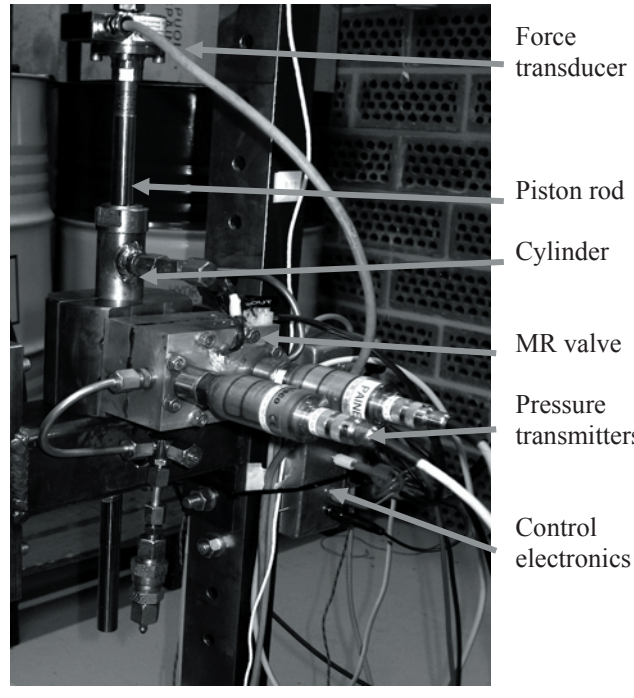

Figure 3: MR damper and sensors used in the experiments.

3.2 Hydraulic actuation system

To measure the properties of the MR damper an excitation system was built. In this case Parker DFplus proportional valve was combined with a hydraulic cylinder designed for servo applications. The hydraulic cylinder used here was Dowty with 160mm^2 effective piston area and 150mm stroke. The hydraulic power was supplied by a gear pump driven by electrical motor. The maximum operating pressure of the system was 14MPa and it was limited by the properties of the gear pump. Thus the maximum output force of the driving system was limited to about 4.5kN. The hydraulic system was controlled by a measurement computer running LabView real time operating system. The same computer was also used for acquiring the measurement data.

4. MEASUREMENT RESULTS

The performance of the damper was analyzed in many ways. First, the quasi static behavior of the device was measured by running the damper at different velocities. This method was used to characterize the flow properties of the valve and to measure the friction of the system. In the second experiment the dynamics of the damper was analyzed by step response experiments. The experimental results are analyzed more closely in the following chapters and the results are compared with theoretical calculations.

4.1 Quasi static measurements

The hydraulic servo system was used to run triangular displacement waveforms to the damper in order to measure the properties of the damper at different velocities. The frequency of the waveform and the amplitude were changed to vary the velocity. The velocity test was then repeated for many different values of coil current to measure the capability of the valve to change the damping properties. The damping force was measured from the piston rod and the pressure difference over the MR valve was recorded simultaneously. The quasi static pressure difference as a function of damper velocity with different coil currents is shown in Figure (4).

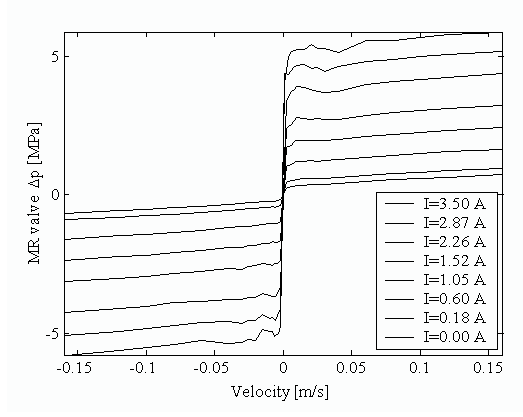

Figure 4: Measured pressure difference over the MR valve and the pressure difference predicted by the Bingham model.

It can be seen the maximum pressure difference which can be controlled by changing the coil current was 4.27MPa. The minimum pressure difference which is caused by the zero magnetic field yield strength of the MR fluid was 0.28MPa. The dynamic range for the MR valve can be calculated using Equation (7) and it is 16.3. The controllable pressure difference multiplied by the effective area of the piston equals to a controllable force of 1.96kN while the minimum resisting force caused by the MR fluid flow is 0.12kN. The friction of the piston is neglected in this calculation to provide a better insight in the performance of the valve. The damping force was also measured during the same experiments and the data is shown in Figure (5).

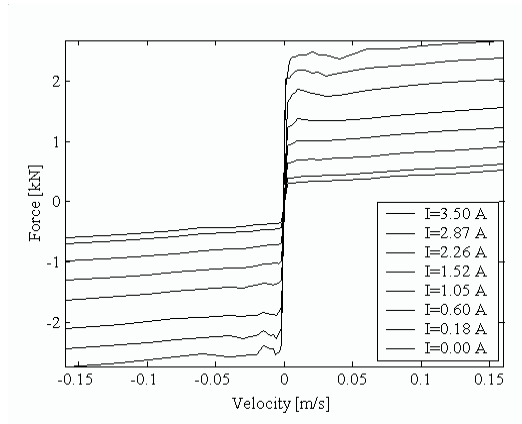

Figure 5: The measured damping force with different values of coil current

Figure (6) shows the measured force and the force estimated by multiplying the pressure difference over the valve by the effective area of the piston. This comparison was carried out to determine if there are any undesired losses in some parts of the damper. Ideally the response predicted by the pressure difference should match with the measured force if the friction of the cylinder seals is added to the calculated result. Figure (6) demonstrates the pressure measurement gives a good estimate of the force at least in quasi static conditions. In this case a frictional force of 240N was added to the calculated result.

One interesting feature which can be noticed from Figures (4-6) is the small increase in damping force or pressure difference at low velocities. Pressure measurements indicate this behavior is caused by the MR fluid flow rather than friction of the cylinder. It is assumed this effect is caused by clogging of the particles in the inlet of the valve. This behavior might have significance on dynamic behavior at low velocities and high magnetic field strengths.

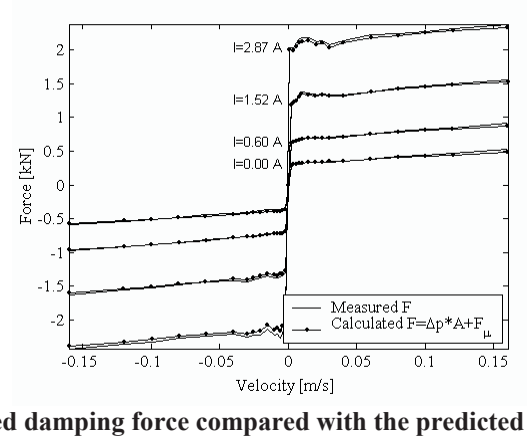

Figure 6: Measured damping force compared with the predicted results derived from pressure measurements.

Next the measured results of the valve were compared with the theoretical calculations. Equation (5) was used to predict the response but for some reason it didn't match very well before the parameter related to the magnetic field induced yield stress was tuned. The equation which predicts the behavior of the valve is

$$4\left(\frac{L}{g\Delta p}\right)^3 {\tau_0}^3 - 3.3\left(\frac{L}{g\Delta p}\right)\tau_0 + \left(1 - \frac{12\eta L q}{w g^3 \Delta p}\right) = 0 . \qquad (9)$$

In the Equation (9) the second term is slightly different compared to the original Equation (5). With this modification the data matches well with theoretical results as Figure (7) demonstrates. The reason for the difference was not fully clarified and more experiments with different parameters of the valve should be done. In addition the Bingham model does not predict any increase of the pressure at very low flow rates which was observed.

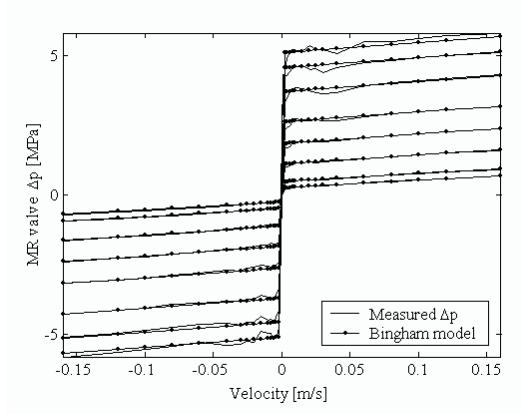

Figure 7: Modified equation of Bingham flow predicts the damping properties of the valve.

To evaluate the magnetic field dependent behavior of the experimental valve, the magnetic field induced yield stress was estimated by fitting a linear curve to the data shown in Figure (4). A linear graph was fitted with least squares method to the curves with positive velocity and the estimated pressure difference at zero speed was then extrapolated. The result for the magnetic field dependent pressure difference is given in Figure (8). The result indicates the valve was not operated very close to the saturation point with 3.5A maximum current applied in these experiments. Almost linear behavior which can be seen in the graph is advantageous considering control applications but more performance could be achieved if current would be increased.

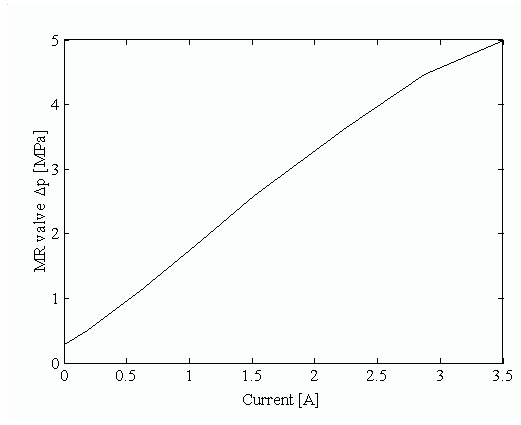

Figure 8: Pressure difference over the MR valve as a function of coil current.

4.2 Friction model

The Stribeck-tanh model proposed for modeling of the valve was fitted to the measured data. The model was fitted by tuning the parameters manually but a good agreement with the measurements can be achieved easily. The Stribeck-tanh model compared with the measured data is shown in Figure (9). It can also be seen the Stribeck-tanh function can be used for capturing the larger initial force caused by the MR fluid properties at low flow rates. The parameters found for the Stribeck-tanh model are: v_s=0.02, k_{tanh}=500 and i=5. The field dependent values for viscosities and initial yield stresses are found by fitting linear curves to the Figure (5).

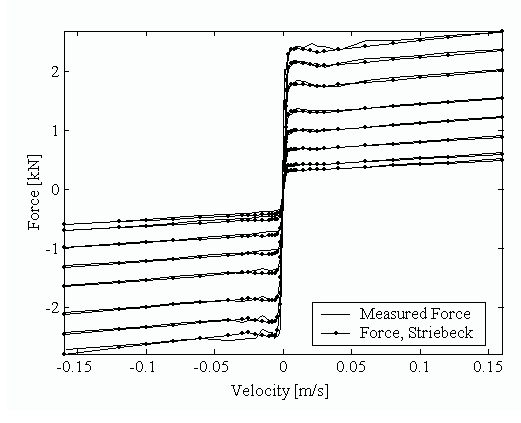

Figure 9: Stribeck-tanh function used for modelling the velocity response of the MR damper.

4.3 Dynamic measurements

The dynamical performance of the damper was measured by analyzing the step responses of the system. The step response test for the pressure difference over the valve and the

damper force were done simultaneously by driving the cylinder with a constant velocity and applying a sudden increase of the coil current.

The pressure step response is shown in Figure (10). It can be seen the current can be applied in less than 0.5ms and the pressure difference of the valve starts to increase almost immediately. The delay is less than 0.2ms. However, there is some oscillation in the pressure and the full pressure difference is achieved after about 2ms. The oscillations are considered to be caused by the compliance of the structure and the compression of the fluid. There is also a possibility of air bubbles in the MR fluid and they might decrease the stiffness. The effect of the air bubbles was tried to be minimized by carefully filling the device and pre pressurizing the valve but even a small amount of free air would have a significant effect on the response time.

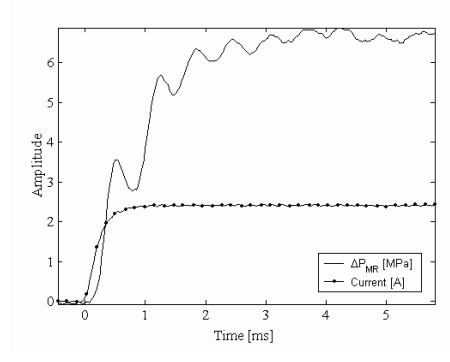

Figure 10: Step response of the pressure difference over the MR valve.

The force response is much similar to the response of the pressure. The measured damper force is shown in Figure (11) and the rise time of the force is about 2ms, too.

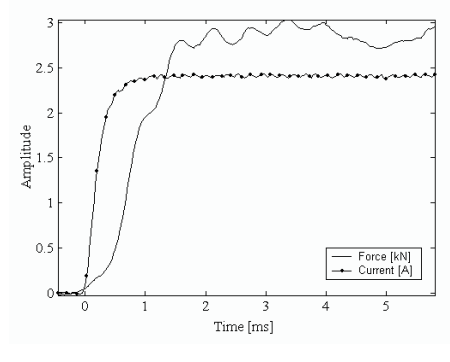

Figure 11: Step response of the damper force.

5. Conclusions

A magnetorheological damper with a fast response time was built and the performance was measured in a test bench set up for this purpose. The response time of the damper presented in this study is only two milliseconds and a force of about 2.5kN could be controlled. Also the dynamic range of the damper and valve are good and comparable to the dampers commercially available. The dynamic response measurements indicate it should be possible to use this kind of damper in real time semi active vibration control at least up to frequency of 150Hz. In this case the period of the vibration is roughly three times longer than the response time of the actuator.

The results of the test showed the behavior of the valve can be predicted with good accuracy. Initially there was a difference between the theoretical result based on Bingham fluid flow and the actual measured results. However, after modifying the model slightly the results matched. The reason for the difference between the theory and practice was not fully clarified but additional experiments could give more insight into this matter.

A simulation model for the damping force was proposed. The Bingham plastic model usually causes numerical problems with dynamic simulations and different models approximating this behavior should be used. The combined Stribeck-tanh model proposed here can be tuned to capture the velocity properties of the damper and the model behaves numerically sound with computer simulations.

The valve presented in this study was implemented by combining a traditional hydraulic cylinder with an external MR damper. This construction was chosen because an integrated device would be considerably more difficult to manufacture. The results with this concept seemed to provide a good performance and future work is planned on developing the device further and integrating the MR valve in the damper.

REFERENCES:

(1) Phillips, R.W. 1969, "Engineering applications of fluids with a variable yield stress", PhD Thesis.

(2) Agrawal, A., Kulkarni, P., Vieira, S.L. & Naganathan, N., G 2001, "An Overview of Magneto- and Electro-Rheological Fluids and Their Applications in Fluid Power Systems", International Journal of Fluid Power, vol. 2, no. 2, pp. 5-36.

(3) Goncalves, F.D., Koo, J.H. & Ahmadian, M. 2006, "A Review of the State of the Art in Magnetorheological Fluid Technologies -- Part I: MR fluid and MR fluid models", Shock & Vibration Digest, vol. 38, no. 3, pp. 203.

(4) Lindler, J.E., Dimock, G.A. & Wereley, N.M. 2000, "Design of a magnetorheological automotive shock absorber", SPIE-Int. Soc. Opt. Eng, , pp. 426.

(5) Milecki, A., Sedziak, D., Ortmann, J. & Hauke, M. 2005, "Controllability of MR shock absorber for vehicles", International-Journal-of-Vehicle-Design, vol. 38, no. 2-3.

(6) Gordaninejad, F. & Kelso, S.P. 2000, "Fail-Safe Magneto-Rheological Fluid Dampers for Off-Highway, High-Payload Vehicles", Journal of Intelligent Material Systems and Structures, vol. 11, no. 5, pp. 395-406.

(7) Ericksen, E.O. & Gordaninejad, F. 2003, "A magneto-rheological fluid shock absorber for an off-road motorcycle", International Journal of Vehicle Design, vol. 33, no. 1-3.

(8) Yang, G., Spencer, J.,Billie F., Jung, H. & Carlson, J.D. 2004, "Dynamic Modeling of Large-Scale Magnetorheological Damper Systems for Civil Engineering Applications", Journal of Engineering Mechanics, vol. 130, no. 9, pp. 1107-1114.

(9) Xinchun, G., Jinhai, L. & Jinping, O. 2005, "Experiment study of large-scale magnetorheological fluid damper", SPIE-Int. Soc. Opt. Eng, , pp. 588.

(10) Goncalves, F.D. 2005, Characterizing the Behavior of Magnetorheological Fluids at High Velocities and High Shear Rates.

(11) Kostamo, J., Kostamo, E., Kajaste, J. & Pietola, M. 2007, "Dynamical performance of a fast magnetorheological (MR) valve", 20th Bath / ASME Symposium on Fluid Power & Motion Control.

(12) Lord Co. "Magnetorheological fluid MRF-132AD", product specification, Available from: www.mrfluid.com. [10.6.2006].

(13) Bossis, G., Lacis, S., Meunier, A. & Volkova, O. 2002, "Magnetorheological fluids", Journal of Magnetism and Magnetic Materials, vol. 252, pp. 224-228.

(14) Barnes, H.A. 1999, "The yield stress - a review or - everything flows?", Journal of Non-Newtonian Fluid Mechanics, vol. 81, no. 1-2, pp. 133-178.

(15) Sims, N.D., Stanway, R., Peel, D.J., Bullough, W.A. & Johnson, A.R. 1999, "Controllable viscous damping: an experimental study of an electrorheological long-stroke damper under proportional feedback control", Smart Materials and Structures, vol. 8, pp. 601-615(15).

(16) Andersson, S., Söderberg, A. & Björklund, S. 2007, "Friction models for sliding dry, boundary and mixed lubricated contacts", Tribology International, vol. 40, no. 4, pp. 580-587.

(17) Jacobson, B. 2003, "The Stribeck memorial lecture", Tribology International, vol. 36, no. 11, pp. 781-789.

Simulation of a piezoelectric high-speed digital valve

XiaoPing OUYANG [1], HuaYong YANG [1], HaoYi JIANG[1], Nigel JOHNSTON[2]

1. The State Key Lab of Fluid Power Transmission and Control, Zhejiang University, Hangzhou 310027, China;
2. Department of Mechanical Engineering, University of Bath, Bath, BA2 7AY, UK

ABSTRACT

As hydraulic transmission and control technology develops, the digital valve is becoming popular, and it has the potential to replace servo or proportional valves in industrial applications for its excellent performance. At present the digital valve can not obtain a high response, high pressure and high flow rate together, which limits its application fields. An innovative idea of a piezoelectric digital valve is outlined to improve the performance of the digital valve. Two piezoelectric stacks are used to open and close the poppet valve. The characteristic of quick-response and high force of the piezoelectric stack is used to kick off the poppet; furthermore the micro displacement of the piezoelectric stack is avoided successfully. Temperature compensation of the piezoelectric actuator is considered in the valve. The structure of the digital valve is discussed, and its mathematical model is built. Simulation results show that the piezoelectric digital valve can get a frequency of 250 Hz, flow rate of 10L/Min, and pressure of 200 bar simultaneously.

Keywords: Piezoelectric actuator, high speed, digital valve, temperature compensation, simulation

1 INTRODUCTION

The digital valve (also called high-speed switching valve), as a new transmission and control technology, is challenging the traditional valve types, namely proportional and servo valves, for it may have the following performance: high-precision control, compact space, high reliability, pollution-proof and low cost. The valve has the potential to replace the servo-valve in many applications, especially in poor environments such as metallurgy, coal, engineering machinery etc [1].

The digital valve can realize precision control based on its fast response that can be improved mainly by increasing the drive force of the actuator. The main kind of actuator in digital valves is the solenoid actuator. The response of the solenoid digital valve can not be improved further owing to the solenoid actuator's space, electromagnetic force and inertia. Furthermore the displacement of the poppet is limited by the on/off time of the poppet; it is very difficult to get a high flow rate and fast response at the same time. Under the same

Fluid Power and Motion Control 2008 Edited by Dr D N Johnston and Professor A R Plummer

drive-force of an actuator, the increasing flow rate results in its response dropping. Moreover high operation pressure of a digital valve induces a high flow force, which delays its response time [1]. Currently, the performance of the digital valve in industry can not be obtained with flow rate of 10 L/min, pressure of 20MPa and frequency of 250Hz together in limited space (Manhartsgruber developed a concept of high speed switch valve with high flow and pressure, but its size is large and application has not been seen seen until now [2]). Therefore one solution of improving the response, flow rate and pressure of a digital valve at the same time is to find a new actuator, and smart actuators may meet the requirement [3].

Applying smart actuators (including piezoelectric actuator, magnetostrictive actuator, magnetorheological fluids) in hydraulic transmission is one important development trend of hydraulic control technology. Perfect performance of smart actuators, such as high-response, high power density, and compactness can be used to improve the competitiveness of hydraulic products [4]. Compared to magnetostrictive and solenoid actuators, the piezoelectric (named PE) actuator has the following advantage: fast response (up to GHz), high output force (up to kN), low energy consumption (power of several watts) and low cost. Therefore the piezoelectric actuator has great potential to improve the performance of the current digital valve [5, 6].

Although the piezoelectric actuator can improve the response of the digital valve, its displacement generally cannot exceed 0.1% of its length, normally about tens of microns, which is much lower than the hundreds of microns that a valve requires. Therefore displacement amplification of the piezoelectric actuator is needed. Currently some methods such as a lever, flexible hinge and fixed hydraulic volume are employed to amplify the displacement of the PE actuator [7], which do realize the function of displacement amplification, but the output force, response and control precision are also reduced at the same time, implying that these methods are not effective.

2 NEW CONCEPT OF A PE DIGITAL VALVE

An innovative concept of a PE digital valve based on fast-response and high output force of the PE actuator has been developed and is shown in Fig.1. The movable valve poppet is composed of three parts, poppet I, spool II and III, which is driven by two piezoelectric actuators PE 1 and PE 2 respectively. Port 1 is the valve inlet, 2 the outlet and 3 tank port. Normally the poppet I is pressed against the seat by high pressure p_1, the force generated by load pressure p_2 is almost zero owing to the special structure in Fig.1, therefore the inlet and outlet is cut off at normal condition. The spool II overlaps the fluid passage D and the spool III underlaps fluid passage E corresponding to zero displacement of the poppet. Chamber C is connected to tank. When the PE 1 actuator is powered on, it outputs an instant force of above 2kN to accelerate the poppet rapidly. The poppet leaves contact with the PE 1 actuator and continues to move under its own momentum. As the valve opens the pressure p_2 increases close to p_1 rapidly. With the poppet moving, Chamber C is connected to passage D and disconnected to passage E, thus the pressure p_3 in Chamber C increases. Pressure p_3 will push the poppet further owing to the cross sectional area difference between II and III. The poppet is stopped by the damper 1 at its right stoke end. On the contrary, when the PE 2 actuator is powered on, it produces a high instant force of 2kN to strike the poppet to move. The poppet continues to move and chamber C connects to pas-

sage E which is at low pressure. With the help of the damper 2 it stops at its left stroke end. Here it is the high instant force of the PE actuator that contributes to movement of the poppet, and the PE actuator only initiates the movement. As a result displacement amplification of the piezoelectric actuator is not necessary. In this case the stroke of the poppet can reach up to 0.7 mm, accordingly the high flow rate can be gained and the conflict among high flow rate, pressure and quick response can be solved.

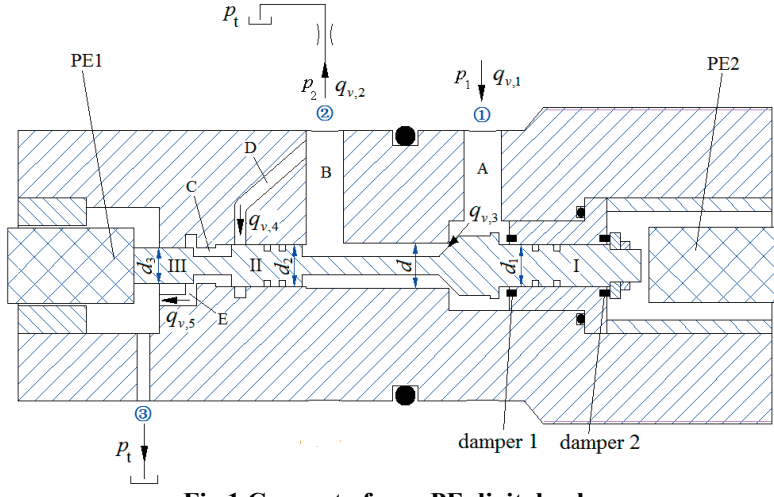

Fig.1 Concept of new PE digital valve

3 MATHEMATICAL MODEL [8]

3.1 Opening of the poppet

The following mathematical model of the PE valve is obtained from Fig.1. Assuming the mechanical and viscous friction force is zero, when the PE actuator is powered on, the force equation is expressed as

$$F_{\mathrm{PE1}}+\frac{\pi}{4}p_1(d^2-d_1^2)+\frac{\pi}{4}p_3(d_2^2-d_3^2)+\sum_{i=1}^{3}F_{fi}-F_{r1}+F_{r2}=m\ddot{x}+c_3\dot{x} \tag{1}$$

Where $F_{f1}=-\rho q_{v,3}v_1\cos\alpha$, $F_{f2}=-\rho q_{v,4}v_2\cos\beta_1$, $F_{f3}=\rho q_{v,5}v_3\cos\beta_2$,

$$F_{\mathrm{PE1}}=\begin{cases}K_{\mathrm{T1}}(\dfrac{\Delta L_{1,\max}}{U_{1,\max}}U_1-x) & (x\le\Delta L_{1,\max})\\ 0 & (x>\Delta L_{1,\max})\end{cases},$$

$$F_{r1}=\begin{cases}k(h+x-x_{\max})+rv & (0\le x_{\max}-x\le h_1)\\ 0 & (x_{\max}-x>h_1)\end{cases},$$

$$F_{r2}=\begin{cases}k(h_2-x)+rv & (x\le h_2)\\ 0 & (x>h_2)\end{cases}.$$

The flow equation of the inlet is given by $q_{v,1} - q_{v,3} + \frac{\pi d_1^2}{4}\dot{x} - \frac{\pi d^2}{4}\dot{x} = \frac{V_A}{\beta_e}\dot{p}_1$ (2)

Where $q_{v,3} = C_{q1}\,\mathrm{A}\sqrt{\frac{2}{\rho}(p_1 - p_2)}$,

$$\mathrm{A} = \pi dx\sin\alpha(1 - \frac{x}{2d}\sin 2\alpha).$$

The flow equation of the outlet is expressed as

$$q_{v,3} - q_{v,2} - q_{v,4} + \frac{\pi d_2^2}{4}\dot{x} - \frac{\pi d^2}{4}\dot{x} = \frac{V_B}{\beta_e}\dot{p}_2 \tag{3}$$

Where $q_{v,2} = K_{\mathrm{L}}\sqrt{p_2 - p_{\mathrm{t}}}$

The flow equation of the chamber C is expressed as

$$q_{v,4} - q_{v,5} + \frac{\pi d_2^2}{4}\dot{x} - \frac{\pi d_3^2}{4}\dot{x} = \frac{V_C}{\beta_e}\dot{p}_3 \tag{4}$$

Where

$$q_{v,4} = \begin{cases} 0 & (\mathrm{x} < \mathrm{e}_1) \\ C_{q2}\pi d_2(x - e_1)\sqrt{\frac{2}{\rho}(p_2 - p_3)} & (\mathrm{x} \geq \mathrm{e}_1) \end{cases},$$

$$q_{v,5} = \begin{cases} C_{q3}\pi d_3(e_2 - x)\sqrt{\frac{2}{\rho}(p_3 - p_{\mathrm{t}})} & (x \leq \mathrm{e}_2) \\ 0 & (x > \mathrm{e}_2) \end{cases}.$$

3.2 Closing of the poppet

Similarly, the mechanical and viscous friction is neglected in the close of the poppet. When the PE actuator 1 is powered off and the PE actuator 2 is powered on, the force equation of the poppet is given by

$$-F_{\mathrm{PE2}} + \frac{\pi}{4}p_1(d^2 - d_1^2) + \frac{\pi}{4}p_3(d_2^2 - d_3^2) + \sum_{i=1}^{3}F_{fi} - F_{r1} + F_{r2} = m\ddot{x} + c_3\dot{x} \tag{5}$$

Where $$F_{\mathrm{PE2}} = \begin{cases} K_{\mathrm{T2}}(\frac{\Delta L_{2,\max}}{U_{2,\max}}U_2 + x - x_{\max}) & (x \geq x_{\max} - \Delta L_{2,\max}) \\ 0 & (x < x_{\max} - \Delta L_{2,\max}) \end{cases}$$

Here the flow equation is as the same as in the open process of the PE valve.

4 SIMULATION

The PE actuator is selected from PI Company, and its parameters are shown in table 1.

Table 1 Parameters of the PE actuator [10]

PE Actuator	Sizes A×B×L/mm	Nominal displacement μm@100V	Blocking force N@ 120 V	Stiffness N/μm	Electrical capacitance μF±20%	Resonant frequency kHz
P-888.91	10×10×36	32	3800	100	13.0	40

The piezoelectric actuators 1 and 2 are driven respectively by a pulse of 120 V, some simulation results are discussed as follows.

Table 2 Parameter values

d	6 mm
k	164100 N/m
r	1520 N/(m/s)
f	250 Hz
U	100 V
β_1	69°
β_2	69°

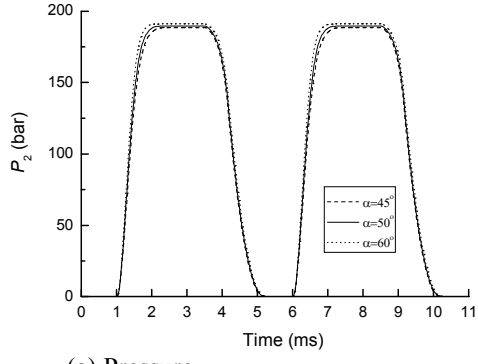

(a) Pressure p_2

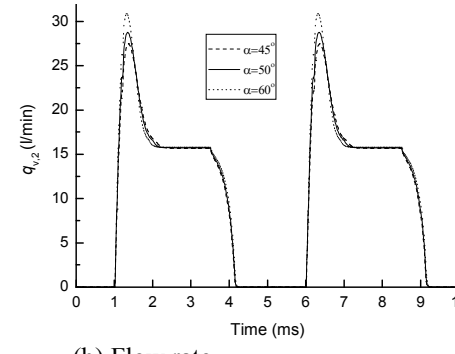

(b) Flow rate $q_{v,2}$

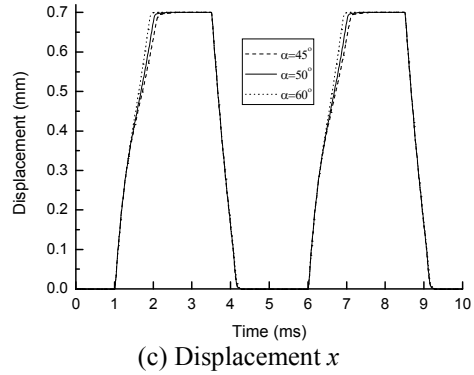

(c) Displacement x

Fig.2 Influence of α

4.1 Influence of jet angle α

While pressure p_1 is 200 bar, and the jet angle of the poppet α varies from 45° to 60°, the pressure p_2 and flow rate $q_{v,2}$ of the outlet are shown in Fig.2. It can be seen that the digital valve can switch oil in a period of 4ms. During the time when the poppet opens, the time to reach the end of the poppet displacement reduces with α increasing, shown in Fig.2c, which contributes to the peak of the flow rate $q_{v,2}$ increasing with α. When the poppet opens, p_2 and $q_{v,2}$ are both being improved a little. Here 60° is selected for the jet angle for the digital valve.

4.2 Influence of pressure p_1

While α=60° and d=6mm, the performance of the PE valve at different input pressure p_1 is shown in Fig.3. It can be seen that the piezoelectric digital valve can switch oil at different input pressure p_1. During the period when the poppet opens, the time of pressure p_2 reaching the steady value reduces with p_1 increasing, shown in Fig.3a, which is because higher pressure p_1 leads to increased resistance of the poppet, therefore the velocity of the poppet reduces, and the poppet needs more time to reach its end, accordingly its stable time at the end displacement reduces, shown in Fig.3c. It can be seen from Fig.3b that flow rate $q_{v,2}$ increases with pressure p_1 increasing.

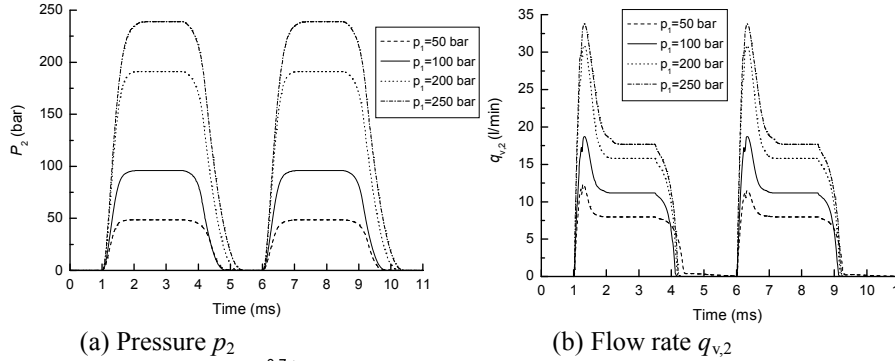

(a) Pressure p_2 (b) Flow rate $q_{v,2}$

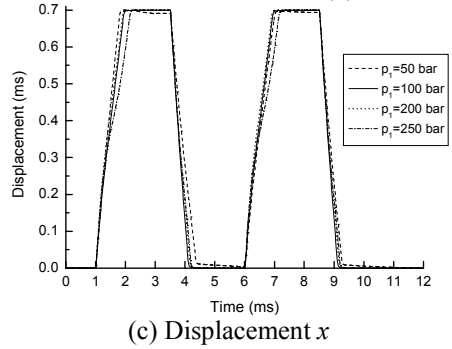

(c) Displacement x

Fig.3 Influence of p_1

Furthermore it can be seen from Fig.3c that at p_1=50 bar, the poppet does not stay in contact with the two end at 0.7 mm and 0 mm, accordingly the flow rate $q_{v,2}$ is not zero when the poppet closes, which is because the closing force generated by p_1 is lower than the

stiffness force produced by the dampers in the valve.

4.3 Influence of pressure p_2

While p_1 is 200 bar and the outlet is connected to different load pressure p_2, the performance of the piezoelectric digital valve is shown in Fig.4. It can be seen that the PE valve can switch high pressure p_1 at different p_2, and the switch time of pressure p_1 reduces with p_2 increasing in Fig.4.

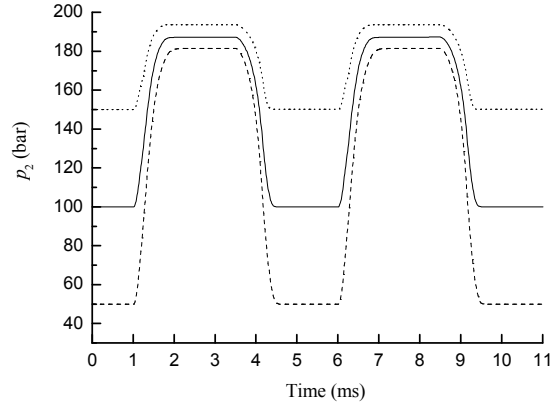

Fig.4 Influence of p_2

4.4 Influence of damper

The importance of the damper in the valve is shown in Fig.5 and Fig.6. It can be seen that the poppet is kicked off by striking force F_{PE1}, and when the poppet arrives at its right end with high speed it will be bounced back by the stiffness of the contact. Resonant vibration happens around its end, and it takes a long time for the poppet to stop at its end with the help of the fluid viscosity force, shown in Fig.6. The relationship between displacement and bounce force of the PE valve with the rubber damper is shown in Fig.7. It can be seen that when the poppet arrives at its right end with high speed, the damper is used to consume the energy of vibration and reduce the extent and times of vibration, so there is only one small bounce force and no displacement ripple at its right end, the same things happens at its left end, therefore the poppet can reach its two ends at the defined time.

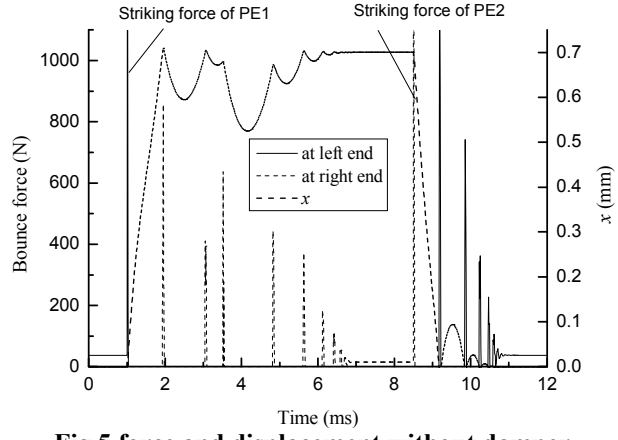

Fig.5 force and displacement without damper

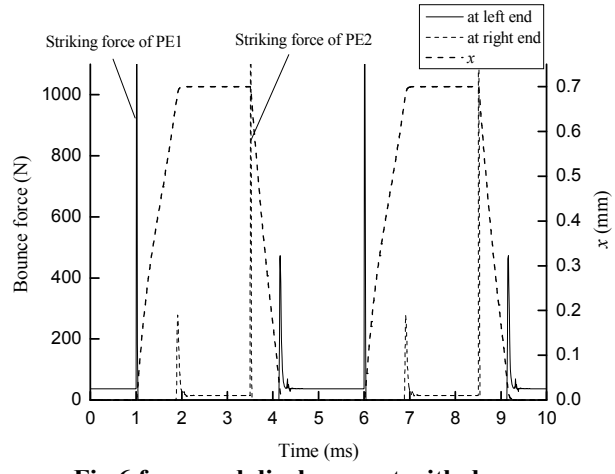

Fig.6 force and displacement with damper

4.5 Performance at p_1=200 bar

Fig.7 shows the comparison between p_1 and p_2 at pressure p_1=200 bar. It can be seen that pressure p_1 stays at about 200 bar and p_2 is zero while the poppet closes. During the poppet opening period, p_1 has a big pressure ripple and p_2 increases from 0 to its maximum. When the poppet stays at its end, pressure p_1 and p_2 are both stable, moreover there is a pressure difference between p_1 and p_2 owing to the throttle effect of the poppet. When the poppet closes, p_2 reduces to zero, and p_1 recovers to its original value.

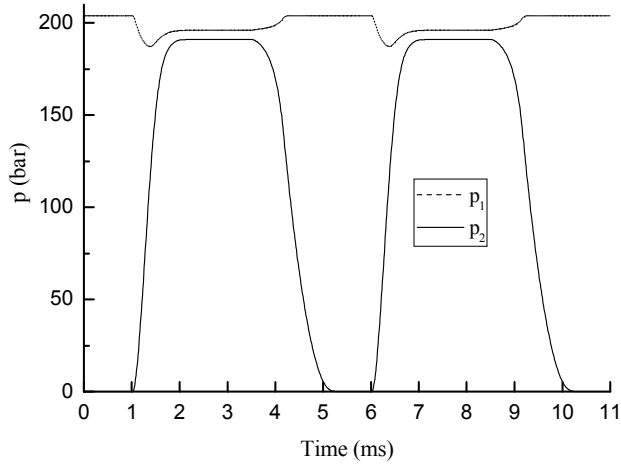

Fig.7 Comparison between p_1 and p_2

Fig.8 shows the relationship between displacement x and flow rate q_v at p_1=200 bar. It can be seen that $q_{v,1}$ is similar to $q_{v,2}$. When x is zero, flow rate $q_{v,1}$ and $q_{v,2}$ are both zero; when x is maximum at 0.7mm, $q_{v,1}$ and $q_{v,2}$ are both 15.7 L/min; while x increases from 0 to 0.7mm, $q_{v,1}$ and $q_{v,2}$ both have a large peak and $q_{v,1}$ is little higher than $q_{v,2}$; when x reduces from 0.7mm to 0, flow rate $q_{v,1}$ and $q_{v,2}$ drop rapidly from 15.7 L/min to 0. When the pop-

pet reaches or leaves its maximal displacement of 0.7 mm, $q_{v,1}$ and $q_{v,2}$ both have flow ripple. Fig.10 shows the relationship between operating voltage U and displacement x. It is the pulse voltage U of 100V that contributes to the movement of the poppet.

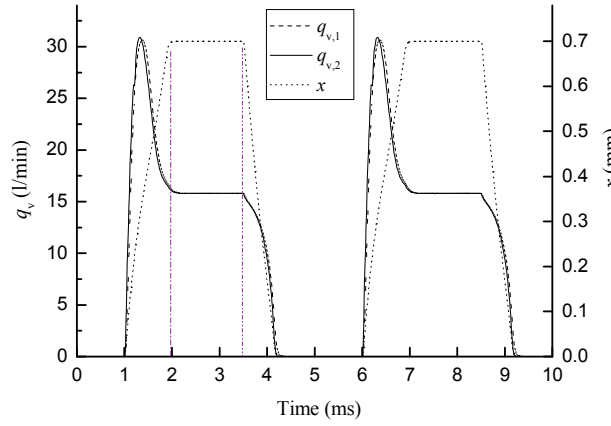

Fig.8 Displacement/flow rate

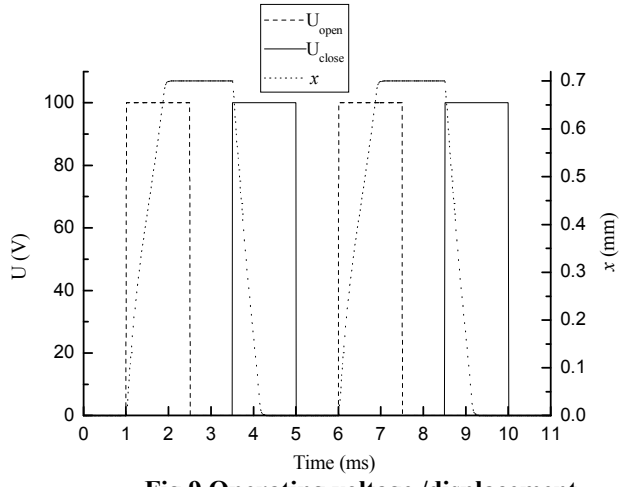

Fig.9 Operating voltage /displacement

5 TEMPERATURE INFLUENCE

The frequent switching of the digital valve may induce a fast rise in oil temperature. Furthermore the piezoelectric ceramics are capacitive loads and require increasing charge and discharge currents with operating frequency, and part of the electric energy is transformed into heat. The high temperature will result in the linear thermal expansion of the piezoelectric actuator, and influence the performance of the PE valve [9] [10]. If there is no temperature compensation for the PE actuator, when the PE actuators are not powered on, some leakage will happen because the expanded length of the PE actuator lifts the poppet a small distance.

Normally, the heat energy produced by throttle loss while oil flows through the poppet is expressed as

$$W_{oil} = \int (p_1 - p_2) q_{v,2} dt \tag{6}$$

If the total volume of oil through the poppet is V, the rising temperature of oil is given by

$$\Delta T_{oil} = \frac{\int (p_1 - p_2) q_{v,2} dt}{c_1 \rho V} \tag{7}$$

If the pressure difference and the flow rate are obtained from Fig.7 and Fig.8, the power loss based on equations (6) and (7) in one period of 4ms is shown in Fig.10. Energy loss is integrated and its value is about 2.74J. If the digital valve continues working for 10 minutes at the same frequency f, the temperature rising ΔT_{oil} is about 10ºC.

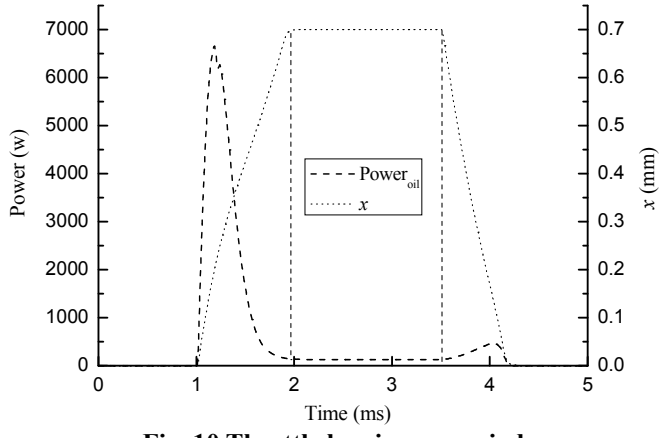

Fig. 10 Throttle loss in one period

The thermal power W_{PE} generated in the PE actuator during harmonic excitation can be estimated with the following equation [11]:

$$W_{\mathrm{PE}} = \frac{\pi}{4} \cdot \tan\delta \cdot f \cdot C \cdot U_{P-P}^2 \cdot t \tag{8}$$

The rising temperature of the PE actuator is given by

$$\Delta T_{\mathrm{PE}} = \frac{\frac{\pi}{4} \cdot \tan\delta \cdot f \cdot C \cdot U_{P-P}^2 \cdot t}{m_p c_2} \tag{9}$$

Similarly, if the valve keeps running for 10 minutes at the same frequency f and there are no measures to reduce temperature, the temperature rise of the PE actuator ΔT_{PE} is about 100ºC.

The above calculation is independent of the digital valve. Here the calculated heat energy W_{oil} and W_{PE} is put into the digital valve and the ambient temperature and initial oil temperature is set as 20 ºC. A temperature field simulation was carried out in ANSYS software in two different valve configurations. Fig.11 shows the temperature simulation of the original digital valve without temperature consideration. Fig.11a shows that the PE digital

valve has a steel ring sleeve. Fig.11b shows its temperature field, where the highest temperature is about 55.5 ºC, inside of the PE actuator, and the lowest temperature is about 28.5 ºC, the oil temperature. Fig.11c shows the thermal deformation of the PE valve and the distance between the poppet and its seat total is about 3.5μm owing to the thermal expansion of the PE actuator. It is obvious that the valve has a poor capability of dealing with rising temperature.

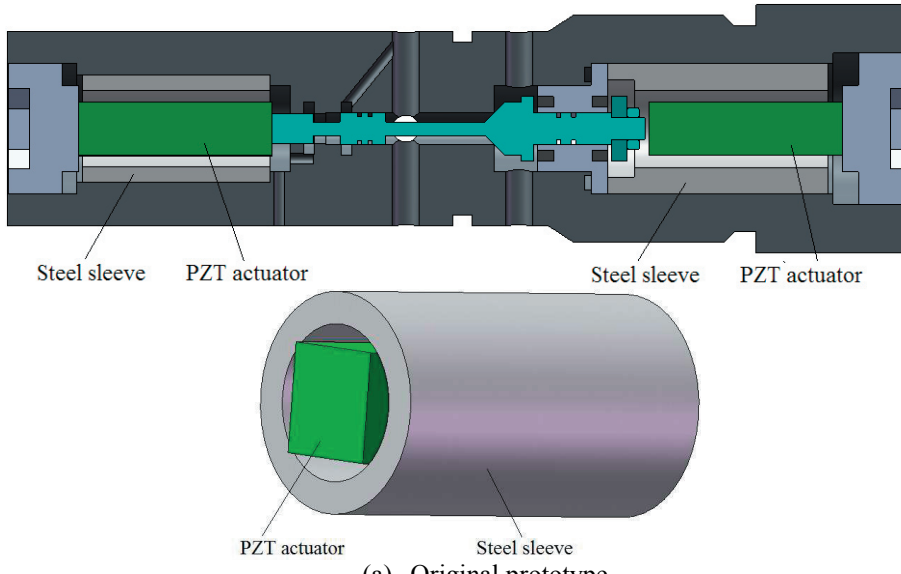

(a) Original prototype

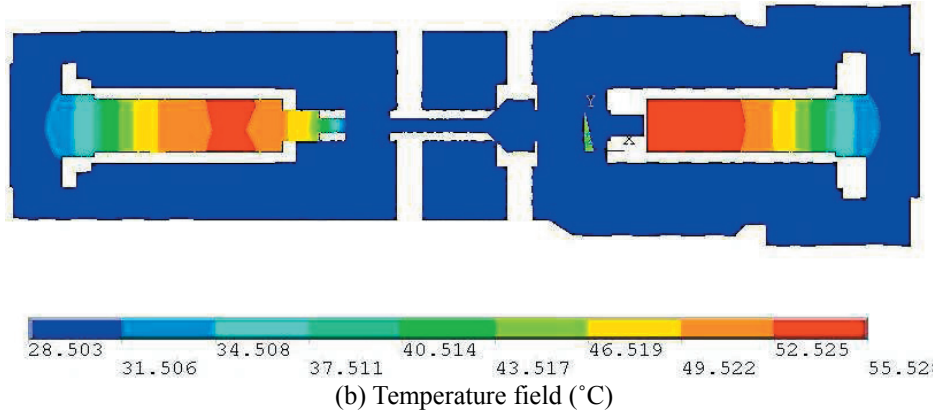

(b) Temperature field (˚C)

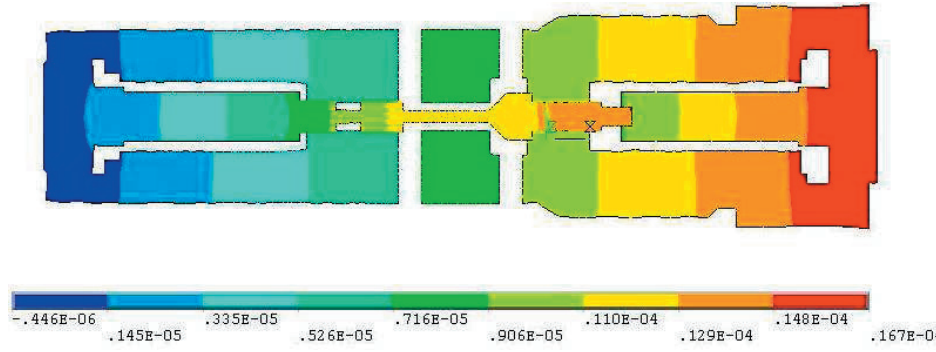

(c) Thermal strain

Fig.11 Without temperature consideration

Fig.12 shows the temperature simulation of the improved digital valve with temperature consideration, where the same heat energy that used in original one is put into simulation model. Fig.12a shows that the PE digital valve has a special copper sleeve and a copper shim between the poppet and the PE actuator, which have a high coefficient of heat conduction. Fig.12b shows its temperature field, where the highest temperature is about 32 ºC, inside of the PE actuator, and the lowest temperature is about 26.5 ºC, the oil temperature. Fig.12c shows the thermal deformation of the PE valve and the distance between the poppet and its seat total is about 0.18μm owing to the thermal deformation. It is obvious that the improved one has a good capability of dealing with temperature rise.

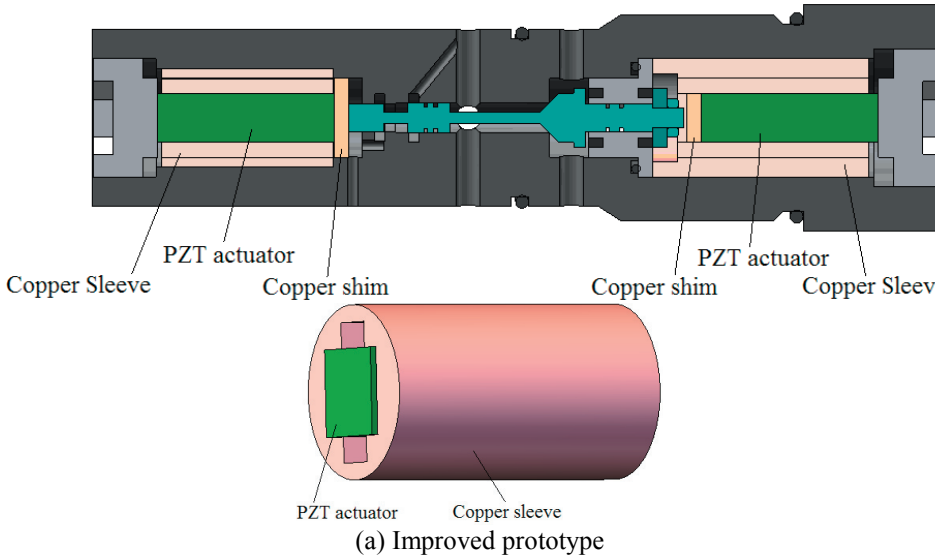

(a) Improved prototype

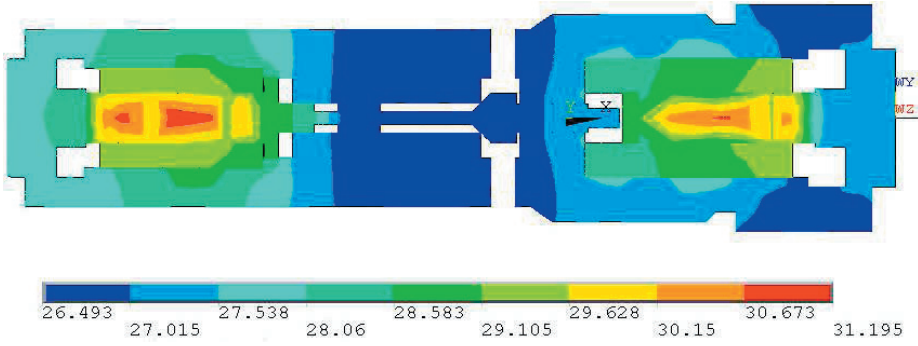

(b) Temperature field (˚C)

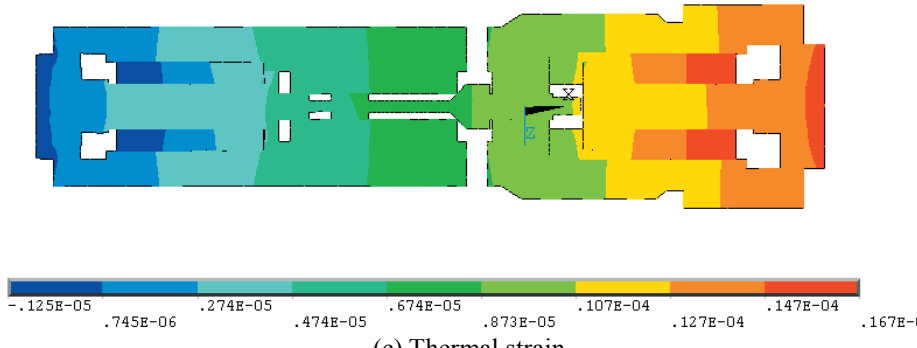

(c) Thermal strain

Fig.12 With temperature consideration

6 CONCLUSIONS

An innovative concept of the piezoelectric high speed valve is outlined, and the characteristic of high instant force of the PE actuator is used to open and close the poppet, and its micro displacement amplification is not necessary in the new PE valve.

The mathematical model of the piezoelectric valve is built and related simulation is carried out. The simulation results show the PE valve can realize oil switching successfully and the performance can be obtained as: pressure of 200 bar, flow rate of 15L/min and frequency of 250Hz. Some key dimensions are also discussed and optimized.

Temperature field simulation is done in ANSYS, and influence of thermal expansion is discussed. Compared to the original prototype, the improved one has a good capability of dealing with rising temperature.

Finally, much more work is still needed to improve the PE valve and to obtain good performance. A prototype and test rig are currently being built.

ACKNOWLEDGMENT

The authors acknowledge "973" Project from the Ministry of Science and Technology of China (Grant No. 2007CB714004) and the Qianjiang excellent project of Zhejiang Province (Grant No. 2007R10024) for supporting the research.

NOTATION

A	poppet valve flow area
c_1	specific heat of oil
c_2	specific heat of the PE actuator
C_{q1}	poppet valve flow coefficient
C_{q2}	flow coefficient of spool II
C_{q3}	flow coefficient of spool III
d	nominal diameter of the poppet valve
d_1	diameter of the poppet guide
d_2	diameter of spool II
d_3	diameter of spool III
e_1	overlap length of spool II
e_2	underlap length of spool III
F_{f1}	poppet valve flow force
F_{f2}	flow force of spool II
F_{f3}	flow force of spool III
F_{PE1}	force generated by the PE actuator 1
F_{PE2}	force generated by the PE actuator 2
h_1	penetration for full damping of damper 1
h_2	penetration for full damping of damper 2
k	stiffness of rubber damper
K_L	flow constant term of throttle valve
K_T	stiffness of the PE stack
ΔL_{max}	maximum displacement of the PE stack
U_{max}	maximum voltage of the PE stack
U	operating voltage of the PE stack
m	poppet mass
m_p	mass of one PE actuator
ρ	oil density
p_1	pump pressure
p_2	load pressure
p_3	chamber C pressure
p_t	tank pressure
$q_{v,1}$	flow rate of inlet
$q_{v,2}$	flow rate of outlet
$q_{v,3}$	discharge flow rate of the poppet
$q_{v,4}$	flow rate of spool II
$q_{v,5}$	flow rate of spool III
r	damper coefficient of the rubber damper
t	running time of the PE valve

x	poppet valve opening
x_{max}	maximal displacement of the poppet
tan δ	dielectric factor
V	total fluid volume through poppet
V_A	fluid volume of chamber A
V_B	fluid volume of chamber B
V_C	fluid volume of chamber C
v_1	oil velocity into Chamber B
v_2	oil velocity into Chamber C
v_3	oil velocity into Chamber E
W_{oil}	heat energy produced by throttle loss of the poppet
W_{PE}	heat energy produced by the PE actuator
α	poppet valve jet angle
β_e	effective bulk modulus, $\beta_e=1.4\times10^9$ N/m^2
β_1	jet angle of spool II
β_2	jet angle of spool III
ΔT_{oil}	temperature rise of oil
ΔT_{PE}	temperature rise of PE actuator

REFERENCES

1. Zhang X Y, Wang X H. Development and application of digital valve. Chinese Hydraulics & Pneumatics. 2001(3):32–33.
2. Manhartsgruber, B. A hydraulic control valve for PWM actuation at 400 Hz. Power Transmission and Motion Control 2006, Bath, 373-385.
3. Bauer F, Murrenhoff H. Piezo actuators-the future for high dynamically driven servo-valves? ICFP2005. Hanghzou: 62–68.
4. Lindler J E, Anderson E H. Piezoelectric Direct Drive Servovalve. Proceeding of SPIE 2002 on Industrial and Commercial Applications of Smart Structures Technologies. San Diego, 2002: 488–496.
5. Reichert M, Murrenhoff H. New concepts and design of high response hydraulic valves using Piezo-technology. Power transmission and motion control 2006. Bath: 2006:401–414.
6. A P Wong, W A Bullough, S B Chin, Y S Chua. Performance of the piezo-poppet valve, Part 1. Proceedings of the Institution of Mechanical Engineers, Part I: Journal of Systems and Control Engineering. 2006, Vol(220): 439–451.
7. Zheng W Z, Xin H B, Zhao F. Design of Micro-displacement Amplifier with Piezoactuator. Mechanical science and technology. 2003.22(6):966–967.
8. Fitch E C and Hong I T. Hydraulic component design and selection, Book 1 of the Computerized Fluid Power Design Series, BarDyne, Inc. (2001) 19-44.
9. Janocha H, Kuhnen K. Real-time Compensation of Hysteresis and Creep in Piezoelectric Actuators [J].Sensors and Actuators A, 2000,79(1) :83–89.
10. Physik Instrumente (PI) GmbH & Co.KG. High performance Piezo Actuators for OEM, Industry and Research. 09/2005.12–13
11. Electrical Requirements for Piezo Operation. http://www.physikinstrumente.com/en/products/prdetail.php?sortnr=400600.75

A Reduced Order Model for a Poppet-Type Relief Valve

Noah D. Manring
Mechanical and Aerospace Engineering Department
University of Missouri – Columbia
Columbia, MO 65211

ABSTRACT

In this paper, the dynamics of a poppet-type relief valve are studied for the purposes of generating an accurate reduced order model that may be used in the simulation of hydraulic systems. This study begins by developing a nonlinear model of the valve system including the steady and transient flow forces that act on the poppet. From here, a linearized third order model is produced from which a stability criterion for the system is deduced using the Routh-Hurwitz method. By neglecting the mass of the poppet, a reduced second order model is developed from which the system's natural frequency and damping ratio are determined. The nonlinear, linearized, and reduced order models are compared using simulation studies and it is shown that the reduced order model correlates well for sufficiently stable systems that are characterized by damping ratios less than 0.718.

1. NOMENCLATURE

A	instantaneous poppet valve flow area
A_o	steady-state poppet valve flow area
A_s	inlet area of the incompressible control volume
C	poppet damping coefficient
C_d	discharge coefficient of the poppet valve
D	inlet diameter of the incompressible control volume
$\mathbf{F}$	vector force acting on the incompressible control volume
F_f	force acting on the poppet from the fluid
F_{ff}	poppet valve flow forces (part of F_f)
F_{sp}	force acting on the poppet from the spring
F'_{sp}	poppet spring force (preload) when $y = 0$
k	poppet spring rate
L	essential length of the fluid column within the incompressible control volume
M	poppet mass

Fluid Power and Motion Control 2008 Edited by Dr D N Johnston and Professor A R Plummer

P	instantaneous fluid pressure
P'	cracking pressure of the valve
P_o	steady-state fluid pressure
Q	instantaneous volumetric flow rate through the poppet valve
Q_o	steady-state volumetric flow rate through the poppet valve
t	time
$\mathbf{u}$	fluid velocity vector within the incompressible control volume
V	volume of the compressible control volume
y	instantaneous poppet displacement
y_o	steady-state poppet displacement
β	fluid bulk modulus of elasticity
ζ	damping ratio predicted by the reduced order model
θ	conical angle of the poppet valve
λ	system eigenvalue
ρ	fluid density
τ	characteristic time constant
φ	jet angle of the fluid discharge flow
ω_n	natural frequency predicted by the reduced order model

2. INTRODUCTION

2.1 Background

Poppet-type relief valves are used to limit pressure levels within hydraulic circuitry. These valves have been used in both mobile and industrial applications for safety and pressure regulation and are commonly constructed in a cartridge design for easy adjustment and / or replacement when the valve fails. Due to the nature and function of the relief valve, these valves are used on an intermittent basis and are accompanied by large power losses and frequent instability problems. Though the poppet valve is a simple looking device, the fluid flow characteristics of this valve are often difficult to predict and model in an analytical way. As a result, when modeling the poppet valve dynamics, the flow forces that act on the poppet valve have either been neglected or oversimplified. Furthermore, the upstream characteristics of the fluid chamber are often neglected. This paper is an attempt to improve the analytical techniques that are frequently used for modeling poppet valves in the simulation of hydraulic control systems.

2.2 Literature Review

Some of the most basic research on poppet valves has been produced by the Dynamic Analysis and Control Laboratory at the Massachusetts Institute of Technology [1]. In this work, the steady-state flow forces acting on the poppet valve were analytically modeled and experimentally shown to be significant. The efforts of this work have shown that downstream conditions of the poppet valve influence the steady-state flow force. This work was assisted by fundamental studies done by von Mises for predicted the steady flow force and the discharge coefficient of the valve as a function of poppet angle. Other

experimental work has been conducted to reduce poppet flow forces by altering the geometry of the poppet [2]. In this work, many operating conditions were studied and it was shown that the discharge coefficient of the valve was fairly constant over a wide range of operating conditions. In other work, the stability of the poppet valve has been studied as it relates to the dynamics of the fluid delivery line and the spring-mass system of the valve [3]. In this work, the poppet valve operated in the reverse direction of conventional poppet valves. The author presented a stability criterion for this system but did not fully address the transient flow forces acting on the valve. To address the frequent instability, noise, and wear issues of the poppet valve, other authors have suggested a closed loop feedback scheme for stabilizing the valve [4]. Though this approach is commendable, it adds cost and reduces the reliability of a device this is supposed to perform a very simple task. As will be shown in the following pages, the modeling efforts of this current study will lend insight into the stable design of an open loop valve and thus eliminating the need for closed loop feedback.

2.3 Valve Description

Figure 1 shows the general configuration of a poppet-type relief valve. In this figure, the poppet is shown to be forced against the seat by a compressed spring. The compression of the spring may be adjusted by altering the vertical position of the cartridge. As the pressure in the bottom port increases, the hydrostatic force acting on the poppet overcomes the spring force and lifts the poppet away from the seat. Once the poppet separates from the seat, fluid is allowed to flow through the poppet valve from the pressurized port to the exhaust port. The release of this fluid achieves the basic function of the poppet valve.

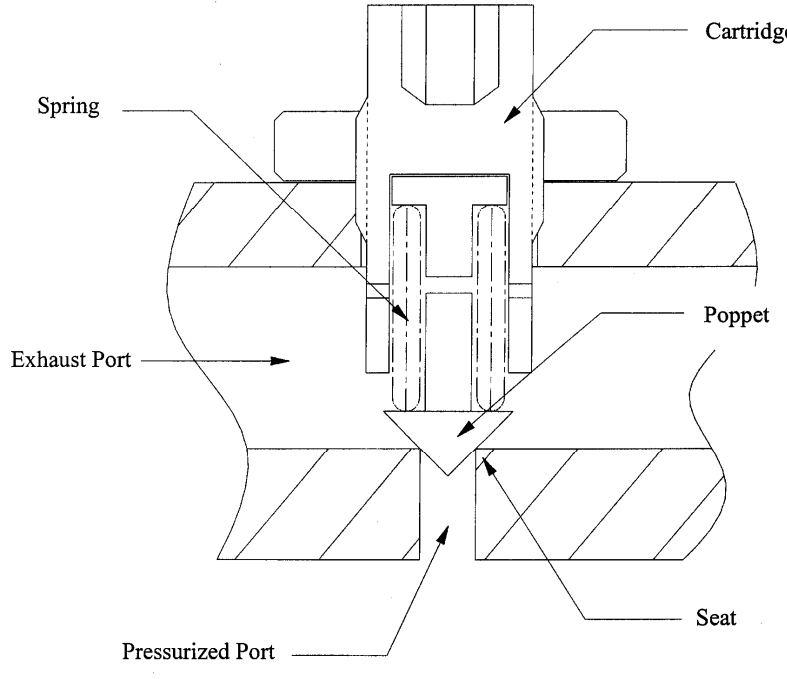

Figure 1 Basic geometry of a poppet-type relief valve

2.4 Objectives

In this paper, the dynamics of a poppet-type relief valve are studied for the purposes of generating an accurate reduced order model that may be used in the simulation of hydraulic systems. This study begins by developing a nonlinear model of the valve system including the steady and transient flow forces that act on the poppet. From here, a linearized third order model is produced from which a stability criterion for the system is deduced using the Routh-Hurwitz method. By neglecting the mass of the poppet, a reduced second order model is developed from which the system's natural frequency and damping ratio are determined. The nonlinear, linearized, and reduced order models are compared using simulation studies and it is shown that the reduced order model correlates well for sufficiently stable systems that are characterized by damping ratios less than 0.718.

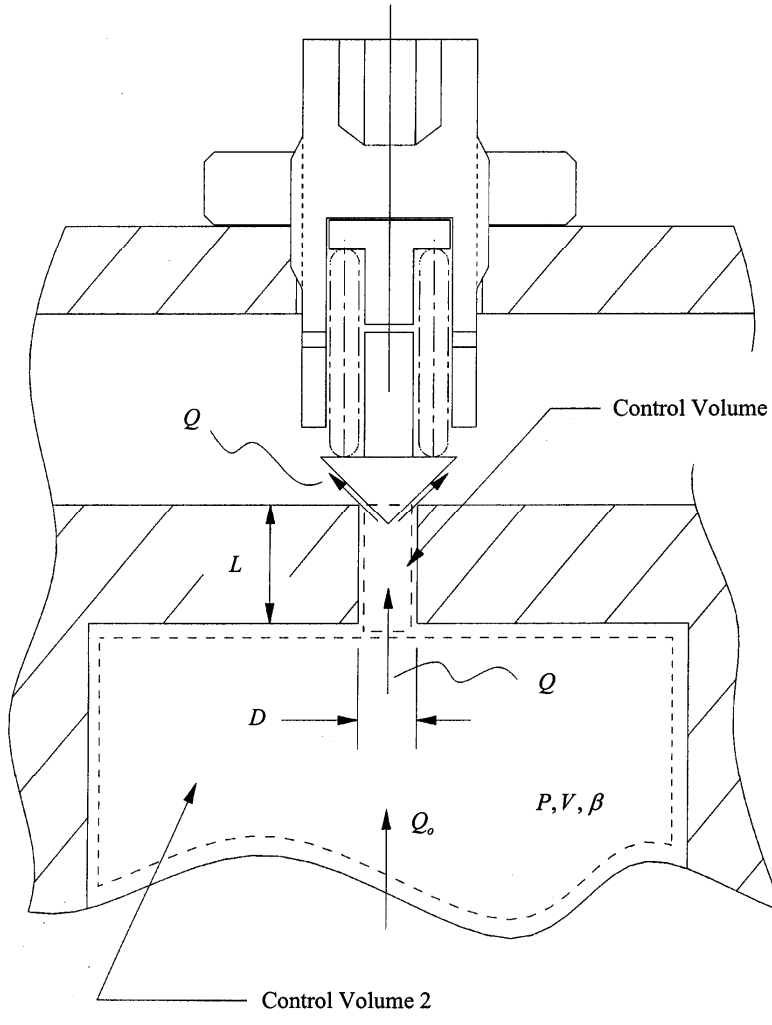

Figure 2 Fluid control volumes

3. NONLINEAR MODELING

3.1 Fluid Control Volumes

Figure 2 shows a schematic of the fluid control volumes that will be considered in this analysis. Control Volume 1 describes a column of fluid that acts directly on the poppet to separate the poppet from the seat. This column of fluid is described by the essential length of the column, L, and the diameter of the pressurized port, D. The fluid within this control volume is assumed to be incompressible with a uniform pressure, P. The conservation of mass for an incompressible fluid requires that the volumetric flow rate into the control volume be equal to the volumetric flow rate out of the control volume. This volumetric flow rate is the flow rate of the valve and is represented by the symbol, Q. Control Volume 2 describes the volume of fluid that is upstream of Control Volume 1. The fluid within Control Volume 2 is slightly compressible with a modulus of elasticity given by β. The fluid pressure within this control volume is uniform and given by the symbol P. The volume of fluid, V, is assumed to be fixed and the volumetric flow rate into Control Volume 2 is given by Q_o. The volumetric flow rate out of Control Volume 2 is the flow rate of the valve, Q. The fluid pressures in Control Volumes 1 and 2 are identical and uniform and are referenced from the fluid pressure in the exhaust chamber of the valve.

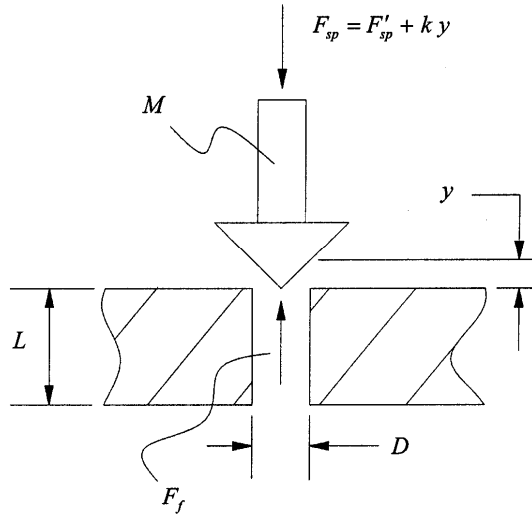

Figure 3 Free-body-diagram of the poppet

3.2 Poppet Forces

Figure 3 shows a free body diagram of the poppet. From this figure, it can be seen that the forces acting on the poppet result from the applied spring force, F_{sp}, and the fluid force, F_f. Summing forces in the vertical direction and setting them equal to the poppet's time-rate-of-change of linear momentum yields the following equation of motion for the poppet:

$$M\,\ddot{y} = -C\,\dot{y} - k\,y - F'_{sp} + F_f \quad , \tag{1}$$

where M is the poppet mass, C is the viscous drag coefficient, k is the spring rate, and F'_{sp} is the preload on the spring.

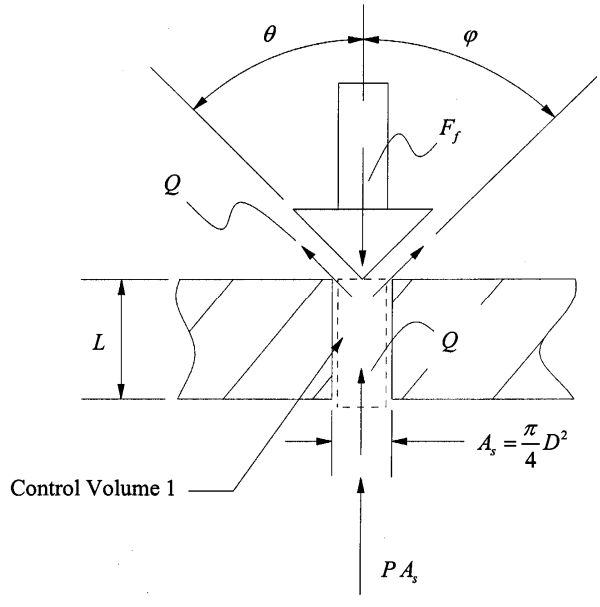

Figure 4 Free-body-diagram of Control Volume 1

3.3 Fluid Forces

Figure 4 shows the free body diagram of Control Volume 1. This figure shows the equal and opposite fluid force reaction against the poppet, F_f, and the hydrostatic pressure force, $P\,A_s$. Note: the fluid shear along the walls of the control volume has been neglected. The momentum effects of the fluid passing through the control volume can be determined using the Reynolds Transport Theorem given by

$$\frac{\partial}{\partial t}\int_{c.v} \rho\,\mathbf{u}\,dv + \int_{c.s.} \rho\,\mathbf{u}\,(\mathbf{u}\cdot\hat{\mathbf{n}})\,da = \mathbf{F} \quad , \tag{2}$$

where ρ is the fluid density, $\mathbf{u}$ is the fluid velocity, v is the fluid volume, $\hat{\mathbf{n}}$ is a unit vector that points out normally from the control volume surface, a is the area of the control surface, and $\mathbf{F}$ is the total vector force acting on the surface of the control volume by its surroundings. The vertical component of Equation (2) may be approximated using the following expression:

$$\rho\,L\,\frac{\partial Q}{\partial t} + \rho\,\frac{Q^2}{A}\cos(\varphi) = A_s\,P - F_f \quad , \tag{3}$$

where φ is the jet angle of the fluid flow exiting the valve and the instantaneous discharge area of the poppet is given by

$$A = \pi\, D \sin(\theta)\, y \quad , \tag{4}$$

where θ is the conical angle of the poppet shown in Figure 4. This expression for the discharge area of the poppet can be determined from geometry and has been used in previous research [1]. In Equation (3), it has been assumed that $A \ll A_s \cos(\varphi)$ which generally means that $y / D \ll 1$. It is also important to recognize that the pressure recovery effects in the exhaust port are assumed to be zero. Since the diameter of the exhaust port is assumed to be very large in comparison with the diameter of the pressurized port, D (see Figure 2); the pressure recovery effects can be neglected [1].

3.4 Fluid Pressure

To describe the fluid pressure in Control Volume 2, we use the classical pressure rise rate equation that has been derived in previous literature [5]. This equation is based upon continuity and the definition of the fluid bulk modulus, β, and is give by

$$\frac{dP}{dt} = \frac{\beta}{V}\left(Q_o - Q\right) \quad , \tag{5}$$

where V is the total volume of the pressurized chamber, and Q_o is the volumetric flow rate into Control Volume 2 (see Figure 2). Since the fluid in Control Volume 1 is assumed to be incompressible, the solution to Equation (5) also describes the essential fluid pressure in Control Volume 1.

3.5 Flow Model

The previous results require an adequate model for the volumetric flow rate through the valve. The model used in this research is the well-known orifice equation given by

$$Q = A\, C_d \sqrt{\frac{2}{\rho} P} \quad , \tag{6}$$

where C_d is the discharge coefficient of the poppet valve that must be determined experimentally [2]. It is important to emphasize that Equation (6) assumes that the flow is incompressible and steady. Though these assumptions are not satisfied everywhere in the previous development of the system model, the use of Equation (6) is justified based upon its wide acceptance in previous research dealing with similar topics [1,2,3,4,5,6] and the mathematical expediency that it offers to this current work.

3.6 Dimensionless Equations

To gain insight into the physical importance of each term in the preceding analysis, the governing equations for the poppet valve will be non-dimensionalized using the following definitions:

$$t = \hat{t}\, \tau \quad , \quad P = \hat{P}\, P_o \quad , \quad Q = \hat{Q}\, Q_o \quad , \quad y = \hat{y}\, y_o \quad , \quad A = \hat{A}\, A_o \quad , \tag{7}$$

where τ is a characteristic length of time, carets denote non-dimensional quantities, and the subscript, o, denotes a nominal, desired, or steady state value for the associated quantity. In other words, for steady state conditions, the symbols with carets are equal to unity. Using the previous analysis, the governing equations for the poppet valve motion and the fluid pressure transients may be written as

$$\Psi_1 \frac{d^2\hat{y}}{d\hat{t}^2} + \Psi_2 \frac{d\hat{y}}{d\hat{t}} + \Psi_3(\hat{y}-1) = (\hat{P}-1) - \Psi_4\left(\frac{\hat{Q}^2}{\hat{A}}-1\right) - \Psi_5 \frac{\partial \hat{Q}}{\partial t} \quad , \tag{8}$$

and

$$\Psi_6 \frac{d\hat{P}}{d\hat{t}} = \left(1-\hat{Q}\right) \quad , \tag{9}$$

where

$$\Psi_1 = \frac{M\ y_o}{A_s\ P_o\ \tau^2} \quad , \quad \Psi_2 = \frac{C\ y_o}{A_s\ P_o\ \tau} \quad , \quad \Psi_3 = \frac{k\ y_o}{A_s\ P_o} \quad ,$$

$$\Psi_4 = \frac{\rho \cos(\varphi)\, Q_o^2}{A_s\ P_o\ A_o} \quad , \quad \Psi_5 = \frac{\rho\, L\, Q_o}{A_s\ P_o\ \tau} \quad , \quad \Psi_6 = \frac{V\ P_o}{\beta\, Q_o\, \tau} \quad . \tag{10}$$

In Equations (8) and (9) all quantities are dimensionless and symbols with carets are scaled so that they are near the value of unity. This means that the physical importance of each term is determined by the dimensionless magnitude of each Ψ-coefficient. For instance, if Ψ_1 is much smaller than, say, Ψ_4 then we can say that poppet inertia is less important than the steady flow forces acting on the valve. Similar comparisons can be made with other coefficients within the same equation. Note: it is not proper to compare Ψ_6 with anything but unity, since it stands within its own equation as a solitary dimensionless group.

4. LINEAR MODELING

4.1 Linearized Model

Equations (8) and (9) represents a nonlinear, third order dynamic system for the poppet valve. By linearizing this system about the steady-state operating conditions, the following two equations may be written to describe the system dynamics:

$$\Psi_1 \frac{d^2\hat{y}}{d\hat{t}^2} + \left(\Psi_5 + \Psi_2\right)\frac{d\hat{y}}{d\hat{t}} + \left(\Psi_4 + \Psi_3 - \frac{1}{2}\frac{\Psi_5}{\Psi_6}\right)(\hat{y}-1) = \left(1 - \Psi_4 + \frac{1}{4}\frac{\Psi_5}{\Psi_6}\right)(\hat{P}-1) \tag{11}$$

and

$$\Psi_6 \frac{d\hat{P}}{d\hat{t}} = -(\hat{y}-1) - \frac{1}{2}(\hat{P}-1) \quad , \tag{12}$$

where again the Ψ-quantities are shown in Equation (10). These equations show that the transient flow force, Ψ_5, contributes to the effective damping of the valve while the steady flow force, Ψ_4, contributes to the effective stiffness of the valve.

At this point, it is useful to consider the magnitude of the Ψ-coefficients to determine the relative importance of each term within the governing equations. Using the design parameters presented in the Appendix, these coefficients may be determined for three different valve designs in which the L/D ratio is given by 2.5, 5.0, and 7.5 respectively. Table 1 shows these results. From Table 1, it may be concluded that poppet inertia is significantly small compared to other effects that have been included in the model, and that this inertia may be safely neglected for most situations. It is also shown from Table 1 that the steady flow force and mechanical spring effects are similar in magnitude, and that the transient flow force becomes more important as the entrance length to the poppet valve increases.

Table 1 A numerical comparison of nondimensional groups shown in Equation (10), based upon the design parameters in the Appendix

		$L/D = 2.5$	$L/D = 5.0$	$L/D = 7.5$
Poppet Inertia	$\Psi_1 =$	3.08E-04	3.08E-04	3.08E-04
Viscous Damping	$\Psi_2 =$	0	0	0
Mechanical Spring	$\Psi_3 =$	4.27E-02	4.27E-02	4.27E-02
Steady Flow Force	$\Psi_4 =$	9.53E-02	9.53E-02	9.53E-02
Transient Flow Force	$\Psi_5 =$	4.75E-03	9.49E-03	1.42E-02
Pressure Transient	$\Psi_6 =$	1	1	1

4.2 Valve Stability

The Routh-Hurwitz stability criterion will be used to determine the stability of the third-order, linearized system presented in Equations (11) and (12). This criterion depends uses the coefficients of the system's characteristic equation which is given by:

$$2\Psi_1\Psi_6\,\lambda^3 + \left(2\Psi_6(\Psi_5+\Psi_2)+\Psi_1\right)\lambda^2 + \left(2\Psi_6(\Psi_4+\Psi_3)+\Psi_2\right)\lambda + \left(2-\Psi_4+\Psi_3\right) = 0 \quad . \tag{13}$$

Using the Routh-Hurwitz stability criteria [7] it may be shown that the following conditions must be satisfied if the poppet valve is to remain stable:

$$\left(2-\Psi_4+\Psi_3\right) > 0$$
$$\left(2\Psi_6(\Psi_5+\Psi_2)+\Psi_1\right)\left(2\Psi_6(\Psi_4+\Psi_3)+\Psi_2\right) > 2\Psi_1\Psi_6\left(2-\Psi_4+\Psi_3\right) \tag{14}$$

Recognizing from Table 1 that $2 \gg \Psi_4 - \Psi_3$, and that by neglecting viscous damping $\Psi_2 = 0$, it may be shown that essential stability criterion for the third order system is approximately given by

$$(\Psi_4 + \Psi_3)\Psi_6\Psi_5 \; > \; \Psi_1 \quad . \tag{15}$$

Substituting Equation (10) into Equation (15), the stability criterion may be written more explicitly as

$$\left(\frac{\rho \cos(\varphi)\, Q_o^2}{A_o} + k\, y_o \right) \frac{V}{\beta} \frac{\rho\, L}{A_s} \; > \; M\, y_o \quad . \tag{16}$$

Physically speaking, this equation says that ability for the system to store energy in the spring effects and the fluid momentum, must exceed the amount of energy that represented by the kinetic energy of the poppet mass. Note: according to Equation (16) an increase in the length L will tend to increase the likelihood of stability.

4.3 Reduced Order Model

From Table 1, it may be shown that the poppet inertia can be safely neglected without much loss in modeling accuracy. Under these conditions the governing equations for the reduced order model may be written as

$$\left(\Psi_5 + \Psi_2\right)\frac{d\hat{y}}{d\hat{t}} + \left(\Psi_4 + \Psi_3 - \frac{1}{2}\frac{\Psi_5}{\Psi_6} \right)(\hat{y} - 1) \; = \; \left(1 - \Psi_4 + \frac{1}{4}\frac{\Psi_5}{\Psi_6} \right)(\hat{P} - 1) \tag{17}$$

and

$$\Psi_6 \frac{d\hat{P}}{d\hat{t}} \; = \; -(\hat{y} - 1) \; - \; \frac{1}{2}(\hat{P} - 1) \quad , \tag{18}$$

where again the Ψ-quantities are shown in Equation (10). Again, recognizing from Table 1 that $2 \gg \Psi_4 - \Psi_3$, and that by neglecting viscous damping $\Psi_2 = 0$, it may be shown that the characteristic equation for this system is given by

$$\Psi_6\Psi_5\lambda^2 + \Psi_6(\Psi_4 + \Psi_3)\lambda + 1 = 0 \quad . \tag{19}$$

From here it may be shown that the undamped natural frequency and the damping ratio of the second order system are given by

$$\omega_n \; = \; \sqrt{\frac{\beta}{V}\frac{A_s}{\rho\, L}} \quad , \quad \zeta \; = \; \frac{1}{2\,\rho\, L\, Q_o\, \omega_n} \left(\frac{\rho \cos(\varphi)\, Q_o^2}{A_o} + k\, y_o \right) \tag{20}$$

For the design listed in the Appendix, the natural frequency and damping ratio for three different configurations of the system are given in Table 2. The undamped natural frequency and the damping ratio can be used to qualitatively (and quantitatively) consider the dynamic response of a second order system [7]. The qualitative considerations may be summarized as follows: 1) increasing the undamped natural frequency, ω_n, reduces the rise

time of the system response, 2) increasing the damping ratio, ζ, reduces the maximum percent overshoot, and 3) increasing the product of the undamped natural frequency and the damping ratio, $\zeta\,\omega_n$, reduces the settling time of the dynamic response.

Table 2 A comparison of the undamped natural frequency and the damping ratio for three different configurations of the system described in the Appendix

		$L/D = 2.5$	$L/D = 5.0$	$L/D = 7.5$
Natural Frequency	$\omega_n =$	730 Hz	515 Hz	420 Hz
Damping Ratio	$\zeta =$	1.015	0.718	0.586

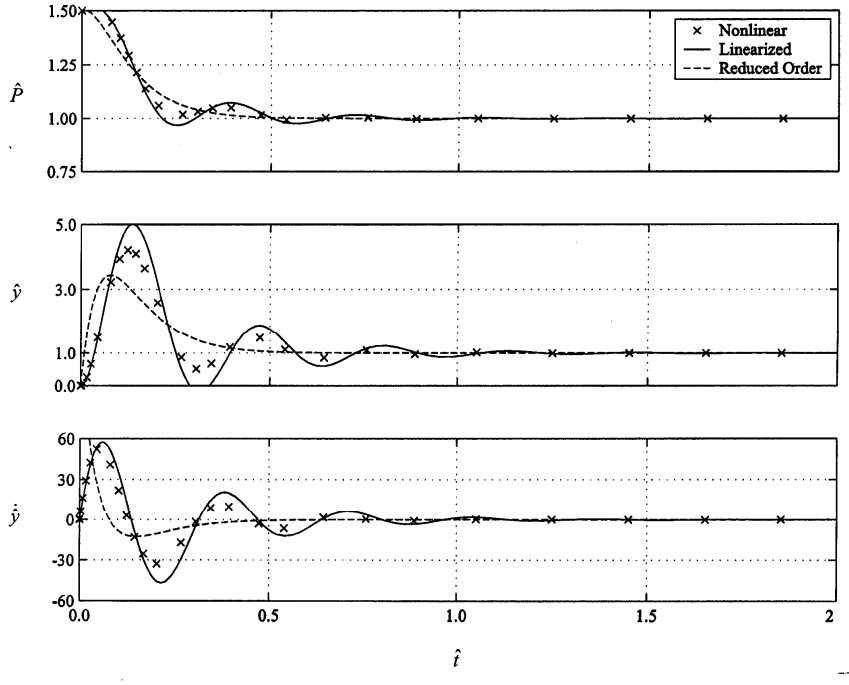

Figure 5 Dynamic response for *L/D* = 2.5

5. SIMULATION STUDIES

Simulation studies were conducted to compare the nonlinear, linearized, and reduced order models of the poppet valve. The parameters used to build these models are included in the Appendix and correspond with the physical design shown in Figures 1 through 4. During the simulation studies, the length of Control Volume 1, L (see Figure 2), was varied to

alter the damping ratio of the reduced order model. Figure 5 shows a comparison of results for $L/D = 2.5$, which corresponds to the geometry shown in Figures 1 through 4. Figure 6 shows a comparison of results for $L/D = 5.0$ while Figure 7 shows a comparison of results for $L/D = 7.5$. For each of these studies, the damping ratio of the reduced order model was given by 1.015, 0.718, and 0.586 respectively.

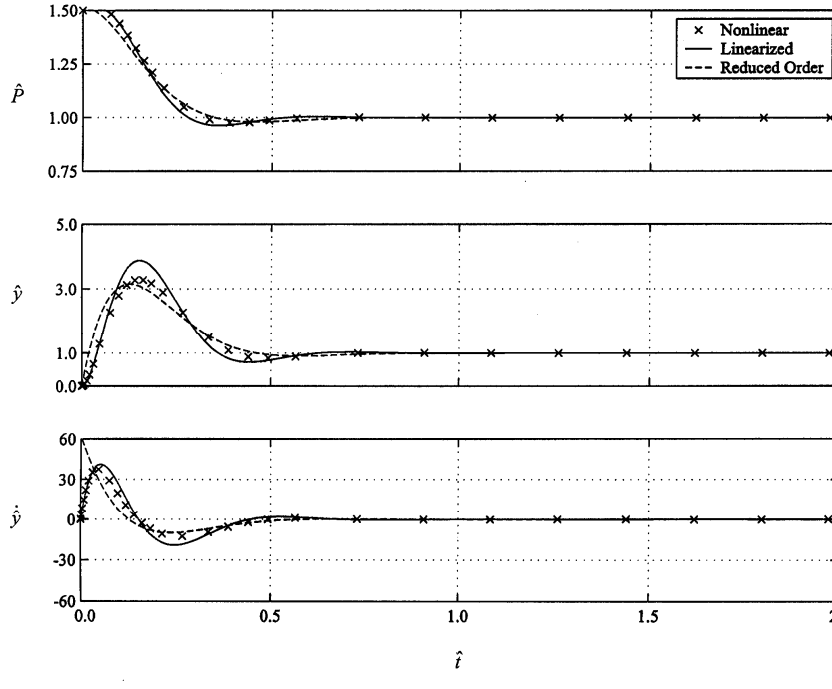

Figure 6 Dynamic response for *L/D* = 5.0

6. DISCUSSION

6.1 Stability

The stability criterion for the valve is shown in Equation (16). As previously mentioned, this criterion states that the stored energy in the spring effects and the fluid momentum, must exceed the amount of energy that represented by the kinetic energy of the poppet mass. If this ratio of storage capability is not satisfied, the poppet valve will be unstable. If stability becomes a problem for a specific application, it is recommended that one increase the length of Control Volume 1, L, or increase the total volume of Control Volume 2, V. Increasing these parameters will help to increase the fluid's ability to store kinetic and potential energy respectively and will thereby improve the system's stability.

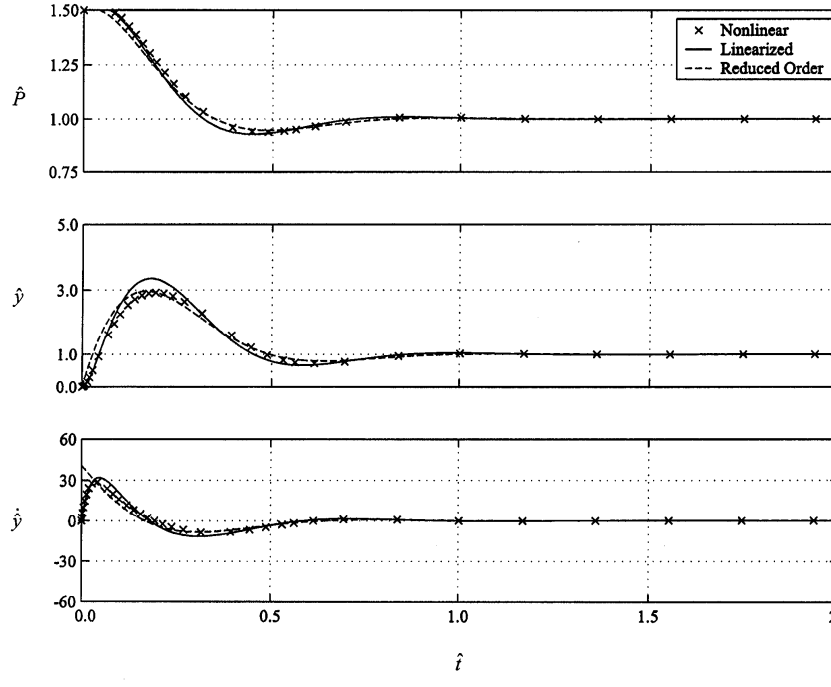

Figure 7 Dynamic response for *L/D* = 7.5

6.2 Modeling Comparisons

Figures 5 through 7 show the comparisons of the nonlinear, linearized, and reduced order models. As shown in these figures, the agreement between all three models improves as the damping ratio of the reduced order model is reduced. This means that the nonlinearities of operation and the mass of the poppet become less important as the damping ratio of the reduced order model decreases. From Table 2, it can be shown that this decrease can be readily accomplished by increasing the length of Control Volume 1, L. Using Equation (20), other system changes may also be introduced to decrease the damping ratio. Though the reduced order model may be used for mathematical expediency even for systems with high damping ratios, it is clear from these studies that the reduced order model at least offers a measure of simplicity (without sacrificing accuracy) for systems characterized by damping ratios less than 0.718.

7. CONCLUSION

The following conclusions are supported by the results of this research:

1. The steady flow forces acting on the poppet always tend to close the valve while the transient flow forces may tend to either open or close the valve depending upon the sign of the time derivative of the volumetric flow rate.

2. The transient flow forces acting on the poppet valve and the compressibility of the fluid in Control Volume 2 are essential for the valve's stability. See the stability criterion given in Equation (16).
3. The agreement between the nonlinear, linear, and reduced order model tends to improve as the damping ratio of the reduced order model decreases. Based upon the observations of this research, the reduced order model is recommended for systems with a damping ratios less than 0.718.
4. The stability of the actual valve and the validity of the reduced order model can be improved by increasing the energy storage capability of the fluid within the system. This increase is best achieved by increasing the length of Control Volume 1, L, or by increasing the total volume of Control Volume 2, V.
5. Increases in stability tend to increase the system rise time, the maximum percent overshoot, and the settling time of the system. Therefore, as usual, a tradeoff must be sought between stability and response.
6. The reduced order model is only valid for systems that exhibit good stability. As a corollary, the reduced order model should not be used to predict stability; rather, Equation (16) should be used for this purpose.

The reduced order model offers a measure of simplicity for the dynamic simulation of poppet-type relief valves that exhibit good stability. The previous conclusions may also be helpful for designing, re-designing, or troubleshooting the dynamic performance of a current poppet valve design.

8. APPENDIX

The following parameters were used in the simulation studies of this research. These parameters are grouped into three categories: 1) fixed geometry parameters, 2) operating conditions, and 3) calculated parameters. The calculated parameters are determined using relationships presented in this paper and the physical quantities reported in groups 1 and 2.

Fixed Geometry Parameters

Symbol	Description	Value	Units
D	Diameter of Control Volume 1	6	mm
k	Spring rate	65	N/mm
L	Length of Control Volume 1	varies	mm
M	Mass of the poppet	4.7	g
V	Volume of Control Volume 2	0.127	liters
θ	Conical angle of the poppet	45	deg

Operating Conditions

Symbol	Description	Value	Units
C	Viscous drag coefficient	0	Ns/m
C_d	Discharge coefficient	0.62	no units
P_o	Steady-state pressure	20	MPa
Q_o	Steady-state volumetric flow rate	40	liters/min
β	Fluid bulk modulus	1.2	GPa
ρ	Fluid density	850	kg/m^3
φ	Jet angle of the discharge flow	45	deg

Calculated Parameters

Symbol	Description	Value	Units
A_o	Steady-state discharge area	5	mm^2
F'_{sp}	Spring preload	487	N
P'	Cracking pressure	17.24	MPa
y_o	Steady-state poppet displacement	0.372	mm

The characteristic time constant for the simulations conducted in this research was selected to be

$$\tau = \frac{V\,P_o}{\beta\,Q_o} = 3.17 \text{ ms} \quad .$$

Note: the selection of this time constant has no physical impact on the simulations (it could have been anything without loss of generality). This particular time constant was used so that Ψ_6 could conveniently be set equal to unity. See Equation (10).

9. REFERENCES

[1] Stone, J.A. 1960. Discharge coefficients and steady-state flow forces for hydraulic poppet valves. ASME *Journal of Basic Engineering*, March, pp. 144-54.

[2] Johnston, D.N., K.A. Edge, and N.D. Vaughan. 1991. Experimental investigation of flow and force characteristics of hydraulic poppet and disc valves. Proc. Instn. Mech. Engrs. 205:161-71.

[3] Funk, J.E. 1964. Poppet valve stability. ASME *Journal of Basic Engineering*, June, pp. 207-13.

[4] Wandling D.E., and B.L. Johnson. 1972. Hydraulic poppet valve stability. SAE National Combined Farm, Construction & Industrial Machinery and Powerplant Meetings. SAE Paper No. 720792.

[5] Zeiger G., and A. Akers. 1985. Torque on the swashplate of an axial piston pump. ASME *Journal of Dynamic Systems, Measurement, and Control*. 107:220-26.

[6] Manring N.D., and R.E. Johnson. 1997. Optimal orifice geometry for a hydraulic pressure reducing valve. ASME *Journal of Dynamic Systems, Measurement, and Control*. 119:467-73.

[7] Franklin, G.F., J.D. Powell, and A. Emami-Naeini. 1994. Feedback Control of Dynamic Systems, 3rd ed. Addison Wesley Publishing Company, Inc., New York, NY. pp. 126-30.

[8] Shin Y.C. 1991. Static and dynamic characteristics of a two stage pilot relief valve. ASME *Journal of Dynamic Systems, Measurement, and Control*. 113:280-88.

[9] Sorensen H.L. 1999. Experimental and numerical analysis of flow force compensation methods for hydraulic seat valve. Sixth Scandinavian International Conference on Fluid Power, Tampere, Finland. pp. 471-81.

Session 5
Pneumatics

Applicability of Servo-pneumatic Positioning Systems for High Loads

Yesid Ernesto Asaff Mendoza, yasaff@hotmail.com
Lidiane Gonçalves de Oliveira, lidiane@emc.ufsc.br
Victor Juliano De Negri, victor@emc.ufsc.br
Federal University of Santa Catarina
Department of Mechanical Engineering – LASHIP – Laboratory of Hydraulic and Pneumatic Systems
Campus Universitário – Zip Code 88040-900 – Florianópolis – SC – Brazil
www.laship.ufsc.br

ABSTRACT

This paper analyzes the applicability of a servo-pneumatic positioning system in the presence of high loads. The model of the servo-valve which includes the non-linear relationship between the mass flow with pressure and electric voltage is presented. Regarding the cylinder modeling, the friction is successfully described with the use of a variable viscous friction model. Based on the model, the system design from the static and dynamic viewpoints is discussed and the theoretical-experimental analysis of a system aimed at the position control of hydraulic turbine blades with 12000N of loading is performed. A classic PID controller with dead-zone compensation of the servo-valve enabled fully satisfactory performance in relation to the settling time and position error established by international standards for power plant control. Thus, the applicability of servo-pneumatic technology with high load was verified and an alternative solution to the hydraulic technology currently used in electrical power plants is proposed.

Keywords: Pneumatic Servo Systems Speed Governing of Turbines.

Parameters

A_A	Cylinder chamber A area	1.227×10^{-2}	m^2
A_B	Cylinder chamber B area	$1.1467 \times 10^{-}$	m^2
b	Critical pressure ratio	0.12	
C	Sonic conductance	1.65×10^{-9}	$m^5/N.s$
M	Total mass	30	Kg
p_0	Pressure at the STP[1]	100	kPa
R	Gas constant	287	J/kg.K
T_0	Temperature at the STP	293.15	K
V_{A0}	Dead volume in cylinder chamber A	98.17×10^{-5}	m^3
V_{B0}	Dead volume in cylinder chamber B	98.17×10^{-5}	m^3

[1] STP = Standard Temperature and Pressure according to ISO 6358 (ISO, 1998).

Fluid Power and Motion Control 2008 Edited by Dr D N Johnston and Professor A R Plummer

γ	Specific heat ratio	1.4	
ρ_o	Density at STP	1.204	Kg/m^3

Variables

a	Pressure ratio	V	Volume in the cylinders (m^3)
Are	Relative opening (m^2)	v	Flow velocity (m/s)
Fc	Load force (N)	x	Piston position (m)
F_{a1}	Friction force of cylinder 2A1 (N)	x_a	Position amplitude
F_{a2}	Friction force of cylinder 2A2 (N)	x_d	Desired position
F_{sn}	Negative static friction force (N)	$\dot{x}_{on}$	Negative stick speed (m/s)
F_{sp}	Positive static friction force (N)	$\dot{x}_{op}$	Positive stick speed (m/s)
f_{vi}	Variable viscous friction coefficient	$\dot{x}_{Limn}$	Negative speed limit (m/s)
p	Pressure in cylinder chambers (Pa)	$\dot{x}_{Limp}$	Positive speed limit (m/s)
p_1	Upstream pressure (Pa)	$\dot{x}_i$	Speed at the operation point (m/s)
p_2	Downstream pressure (Pa)	$_{A,B}$	Subscripts for chambers A and B
q_m	Mass flow rate (Kg/s)	^{2A1}	Superscript for cylinder 2A1
T_1	Upstream temperature (K)	^{2A2}	Superscript for cylinder 2A2

1. INTRODUCTION

In the area of automation and control of equipment and processes three technologies have been used to generate mechanical movement, which are: hydraulics, electrical and pneumatics. Each one has inherent characteristics which make them appropriate for a specific domain, although there is some overlapping, especially when the levels of force (or torque) and speed are attainable through more than one constructive principle. In this paper the use of pneumatic position control is investigated in a force domain common in hydraulic systems. The domain field is electrical power generation using hydro turbines where the position control of the turbine blades is required. The motivation behind the substitution of hydraulic drives with pneumatic ones in small hydroelectric power plants is based on several aspects, including: (a) Equipment cost reduction,; (b) Attainment of lightweight systems; (c) Reduction in component quantity and dispensing with need for a hydraulic power unit; (d) Mineral oil is not required, reducing the environmental risks; and (5) Capacity to store energy in a simple way (through air reservoirs) to carry out emergency operations. As discussed in this paper, the levels of force, settling time and position error required for turbine speed governors in small hydroelectric power plants (SHPP) with a power of up to 2MW can be achieved through appropriate design of a pneumatic positioning system. Specifically, in section 2 the specifications of the servo-pneumatic system are presented and in section 3 the mathematical modeling is detailed. The test rig is described in section 4, the theoretical-experimental results are given in section 5 and in section 6 the conclusions are presented.

2. SERVO-PNEUMATIC SYSTEM

Figure 1 shows a general view of a Francis turbine with details of the shift ring and the servo-motor required for its movement.

Through the shift ring position control the blades will be positioned such that the flow through the rotor will produce the desired rotation speed.

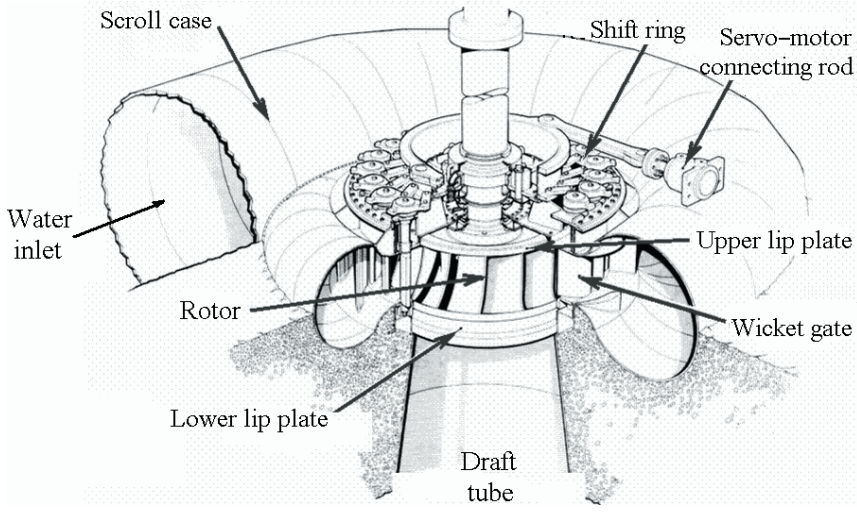

Figure 1. Francis turbine scheme (Littler (1))

The main design specifications for a positioning system for speed governors originate from the static and dynamic behavior requirements established by the ANSI/IEEE 125 (2) and IEC 61262 (3) standards. Additional requirements for Small Hydroelectric Power Plants (SHPP) are used, which were provided by Reivax Automation and Control Company and correlated research project results. The opening/closing times of the servo-motor[1] (*ta* and *tf*) are important specifications such that overspeed and water hammer in the penstock can be avoided. Considering previous results reported by Rodrigues & De Negri (4), the minimum opening/closing times of 5s were defined.

The standards cited above make reference to the use of hydraulic circuits where the installation of flow control valves between the continuous control valve (distributing valve) and the servo-motor is required. These valves must be adjusted so that the maximum opening/closing speeds (minimum times) of the wicked gate servo-motor are achieved. Furthermore, according to IEC 61362 (3), the time constant (τ) of the servo-positioner that controls the wicket gate opening must be between 0.1 and 0.25s. The maximum positioning error of the servo-motor is established as 1% of the total stroke. A generation setup composed of a Francis turbine with 400kW of power and 50m of head was chosen for this study.

The pneumatic circuit designed for this system is shown in Figure 2. Two double-acting cylinders are connected to one 5-port servo-valve that simultaneously puts in motion the two cylinders through a signal originated in the controller. The proportional pressure regulation valve, together with the air reservoir, has the function of keeping a constant air supply pressure for the servo-valve.

[1] In the domain of hydroelectric power plants, the cylinder is called the servo-motor.

The volume V_A is calculated with the addition of the volumes of the cylinder A chambers; the position $x^{2A1}=0$ is attained when cylinder 2A1 is retracted and position $x^{2A2}=0$ when cylinder 2A2 is in the advanced position. The system that emulates the mechanical work required in the regulating ring is formed by a lever pivoted at its center and connected at its extremities to the pneumatic cylinders and load hydraulic cylinder. The mechanical assembly of the cylinders includes swivel flanges that allow their angular movement, as shown in Figure 6.

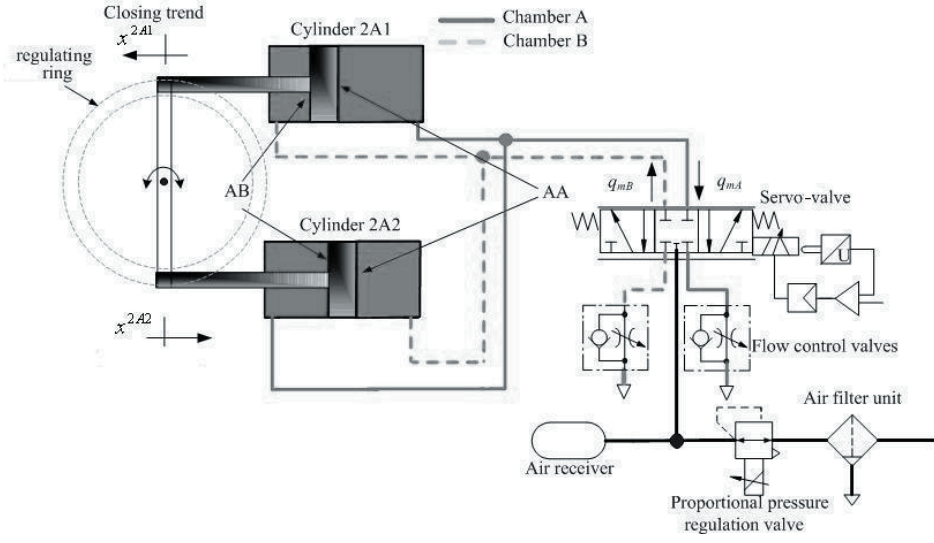

Figure 2. Pneumatic circuit for the speed-governing system

3. MATHEMATICAL MODELING

The analysis of the static and dynamic response was carried out through a non-linear model that includes both the dead-zone compensation of the servo-valve and the non-linear function of the mass flow rate with the pressures and electric voltage in the servo-valve. Based on experimental data, the friction in the cylinders is also represented by a non-linear model.

As presented in Scholz (5) and Vieira (6), the mass flow rate through the valve is modeled according to ISO 6358 (7):

$$q_m = A_{re} C p_1 \rho_o \sqrt{\frac{T_o}{T_1}} w(a) \tag{1}$$

where,

$$w(a) = \begin{cases} = \sqrt{1 - \dfrac{(a-b)^2}{(1-b)^2}} \;\; if \;\; a > b \\ = 1 \;\; if \;\; a \le b \end{cases} \quad \text{where} \quad a = \frac{p_2}{p_1} \text{ and } b = \left.\frac{p_2}{p_1}\right|_{cr} \tag{2}$$

The dead-zone (DZ) is a static input-output relationship where there is no output for a range of input values, as shown in Figure 3(a), where u is the input signal and u_{zm} is the output signal. In general, the right (z_{md}) and left (z_{me}) limits and the slopes (*md* and *me*) are not equal. The dead-zone compensation of the servo-valve is obtained by placing the inverse of the dead-zone function linearly smoothed at the origin (Figure 3(b)) between the control signal generated by the compensator u_{czm} and the valve signal input u. This compensation was presented by Tao and Kokootovic (8) and successfully implemented by Machado *et al*. (9), and is described by Eq.3.

$$u_{czm}(t) = \begin{cases} \dfrac{u(t)}{md} + zmd & if \quad u(t) \geq lc \\ \dfrac{u(t)}{me} - |zme| & if \quad u(t) \leq -|lc| \\ \left(\dfrac{zmd + lc/md}{lc} \right) u(t) & if \quad 0 \leq u(t) < lc \\ \left(\dfrac{|zme| + |lc|/me}{|lc|} \right) u(t) & if \quad -|lc| \leq u(t) < 0 \end{cases} \tag{3}$$

In this equation, u is the required input voltage in the absence of DZ, u_{czm} is the compensated signal and *lc* is the compensation width that defines the region of linear smoothing. The following values can be assumed for the servo-valve used in this study: *md* = *me* = 1, *zmd* = 0.61V, *zme* = 0.69V and *lc* = 0.4 (Vieira (6)).

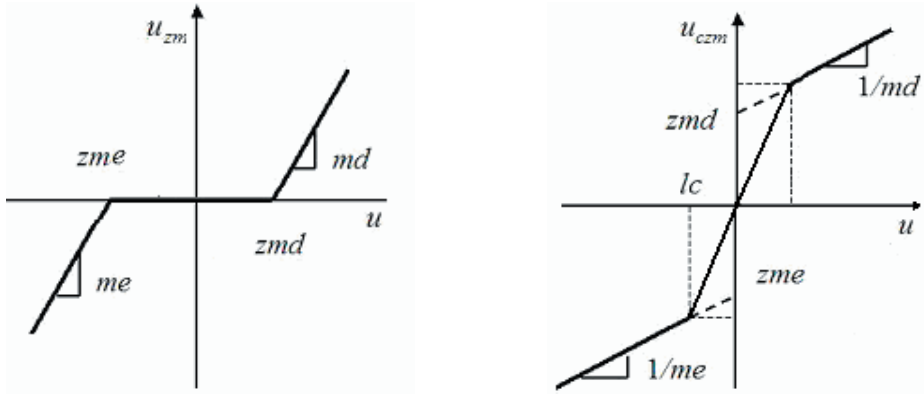

(a) **(b)**

Figure 3. Dead-zone: (a) Graphical representation of the dead-zone. (b) Graphical representation of the inverse of the dead-zone (Valdiero (10))

For the cylinders, Eqs. 4 and 5 describe the dynamic behavior of the air in the chambers, according to the pneumatic circuit shown in Figure 2 where the two cylinders are connected to the same servo-valve (Asaff (13)).

$$\frac{dp_A}{dt} = -\frac{v\gamma\left(A_A^{2A1} + A_B^{2A2}\right)}{V_{A0}^{2A1} + A_A^{2A1}x^{2A1} + V_{A0}^{2A2} + A_B^{2A2}x^{2A2}}p_A$$

$$+\frac{RT_A\gamma}{\left(V_{A0}^{2A1} + A_A^{2A1}x^{2A1} + V_{A0}^{2A2} + A_B^{2A2}x^{2A2}\right)}q_{mA} \tag{4}$$

$$\frac{dp_B}{dt} = \frac{v\gamma\left(A_B^{2A1} + A_A^{2A2}\right)}{V_{B0}^{2A1} + A_B^{2A1}\left(L - x^{2A1}\right) + V_{B0}^{2A1} + A_A^{2A2}\left(L - x^{2A1}\right)}p_B$$

$$-\frac{RT_B\gamma}{\left(V_{B0}^{2A1} + A_B^{2A1}\left(L - x^{2A2}\right) + V_{B0}^{2A2} + A_A^{2A2}\left(L - x^{2A2}\right)\right)}q_{mB} \tag{5}$$

Considering that the rod extremities of the cylinders are connected and neglecting the rod angle variation related to the interconnection lever, Newton's Second Law results in:

$$p_A A_A^{2A1} - p_B A_B^{2A1} + \left(-p_A A_B^{2A2} + p_B A_A^{2A2}\right) - F_{a1} - F_{a2} - Fc = M\frac{d^2x^{2A1}}{dt} \tag{6}$$

The friction forces (F_{a1} and F_{a2}) are modeled using the variable viscous friction coefficient presented by Gomes and Rosa (12) and improved by Machado (13), as presented in Figure 4 and described by Eq. 7:

$$F_{ai} = f_{Vi}\dot{x}_i \tag{7}$$

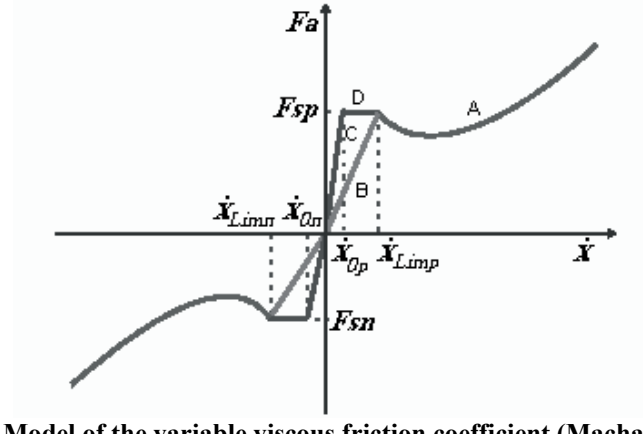

Figure 4. Model of the variable viscous friction coefficient (Machado (13))

In this model, the friction force for speeds above the speed limit ($\dot{x}_{\lim}$) (curve A in Figure 4) is obtained from friction-velocity maps experimentally determined for each of the

cylinders, as shown in Asaff & De Negri (11) and Asaff (14). When the speed is lower than the speed limit, the friction force is represented by curves B, C and D. In the slip mode, which occurs when the static friction force is overcome, the friction force is represented by trajectory B and in the stick mode it is represented by the trajectory C and D. The equations for the implementation of the friction model and their corresponding parameters are given in Asaff (14).

Finally, the control signal generated by the PID controller can be generically express by Eq. (8).

$$u(t) = Kp(e(t)) + \frac{1}{Ti}\int_0^t e(\tau)d\tau + T_d \frac{de(t)}{dt} \tag{8}$$

The set of equations presented was implemented in MATLAB/SIMULINK as shown in Figure 5. The acquisition and control system used was a dSPACE board, composed of four analog inputs (A/D) and four analog outputs (D/A), installed in a desk top computer.

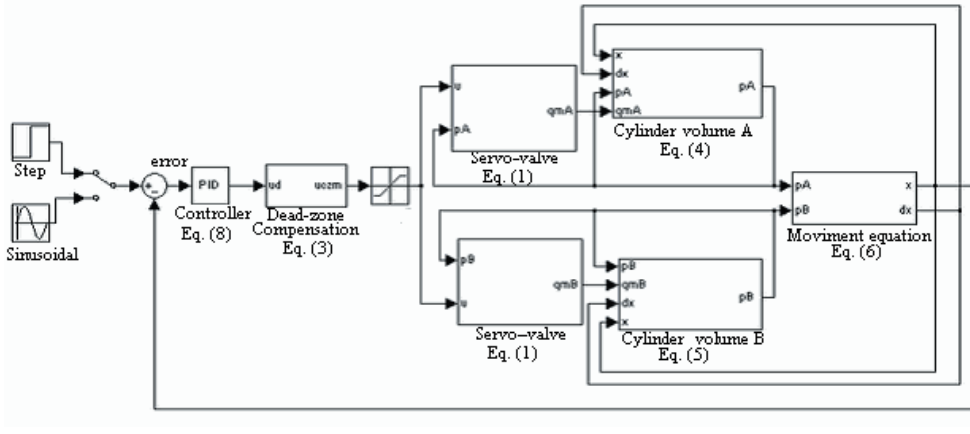

Figure 5. Block diagram of the pneumatic positioning system

3.1 Actuation circuit sizing

The starting point for the sizing of the positioning system for speed governors for hydroelectric power plants is the maximum mechanical work required. According to Júdez (15), this is a function of the maximum power, the head and the type of turbine, which is characterized by the proportionality constant *k*, as expressed by:

$$\tau_{máx} = \frac{k}{75}\frac{P_{máx}}{\sqrt{H}} \tag{9}$$

For a Francis turbine with maximum power (P_{max}) of 400KW and head (H) of 50m, the k value is 2.5 (Júdez (15)), resulting in a maximum work of 1885.6Nm. In turn, considering that a servo-motor stroke (l) is typically in the range of 115mm to 200mm for a SHPP up to 5.000KW, a stroke of 160mm was adopted for this design. The maximum force required to

move the distributor can be estimated by Eq. 10, assuming that the work is constant throughout the stroke.

$$F_{máx} = \frac{\tau_{máx}}{l} \tag{10}$$

In this case, the resulting maximum force is 12000 N. Considering a load pressure on the cylinders of 0.66MPa$_{abs}$ two single-rod double-acting cylinders of 125mm piston diameter and 32mm rod diameter (see Figure 2) are required. On the other hand, based on the opening/closing times established in section 2, the maximum mass flow rate required in the servo-valve is 6.286x10^{-3}Kg/s. Using Eqs. 1 and 2 one can conclude that the servo-valve commercially available with a sonic conductance (C) of 1.65x10^{-9} m5/Ns and critical pressure ratio (b) of 0.12 meets the static specifications. The air reservoir, installed in the supply pressure line of the servo-valve (see Figure 3), aims both to reduce the pressure fluctuations due to air consumption during the system operation and to ensure the continuous system operation at least for one sequence, regarding the closing, opening and closing of the wicket gate, when the external air supply is not available.

4. TEST RIG

The experiments were carried out using the test rig shown in Figure 6. The main components are a position transducer connected to one of the two double-acting pneumatic cylinders and one 5-port servo-valve. A pressure proportional valve and an air reservoir are installed under the test rig.

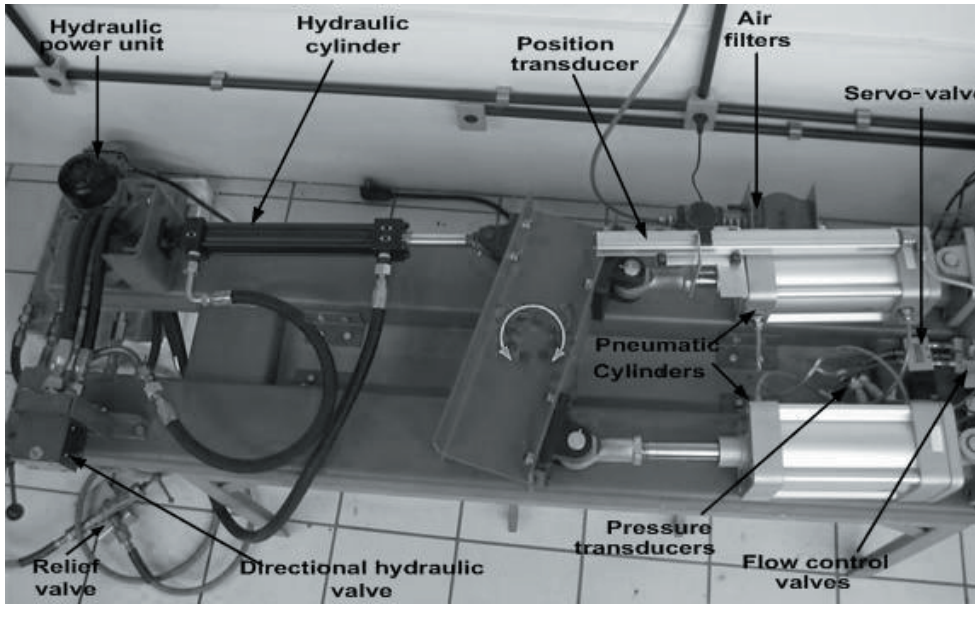

Figure 6. Test rig

The system that generates the loading comprises a hydraulic circuit, which is composed of a double-acting hydraulic cylinder commanded by a directional valve supplied by a hydraulic power unit including a relief valve that controls the hydraulic supply pressure.

5. RESULTS

The main theoretical and experimental results obtained in this research are presented in this section. Firstly, the model validity is verified. The step and sinusoidal experimental responses of the positioner are then analyzed, demonstrating that the design specifications established in section 2 were achieved. The loading conditions, the initial position of the cylinders and reference signals (sinusoidal and step input) used in this study are related to the operational conditions of a speed governor system. As discussed in Asaff & De Negri (11) and Asaff (14), there are two critical operational regions: 1) the speed-no-load condition, which occurs with approximately 15 % of the servo-motor stroke, and 2) the turbine rated power condition, corresponding to 80 to 90% of the servo-motor stroke.

5.1 Validation of the mathematical model

Firstly, Figure 7 allows a comparison of the experimental behaviors of the system with and without dead-zone compensation. A better performance is obtained when compensation is used since this strategy eliminates the effect of the valve asymmetry and shifts the voltage that commands the valve to guarantee a flow rate different to zero when necessary, reducing the settling time of the system.

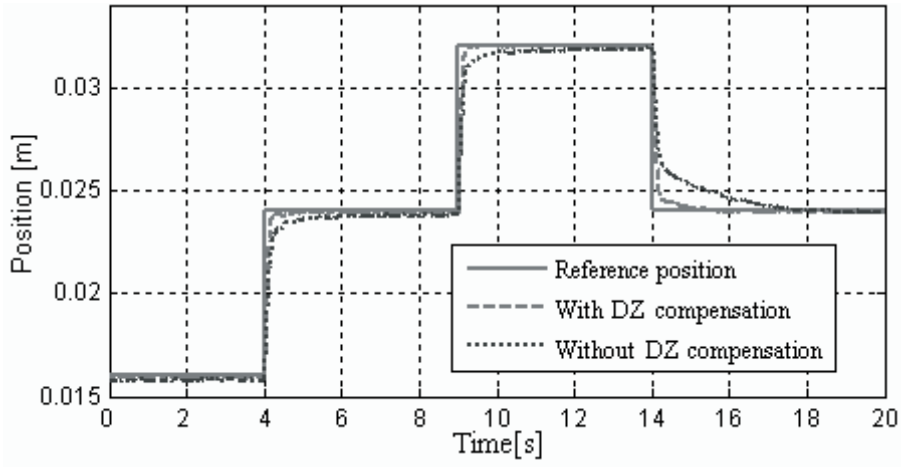

Figure 7. System response for a step sequence of 10% of the stroke with and without dead-zone compensation (Cylinder initial position = 136mm; No loading; PID gains: K_P=280, K_I=0.2, K_D=6)

In Figure 8 and Figure 9 the theoretical and experimental results with an input step of 2% of the cylinder stroke and for F_C=2300N are presented. A settling time of t_s=0.57s can be identified in the response to the step at 4s and 9s and t_s=0.8s to the step at 14s, for a maximum steady state error of 0.30mm.

Based on these graphs and other results presented in Asaff & De Negri (11) and Asaff (14), the model adequacy can be shown, allowing it to be applied to the speed governor design of other small hydroelectric power plans.

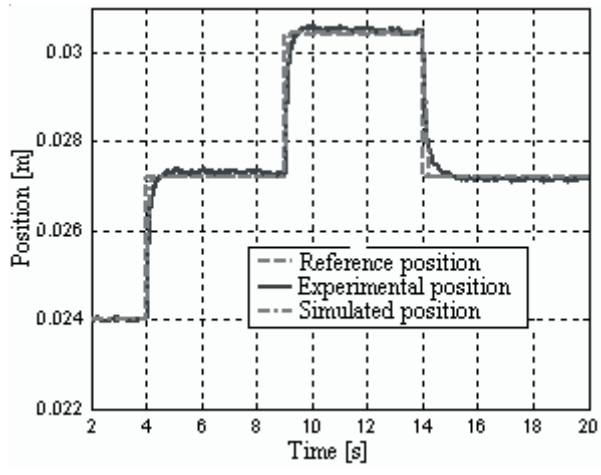

Figure 8. System response with F_C=2300N (positive) for a step sequence of 2% of stroke (Cylinder initial position = 24mm; PID gains: K_P=280, K_I=0.2, K_D=20)

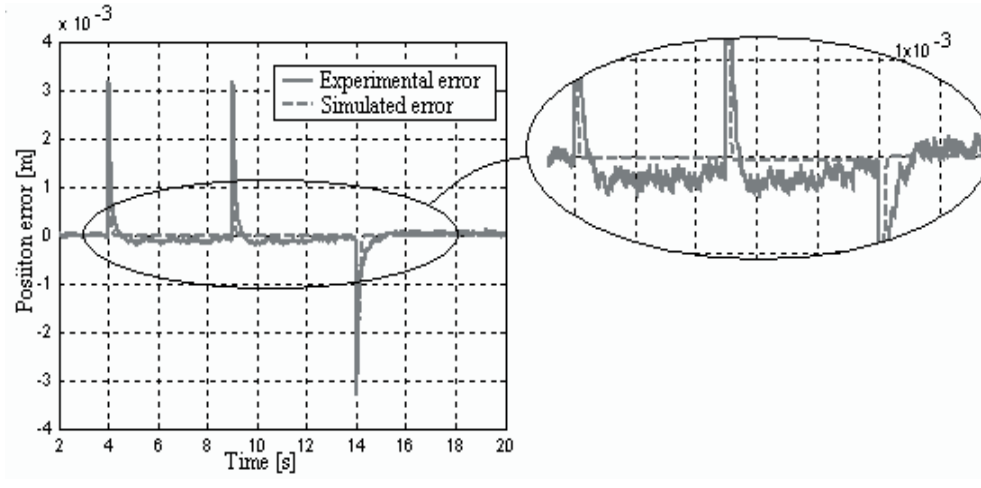

Figure 9. Position error related to Figure 8

5.2 Test results for the speed governor

For the tests related to the application as a speed governor, the installation and adjustment of the flow control valves (see Figure 2) was carried out aiming to achieve the opening and closing times of 5s and 5s, respectively, when a load force of 5700N (approximately 50% of the F_{Cn}) is applied. With this setup, the system behavior was observed under different operational conditions, as discussed below.

In Figure 10, the positioning system response for a step of 5% of the cylinder stroke is shown. Settling times (t_s) of approximately 0.33s for the positive step and t_s=0.56s for the negative step were obtained. The maximum steady state error identified in Figure 11 is 0.24mm. In this experiment, the initial position of the servo-motor corresponds to 80% of the stroke, verifying the system behavior under the turbine rated power condition.

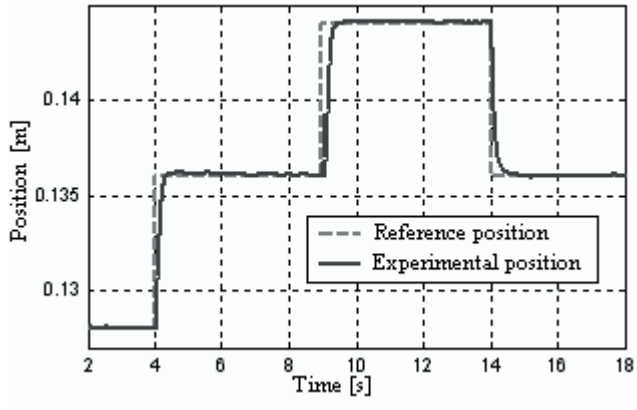

Figure 10. System response with F_C=11200N (positive) for a step sequence of 5% of stroke (Cylinder initial position = 128mm; PID gains =K_P=280, K_I=0.2, K_D=20)

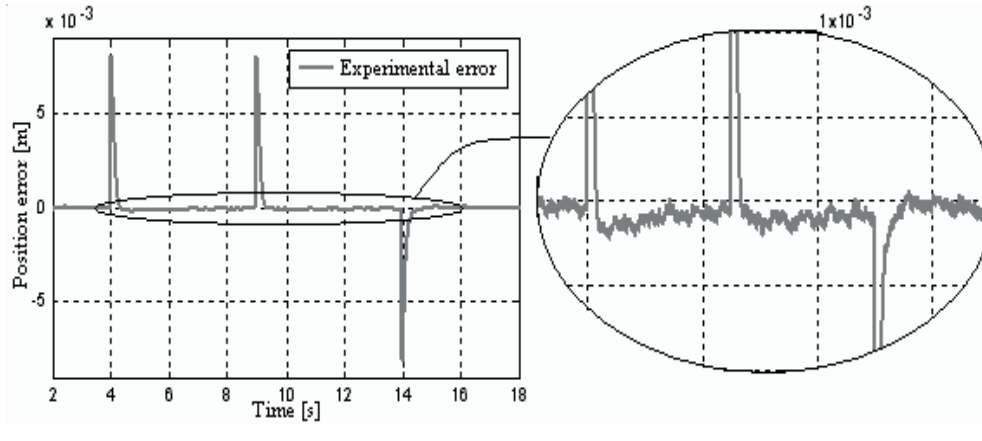

Figure 11. Position error related to Figure 10

On the other hand, the speed-no-load condition needs to be analyzed at near to 15% of the servo-motor stroke. Despite the designation, the water flow throughout the turbine can produce a positive force, trying to close the wicked gates, or a negative fore, trying to open the wicked gates. Figure 12 describes the test for a negative force, achieving a settling time of around 0.64s with a position error of 0.8mm. Tests with positive load were also carried out achieving equally appropriate results (Asaff & De Negri (11)).

This test gives the lowest dynamic response observed in this study. Considering a second-order critically damped response, the maximum time constant of the system is 0.22 s.

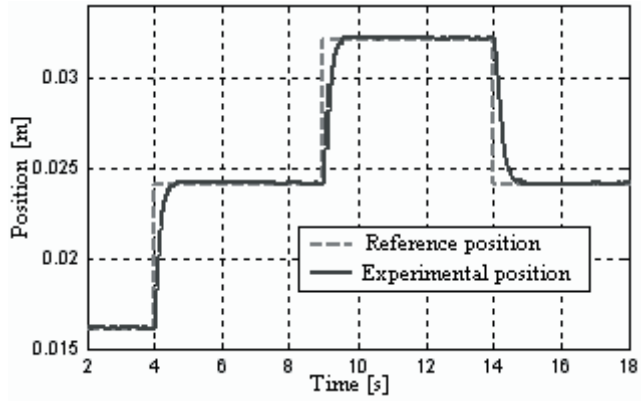

Figure 12. System response with F_C=2300N (negative) for a step sequence of 5% of stroke (Cylinder initial position = 16mm; PID gains =K_P=280, K_I=0.2, K_D=20).

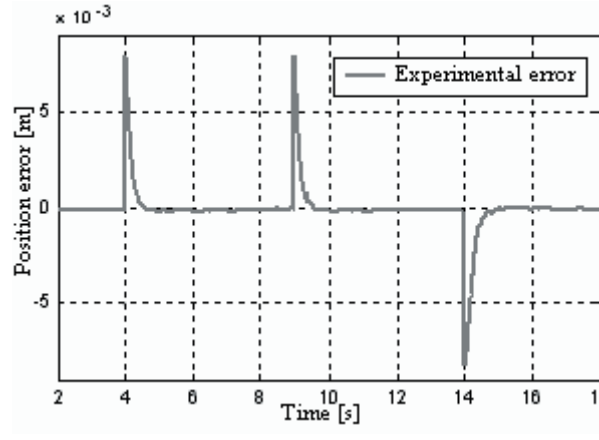

Figure 13. Position error related to Figure 12.

Another important aspect in the governing system operation is the synchronization of the power plant when it is operating on an interconnected electricity distribution network. Considering that the synchronization phase occurs with low loading and tracking a sinusoidal trajectory, an experiment was carry out with a positive force (F_C) of 2300N and an input signal expressed by $xd(t)= x_a sin(\omega t)$, where x_a = 8mm (5% of the cylinder stroke) and $\omega= \pi/10$rad/s (0.05 Hz). A delay in the system response in the demarcated areas of Figure 14 is observed, which increases the position error (0.52mm) at the beginning of the cylinder 2A1 retracting (cylinder 2A2 extending). This is caused by the one-directional load, such that the pressure in chamber A is higher than that in chamber B throughout the trajectory.

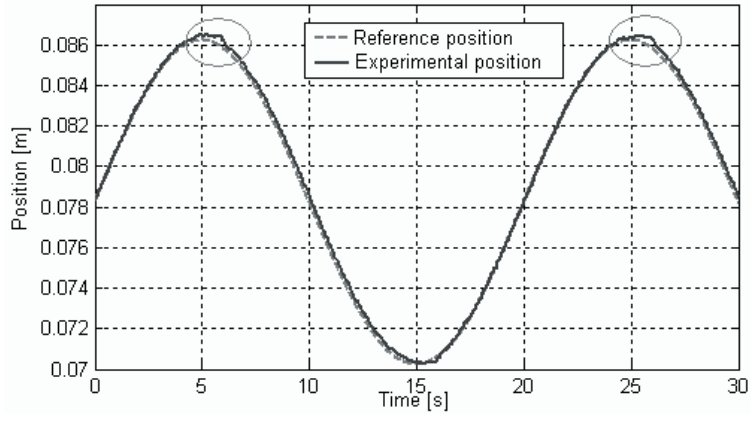

Figure 14. System response for synchronization (PID gains: K_P=280, K_I=0.2, K_D=20.

6. CONCLUSIONS

The theoretical and experimental results presented in this paper show the applicability of pneumatic positioning systems for high loads as required in the speed-governing of small hydroelectric power plants. The servo-valve dead-zone compensation improved significantly the system behavior allowing the obtainment of steady state errors between 0.5 and 0.8% of the cylinder stroke, these being below the 1% required for speed governors. The settling times were limited to 0.64s resulting in a time constant of 0.22s, satisfying the international standards specifications. Furthermore, the mathematical model was shown to be appropriate for description of the physical phenomena, including the non-linear friction and valve behavior, this being useful in servo-pneumatic system design. Considering the pneumatic component size available on the market, mainly regarding the cylinder and servo-valve, and the sizing rules discussed in this paper, it is presumed that a pneumatic system can be applied to a hydroelectric power plant of up to 2MW.

7. ACKNOWLEDGMENTS

This research was sponsored by Reivax Automação e Controle Company and CNPq (Brazilian National Council for Scientific and Technological Development), to whom the authors are grateful.

REFERENCES

(1) Littler, D. J., 1991, Modern power station practice. Third Edition. British Electricity Ineternational. Pergamon Press.

(2) IEEE. ANSI/IEEE Std. 125, 1988, “Recommended Practice for Preparation of Equipment Specifications for Speed-Governing of Hydraulic Turbines Intended to Drive Electric Generators”, USA, 28p.

(3) IEC. IEC 61362, 1997, “Guide for Specification of Hydroturbine Control Systems”, Switzerland, 105p.

(4) Rodrigues, L. A. H., De Negri, V. J. 2004. “Project: Development of Intelligent Valves and Electro-Hydraulic Equipment Applicable to Electricity Generation”. Technical report FINEP: 01.02.0031-00 - FNDCT / CT – ENERG. (In Portuguese), Brazil.

(5) Scholz, Dieter., 1990, “Auslegung Servopneumatischer Antriebssystemse, Doctorate Thesis, IHP-RWTH, Aachen, Germany.

(6) Vieira, A. D., 1998, “Theoretical and Experimental Analysis of Pneumatic Linear Position Servo Systems” (In Portuguese), Master’s Thesis, Mechanical Engineering Department, Federal University of Santa Catarina, Brazil.

(7) ISO International Organization for Standardization, 1989, “ISO 6558 - Pneumatic Fluid Power - Components Using Compressible Fluids – Determination of Flow Rate Characteristics”, Switzerland, 13p.

(8) Tao, G., Kokotovic. 1996. “Adaptive Control of Systems with Actuator and Sensor Nonlinearities. John Wiley & Sons. New York.

(9) Machado, C., Guenther, R., De Negri, V. J. Pinheiro, S. 2006. “Cascade Control with Friction Compensation Based on Artificial Neural Network for a Hydraulic Actuator” Proceedings of IMECE2006 - 2006 ASME International Mechanical Engineering Congress and Exposition. Chicago, Illinois, USA.

(10) Valdiero, A., 2004, “Control of Hydraulic Robots with Friction Compensation”, (In Portuguese), Doctor Thesis, Mechanical Engineering Department, Federal University of Santa Catarina, Brazil, 188 p.

(11) Asaff, Y. E. and De Negri, V. 2007. “Development of a High Power Pneumatic Servo-Positioning System for Speed Governors of Hydraulic Turbines”. Proceedings of COBEM2007. 19th International Congress of Mechanical Engineering. Brasilia, Brazil.

(12) Gomes , S. C. P.; Rosa, V. S., 2003, A new Approach to Compensate Friction in Robotic Actuators. In: International Conference on Robotics and Automation, 2003, Taipei, Taiwan. Proceedings... (S.I).

(13) Machado, C., 2003, “Friction Compensation in Hydraulic Actuators using Artificial Neural Network”, (In Portuguese), Master‘s Thesis, Mechanical Engineering Department, Federal University of Santa Catarina, Brazil.

(14) Asaff, Y. E., 2006, “Development of a Pneumatic Servo-Positioning for Driving Speed Governors for Turbines of Small Hydroelectric Power Plants”. (In Portuguese), Master’s Thesis, Mechanical Engineering Department, Federal University of Santa Catarina, Brazil, 143 p.

(15) Júdez, G. Z., 1965, “Power Plants: Study, Installation, Testing and Regulation”. (In Spanish), John Wiley & Sons, Editorial Gustavo Gili S.A.

Experimental Assessment of a Free Elastic-Piston Engine Compressor With Separated Combustion Chamber

José A. Riofrío and Eric J. Barth
Center for Intelligent Mechatronics
Mechanical Engineering, Vanderbilt University
Nashville, TN, USA

ABSTRACT

This paper presents the experimental assessment of a free elastic-piston compressor (FEPC) equipped with a separated combustion chamber. The FEPC is a proposed device that utilizes combustion of a hydrocarbon fuel to compress air into a high-pressure supply tank, thus potentially serving as a portable power supply candidate for untethered pneumatic systems of human-scale power output. The design and simulation of the FEPC concept have been shown in previous work, and the device's energetic merit outlined. The free "piston" consists of a custom-molded silicone-rubber membrane, clamped at the circumference, thus providing perfect blow-by sealing and near zero friction. The device is equipped with a custom-built separated combustion chamber, which dynamically channels high-pressure combustion products of a hydrocarbon fuel in order to produce power strokes. Experimental results coupled with high-speed video are presented which verify 1) the operation of the separated combustion chamber including its air/fuel mixture control, 2) the dynamics of the combustion valve in first sealing the pre-combustion gases and then venting the combustion products into an expansion chamber, 3) the dynamics of the free piston in converting pressure energy in the expansion chamber into kinetic energy, and 4) successful pumping of air into a reservoir.

1. INTRODUCTION

Ongoing research endeavors in electromechanical untethered robotic systems of human-scale power output (in the neighborhood of 100 Watts, as defined in [1]) have found significant roadblocks in their overall systems-level energy and power densities. Take, for example, the Honda P3 humanoid robot: this state-of-the-art humanoid has an "idling" operation time of 15 to 25 minutes before its 30-kg Ni-Zn battery needs to be recharged. Put simply, the problem is that state-of-the-art batteries are too heavy for the amount of energy they store, and electric motors are too heavy for the mechanical power they can deliver, in order to present a viable combined power supply and actuation system capable of delivering human-scale mechanical work in a human-scale self contained robot package, for a useful duration of time.

Fluid Power and Motion Control 2008 Edited by Dr D N Johnston and Professor A R Plummer

A relatively new approach to developing such robotic systems is being undertaken in the pneumatic domain, where motion is typically carried out with linear pneumatic actuators. Control issues aside, linear pneumatic actuators have approximately an order of magnitude better volumetric power density and five times better mass specific power density than state of the art electrical motors [2]. Regarding power delivery, on-board air supply has shown to be a non-trivial issue, since standard air compressors are too heavy for the intended target scale, as are portable tanks with enough compressed air to supply the actuators for a useful duration of time. Goldfarb et al [3] have experimentally demonstrated the viability of utilizing hot gas released by the catalytic decomposition of hydrogen peroxide to drive pneumatic actuators, whereby the on-board supply of hot gas is carried out by a small tank of hydrogen peroxide in line with a small catalyst pack. An experimental energetic analysis carried out by Fite and Goldbarb [4] showed an achieved 45% conversion efficiency from stored chemical energy of a 70% concentration of H_2O_2 (whose lower heating value is 400 kJ/kg) to controlled mechanical work in a linear actuator. Despite its promising energetic characteristics, however, one of the biggest challenges still posed by a monopropellant-based actuation system is its high-temperature working fluid, which can present difficulties associated with valves and seals in pneumatic components.

An alternative approach for developing an on-board supply of cool air via a free elastic-piston compressor (FEPC) is hereby presented. The FEPC is a compact internal combustion engine with a free-piston configuration, dynamically arranged to efficiently match the load of a pneumatic compressor of human-scale power output capability. Put simply, it serves the function of converting chemically stored energy of a hydrocarbon fuel into pneumatic potential energy of compressed air, with a combustion-driven free-piston acting as an air pump. The combined factors of a high energy-density hydrocarbon fuel, the efficiency of the device, the compactness and low weight of the device, and the use of the device to drive lightweight linear pneumatic actuators (lightweight as compared with power comparable electric motors) are projected to provide at least an order of magnitude greater total system energy density (power supply and actuation) than state of the art power supply (batteries) and actuators (electric motors) appropriate for human-scale power output. More in-depth discussion on this energetic motivation is provided in [3], [4] and [5].

Figure 1 shows a Pro/ENGINEER drawing of the FEPC design, and Figure 2 shows a fabricated prototype assembly . A custom-molded silicone-rubber membrane constitutes the "elastic piston", essentially a mass-spring system. To the left of the piston is the "expansion" chamber, where the combustion gasses expand and perform PV work on the piston, while squeezing the air out of the pump chamber (right of the piston) into a reservoir. The inner walls of this pump chamber are hemispherically shaped to match the contour of a "spherical segment" displacement profile of the expanding piston, thus minimizing the pump dead volume. The dynamics are tuned such that the piston resonates at a given frequency, with combustion pressures representing the required pulsating inputs to maintain the system in oscillation. A "separated" combustion chamber was introduced as a constant-volume space in which pressurized air and propane are injected and ignited, and whose high-pressure combustion products are quickly vented into the "expansion" chamber (thereby performing PV work against the free piston). Coupled with a passive, high-flow "combustion valve" that channels these combustion products, the separated combustion chamber effectively decouples the fuel injection dynamics from the free-piston dynamics. This configuration has several benefits, most notably 1) its lack of traditional "intake" and "compression" strokes

associated with typical 4-stroke cycles, 2) its lack of scavenging issues associated with typical 2-stroke cycles, and 3) its ability to start and stop on demand, without the need for "idling" or an additional starting cycle. In essence, 2-stroke power is combined with 4-stroke efficiency, without bulky kinematic linkages that would be terribly inadequate for the target size and power scale of the overall application.

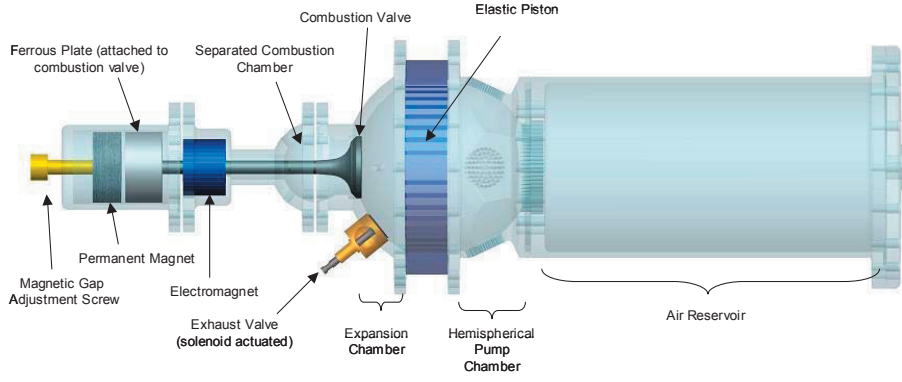

Figure 1: Pro/ENGINEER Drawing of Free Elastic-Piston Compressor (FEPC).

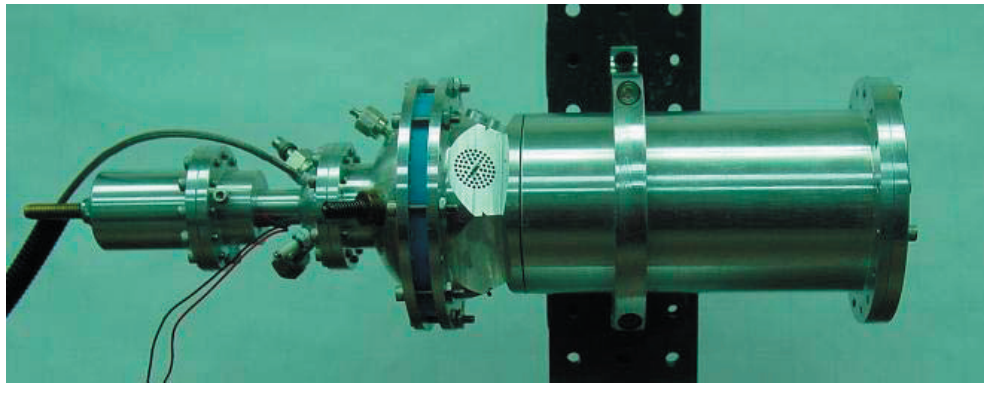

Figure 2: Fabricated FEPC Assembly.

The design, fabrication, thermodynamic analysis and dynamic simulation of a free "liquid-piston" compressor was presented in [6] and constitutes the conceptual framework on which the FEPC is based. A thick silicone-rubber membrane used as a piston exhibits identical dynamic characteristics as a liquid-piston (as defined in [6]), while providing more mechanical robustness.

2. COMBUSTION VALVE DYNAMICS

The "combustion valve", which can be seen in Figure 1, is carefully designed such that its passive dynamic characteristics comply with the following fourfold operational principle: 1) The valve must be shut against a pressurized air/fuel mixture (i.e. "injection pressure"), 2) it must immediately open upon ignition, such that the high-pressure combustion products can quickly vent into the expansion chamber with minimal flow restrictions, 3) it must remain open for a long enough duration of time in order for the pressure in the combustion chamber to come all the way down to (and slightly below) atmospheric, thus inducing a breathe-in check valve to allow fresh ambient air to enter the combustion chamber (passive cooling), and finally 4) it must close just before the end of the power stroke and remain closed for the entire exhaust stroke, so as to not allow combustion products to flow back into the combustion chamber. An automotive valve was selected due to its high flow capacity, and a ferrous plate was attached to its stem so that its opening and closing can be influenced by magnetic fields. A strong permanent magnet holds the valve shut against the pressurized injection of air and propane, and after a sparked ignition, the combustion pressure becomes high enough to overcome the magnetic force and throw the valve open. Similarly, an "emergency" electromagnet is included to hold the valve open (only in the unlikely event where the valve finishes its stroke before overexpansion of the combustion gases).

The main designable dynamic elements present in the combustion valve are its mass (variable through design of its attached ferrous plate) and the stiffness of its return spring. A comprehensive dynamic model of the FEPC, presented in [6], calculates the flow through the combustion valve based on its revealed flow area (which itself is a function of valve position). A free-body diagram showing the horizontal forces acting on the combustion valve is shown in Figure 3.

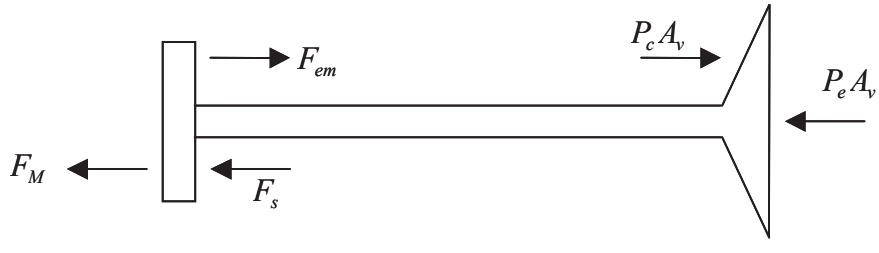

Figure 3: FBD of Combustion Valve

Applying Newton's second law, the valve dynamics are thus given:

$$m\ddot{x}_v = -k_s x_v + P_c A_v + F_{em} - F_M - P_e A_v \tag{1}$$

where x_v is the position of the valve, m is the mass of the valve, k_s is the return spring constant, F_{em} and F_M are the magnetic forces generated by the electromagnet and permanent magnet, respectively, and A_v is the cross-sectional area of the valve head. Furthermore, the valve flow area $a_2(x_v)$ can be described by the following:

$$a_2(x_v) = \max\left\{2\pi r_v x_v ,\ \pi\left(r_v^{\,2} - r_{stem}^{\,2}\right)\right\} \tag{2}$$

where r_v and r_{stem} are the radii of the valve head and valve stem, respectively. It can be seen that this combustion valve constitutes a highly tunable dynamic element within the system; its yielded simulated performance was demonstrated in [6], and its experimental validation will be shown hereby.

3. EXPERIMENTAL ARRANGEMENT

3.1 Control of Air/fuel Ratio and Injection

For preliminary experimental assessment, the air used for injection comes from an external supply, whereas the fuel source is a 0.5-kg bottle of Coleman® propane, which at room temperature has a vapor pressure of near 1 MPa [7]. In addition to injection pressure, there are 2 essential criteria that must be met in order to achieve proper combustion: 1) mixture quantity, in terms of having a near stoichiometric mass ratio of air-to-fuel, (15.63 for propane); and 2) mixture quality, in terms of proper mixing of the two substances. Finally, from a systems-level perspective, the injection process has to be fast enough to comply with the desired operational frequency of the device. Recall that since the "separated" combustion chamber decouples the fuel injection from the piston dynamics, the potential to achieve higher frequencies will depend on the slower of these two.

A simple and effective fuel injection scheme has been implemented, with achieved injection durations as short as 30 milliseconds. As shown in Figure 4, its principle operation is as follows: air and fuel are streamed into a common mixture line, at the end of which there is an on/off valve that allows a pressurized mixture into the combustion chamber. For adequate air/fuel mixture quantity, a properly adjusted metering valve maintains the fuel flow smaller than the air flow, such that the mixture line contains stoichiometric air-to-fuel ratio at all times.

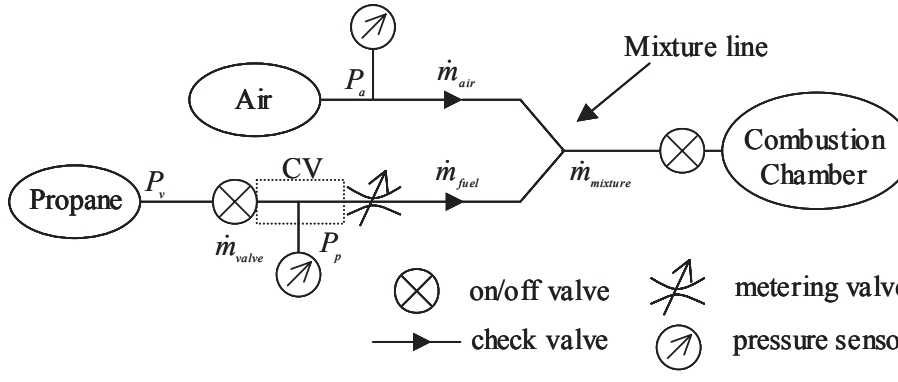

Figure 4: Schematic of Fuel Injection Configuration.

From Figure 4, $\dot{m}_{air}$, $\dot{m}_{valve}$, $\dot{m}_{fuel}$, and $\dot{m}_{mixture}$ are the mass flow rates through the air line, propane on/off valve, propane metering valve and mixture line, respectively, and P_a , P_v and P_p are the air pressure, vapor pressure of propane, and regulated propane pressure, respectively. Since the vapor pressure of propane is much higher than the target injection pressure, a simple feedback control loop was implemented so that the upstream propane pressure (i.e., in the control volume, as defined by dashed space in Figure 4) is the same as the air pressure. Essentially, this fuel pressure regulator looks at the pressure in the pre-mixture air line, and regulates the pressure in the control volume (CV) by controlling an on/off valve between the propane bottle (at high vapor pressure) and the CV. The mass flow rate through the metering valve, $\dot{m}_{fuel}$ essentially constitutes a disturbance in the loop, since pressure dynamics in the control volume depend on the net mass flow rate. Figure 5 shows the block diagram of this pressure regulator.

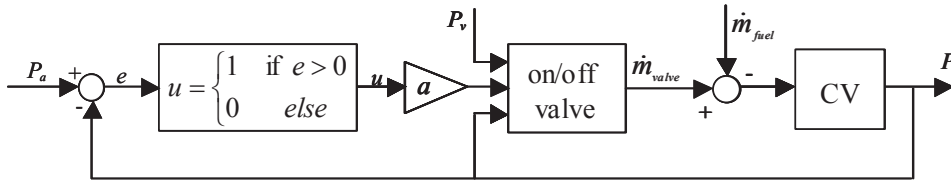

Figure 5: Block Diagram of Propane Pressure Regulator.

The mass flow rate through a valve, as outlined in [8], can be characterized by the following expression:

$$\dot{m} = a\,\psi\left(P_u, P_d\right) \tag{3}$$

where a is the effective cross-sectional flow area of the valve orifice, and $\psi\left(P_u, P_d\right)$ is a nonlinear function of upstream and downstream pressures across the valve, and its discharge coefficient. Furthermore, the mass flow rates through the air and propane lines can be related in the following way:

$$\dot{m}_{mixture} = \dot{m}_{air} + \dot{m}_{fuel} \tag{4}$$

To achieve a stoichiometric ratio in the air/fuel mixture, the following condition must be met:

$$\frac{\dot{m}_{air}}{\dot{m}_{fuel}} = 15.63 \tag{5}$$

Combining Equations (3) and (5), and noting that by virtue of the fuel pressure regulator the upstream and downstream pressures are the same for both the air and fuel lines, we obtain:

$$\frac{\dot{m}_{air}}{\dot{m}_{fuel}} = \frac{a_{air}}{a_{fuel}} \tag{5}$$

This demonstrates that the mass flow-ratio between the air and propane are dependent only on the ratio of their effective flow areas. Therefore, provided that the air and fuel lines have equal upstream and downstream pressures, a properly adjusted metering valve in the fuel line suffices in order to achieve a continuous stoichiometric air-to-fuel ratio.

3.2 Ignition

Ignition is carried out with a traditional coil and spark plug. Miniature ignition components (ignition coil, spark plug and spark plug cable) were acquired from an independent RC enthusiast, and proved to be very adequate for this application. A computer-signaled transistor allows a current flow through the primary wire in the coil, and is suddenly stopped after a very short duration of time. This "instantaneous" current drop in the primary wire (which results in a sudden change in the magnetic field) induces a high voltage in the much longer secondary coil, which is finally discharged across the spark plug gap. A 6-volt battery powers the small coil, and an opto-coupler separates the computer input signaling from the high-current coil circuit. Figure 6 shows a picture of the fuel injection and ignition components.

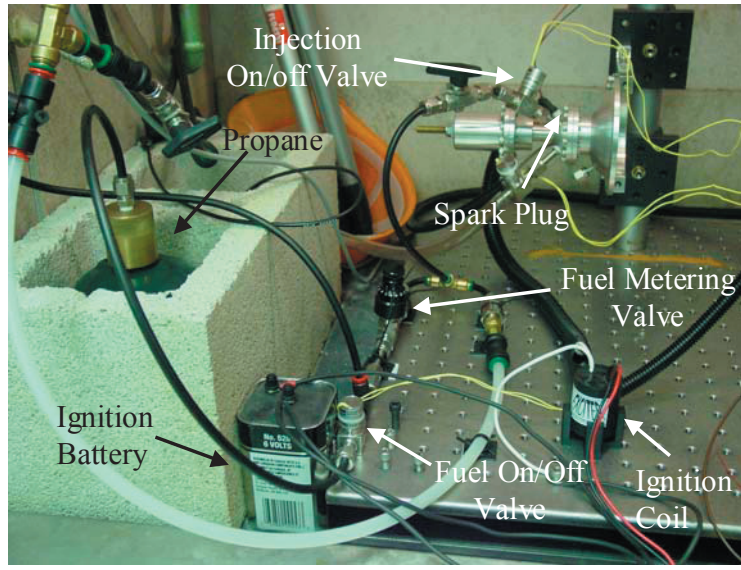

Figure 6: Fuel Injection and Ignition Components

4. EXPERIMENTAL RESULTS

4.1 Validation of Combustion Valve Dynamics

The first immediate concern regarding valve design validation was to ensure that the combustion valve being held shut by the magnet could provide adequate sealing at the valve

seat. This was tested by injecting pure air into the combustion chamber at the maximum target injection pressure of 650 kPa. After proper tuning of the magnet adjustment screw, no leakage through the valve was observed. The fuel injection scheme presented above was then implemented, and the fuel metering valve was adjusted by trial and error until optimal combustion was achieved ("optimal" in relative terms of repeatability and yielded combustion pressures).

The next concern involved valve behavior. It is desired for the combustion valve to "throw" open immediately upon combustion, and stay open (ideally by its own inertia) long enough to allow for the pressure in the combustion chamber to vent all the way down to atmospheric. To observe this, the piston was removed and a high-speed video camera, aimed at the expansion chamber, was utilized to record the fast motion of the valve. A MotionScope® camera was used, taking video at 1000 frames per second. Figure 7 shows a series of screen shots taken from the captured video, containing an complete valve cycle. The instant where the spark ignites is denoted as 0 milliseconds, and intervals of 2 milliseconds are shown. An LED was connected to the ignition command (i.e., the command sent to charge the ignition coil) and placed next to the valve so that the instant of spark was known with respect to the valve motion. Therefore, this instant corresponds to the exact moment at which the LED becomes unlit.

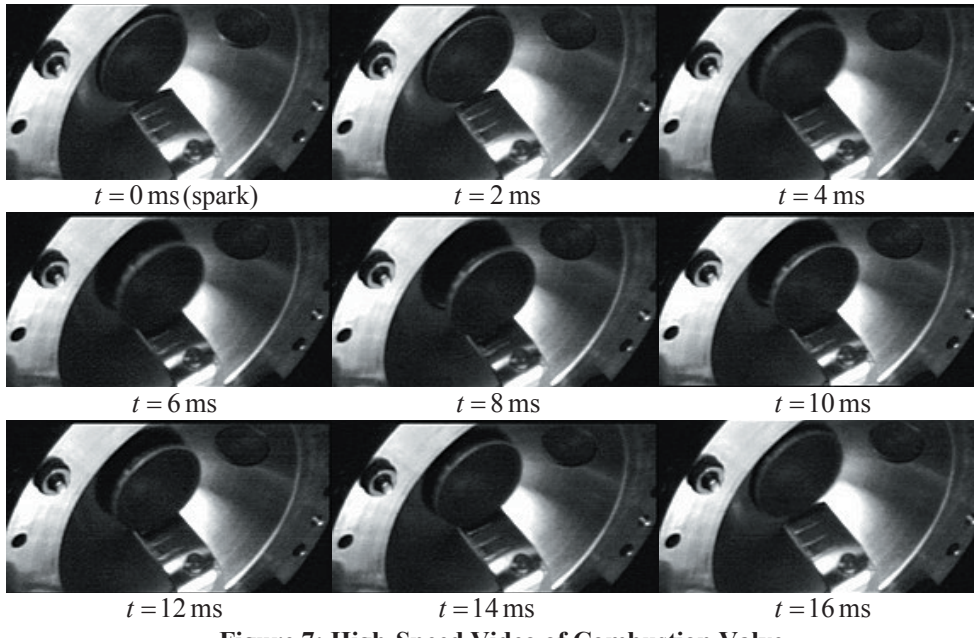

Figure 7: High-Speed Video of Combustion Valve

From Figure 7, it can be seen that the combustion valve takes somewhere between 2 and 4 milliseconds to begin to open, and that it quickly overcomes the magnetic force and performs its full 10mm stroke. It can also be seen that it is fully re-shut 16 milliseconds after spark. A corresponding experimental pressure signal in the combustion was recorded, and is

shown in Figure 8. An undesired (albeit convenient) noise spike indicates the instant of spark, and therefore the time axis was modified so that it is in sync with Figure 7.

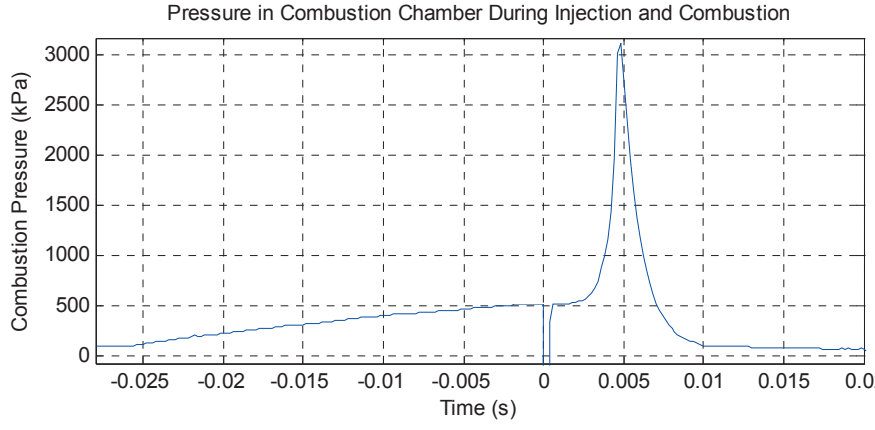

Figure 8: Pressure in Combustion Chamber

By looking at both Figures 7 and 8, it should be noticed that the combustion pressure vents all the way down to atmospheric pressure well before the valve finishes its return stroke. This means that an over-expanded engine cycle can be achieved with a completely passive combustion valve, with enough additional time for breathe-in to occur through the combustion chamber.

Additional open combustion testing (i.e., with the piston removed) was undertaken to test higher combustion frequencies. Successful firing was achieved at the targeted 10 Hz, as is shown in Figure 9. The inconsistencies of the peak values are believed to be a result of inadequate resolution and response time of the pressure sensor; after all, capturing combustion phenomena is not within the scope of this standard pneumatic sensor. This issue will be addressed in the near future by implementing a combustion-specific pressure sensor.

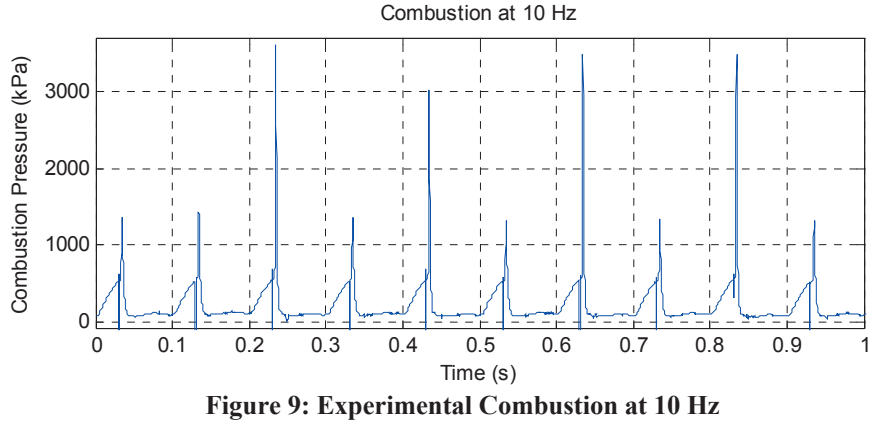

Figure 9: Experimental Combustion at 10 Hz

4.2 Silicon-Piston Dynamic Validation

Another experiment was carried out to analyze the behavior of the silicon piston under no load. The piston was connected to the expansion chamber, but this time the pump chamber was left disconnected. High-speed video was taken to capture the response of the piston to a combustion event. This is shown in Figure 10.

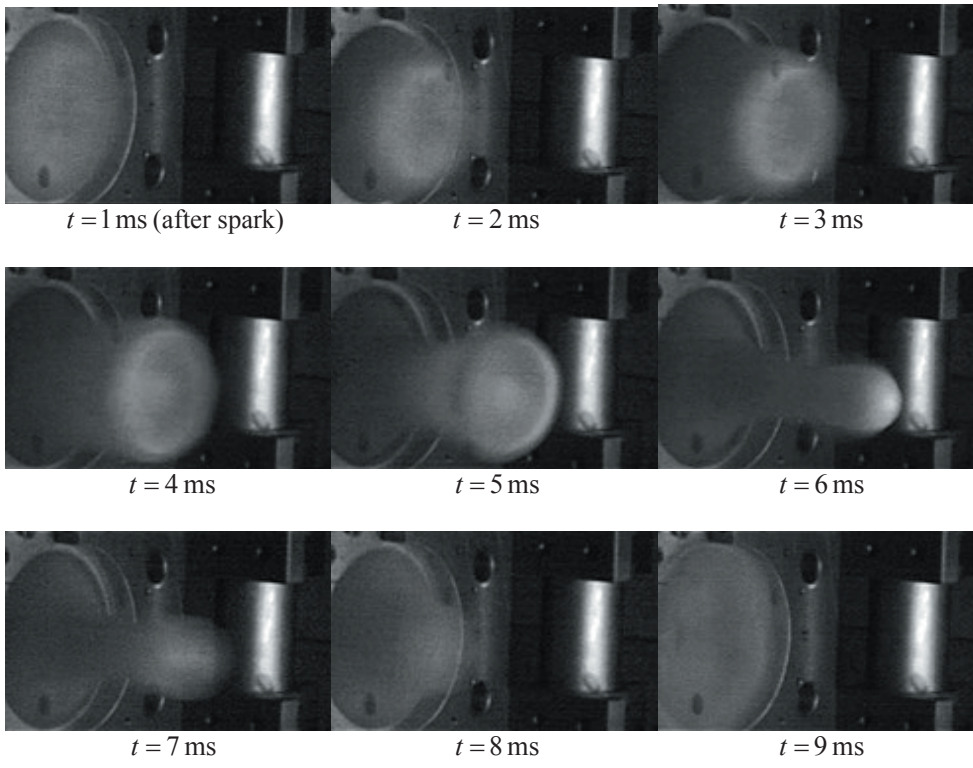

Figure 10: High-Speed Video of Silicone-Rubber Piston (with no load)

The extent of the inertial loading of the piston can be appreciated from looking at Figure 10. In addition, it was observed that short-term thermal effects, as well as combustion-related phenomena, did not affect the diaphragm, since no signs of stress or irregularities in general were found. The fast dynamics observed are due to the fact that the mass of this particular silicone membrane (used for demonstration and preliminary validation purposes) is significantly below the value required for optimal performance. As suggested by the simulation in [6], this mass should be around 0.5 kg.

4.3 Full Device Operation

After experimentally validating the combustion valve and the silicone piston without a load, the FEPC device was fully assembled and full operation was obtained. Successful pumping was achieved at low pressures (up to 260 kPa). Figures 11 and 12 show experimentally obtained plots of the combustion and reservoir pressures for a series of five consecutive strokes.

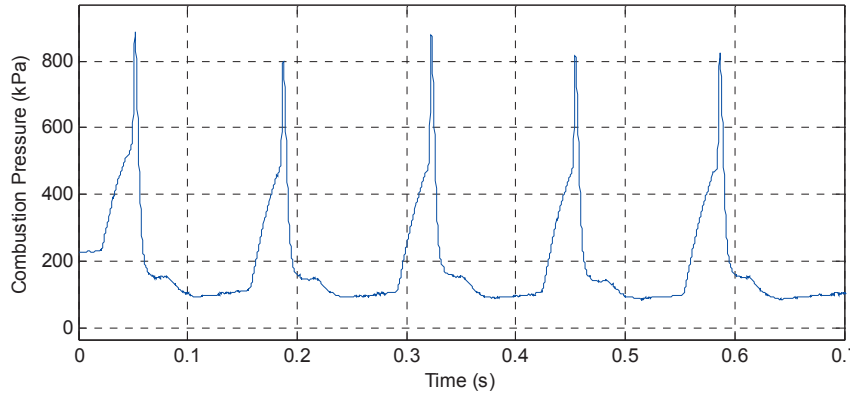

Figure 11: Combustion Pressure Versus Time

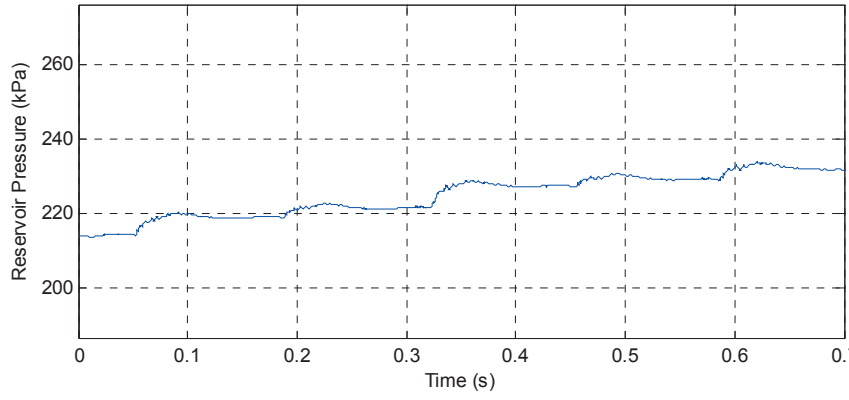

Figure 12: Reservoir Pressure Versus Time

It is important to point out that the experimental plots shown in Figures 11 and 12 are only preliminary, and are hereby used only to show pumping potential of the device. Crucial dynamic elements such as mass of the piston and response times of the pump inlet and outlet check valves have not yet been optimized, and as demonstrated in [6], these have to be properly and carefully tuned in order to achieve target power and efficiency. The slow speed of response of the pump outlet valve, in particular, can be observed by the small overshoot present at each "pumping step" in Figure 12. This essentially indicates that some air manages to escape the reservoir and flow back into the pump chamber at the very beginning of the exhaust stroke. By stiffening these check valves, however, their effective flow area is reduced (i.e., the valves become more flow restrictive). Therefore there is a trade-off between flow capability and response time. However, since the observed overshoot is low, it is reasonably assumed that other factors play a greater role in the pumping limitation of the system. It is believed that the pump inlet check valves are likewise slow in response, causing air to escape through them during the beginning of the power strokes. In addition, and most importantly, the silicone piston is not properly tuned, in terms of its mass and spring

constant. According to the model-based simulation presented in [6], very low masses (such as this one) should result in very inefficient operation. These shortcomings are being addressed in current and upcoming research.

5. CONCLUSIONS

A free elastic-piston compressor (FEPC) was presented. As a follow up to its design, fabrication, thermodynamic analysis and dynamic simulation presented in [6], successful experimental validation of its main design elements was demonstrated: 1) The principle of operation and designed dynamic response of the combustion valve, 2) a fast and repeatable fuel injection scheme, and 3) preliminary operation of the full-device, with low pressure pumping.

REFERENCES

[1] Dunn-Rankin, D., Leal, E. M., and Walther, D. C., "Personal Power Systems". *Progress in Energy and Combusion Scence,* vol. 31, pp. 422–465, 2005

[2] Kuribayashi, K., "Criteria for the evaluation of new actuators as energy converters," *Advanced Robotics*, vol. 7, no. 4, pp. 289-37, 1993.

[3] Goldfarb, M., Barth, E. J., Gogola, M. A., and Wehrmeyer, J. A., "Design and Energetic Characterization of a Liquid-Propellant-Powered Actuator for Self-Powered Robots," *IEEE/ASME Transactions on Mechatronics*, vol. 8, no. 2, pp. 254-262, June 2003.

[4] Fite, K. B., and Goldfarb, M., "Design and Energetic Characterization of a Proportional-Injector Monopropellant-Powered Actuator," *IEEE/ASME Transactions on Mechatronics,* vol. 11, no.2, pp. 196-204, April 2006.

[5] Riofrio, J. A., and Barth, E. J., "A Free Piston Compressor as a Pneumatic Mobile Robot Power Supply: Design, Characterization and Experimental Operation," *International Journal of Fluid Power,* vol. 8, no. 1, pp 17-28, February 2007.

[6] Riofrio, J and Barth, E. J., "Design and Analysis of a Resonating Free Liquid-Piston Engine Compressor," *2007 ASME International Mechanical Engineering Congress and Exposition (IMECE),* IMECE2007-42369, November 11-15, 2007, Seattle, WA.

[7] Lide, David R. (ed), *CRC Handbook of Chemistry and Physics, 84th Edition*. CRC Press. Boca Raton, Florida, 2003

[8] Richer, E., and Hurmuzlu, Y., "A High Performance Pneumatic Force Actuator System: Part I – Nonlinear Mathematical Model," *Transactions of ASME,* vol. 122, pp. 416-425, September 2000.

Modeling and Control of a Free Liquid-Piston Engine Compressor

Chao Yong, Eric J. Barth, José A. Riofrío
Center for Intelligent Mechatronics
Department of Mechanical Engineering, Vanderbilt University
Nashville, TN, USA

ABSTRACT

This paper presents the modeling and control of a prototype compact free liquid-piston engine compressor. The dynamic model includes 1) the injection dynamics of the air/fuel mixture, 2) the dynamics of heat release during combustion, 3) the inertial dynamics of the magnetically latched combustion valve, 4) the mass flow dynamics of the combustion and exhaust valves, 5) the inertial dynamics of the free piston, and 6) the compression and pumping dynamics. The model is then utilized to design an iterative control scheme to control the amount of fuel injected for each cycle, the timing of the spark, and the timing and duration of the exhaust valve. Simulation results show a good correlation with experimentally obtained data, and simulated closed-loop control of the engine is demonstrated.

1. Introduction

Motivated by high energy and power densities, pneumatic power supply and actuation systems are being investigated by various researchers [1][2] for untethered robotic applications requiring controlled human-scale power motion output. Such systems utilize linear pneumatic actuators that have approximately an order of magnitude better volumetric power density and five times better mass specific power density than state of the art electrical motors [3]. Regarding power supply, on-board air supply has shown to be a non-trivial issue, since standard air compressors are too heavy for the intended target scale, as are portable tanks with enough compressed air (stored energy) to supply the actuators for a useful duration of time. For this purpose, a free liquid-piston engine compressor (FLPEC) with a separated combustion chamber has been developed by Riofrio and Barth [3] to provide an on-board supply of compressed air. Various incarnations of free-piston engines for various applications have been attempted for more than 70 years since their conception [4-13]. The progenitor free-piston engine patent by Pescara [4] was actually intended as an air compressor.

The FLPEC discussed in this paper is a compact internal combustion engine with a free-piston configuration, dynamically arranged to match the load of compressing and pumping air. The combined factors of a high-energy density fuel, the efficiency of the device, the compactness and low weight of the device, and the use of the device to drive lightweight linear pneumatic actuators (lightweight as compared with similar power electric motors) is

Fluid Power and Motion Control 2008 Edited by Dr D N Johnston and Professor A R Plummer

projected to provide at least an order of magnitude greater total system energy density (power supply and actuation) than state of the art power supply (batteries) and actuators (electric motors) appropriate for human-scale power output [16].

The FLPEC is shown in Figure 1. It consists of a combustion chamber, an expansion chamber, a liquid piston, and a compression/pumping chamber. The combustion chamber is separated from the expansion chamber by a magnetically latching valve that seals in the face of high pressure air and fuel injected into the chamber, and opens in the face of higher pressure combustion products. The expansion chamber allows for the combustion products to perform PV work on a free-piston consisting of a liquid slug trapped between two high-temperature elastomeric diaphragms. Please refer to [3] for more details.

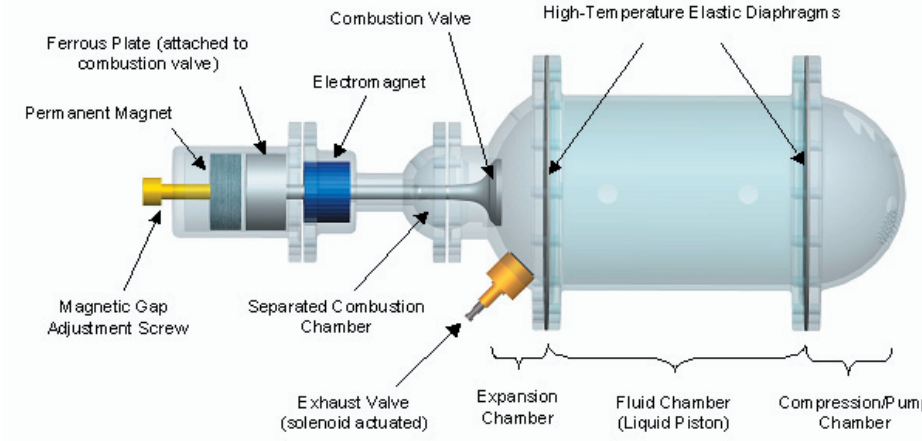

Figure 1 The free liquid-piston engine compressor configuration [3]

This paper is organized as follows: First, details of the dynamic system model of the FLPEC are presented in Section 2. Section 3 presents an experimental validation of the combustion model. Section 4 presents a pressure-based iterative control approach. Finally, Section 4 presents a simulation of the FLPEC controlled with this approach.

2. Dynamic System Model of the FLPEC

The FLPEC was modeled as a lumped-parameter model with a level of fidelity appropriate for only those states of interest, and with accuracy adequate for control purposes. Therefore the system is simplified as the forced mass-spring-damper system shown in Figure 2. A control volume (CV) approach was taken to model the pressure and temperature dynamics in the combustion constant-volume chamber (subscript "c"), the expansion chamber (subscript "e"), and the pump chamber (subscript "p"). Mass flow rates were modeled through all six channels: 1) air/fuel injection mass flow through a controlled on/off valve ($\dot{m}_{inj}$), 2) breathe-in check-valve inlet mass flow into the combustion chamber ($\dot{m}_1$), 3) mass flow through the magnetically-latched combustion valve between the combustion and expansion chambers ($\dot{m}_2$), 4) mass flow through the exhaust valve of the expansion

chamber ($\dot{m}_3$), and 5) inlet ($\dot{m}_4$) and 6) outlet ($\dot{m}_5$) check-valve mass flow of the pump chamber. The arrows in Figure 2 indicate the directions of the mass flow, where $\dot{m}_2$ and $\dot{m}_3$ are modeled as two-way flow dependent upon time varying upstream and downstream pressures. Finally, the inertial dynamics of the liquid piston and the combustion valve were included to relate the time-based behavior of all three control volumes.

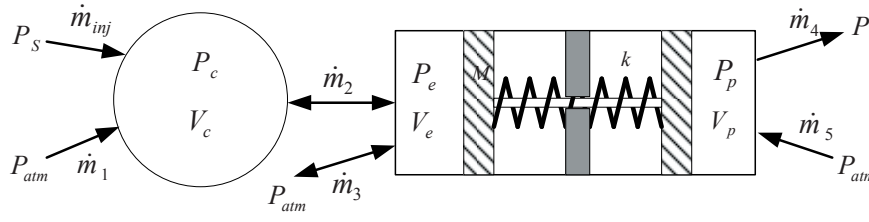

Figure 2 Schematic of the lumped-parameter dynamic model of the FLPEC

A power balance equates the energy storage rate to the energy flux rate crossing the CV boundaries. The rate form of the first law of thermodynamics is given as follows:

$$\dot{U}_j = \dot{H}_j + \dot{Q}_j - \dot{W}_j \tag{1}$$

where j is a subscript (c, e or p) indicating each of the three CVs, $\dot{U}$ is the rate of change of internal energy, $\dot{H}$ is the net enthalpy flow rate into the CV, $\dot{Q}$ is the net heat flux rate into the CV, and $\dot{W}$ is the rate of work done by the gas in the CV. Expressions for $\dot{H}$, $\dot{W}$ and $\dot{U}$ are given as:

$$\dot{H}_j = \sum \dot{m}_j \left(c_{p_{in/out}}\right)_j \left(T_{in/out}\right)_j \tag{2}$$

$$\dot{W}_j = P_j \dot{V}_j \tag{3}$$

$$\dot{U}_j = \dot{m}_j \left(c_v\right)_j T_j + m_j \left(c_v\right)_j \dot{T}_j = \frac{1}{\gamma_j - 1}\left(\dot{P}_j V_j + P_j \dot{V}_j\right) \tag{4}$$

where $\dot{m}$ is an individual mass flow rate entering (positive sign) or leaving (negative sign) the CV, $c_{p_{in/out}}$ and $T_{in/out}$ are the constant-pressure specific heat and the temperature of the substance entering or leaving the CV, respectively, P , V and T are the pressure, volume and temperature in the CV, respectively, c_v is the constant-volume specific heat of the substance in the CV, and γ is the ratio of specific heats of the substance in the CV. Combining Equations (1-4), the following differential equations can be obtained for the pressure and temperature dynamics:

$$\dot{P}_j = \frac{\left(\gamma_j - 1\right)\sum \dot{m}_j \left(c_{p_{in/out}}\right)_j \left(T_{in/out}\right)_j + \left(\gamma_j - 1\right)\dot{Q}_j - \gamma_j P_j \dot{V}_j}{V_j} \tag{5}$$

$$\dot{T}_j = \frac{\sum \dot{m}_j [\left(c_{p_{in/out}}\right)_j \left(T_{in/out}\right)_j - \left(c_v\right)_j T_j] - P_j \dot{V}_j + \dot{Q}_j}{m_j \left(c_v\right)_j} \tag{6}$$

The mass flow rates crossing all six valves depend on the upstream and the downstream pressures where a positive sign convention indicates mass flow into the CV. Upstream and downstream pressure roles will switch for the two two-way mass flow rates shown ($\dot{m}_2$ and $\dot{m}_3$) as the pressures P_c and P_e change dynamically according to Equation (5). The following equations give the mass rate under subsonic and sonic conditions [15]:

$$\dot{m}_j = \psi_j \left(P_u, P_d\right) = \begin{cases} C_d a_j C_1 \dfrac{P_u}{\sqrt{T_u}} & \text{if} \quad \dfrac{P_d}{P_u} \le P_{cr} \\ C_d a_j C_2 \dfrac{P_u}{\sqrt{T_u}} \left(\dfrac{P_d}{P_u}\right)^{1/\gamma_u} \sqrt{1 - \left(\dfrac{P_d}{P_u}\right)^{\gamma_u - 1/\gamma_u}} & \text{if} \quad \dfrac{P_d}{P_u} > P_{cr} \end{cases} \tag{7}$$

where C_d is a nondimensional discharge coefficient of the valve, a is the area of the valve orifice, P_u and P_d are the upstream and downstream pressures, T_u is the upstream temperature, γ_u is the ratio of specific heats of the upstream substance, and C_1 , C_2 and P_{cr} are substance-specific constants given by

$$C_1 = \sqrt{\frac{\gamma_u}{R_u} \left(\frac{2}{\gamma_u + 1}\right)^{\gamma_u + 1/\gamma_u - 1}} \tag{8}$$

$$C_2 = \sqrt{\frac{2\gamma_u}{R_u \left(\gamma_u - 1\right)}} \tag{9}$$

$$P_{cr} = \left(\frac{2}{\gamma_u + 1}\right)^{\gamma_u / \gamma_u - 1} \tag{10}$$

where R_u is the gas constant of the upstream substance. The valve orifice areas of the combustion and exhaust valves (a_2 and a_3) are dynamically determined by the inertial dynamics of their respective valve stems.

2.1 Modeling of the Combustion Process

Since the expansion and pumping processes occurs very quickly, heat lost during these two processes is neglected. That is $\dot{Q}_e = \dot{Q}_p = 0$. However, the heat flux rate for the pressure and temperature dynamics of the combustion chamber is primarily determined by the heat released during the combustion. The combustion process is coupled to the temperature dynamics in the combustion CV. Given that the *PV* work term in Equation (6) changes on a time-scale of the same order as the combustion process, a model of the heat release rate during combustion must be included. The total energy stored in the air/fuel mixture at the time of the spark can be computed by $E_c = \Delta H_r m_c \Big|_{t_{spark}}$, where m_c is the total mass in the

combustion chamber, and ΔH_r is computed from the lower heating value for the stoichiometric combustion of propane,

$$\begin{aligned}\Delta H_r &= \frac{46350\,\text{kJ}}{\text{kg fuel}} \times \frac{1\,\text{kg fuel}}{16.63\,\text{kg air/fuel mixture}} \\ &= 2787\,\frac{\text{kJ}}{\text{kg air/fuel mixture}}\end{aligned} \tag{11}$$

The rate at which heat is released by combustion in the combustion chamber is given by,

$$\dot{Q}_c = \Delta H_r \dot{m}_{cc} \tag{12}$$

where m_{cc} is the mass of the combustion products.

In the combustion research community, the Arrehnius law [14] is often used to compute the reaction rate. Using this method, the following equation is obtained giving the reaction rate of the temperature dependent combustion,

$$\dot{m}_{cc} = Ke^{-E_a/R_cT_c} m_{uc} \tag{13}$$

where $\dot{m}_{cc}$ is the rate of emergence of combustion products, E_a is the activation energy, and K is the pre-exponential factor. The mass of uncombusted material m_{uc} in the combustion chamber is given by

$$m_{uc} = m_c - \int_{t_{spark}}^{t} \dot{m}_{cc} dt \tag{14}$$

In the Laplace domain, Equation (12), (13) and (14) can be more compactly represented by the following,

$$Q_c = \frac{E_c}{\tau s + 1} \tag{15}$$

where

$$\tau = \frac{1}{Ke^{-E_a/R_cT_c}} \tag{16}$$

The Arrehnius law assumes that the fuel is homogeneously combusted and the temperature is same within all regions of the combustion chamber. However, the combustion is spark-ignited in the FLPEC. Hence, the first order model will not adequately capture the spatial propagation dynamics of the combustion process. Instead, a second-order model is applied to account for the complexities associated with combustion flame propagation and temperature distribution within the chamber. The overall heat release rate is then given as,

$$Q_c = \frac{E_c \tau_c^2}{s^2 + 2\xi\tau_c s + \tau_c^2} \tag{17}$$

Given that the reaction is assumed irreversible, the damping ratio must satisfy $\xi \geq 1$. The temperature-dependent rate is still given by the Arrehnius law: $\tau_c = Ke^{-E_a/R_cT_c}$.

$\dot{Q}_c$ is regarded as the ***effective heat release rate*** which "contributes" to pressure and temperature dynamics as shown in Equations (5) and (6). τ_c can be further simplified as,

$$\tau_c = Ke^{-A/T_c} \tag{18}$$

where K and A are empirically obtained constants.

2.2 Combustion Valve Dynamics

Since the combustion valve has dynamic characteristics that influence its flow area, it has to be properly modeled so that Equation (7) can be computed in real-time. Figure 3 shows the free-body diagram of this valve.

Applying Newton's second law, the valve dynamics are thus given:

$$m_{c\_v}\ddot{x}_v = P_c A_{c\_v} + F_M - F_{EM} - P_e A_{c\_v} \tag{19}$$

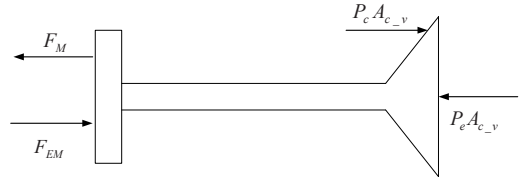

Figure 3 Free-Body Diagram of Combustion Valve

where m_{c_v} is the mass of the valve, x_v is the position of the valve, F_M is the magnetic force generated by the permanent magnet, respectively, and A_{c_v} is the cross-sectional area of the valve head. Furthermore, the valve flow area $a_2(x_v)$ can be described by the following:

$$a_2(x_v) = \max\left\{2\pi r_v x_v,\ \pi\left(r_v{}^2 - r_{v\_stem}{}^2\right)\right\} \tag{20}$$

where r_v and r_{v_stem} are the radii of the valve head and valve stem, respectively.

2.3 Exhaust Valve Dynamics

The dynamics of the exhaust valve, as shown in Figure 4, are given similarly to the combustion valve as follows,

$$m_{e\_v}\ddot{x}_{e\_v} = (P_{atm} - P_e)A_{e\_v}^2 - k_{e\_v}(x_{e\_v} + x_{e\_v0}) - b_{e\_v}\dot{x}_{e\_v} + F_{solenoid} \tag{21}$$

where x_{e_v} is the displacement of the exhaust valve into the expansion chamber side, A_{e_v} is the cross-sectional area of the exhaust valve, b_{e_v} is the effective viscous friction, x_{e_v0} is the pre-compressed spring force giving the valve returning force, and $F_{solenoid}$ is the force exerted on the exhaust valve by the solenoid valve controller.

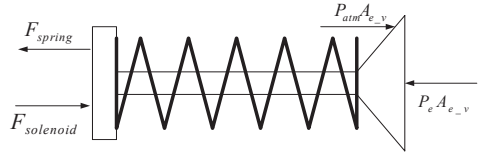

Figure 4 Free-Body Diagram of Exhaust Valve

Similarly, the valve flow area $a_3(x_{ex})$ can be described by the following:

$$a_3(x_{ex}) = \max\left\{2\pi r_{ex} x_{ex},\ \pi\left(r_{ex}{}^2 - r_{ex\_stem}^2\right)\right\} \tag{22}$$

where r_{ex} and r_{ex_stem} are the radii of the exhaust valve head and stem, respectively.

2.4 Free-Piston Inertial Dynamics

The dynamics given by the liquid piston are modeled by the following differential equation:

$$\ddot{V}_e = \frac{1}{M}\left[\left(P_e - P_p\right)A^2 - kV_e - b\dot{V}_e + kV_{e\_rlx}\right] \tag{23}$$

where V_e is the volume in the expansion side, A is the cross-sectional area of the liquid-piston, b is the effective viscous friction assumed for a 50% overshoot, and V_{e_rlx} is the "relaxed" volume in the expansion chamber when the diaphragms are unstretched.

3. Simulation and Validation of the Combustion Chamber

This section shows experimental model validation of three processes inside the combustion chamber: 1) pressure dynamics inside the chamber during the injection of the air/fuel mix, 2) the dynamics of heat release during combustion and the resulting influence on pressure, and 3) the opening of the combustion valve and its effects on the pressure.

Figure 5 shows the simulated and experimentally measured pressure in the combustion chamber during the injection of the air/fuel mixture. The model is given by Equations (5) and (7). The only parameter empirically determined was $C_d a$ in Equation (7). Figure 6a shows the pressure in the combustion chamber immediately after air/fuel injection stops and the spark occurs (at 0.04 seconds). Since the temperature during the combustion is difficult to measure on the real device, only the pressure dynamics can be compared between simulated and experimental data. As will be introduced in the next section, the system-level controller is based on pressure dynamics. Therefore, it is important to validate the pressure dynamics in all three CVs, especially in the combustion chamber given that it provides all of the driving power to the remainder of the system. The device was tested as an open system, where the expansion chamber was not attached to the combustion chamber; that is, the combustion valve was exposed to the atmosphere. The results show the pressure in the combustion chamber immediately after the spark. The dynamics of heat release during combustion cause a rapid rise in pressure, and the opening of the combustion valve causes the pressure drop. The two constants K and A in Equation (18), and the magnitude of F_M in Equation (19) were empirically adjusted to fit the overall combustion chamber pressure dynamics to the experimental results of the combustion pressure. The electromagnetic force F_{EM} in Equation (19) was set to zero as this electromagnet was not utilized in this experiment.

Figure 6b shows the total heat released by combustion as described by Equation (17). The total heat E_c stored in the air/fuel mixture is 130.2 kJ for this combustion event. However, in matching the simulated pressure dynamics to the experimentally obtained data, the values of K and A yield an effective heat release E_c of 93.8 kJ, which means that the experimental combustion lost 36.4 kJ to some combination of incomplete combustion and heat losses through the combustion chamber walls.

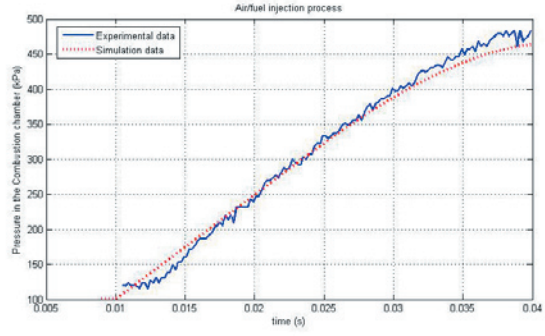

Figure 5 Simulation results and experimental data of the air/fuel injection process

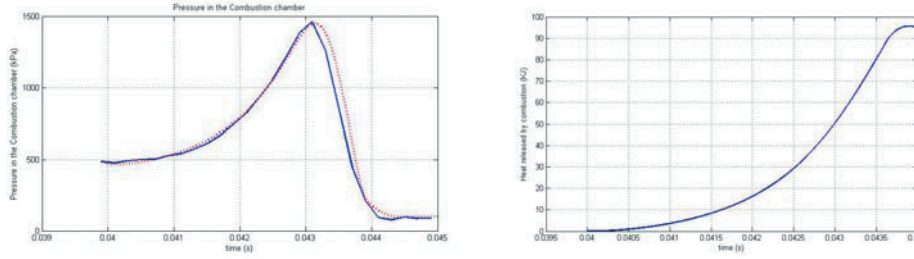

(a) Second-order model (b) Heat released by combustion

Figure 6 Simulation results (solid blue) and experimental data (dashed red) of the combustion pressure dynamics in the combustion chamber.

4. Pressure-Based Iterative Control for the FLPEC

The basic idea behind this approach is to control the overall system by regulating the control variables. The objective is to drive the system in an efficient manner by extracting the maximum amount of *PV* work from the combustion products. The controller should be able to dynamically adjust the control variables, such as the fuel injection duration. For instance, the pressure in the reservoir will be increased by continuous pumping, or decreased by supplying air to the end application. The duration of air/fuel injection must be adaptively controlled so that optimal efficiency can be achieved and the compressor can be kept running in a desired way in face of uncertainties. Furthermore, proper timing of *all* of the valves is critical in achieving the best performance of the FLPEC. For the FLPEC, the period from cycle to cycle is not fixed. Hence, the controller also aims at achieving the highest operational frequency possible. In order to achieve the optimal control parameters, the performance of the immediately previous cycle will be recorded and analyzed to adjust or set the control variables for the current cycle.

4.1 Pressure-based Iterative Controller

Although in simulation one can obtain every signal, some signals are not available on the actual device. Furthermore, using as few signals as possible is preferred for reducing the

sensors attached to the FLPEC. Basically, the pressures in different chambers are the most convenient signals to obtain, and these pressures directly represent the dynamics in three CVs. In particular, the pressures in the expansion and pump chambers, namely P_e and P_p, carry valuable information regarding the dynamic behavior of the piston and the pumping process. As it will be shown, event-based control of all relevant valves can be determined solely by these dynamics.

In short, there are five control variables to be regulated: 1) The amount of air/fuel mix injected for each cycle, or the time duration of the air/fuel injection process (T_{inj_d}); 2) The initiating time of air/fuel injection (t_{inj}); 3) The timing of the spark (t_{spark}); 4) The initiating time to open the exhaust valve (t_{ex}); 5) The duration of opening of the exhaust valve (T_{ex_d}). All these control variables are decided by pressured-based events.

Successful pumping is manifested by a slightly higher pump chamber pressure P_p than the reservoir pressure P_s. The pumping process begins at the time when P_p is increasing and is higher than P_s (crossing P_s from below). On the one hand, the duration of the air/fuel injection needs to be increased if P_p has never been higher than P_s. On the other hand, too much air/fuel injected into the combustion chamber may result in unutilized energy, which consequently decreases the energy efficiency.

The two strokes of the FLPEC are the power stroke, which begins with the spark and ends with the finishing of pumping, and the return stroke. The pressure P_e at the end of the pumping, denoted by $P_e\big|_{P_P=P_s\downarrow}$, can be used to indicate if there is too much fuel injected and combusted. (Note that the subscripted condition $P_P = P_s\downarrow$ refers to the instant at which the pump pressure drops "across" the reservoir pressure). For instance, if too much fuel is used, $P_e\big|_{P_P=P_s\downarrow}$ will be high. Therefore, the duration of the air/fuel injection can be adaptively adjusted in the next cycle based on $P_e\big|_{P_P=P_s\downarrow}$. Without enough air/fuel injection, on the other hand, there will be no pumping during one cycle, and P_p will be lower than P_s for the entire duration of the stroke. Hence, the maximum value of P_p in one cycle is also recorded as $\max P_p$. Thus, the control command for the duration of the air/fuel injection is given as follows:

$$T_d(k+1) = \begin{cases} T_d(k) - L_k(P_e\big|_{P_P=P_S\downarrow} - P_{atm}) & \text{if } \max P_p > P_s \\ T_d(k) - L_k(\max P_p - P_s) & \text{otherwise} \end{cases} \tag{24}$$

Where $T_d(k+1)$ is the duration of air/fuel injection of the current cycle while $T_d(k)$ is that of the immediately previous cycle. Each cycle is defined as starting and ending at the spark time. The gain L_k is a positive constant serving to drive the error $e = P_e\big|_{P_P=P_S\downarrow} - P_{atm}$ to zero.

$$L_k = \begin{cases} \text{small} & \text{if } \max P_p > P_s \\ \text{large} & \text{otherwise} \end{cases} \tag{25}$$

Once pumping has finished, V_e starts to decrease in the return stroke. The combustion valve at this point has already closed, and it is allowable to begin the injection of the air/fuel for the next cycle. Meanwhile, the piston is moving back toward the combustion side, at which point the exhaust valve should immediately be opened to allow the combustion products in the expansion chamber to be exhausted. Thus, the time to open the exhaust valve should be when $P_P = P_s \downarrow$ (the end of pumping).

To avoid a large dead volume in the expansion chamber, the best spark time is right at the time when V_e is at a minimum (ideally zero). However, the injection will take longer than the duration of the return stroke of the piston. Hence, the timing of the spark must be delayed until V_e bounces back to a minimum after another period of resonance, which will provide the injection with enough time to complete. Although V_e cannot be directly measured, it can be inferred from P_p since the pump chamber acts as a bounce chamber during this period. Since $\dot{V}_p = -\dot{V}_e$, $\dot{V}_p$ is positive when V_e is decreasing to its minimum, and therefore $\dot{P}_p$ is negative. When $V_e = \min$, $\dot{V}_p = \dot{V}_e = 0$, which implies P_p is at its minimum value. Thus, the spark takes place while $\dot{P}_p < 0$ and P_p is approaching atmospheric pressure.

4.2 Simulation of the Controlled System

Figure 7 shows the timings and durations of the control commands and their conditions. The pressure-based event observer and the proposed controller were applied to the simulation model described in section 2. The initial pressures and temperatures in the three chambers were set to atmospheric pressure and ambient temperature, the free piston started at its "relaxed" position, and all the valves are initially closed.

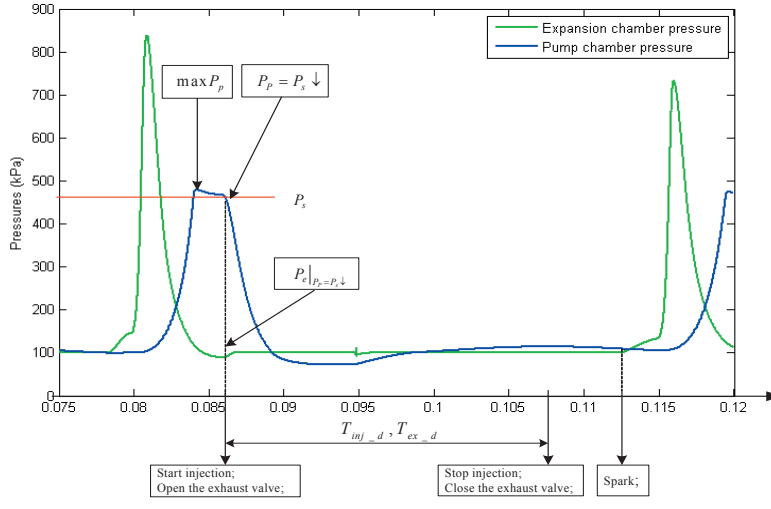

Figure 7 Timings and durations of the control commands and their conditions

The pressure-based iterative controller tracks the critical events represented by P_e and P_p. In Figure 7 above, the straight line indicates the reservoir pressure. It was set as the threshold for P_p. At the time when P_p is decreasing and crossing the reservoir pressure, P_e is recorded as $P_e\big|_{P_p=P_s\downarrow}$ and used for calculating the injection duration for the next cycle, as given by Equation (24). The injection is started and the exhaust valve is opened at this moment. As P_p continues to evolve, the spark is initiated when P_p decreases a second time through or near P_{atm} after the return bounce (please refer to Figure 7). Comparing P_p with V_e in Figure 8 demonstrates that P_p can be used to indicate the times when V_e is at a minimum.

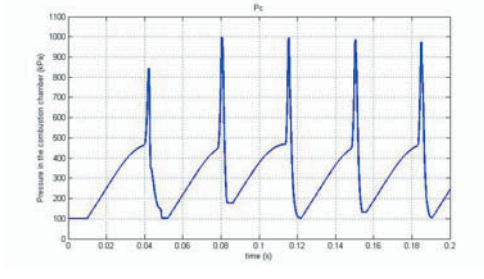

(a) Combustion Chamber Pressure P_c

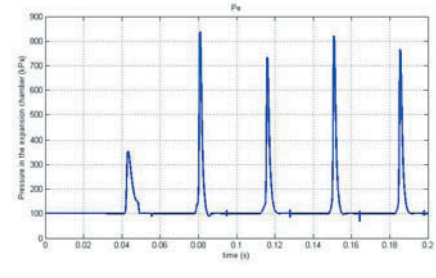

(b) Expansion Chamber Pressure P_e

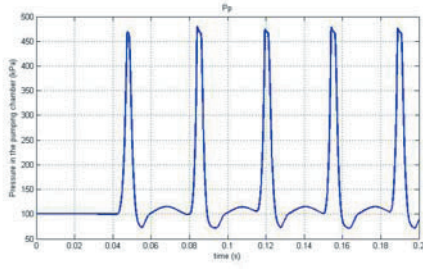

(c) Pump Chamber Pressure P_p

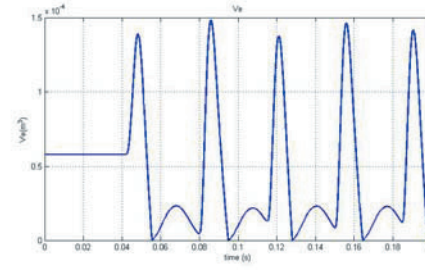

(d) Piston Inertial Dynamics V_e

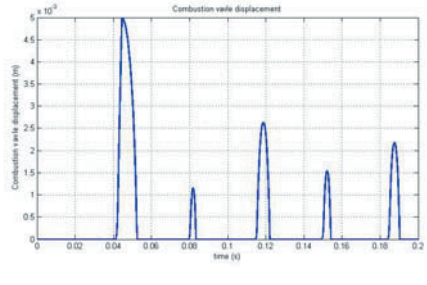

(e) Combustion Valve Dynamics

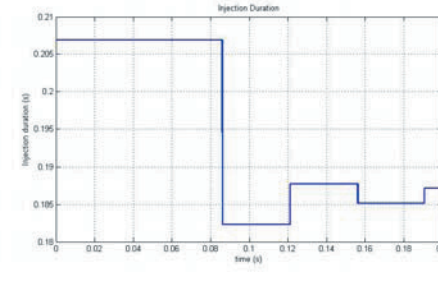

(f) Duration of the Air/Fuel Injection

Figure 8 Simulation results using the pressure-based iterative controller

Applying the pressure observer and the pressure-based iterative controller to the simulation, a typical system performance is shown in Figure 8. Band-limited white noise was added to P_p to simulate sensor noise. One can notice that the duration of the fuel injection is dynamically changed from cycle to cycle. As shown in Figure 8f, the duration of the fuel injection is converging to about 0.027s after a few cycles.

5. Conclusions

This paper presented the modeling, simulation, and control of a new free liquid-piston engine compressor. The combustion process was modeled as a second order dynamic with the heat release rate governed by the Arrhenius law. The dynamics of three control volumes, the combustion chamber, the expansion chamber and the pump chamber respectively, were modeled. The mass flows in/out of these control volumes were also modeled. The simulation results for the pressures in the combustion chamber show good agreement with the experimentally measured pressure. A pressure-based iterative control scheme for this device was developed to control 1) The duration of air/fuel injection for each cycle; 2) The timing of the fuel injection; 3) The timing of the spark; 4) The timing and duration of the exhaust valve. Applying the proposed controller to the simulation model results in good dynamic performance. By tracking the pumping pressure, the fuel injection can be adjusted from cycle to cycle. However, the proposed controller lacks a fault-tolerant mechanism for some special cases, such as misfiring. Future work will investigate this, as well as implement the proposed control scheme on the real device and test its performance.

REFERENCES:

[1] Goldfarb, M., Barth, E. J., Gogola, M. A., and Wehrmeyer, J. A., "Design and Energetic Characterization of a Liquid-Propellant-Powered Actuator for Self-Powered Robots," *IEEE/ASME Transactions on Mechatronics*, vol. 8, no. 2, pp. 254-262, June 2003.

[2] McGee, T. G., Raade, J. W., and Kazerooni, H., "Monopropellant-Driven Free-piston Hydraulic Pump for Mobile Robotic Systems," *ASME Journal of Dynamic Systems, Measurement, and Control*, vol. 126, pp. 75-81, March 2004.

[3] J. Riofrio, E. J. Barth, "Design and analysis of a resonating free liquid-piston engine compressor," IMECE 2007, November 11-15, 2007, Seattle, WA.

[4] Pescara, R. P., "Motor Compressor Apparatus," U.S. Patent No. 1,657,641, Jan. 31, 1928.

[5] Achten, P. A.., Van Den Oeven, J. P. J., Potma, J., and Vael, G. E. M. 2000. Horsepower with Brains: the design of the CHIRON free piston engine, *SAE Technical Paper* 012545.

[6] Aichlmayr, H. T., Kittelson, D. B., and Zachariah, M. R., "Miniature free-piston homogenous charge compression ignition engine-compressor concept – Part I: performance estimation and design considerations unique to small dimensions," *Chemical Engineering Science*, 57, pp. 4161-4171, 2002.

[7] Aichlmayr, H. T., Kittelson, D. B., and Zachariah, M. R., "Miniature free-piston homogenous charge compression ignition engine-compressor concept – Part II: modeling HCCI combustion in small scales with detailed homogeneous gas phase chemical kinetics," *Chemical Engineering Science*, 57, pp. 4173-4186, 2002.

[8] Barth, E. J., and Riofrio, J., “Dynamic Characteristics of a Free Piston Compressor,” *2004 ASME International Mechanical Engineering Congress and Exposition (IMECE),* IMECE2004-59594, November 13-19, 2004, Anaheim, CA.

[9] Underwood, A. F., “The GMR 4-4 ‘Hyprex’ Engine: A Concept of the Free-Piston Engine for Automotive Use,” *SAE Technical Paper Series*, 570032, vol. 65, pp. 377-391, 1957.

[10] Beachley, N. H. and Fronczak, F. J., “Design of a Free-Piston Engine-Pump,” *SAE Technical Paper Series*, 921740, pp. 1-8, 1992.

[11] Johansen, T. A., Egeland, O., Johannessen, E. A., and Kvamsdal, R., "Dynamics and Control of a Free-Piston Diesel Engine," *ASME Journal of Dynamic Systems, Measurement, and Control*, Vol. 125, pp. 468-474, 2003.

[12] Klotsch, P., “Ford Free-Piston Engine Development,” *SAE Technical Paper Series*, 590045, vol. 67, pp. 373-378, 1959.

[13] Mikalsen, R., and Roskilly, A. P., "A Review of Free-Piston Engine History and Applications," *Applied Thermal Engineering,* vol. 27, pp. 2339-2352, March 2007.

[14] K. Annamalai, I. K. Puri, “Combustion Science and Engineering,” CRC, pp.195-196, 2006

[15] Richer, E., and Hurmuzlu, Y., "A High Performance Pneumatic Force Actuator System: Part I – Nonlinear Mathematical Model," *Transactions of ASME,* vol. 122, pp. 416-425, September 2000.

[16] Riofrio, J. A., and Barth, E. J., "A Free Piston Compressor as a Pneumatic Mobile Robot Power Supply: Design, Characterization and Experimental Operation," *International Journal of Fluid Power,* vol. 8, no. 1, pp 17-28, February 2007.

Session 6
Efficient and intelligent systems

The Center for Compact and Efficient Fluid Power

Kim A. Stelson
Professor and Director
Center for Compact and Efficient Fluid Power
Department of Mechanical Engineering
University of Minnesota
Minneapolis, MN 55455
U.S.A.
e-mail:kstelson@me.umn.edu

ABSTRACT

The Center for Compact and Efficient Fluid Power (CCEFP) is a network of researchers, educators, students and industry working together to transform the fluid power industry. CCEFP includes seven universities: Georgia Tech, Illinois Urbana-Champaign, Milwaukee School of Engineering, Minnesota, North Carolina A&T, Purdue and Vanderbilt. The CCEFP fills a void in fluid power research that existed for decades. Until the Center was established, the U.S. had no major fluid power research center (compared with more than thirty centers in Europe). Fluid power researchers, who were previously disconnected, are now linked through the CCEFP. A team of thirty-five faculty researchers is engaged in work on twenty-two research projects and four test beds. These projects are organized in three thrusts (efficiency, compactness and effectiveness) that achieve the following societal benefits: creation of a new fluid power technology that, with improved efficiency, will significantly reduce petroleum consumption, energy use and pollution; creation of a new fluid power technology that, with improved effectiveness, will make fluid power clean, quiet and safe for its millions of users; and creation of a new fluid power technology that, with improved compactness, will exploit its attributes in a new generation of devices and equipment—orthoses that increase mobility for an aging population and autonomous rescue and service robots needed in our complex world. The CCEFP's education and outreach program is designed to transfer this knowledge to diverse audiences—students of all ages, users of fluid power and the general public

1. INTRODUCTION

The vision of the Engineering Research Center for Compact and Efficient Fluid Power (CCEFP) is to create new fluid power systems that are compact and efficient. This will lead to significant fuel savings as the new systems technologies are implemented in existing and new applications. The new technologies will enable new products and systems requiring

Fluid Power and Motion Control 2008 Edited by Dr D N Johnston and Professor A R Plummer

portable high-power, un-tethered operations over long time periods. As the vision of the CCEFP is realized, both short and long term advantages will accrue. Improved efficiency will greatly reduce petroleum consumption and pollution, recovering the Center's cost many times over. Improved compactness will enable fluid power to perform tasks that are not presently possible, spawning whole new industries to commercialize these systems.

CCEFP has created a highly qualified multi-disciplinary team to realize this vision. CCEFP includes seven universities: Georgia Tech, Illinois Urbana-Champaign, Milwaukee School of Engineering, Minnesota, North Carolina A&T, Purdue and Vanderbilt. The center is becoming recognized as a world leader in fluid power. In the November 2007 issue of *Hydraulics and Pneumatics,* the leading trade magazine in fluid power, Paul Heney, Senior Editor writes: "I've said it before, and I'll say it again. I think the newly formed Center for Compact and Efficient Fluid Power is key to moving fluid power in the U.S. forward. The center is something that both industry and manufacturers should pay attention to and support. Take a look at their website, www.ccefp.org. Their dedication, research and education may be the linchpin that we need to figure out how to keep fluid power strong, competitive, and on the minds of the youngest, brightest students mulling over career choices."

2. RESEARCH

The CCEFP has four goals. The first goal is to dramatically improve the energy efficiency of fluid power in current applications; the second goal is to improve the efficiency of the transportation sector using fluid power by developing fuel efficient hydraulic hybrid technologies for small passenger vehicles; the third goal is to develop un-tethered portable human-scale fluid power devices; and the fourth goal is to make fluid power more acceptable and ubiquitous.

When these goals are achieved, society will benefit from much lower energy consumption and pollution in existing fluid power applications and in transportation. Whole new industries will be created for the new human-scale applications that will improve quality of life in many ways. Autonomous rescue robots will aid in emergencies, and free-roving service robots and a new generation of protheses and orthoses will aid those who are mobility impaired or suffering from other afflictions. These and many other applications will greatly benefit humanity.

2.1 Test beds

The CCEFP systems level test beds are the focus of technology integration activity. Through integration of research from the three thrusts (efficiency, compactness and effectiveness), they provide concrete demonstrations of achieving the four CCEFP goals. Test bed demonstrations not only create excitement for faculty and students but also credibility in the industry's eyes. Because of the integrative nature of the research challenges, research activities are directed in ways not possible in single investigator projects. CCEFP test beds are described below.

2.1.1 Excavator: The excavator demonstrates improved efficiency in current applications by using more efficient components, including fluids, and more efficient control strategies. It is also being used to demonstrate progress toward the goals of the Center's effectiveness thrust: easier, quieter and leak-proof operation. An excavator, donated by a CCEFP partner, was instrumented and a real-world energy consumption baseline was established. Detailed dynamics models have been created, predicting a 30% reduction in energy consumption with the implementation of CCEFP developed technologies. Modifications to incorporate these technologies, such as pump controlled linear actuation and engine management, are underway.

2.1.2 small Urban Vehicle (sUV): The small Urban Vehicle (sUV) is nearly operational. This vehicle has a novel power train system (a hydro-mechanical transmission with energy regeneration) which is expected to be significantly more efficient than existing approaches. A patent has been applied for. The sUV will demonstrate more efficient control strategies, more efficient pumps and motors and more compact energy storage. The sUV also provides a test bed for demonstrating improved drivability and noise reduction.

2.1.3 Rescue Robot: The rescue robot provides an example of a small-scale fluid power application where tether-less operation is required for long periods of time. The rescue robot is also being used to demonstrate a compact fluid power energy source. The first version, which is nearly operational, uses existing chemo-fluidic propulsion. Later versions will test two new compact power sources being developed by CCEFP: the chemo-fluidic hot gas vane motor and the free-piston engine compressor. The rescue robot is a cooperative project between Georgia Tech and Vanderbilt. Development of the control approach is now shared between the two universities, but eventually will be integrated into a seamless whole.

2.1.4 Orthosis: The orthosis stretches the capabilities of engineering a compact fluid power application to the limits. The first orthosis prototype was passive, using energy harvesting from walking for power. Now nearing completion, the first prototype has proven to provide important clinical results for patients with walking problems. Efforts are now being focused on a powered orthosis using a compact chemo-fluidic power source. The new device must be housed in a small, light package despite conflicting demands for power, mechanical strength, heat transfer, and minimal noise.

2.2 Strategic research plan

The mission of the CCEFP is to utilize system driven, cross functional research to transform fluid power so that it becomes more compact, efficient, and effective to use. By doing so, societal benefits in the areas of energy conservation, productivity and improved quality of life are expected. Direct energy savings will be realized on existing fluid power applications by improving the efficiency of fluid power components and systems. By combining these efficiency gains with advancements in compactness, the possibility of a viable fluid power enabled, fuel efficient passenger automobile becomes a reality. When these gains in compactness are combined with new ways of generating fluid power that is energy dense and mobile, entirely new systems and applications are possible. None of these perceived benefits will be realized unless fluid power becomes more effective, that is, easier and safe to use, quiet and leak free. CCEFP research is targeted at four goals described next.

2.2.1 Goal 1: Efficiency of existing applications

Fluid power in the agriculture, mining and construction sector consumes $56 billion of energy in the U.S. annually, and fluid power in the machine drives sector of manufacturing consumes $42 billion annually. A ten percent improvement in the energy efficiency of these sectors would save $9.8 billion in the U.S.A. annually. The energy data is provided by the United States Department of Energy (1.) Dollar values are calculated assuming a price of crude oil of $100 per barrel. Our goal is to significantly reduce energy consumption in existing applications of fluid power through development of efficient system configuration, control methodologies, and efficient components.

The excavator and the injection molding machine, representing the mobile construction and stationary manufacturing sectors respectively, were initially chosen when CCEFP started in June 2006 as the intended test beds for demonstrating efficiency improvement in existing fluid power applications. The injection molding machine was later eliminated because electric injection molding machines are displacing hydraulic injection molding machines especially at smaller capacities. Electric injection molding machines are more energy efficient than hydraulic injection molding machines.

State-of-the-art excavators make use of a load sensing pump and throttling valves for control. Although the pump is controlled to match the load of the circuit with the highest pressure, a third of the energy is still lost via throttling valves in the other circuits, another third of the energy is lost through inefficient components, leaving only a third of the energy for useful work.

Control configurations that do not involve throttling, systems that allow energy regeneration and appropriate energy and engine management schemes are needed to significantly increase system efficiency. Improvement in pump and motor efficiency, especially at partial load conditions will also be needed. Effective and intuitive human/machine interfaces are also needed to improve operation efficiency leading to reduced energy use.

2.2.2 Goal 2: Hydraulic hybrid passenger vehicles

The transportation sector consumes $480 billion of energy in the U.S. annually of which $200 billion is consumed by passenger cars. The energy data is provided by the United

States Department of Energy (2.) Again, dollar values are calculated assuming a price of crude oil of $100 per barrel. Hydraulic hybrid vehicles combine an internal combustion engine with energy storage in hydraulic accumulators. Hydraulic hybrid vehicles are just coming on the market. Prototype or near market vehicles include refuse trucks, city busses, SUVs and delivery vans. Energy savings in these sectors are expected to be a few hundred million dollars a year for each sector. A ten percent improvement in the energy efficiency of passenger vehicles would save $20 billion annually, a much larger amount. Accompanying this saving is a corresponding reduction in harmful emissions. Our goal is to develop hydraulic hybrid drive trains suitable for passenger vehicles.

Current hydraulic hybrid technology (e.g. by the U.S. EPA and various industry partners) can be used for heavier vehicles, but it is too large and heavy for competitive use in passenger vehicles. Electric hybrids, while already on the market after decades of research and development, rely on electric motor/generators with power densities are an order of magnitude lower than hydraulic pump/motors. This means that hydraulic hybrids can be more powerful for the same size can accelerate faster and are able to re-capture more braking energy during hard braking. Hydraulic hybrids are also potentially more reliable and cost-effective.

The small Urban Vehicle (sUV), is the test bed to demonstrate the technologies needed for hydraulic hybrid passenger vehicles. The unique challenge for small hydraulic hybrid vehicles lies in the weight and size requirements. State-of-the-art hydraulic accumulators have energy storage densities that are two orders of magnitude lower than electric batteries. Energy storage for fluid power systems that are five to ten times more compact than presently possible will be sufficient for hydraulic regenerative hybrid passenger vehicles. Other components, such as pumps and motors, must also be made more efficient over a broad operating range, quieter and more compact. Appropriate system architecture, operational strategy including engine and energy management, and precise control are all needed to realize the energy savings.

2.2.3 Goal 3: Portable, un-tethered, human-scale applications

Personal service robots are just one example of un-tethered portable human-scale fluid power devices. The market for service robots is estimated to be worth $10 billion in a decade (Japan Government Report, March 2005). These robots must be energetically autonomous to be truly effective, but there currently exists no power supply or actuation system capable of powering a human-scale robot for extended periods of time. Because electric motors and batteries are heavy, this approach cannot provide the required energy, and typical running times for these systems are limited to about twenty minutes. Because of the intrinsic power density advantage of fluid power, it is the natural technology for human-scale, un-tethered applications. The CCEFP will develop novel fluid power based compact power and actuation systems that will provide an order of magnitude greater energy and power density than state-of-the-art batteries and motor drives, thus overcoming one of the major barriers to the development of portable human-scale fluid power devices.

Two CCEFP test beds, the compact rescue crawling robot and the fluid powered orthosis, are designed to capture the vision of human-scale applications made possible by fluid power technologies that will be tetherless, portable and self-powered. The key functional barriers to these systems lie in the need for compactness. Specifically, compact and portable power

supplies suitable for long periods of operation, compact power generation and actuation (pumps, motors and actuators), and compact energy storage for regenerative modes of operation must be developed. Safe and intuitive human machine interfaces are key to the functional success of these test beds and applications.

2.2.4 Goal 4: Ubiquity

Key barriers to making fluid power widely accepted and having greater societal impact are: 1) unfriendliness to human operators, 2) noise and vibrations, and 3) leakage of hydraulic fluids. The image that fluid power is an outdated technology must be overcome. The test beds were selected to demonstrate societal impact and create excitement. New technologies that mitigate noise and vibration, leakage, cavitation are being demonstrated in all four test beds. Development of these technologies is especially critical for the success of several test beds: intuitive and safe human machine interfaces for the excavator, compact rescue crawler and fluid powered orthosis; quiet and leak free operation for the small Urban Vehicle, compact rescue crawler and fluid powered orthosis.

In summary, the technical barriers, as motivated by the engineered systems test beds, to accomplishing the four goals of CCEFP are: inefficient throttling control approach, lack of energy management, inefficient components, lack of compact power supplies, lack of compact energy storage, lack of compact integration and distribution, inability to achieve high pressure operation, lack of effective human/machine interfaces, noise and vibration, and leakage. The major barriers to each of the four goals and the test beds that drive the research to remove these barriers are summarized in Table 1 below.

Table 1: Test beds, Thrust Areas and Major Research Goals

Center Test Beds	Efficiency	Compactness	Effectiveness
Excavator	Meterless systems, more efficient pumps and motors, power management, energy regeneration	High pressure operation	Leak-free and quiet systems, productivity enhancing and intuitive user interfaces
sUV	Powertrain management, energy regeneration, more efficient pumps and motors	New compact energy storage concepts	Leak-free and quiet systems
Compact Rescue Robot		Compact power source	Remote user interfaces with haptic feedback
Human Orthosis		Compact fluid power components	Safe and passive user interface
	Major Research Barriers		

The three-plane diagram was developed by the National Science Foundation as a mechanism to concisely show the interrelationship of the research programs within an ERC. The three-plane diagram for CCEFP is shown in Figure 1. The highest level of the diagram contains the integrated engineered systems or test beds. The middle level of the diagram contains the enabling technology to create the integrated systems. The lowest level of the diagram contains the fundamental research needed to create the enabling technology. The diagram is organized into the three CCEFP research thrusts, efficiency, compactness and effectiveness.

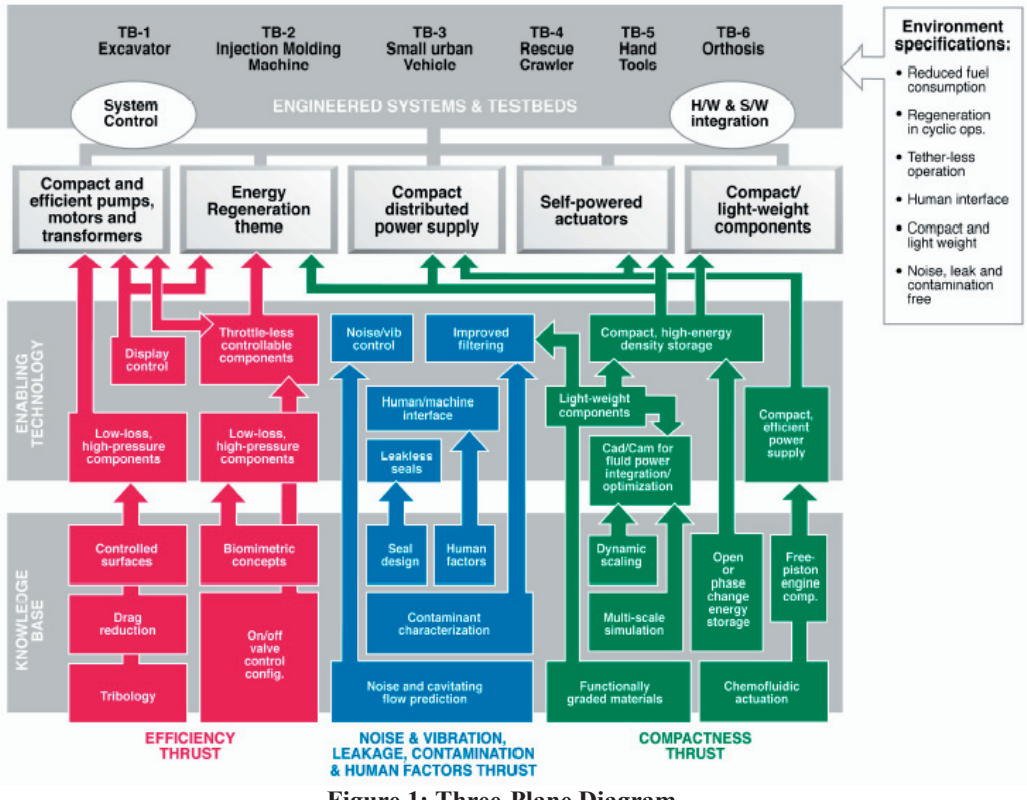

Figure 1: Three-Plane Diagram

3. EDUCATION AND PRE-COLLEGE OUTREACH

The Center's Education and Outreach program fills a long-recognized need. Despite fluid power's ubiquitous presence as an industry enabler, hydraulics and pneumatics instruction is typically scant. But the CCEFP is now transferring knowledge about fluid power and the work of the Center to diverse audiences—students of all ages, users of fluid power and the general public. Some of these programs are focused on STEM (science, technology, engineering and mathematics) education with examples drawn from fluid power when appropriate, while others are specific to fluid power and its application. All are designed as multipliers—leveraging the benefits of working with established partners or with the potential to be duplicated by others.

Informed by the CCEFP's research, the Center's Education and Outreach programs enrich understandings of fluid power technology. But its twenty-three projects share in a broader goal: to heighten interests in technology and engineering among an increasingly diverse student population. Some of the major education and outreach activities are described below.

3.1 Fluid power content in Project Lead The Way (PLTW) curricula

In partnership with PLTW and the National Fluid Power Association (NFPA), the CCEFP is working to enhance and expand fluid power content in several PLTW courses that are a part its middle and high school curricula. PLTW programs are now established in all 50 states and the District of Columbia, engaging 7,000 teachers and 5,000 counselors who work with 200,000 students. PLTW's fluid power course content is focused and enriched with the help of subject matter experts from industry (through the help of NFPA) and from the Center's faculty and staff.

3.2 Pneumatic training for FIRST Robotics teams

FIRST is an international robot competition for high school students. In 2008 there are 1,500 FIRST Robotics teams involving 37,000 high school students. Since inception, FIRST programs have impacted 156,000 students. In a pilot program for 2008, the Center has developed a pneumatics workshop and field-tested it among several Minnesota- and Georgia-based FIRST teams. Next year, this workshop will be made available to other FIRST teams in other locations. The Center is connecting its diversity efforts to FIRST by sponsoring a rookie, all Native American, FIRST Robotics team located in Cloquet, MN.

3.3 Delivering fluid power education through the core curriculum of mechanical engineering

Consensus reached at a recent NFPA Education/Industry Summit (3) reaffirmed what has long been widely assumed: new departments and new four-year undergraduate degrees in fluid power are not realistic goals. But, inserting fluid power into the core mechanical engineering curriculum is. The CCEFP is working to develop curriculum material to insert into controls and fluid mechanics courses, which are part of every mechanical engineering program in the world. This material is being written now, and dissemination will start in the fall of 2008 with the seven CCEFP schools. With this start as a foundation, the Center's goal is to reach all 283 ABET accredited mechanical engineering programs in the United States. Universities in other parts of the world come next.

3.4 Interactive learning models

Staff from the Science Museum of Minnesota (SMM) and Center faculty are developing interactive exhibits on fluid power that engage the public. The Hydraulic Hybrid Vehicle Exhibit, the first in the exhibit series, and already on the SMM's floor, made a trip to the Minnesota State Fair where it was seen by thousands of fair goers, and was featured in the CCEFP's booth at the International Exposition for Power Transmission and its show partner, CONEXPO – CON/AGG. Together, these shows will host more than 100,000 attendees.

4. INDUSTRIAL COLLABORATION AND TECHNOLOGY TRANSFER

Data on the size and reach of the current fluid power industry speak to the potential for the Center's impact. The National Fluid Power Association (NFPA) estimates that direct fluid power component sales exceed $33 billion worldwide. End application sales were easily an order of magnitude greater since fluid power technology is utilized in a wide range of industries: construction, manufacturing, transportation, agriculture, packaging, and many

more. The use of fluid power is so prevalent that improvements in its use, driven by the Center's research, will have a profound societal impact.

Industry has supported the CCEFP since its proposal stage. Today, fifty-seven companies support the Center with funding and in-kind donations. CCEFP annual industrial membership fees are around $650,000, and CCEFP companies have donated $250,000 worth of fluid power equipment to the Center. Twenty-two CCEFP member companies are represented on the Industrial Advisory Board (IAB).

Through its committees and conferences, project mentoring, internships, and a host of other projects and individual contacts, the CCEFP is a forum that not only facilitates knowledge transfer between academia and industry but also a growing appreciation of each other's culture. These emerging partnerships will be among the Center's key legacies.

Benefits await industry members who take an active role in the Center. Industry feedback indicates that a "pipeline for future talent" is at or near the top of this list. Another major benefit is insight into breakthrough technologies which only the Center is uniquely positioned to provide. CCEFP technologies could be commercialized in several ways.

Near term developments are expected to be in the business area of CCEFP member companies, so the companies themselves would provide commercialization. Many of these technologies would be demonstrated on the excavator test bed.

Medium term developments are expected in the hydraulic hybrid vehicle market. It is unlikely that the hydraulic hybrid vehicle would be commercialized by the established automobile industry. Hydraulic hybrid vehicles are disruptive technology, meaning they would undermine established business practice. Further, the early market for these vehicles would be too small to interest automobile manufacturers. The more likely path for hydraulic hybrid vehicle commercialization would be by a vehicle manufacturer other than an auto maker. Examples are manufacturers of ATVs, snowmobiles and street and floor sweeping equipment. These companies are much smaller and do not have competing products, so the hydraulic hybrid vehicle business would be more attractive to them. These companies also use many of the same manufacturing methods of automobile companies. A parallel fluid power hybrid vehicle development path is expected for heavy trucks and buses. Heavy hydraulic hybrid vehicles are viable with off-the-shelf technology, so the market can be expected to develop faster. This growing market will encourage improvements in the technology that could migrate to the hydraulic hybrid passenger market and speed development.

Longer term developments may be in businesses far removed from current fluid power markets. Fluid power companies could move into these markets, but companies from other sectors could also be attracted. Startup companies often result from this type of new technology. Examples of areas that could produce startup companies would be compact fluid power energy sources, compact energy storage devices, service and rescue robots, fluid power hand tools, and biomedical devices.

Figure 2 shows major commercialization opportunities for emerging technologies of the Center as a function of the potential of the Center to lead this technology and the potential of the Center to achieve technology transfer. The most promising opportunities are for those projects in the upper right hand corner of Figure 2. Nearer term opportunities identified for early migration into industry includes new seal design concepts, CFD code for predicting cavitation, free piston engine compressors and fluid power noise silencers. Longer term technologies with high impact potential include compact fluid power based energy storage devices, new high speed/high flow valve concepts, new fluid power system control methodologies, high performance fluids with nano-particle additives, autonomous robots with fluid power based propulsion and work circuits and fluid power based transmissions for automobiles that can regenerate energy.

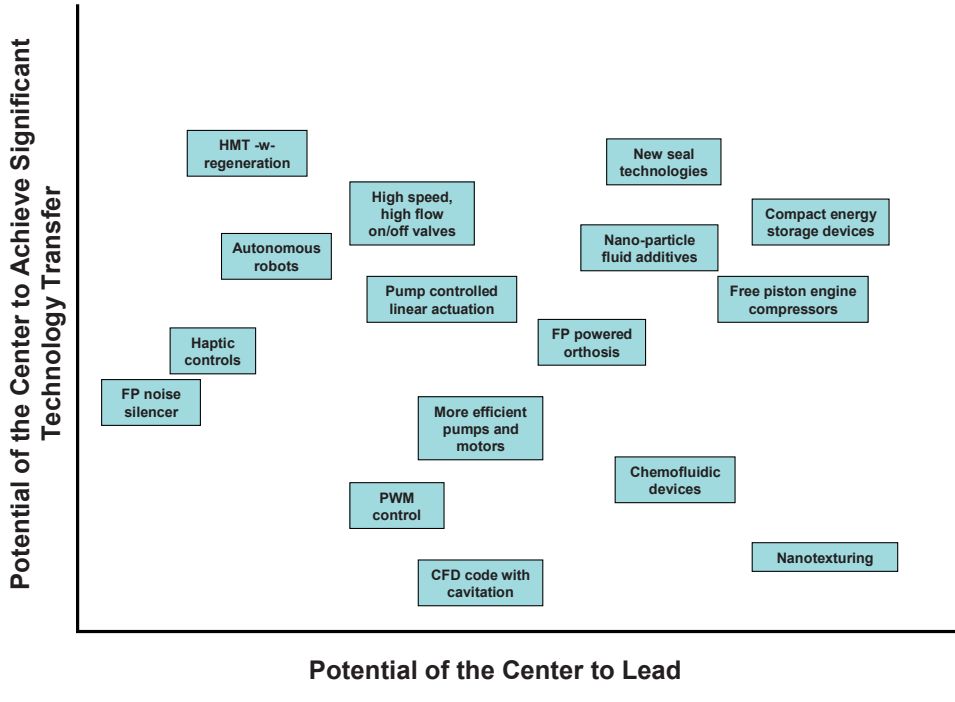

Figure 2: Technology Transfer and CCEFP Leadership

5. CONCLUSION

The Center for Compact and Efficient Fluid Power (CCEFP) is a major new fluid power education and research initiative in the United States. CCEFP was founded in June 2006 and includes seven universities: Georgia Tech, Illinois Urbana-Champaign, Milwaukee School of Engineering, Minnesota, North Carolina A&T, Purdue and Vanderbilt. Research projects are organized in three thrusts (efficiency, compactness and effectiveness) that achieve the

following societal benefits: creation of a new fluid power technology that, with improved efficiency, will significantly reduce petroleum consumption, energy use and pollution; creation of a new fluid power technology that, with improved effectiveness, will make fluid power clean, quiet and safe for its millions of users; and creation of a new fluid power technology that, with improved compactness, will exploit its attributes in a new generation of devices and equipment. CCEFP technology is demonstrated on four test beds: an excavator, a hydraulic hybrid passenger vehicle, a rescue robot and an orthosis. CCEFP research activities are complemented by an education and outreach program designed to transfer this knowledge to students of all ages, to users of fluid power and to the general public.

REFERENCES

(1.) Department of Energy, 2001, Energy Information Administration (EIA), Annual Energy Outlook 2002, DOE/EIA-0383(2002), Washington, DC.

(2.) Department of Energy, 2004, Energy Information Administration (EIA), Annual Energy Review 2003, DOE/EIA-0384(2004), Washington, DC.

(3.) NFPA 2007, 5th NFPA Summit for Fluid Power Engineering and Research Technology, August 21, 2007, Roundtable Discussion: Fluid Power in Universities – Should there be a degree?

Towards intelligent mobile machines – GIM research

Kalevi Huhtala*, Jussi Suomela, Matti Vilenius* and Aarne Halme****
* Department of Intelligent Hydraulics and Automation (IHA) in Tampere University of Technology
** Automation Technology Laboratory (ATL) in Helsinki University of Technology

ABSTRACT

This paper will give the state-of-art of the Generic Intelligent Machines (GIM) research group work results. The main focus is in this paper in the skid-steered mobile machines. A portable remote control for short-range teleoperation is developed. Electronics of the controller is designed and the wireless communication between the remote control and the machine is carried out with lightweight low-cost radio modems.

The problematic of the control and steering of the skid-steered machines in the teleoperated and autonomous machines is considered. Another studied field is autonomous excavation. Special requirements due to demanding operating conditions and different soil types are considered. The control system is installed and software is designed. The test system and results are presented.

The paper describes also the components of a multi-machine teleoperation system. The main components of the system are: work site, work machines, teleoperation/control station and a simulator. The components are joined together with a software architecture that enables the flexible implementation of distributed systems. The control of the system is done via the Internet. As a result the system presents a full featured test platform for multi work machine teleoperation with real work machines at a real work site.

1. INTRODUCTION

Robots are slowly moving from factories to mines, construction sites, public places and homes. The first real robotic systems replacing human driven work machines are already on the market. AutomineTM /1/ by Sandvik is a good example of commercial robotic work machines. Automine is a semiautonomous loading and hauling system for underground mines. It includes Loading and Hauling Devices (LHDs) and dumpers, which both are capable to navigate autonomously without any additional infrastructure. Only loading and exceptional situations need the help of operator, who supervises and occasionally teleoperates several machines from a control room (Figure 1).

Fluid Power and Motion Control 2008 Edited by Dr D N Johnston and Professor A R Plummer

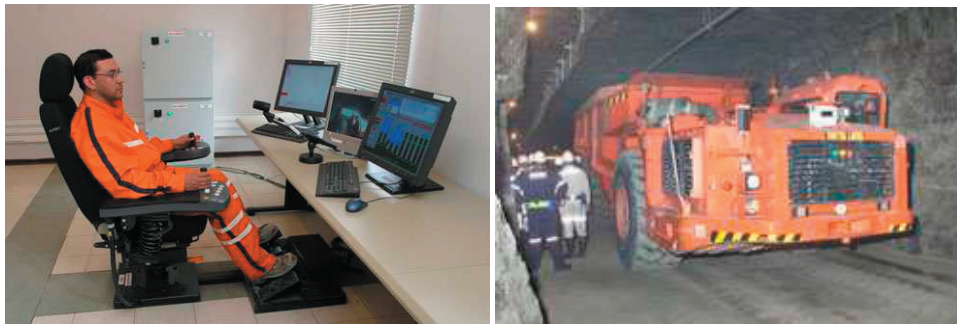

Figure 1 Views of AutomineTM control room and dumper in a tunnel /1/.

By means of this example it is easy to understand the demands what teleoperation or autonomous functions set for instance to hydraulics, controls, navigation or human-man interactions.

2. GIM RESEARCH

The newly founded Finnish Center of Excellence (CoE) in Generic Intelligent Machines Research (GIM) is focusing to the development of robotic like mobile machines. The CoE period for GIM is 2008-2013. GIM has started its operation as a research project to build up the infrastructure in 2005. During the CoE period GIM will carry applied basic research projects covering the area of robotic like mobile machines from locomotion systems up to human robotic interfacing. All research results are tested and demonstrated with real hardware in the GIM worksite. The background of GIM is in strong research tradition of the participating institutes: Automation Technology Laboratory (ATL) in Helsinki University of Technology and Department of Intelligent Hydraulics and Automation (IHA) in Tampere University of Technology. GIM has been and will be supported by the Finnish Academy, National Agency of Finland (TEKES) and the wide mobile working machine industry in Finland.

GIM collects totally 40 scientists from its host units to carry out research during the years 2008-2013. In a way it's a big six years long research project. Research is divided in 9 research packages, which are

- RP 1: Internal Re-evaluation and Education
- RP 2: Modularity of Generic Machines
- RP 3: Power and Energy Systems
- RP 4: Transmission of Power and Data
- RP 5: Control Architectures (task manager and planning system)
- RP 6: Perception and Navigation Systems
- RP 7: Human – Robotic Machine Interaction
- RP 8: Motion systems
- RP 9: INTEGRATOR project – integrate, validate and demonstrate

As the name indicates the first package is for internal evaluation and education in form of internal seminars, conferences and development meetings. RPs from 2 to 8 include the real research work. Each RP represents roughly a subsystem in a mobile robot. Naturally the research can't cover each RP area fully but it is a frame where interesting research topics are raised and studied. Each RP is a studied by a team consisting of 3-5 senior scientists and several doctoral students. Senior scientists are typically involved in several RPs when doctoral students concentrate on a topic.

In the case of mobile robotics the paper research and simulations are good tools but to be really credible the research results have to be proved with real hardware. RP 9, the integrator project, is a tool for this purpose. It includes a "Future worksite" type of infrastructure with several robotic machines and a control architecture, which allows easy (tele)control of the robots. All research results are integrated into the worksite and tested in practise.

3. FUTURE WORKSITE /2/

With "Future Worksite" the authors mean any type of worksite where mobile work machines carry their tasks in high level of autonomy (Figure 2). It doesn't need to be fully automated. Human workers as well as manually driven machines may also exist there.

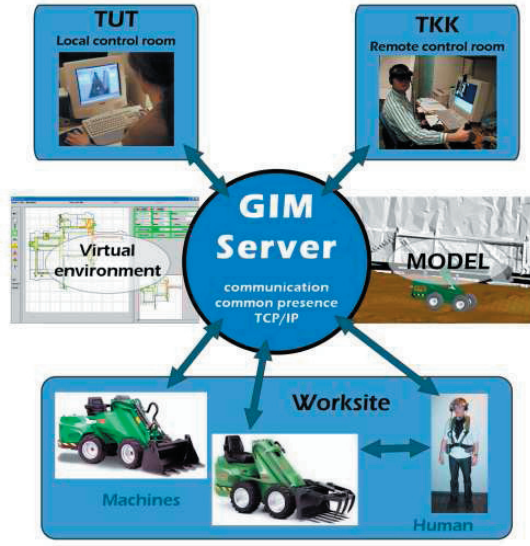

Figure 2 Concept of Future Worksite.

The idea is that most of the work can be performed with robotic vehicles and vehicle operators are not physically bound to the physical worksite. In fact the system includes three kinds of worksites: the physical work sites, operators' worksites and virtual worksites where operators and machines meet. Physical worksites can be located globally – or even universally – anywhere. It could be somehow compared to the existing situation with

telephone exchanges. A call to a company can end up to different continent than the company is located. After the answer it can be forwarded to a person sitting physically in the company or working in a third continent. This has become possible due to the development in telecommunication. If the development in robotic machines is added – as Automine show this is possible already today – the operation of a worksite can really be outsourced or locate freely. However, even the future worksite already exists, there is a lot to do before the idea can be applied in all type of worksites such as construction sites, forestry, janitorial services, etc. At the moment the basic level navigation and perception of robotic work machines is sufficient for certain tasks but especially the machine learning, rapid task teaching, human robot interaction and the common situational awareness of the worksite entities have to be improved.

4. EXISTING RESEARCH ENVIRONMENT AND MACHINES /5, 6, 7/

The basic infrastructure of the GIM research environment was under development in "Integrator"-project during the years 2006 and 2007. The target was to construct basic infrastructure to serve the GIM research. Worksite includes a 20 m x 20 m test hall with 2-3 robotic work machines and a control/communication architecture allowing teleoperation and supervisory control over the Internet. Worksite and the machines are modelled in 3D in order to help the off-line testing of control algorithms.

The skid steered loaders are located in the covered worksite in Tampere. The worksite is equipped with supporting sub-systems such as cameras, WLAN communication, etc. A local remote control room is located in the vicinity of the worksite. The "real remote control room", which basically can be anywhere or even distributed (where internet is available), is located in Espoo. The physical distance between Espoo and Tampere is 180 km. The interface between a machine/robot and the GIM-architecture is independent of the robot structure thus it's easy to connect different type of machines to the system.

The remote machines are modified to be computer controlled. The leading idea in the instrumentation of the machines was to maintain them as a real mobile work machines (robust, environment tolerance, etc). The mobile machine (Figure 3) has four instrumentation parts needed for computer control. Number one includes all electronic components, number two is a control and display module, which runs the main program, number three is the radio modem and number four is the place of the proportional valve block, which is installed in the front of the machine. The hydraulic circuit is illustrated in Figure 4.

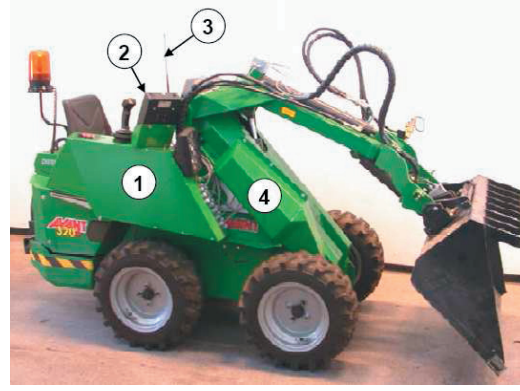

Figure 3 The most important components of the studied machine. (1) I/O modules, (2) display module, (3) radio modem, (4) proportional mobile valves.

The electronics of the machine consists of a display module, I/O modules, a radio modem, an electric gas, controls, and sensors. All electronic components are robust and selected for mobile use.

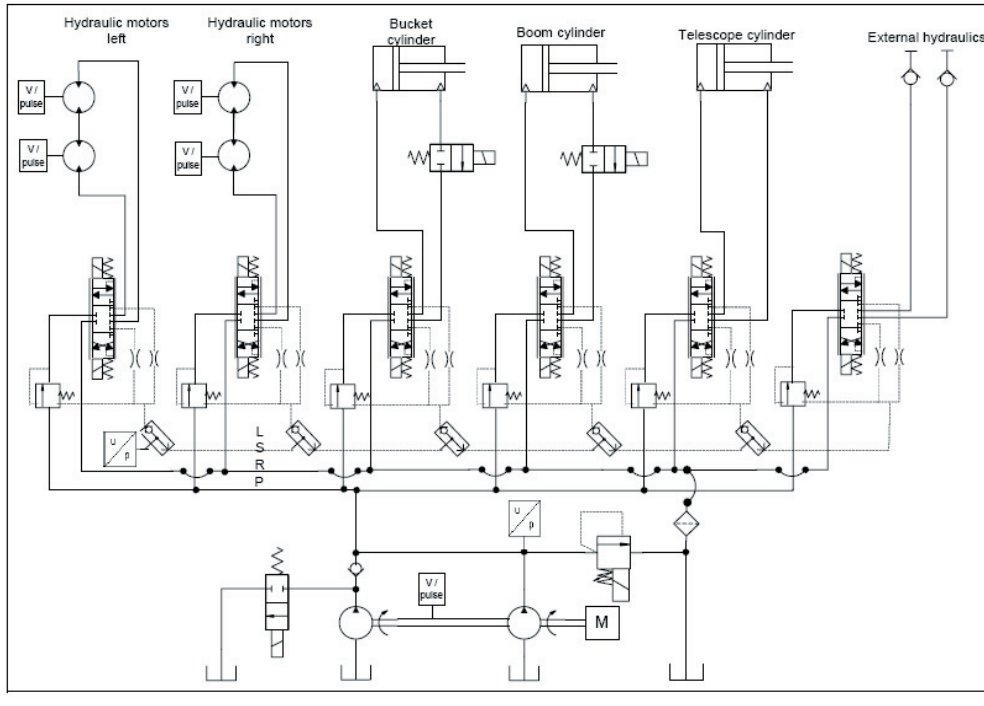

Figure 4 Hydraulic diagram of the studied machine.

The display module DM586 is the master module of the system. It carries out all high level control tasks of the system. The display module is also a user interface for the operator

while the machine is operated manually. Multipurpose I/O modules control the valves and the electric gas. As input, the modules read values from the sensors. The display module and I/O modules communicate via CAN bus. /3, 4/

The wireless link between the machine and the operator is carried out with commercial radio modems. Radio modems are cost-effective, robust (temperature range, supply voltage etc.), and free to use (license free frequency band). Delays of the data transmission are also predictable and with intelligent software possible data losses can be compensated. Two different types of radio modems are used. Serial transmission (RS-232/RS-422) is used in both cases. In the machine the radio modem is connected to the serial port of the display module.

Simplified block diagram of the connections between the modules, sensors, valves, and control devices in the machine is shown in Figure 5. Direction of the arrows in figure 5 describes the direction of the signals. Lines without arrows are busses. Power feed lines have not been drawn.

At the moment the two machines can be directly teleoperated over the internet. Additionally to the real machines there is a fully dynamic model of the loader having the same control electronics (HIL) as the real machines. The model can be teleoperated as the real ones and it can also be augmented into the worksite by rendering it to the video image (Figure 6). The worksite is also modelled in 3D with 3D-laser scanner and the model can be used as virtual worksite for the vehicle model and also for the real ones. In the latter case the real machines are located with the aid of the worksite cameras and added into the model.

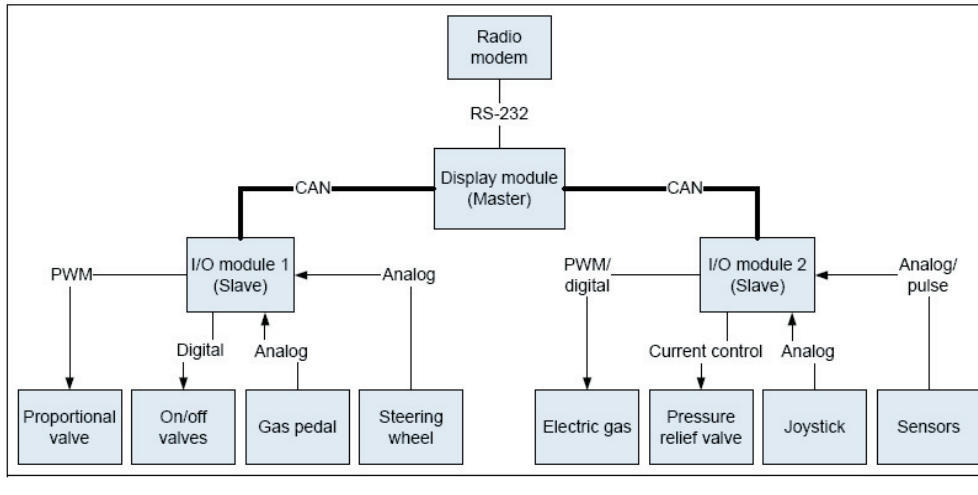

Figure 5 Block diagram of the electronics in the machine.

Figure 6 Two real machines and one simulated in the worksite. A snapshot from operation screen.

With computer control, we can add some extra features to the machine, an important one developed to improve controllability being the automatic virtual gear box based on the ELS-system. The machine is difficult to control with a constant pressure system, because the supply pressure is high when the control valve starts to open. In skid-steered machines, in which the power transmission control valves open and close frequently, a constant pressure system does not work well. With the control valves closed, the diesel's power is greatly limited, because if the supply pressure level is set as high as possible, the diesel engine chokes. Contrariwise, if the pressure level is set so that the diesel works well, the pressure is too low for the actuators. This means that though one purpose of the ELS is to improve the efficiency of the hydraulic system, the focus of the study was to improve the overall control of the machine. The system was based on an electrically controlled pressure relief valve, regulated by the control and display module. When the highest load pressure was measured at the proportional valve block, the necessary supply pressure was known.

It is challenging to use this ELS in a hydraulic system with a constant displacement hydraulic pump. The pump's output flow was regulated by changing the rotational speed of the diesel. The output speed of the diesel engine was controlled with an electric gas pedal with the controller located in the control and display module, which housed also the program of the automatic virtual gear box.

The automatic virtual gear box consisted of three gears, neutral, reverse, and drive. In drive or reverse, the machine crawls forward or backward. With more gas, the machine control becomes smoother, because the valve's death zone is not in effect anymore. The joystick has two buttons for the gear box to shift gear up and down. The operator can see on the display module the engaged gear and the supply and load pressures.

A simulator is embedded as a part of the system. The simulator is a hardware-in-the loop (HIL) simulator, which uses the same control electronics as the real machine, but the mechanics, hydraulics and the environment are simulated. The simulator provides valuable

information in the testing and development phase. The system communication is based on TCP/IP. Basically the only communication links in the system that do not use the Internet are the radio modem channel between the local network and the work machines and the on board communication, which uses CAN.

The basic architecture of the mobile machine simulator is presented in Figure 7. Computers used for the calculation of the simulation model and visualization were standard personal computers equipped with fast AMD Athlon 64 processors. The simulation model was made in the Matlab/Simulink environment and compiled to the embedded xPC target kernel. The visualization of the mobile machine was made with OpenGL–based software. The visualization model was created from the laser scan of the mobile test hall at TTY (see Figure 7). Controls were the same as for the real mobile machine.

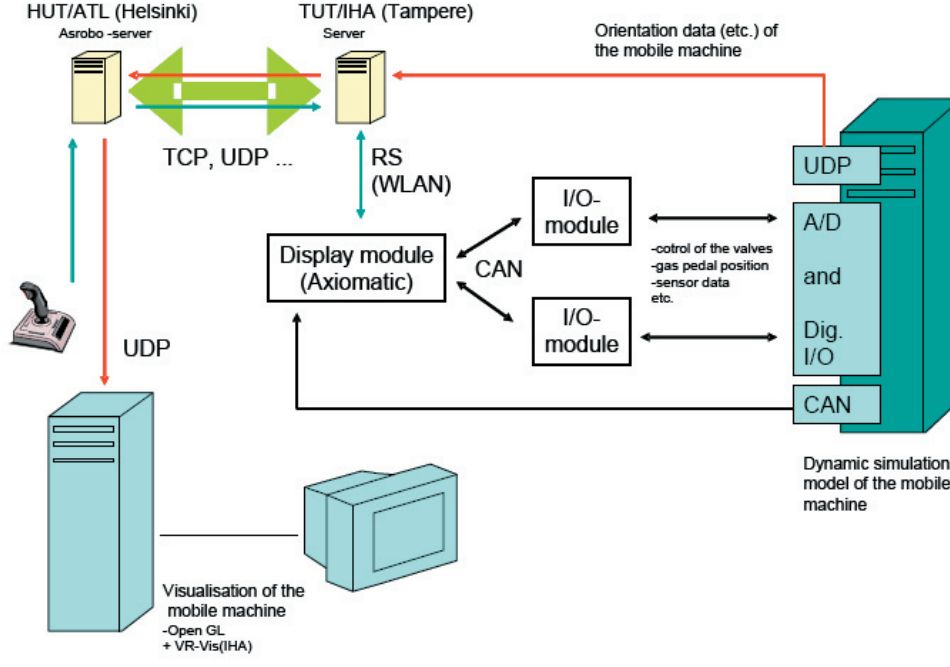

Figure 7 Teleoperated real-time mobile machine simulator with hardware-in-the-loop.

The hardware connected to the simulator consists of the same hardware setup as the real mobile, except that the radio modem was replaced by direct RS232 cable and the PWMvalve control signal was filtered by passive low pass filter. The control software was exactly the same as in the real machine. Other hardware include a display module (Axiomatic) and I/O valve control modules. The I/O interface between the simulation model and the HIL consists of several AD, DA and Digital I/O connections and a CAN bus card. An Ethernet card was used to transfer the simulated data to the visualization computer.

The simulation model is a simplification of the accurate offline simulation model of the same mobile machine presented in /8/. For real-time purposes semiempirical component models are used instead of analytical models. Dynamic friction models are also replaced with simplified friction models.

5. RESEARCH RESULTS

5.1. Study of Advanced Velocity Control (AVC) via simulations in direct drive /7, 15/

The mobile machine was equipped with robust velocity sensors of the hall type with a measurement frequency of 20 pulses per revolution. This type is unsuitable for closed-loop velocity control with a proportional mobile valve, because its sampling rate is too low, and because the valve, too, sets limits to closed-loop control. If the sampling rate were to be increased with a better sensor with a proportional mobile valve, the system would become unstable because of the valve characteristics discussed earlier in this study.

This simulation sought to study advanced velocity control (AVC), based on standard mobile hydraulic components and sensors. The output angular speeds of the left and right tires were measured, and the left and right side were controlled by their own valves. Angular speed was controlled with a PI-controller, which was activated when the valve control signal registered +/- 3% more than the valve's dead zone. This limiting value ensured that the machine moved forward or backward instead of vibrating. The simulation was conducted with a progressive spool with a +/- 15% dead zone.

The simulation was run with step input response, a progressive spool, an LS-system, and with a constant diesel rotation of 3500 rpm. Figure 8 shows the results compared to those of a progressive spool without advanced velocity control. Because engine size limited the diesel's effective control area, advanced velocity control was tested at full engine rotation. With advanced velocity control, simulation shows slight vibration in acceleration, but the velocity curve is much better with hardly any overshooting.

The simulation result shows that velocity curve is acting much better and smoothly with AVC-control. More about measurement and simulation system is presented in reference /7/. Figure 9 compares simulation results of advanced velocity control of a machine with a progressive spool without and with an LS-system. The vibration in acceleration has now disappeared, and the velocity curve shows no overshooting.

The results show that advanced velocity control is useful in autonomous mobile machine applications. Because vibration and overshooting can be avoided in the angular speed curve, the machine responds accurately to control.

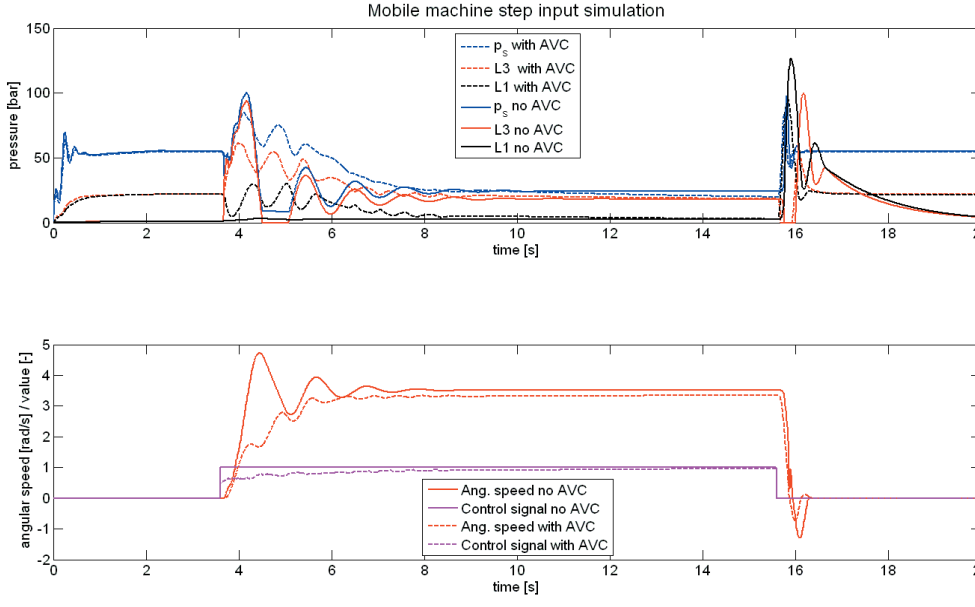

Figure 8 Simulation with LS-system and advanced velocity control and without AVC /15/.

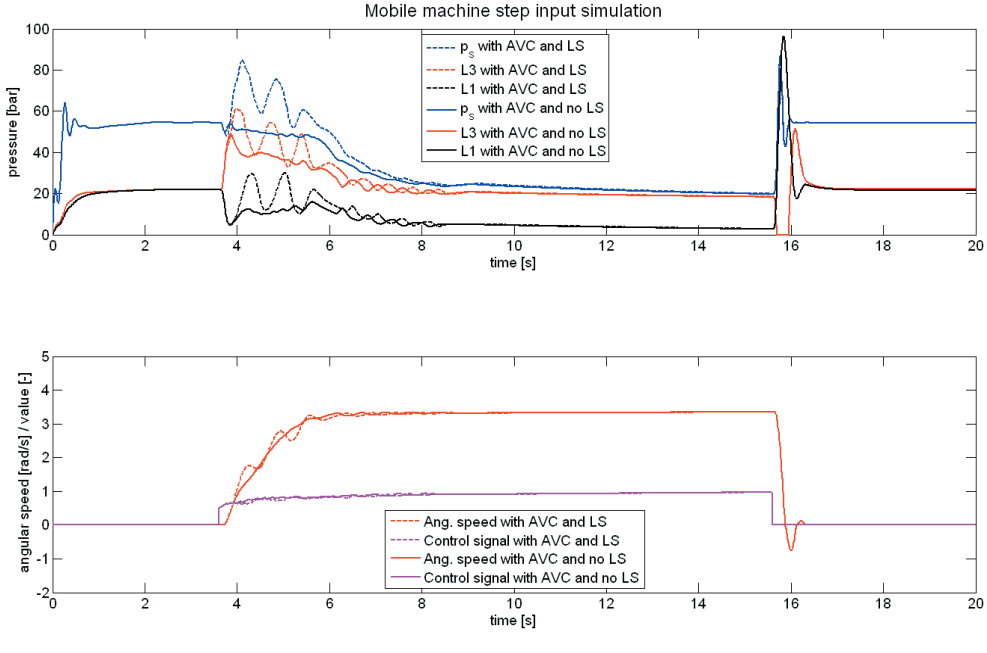

Figure 9 Simulations of advanced velocity control with an LS-system without it /15/.

5.2. Autonomous functions of hydraulic excavator /16/

Autonomous work cycles require advanced control algorithms. The control system typically consists of several layers. Low-level motion controllers may be similar to normal operation. On the next layer autonomously travelling machines usually have a navigation controller that does short range path planning, mainly obstacle avoidance. The top level of control is mission or path planning that is normally coordinated by the operator. /9/ In an autonomous excavator a similar approach is applicable. The motion controllers can be simple position controllers. Depending on the following layer, trajectory tracking properties may be required. Resolved-mode control in mobile machines has been researched in some projects /10, 11/. It makes the user interface more intuitive for the operator and helps when straight bucket trajectories are needed. Resolved-mode control is, however, not necessarily required for autonomous operation, at least not at motion control layer. The target trajectories may be continuous but in many cases a phased position control through a couple of points could be adequate. The work of professional excavator operators could be observed to generate efficient and economical bucket trajectories /12/.

If the trajectory points are given in values of joint angles or by manually producing the desired trajectory at first, the control algorithms can be kept rather simple. For more advanced user interfaces with Cartesian coordinates, at least inverse kinematics of the excavator has to be calculated.

The most demanding part in autonomous excavation is probably the interface between the bucket and soil when the bucket is filled. Different soil types, rocks, and varying temperatures affect substantially the behaviour of the excavator. A general solution may be difficult to find. One option is to monitor the velocity of the bucket as it approaches the soil. If the velocity drops enough before the target position is reached, the bucket can be filled, emptied, and the cycle can be repeated. Learning or fuzzy control might improve the efficiency of the bucket filling algorithm and make it suitable for more soil types and conditions.

A hydraulic excavator attachment is used as an example. The excavator is a commercial product that has been slightly modified. An electronic control unit for the excavator has been designed and built. /13/ The attachment is installed to a skid steered mobile machine that has been developed at the Institute of Hydraulics and Automation /14/.

The performance of the controller was tested with a couple of different cases. Figure 10 (above) shows the angle error signal as the excavator is moved to a target position of -45°. The boom, stick, and bucket are oriented so that the centre of mass is as far as possible, making the control of the excavator demanding. To test longer movements, the target value was set to 0°. The angle error is shown in Figure 10 (below). The excavator was moved from extreme positions, about ±70°, to the centre position.

As it can be seen from Figure 10, the steady-state error is about 1°. This results in a position error of about 5 cm when the excavator is fully extended. This is probably sufficient for most applications taking into account the diverse behaviour of soil. Moreover, the repeatability of the steady-state error is very good: about 0.5° when the excavator is moved between two targets. This is the most typical case in excavation. The proportional gains of the position controller were set rather low to limit the acceleration of the excavator. This

prevents the machine from jerking and therefore decreases the absolute position error of the bucket. The settling times are not very constant, probably because of the low-cost valve actuation unit. In addition, the construction of the excavator makes the position controller slightly asymmetric. The valve seems, however, quite suitable to autonomous excavation.

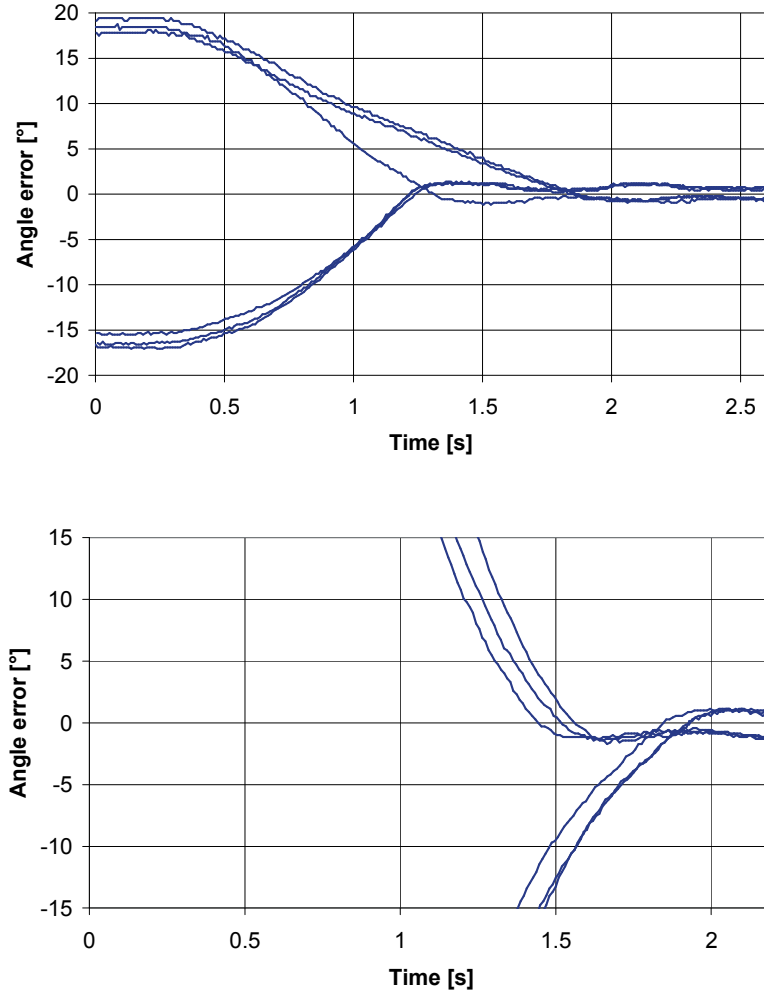

Figure 10 Angle errors when target value is -45° (above) and when moving from extreme postions to centre (below) /16/.

6. CONCLUSIONS

GIM is a Finnish research centre focusing to the mobile, field and service robotics. Research covers all subsystems of a mobile robot from locomotion to task learning and human robot interaction. All research results will be demonstrated and integrated into a

multi machine test system, which will gradually develop towards Future Worksite concept. Future Worksite includes a physical worksite with autonomous and semiautonomous machines, which are controlled from a remote control station. Operator and worksite are connected with a virtual worksite, where the work tasks are planned and the progress of the work can be followed.

At the moment the basic infrastructure including the robotic machines and worksite is ready. The user interface and communication architecture is partly done but they will be updated during th research work. Results show that the communication architecture and low level control of the work machines are performing well forming a good basis for future development.

7. REFERENCES

/1/ http://www.miningandconstruction.sandvik.com/

/2/ Suomela J., Saarinen J., Halme A, Vilenius M., Huhtala K. , GIM, Towards the future worksite, Proceedings of the 26th IFAC Symposium on Intelligent Autonomous Vehicles, IAV 2007, Toulouse, France, 3-5 September 2007.

/3/ Display module DM586, Technical Datasheet. Tampere, Finland 2003, Axiomatic Technologies Inc.

/4/ Multipurpose I/O module MVMIO24, User Manual. Tampere, Finland 2002, Axiomatic Technologies Inc.

/5/ Saarinen, J., Hyvönen, M., Suomela, J., Vilenius, J., Halme, A. & Huhtala, K. 2007. Development of multi-machine remote control platform. In: Vilenius, J. & Koskinen, K.T. (eds.) The Tenth Scandinavian International Conference on Fluid Power, May 21-23, 2007, Tampere, Finland, SICFP'07 2 Tampere. Tampere University of Technology. pp. 9-23.

/6/ Uusisalo, J., Vilenius, J., Vuohijoki, A., Hirvonen, S-M., Karhu, O. & Huhtala, K. 2007. Portable remote control for teleoperated hydraulic mobile machine. In: Vilenius, J. & Koskinen, K.T. (eds.) The Tenth Scandinavian International Conference on Fluid Power, May 21-23, 2007, Tampere, Finland, SICFP'07 3 Tampere. Tampere University of Technology. pp. 35-45.

/7/ Vilenius J., Characteristics of Valve Controlled Hydraulic Power Transmission in Teleoperated Skid Steered Mobile Machine, Dissertation NO 654, Tampere, Finland, 2007.

/8/ Hyvönen M., Vilenius J., Vuohijoki A., Huhtala K., Mathematical model of the valve controlled skid steered mobile machine, 2nd International Conference on Computational Methods in Fluid Power, FPNI'06.

[9] Durrant-Whyte, H. Autonomous land vehicles. Proceedings of IMechE. Part I: Journal of systems and control engineering 219(2005)1, pp. 77-98.

/10/ Münzer, M. & Pedersen, P. Tool centre control of mobile hydraulic manipulators. Proceedings of FPNI-PhD, Modena, Italy, July 3-5, 2002.

/11/ Sepehri, N., Lawrence, P., Sassani, F. & Frenette, R. Resolved-mode teleoperated control of heavy-duty hydraulic machines. Journal of dynamic systems, measurement, and control 116(1994)2, pp. 232-240.

/12/ Hall, A. & McAree, P. A study of the interaction between operator style and machine capability for a hydraulic mining excavator. Proceedings of IMechE. Part C: Journal of mechanical engineering science 219(2005)5, pp. 477-489.

/13/ Karhu, O., Vilenius, J., Uusisalo, J. & Huhtala, K. Developing intelligent hydraulic excavator. Proceedings of PTMC, Bath, UK, September 13-15, 2006. pp. 265-274.

/14/ Raneda, A., Vilenius, J. & Huhtala, K. Development of a teleoperated hydraulic mobile machine. Proceedings of SICFP, Tampere, Finland, May 7-9, 2003. pp. 449-459.

/15/ Vilenius J., Huhtala K., Simulation Model of Hydraulic Power Transmission of Teleoperated Mobile Machine and Development and Research Work of Advanced Velocity Control via Simulations. The 6th International Fluid Power Conference Dresden, 2008.

/16/ Karhu, O., Moya, J., Uusisalo, J. & Huhtala, K. 2007. Enabling autonomous functions on hydraulic excavator attachment. In: Vilenius, J. & Koskinen, K.T. (eds.) The Tenth Scandinavian International Conference on Fluid Power,May 21-23, 2007, Tampere, Finland, SICFP'07 2 Tampere. Tampere University of Technology. pp. 35-45.

Efficiency Study of an Excavator Hydraulic System Based on Displacement-Controlled Actuators

Christopher Williamson, Joshua Zimmerman, Monika Ivantysynova

Purdue University, Department of Agricultural and Biological Engineering, West Lafayette, Indiana, USA

ABSTRACT

One proposed solution for improving the energy efficiency of mobile hydraulic machinery is displacement controlled actuation, in which cylinders and motors are controlled hydrostatically via variable displacement pumps. This paper compares pump displacement control to traditional load-sensing valve control for a mini-excavator application. Detailed dynamic models of the excavator with both hydraulic systems were constructed, and a trench digging cycle was simulated. The displacement controlled excavator consumed 39% less total energy than the LS excavator for the simulated operation. In this study, the efficiency improvement was almost entirely due to the elimination of valve metering losses rather than energy recovery.

1. INTRODUCTION

Fluid power systems are used in many industrial and mobile applications where high power density and dynamic performance are required. Compared to mechanical and electrical transmissions, the flexibility and relatively small size and weight of fluid power components makes hydraulic systems an attractive choice for mobile applications. It is for these reasons that fluid power is ubiquitous for power transmission in mobile construction, agriculture, and mining applications. However, the energy efficiency of fluid power systems is relatively low. Efficiency was a secondary consideration in the past, but the high cost of petroleum in recent years has motivated research and development of more energy efficient hydraulic components and systems (1-2)

1.1 Displacement-Controlled Actuation

A large fraction of the power wasted in mobile hydraulic systems can be attributed to metering fluid flow through directional control valves (3). One method to reduce these losses is displacement-controlled (DC) actuation, in which a variable displacement pump

Fluid Power and Motion Control 2008 Edited by Dr D N Johnston and Professor A R Plummer

controls the motion of a single or double-rod cylinder. This "valveless" or "pump controlled" concept improves energy efficiency by eliminating metering losses and recovering power when the pump operates in motoring mode (4-5). DC is also attractive from the point of view of system control. Valve-controlled actuators typically have highly coupled, nonlinear system dynamics. Displacement control decouples the actuators and gives a more linear input/output relationship (6). Figure 1 depicts a basic closed circuit displacement control scheme which is the basis for the authors' current work. Other configurations may also be used for DC actuation (7).

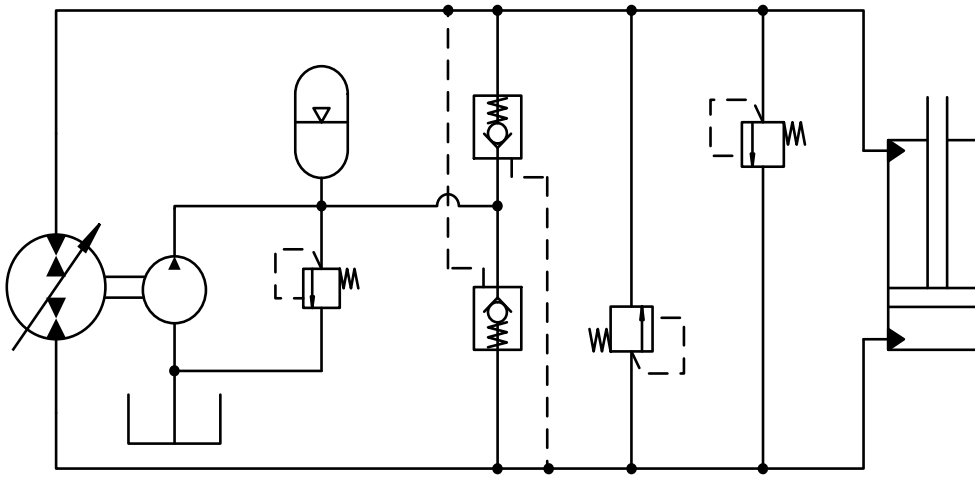

Figure 1 Closed circuit displacement controlled actuation

1.2 Current Research

In previous research, the authors have developed displacement-controlled systems for wheel loader and skid-steer loaders with measured fuel savings in the range of 10% to 20%. The work described in this paper is part of a project to develop energy saving systems and controls for excavators and other multi-actuator machines. Modeling and simulation of a compact excavator with a load-sensing (LS) hydraulic system was published previously (3). The current work considers the same mini-excavator with displacement-controlled actuators. Modeling of system dynamics and energy dissipation is discussed along with the actuator control algorithm. The primary goal of this paper is to compare excavator energy efficiency during simulated operation with LS and DC hydraulic circuits. After the prototype excavator is retrofitted with new DC components, this comparison will be repeated experimentally and the results will be presented in a future publication.

2. MACHINE DESCRIPTION

Compact excavators are multi-purpose machines frequently used for earth-moving as well as other tasks with auxiliary attachments. The excavator workgroup is an open kinematic linkage consisting of three main links known as the boom, stick, and bucket. These links are connected in a plane by revolute joints and are controlled by hydraulic cylinders. The

cabin and workgroup are rotated about the undercarriage by a hydraulic motor. The excavator uses tracks for propulsion which are driven by hydraulic motors. A Bobcat 435 compact excavator has been selected as a representative example. Gross vehicle weight is approximately five tons with a standard rated bucket capacity of 0.14 m^3 (0.18 cu. yards).

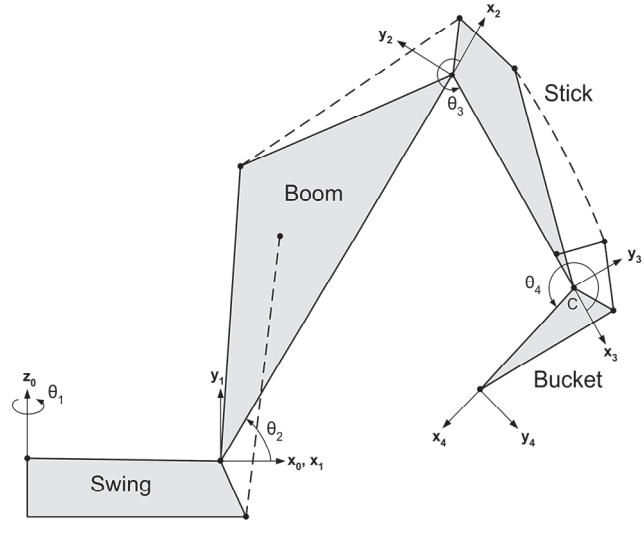

Figure 2 Excavator kinematic diagram

The standard Bobcat excavator is equipped with LS hydraulics for the operating functions and dual hydrostatic transmissions to drive the tracks. This machine was selected for study because it adequately represents the features of larger excavators while being sufficiently compact for use in a laboratory environment. The hydraulic circuit has been modified for displacement control. A simplified schematic is shown in Figure 3. The compact excavator has eight independent functions which do not all operate simultaneously. To reduce the number of pumps required, switching valves allow a single pump to control two actuators, one at a time. A single charge pump and low pressure accumulator are connected to all of the actuator circuits.

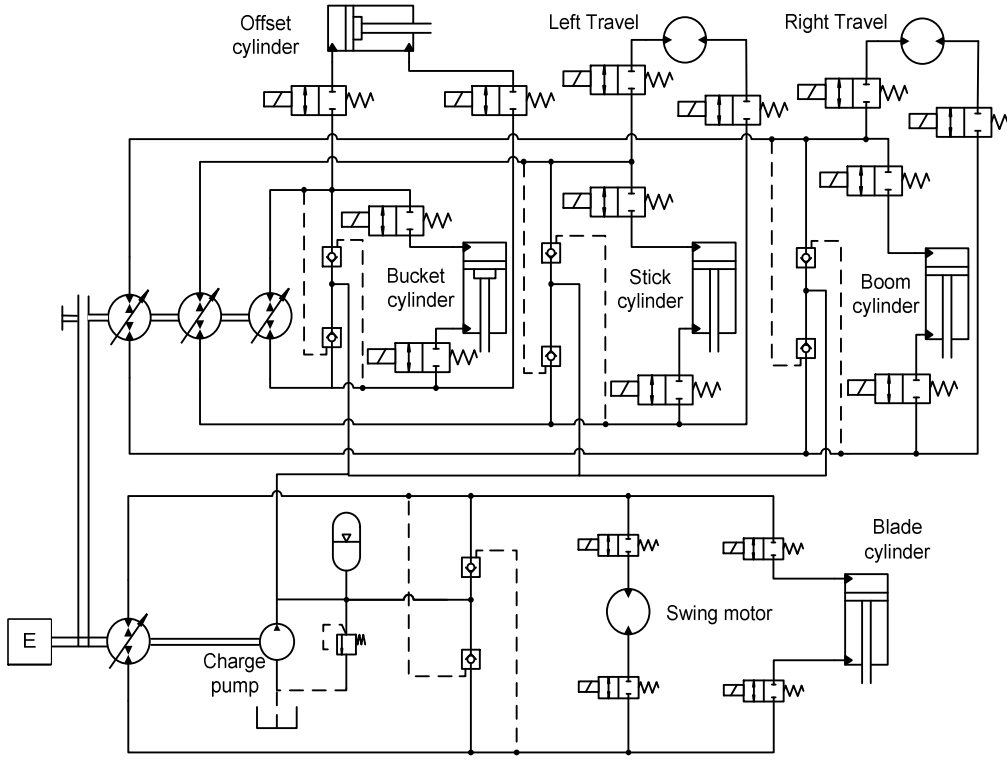

Figure 3 DC excavator hydraulic circuit

3. MATHEMATICAL MODEL

A complete model of dynamic and steady-state characteristics is needed to accurately calculate energy distribution through the machine. Such a model was developed previously for the excavator under study with load-sensing hydraulics (3). A new model with DC hydraulics has been created, as will be described in this section.

3.1. Multi-body Mechanics

The excavator's mechanical structure was simulated with the Matlab/SimMechanics toolbox. The mechanical model is fully coupled to the hydraulic model in Simulink. Mass and inertial properties of the excavator bodies were obtained from CAD models supplied by the manufacturer. Rigidity is assumed, and friction at the revolute joints is neglected (or more precisely, lumped with the actuator friction). To visualize the machine motion, CAD parts were converted into virtual reality markup language (VRML) and assembled into a 3D animated model. More information about the mechanical model may be found in (3).

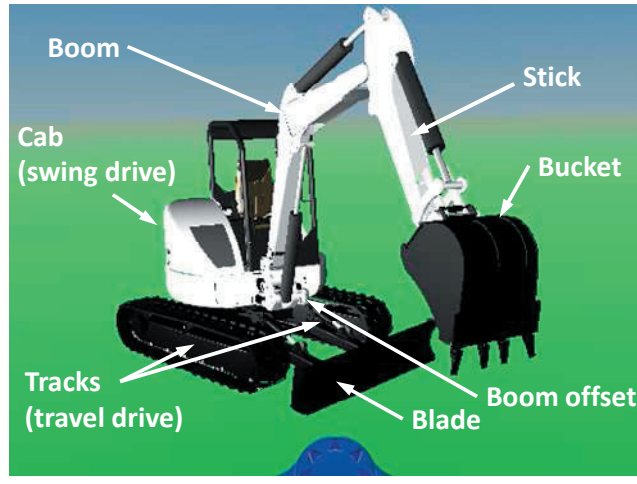

Figure 4 Mechanical model animation with labeled functions

3.2. Linear Actuator

Figure 5 depicts a single-rod cylinder with flow and velocity variables defined to be positive when the cylinder is extending. The pressure build-up equations are expressed as:

$$\dot{p}_A = \frac{1}{C_{H_A}}\left[Q_A - A_A\dot{x} - Q_{Li}\right] \tag{1}$$

$$\dot{p}_B = \frac{1}{C_{H_B}}\left[-Q_B + A_B\dot{x} + Q_{Li}\right] \tag{2}$$

The hydraulic capacitance associated with each cylinder volume is a function of the piston position, line volume and fluid bulk modulus, as shown in Eq. 3-5. Internal leakage Q_{Li} across the piston seal is assumed to depend only on pressure, and external leakage is neglected.

$$C_{HA} = \frac{V_A}{K_{oil}} \quad \text{and} \quad C_{HB} = \frac{V_B}{K_{oil}} \tag{3}$$

$$V_A = V_{\text{line}} + A_A x \tag{4}$$

$$V_B = V_{\text{line}} + A_B\left(h - x\right) \tag{5}$$

$$Q_{Li} = k_{Li}\left(p_A - p_B\right) \tag{6}$$

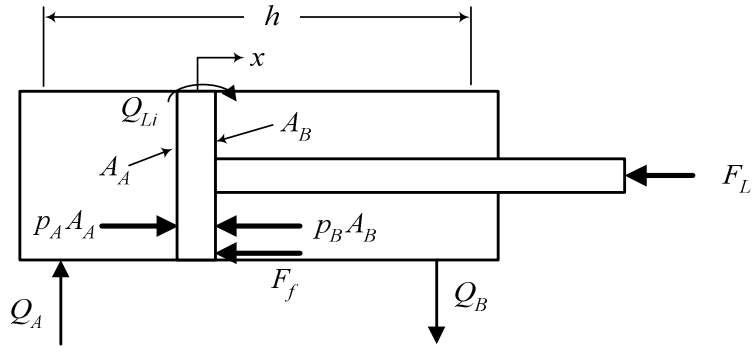

Figure 5 Single-rod linear actuator

Summing forces on the cylinder piston and rod gives Eq. 7. Here F_p represents the pressure force, F_f is the force due to viscous and Coulomb friction, and F_L is the external load force including forces due to gravity and soil mechanics.

$$F_p - F_f - F_L = m_{eq}\ddot{x} \tag{7}$$

$$F_p = A_A p_A - A_B p_B \tag{8}$$

$$F_f = f_v \dot{x} + f_C \cdot \text{sign}(\dot{x}) \tag{9}$$

The friction coefficients used in simulation were identified experimentally by measuring the pressure and position of each workgroup joint while moving with no load on the excavator bucket. Cylinder position, velocity and acceleration were calculated from the measured joint positions and filtered to reduce noise. With this kinematic data, the SimMechanics model previously described was used to calculate the forces on the actuator due to gravity and inertia. The friction force could then be found by rearranging Eq. 7 to form Eq. 10.

$$F_f = F_p - \left(F_L + m_{eq}\ddot{x}\right) \tag{10}$$

The coefficients f_v and f_C in Eq. 9 were estimated with robust linear regression (Matlab's *robustfit* routine), using an iteratively reweighted least squares algorithm. Coefficient values are listed in Table 1 along with the standard deviation s of the regressed friction model.

Table 1 Friction coefficients

Function	f_v (Ns/m)	f_C (N)	s (N)
Swing	1.72	87.5	145
Boom	2.25E3	1.26E4	1.53E3
Stick	1.93E4	1.45E3	2.40E3
Bucket	2.88E4	0	1.40E3

3.3. Rotary Actuator

A fixed displacement radial piston motor (Figure 6) rotates the excavator cabin through a circular rack and pinion gear. The mathematical model for the hydraulic motor is quite similar to that derived for the linear actuators.

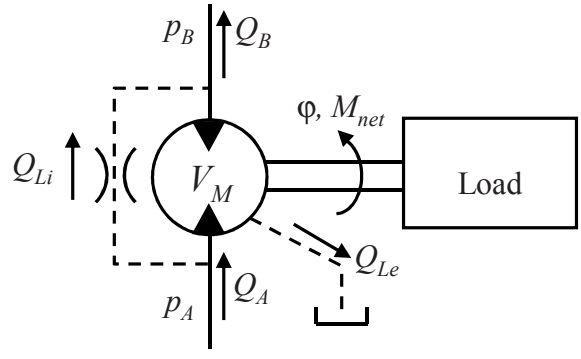

Figure 6 Rotary actuator (swing motor)

$$\dot{p}_A = \frac{1}{C_{HA}} \cdot \left(Q_A - Q_{Li} - Q_{LeA} - \frac{V_M}{2\pi} \cdot \dot{\varphi} \right) \tag{11}$$

$$\dot{p}_B = \frac{1}{C_{HB}} \cdot \left(-Q_B + Q_{Li} - Q_{LeB} + \frac{V_M}{2\pi} \cdot \dot{\varphi} \right) \tag{12}$$

The internal leakage is still as shown in Eq. 6. The external leakage cannot be neglected as it was for the cylinders. Assuming zero case pressure:

$$Q_{Le} = \overbrace{k_{Le} \cdot p_A}^{Q_{LeA}} + \overbrace{k_{Le} \cdot p_B}^{Q_{LeB}} \tag{13}$$

The hydraulic capacitances are also calculated using Eq. 3, with corresponding volumes for the motor from Eq. 14. The net torque exerted by the swing motor is coupled to the multi-body mechanical system as in Eq. 15:

$$V_A = V_B = V_M + V_{\text{line}} \tag{14}$$

$$M_{net} = (p_A - p_B) \cdot \frac{V_M}{2\pi} - f_v \dot{\varphi} - f_C \text{sign}(\dot{\varphi}) \tag{15}$$

Friction coefficients were identified experimentally as described in section 3.2.

3.4. Variable Displacement Pump

Each actuator is independently powered and controlled by a variable displacement axial piston pump. An accurate model of pump efficiency characteristics is essential for calculating realistic energy simulations. Due to the complex behavior of mixed friction and volumetric losses, an empirical model based on measured data is required. Steady-state torque and volumetric losses were measured on a laboratory test rig according to ISO 4409. The simulation model consists of a least-squares polynomial interpolation of pump losses as a function of displacement, speed and pressure (8). The polynomial surface and measured data points for a single speed are shown in Figure 7.

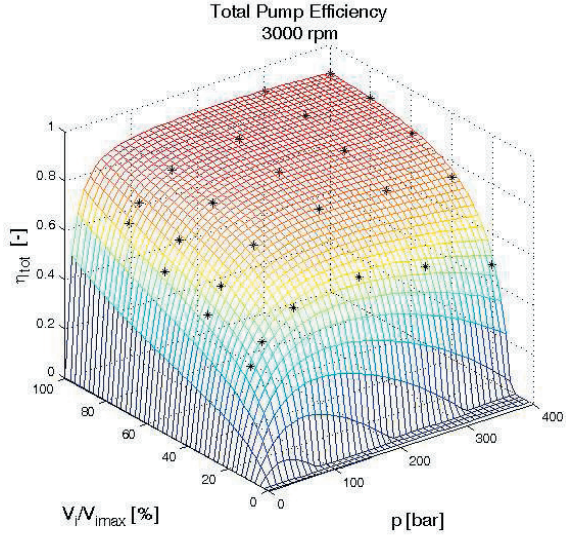

Figure 7 Pump power efficiency map

One difficulty presented by this approach is that it requires measurements of an existing pump, not a future design. The DC hydraulic system being modeled and simulated will use 18 cc/rev axial piston pumps which have not yet been obtained from the supplier. In lieu of this discrepancy, a loss model for a similar axial piston pump was simulated instead. Simulations of the LS and DC excavators both included the same pump efficiency model to allow a fair comparison of the hydraulic system configurations rather than the characteristics of two different pumps. Differences in displacement volume between the measured and simulated pumps were accounted for with linear scaling laws.

Although the primary goal of the pump model was to describe power efficiency, dynamic characteristics were also considered. Dynamic equations were included for the displacement control valve, control piston pressure and swash plate motion. The interested reader is referred to (6) for more information about the pump dynamic model.

3.5. Charge Pump

A 14 cc/rev constant displacement gear pump serves several purposes in the hydraulic circuit. It powers a variable speed engine fan motor, provides pressure and flow to the pump control valves, replenishes the volumetric losses of the other pumps and motors and compensates for the differential flow rate through the single-rod actuators. Nominal charge pump pressure is 45 bar. The fan motor pressure varies with engine temperature; a constant 30 bar drop is assumed. The pump control pressure is maintained at 30 bar minimum with a pressure reducing valve. The charge line relief valve is set to 15 bar. Efficiency curves for the charge pump were obtained from the manufacturer's specifications. Constant operating speed at 2500 rpm is assumed.

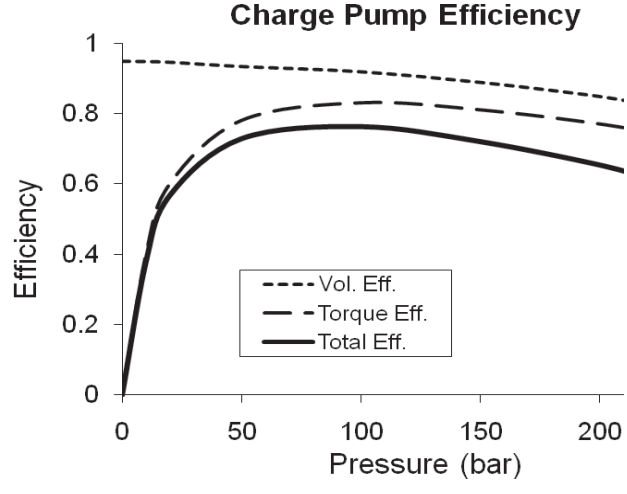

Figure 8 Charge pump efficiency curves

3.6. Other Hydraulic Components

Other components in the hydraulic circuit also add power losses. Pilot-operated check valves, low pressure piston accumulator, relief valves, hoses and fluid connectors were all modeled using standard equations for dynamic and steady-state behavior. Power losses due to these components are relatively small during normal operation, but are nonetheless important to consider. For details, the reader is referred to references (3) and (9).

4. EXCAVATOR CONTROL

Electrohydraulic feedback control of the pump displacement is required for DC actuation. The actuators' position and velocity may be controlled in either open or closed loop configurations. Simulating a defined operating cycle requires closed-loop control of the actuator motion. The control algorithm is presented in block diagram form in Figure 9. The basic design consists of two cascaded feedback loops, with the pump displacement controlled in the inner loop and the actuator motion controlled in the outer loop. The inner loop is simple proportional control, with a more sophisticated control law in the outer loop for reference tracking and disturbance rejection. This approach has been successfully proven in previous work with DC actuation (5,10).

There are many works in the literature regarding control of hydraulic manipulators A few relevant examples are listed in (11-14). In this study, the manipulator control law is based on feedforward input/output linearization combined with feedback of measured joint position, velocity and acceleration.

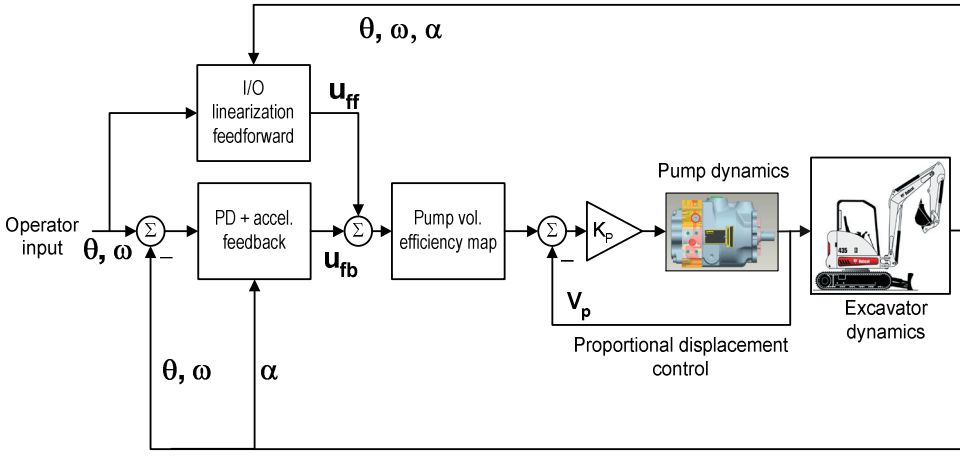

Figure 9 Excavator control scheme

Robotic manipulators are usually modeled with Lagrange-Euler dynamics, as in Eq. 16. In this equation, the terms in parenthesis represent joint torques due to actuator force $\boldsymbol{\tau}$, coriolis and centripetal acceleration $\boldsymbol{C}$, friction $\boldsymbol{F}$ and gravity $\boldsymbol{G}$, respectively. Actuator pressure

dynamics are captured by Eq. 17, where the input u represents the effective pump flow rate to the actuator. As written in vector-matrix form, these two state equations compactly describe the dynamics of all four joints in the excavator workgroup (swing, boom, stick and bucket). The linear force due to actuator pressure is related to the torque about the corresponding revolute joint by a Jacobian matrix, as in Eq. 18.

$$\ddot{\boldsymbol{\theta}} = \mathbf{M}^{-1}\left(\boldsymbol{\tau} - \boldsymbol{C} - \boldsymbol{F} - \boldsymbol{G}\right) \tag{16}$$

$$\dot{\boldsymbol{p}} = \mathbf{C}_{\mathbf{H}}{}^{-1}\left(\boldsymbol{u} - \mathbf{A}\frac{\partial \mathbf{x}}{\partial \boldsymbol{\theta}}\dot{\boldsymbol{\theta}} - \mathbf{K}_{\mathbf{L}}\boldsymbol{p}\right) \tag{17}$$

$$\boldsymbol{\tau} = \mathbf{A}\frac{\partial \boldsymbol{x}}{\partial \boldsymbol{\theta}}\boldsymbol{p} \tag{18}$$

The feedforward input u_{ff} commands a flow rate corresponding to the desired velocity and linearizes the relationship between Q and θ by canceling the nonlinearities in Eq. 16 and 17. Since the terms in Eq. 13 are unmatched, integrator backstepping requires inputting their derivatives. The feedback input u_{fb} compensates for disturbances and modeling error. Joint velocity is estimated from measured position. Acceleration feedback eliminates undesirable oscillation by increasing the damping of the closed-loop actuator system. Alternatively, pressure feedback or pole-zero cancellation (2nd order filter) could be similarly used to increase the actuator damping.

$$\begin{aligned} \boldsymbol{u} &= \boldsymbol{u}_{ff} + \boldsymbol{u}_{fb} \\ \boldsymbol{u}_{ff} &= \mathbf{A}\frac{\partial \boldsymbol{x}}{\partial \boldsymbol{\theta}}\dot{\boldsymbol{\theta}}_d + \mathbf{K}_L\boldsymbol{p} + \boldsymbol{C}_H\frac{\partial \boldsymbol{\theta}}{\partial \boldsymbol{x}}\boldsymbol{A}^{-1}\left(\dot{\mathbf{V}} + \dot{\mathbf{F}} + \dot{\mathbf{G}}\right) \\ \boldsymbol{u}_{fb} &= \frac{\partial \boldsymbol{\theta}}{\partial \boldsymbol{x}}\left(\mathbf{K}_s\left(\boldsymbol{\theta} - \boldsymbol{\theta}_d\right) + \mathbf{K}_v\left(\dot{\boldsymbol{\theta}} - \dot{\boldsymbol{\theta}}_d\right) + \mathbf{K}_a\ddot{\boldsymbol{\theta}}\right) \end{aligned} \tag{19}$$

Both the LS and DC excavators were simulated with the same joint position controller (Eq. 19, the outer feedback loop). The inner flow control loop is realized differently, with post-compensated valves for load independent flow distribution in the LS system and pump displacement control for the DC system.

5. SIMULATION

5.1. Duty Cycle

The simulated working cycle was based on measurements of the LS excavator in actual operation. The cycle consisted of one minute of trench digging in loose soil while measuring pump pressure, cylinder pressure and joint position. Cylinder positions during

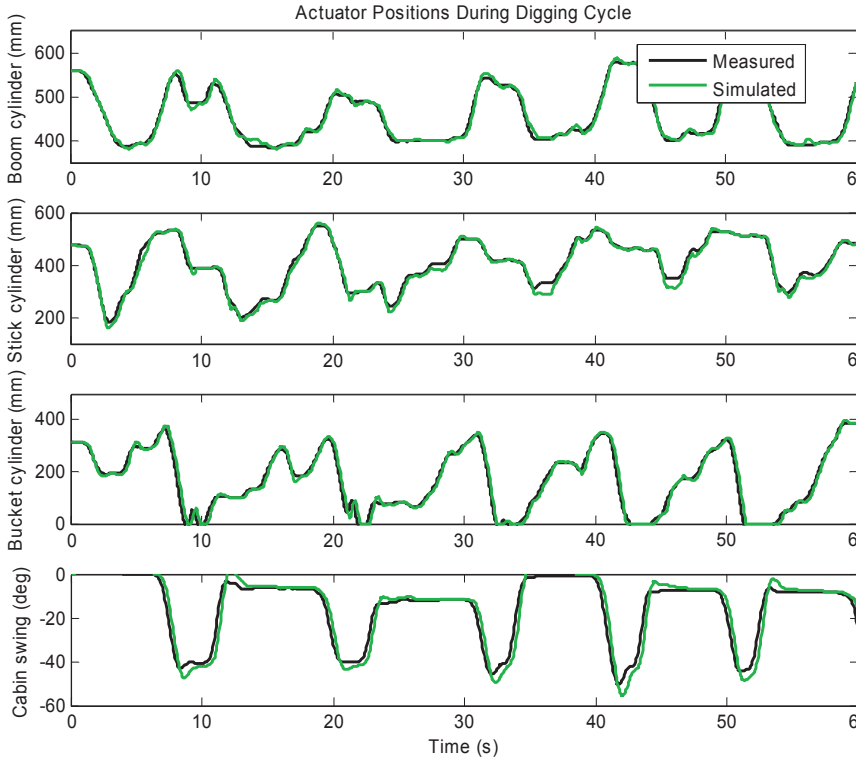

Figure 10 Measured and simulated LS excavator operation

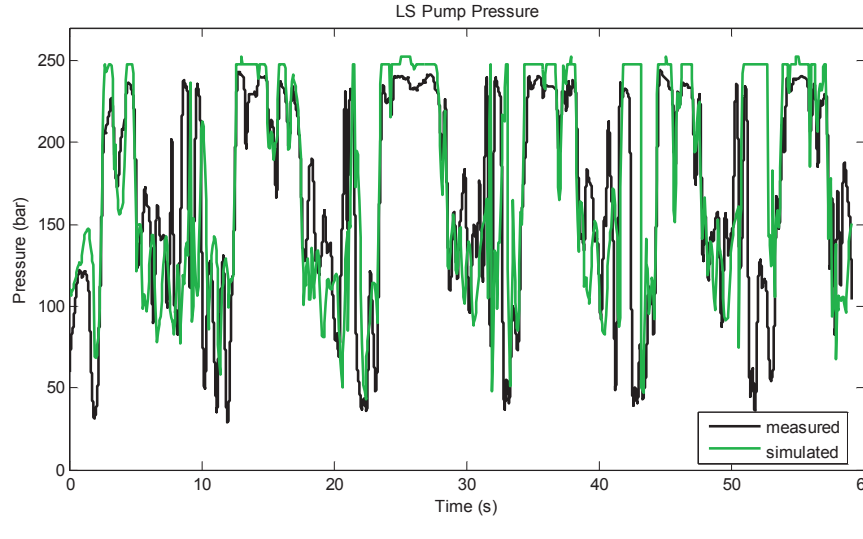

Figure 11 Measured and simulated pump pressure

the cycle are shown in Figure 10, where essentially the same digging motion is repeated six times. Load forces on the bucket from breaking and lifting soil were estimated from measured data according to Eq. 20. Friction and inertial forces are calculated with the excavator dynamic model and subtracted from the measured pressure force to obtain the actuator load. These load forces are then applied to the actuators to simulate digging and moving earth.

$$F_L = F_p - F_f - m_{eq}\ddot{x} \tag{20}$$

Figure 11 and Figure 12 compare measured and simulated pressures for the LS excavator, indicating accurate duplication of the measured work in simulation. With this confidence, the same loads are applied to the DC excavator in simulation to compare the energy performance of the two hydraulic systems.

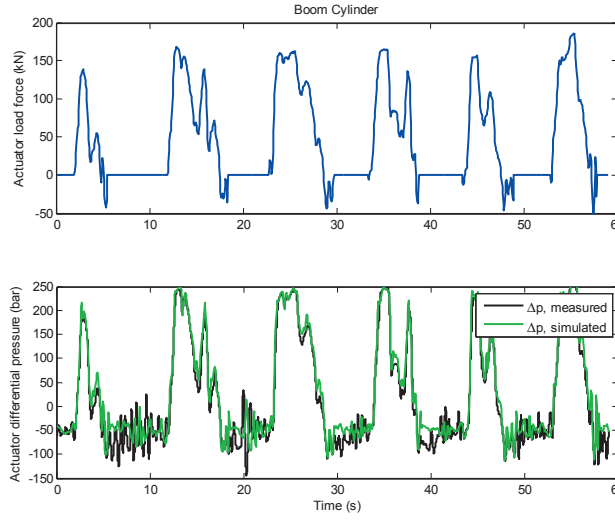

Figure 12 LS boom cylinder during digging cycle

5.2 Results

The primary goal of this paper is to compare the energy consumption of load-sensing and displacement-controlled control systems for a compact excavator in typical operation. To this end, both systems were simulated for the 60 second digging cycle. Simulation results are summarized in Table 2 and Figure 13. The power distribution categories are defined in the following bulleted list.

Table 2 Simulated energy comparison for 60 s digging cycle

	Actuator Work	Valve Losses	Pump Losses	Friction, Other	Charge & Drive	Total	Unit
LS	241	724	184	102	414	1665	kJ
DC	259	4.8	392	129	229	1013	kJ
Relative difference	+7.4	-99.3	+113.2	+26.4	-44.7	**-39.2**	%

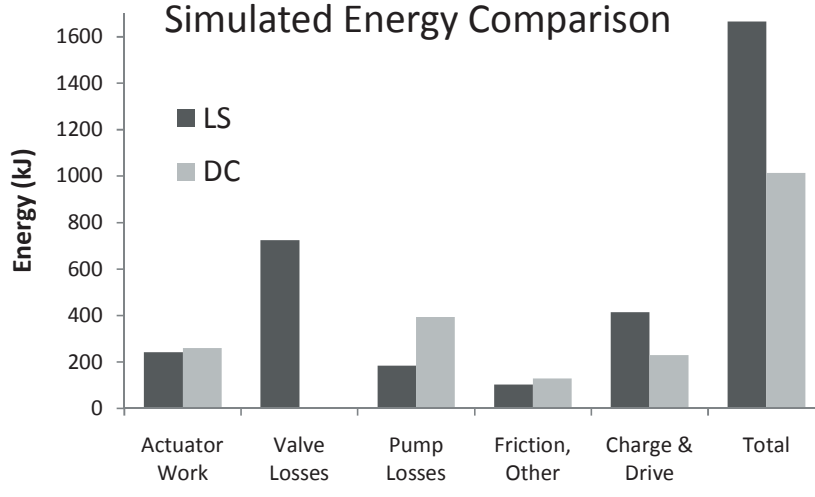

Figure 13 LS/DC energy comparison for 60 s digging cycle

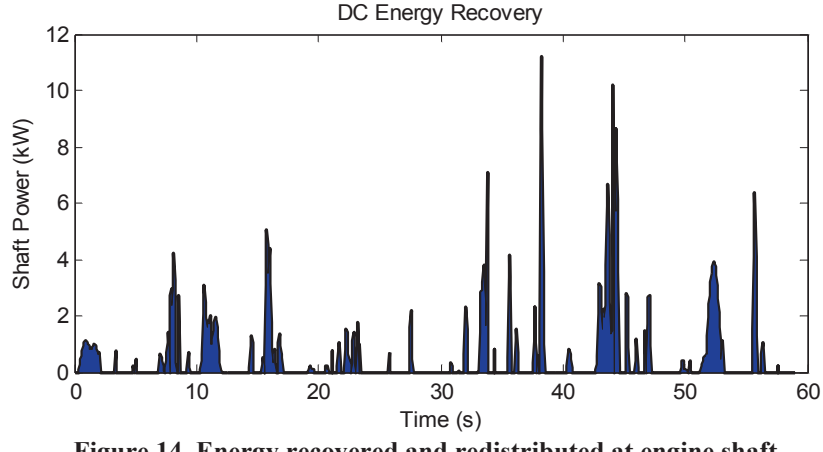

Figure 14 Energy recovered and redistributed at engine shaft

- "Actuator work" is the product of net actuator force/torque and velocity, after friction

- "Valve losses" includes metering losses from relief valves and LS control valves

- "Pump losses" includes the volumetric and mechanical losses associated with the LS pump and DC actuator pumps

- "Friction, Other": Power losses due to actuator friction, actuator leakage and transmission line resistance.

- "Charge & Drive": Both systems use the same gear pump for charge and auxiliary functions. This pump powers a cooling fan motor, replenishes volumetric losses in the hydrostatic circuits and supplies low pressure power for pilot lines (LS), pump control valves (DC) and actuator volume compensation (DC). Although the simulated cycle does not include driving, the hydrostatic track drives generate losses as the twin drive pumps spin at zero displacement (LS).

5.3 Discussion

Consideration of the simulation results prompts several points of discussion. Of course, the salient result is that the DC system requires 39% less total energy for the same operating cycle. Energy savings are primarily due to the elimination of valve metering losses. One might expect that metering losses would not be so high in a load sensing system, but high losses result from multiple actuators operating simultaneously at different pressure levels (3). The DC excavator also recovers energy when the pumps operate in motoring mode (see Figure 14). In this cycle, however, energy recovery is negligible. Only 26.5 kJ of the actuator work is recaptured, which is 10% of the useful work output or about 1% of the primary power input to the DC system. Half of this energy is recaptured while lowering the boom. More energy recovery would be expected in a different operating cycle involving lowering a load or with a larger machine having a more massive manipulator.

Displacement controlled actuation eliminates metering losses, but increases pump losses. In this case, the pump power losses are doubled. These losses are partly due to more installed pump flow capacity and partly due to their frequent operation at low displacements (9). One would expect the same amount of actuator work for both the LS and DC simulations. Variations in actuator work and friction are due to differences in control input and system dynamic response while tracking the same reference signal. These discrepancies do not significantly affect the total energy consumption.

The "Charge & Drive" category refers to energy losses from auxiliary components not directly used for digging. The LS system includes two track drive pumps which, being physically connected to the engine, continue consuming power while the machine is stationary. The DC configuration illustrated in Figure 3 does not have dedicated drive pumps, but rather switches two of the workgroup pumps for propulsion. This arrangement results in 10% total energy savings for the cost of limiting machine functionality in certain unusual cases where the workgroup and drive operate simultaneously.

6. CONCLUSION

Based on a comparison of simulated operation, a compact excavator with displacement controlled hydraulic actuators is significantly more energy efficient than the same machine with a load sensing hydraulic system. Energy savings of 39% were obtained for a trenching maneuver. Reduced power consumption is predominantly due to the elimination of metering losses. DC actuation allows power recovery, but energy recuperation was negligible in this study. Although the precise energy distribution depends on many variables, the simulated duty cycle is a typical operation for the given application and the simulated performance is quite close to the available measured data.

This paper focuses on the energy efficiency characteristics of competing hydraulic system configurations. Future research will also consider engine characteristics. The goal is to not only reduce the required power, but also to control the engine's operating point so as to minimize fuel consumption. Implementation and measurement of the proposed DC hydraulics and controls on a mini-excavator are also planned.

NOMENCLATURE

φ	angular position of hydraulic motor	[rad]
Δp	actuator differential pressure	[Pa]
θ	joint angle	[rad]
ω	joint angular velocity	[rad/s]
α	joint angular acceleration	[rad/s^2]
A_A	cylinder piston area	[m²]
A_B	cylinder rod-side annular area	[m²]
C_H	hydraulic capacitance	[m^3/Pa]
F_f	friction force	[N]
F_L	load force	[N]
F_p	pressure force	[N]
K_{oil}	fluid bulk modulus	[Pa]
Q	flow rate	[m^3/s]
V_A	cylinder piston-side volume	[m^3]
V_B	cylinder rod-side volume	[m^3]
V_{line}	actuator line volume	[m^3]
V_M	motor volumetric displacement	[m^3/rev]
V_p	pump volumetric displacement	[m^3/rev]
f_v	coefficient of viscous friction	[Ns/m]
f_C	coefficient of Coulomb friction	[N]
h	cylinder stroke	[m]
k_{Li}	coefficient of internal leakage	[m^3/Pa·s]
m	mass	[kg]
p	hydraulic pressure	[Pa]
x	cylinder piston position	[m]

REFERENCES

1 **Nanjo, T., Imanishi, E., Ootani, K.** and **Tsutsui, A.**, 2007. "Simulation and Evaluation Technique for Power System and Related Energy Saving on Hydraulic Excavator," *Kobelco Technology Review*, No. 27, pp. 28-34.

2 **Kagoshima, M., Komiyama, M., Nanjo, T.** and **Tsutsui, A,** 2007. "Development of New Hybrid Excavator", *Kobelco Technology Review*, No. 27, pp. 39-42.

3 **Zimmerman, J., Pelosi, M., Williamson, C.** and **Ivantysynova, M.**, 2007. "Energy Consumption of an LS Excavator Hydraulic System," *Proceedings of 2007 ASME International Mechanical Engineering Congress & Exposition (IMECE2007),* Seattle, Washington, USA.

4 **Ivantysynova, M.**, 2000. "Displacement Controlled Linear and Rotary Drives for Mobile Machines with Automatic Motion Control," SAE Technical Papers 2000-01-2562, *2000 SAE International Off-Highway & Powerplant Congress*, Milwaukee, Wisconsin, USA.

5 **Rahmfeld, R.,** 2002. *Development and Control of Energy Saving Hydraulic Servo Drives for Mobile Systems*. PhD Thesis. Technical University of Hamburg-Harburg, Germany.

6 **Grabbel, J. and Ivantysynova, M.** 2005. "An investigation of swash plate control concepts for displacement controlled actuators." *International Journal of Fluid Power, Vol. 6 (2005), No.2 August 2005. pp.19- 36.*

7 **Heybroek, K., Larsson, J.,** and **Palmberg, J.O.**, 2006. "Open Circuit Solution for Pump Controlled Actuators," *Proceedings of 4th FPNI PhD Symposium*, Sarasota, FL, USA, pp. 27-40.

8 **Mikeska, D.** 2002. A precise steady-state model of displacement machines for the application in virtual prototyping of power-split drives. *2nd FPNI-PhD Symposium Modena 2002*, University of Modena, Italy.

9 **Williamson, C. and Ivantysynova, M.,** 2007. "The Effect of Pump Efficiency on Displacement-Controlled Actuator Systems," *Proceedings of the Tenth Scandinavian International Conference on Fluid Power (SICFP '07)*, Vol. 2, pp. 301-326.

10 **Grabbel**, J. 2004. *Robust Control Strategies for Displacement Controlled Rotary Actuators using Vane Type Motors*. PhD Thesis. Technical University of Hamburg-Harburg, Germany.

11 **Lawrence, P., Salcudean, S., Sepehri, N.,** et al., 1995. "Coordinated and Force-Feedback Control of Hydraulic Excavators," *Proceedings of the Fourth International Symposium on Experimental Robotics (ISER95),* Stanford, California, USA.

12 **Salcudean, S., Tafazoli, S., Lawrence, P.,** and **Chau**, I., 1997. "Impedance Control of a Teleoperated Mini Excavator" *Proceedings of the 8th International Conference on Advanced Robotics (ICAR '97)*, Monterey, California, USA, pp.19-25.

13 **Bu, F.** and **Yao, B.,** 2001. "Nonlinear Model Based Coordinated Adaptive Robust Control of Electro-Hydraulic Robotic Manipulators: Methods and Comparative Studies", *2001 ASME International Mechanical Engineering Congress and Exposition (IMECE'01*), New York, New York, USA.

14 **Gu, J., Taylor, J.,** and **Seward, D.,** 2004. "Proportional-integral-plus control of an intelligent excavator", J. of Computer-Aided Civil and Infrastructure Engineering, Vol. 19, No. 1, pp. 16-27.

New Electro-Hydraulic Control Systems for Mobile Machinery

R FINZEL and **S HELDUSER**
Institute for Fluid Power, Technische Universität Dresden, Germany

ABSTRACT

The paper outlines a new electro-hydraulic control system for the working hydraulics of mobile machines. The new control system basically uses the command signals from the joysticks to control the volume flow delivered by the pump. The valves that control the flow for the actuators operate like flow dividers, again controlled by the joystick signal. The new electro-hydraulic system offers better energy efficiency, better controllability and a better damping than hydraulic-mechanical systems supplied today.

1. INTRODUCTION

In mobile machinery, several hydraulic drives can be operated independently at the same time. The hydraulic control system has to distribute the hydraulic power among the actuators depending on their requirements. In the European market, load-sensing systems (LS) are often used to control the working hydraulics. These systems have reached a very high degree of development and exceed other systems in terms of their capability. They are economically priced and reliable. However, they can be prone to oscillations in some cases and often demand high commissioning costs.

Due to the development of robust electro-hydraulic pumps and valves, new electro-hydraulic control systems have been developed in recent years. This paper presents new electro-hydraulic control systems for excavators. They combine the advantages of the hydraulic-mechanical LS systems with the flexibility, good controllability, energy efficiency and high dynamic performance of the electro-hydraulic ones.

2. LOAD-SENSING TECHNOLOGY

The idea of load sensing is to control the swivel angle of the pump by using a load signal. The pump is swivelled out in a way that the pressure difference $\Delta p_{RS}=p_1-p_{LS}$ (set by the pump controller) is adapted in the system. As a result, the load-sensing system causes a small but constant pressure drop in the system, usually 20 - 30 bar and nearly no excess

Fluid Power and Motion Control 2008 Edited by Dr D N Johnston and Professor A R Plummer

flow. Therefore, the excess pressure $\Delta p=p_1-p_{LS}$ is chosen as the characteristic parameter to compare the LS system with the new electro-hydraulic ones.

The pressure drop and the resulting energy losses can be divided into power losses, which occur from the pipe, and into those power losses caused in the control edges of the mobile valves as well as principal losses on the control edge of the lower loaded actuator. To minimize the power losses in the system it is necessary to reduce the excess pressure in the system.

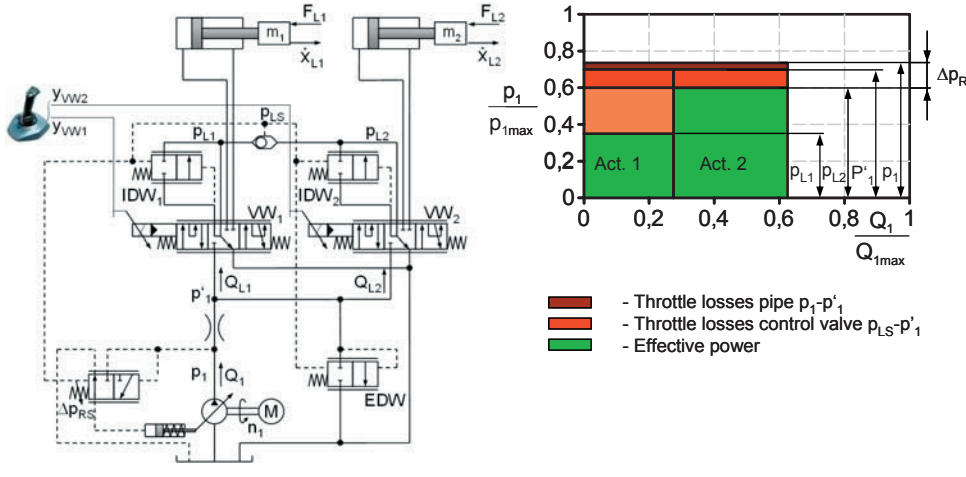

Figure 1: Hydraulic-mechanical load-sensing system

To avoid an interaction between the actuators, individual pressure compensators are used. In co-operation with the control valves, these compensators guarantee a load-independent operation of the system. A circuit with pressure compensators placed between the control valve and the actuator causes the same pressure drop over all active control valves (**Figure** 1). The division of the volume flow is proportional to the active flow areas of the valve spools. Due to the losses in the inlet pipe, the pressure drop over the control valve is not constant and depends on the actual flow in the system.

In case of an insufficient pump, the pressure drop over all the active control valves will be reduced so that all actuator speeds are reduced proportionally to their operator demands. Due to this characteristic, this system is suitable for machines used for constructing buildings.

A pressure compensator in the inlet section of the valve block avoids pressure peaks by opening in cases of high pressure drop in the system. In such cases, the damping characteristics of the system will increase.

3. NEW ELECTRO-HYDRAULIC SYSTEM CONCEPTS

Based on the characteristic of the hydraulic mechanical LS system, customer demands on the development of new electro-hydraulic system solutions can be described as follows.

1. Reduction of excess pressure

2. Improved damping characteristics

3. Simplification of current valve design

4. Reduced commissioning costs

5. Greater flexibility and user friendliness

6. Avoidance of additional sensors

Figure 2 presents the structure of the new electro-hydraulic LS systems. The drive delivers the required flow which can be adjusted to the operator demands via a pump controller or by changing the motor speed. The control valves divide the flow according to the demands of the actuators.

It is the general idea of the new systems that the pump flow Q_1 meets exactly the total flow demand $\sum Q_{Lj}$. Based on the position of the joysticks, a set actuator velocity can be calculated. With the help of an electro-proportional pump controller, the pump can be exactly swivelled out in a position to meet the requirement. Thanks to this, a load feedback to the pump is no longer necessary and the system is no longer pressure-controlled. By changing this principal control philosophy into a flow-controlled system, the control pressure drop in the system is not required anymore.

The clear separation of the fields of activity (drive, control system, controller, actuator and operator) enables a systematisation of the different drive and control tasks which were freely combined into functional LS systems in previous works(1,2). The many new possible system solutions are evaluated by their functions and economic characteristics.

The solutions developed, work with minimum technical effort but can be complemented by appropriate components. To improve the transmission features, the system can be enlarged to a closed-loop control system. This results in a high accuracy of the flow supply to several actuators, which is necessary to drive automated trajectories, for an example.

To attain load independence of the system, flow control over the control valves is done individually. This is performed by means of individual pressure compensators. In contrast to sensors, they react directly and fast on disturbance variables in the system. When using a sensor, the main control valve must compensate for the disturbances.

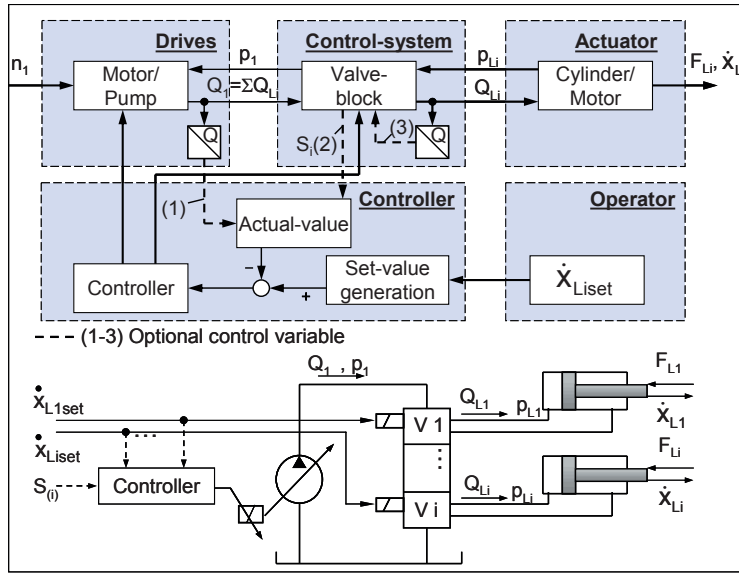

Figure 2: Generalised structure of the new electro-hydraulic LS systems (EFM)

The new electro-hydraulic systems (EFM) can be classified through the position of the pressure compensator. The EFM systems can be classified in EFM systems with primary and secondary pressure compensators. The solutions with primary pressure compensators are developed for agricultural machines and have been described in recent literature (2,4). The new electro-hydraulic control systems with secondary pressure compensators are presented in this paper.

3.1 Open loop control EFM system with secondary pressure compensator

The simplest and therefore most practical solution of a new EFM system is an open-loop control EFM system. **Figure 3** shows two open-loop solutions with different control algorithms.

The pump flow is directly calculated from the operator setting of the joystick. In the simplest version, the operator setting is directly sent to the valve electronic. For a further reduction of the energy consumption, an extra output from the control algorithm becomes necessary to control the valve opening in addition to the pump flow calculation.

Basically, the common load-sensing valve technology can be used for the new electro-hydraulic control systems. The only important hardware modification in comparison to the hydraulic-mechanical reference system is the application of an electrically controlled pump, the associated reduction of the hydraulic load sensing and the necessity of an electronic control unit. Even manually operated valves are conceivable when a position sensor is integrated in the valve. However, electrically operated valves are recommended to simplify the control effort and increase the system performance.

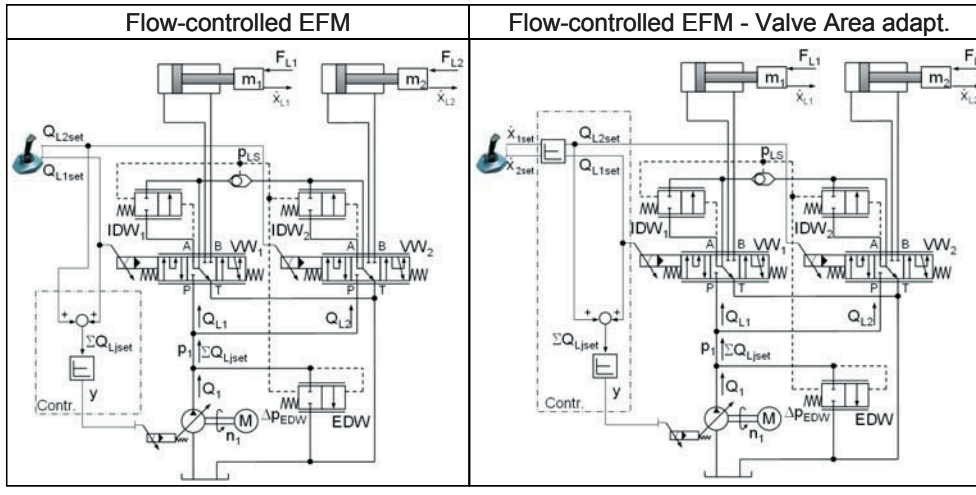

Figure 3: Solutions for open loop control EFM systems

3.2 Design and constraints of the EFM-control algorithm

It is the task of the control algorithm in the EFM system to realise the best transmission characteristic of the new electro-hydraulic control systems. The control algorithm calculates the flow demand from the operator settings and increases the user friendliness of the machine by taking control measures. The simplest solution is to control the valves directly by the joysticks (Figure 3, left). The pump flow is calculated by means of the throttle equation /1/

$$Q_1 = \alpha \cdot \sqrt{\frac{2}{\rho}} \cdot A \cdot \Delta p \cdot \qquad /1/$$

The flow area A is directly set by the joystick signal and depends on the valve design parameters. The set pressure drop Δp in the control valves has to be chosen in the control algorithm according to the actual pressure drop which occurs in a fully opened control valve in combination with the maximum possible flow. This results in a minimum pressure drop of 7 - 10 bar depending on the control edge geometry. If a lower pressure drop is used in this control algorithm, the maximum pump flow cannot be fully utilized.

The concepts of open-loop control systems are practicable and easy to realize but do not take account of pump losses. The systems can not compensate for these losses and hence, the actuators are under-supplied by this amount. In this case, the operator would slightly increase the joystick signal to achieve the set velocity of the actuators. He would not notice this system feature.

Assuming the customer already has the control valves and only wishes to change the system into an EFM system, the minimum practicable pressure drop in the system is 7-10 bar. There are two ways to further reduce energy consumption in the system:

1. further opening of the valves by the control algorithm, which will reduce the energy consumption in cases of lower volume flow

2. use of the simple control strategy with a new design of the control edges in the control valve which may involve a larger valve dimension.

3.2.1 Minimum pressure excess by maximum valve opening

The maximum overall efficiency of the system is achieved when the control system causes no extra throttle losses in the line to the actuator with the highest flow demand. In order to achieve this, the corresponding control valve must be fully open. The actuator with the highest flow demand can be easily detected via the joystick signal. The actuators with lower flow demands need to be further opened, in proportion to the operator settings because of the flow dividing characteristic of the system.

Figure 4 presents the control algorithm of the new electro-hydraulic EFM solutions. The operator signal $U_{operator}$ is directly transformed into a volume flow demand. Via the correction factor K_1, this signal can be adapted to the operator demands. Hence a better fine tuning characteristic can be reached without the use of difficult control edge designs. Furthermore, the machine characteristic can be adjusted to the specific task to increase user friendliness and effectiveness of the mobile machine.

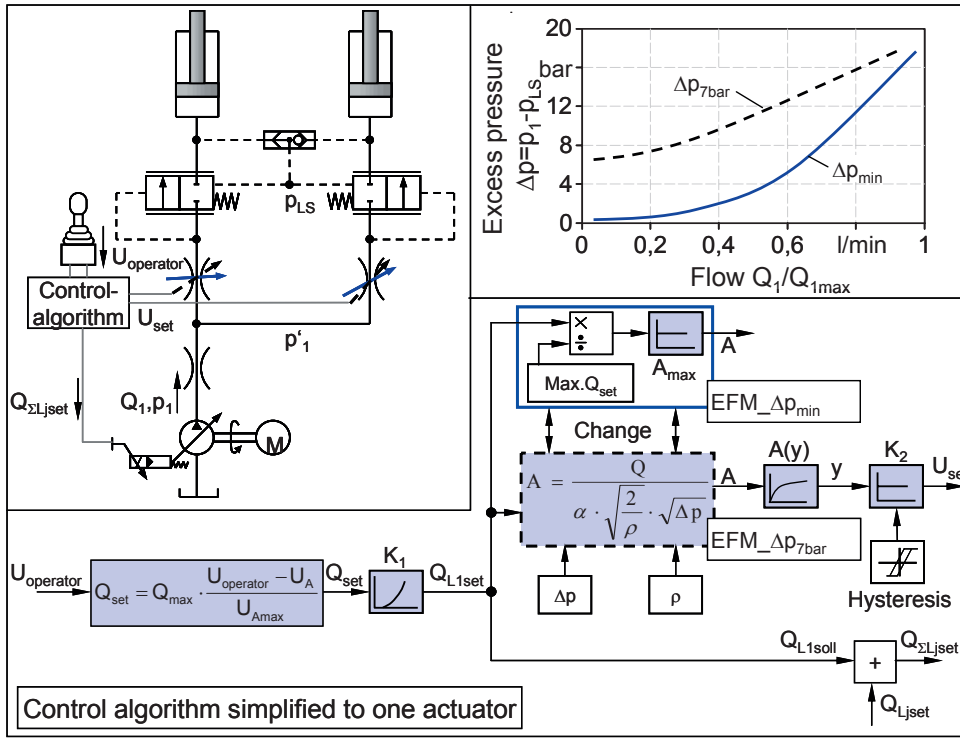

Figure 4: Controlling architecture for new EFM solutions

The set volume flow is sent directly to the pump controller. The valve opening is calculated via a chosen pressure difference and the volume flow Q_{set}. In case of maximum valve opening, only the proportion of the volume flow demands of the actuators has to be known. The spool position can be calculated from the valve opening using constructive parameters. Using correction factor K_2, hysteresis characteristics can be compensated for cases where the spool is not position-controlled.

Examining the calculated pressure excess of the system with different control algorithms (Figure 4 right,) an increasing excess pressure in the case of a rising flow occurs. This refers to the throttle losses in the inlet pipe and the increasing throttle losses in the control valves for systems with reduced pressure drop (Δp_{min}, Δp_{7bar}).

The control algorithm with maximum valve opening is the most energy-efficient but fails in the case of pulling loads. To lower the load in a controlled way, the flow is controlled via the tank edge in the control valve. In the system, shown in Figure 4, at maximum opening of the valve, the tank edge would also open to its maximum value and thus would not provide controlled lowering of the load. Nevertheless, this algorithm can be used for pushing loads. Based on the joystick position, the load cycle parts that are suitable for pushing loads can be detected. The control algorithm can be used in these cases to reduce the energy consumption to a minimum.

Furthermore, the maximum opening of the valves has a negative effect on the accuracy of the flow division in the system. The actual pressure drop over the control valve is influenced by the pressure compensator and the loads. Assuming that there are two active actuators in the system: one with a small flow demand of 5l/min and a second with an increasing flow demand of 5 - 90 l/min. The pressure difference between the actuators is varied within 180 and -180 bar. Pressure p_{IDW} changes because of the spring stiffness in the pressure compensator and varies depending on the load difference of the actuators. As the pressure behind the control valves is not equal anymore, the accuracy of the flow division is affected.

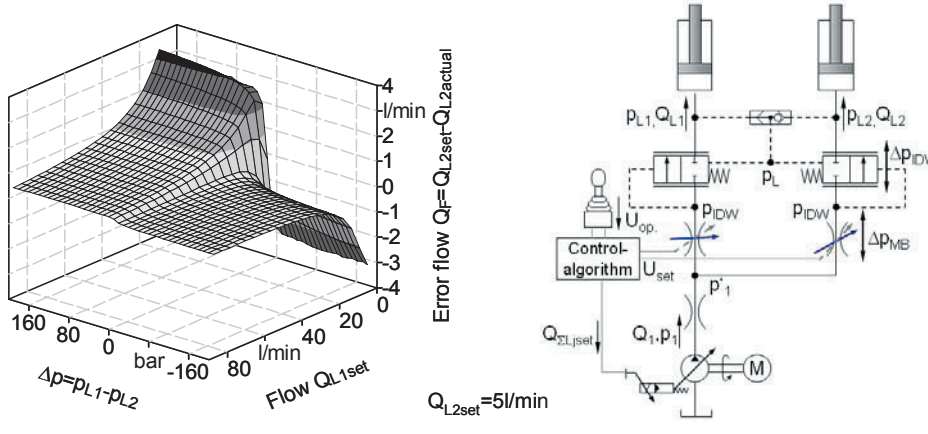

Figure 5: Calculated error flow in the case of two active actuators

Figure 5 shows this effect as the error flow $Q_F = Q_{L2set} - Q_{L2act}$ to the lower-supply actuator. Especially in case of low-volume flows, the error increases up to 70 % of the set value because of the low pressure drop over the valve compared to the error pressure of the compensator. If the pressure drop Δp_{MB} rises in the control valve due to the control edge design in combination with a rising flow, the pressure inaccuracy of Δp_{IDW} has less influence on the system. The error flow will be reduced in a characteristic of a root function as a result of the throttle equation.

The error can be minimized due to an ideal load sensing scheme and the avoidance of the spring in the pressure compensators.

The valve block characteristic can be maintained by adopting the valve opening in consideration of a minimal allowed flow error via the control algorithm. **Figure 6** presents the results of the maximum allowed flow area calculation. A minimisation of the flow error up to 10% requires the valve opening to be reduced depending on the flow demand of the actuators. Due to the smaller opening A_{max}* of the control valve, the pressure drop over the control valve Δp_{MB} increases. The additional energy losses in the system have to be accepted in order to realise good controllability and to avoid interaction between the actuators. Principally, this adapted control algorithm can handle pushing loads because of controllable valve openings.

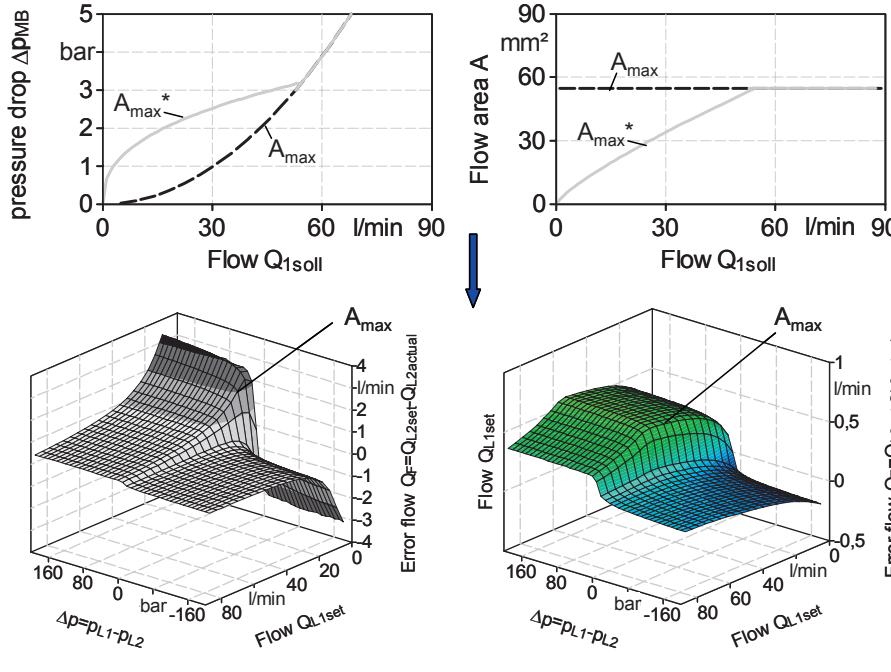

Figure 6: Adaptation of valve opening area to increase the flow division accuracy

*

3.2.2 Valve edge design reduces excess pressure

To avoid such a complicated control algorithm in a newly designed EFM system, the control edges have to be designed taking account of the operator demands in the engineering process. The control edge is adapted to the system volume flow set by the operator. Therefore, the control edge can easily be divided into three parts. First: an overlapping area, second: a fine tuning area which the operator needs for exact and comfortable positioning and third: the rest of the control edge with no special features. The control area has to be designed in a way that a calculated pressure drop of about 3 bar occurs at every operating point. A pressure drop Δp_{MB} of 3 bar is chosen because of the calculated flow error discussed in section 4.2.1. As a result, a simple control algorithm, which controls the pump only, can be used (**Figure 7**).

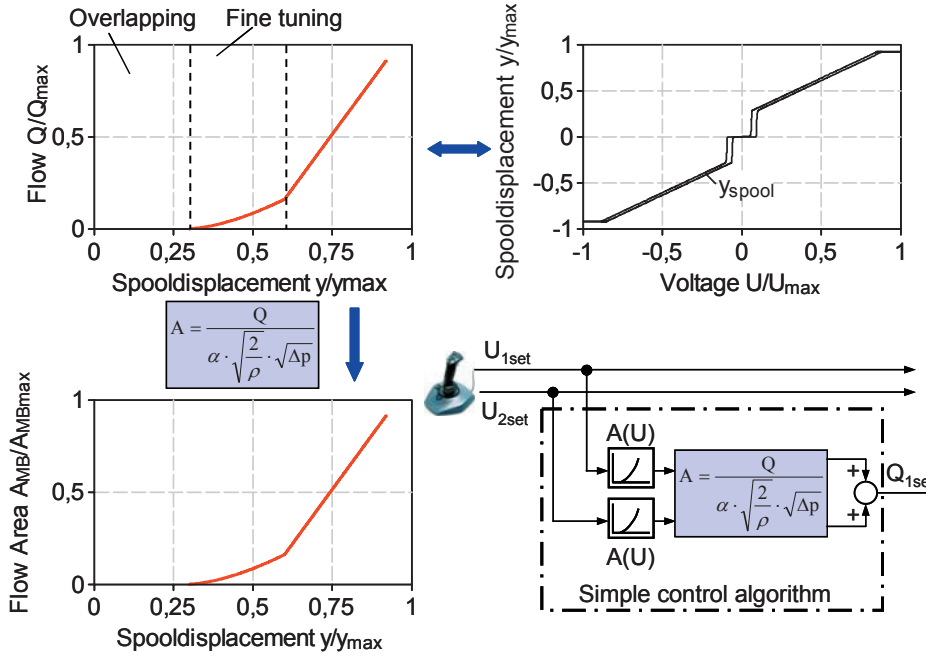

Figure 7: Design of main control edge

Furthermore, the control edge can be designed in a simple way. Theoretically, the complicated fine tuning area of common spools can be avoided. Using the correction factor K1, an operator-specific machine characteristic can be achieved in the electrically controlled machine. In this case, it is again necessary that the control algorithm takes account of the valve control.

Assuming that a system with one spool for both the main control edge and the tank edge is used, the tank edge has to be designed in close connection with the main control edge. Spool position and volume flow over the tank edge are well known from the calculation of the main control edge. The tank edge has to be designed such that energy consumption is reduced and cavitation avoided in the case of pulling loads (in connection with anti-cavitation valves).

4. INVESTIGATION RESULTS

The static and dynamic characteristics of the LS systems shown and their control algorithms are investigated by simulation and rig testing. The software used as the simulation tool was ITI®-SimulationX. **Figure 8** shows the LS test rig in the test facility of the IFD at TU Dresden. The LS test rig is developed for hydraulic-mechanical and electro-hydraulic system solutions with up to three actuators. It is based on LUDV valves (series M7-20) as well as the axial piston pump A10VO63 manufactured by Bosch Rexroth AG. In addition to the three actuators (throttle, hydromotor, cylinder), the working equipment of an excavator has been installed which can be used optionally as a realistic actuator. The open and closed loop control concepts of the new electro-hydraulic system solutions are realized by means of the real-time hardware by dSpace GmbH.

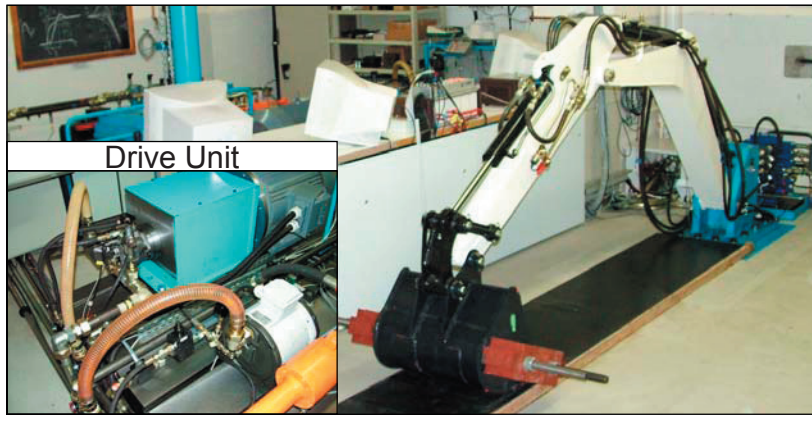

Figure 8: LS test rig with drive unit and excavator demonstrator

4.1 Results of the static investigation

Figure 9 shows the static investigation results obtained for the new systems in comparison with a conventional hydraulic mechanical LUDV system. The figure illustrates the steady-state command response while the volume flow of the first actuator increases. The control pressure difference Δp_{RS} of the hydraulic mechanical reference system is set at 20 bar.

Due to the new electro-hydraulic control system, the excess pressure can be reduced by about 15 bar. This reduction of the energy consumption greatly depends on the working point of the system. In particular, low volume flow demands and low loads can help achieve a remarkable reduction of energy consumption. The absolute power losses over the control edge is shown for the EFM Systems in comparison to the HMLS systems. The maximum absolute power saving is about 2 kW. The relative energy saving during a load cycle, like for example an unloaded level finishing (*planum*), is up to 14%. Depending on the load and the specific load cycle, the predicted energy saving is lower than this test result.

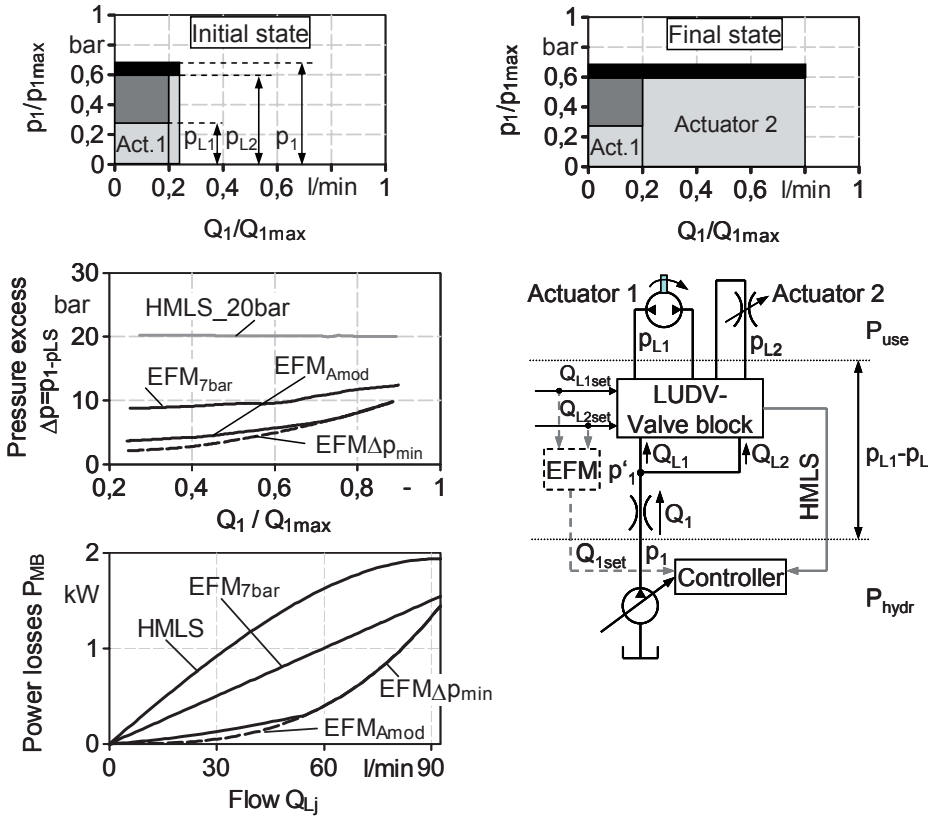

Figure 9: Results of the static investigation

4.1 Results of the dynamic investigation

The excavator in the test facility is used as an actuator for the dynamic investigations. A reasonable damping ratio and eigenfrequency can be adjusted only with a realistic actuator. The working equipment of the excavator is rigidly connected with the floor in the test facility. Therefore, outside influences like machine oscillations or tyre parameters are excluded from the evaluation of the dynamic system performance.

Figure 10 shows the dynamic command response of the EFM system in comparison with the hydraulic-mechanical reference system. The new electro-hydraulic LS systems are better damped with a shorter settling time. The pump in an EFM system is not pressure-controlled any longer, instead it is adjusted via an open-loop control to the set value. A feedback of the load signal is no longer necessary. Therefore, better damping and stability of the system also result in a faster response. In the hydraulic system of a real excavator, the system oscillations can be influenced by the machine oscillations. Under special conditions the hydraulic-mechanical system is less vulnerable to oscillations. The oscillations of the system can counteract the machine oscillations, which is not possible in the EFM systems because of the constant displacement of the pump. Using simple control strategies or higher

ramp responses, the problems can easily be solved on the control side of the new systems, which reduces their commissioning costs.

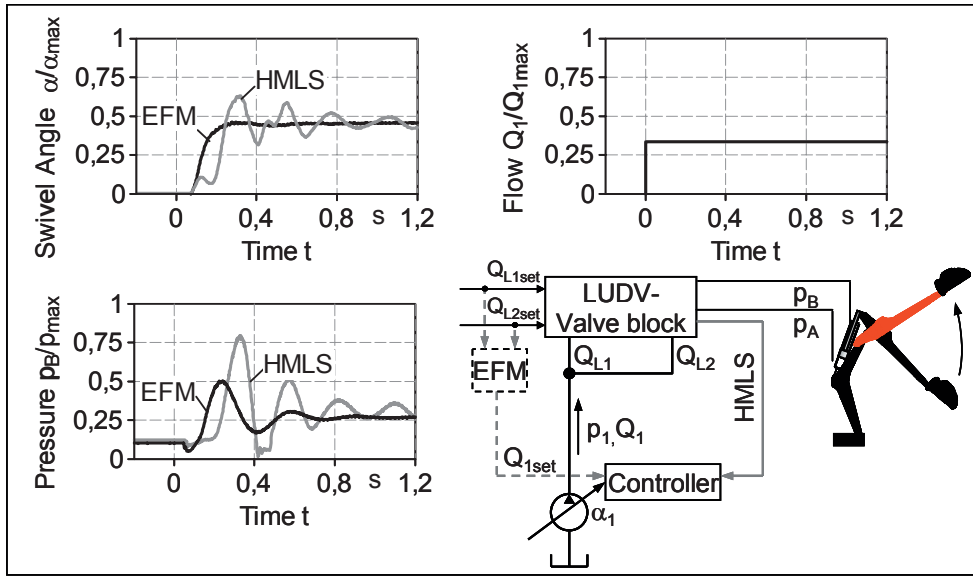

Figure 10: Results of the dynamic investigation

4. CONCLUSIONS AND PERSPECTIVE

The new electro-hydraulic systems presented combine the simplicity and robustness of the hydraulic-mechanical LS systems with good controllability, flexibility and user friendliness of the electro-hydraulic components. Principally their design is based on the conventional system with small modifications so that standard mobile components can still be used. The energy consumption can be reduced by about 14%. The damping characteristic is enhanced due to the uncoupling of the pump control from the load signal. As a result, practical and cost-effective solutions are ready for implementation in mobile machinery.

NOMENCLATUR

α	Swivel angle	°
ρ	Density	Kg/m³
A	Flow area	mm²
E	Energy	J
p	Pressure	bar
Δp	Excess pressure	bar
Δp_{RS}	Pressure drop in the control path of the system	bar
Δp_{IDW}	Pressure drop over the compensator	bar
Δp_{MB}	Pressure drop over the control valve	bar
P	Power	kW
Q_1	Pump flow	l/min

REFERENCES

(1) Djurovic, M.; Helduser, S.
Elektrohydraulisches Load Sensing
O+P – Ölhydraulik und Pneumatik 48, 2004

(2) Djurovic, M.
Energiesparende Antriebssysteme für die Arbeitshydraulik mobiler Arbeitsmaschinen „Elektrohydraulisches Flow-Matching“,
Dissertation, TU Dresden 2007

(3) Jongebloed, H.; van Büren, D.; Völkel, U.; Jabs, C.
Energy-Saving Valve System for Mobile Hydraulic Applications – Load-Control-System (LCS)
4th International Fluid Power Conference, Dresden 2004

(4) Fedde, T.; Harms, H. H.
Adaptives Hydrauliksystem für Traktoren
Tagung Landtechnik, Hannover 2005

Session 7
Pumps and noise

Active Systems for Noise Reduction and Efficiency Improvement of Axial Piston Pumps

Nafz, Timo
Bosch Rexroth AG, Horb a.N., Germany
Murrenhoff, Hubertus
Institute for Fluid Power Drives and Controls (IFAS), Aachen, Germany
Rudik, Ruslan
Bosch Rexroth AG, Horb a.N., Germany

ABSTRACT

The development of hydraulic pumps will more and more focus on fuel efficiency and noise emissions. Nowadays, common methods to reduce noise and flow ripple in axial piston pumps are to use grooves or boreholes in the valve plate, and more recently, the use of pre-compression volumes (PCV). Whenever operating parameters such as speed, delivery pressure and pump displacement change, those geometrically fixed methods no longer achieve the optimum in noise and flow ripple reduction. Therefore adjustable systems, such as variable valve plate timing or check valves have been investigated in the past, but none of these systems made it into series production. In this paper, formerly investigated adjustable systems are presented and their advantages and disadvantages are discussed. From a current point of view, systems using control valves combined with the recently available high speed measurement and control devices provide the most promising systems. Using AMESim, detailed simulations of such systems were made. Changes in flow ripple, axial forces, swash plate torque and efficiency are presented and discussed at different operating points.

Keywords: flow ripple, noise, efficiency, hydraulic pump, active valve control

1. INTRODUCTION

Two of the main targets of pump development are fuel efficiency and noise, including fluid-borne noise, structure-borne noise and air-borne noise. Until now a lot of methods for noise reduction have been developed and investigated. In general, these methods can be categorized as shown in figure 1. The methods can be split into primary and secondary methods. Secondary methods reduce the pulsation after its creation and are generally located outside the pump. Primary methods avoid the creation of pulsation and are located inside the hydraulic pump. They can be divided into geometrically fixed methods such as

Fluid Power and Motion Control 2008 Edited by Dr D N Johnston and Professor A R Plummer

grooves and adjustable systems that guarantee an optimal performance at all operating points. Depending on the type of control, adjustable methods divide into passive methods such as check valves and active methods such as electronically actuated control valves. The configuration of the valve plate plays a key role concerning efficiency and noise, but also affects other important pump characteristics as shown in figure 2.

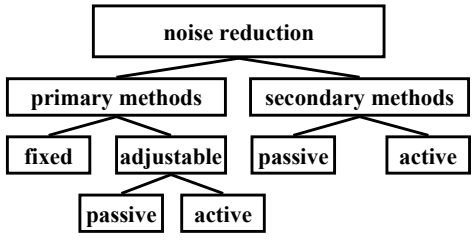

Figure 1 Methods for noise reduction

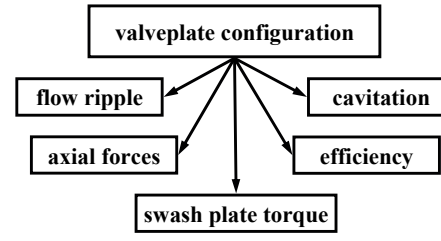

Figure 2 Influence of the valve plate

Influencing the flow ripple, the valve plate affects the pulsation of the delivery pressure that leads to vibrations in the hydraulic circuit. Influencing the cylinder pressure, axial forces and swash plate torque are affected, forcing the pump housing to vibrate and emit air-borne noise. Furthermore, the swash plate torque generates pulsation of the control pressure. Efficiency is mainly affected by the overlap between the suction and the delivery port at the inner dead centre (IDC) and outer dead centre (ODC). Another loss of efficiency occurs, when the pressurized dead volume of the cylinder enters the suction port. The respective flow rates and flow directions influence the creation of cavitation.

This paper mainly focuses on flow ripple, but also takes axial forces and swash plate torque into account. The creation of flow ripple of an axial nine piston pump is shown in figure 3.

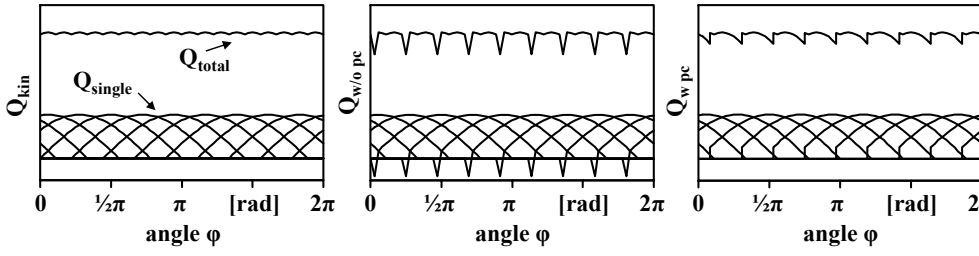

Figure 3 Different forms of flow ripple

The left figure shows the kinematic flow ripple Q_{kin} at zero pressure, which is only due to pump kinematics. At higher pressures, compressibility leads to a back flow from the delivery port into the piston chamber, increasing flow ripple significantly ($Q_{w/opc}$). The right figure shows the flow ripple with pre-compression Q_{wpc} at optimal timing, meaning that the delivery port is delayed so that the oil is ideally pre-compressed by the piston movement. This ideal pre-compression can only be designed for one operating point, making adjustable systems desirable that can be adjusted to the operating parameters speed, pump displacement and delivery pressure.

2. ADJUSTABLE SYSTEMS

In the following, formerly investigated adjustable primary systems are systematized into six main principles. These main principles are described and their advantages and disadvantages are discussed.

2.1 Check Valves

The principle of the check valve system is shown in figure 4. The check valve triggers the delivery cycle as soon as the cylinder pressure equals the delivery pressure. This way flow ripple due to not-optimal timing can be eliminated. In this system pre-compression is done by the piston movement so that the delivery kidney has to be extremely shortened for variable displacement pumps. Another disadvantage is the wear of the valve seats, the conflict of valve stability versus dynamical performance and the noise of the valve itself.

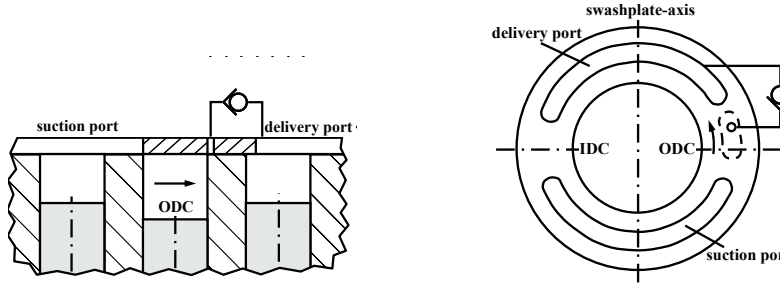

Figure 4 Check valve principle

Lechner [11] investigated a system where each piston had an individual check valve located in the barrel and achieved a noise reduction at high speeds. Grahl [5] investigated the use of a commercial check valve in the valve plate and achieved a reduction of airborne noise of 3 dB at a delivery pressure of 2.5 MPa in comparison to a common valve plate. However, the noise level dramatically increased with pressure. Due to the disadvantage of wear, Pettersson [13] investigated the use of a vortex diode instead of a check valve but found the dynamic properties to be too weak for this application. Jarchow [8] used small plates as check valves and put them in parallel with an orifice, allowing a slight pre-compression via the delivery port. At low speeds, he achieved a pressure ripple reduction of 50 % compared to a standard pump. However, the pressure ripple increased with speed. Due to stability reasons, the highly dynamic spring plates could only be used for low pressure applications. Jarchow also investigated a check valve controlled PCV (pre-compression volume) by introducing a check valve between the borehole and the PCV in parallel to the regular connection. Hereby, a higher cross sectional area was provided for the discharge of the PCV being controlled by the check valve. Due to the high dynamic performance needed, no significant improvement in flow ripple was achieved. Harrison and Edge [6] investigated heavily damped check valves (HDCV) being damped by a hydraulic orifice connected to the delivery port. For a pressure range of 10 MPa to 25 MPa and pump displacements between 20 % and 100 %, flow ripple and noise were reduced. Becher [1] investigated a flexible ring working as check valve and achieved a reduction of flow ripple between 20 % and 50 %, depending on the operating point.

2.2 Variable Valve Plate Timing

The principle of variable valve plate timing is shown in figure 5.

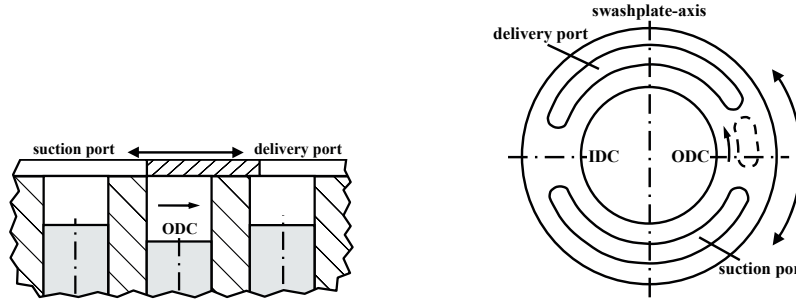

Figure 5 Variable valve plate timing

Rotating the valve plate relatively to the dead centres, the timing of the suction and delivery cycle can be adjusted, so that an optimal timing can be achieved at all operating points. However, turning the valve plate negatively affects the timing of the suction port.

Reimers [14] investigated the influence of the valve plate timing and suggested an adjustable valve plate. Edge and Liu [4] determined a significant reduction of pressure ripple by altering valve plate timing and proposed a microprocessor controlled valve plate. Grahl [5] found an optimal valve plate turning angle of 4° for minimal flow ripple and proposes an adjustable system where the valve plate is positioned with a control valve.

2.3 Adjustable Valve Plate Geometry

Several systems providing adjustable valve plate geometry have been suggested in the past. Systems with steadily adjustable valve plate geometry allow adjustment of timing and cross section. Systems using different holes can only be adjusted within discrete steps. Most ideas are very complex and should be electronically activated to provide full flexibility.

Grahl [5] investigated a system that could adjust the end of the suction cycle in three stages and achieved noise reductions for pressures below 2.5 MPa and small pump displacements. Weingart [15] suggested relief grooves with a membrane that can be deformed by a piezo actuator. However, new materials are needed for this technology. Beerman and Eichhorst [2] suggested an adjustable orifice for pre-compression. Using sensors for speed, pump displacement and delivery pressure, a control unit can determine the optimal conduit for each operating point.

2.4 External Pre-Compression

The principle of external pre-compression by a piezoelectric actuator is shown in figure 6.

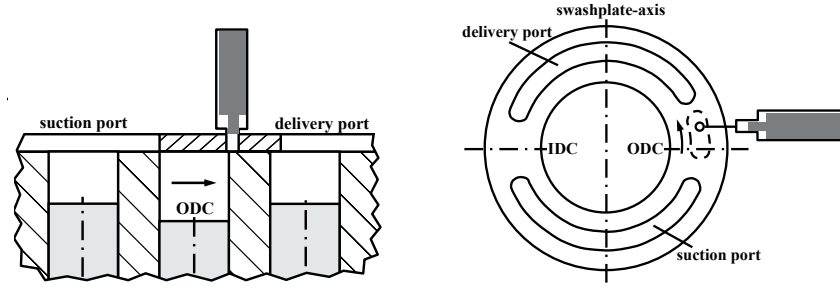

Figure 6 External pre-compression using a piezoelectric actuator

Dantlgraber [3] suggested a piezoelectric actuator to pressurize the cylinder volume. Another possibility is to use a valve controlled external pressure source. Ideally such a system can reduce flow ripple down to kinematic flow ripple (see figure 3). Dantlgraber also suggested using the delivery port as pressure source. Using sensors to determine the operating point, control valves can be actuated in such a way that flow ripple is minimized. Helduser and Weingart [7] investigated a piezo actuated pre-compression and simulated a reduction of pressure ripple of 30 % compared to a grooved valve plate. However, the size of the piezo actuator and the cooling effort were considered as severe disadvantages.

2.5 Cross-Angle

By tilting the swash plate around the axis perpendicular to the swash plate axis, the angular positions of the ODC and IDC change with the pump displacement. Similar to the principle of variable valve plate timing, the timings of the suction and delivery ports change in the same manner. Johansson [9] found a cross angle of 3.5° to be an optimal compromise for flow pulsation, piston forces and swash plate torque. Helduser and Weingart [7] investigated an active cross angle system. They found a slight reduction of pressure ripple but predict better results for low displacements and low pressures. However, an active cross-angle system is hardly realistic due to the enormous piston forces.

2.6 Pressure Equalization at Dead Centres

Another principle for noise reduction and efficiency improvement is pressure equalization between ODC and IDC. Hereby the hydraulic energy stored in the dead volume at IDC can be used to pressurize the cylinder volume at ODC. Recuperating hydraulic energy from IDC to ODC can improve efficiency and may lead to a reduction of flow ripple. However, a valve controlled energy accumulator is required for an odd piston number.

Kahrs [10] investigated a system with a hydraulic restrictor between ODC and IDC and found a noise reduction. He also proposed several systems that can be adjusted to the operating point. A similar system with additional hydraulic chambers is proposed by Lemmen and Schmitt [12]. They also proposed a staged pressurisation.

3. SIMULATION MODEL

In order to investigate the active systems, a simulation model of a standard nine piston pump was built in AMESim. The simulation model for one piston is shown in figure 7.

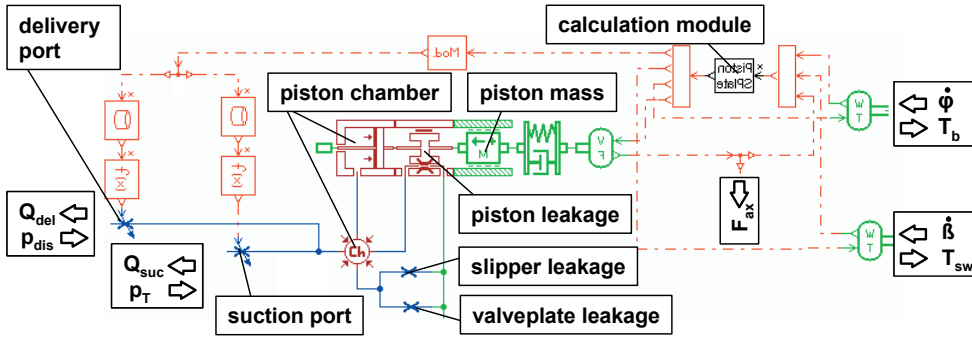

Figure 7 Simulation model of one piston

The piston position $x(\varphi)$ and the velocity of the piston $\dot{x}(\varphi)$ are calculated from the actual pump angle φ, the swash angle β and the radius R of the piston around the driveshaft by equation (1). Herby the piston angle is defined as φ=0 at ODC. The actual cylinder pressure is then calculated by integrating equation (2) with the bulk modulus E_{oil} being a function of the pressure according to equation (3).

$$x(\varphi) = -R \cdot \tan\beta \cdot \cos\varphi \qquad \dot{x}(\varphi) = \dot{\varphi} \cdot R \cdot \tan\beta \cdot \sin\varphi \tag{1}$$

$$\frac{dp}{dt} = \frac{E_{oil}}{V_{cyl}} \cdot \sum Q = \frac{E_{oil}}{V_{cyl,0} - A_{pis} \cdot x} \cdot \left(Q_{suc} - Q_{del} - Q_L - A_{pis} \cdot \dot{x}\right) \tag{2}$$

$$E_{oil} = \frac{(1-\alpha) \cdot \left(1 + \frac{m \cdot p}{E_0}\right)^{-1/m} + \alpha \cdot \left(\frac{p_0}{p}\right)^{1/n}}{\frac{1-\alpha}{E_0} \cdot \left(1 + \frac{m \cdot p}{E_0}\right)^{-(m+1)/m} + \frac{\alpha}{n \cdot p_0} \cdot \left(\frac{p_0}{p}\right)^{(n+1)/n}} \tag{3}$$

The used parameters are m = 10, the polytropic index of gas n, the fluid bulk modulus at ambient pressure E_0 and the content of unsolved air α. Since the simulations were made at constant temperature of 50°C, dynamic viscosity μ was held constant. The delivery and suction kidneys were modelled as circular orifices with the cross sectional areas $A(\varphi)$ being deposited as data files, so that the flow rates $Q_{suc}(\varphi)$ and $Q_{del}(\varphi)$ are given by equation (4).

$$Q(\varphi) = C_q \cdot A(\varphi) \cdot \sqrt{\frac{2 \cdot \Delta p(\varphi)}{\rho}} \tag{4}$$

In order to include laminar flow, the flow coefficient C_q is modelled as a function of the maximum flow coefficient $C_{q,max}$ the flow number λ, and the critical flow number λ_{crit}:

$$C_q = C_{q,\max} \cdot \tanh\left(\frac{2 \cdot \lambda}{\lambda_{crit}}\right) \tag{5}$$

The Leakage flow rate Q_L consists of piston leakage, slipper leakage and valve plate leakage. Assuming that the piston is located in the cylinder bore in a central position, the piston leakage $Q_{L,pis}(\varphi)$ was modelled as an annular gap with variable gap length.

$$Q_{L,pis}(\varphi) = \frac{D \cdot \pi \cdot h_{pis}^{\ 3}}{12 \cdot \mu \cdot l_{pis}(\varphi)} \cdot (p_{cyl}(\varphi) - p_T) \quad , \quad l_{pis} = l_{init} + x(\varphi) \tag{6}$$

Hereby p_T is the tank pressure, D the diameter of the cylinder bore. h_{pis} the gap height and l_{init} the initial gap length. The valve plate leakage $Q_{L,VP}(\varphi)$ was modelled by assuming a constant gap height $h_{L,VP}$ between the valve plate and the cylinder by equation (7).

$$Q_{L,VP}(\varphi) = \frac{h_{\mathrm{L,VP}}^{\ 3} \cdot l_{\mathrm{L,VP}}}{12 \cdot \mu \cdot b_{\mathrm{L,VP}}} \cdot (p_{del}(\varphi) - p_T) \tag{7}$$

Hereby $l_{L,VP}$ is the circumference of the delivery port and $b_{L,VP}$ the gap width. The slipper leakage $Q_{L,slip}$ is due to the flow through the piston bore (*pb*), the slipper bore (*sb*) and the gap between slipper and swash plate (s*wash*). Assuming a constant gap height $h_{L,slip}$, the slipper leakage can be calculated by equation (8).

$$\begin{aligned} Q_{L,slipper}(\varphi) &= \frac{C_{pb} \cdot C_{sb} \cdot C_{swash}}{C_{pb} \cdot C_{sb} + C_{pb} \cdot C_{swash} + C_{sb} \cdot C_{swash}} \cdot (p_{cyl}(\varphi) - p_T) \\ C_{pb} &= \frac{\pi \cdot d_{pb}^{\ 4}}{128 \cdot \mu \cdot l_{pb}} \qquad C_{sb} = \frac{\pi \cdot d_{sb}^{\ 4}}{128 \cdot \mu \cdot l_{sb}} \qquad C_{swash} = \frac{\pi \cdot h_{L,slip}^{\ 3}}{6 \cdot \mu \cdot \ln(R_{slip} / r_{slip})} \end{aligned} \tag{8}$$

Hereby d_x are the diameters and l_x the lengths of the corresponding bores. R_{slip} is the outer radius and r_{slip} the inner radius of the slipper.

Neglecting friction effects, the cylinder pressure p_{cyl} is used to calculate the axial piston force F_{ax}, the torque on the swash plate T_{sw} and the driving torque T_b for a single piston:

$$F_{ax}(\varphi) = p_{cyl}(\varphi) \cdot A_p(\varphi) + m_p \cdot \ddot{x}(\varphi) \tag{9}$$

$$T_{sw}(\varphi) = -F_{ax,x}(\varphi) \cdot l_y(\varphi) = -\frac{F_{ax}(\varphi) \cdot R \cdot \cos\varphi}{\cos^2\beta} \tag{10}$$

$$T_b(\varphi) = -F_{ax}(\varphi) \cdot R \cdot \sin\varphi \cdot \tan\beta \tag{11}$$

Using the described single piston model, a simulation model for a nine piston pump was built as shown in figure 8. This model allows an investigation of different operating points by adjusting the pump speed n, pump displacement β and the delivery pressure p_{del}.

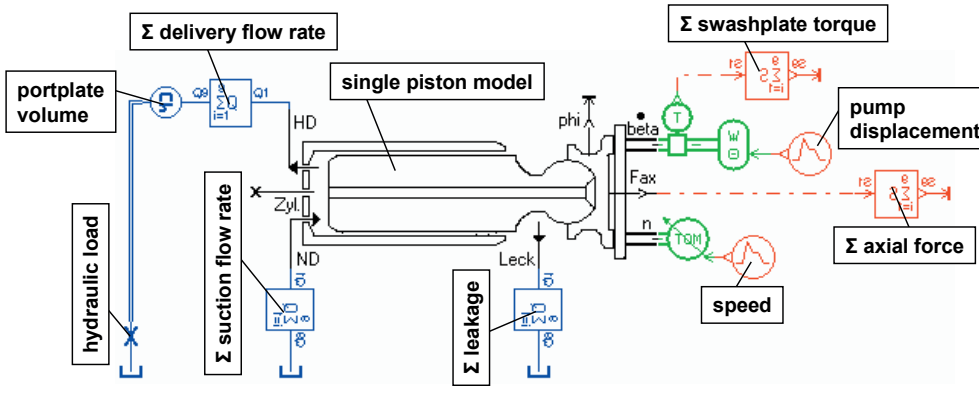

Figure 8 Simulation model of the whole pump

In order to save computational time, the inputs and outputs X_1 of the single piston model are used to derive the total values X_{total} of an n-piston pump by equation (12).

$$X_{total}(\varphi) = \sum_{i=1}^{n} X_1\left(\varphi + (i-1)\cdot 360°/n\right) \tag{12}$$

The capacities of the other piston chambers are taken into account by enlarging the simulated port plate volume. According to the test stand, the hydraulic load was modelled as an orifice using equation (4). The hydraulic pipe between port plate volume and hydraulic load was modelled by a lumped capacitive and resistive element. Since the main interest is on flow ripples, a more complex pipe-model isn't reasonable because of computational time.

The described simulation model was verified with cylinder pressure measurements of a standard hydraulic pump. The grooved valve plate of this standard pump and a comparison of simulation results and measurements are shown in figure 9.

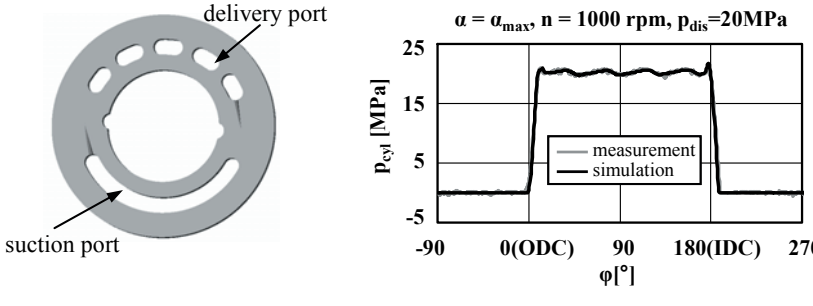

Figure 9 Grooved valve plate and corresponding cylinder pressure

As to be seen from figure 9, the delivery pressure ripples could be modelled very precisely. In order to provide a closer view on the pressure rise and fall, these regions are shown in figure 10 at two different speeds and two different delivery pressures (10MPa and 30MPa).

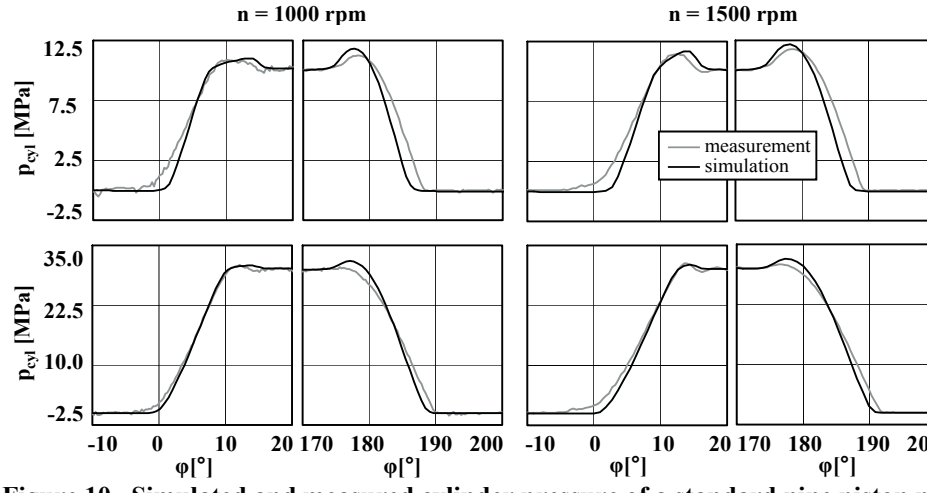

Figure 10 Simulated and measured cylinder pressure of a standard nine piston pump

The simulated pressure rise fits the measurements pretty well, with the simulated pressure rise starting later than the measured one. This might be due to the very low bulk modulus at low pressures coming from equation (3). The differences at the pressure fall might be due to manufacturing inaccuracy or due to flow conditions which cannot be modelled in a one dimensional simulation. However, this work mainly focuses on delivery flow ripple, which are not influenced by the pressure fall but only by the pressure rise. Furthermore, this comparison between measurement and simulation demonstrates the ability of the simulation model to react to a change of the operating point.

4. INVESTIGATED SYSTEMS

In the following, the thoughts of chapter 2 are continued and active systems are developed. The simulation model described in chapter 3 is used to investigate the pure systems. This way, the working principles of the systems and their advantages and disadvantages can be investigated more clearly. However, their performance might be better in combination with additional grooves or in combination with each other.

4.1 Control Valve System

Expanding the discussion of check valves of chapter 2.1, adjustable valve plate geometry of chapter 2.3 and external pre-compression of chapter 2.4, a concept using highly dynamic control valves with variable stroke limitation was developed. This way no pressure peak would be needed for opening and pre-compression flow can be withdrawn from the delivery port. Being electronically actuated, such a system allows to actively adjust the timing as well as the size of the cross sectional area in order to achieve optimal performance. However, such dynamical valves with variable stroke limitation are difficult to realize, so that the system was simplified as shown in figure 11.

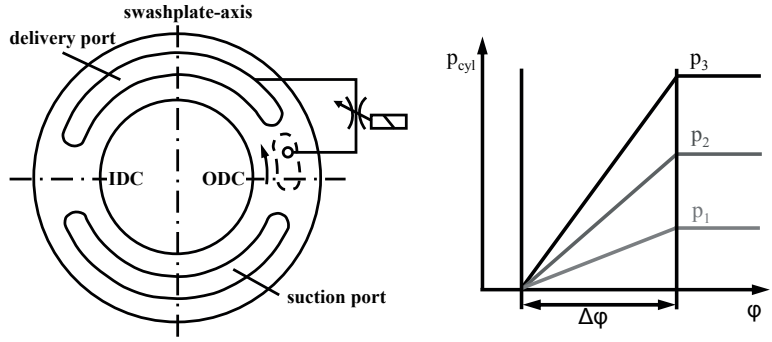

Figure 11 Principle of the control valve system

The control valve can be adjusted to the operating point by varying the cross sectional area. Figure 11 also shows the schematic pressure rise being adjusted to different delivery pressures. In the simulation model, the control valve system was modelled as a fixed orifice with a diameter of 5 mm in the valve plate and a variable orifice in series. Both orifices use equation (4). The fixed orifice opens just as early that no back flow occurs into the suction port and the cross sectional area of the variable orifice was adjusted to the operating point in order to minimize flow ripple. Figure 12 shows the resulting flow ripple, axial forces and swash plate torque of this control valve system compared to the grooved standard valve plate of figure 9 at two different operating points.

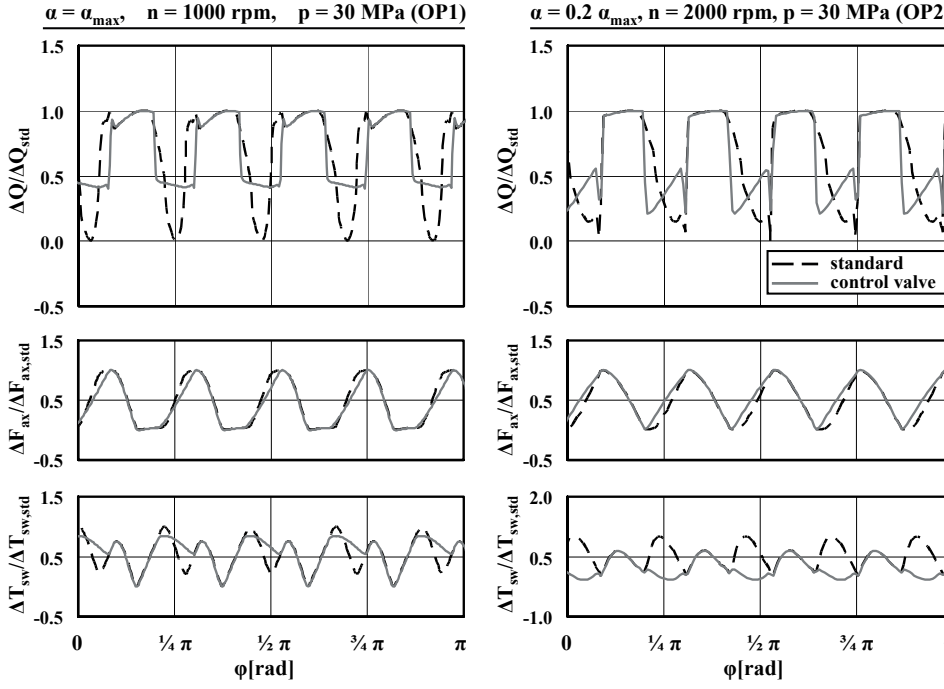

Figure 12 Simulation results of the control valve system

All values are presented in relation to the maximum magnitude of the standard valve plate. At operating point 1 (OP1), flow ripple can be reduced by 40 %, combined with a reduction of swash plate torque amplitude. The reduction in flow ripple decreases with higher speeds and lower displacements. At OP2, flow ripple amplitude is only little less and an additional frequency is introduced, which can only be eliminated by a higher flow ripple. Concerning swash plate torque, a significant reduction of amplitude is achieved and the second order frequency is almost eliminated, which might lead to a significant noise reduction. Since the standard valve plate is designed for higher speeds, only smaller improvements can be achieved. As stated in figure 11, the pressure rise is significantly lower in both operating points. This can be seen in the axial force plot, because the piston force is almost proportional to the cylinder pressure.

4.2 Valve Controlled Pre-Compression Volume

Following the discussion of the control valve concept of chapter 4.1, the check valve controlled PCV of chapter 2.1, and external pre-compression in chapter 2.4, a valve controlled PCV was developed (figure 13).

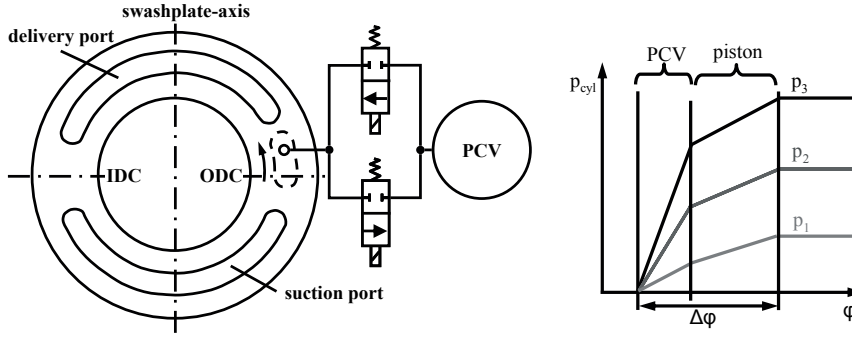

Figure 13 Principle of the valve controlled PCV

With this system the charge and discharge of the PCV can be independently controlled with a higher cross sectional area for the discharge and a smaller one for the charge. Since the PCV is of finite size, the cylinder volume cannot be pressurized up to the delivery pressure. The remaining pressure difference has to be realized by the piston stroke. During this phase, the PCV is disconnected from the cylinder volume, so that only the cylinder volume has to be pressurized. By introducing grooves, the remaining pressure difference could be realized much faster than by the piston movement. As mentioned before, the intention was to investigate the systems individually. Therefore, the simulated strategy is to discharge the PCV very fast in order to maximize the time for the pressurization by the piston movement. The PCV is then reconnected to be charged when flow ripple is high due to pump kinematics (compare figure 3). In the simulation model, the control valves were modelled as variable orifices using equation (4) with cross sectional areas of A_{dis}=7 mm² for the discharge and A_{charge}=2.5 mm² for the charge of the PCV. The valves were modelled with a linear opening and closing time of 0.3 ms. The volume of the PCV was set equal to that of the comparable series PCV, providing a ratio of PCV to cylinder volume at zero pump displacement of 7.5.

The obtained simulation results are shown in figure 14 in comparison to the standard PCV.

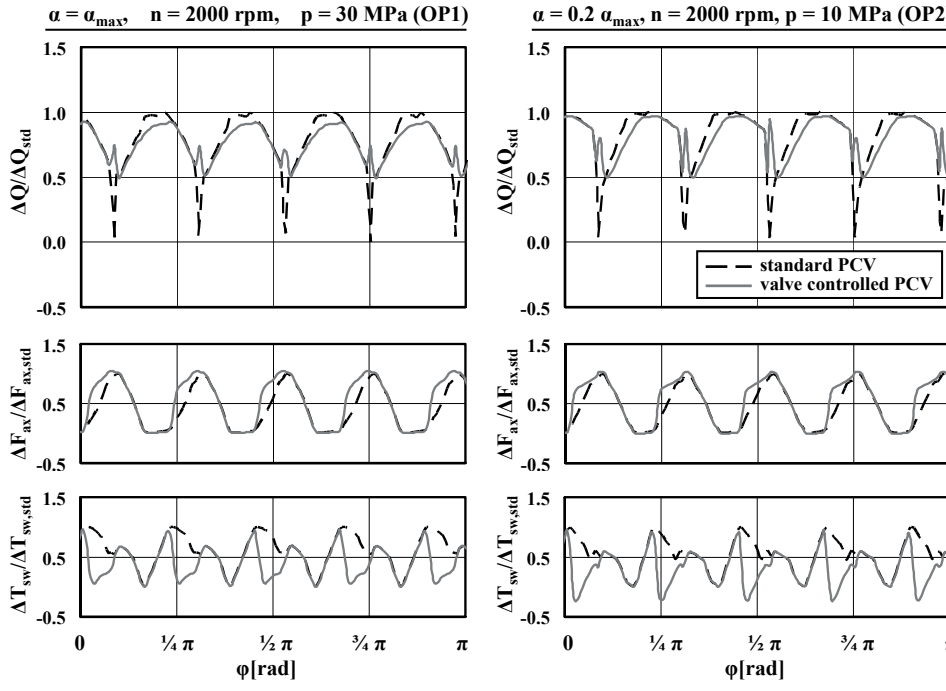

Figure 14 Simulation results of the valve controlled PCV

In these two operating points, flow ripple was reduced by at least 50 % compared to the standard PCV version. However, a second peak has to be tolerated at both operating points, when the cylinder kidney enters the delivery port. This could be smoothened by short grooves at the delivery port. Compared to the standard PCV, the charge and discharge cycle of the PCV can be exactly separated. This way, the charge of the PCV can be done over a longer time, which leads to a lower maximum of the flow ripple.

Since the cylinder pressure and the axial piston force are almost proportional, the force plot shows the expected characteristics of the cylinder pressure as expected in figure 13. The pressure rise is very fast when the PCV is discharged and slow when the remaining pressure difference is done by the piston movement. This rapid pressure rise leads to a slightly higher swash plate torque and introduces a high peak of the second order frequency, which might increase structure borne noise emission of the pump. The disadvantages of this concept, which are due to the slow pressurization of the piston movement, can be eliminated by adding grooves for the second stage of pressurization. Even better performance could be achieved in combination with the control valve system (chapter 4.1). This is even more important at high delivery pressures and low pump displacements, where the dead volume of the cylinder chamber is high while the piston stroke is low. Furthermore the charging of the PCV leads to a significant low in the delivery flow. A solution might be the recuperation of the hydraulic energy stored in the piston chamber at IDC.

4.3 Pressure Recuperation Volume (PRV)

The discussion of the valve controlled PCV in chapter 4.2 and the pressure equalization at the dead centres in chapter 2.6 results in a concept using a pressure recuperation volume (PRV), to recuperate the hydraulic energy of the cylinder chamber at IDC (figure15).

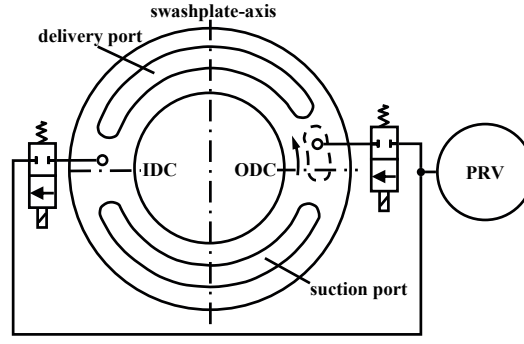

Figure 15 Pressure recuperation volume (PRV)

In this system the hydraulic energy is recuperated from IDC to ODC via the PRV. This way pump efficiency can be increased and positive effects on the flow ripple can be achieved. Such a PRV system was simulated and compared to a standard valve plate configuration in order to determine the possible efficiency improvement. In this simulation, leakage was not modelled. The valves were simulated as described in chapter 4.2 with a cross sectional area of 3.3mm². Those valves are active when the cylinder kidney neither contacts the delivery kidney nor the suction kidney. The size of the volume that can be recuperated depends on the size of the PRV. For a maximum amount of recuperated volume, the size of the PRV was found to be at least 8 times the size of the dead volume of one piston chamber at zero displacement. At full pump displacement efficiency improvements of 1 % at 10 MPa and 2 % at 30 MPa were determined. At a displacement of 20 %, efficiency could be improved by 5 % at 10 MPa and 11 % at 30 MPa. A change in pump speed can be neglected for these results. The electrical energy needed to switch the control valves is not considered. Especially pumps with trunk pistons can profit of such a system, since a higher dead volume results in higher losses due to compressibility when entering the suction port.

5. CONCLUSION

Due to the enormous influence of the valve plate geometry, several adjustable systems have been investigated in the past. The principles of these systems and their advantages and disadvantages have been discussed. Following this discussion, new active systems using control valves have been developed, described and investigated by simulation. Integrating these systems preceding the delivery kidney, simulation results predict improvements in flow ripple, axial force, swash plate torque and efficiency depending on the system and the operating point. By additionally introducing the active systems preceding the suction port, further improvements in flow ripple, axial forces, swash plate torque and efficiency can be achieved. Furthermore, combining these systems will improve pump performance.

REFERENCES

[1] Becher, D. (2003): Untersuchungen an einer Axialkolbenpumpe mit Ringsystem zur Minderung von Pulsationen. Dissertation, Institut für Fluidtechnik, TU Dresden

[2] Beermann, Karl and Eichhorst, Bernd (2007): Druckmittelaggregat mit kontinuierlich steuerbarem Strömungsquerschnitt in der Umsteuerung. Patent, DE10135800B4

[3] Dantlgraber, Jörg (1999): Hydrostatische Maschine. Patent, DE19818721A1

[4] Edge, K. A. and Liu, Y. (1989): Reduction of Piston Pump Pressure Ripple. Fluid Power Transmission and Control, Proc. of the 2nd Int. Conference, Hangzhou, China

[5] Grahl, T. (1989): Geräuschminderung an Axialkolbenpumpen durch variable Umsteuersysteme, Ölhydraulik und Pneumatik 33, 1989, no 5

[6] Harrison, A. M. and Edge, K.A. (1999): Reduction of Axial Piston Pump Pressure Ripple. Proc Instn Mech Engrs, Vol. 214 Part I

[7] Helduser, S. and Weingart, J. (2004): Piezoaktor zur aktiven Pulsationsminderung bei hydraulischen Verdrängereinheiten, Proceedings of the 4th IFK, Dresden

[8] Jarchow, M. (1997): Maßnahmen zur Minderung hochdruckseitiger Pulsationen hydrostatischer Schrägscheibeneinheiten. Dissertation, IFAS, RWTH Aachen

[9] Johansson, A. (2005): Design Principles for Noise Reduction in Hydraulic Piston Pumps – Simulation, Optimisation and Experimental Verification, Dissertation, Division of Fluid and Mechanical Engineering Systems, Linköping

[10] Kahrs, M. (1968): Die Verbesserung des Umsteuervorganges schlitzgesteuerter Hydro-Axialkolbenmaschinen mit Hilfe eines Druckausgleichkanals, Ölhydraulik und Pneumatik 12, 1968, no 1

[11] Lechner, E. (1980): Untersuchung des Betriebs- und Geräuschverhaltens einer verstellbaren Axialkolbenpumpe mit Ventil-Vorsteuerung. Dissertation, Institut für Produktionstechnik (WBK), Universität Karlsruhe

[12] Lemmen, R. and Schmitt, J. (2004): Axialkolbenmaschine mit Mitteldrucköffnung. Patent, DE19804374B4

[13] Pettersson, M. (1995): Design of Fluid Power Piston Pumps with Special Reference to Noise Reduction. Dissertation, Linköping University, Sweden

[14] Reimers, E. (1984): Möglichkeiten zur Lärmminderung an Axialkolbenpumpen mit wasserhaltigen Druckflüssigkeiten. Fortschr.-Ber. VDI-Z., Reihe 11, Nr. 60

[15] Weingart, J. (2004): Geräuschminderung von Hydraulikpumpen durch aktive Verminderung der Volumenstrom- und Druckpulsation, METAV München

Design and Optimization of a Novel Hydraulic Free Piston Engine with Liquid-propellant-power

Haoling REN, Haibo XIE, Huayong YANG

The State Key Laboratory of Fluid Power Transmission and Control, Zhejiang University, Hangzhou, 310027, China
Corresponding Author: **Haibo XIE, hbxie@zju.edu.cn**

ABSTRACT

This paper describes a new design of a hydraulic free piston engine for human scale power systems. The piston assembly is driven by the energy released by the decomposition of the high test hydrogen peroxide (HTP) through the catalyst. The elimination of the starter, air/fuel mixing and ignition enables a compact and reliable design. Incorporating two 2/2 exhaust valves to discharge the exhaust gas after the power process allows a higher and stable performance. This paper discusses the effect of the design and structural parameters' on the output and the conversion efficiency of the HTP. Especially, the performance of the 2/2 exhaust valve plays an important role on the frequency, output and gas pressure of the engine. The ragone plot is used to evaluate the engine with the exhaust valves and without the valves (natural exhaust system). The theoretical analysis and the simulation results prove that the engine with the exhaust valves has higher output and stable performance.

KEYWORDS： Hydraulic free piston engine (HFPE) High test hydrogen peroxide (HTP) Ragone plot Power stroke Stable performance

1. INTRODUCTION

Hydraulic free piston engine (HFPE) is the simplest, most effective device which combined the engine and hydraulic pump integral to supply the power to hydraulic systems. A free piston engine extracts work from the burning fuels by directly propelling linear motion of the free piston assembly (FPA) and pressuring the hydraulic fluid. The HFPE has higher efficiency by eliminating the rotational motion and the side force comparing to the crank

Fluid Power and Motion Control 2008 Edited by Dr D N Johnston and Professor A R Plummer

shaft engine. Due to the potential advantages, many efforts have been done on the HFPE, especially the Innas BV [1] from Dutch, Toyohashi University of Technology [2] from Japan, Tampere University of Technology [3] from Finland, and Zhejiang University [4] from China. They all have achieved some success in their research.

A novel type HFPE is introduced here for the human scale power supply. This novel engine extracts energy from the decomposition of Liquid-propellant-power, say the high test hydrogen peroxide (HTP) through the catalyst. The HTP can decompose into oxygen and steam when brought into contact with a catalyst, say sliver, requiring no oxidizer in this heat release process. The HTP is safe and friendly to the environment and the operators because its decomposition products are oxygen and steam. The most interesting property of HTP is that it has a higher energy density compared with other human scale power sources, such as batteries, fuel cells and DC motors. Table 1 outlines the energy density comparison of various power sources.

Table 1. The energy density comparison of various power sources

Power Source	Lower Heating Value
100% HTP	1.6 MJ/kg
90% HTP	1.2 MJ/kg
Battery	0.43 MJ/kg
Fuel Cell	1.5 MJ/kg
DC Motor	0.53 MJ/kg

The HTP is widely used in military affairs, say the torpedoes and rockets, as the monopropellant or the oxidizer of the bipropellant. Using the HTP as the power source in the civil fields has existed in some patents [5] and some researchers already use the HTP as the power source in their research. Barth etc. in Vanderbilt University [6,7] has explored the use of the HTP to move the pneumatic actuator and receive good experimental results. Raade and McGee [8,9] in U.C. Berkeley explored the HTP as the fuel to move the free piston in the free piston hydraulic pump (FPHP) and verified that the FPHP can work well by testing the sample. The prior researches work proves the feasibility of the HTP in the civil fields.

This paper firstly sets up the models of the HFPE, and then discusses the effects of the design and structural parameters on the output of the system and the conversion efficiency of the HTP. The ragone plot is employed to assess the two systems performance.

2. DESCRIPTION OF THE HFPE

Figure 1 provides a principal sketch of the engine which based on the dual pistons HFPE. Compared to the traditional internal HFPE, this novel HFPE eliminates the burning process, and thus the starter, the air/fuel or ignition are no longer needed. But it adds a catalyst bed to each head of the gas cylinder seen from figure 1. The HTP decomposes according to the following reaction.

$$2H_2O_2(l) \xrightarrow{catalyst} 2H_2O(g) + O_2(g) + Q_{LHV} \quad (1)$$

Where Q_{LHV} denotes the lower heating value of the reaction, for the 90% concentration HTP, this value is 1.2MJ/kg.

The operation process of this novel HFPE can be expressed as: The operation of the engine begins with the injection of high-pressure HTP into the catalyst bed 1 on the left (right) side by opening the left (right) fuel valve 7. The HTP decomposes into steam and oxygen as it passes through the left (right) catalyst bed 1, typically a sliver meshes. These hot gases expand within the left (right) hot gas cylinder 2 and propel the FPA 5 to the right (left). The movement of the FPA pumps the hydraulic fluid at high pressure from the right (left) cylinder 3 while simultaneously drawing in low pressure fluid from the reservoir into the left (right)of the hydraulic cylinder. The hydraulic fluid into and out of the hydraulic cylinder is controlled by the check valves 4 shown in figure 1. The hot gases expand until the hot gas piston uncovers the left (right) exhaust ports, and at this point the gases vent to the atmosphere and the piston decelerate gradually. This is one stroke when the FPA stops completely. The right (left) fuel valve is then opened to begin another stroke on the opposite side of the engine, pushing the FPA from the exhaust ports towards the gas cylinder head. When the FPA returns to its initial position, an operation cycle is completed. A repetition of this cycle results in a pulsating flow of hydraulic fluid from the reservoir to the high pressure accumulator and load.

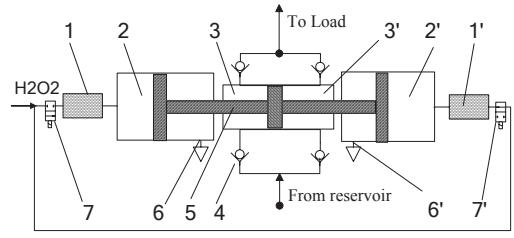

1/1′.catalyst bed 2/2′.gas cylinder 3/3′.hydraulic cylinder 4.check valves 5. FPA 6/6′. Exhaust ports 7/7′.fuel valves

Figure 1 The schematic structure of the novel HFPE

The structure shown in figure 1 has some problems. After the exhaust ports open completely, the FPA stays there until the pressure in the hot gas cylinder approaching the environment pressure to avoid the accumulation of hot gases in the gas cylinder. This leads to a low operation frequency and results a low output of the engine. If improving the operation frequency, the gases in the gas cylinder will not vent completely, and thus the gases will accumulate cycle by cycle and the gas pressure will also increase simultaneity. The FPA will stall when the gas pressure almost the same as the pressure of the newly decomposed gases in the opposite cylinder. This will lead to the unstable performance of the engine.

To solve the above problems, another structure with 2/2 exhaust valves which are added to the gas cylinder is shown in figure 2. The right side has the similar structure and operation. The difference of this structure from the above is that when the FPA moves to left, the 2/2 exhaust valve opens simultaneity to vent the gases in the left gas cylinder and avoids the gas accumulation. In this structure, the FPA can move continuously and the engine can achieve a higher operation frequency.

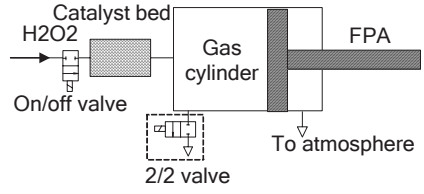

Figure 2 The novel HFPE with the accessorial 2/2 exhaust valves

The following parts will discuss the two structures and evaluate their performance. And the system is optimized based on the evaluation.

3. MODEL THE HFPE

3.1 The force balance of the FPA

The FPA is the only moving part in the HFPE and is controlled by the dynamic balance not the kinetic balance. The dynamics of the FPA motion is governed by:

$$\sum F = m_p \ddot{x}_p \tag{2}$$

Where m_p denotes the mass of the FPA; $\ddot{x}_p$ is its linear acceleration and $\sum F$ is the sum of the forces acting on the FPA, which are illustrated in figure 3.

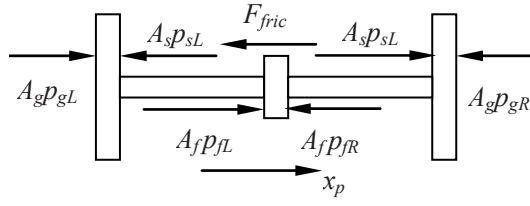

Figure 3 The sketch of forces on the FPA

Inserting the above force terms in the figure 3 into the equation (2) yields:

$$m_p \ddot{x}_p = A_g (p_{gL} - p_{gR}) + A_f (p_{fL} - p_{fR}) - A_s (p_{sL} - p_{sR}) - F_{fric} \tag{3}$$

Where p_{gL}, p_{gR} denote the pressure in the left and right hot gas cylinder respectively; p_{fL}, p_{fR} denote the pressure in the left and right hydraulic pump cylinder respectively; p_{sL}, p_{sR} denote the pressure in the left and right insulating cylinder respectively; A_g, A_f, A_s denote the area of the hot gas piston, hydraulic pump and insulating cylinder respectively, F_{fric} denotes the friction of the FPA, x_p, $\dot{x}_p$, $\ddot{x}_p$ denote the position, velocity and acceleration of the FPA respectively.

For the FPA, the friction is composed of the coulomb friction which can be seen as constant during the stroke and viscous friction relating to velocity, and can be defined as follows:

$$F_{fric} = F_{coul} + F_{visc} = F_{coul} + b\dot{x} \tag{4}$$

3.2 The model of the HTP decomposition

The decomposition of the HTP is considered as the first order reaction. It can be defined as:

$$r = \frac{dc_P}{dt} = K(c_0 - c_P) \tag{5}$$

Where r denotes the reaction ratio, K denotes the ratio constant of the reaction, it depends on the type of the catalyst, c_0 denotes the initiative concentration of the HTP, and c_p denotes the concentration of the production.

Substitute the equation (5) with its differential equation, suppose the decomposition time constant $\tau_r=1/K$, and the released heat are proportional to the decrease of the reactant, so the equation (5) can be rewritten as:

$$\tau_r \ddot{Q}_r + \dot{Q}_r = Q_{LHV}\dot{m}_{fuel} \tag{6}$$

Where Q_r denotes the heat released through the reaction, Q_{LHV} denotes the lower heating value of the HTP, and $\dot{m}_{fuel}$ denotes the mass flow rate of the HTP.

Equation (6) is the dynamic model of the HTP decomposition.

3.2 The model of the catalyst bed

The catalyst bed is the place where the HTP transfers from liquid to hot gases. In this process, the catalyst bed can be seen as the control volume, as the figure 4 shows. Where $\dot{m}_{decom}$ denotes the mass flow rate of the decomposed gases out of the catalyst bed.

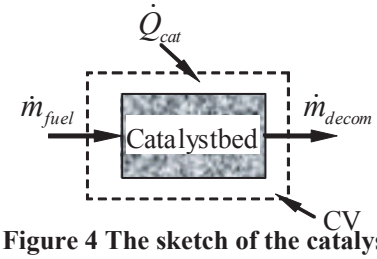

Figure 4 The sketch of the catalyst bed

The catalyst bed can be seen as an open system, and the power balance relating the rate of energy storage to the energy flux rate across the catalyst bed can be written as:

$$\dot{U}_{cat} = \sum \dot{H}_{cati} - \sum \dot{H}_{cate} + \dot{Q}_{cat} - \dot{W}_{cat} \tag{7}$$

To simplify the equation, some assumptions are made:(1)The volume of the catalyst bed is small, and thus the internal energy (IE) can be ignored, so $\dot{U}_{cat} = 0$. (2)The enthalpy into the catalyst bed is the energy to push the HTP into the bed. Compared to the enthalpy exiting the bed, the entry enthalpy can be neglected. (3)The enthalpy exiting the catalyst bed is the energy released through the decomposition, and it can be written as $\sum \dot{H}_{cate} = \dot{m}_{decom} c_p T_{ADT}$. (4)The heat enters into the catalyst bed is the heat released by the decomposition, and the heat loss in form of conduction or convection can be neglected,

so $\dot{Q}_{cat} = \dot{Q}_r$. (5)The volume of the catalyst bed is constant, so any work is done to the environment, then $\dot{W}_{cat} = 0$.

Taking the above assumptions into account, and the equation (7) can be rewritten as:

$$\dot{Q}_r = \dot{m}_{decom} c_p T_{ADT} \tag{8}$$

3.4 The model of the gas cylinder

The figure 5 shows the sketch of the gas cylinder before the exhaust ports open, and the FPA is propelled by the decomposed gases from the catalyst bed.

The gas cylinder can also be seen as an open system, and the power balance can be expressed as: $$\dot{U}_{ch} = \sum \dot{H}_{chi} - \sum \dot{H}_{che} + \dot{Q}_{ch} - \dot{W}_{ch} \tag{9}$$

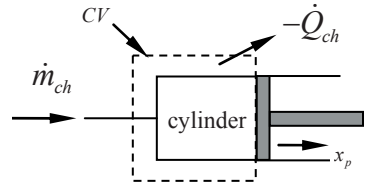

Figure 5 The sketch of the gas cylinder

To simplify the equation, some assumptions are made:

(1)The internal energy (IE) can be calculated from gas temperature in the gas cylinder, T, the mass of the gas, m_{ch}, and the specific energy, c_v through an ideal gas approximation: $U_{ch} = m_{ch} c_v T$.

Since the ideal gas properties are assumed, the derivative of the IE can be expressed as

$$\dot{U}_{ch} = \frac{d}{dt}(m_{ch} c_v T) = \frac{d}{dt}(\rho_g V_g \frac{R}{k-1} T) = \frac{d}{dt}(\frac{p_g V_g}{k-1}) = \frac{\dot{p}_g V_g + p_g \dot{V}_g}{k-1} \tag{10}$$

Where k denotes the adiabatic coefficient of the ideal gas, ρ_g denote the gas density, R denotes the ideal gas constant, V_g denotes the gas volume.

(2)The enthalpy into the gas cylinder is the energy flow from the catalyst bed, so it can be written as $\sum \dot{H}_{chi} = \sum \dot{H}_{cate} = \dot{m}_{decom} c_p T_{ADT}$. (3)Before the exhaust ports open, no mass flows out of the cylinder, so $\sum \dot{H}_{che} = 0$ (4)The heat loss in form of conduction or convection can be neglected because of the good insulation, so $\dot{Q}_{ch} = 0$. (5)The derivative of work is calculated as $\dot{W}_{ch} = A_g p_g \dot{x}_p$. Where p_g denotes the hot gas pressure. (6) The

loss between the catalyst bed and the gas cylinder can be neglected and the boundaries of the two control volumes are match, then $\dot{m}_{ch} = \dot{m}_{decom}$.

Using the above assumptions into the equation (9), the power balance can be rewritten as:

$$\dot{p}_g = \frac{k}{x_p}[\frac{R\dot{m}_{ch}T_{ADT}}{A_g} - p_g\dot{x}_p] \tag{11}$$

Since the pressure in the hot gas cylinder provides the pumping forces in the engine, the equation (11) is crucial to analyze the system.

3.5 The model of the compression process

When the engine is a natural exhaust system, the gas in the gas cylinder is compressed and assumed that this is an adiabatic process. The pressure in the cylinder can be expressed as:

$$p_g = p_{atm}(\frac{L}{L - x_p})^k \tag{12}$$

Where L denotes the whole stroke of the FPA, p_{atm} denotes the atmosphere pressure of the surroundings.

When the engine has an accessorial 2/2 exhaust valves, the left hot gas cylinder is connected to the atmosphere during this process. Therefore, the pressure in the left hot gas cylinder is the same to the atmosphere, and can be written as: $p_g=p_{atm}$.

4. THE CONVERSION EFFICIENCY

The efficiency is an important parameter to evaluate the performance of an engine. The conversion efficiency of the HTP can be defined as: $\eta_c = \frac{P_{out}}{P_{in}}$.

The output power P_{out} which represents the power lever of the engine can be expressed by the area of the hydraulic pump, A_f, the stroke of the FPA, L, the pressure of the pump, (p_{load}-p_{supply}), and the operation frequency, f. Thus the output can be written as:

$$p_{out} = 2A_f Lf(p_{load} - p_{\sup ply}) \tag{13}$$

The input power is defined by the energy stored in the HTP. It can be calculated through the maximum mass of hot gases in the gas cylinder.

$$P_{in} = A_g \times (L + L_c) \times \rho_{gas} \times f \times Q_{LHV} \tag{14}$$

Where L_c denotes the clearance length in the hot gas cylinder.

Thus the efficiency of the engine can be expressed as follows:

$$\eta_c = \frac{P_{out}}{P_{in}} = \frac{2(p_{load} - p_{\sup ply})}{\varepsilon \cdot (1 + L_c / L_e) \cdot \rho_{gas} \cdot Q_{LHV}} \tag{15}$$

Where ε denotes the area ratio which is defined as: $\varepsilon = \frac{A_g}{A_f}$.

5. INFLUENCE OF THE PARAMETERS

The engine is greatly influenced by the engine dimensions and operation parameters. The interesting performance values are the hot gas pressure, the power level of the engine, the conversion efficiency. The interesting design and operation parameters which determine the engine performance are the gas cylinder area, the hydraulic pump area, the mass of the FPA, the stroke, supply pressure, load pressure and the mass flow rate of the HTP. To evaluate the influence of the parameters on the engine performance can help the design and optimization of the prototype.

The studied parameter range is set as [20，25，33，50，75，100，150，200，300，400，500]%, though some range of them are not rational in a real system. When changing the given parameter, the other parameters keep in the reference values.

The basic reference parameters for the analysis are: the gas cylinder diameter D_g=50mm, the hydraulic pump diameter D_h=25mm, the piston rod diameter d_h=16mm, the stroke L=50mm, the mass of the FPA m_p=0.7kg, the load pressure P_{load}=7MPa, the supply pressure P_{supply}=0.3MPa, the fuel mass for one stroke m_{fueli}=3g.

Based on the above models, the influence of the parameters is plotted in figure 6.

The first chart shows the influence of the parameters on the pressure in the hot gas cylinder. The gas pressure decreases quickly with the increase of the area ratio, which is the ratio of the gas cylinder to the hydraulic pump, to keep the force balance on the FPA. The load pressure increase will results the increase of the gas pressure also to keep the force balance. The increase of the mass flow rate of the fuel will release more heat in one stroke, and thus leads to the increase in the gas pressure shown in figure 6. The increase of the stroke leads to a slight increase of the gas pressure and thus the FPA can have enough impulse to pass the exhaust ports. The supply pressure has slightly influence on the gas pressure though it will decrease the value of the gas pressure when it increases.

The second chart shows the influence of the parameters on the output power. The increase of the supply pressure decreases the output slightly. According to the equation (13), the other three parameters, the area of hydraulic pump, the stroke and the load pressure are proportionate to the output, so the increase of these three parameters can improve the output quickly, seen in figure 6. The larger these three parameters are, the larger power the engine exports.

The third chart shows the influence of the parameters on the efficiency. The increase of the area ratio can reduce the efficiency of the engine. And the increase of the load pressure can improve the efficiency. The other two parameters have slight influence on the efficiency.

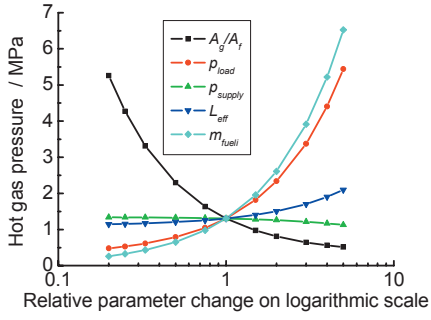

a) Influence on the gas pressure

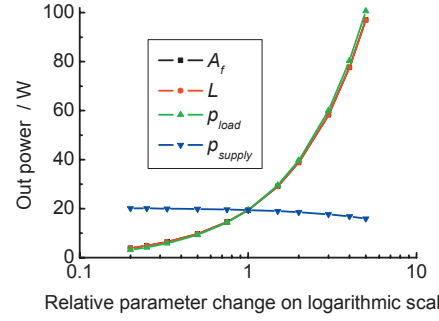

b) Influence on the output

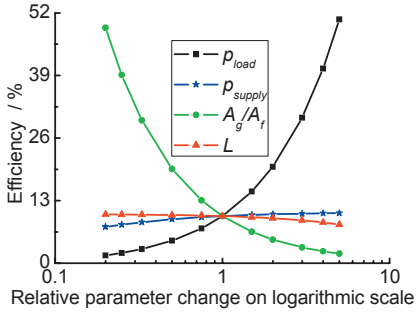

c) Influence on the efficiency

Figure 6 The influence of the parameters on the performance of the engine

Seen from the figure 6, to increase the load pressure and reduce the area ratio can improve the output and the efficiency of the engine. But to reduce the area ratio means to reduce the area difference of the gas cylinder and the hydraulic pump. And according to equation (3), the load pressure will be little when the gas pressure is the same. This will reduce the output. So when design the engine, these two parameters should be weighed carefully.

6. THE COMPARISON OF THE TWO SYSTEMS

A dynamic model is set up in the simulation software-AMESim. The two structure systems have the same components except the system with the accessorial exhaust device has two 2/2 valves. This increases the engine mass slightly but improves the operation frequency about 5 times. Therefore, the system output of the 2/2 exhaust valves is nearly 5 times to the natural exhaust system. Table 2 records the primary results of the systems from the simulation models. The HTP mass consumed in one stroke in 2/2 exhaust valves system is less than the natural exhaust system because of the less resistance in the opposite gas cylinder and thus leads to an higher conversion efficiency of the engine.

Table 2. Primary Results Comparison of the Two Systems

Primary Results	Structure	
	Natural Exhaust	2/2 Exhaust valves
Max Velocity [m/s]	1.84	2.52
Mean Velocity [m/s]	0.93	1.13
Max mass Flow Rate of HTP [g/s]	16.44	13.53
Consumed Mass of HTP [g]	0.74	0.55
Max Pressure of the Gas Cylinder [MPa]	1.142	0.853
Max Output [W]	160	800

The specific energy and the specific power are the two crucial parameters to evaluate the engines. For the short operation times, the specific power is more important than the specific energy. The larger specific power can run a heavier load in short time. Otherwise, for a long operation time, the most interesting parameter is the specific energy. The larger specific energy can keep the engine run for a longer time and provide more energy.

Ragone plot is employed to evaluate the performance of the two systems. A ragone plot is usually used to compare the performance of various energy storing devices. Specific energy and specific power are the interesting parameters in the chart. For the two compared systems here, they share the same components except the 2/2 valves.

The specific energy $\hat{E}$ can be defined as

$$\hat{E} = \frac{E_{sys}}{m_{sys}} = \frac{P_{out} t}{m_{fuel} + m_{\tan k} + m_{eng}} \tag{16}$$

Where E_{sys} is the output energy of the system, it is depended on the fuel consumed, and their relationship is

$$m_{fuel} = \frac{E_{sys}}{\eta_{sys} Q_{LHV}} \tag{17}$$

Thus the specific energy can be rewritten as:

$$\hat{E} = \left(\frac{1}{\eta_{sys} Q_{LHV}} + \frac{m_{\tan k} + m_{eng}}{P_{out} t}\right)^{-1} \tag{18}$$

The specific power $\hat{P}$ can be defined as

$$\hat{P} = \frac{P_{out}}{m_{sys}} = \frac{\hat{E}}{t} \tag{19}$$

Therefore, for a given operation time, one $(\hat{E}(t), \hat{P}(t))$ point is put on the ragone plot. For the two systems, the parameters used in computation are set in table 3. The parameters are from the sample design and used in the simulation.

Table 3. Parameter Values Used for Ragone Plot

Parameters	symbols	Natural Exhaust	2/2 Exhaust Valves
conversion ratio	η_{sys}	0.15	0.15
engine mass	m_{eng}	6kg	6.4kg
total mass in the tank	m_{fuel}	14kg	14kg
tank mass	m_{tank}	2.0 kg	2.0kg
lower heating value	Q_{LHV}	1.2MJ/kg	1.2 MJ/kg
maximum output	P_{out}	160W	800W

The ragone plot is plotted in figure 7 based on the above equations and the values.

Note that the 2/2 exhaust valves system has approximately 4.5 times the specific power and specific energy in the short operation time to the natural exhaust system. Thus the system with the valves can provide larger power to the load in short time. Because the two systems have the same volume fuel tanks, thus they can provide approximately the same energy in the end of the operation. Therefore, when the operation time is longer, say as 10 hours as shown in figure 7, the two systems have the approximate specific energy and specific power. The exhaust valves system has more advantages when the operation time is less than 1 hour.

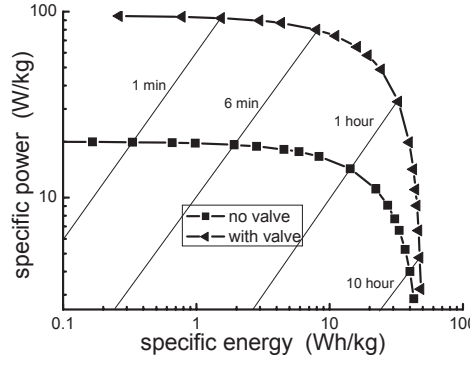

Figure 7 Ragone plot of the two power systems

The two systems can be further compared by the engine potential E_p , which can be expressed by the energy density of the HTP e_{fuel}, the conversion efficiency of the system η_{sys} and the power density of the engine p_{sys}, and then the engine potential is $E_p = e_{fuel}\,\eta_{sys}\,p_{sys}$.

The lower heating value of 90% HTP is Q_{LHV}=1.2MJ/kg. Because of the HTP stored in the tank, the energy density of the fuel is effectively reduced by the additional weight of the

tank, as given by $e_{fuel} = \frac{m_{fuel} Q_{LHV}}{m_{fuel} + m_{\tan k}}$. Then the energy density reduced from 1.2 to 1.05MJ/kg. The power density is found by measuring the maximum output power and normalizing mass of the system and thus the power density of the two systems are 20W/kg for the natural exhaust system and 95W/kg for the 2/2 exhaust valves system respectively.

Then for the natural exhaust system, the engine potential E_p =3.15 KJ·KW/kg^2, and for the 2/2 exhaust valves system, the engine potential E_p =14.96 KJ·KW/kg^2. The engine potential of the 2/2 exhaust valves system has almost 4.5 times to the natural exhaust system and can adapt to the large load in the same scale.

7. SUMMARY AND CONCULSIONS

The hydraulic free piston engine with liquid-propellant-power represents a new power source for the motion devices. The load pressure and the area ratio are vital in the engine design and crucial to the engine optimization. The employing of the 2/2 exhaust valves can not only improve the operation frequency, the output power and the conversion efficiency of the engine, but also can improve the stable operation of the engine. The employing of the ragone plot analysis is necessary to compare the performance of the power sources. The ragone plot intuitively shows the relationship between the operation time and the specific energy or the specific power.

ACKNOWLEDGEMENTS

This work is supported by the National Nature Science Fund of China (No.50425518) and the National basic Research Program of China (973) (No. 2007CB714000). The authors also acknowledge Doctor XIA Bizhong who sparks the idea of using the liquid-propellant-power in the hydraulic free piston engine.

REFERENCES

[1] Peter A. J.Achten. A review of free piston engine concepts [J]. SAE paper，941176:1836-1847.

[2] Hibi A，Hu，Y. A prime mover consists of a free piston internal combustion hydraulic power generator and a hydraulic motor [J]. SAE paper，930313，1993：1-10.

[3] Tikkanen S.Evolution of engine-hydraulic free piston engine[C].Acta Polytechnica Scandinavica, Mechanical Engineering Series N0.145,ESPOO 2000：1-147.

[4] XIA Bizhong, Wang Jinsong, FU Xin, etc. Development of a dual piston hydraulic free piston engine prototype and its compression ratio [J]. Chinese journal of mechanical engineering. 2006, Vol 42(3): 117-123. (In Chinese)

[5] Amendola, S.C., Petillo, P.J.. Engine cycle and fuels for same. US patent, #6250078B1,2001.

[6] Michael Goldfarb, Eric J. Barth, Michael A. Gogola. Design and energetic characterization of a liquid-propellant-powered robots [J]. IEEE/ASME transactions on mechatronics,2003,Vol.8(2):254-262.

[7]Eric J. Barth, Michael A. Gogola , Michael Goldfarb . Modeling and control of a monopropellant-based pneumatic actuation system [C]. Proceedings of the 2003IEEE International conference on robotics & automation, Taipei, Taiwan, September 14-19,2003:628-633.

[8] J. W. Raade, T.G. McGee，H. Kazerooni. Design, construction, and experimental evaluation of a monopropellant powered free piston hydraulic pump [C]. Proceedings of IMECE'03，2003(11): 651-658.

[9] J. W. Raade , H. Kazerooni. Analysis and design of a novel hydraulic power source for mobile robots [J]. IEEE transactions on automation science and engineering, Vol.2, No.3, July 2005:226-232

Adaptive active attenuation of narrow-band fluid borne noise in a simple hydraulic system

Lin Wang and Nigel Johnston
Department of Mechanical Engineering
University of Bath

ABSTRACT

This paper describes the active cancellation of fluid borne noise for several harmonic orders caused by a pump in a simple hydraulic system. A servo valve is applied as an actuator, which generates an anti-noise signal in real time. The filtered reference least mean square (FXLMS) adaptive control method with a notch adaptive filter is used. It was found that ripple reflection from both ends of the hydraulic circuit affected the performance and stability of the cancellation method. In order to execute the cancellation without any prior information about the dynamics of the hydraulic system, the online secondary path identification method was used. For efficiency and robustness, a fast block LMS (FBLMS) online secondary path identification algorithm was applied to give fast adaptive performance. However, an auxiliary white-noise signal applied to the system for this on-line method may increase residual noise.

In addition to the experiments, simulations of the active cancellation system were performed. The dynamic behaviour of the system was modelled using the method of characteristics (MOC). It was found experimentally that selected harmonics of fluid-borne noise could be attenuated by about 20dB under normal working conditions.

1. INTRODUCTION

The harmful effects of unwanted noise are becoming of more concern, especially in relation to factory workers. Fluid-borne noise, which is produced by hydraulic fluid power equipment, is one of the main sources of the unwanted noise in the workplace. Therefore effective methods for the control of fluid-borne noise are needed to realize comparatively quiet working conditions. Active noise control methods, especially adaptive control algorithms, may produce excellent results, surpassing those that can be achieved using passive noise control methods. The aim of this work was to develop efficient active control

Fluid Power and Motion Control 2008 Edited by Dr D N Johnston and Professor A R Plummer

methods for the attenuation of fluid borne noise on the basis of analysis and evaluation of different noise control algorithms.

2. LMS ADAPTIVE FILTER

A widely used method, which is known as least-mean-square (LMS) algorithm, deduced by Widrow and Hoff (1960), was developed. This algorithm is an important member of the "stochastic gradient algorithm" family [1] and inherits the concept of the method of steepest descent, but uses a special gradient estimation [2]. For cancelling the noise in a duct system using active control algorithms, an LMS filter is a simple and effective method. Figure 1 presents a schematic basic structure of an LMS filter to cancel the noise from a plant without prior knowledge of its dynamic characteristics.

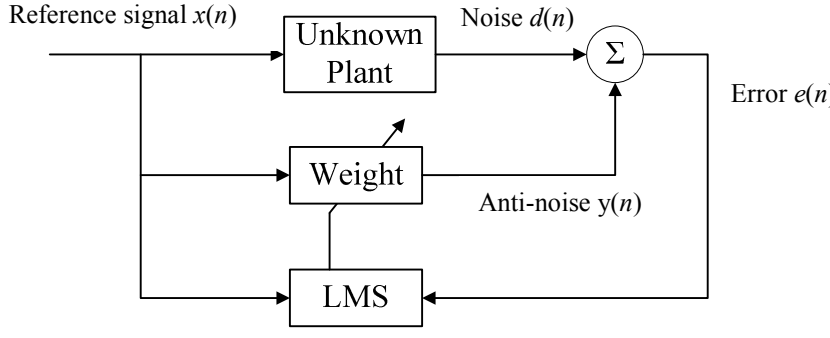

Figure 1 Noise cancellation using LMS adaptive filter

$x(n)$ is the reference signal picked up by a sensor, $d(n)$ is the noise that needs to be cancelled, $w(n)$ is a weighting vector, and $y(n)$ is anti-noise, all at the n^{th} sample time. The whole process can be represented using the following equations:

$$\overline{w}(n+1) = \overline{w}(n) + \mu \overline{x}(n)e(n) \tag{1}$$

Where,

$$\overline{w}(n) = [w_0(n) \quad w_1(n) \quad \cdots \quad w_{M-1}(n)]^T$$
$$\overline{x}(n) = [x(n) \quad x(n-1) \quad \cdots \quad x(n-M+1)]^T$$

and μ is the convergence factor, M is the length of the filter.

$$y(n) = \overline{w}^T(n)\overline{x}(n) \tag{2}$$

$$e(n) = d(n) - y(n) \tag{3}$$

It is assumed that both $d(n)$ and $x(n)$ are statistically stationary [3].

In practice, there are two types of noise in the environment, broadband and narrow band. In this work, as the periodic noise generated by a rotating pump is being considered, the narrowband feed forward adaptive LMS filter is utilized, as described in the next section.

3. FILTERED REFERENCE LMS (FXLMS) ADAPTIVE FILTER WITH ON-LINE SECONDARY PATH IDENTIFICATION

A simple practical structure using a narrowband LMS adaptive filter in a hydraulic system is presented in Figure 2. Rather than picking up a noise signal from a sensor at the entrance of the duct, for narrowband application in this paper the reference signals are synchronized by mounting a sensor on the pump shaft to give one pulse per revolution [4]. Therefore, the fundamental frequency of the harmonic noise can be obtained.

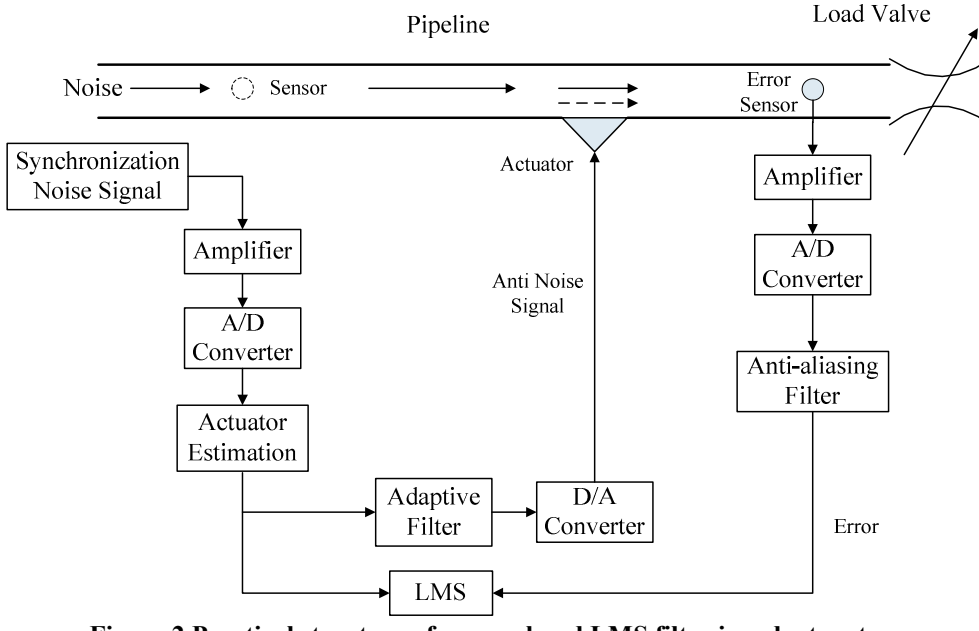

Figure 2 Practical structure of narrowband LMS filter in a duct system

As shown in Figure 2 the anti-noise signal is not applied into the duct directly but through a 'secondary path', which contains D/A and A/D converters, an anti-aliasing filter, amplifiers and an actuator. This can result in a complex transfer function between the actuator signal and the response at the error sensor. It is necessary to compensate for the transfer function of these devices in order to ensure convergence of the adaptive filter and hence stability.

To ensure that the adaptive filter converges to a desired solution, a compensation transfer function should be added in the controller to cover the response of the secondary path. A filtered reference LMS (FXLMS) adaptive filter, which can overcome this problem, is shown in Figure 3 (disregard for now the blocks within the dotted line).

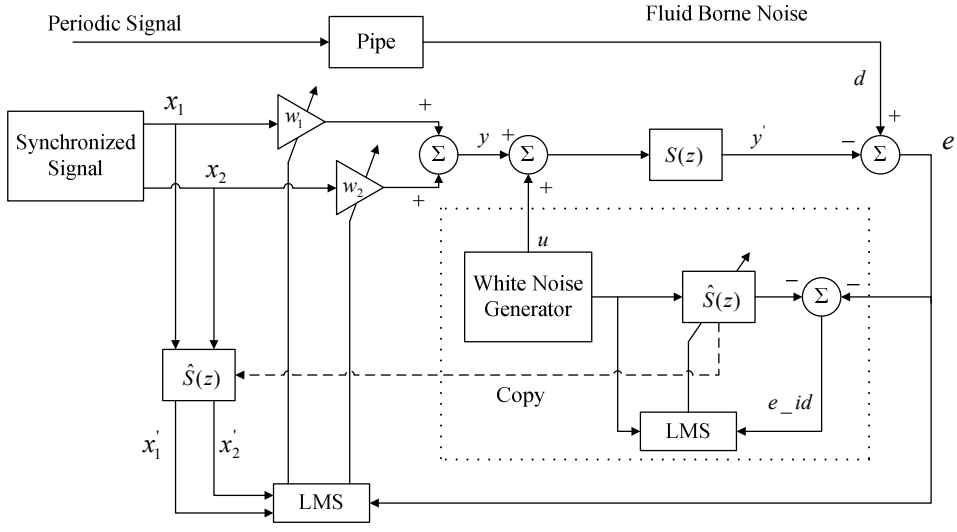

Figure 3 FBN cancellation using FXLMS with on-line time-domain identification

$S(z)$ represents the secondary path transfer functions as mentioned above. In this application the narrowband LMS filter acts as a notch filter, as this is efficient and simple [5, 2]. Instead of $\bar{x}(n)$, at the n^{th} time point x_1 and x_2 are used as reference input signals. Comparing with Figure 1 and equation (1) to (3):

$$x_1(n) = A\sin(2\pi f_j n\Delta t)$$
$$x_2(n) = A\cos(2\pi f_j n\Delta t)$$

Where A is the amplitude, f_j is the j^{th} harmonic order of the fundamental frequency and Δt is the sampling period.

$x_1'(n)$ and $x_2'(n)$ can be obtained by convolving $\bar{x}_1(n)$ and $\bar{x}_2(n)$ with $\hat{S}(z)$.

$$x_1'(n) = \bar{x}_1(n)\hat{S}(z)$$
$$x_2'(n) = \bar{x}_2(n)\hat{S}(z)$$

Where
$$\bar{x}_1(n) = [x_1(n) \quad x_1(n-1) \quad \cdots \quad x_1(n-M+1)]$$
$$\bar{x}_2(n) = [x_2(n) \quad x_2(n-1) \quad \cdots \quad x_2(n-M+1)]$$

These values are accumulated in a buffer.

$\hat{S}(z)$ is the estimation vector of the impulse response of the secondary path $S(z)$, and can be represented as:

$$\hat{S}(z) = [\hat{s}_1(n) \quad \hat{s}_2(n) \quad \cdots \quad \hat{s}_M(n)]^T$$

M is the length of the secondary path impulse response vector.

$$w_1(n+1) = w_1(n) + \mu x_1'(n)e(n)$$
$$w_2(n+1) = w_2(n) + \mu x_2'(n)e(n)$$
$$\text{And} \qquad e(n) = d(n) - y'(n)$$
$$y(n) = w_1(n)x_1(n) + w_2(n)x_2(n)$$
$$y'(n) = \overline{y}(n)S(z) \quad \text{(assuming } u \text{ is zero)}$$

Where
$$\overline{y}(n) = [y(n) \quad y(n-1) \quad \cdots \quad y(n-M+1)]$$

The convergence condition for this FXLMS adaptive filter is only that the phase difference between $S(z)$ and $\hat{S}(z)$ is in the range of $\pm 90^\circ$ [3].

Generally there are two methods of estimating $S(z)$: off-line and on-line algorithms in real time. For the off-line identification case, assuming the dynamic characteristics of the secondary path are time invariant but unknown, this can be realized using the strategy shown in Figure 1 prior to the noise cancellation, with white noise applied as the reference and excitation signal. However, in most applications the actuator and system's dynamic properties are time-varying or change with different working conditions. Therefore the on-line algorithm with FXLMS adaptive filter is discussed and applied in this paper.

One on-line secondary path identification method with auxiliary random noise signal is illustrated in Figure 3 including the blocks within the dashed line [6]. $\hat{S}(z)$ is the estimation of the impulse response of $S(z)$, which can be achieved by adding an extra simultaneous LMS adaptive filter and which can be used for compensation at the same time. The random noise *u* is uncorrelated with *d* and is supplied by a white noise generator with zero mean and low power level. This identification process is also realized using equations (1) to (3). However, there is a problem: the control flow from the actuator is not y' but $y'+u$, therefore the error signal *e_id* used to adapt $\hat{S}(z)$ now is $u * S(z) - u * \hat{S}(z) + (d - y')$. In the third part of this equation, *d* consists of multiple harmonic frequency signals from the pump, which may not have been cancelled by y'. These signals will increase on-line identification time and may result in instability of the whole system. Furthermore, this problem may still occur during the adaptive process if $(d - y')$ becomes small. There are several methods that have previously been used to solve this problem [7, 8, 9]. Because of its robustness and efficiency, the fast block LMS

(FBLMS) adaptive algorithm is implemented in this work in the frequency domain [10]. Figure 4 illustrates the structure of FBLMS, which can replace the dashed line block in Figure 3. In this application the block length L is the same as M, which is the length of the weighting function [1]. This length of weighting function strongly affects the processing time and limits the maximum sample rate. The required length of the weighting function depends on the working conditions in the hydraulic circuit which will be discussed in the next section.

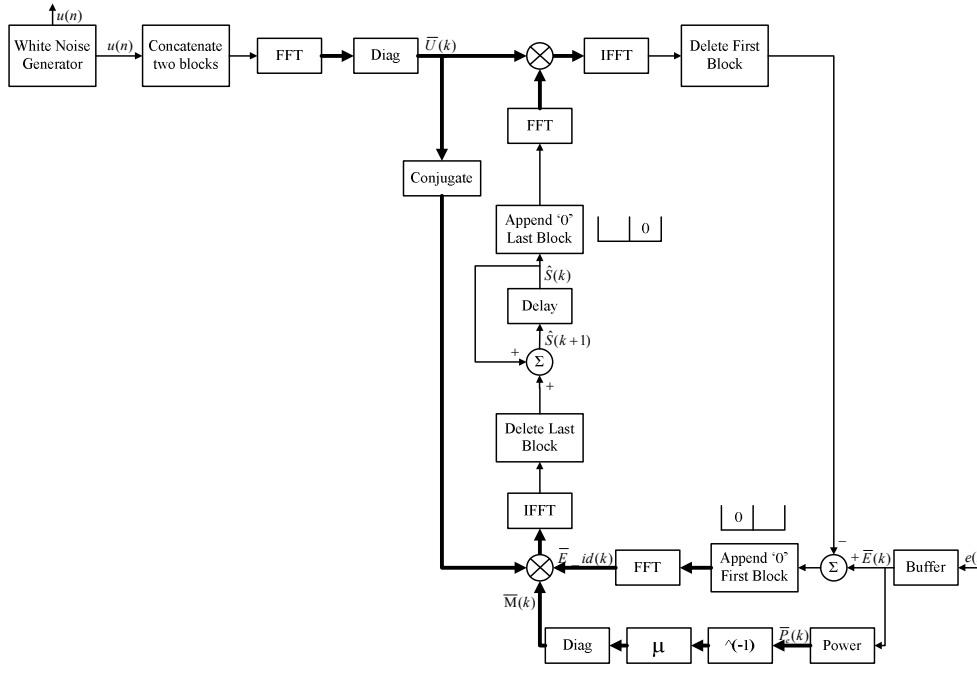

Figure 4 Frequency-domain secondary path identification

In this algorithm, rather than sample by sample, the signals are processed block by block. The weighting function is not updated until the next block. Therefore the last term on the right side in equation (1) becomes:

$$\mu \sum_{i=0}^{L-1} \bar{x}(kL+i)\, e(kL+i)$$

$$= \mu \sum_{i=0}^{L-1} x_j(kL+i-j)\, e(kL+i)$$

where $j = 0, 1, \cdots, M-1$. This is a cross correlation form between x and e.

Equation (2) becomes: $\overline{y}(kL + i) = \overline{w}^T(k)\overline{u}(kL + i)$

$$= \sum_{j=0}^{M-1} w_j(k)u(kL + i - j)$$

where $i = 0, 1, \cdots, L-1$. This is a convolution form between *w* and *u*.

In order to increase the computation speed, fast convolution and fast cross correlation using the "overlap-save" method are applied in the frequency domain [1, 11].

In Figure 4 the frequency domain calculation is denoted by the thick line. The whole computation process can be described by following equations:

$$\overline{U}(k) = diag\{FFT[\overline{u}(k-1) \quad \overline{u}(k)]\}$$

$$\hat{S}(k+1) = \hat{S}(k) + IFFT\{conj[\overline{U}(k)]\overline{\mathrm{M}}(k)\overline{E}\_id(k)\}_{last\_block}$$

where *k* denotes the number of the block, and $\overline{E}\_id$ is the block error signal used to obtain secondary path estimation:

$$\overline{E}\_id(k) = FFT\left\{ \begin{bmatrix} 0_{L\times 1} \\ \overline{E}(k) - IFFT\left[\overline{U}(k) \cdot FFT\begin{bmatrix} \hat{S}(k) \\ 0_{L\times 1} \end{bmatrix} \right]_{last\_block} \end{bmatrix} \right\}$$

L is the length of the block and weighting function.

Unlike Eriksson's method in which the step size μ is a constant value during the adaptive process, the convergence factor is an adaptive function $\overline{\mathrm{M}}(k)$ of the estimated power of *e*, which can be found in Figure 3. This is deduced in the frequency domain and assigned into individual frequency bins in order to increase convergence speed and stability.

$$\overline{\mathrm{M}}(k) = diag\left[\mu \frac{1}{\overline{P}_e(k)} \right]$$

Where $\overline{P}_e(k)$ is the power of the error signal *e*. This is estimated using a first-order low pass filter:

$$\overline{P}_e(k+1) = \gamma\overline{P}_e(k) + (1-\gamma)\left| FFT\begin{bmatrix} 0_{L\times 1} \\ \overline{E}(k) \end{bmatrix} \right|^2$$

γ controls the amount of smoothing of $\overline{P}_e(k)$. The initial value of $\overline{P}_e(k)$ can be set to zero or small positive value in this case.

As mentioned above, the selection of weighting function length for secondary path identification is critically associated with system behaviour, specifically the decay time of the actuator impulse response. The length of the weighting function needs to be sufficient

to capture the important features of the impulse response. Therefore the dynamic characteristic of the secondary path was investigated by computer simulation. The simulation model was built up using the method of characteristics (MOC) [12] to investigate the effect of different working conditions.

The impulse response of the actuator in the hydraulic system was deduced using the signal detected from the sensor downstream in Figure 2. The impulse response is affected by the transfer function of the actuator as well as the hydraulic system transfer function. This is strongly affected by wave propagation in the pipe and the reflections from both ends of the pipe, and large reflections may give a slow transient decay. The decay rate is affected by valve flow and pressure drops, fluid properties, length of pipe and sensor position [13]. Generally a small valve flow and high pressure drop may result in a large reflection and slow transient decay. In Figure 5 the simulated actuator impulse response is plotted with different reflection levels.

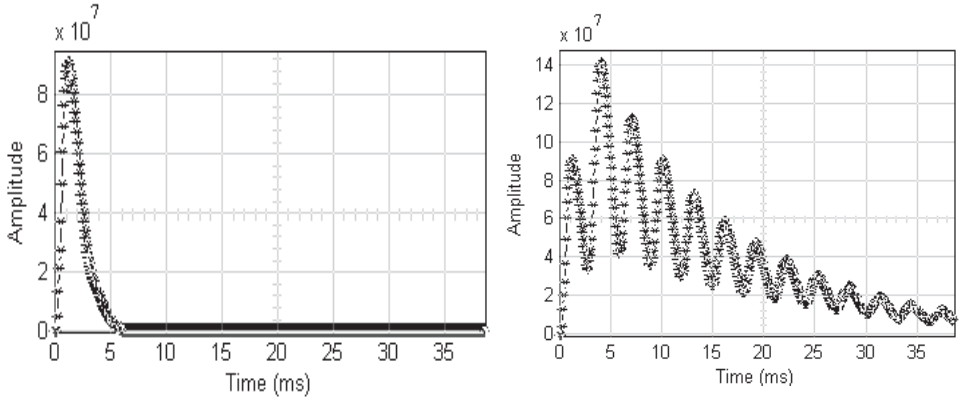

(a) small reflection **(b) large reflection**

Figure 5 Actuator impulse responses with different reflection level in the pipe

In this model an arbitrary actuator transfer function with high damping ratio is applied and 512 is selected as the length of the actuator impulse response for identification.

Firstly the load valve was set to give a reflection coefficient amplitude of approximately 0.1. A small reflection is given from this situation and the result is shown in Figure 5(a). Then setting the load valve to give a reflection coefficient amplitude of approximately 0.9, more reflections were predicted at the error sensor after some delays affected by pipe length and error sensor position. From the impulse response result illustrated in Figure 5(b) under this condition, the actuator can be represented as a transfer function with low damping ratio with delays. Hence the length of impulse response in the controller must be long enough to cover a sufficient part of the dynamic characteristic of the actuator and system to obtain accurate compensation and make the system stable. In addition, a suitable value of real time sampling frequency is also a critical factor in order to obtain accurate secondary path identification whilst being sufficiently high compared to the maximum harmonic frequency of the fluid borne noise to be cancelled.

4. REAL TIME TEST USING A PUMP AND ANALYSIS OF RESULTS

The algorithm discussed above was applied on a test rig using a real pump which was running at 16.47 Hz (approximately 1000 rev/min). The pump was of the axial piston type with three pistons, a maximum pressure of 56 bar and a maximum flow rate of 12.2 L/min. A high response servo valve was used as the actuator, with a supply pressure of 105 bar, supplied remotely from another pump. A pressure sensor was located a short distance downstream of the servo valve. The pipe was 10mm in diameter and 4 metres long with a load valve at the end. A simple structure of the rig is shown in Figure 6. The oil flow route is plotted using thick lines and electrical signals are denoted by thin lines.

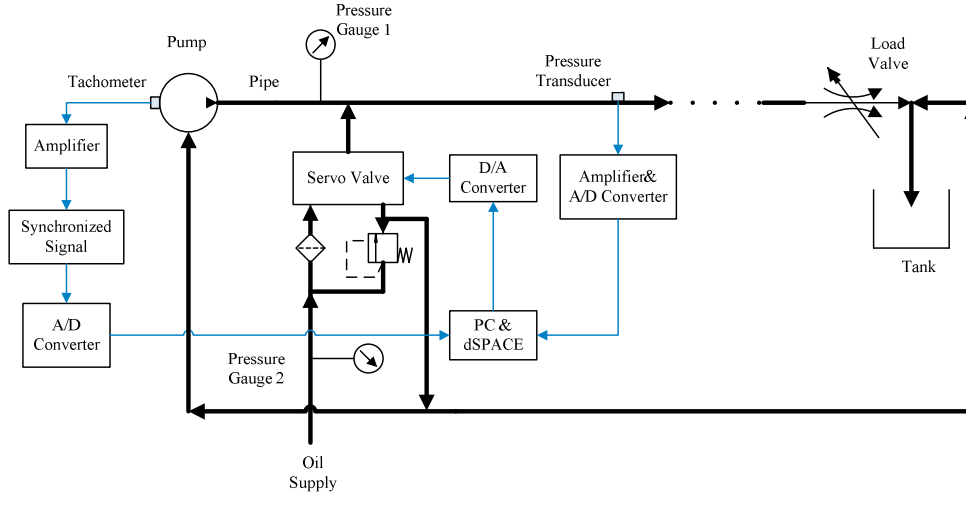

Figure 6 Simple structure of test rig

Firstly the secondary path response including the servo valve, amplifiers A/D and D/A converters was identified using the off-line method without the pump running, with 25bar applied in the pipe from the remote pump. The white noise was generated using a dSPACE® model 1005 system. The secondary path amplitude and phase spectrum was also deduced from the ratio of the output and input signals in the frequency domain using Hanning windows. A comparison between this (named Frequency domain) and the Fourier transform of the weighting function is plotted in Figure 7, and a well matched result is obtained. From this figure, the performance at with different frequencies can also be investigated. In this experiment the length of the weighting function was 128 and the sampling frequency was 3125 Hz.

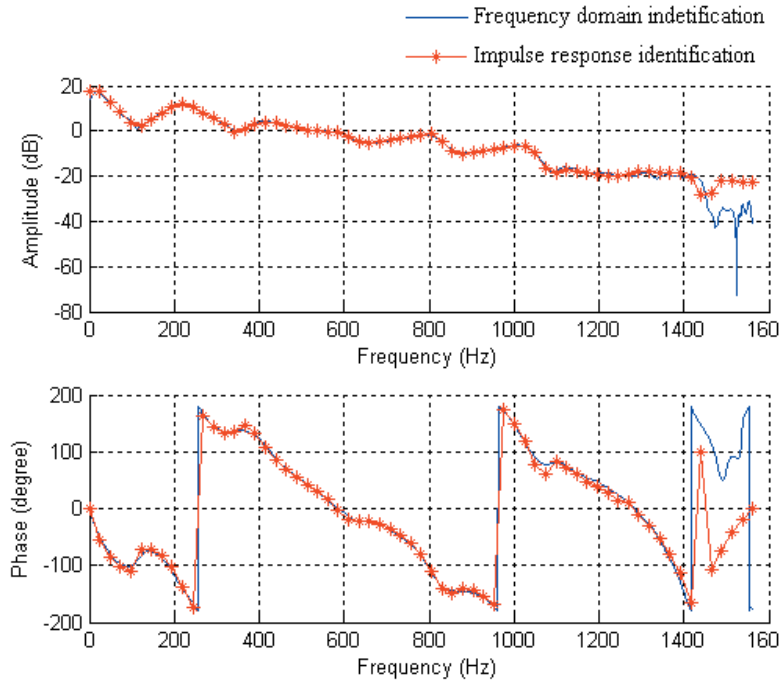

Figure 7 Comparison between Frequency domain and offline identification method, 25 bar pressure

Secondly, the FBLMS online identification algorithm discussed above was realized on the same test rig. White noise was used as the auxiliary signal, with a low power level compared with that of the fluid borne noise. Both the control signal and the white noise were generated by the servo valve. As the pump was a three piston device, the fundamental frequency of the fluid borne noise was three times the pump rotating speed. In order to cancel more harmonic components, x_1, x_2 and w_1, w_2 in Figure 3 are replaced by vectors, which can be written as:

$$\bar{x}_1(n) = \begin{bmatrix} x_1^1 & x_1^2 & \cdots & x_1^j \end{bmatrix};\ \bar{x}_2(n) = \begin{bmatrix} x_2^1 & x_2^2 & \cdots & x_2^j \end{bmatrix}$$
$$\bar{w}_1(n) = \begin{bmatrix} w_1^1 & w_1^2 & \cdots & w_1^j \end{bmatrix};\ \bar{w}_2(n) = \begin{bmatrix} w_2^1 & w_2^2 & \cdots & w_2^j \end{bmatrix}$$

j is the number of harmonic components to be cancelled, and hence the control signal y can be presented as:

$$y = \bar{x}_1(n)\bar{w}_1^T(n) + \bar{x}_2\bar{w}_2^T$$

9 orders of the harmonic frequencies were attenuated using this method under two different pressures which were set using the load valve.

The secondary path impulse response was also obtained and compared with that using the offline identification method, and is shown in Figure 8. The offline and online identification methods agree well. From these experimental results, an accurate impulse response could be obtained using the online identification algorithm with a buffer length of 128 and sampling frequency of 3125 Hz, which means fine compensation and stability of the whole system. On the other hand, the higher load pressure results in larger reflections and a slower decay, as discussed previously.

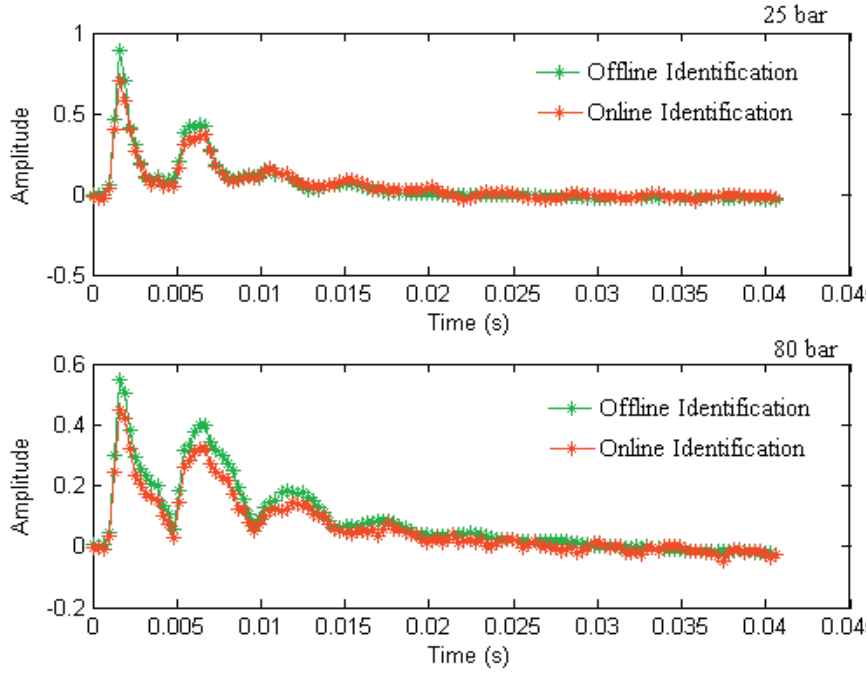

Figure 8 Comparison of secondary path impulse response between offline and online methods with different pressures

The measured fluid-borne noise spectra with active cancellation of the first nine pumping harmonics are shown in Figures 9 and 10, together with the corresponding spectra without cancellation. The cancellation frequencies are marked with their order number relative to the shaft frequency. It can be seen that the signals at these frequencies are reduced by typically 20dB to insignificant levels when cancellation is applied. There is a slight increase in some higher frequency, uncancelled harmonics, which may be due to non-linearity and distortion in the servo valve response.

The algorithm is able to adapt to changes in the system conditions. It was found that the adaptive setting time for cancellation is less than 1 second in this experiment for small changes of the load pressure. However it was found that the system could go unstable following sudden, large changes in the working conditions.

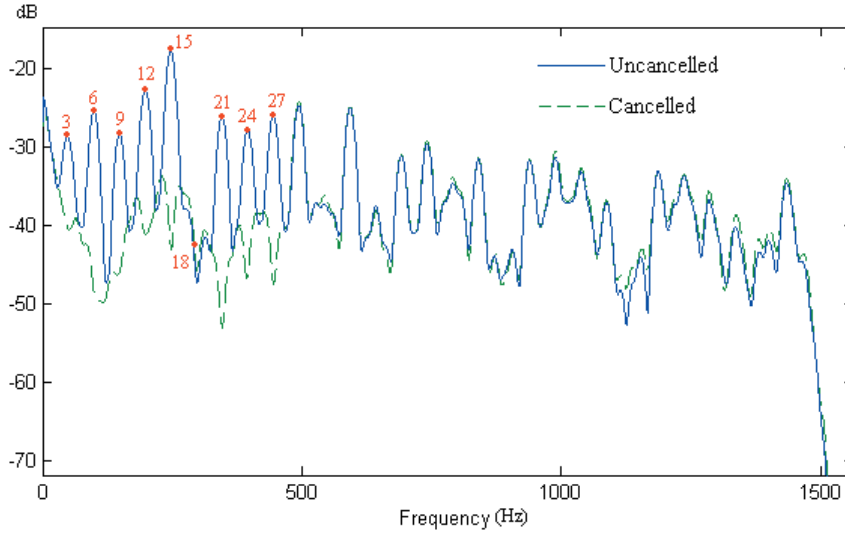

Figure 9 Measured frequency spectra with cancellation of 9 harmonics at 25 bar

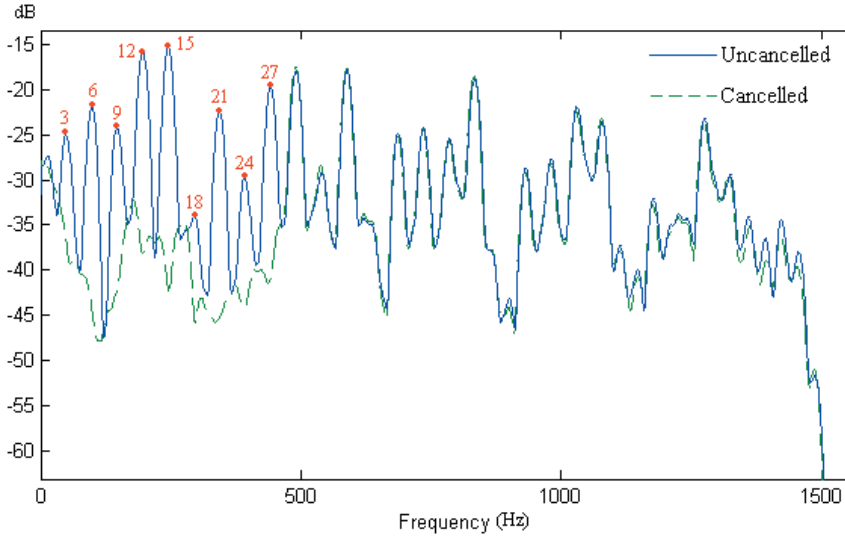

Figure 10 Measured frequency spectra with cancellation of 9 harmonics at 80 bar

Because of computing limitations of the dSPACE® 1005 system, it was only possible to cancel 9 orders of fluid borne noise. A more powerful processor may give cancellation of more harmonic orders with increased sampling frequency; it should be remembered that the pump that was used had only three pistons and a relatively low pumping frequency of 50 Hz.

Although the fluid-borne noise is reduced very effectively at the cancellation frequencies, the effect on structure-borne and airborne noise may not be as great. This may be due to a number of reasons: noise may be caused by direct mechanical vibration from the pump's moving parts; additional vibration may be caused by the motion of the servovalve; the higher frequency components may be more significant; and additional noise may be caused by the hydraulic supply for the servovalve. In this example, whilst a difference in the timbre of the sound could be noticed, there was not a significant reduction in sound level. It is likely that it would not be the practical to use a servovalve as the cancellation device in a real application, for reasons of cost, contamination tolerance, bandwidth, efficiency and complexity. A piezoelectrically operated actuator or valve may be a more suitable commercial solution. Nonetheless, significant improvements in fluid-borne noise levels have been achieved here, so the method shows sufficient promise to be a solution to some noise and vibration problems, particularly if a faster computing system and actuator are available.

5. CONCLUSIONS

This paper presents a method for cancelling fluid borne noise using a FXLMS algorithm. FBLMS online secondary path identification was used, which does not require any prior information about the dynamic response of the actuator and system. Wave reflections in the hydraulic system needed to be considered and the length of the impulse response identification vector needed to be sufficient to capture the reflections in the impulse response. The impulse response can be obtained accurately using an online identification method. Very effective reduction of fluid-borne noise could be achieved at selected cancellation frequencies. The system can adapt to changes in conditions and is reasonably robust for small or gradual changes; however instability can occur for large, sudden changes in working conditions.

Further work is needed to develop a more suitable actuator to act as a cancellation device, perhaps using piezoelectric technology. It would then be desirable to implement the technique on a real application with a known noise problem.

REFERENCES

[1] Haykin, S., "*Adaptive filter theory*", Prentice-Hall Inc, 2002.

[2] Widrow, B. and Stearns, S.D., "*Adaptive signal processing*", Prentice-Hall Inc, 1985.

[3] Kou, S.M. and Morgan, D.R., "*Active noise control systems algorithms and DSP implementations*", John Wiley & Sons Inc, 1996.

[4] Chaplin, B., "*The cancellation of repetitive noise and vibration*", Proceeding of Inter-noise, 1980, pp.699-702.

[5] Glover Jr, J.R."*Adaptive noise canceling applied to sinusoidal interferences*", IEEE transaction on acoustics, speech and signal processing, Vol. ASSP-25, No.6, December, 1977.

[6] Eriksson, L.J. and Allie, M.C. "*Use of random noise for on-line transducer modelling in an adaptive active attenuation system*", Journal of Acoustical Society of America, 85, pp.797-802, 1989.

[7] Kou, S.M. and Vijayan, D. "*A secondary path modelling technique for active noise control systems*", IEEE transaction on speech and audio processing, Vol. 5, No.4, July, 1997.

[8] Zhang, M., Lan, H. and Ser, W. "*A robust online secondary path modelling method with auxiliary noise power scheduling strategy and norm constraint manipulation*", IEEE transaction on speech and audio processing, Vol. 11, No.1, January, 2003.

[9] Shynk, J.J. "*Frequency-domain and multirate adaptive filtering*", IEEE Signal Processing Magazine, Vol.9, Issue 1, January, 1992.

[10] Hillis, A.J. "*Adaptive control of active engine mounts*", Ph.D thesis, University of Bristol, 2004.

[11] Ifeachor, E.C. and Jervis, B.W. "*Digital signal processing a practical approach*", Addison-Wesley Publishing Company Inc, 1993.

[12] Johnston, D.N. "*Efficient methods for numerical modeling of laminar friction in fluid lines*", Journal of Dynamic System, Measurement and Control, ASME, Vol.128, December, 2006.

[13] Johnston, D.N. "*Measurement and prediction of the fluid borne noise characteristics of hydraulic components and systems*", Ph.D thesis, University of Bath, 1987.

Session 8
Control II

The design and study of Fuzzy Parameters Self-tuning PID temperature Controller for Large-Scale Hydraulic power unit

CHEN Chao, GONG Guofang, YANG Huayong, FENG Bin
State Key Laboratory of Fluid Power Transmission and Control, Zhejiang University, Hangzhou, 310027 China

ABSTRACT

A fuzzy parameters self-tuning PID controller was designed to obtain the high control precision of the oil temperature in the large scale hydraulic power unit. The flow rate in the pump unit is up to 2157L/min, and the total power is 700kW.
Considering the feature of the large time delay, the nonlinearity, and slow-time varying for hydraulic temperature field, the previous control scheme for large time delay course is inadequate. Firstly, the conventional PID control algorithm is sensitive to time-varying parameters of the system, it depends on system model. What's more, the steady-state accuracy of mere fuzzy control is not enough. In order to avoid the shortcomings of them, parameters self-tuning fuzzy PID control algorithm is studied. By online Fuzzy reasoning, three PID parameters are adjusted. This will ensure the system to have more excellent performance in responsivity, stability and accuracy.
The mathematical modeling of the Fuzzy PID controller is accomplished, and the simulation is completed by Simulink and Fuzzy toolbox in Matlab environment. The temperature control experiment is conducted in the actual hydraulic power unit with high power and flow. Both the simulation and experimental results show that the controller is effective in oil temperature control.
Keywords: Fuzzy PID control, Parameters Self tuning, Temperature control, Hydraulic power unit.

1. INTRODUCTION

The oil temperature control of hydraulic system is very important in some applications. This paper presents a temperature controller for a large hydraulic power unit. The power unit had three different operation conditions. It was a totally enclosed system with closed pressurized oil tank. The flow rate in the power unit was up to 2157L/min, and the total power was 700kW. The temperature control system had a high performance requirement owing to characteristics of high flow and power.
The temperature field between the hydraulic system and heat exchanger is nonlinear, time-varying and with large time delay (1). Considering the complexity and randomicity of the heat exchange process related to hydraulic system temperature field, the previous control schemes for large time delay course such as the Smith predicted controller and Dahlin algorithm controller show performance limitations (2-4). This hydraulic system has three different working conditions. Moreover, some system parameters will vary after long-time

Fluid Power and Motion Control 2008 Edited by Dr D N Johnston and Professor A R Plummer

running owing to pipes corrosion and decrease of motor efficiency etc. Thus, the temperature control system must be independent of system model, and robust for diverse conditions. This paper proposes a fuzzy parameters self-tuning PID controller. Firstly, the conventional PID control algorithm is sensitive to time-varying parameters of the system. It depends on system model as well as shows poor performance in the dynamic response (5). What's more, the steady-state accuracy of fuzzy proportional control is not enough (6). The fuzzy PID controller can avoid the shortcomings of them and integrate their advantages. It ensures the system to have better performance in responsivity, stability and accuracy. The simulation of the controller was accomplished, and the temperature control experiments were conducted in the actual hydraulic power unit. The experimental and simulation results showed that the controller was simple in structure, easy in implementation, and better in performance than conventional controls.

2. WORKING PRINCIPLE OF TEMPERATURE CONTROL SYSTEM

The large-scale hydraulic power unit had three different operation conditions. It was a totally enclosed system with closed pressurized oil tank. The overall input electrical power was up to 700kW. The pressurized oil supply involved control oil and power oil. Their respective highest flow rate was 355L/min and 1802L/min. So the hydraulic system return oil in all can be up to 2157L/min. The set point of the oil temperature was 45℃ with an accuracy of ±2℃. The overall cooling water owned a flow rate of 45m^3/h. The temperature control system had a high performance demand owing to characteristics of high flow and power. The principle of temperature control system was presented in Fig. 1.

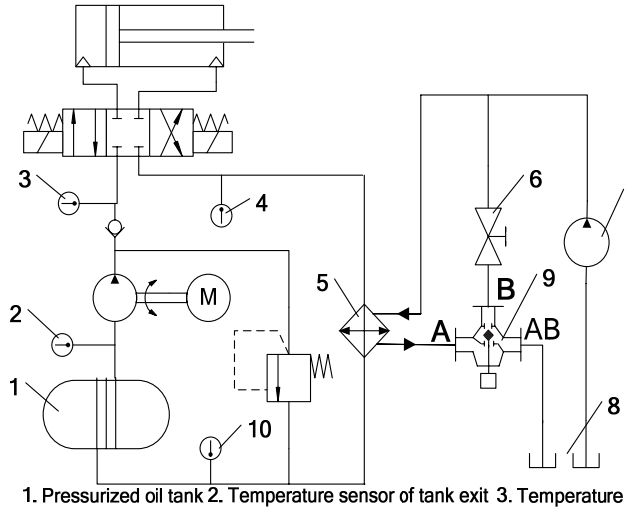

1. Pressurized oil tank 2. Temperature sensor of tank exit 3. Temperature sensor of power oil (main set point) 4. Temperature sensor of return oil 5. Plate heat exchanger 6. Static-state balance valve 7. Centrifugal water pump 8. Water tank 9. Three-way proportional water valve 10. Temperature sensor of tank return opening

Fig. 1 Principle of temperature control system for hydraulic power unit

In the temperature control system, the plate heat exchanger was selected for cooling components, and the cooling water was supplied by centrifugal water pump. The

temperature of power oil 3 was defined as the main set point. The cooling effect of the heat exchanger would determine the temperature of this set point, if the relief valve pressure and pumps flow rate were fixed. By adjusting the three-way proportional valve spool position, the temperature control system can regulate the flow of water through the heat exchanger (0~45m^3/h), which will change the heat transfer capability of heat exchanger. Thus the purpose of temperature control was achieved. Simultaneously, the temperature of tank exit 2, return oil 4 and tank return opening 10 were monitored, as the assistant control reference.

3. DESIGN OF FUZZY PID CONTROLLER

The conventional PID control methodology possesses advantages of simplicity, good stability and high reliability. It is especially applicable to linear system without time varying. However, it's sensitive to time-varying parameters as well as deficient in the system dynamic response. On mere fuzzy control, the robustness and fast responsivity can't cover up its disadvantage of poor steady-state accuracy. The fuzzy PID hybrid control strategies combine their advantages together, avoiding their respective shortcomings simultaneously.

3.1 Mathematical model of controlled object

The temperature control system is composed of generalized controlled object and temperature controller. The generalized controlled object includes temperature sensors, adjusting valves etc. besides technological object. The dynamic characteristics of the generalized controlled object can be defined by approximate forms with pure time delay. As to this hydraulic power unit, the transfer function of the controlled object was described as the first-order inertia link with pure time delay. It was expressed by:

$$\begin{cases} \mathrm{G(s)} = \dfrac{K}{1+Ts} e^{-\tau s} = \dfrac{3.2}{1+300\mathrm{s}} e^{-80\mathrm{s}} \\ K = \mathrm{y}(\infty)/x(\infty) \end{cases} \tag{1}$$

Where K represents the system gain, T is the time constant, τ represents the lag of time, x(t) is the input step signal of the experimental response curve method, and y(t) represents the system output of that method. The principle of this method is shown in Fig.2 (7). By making tangent in the inflexion of the response curve, values of τ, T could be found out from the figure. The gain coefficients are determined as K=3.2, T=300s, τ=80s.

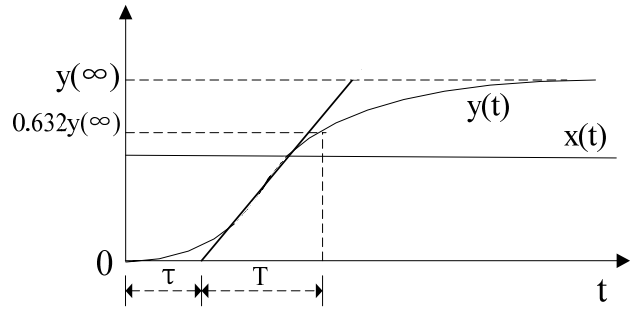

Fig. 2 Principle of experimental response curve method

3.2 System structure

The structure of the parameters self-tuning fuzzy PID controller is depicted in Fig. 3. Where r(t) is the set value and y(t) is the output value. Likewise the conventional PID algorithm, the input variables are the temperature error E and its derivatives EC. For the purpose of obtaining appropriate control parameters for different E and EC, three PID parameters K_p, K_i, K_d (refer to gain coefficients of PID controller) are online self tuned by fuzzy inference. Thus, the controlled object will gain high-quality static and dynamic behavior.

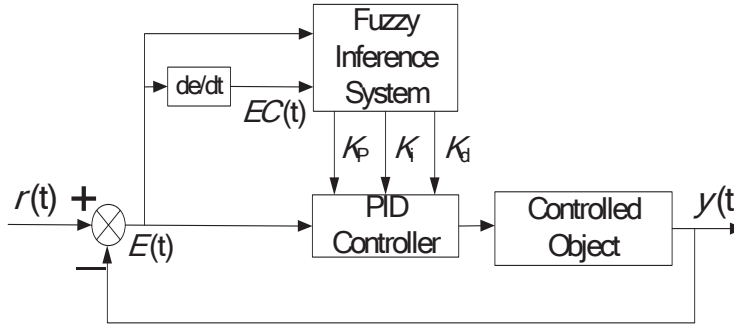

Fig. 3 Hybrid fuzzy–PID control structure

3.3 Fuzzy controller design

The fuzzy controller used for adjusting the PID parameters had two inputs of *E and EC,* three outputs of $\triangle K_p$, $\triangle K_i$, and $\triangle K_d$ (refer to increment of gain coefficients). These inputs and outputs fuzzy sets were marked with the following labels: positive big (PB), positive medium (PM), positive small (PS), zero (ZO), negative small (NS), negative medium (NM), and negative big (NB). {NB, NM, NS, ZO, PS, PM, PB} Their numerical range is in relation to [-6, 6]. According to the output ranges, ranges of reference input values for E and EC were [-48, 48] and [-0.4, 0.4] respectively. Accordingly, the gain coefficients for error and error derivatives were determined as: K_e=1/8, K_{ec}=15.

The membership functions (μ) and their corresponding labels of error (E), error derivatives (EC) and outputs ($\triangle K_p$, $\triangle K_i$, $\triangle K_d$) are presented in Fig. 4.

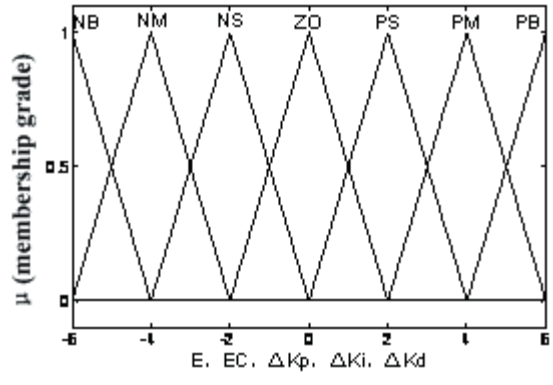

Fig. 4 Membership functions of E, EC, $\triangle K_p$, $\triangle K_i$ and $\triangle K_d$

In the triangular membership functions, membership grade of any input or output value can be represented by:

$$\begin{cases} \mu_{LV}(a) = (a-p)/(q-p) & p \le a \le q \\ \mu_{LV}(a) = (r-a)/(r-q) & q \le a \le r \\ q = (p+r)/2 \end{cases} \tag{2}$$

In Eq. (2), a represents any input or output value, LV refers to different rules in corresponding conditions and μ is the membership function. P represents the lower limit of every variable in a particular variation section. Similarly, r represents the upper limit of every variable in a particular variation section.

The reasoning rules for PID parameters are as follows:

When the sign of E is same to that of EC, it suggests that the absolute value of error is increasing. If $|E|$ is large, large K_P should be adopted to make the $|E|$ decrease as soon as possible. Medium K_d and small K_i can be chosen to improve the dynamic performance. If $|E|$ is small, the moderate control can be used to change the error development trend. So K_P ought to be medium. In the meantime, employ of big K_i and small K_d will keep the control system stable.

When the sign of E is reverse to that of EC, it suggests that the absolute value of error is decreasing. If $|E|$ is large, implementing the moderate control is appropriate to decrease $|E|$ quickly. Medium K_d, K_P and small K_i are selected to improve the dynamic and steady performance. If $|E|$ is small, the small control can be used. So K_P and K_d ought to be small, and K_i is big to avoid arising oscillation.

According to the reasoning rules for PID parameters, the fuzzy rules for $\triangle K_p$, $\triangle K_i$ and $\triangle K_d$ could be obtained. Taking $\triangle K_p$ for instance, the rules are expressed as Table 1.

Table 1 Fuzzy logic rules for determination of $\triangle K_p$

EC / $\triangle K_p$ / E	NB	NM	NS	ZO	PS	PM	PB
NB	PB	PB	PM	PM	PS	ZO	ZO
NM	PB	PB	PM	PS	PS	ZO	NS
NS	PM	PM	PM	PS	ZO	NS	NS
ZO	PM	PM	PS	ZO	NS	NM	NM
PS	PS	PS	ZO	NS	NS	NM	NM
PM	PS	ZO	NS	NM	NM	NM	NB
PB	ZO	ZO	NM	NM	NM	NB	NB

(1) If E is NB and EC is NB then $\triangle K_p$ is PB;

(2) If E is NM and EC is NB then $\triangle K_p$ is PB;

……

(49) If E is PB and EC is PB then $\triangle K_p$ is NB.

Similarly, fuzzy logic languages of $\triangle K_i$ and $\triangle K_d$ could be expressed as above. Membership functions for each fuzzy logic language are calculated by:

(1) $\mu \triangle K_{p1}$ (PB) $= \mu$ NB$_{E(x)} \wedge \mu$ NB$_{EC(x)}$;

(2) $\mu \triangle K_{p2}$ (PB)$= \mu$ NM$_{E(x)} \wedge \mu$ NB$_{EC(x)}$;

……

(49) $\mu \triangle K_{p49}$ (PB)$= \mu$ PB$_{E(x)} \wedge \mu$ PB$_{EC(x)}$.

As soon as fuzzy inference is applied to each rule, $\triangle K_p$'s all membership grades corresponding to different E and EC are obtained, and the defuzzification procedure takes place. The output result in discrete terms is:

$$u = \sum x_i \times \mu_n(x_i) / \sum \mu_n(x_i) \tag{3}$$

Where u refers to values of $\triangle K_p$, $\triangle K_i$ and $\triangle K_d$, n =1, 2……49.

The following equation is employed to determine the online PID parameters:

$$K_j(j = p, i, d) = K'_j(j = p, i, d) + \Delta K_j(j = p, i, d) \tag{4}$$

Where K'_j is the former value of K_j.

4. SIMULATION

The fuzzy controller was installed by Fuzzy toolbox of Matlab. Following this, the controller was embedded in the Simulink as a submodel. The simulation of the Fuzzy PID temperature controller was carried out in Matlab/Simulink environment. Fig. 5 presented the system simulation model. The simulation sampling period was set 1s, and required temperature control precision was 45±2℃. The initial tuning of the PID controller was accomplished based on the quarter wave damping criteria suggested by Zigler–Nicholes (8), and the gain coefficients are determined as K_p=0.4, K_i=0.002, K_d=35.

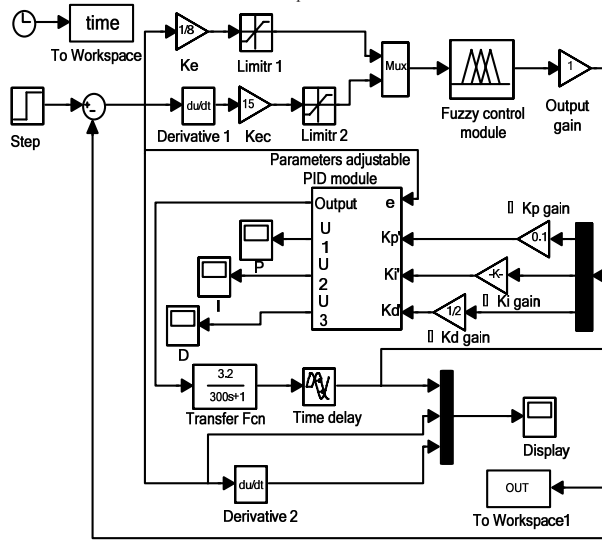

Fig. 5 Controller simulation model

A comparative study between fuzzy PID and PID controller was performed. In the majority working conditions, the system transfer function is unchanging. Fig. 6 showed temperature step responses of controllers. The results suggested that the steady state precision was up to ±0.5℃ using fuzzy PID control. It would only take 200s to achieve desired 45±2℃. Compared with conventional PID controller, fuzzy PID controller had a smaller system overshoot, faster response and improved the dynamic behavior of the system obviously.

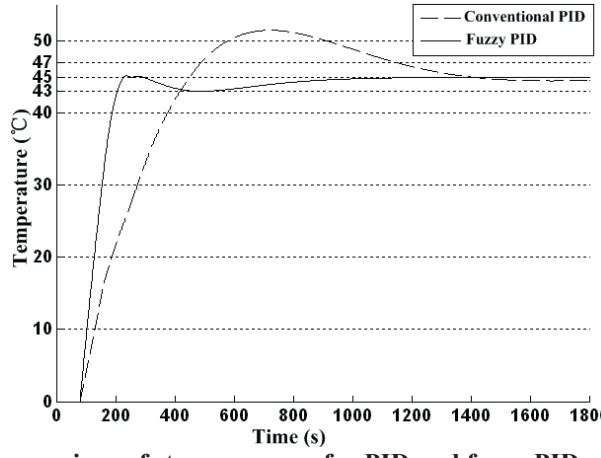

Fig. 6 Comparison of step responses for PID and fuzzy PID controllers

Since the hydraulic system was time varying, parameters of the controlled object would change in some conditions. Simulation was carried out under changed controlled object, with changed transfer function gain K of 4.5, time constant T of 330s and time delay τ of 60s. Meanwhile, the fuzzy PID and PID controller kept invariant. Simulation results of controllers' step responses were presented in Fig. 7. It was observed that fuzzy PID controller had a smaller system overshoot, faster response than conventional PID controller. More importantly, the fuzzy PID controller was able to control the temperature effectively when the controlled object had changed. It was robust and satisfactorily adaptable to hydraulic system oil temperature control.

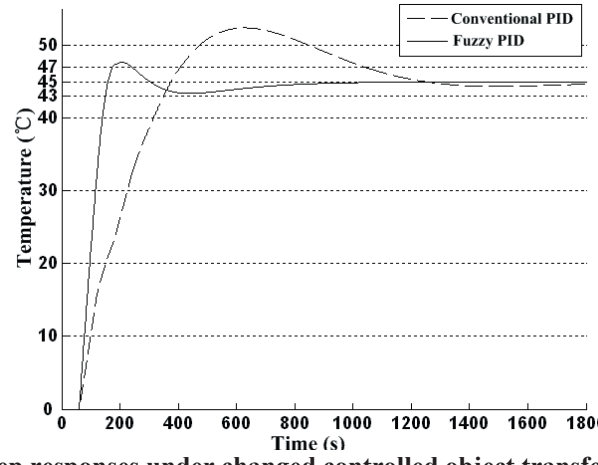

Fig. 7 Step responses under changed controlled object transfer function

5. EXPERIMENTS

The temperature control experiment was conducted in the actual hydraulic power unit with high power and flow. Principles of the temperature control system for hydraulic power unit were simplified in Fig. 1. The experimental test rig, large-scale hydraulic power unit, was shown in Fig. 8.

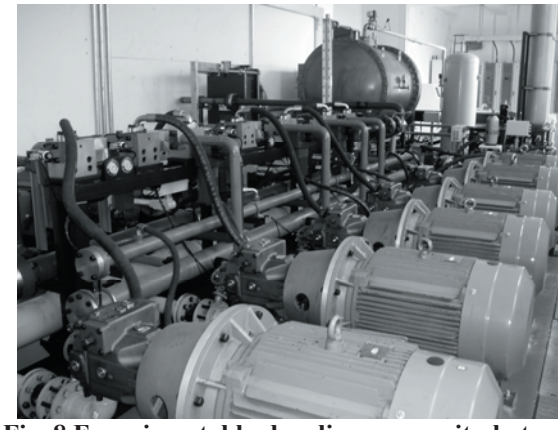

Fig. 8 Experimental hydraulic pump unit photo

Experimental studies were performed under two different working conditions. The temperature of the hydraulic oil was controlled using the fuzzy PID controller. Firstly, experiments were carried out under limited-flow conditions with system flow rate of 774L/min, three pumps operating in the pressure of 10MPa and input power of 165kW. The water pump supplies 45m^3/h cooling water. So the flow rate of water through the heat exchanger is 0~45m^3/h, which is the controlled variable. Temperature set points were 35℃, 40℃ and 45℃ sequentially. Fig.9 shows the experimental results of oil temperature under fuzzy PID control, with flow rate of 774L/min. It can be seen from that temperature fluctuations of all three set points were within ±1℃, and the controller was able to achieve the system control accuracy.

Experiments under full-flow conditions were conducted, with the highest flow rate of 2157L/min, nine pumps operating in the pressure of 10MPa and input power of 700kW. The water pump supplies 45m^3/h cooling water. So the flow rate of water through the heat exchanger is 0~45m^3/h, which is the controlled variable. The temperature set point was 45℃. Based on full-flow status, the system working pressure was adjusted from 10MPa to 4MPa, to make the experimental hydraulic system operate in varying condition. Experimental results were presented in Fig.10. The curve showed that temperature fluctuation of the set point was within ±1℃, under the varying operation condition. The temperature control system is applicable to the hydraulic pump unit. It was robust and capable of achieving the desired control precision satisfactorily.

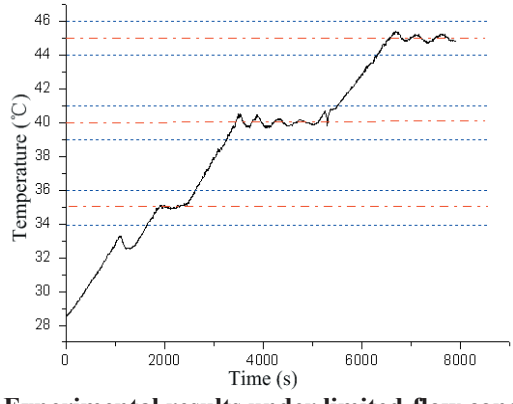

Fig. 9 Experimental results under limited-flow conditions

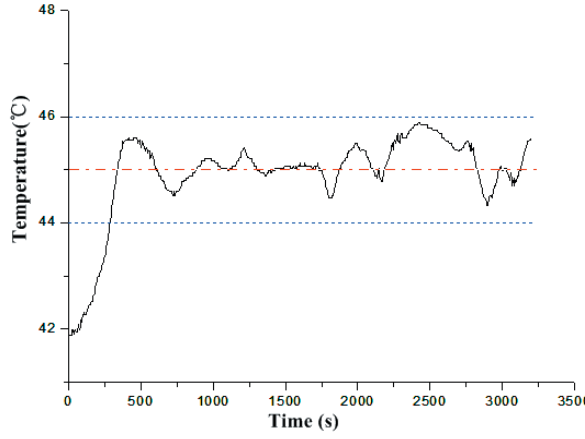

Fig. 10 Experimental results under full-flow conditions

6. CONCLUSIONS

The present work was concerned with the design, simulation and experimental testing of a fuzzy PID controller for oil temperature control of a large scale hydraulic power unit. The desired behavior of the controller was fast responsivity, robustness and a steady-state accuracy of 45±2℃. What's more, it should be adaptable to varying controlled object.

The simulation was completed by Simulink and Fuzzy toolbox. The simulation results suggested that fuzzy PID controller had a smaller system overshoot, faster response, and more robustness than conventional PID controller. Temperature control experiments were conducted in the actual hydraulic power unit with full flow rate and varying operation conditions. The experimental results showed that the controller was satisfactorily applicable to the hydraulic pump unit. It was robust, adaptable to varying controlled object and capable of achieving the control accuracy of 45±1℃, with fast responsivity.

The fuzzy parameters self-tuning PID controller was successfully applied to the hydraulic oil temperature control, with the feature of large time delay, nonlinearity, and slow-time varying. It provided significant reference for temperature control system study, especially for hydraulic systems.

7. ACKNOWLEDGEMENTS

This work was supported by the National Basic Research Program of China (also called 973 Program) under Grant 2007CB714004.

REFERENCES

(1) Zhou, S. C., He, H., The Neural Network Self-learning Fuzzy Control of the oil temperature in hydraulic system, *Proceedings of the 2th International symposium on Fluid Power Transmission and Control,* Shanghai, China, 1995, pp.94-99.

(2) Hang, C., A performance study of control system with dead time, *IEEE Transactions on*

Fuzzy Systems, 27(4), 1990: 234-241.
(3) Cui, Y., Hang, C., Research on fuzzy PID methods based on Smith Predictor, *Master thesis of Dalian University of Technology,* 2005: 3-5.
(4) Zhu, X. F., Dahlin algorithm and Smith Predictor, *Automation &Instrumentation,* 4(1), 2001: 32-35.
(5) Ho, K., Lira, W., Xu, W., Optimal gain and phase margin tuning for PID controllers, *Automatica,* 34(3), 1998: 1009–1014.
(6) Zhang, Q., Litchfield, J. B., Fuzzy logic control for a continuous crossflow grain dryer, *Journal of Food Process Engineering,* 16(1), 1993: 59–77.
(7) Li, H. X., A comparative design and tuning for a conventional fuzzy control, *IEEE Transactions on Systems and Cybernetics,* 27(5), 1997: 884–889.
(8) Ziegler, JG., Nichols, NB., Optimum setting for automatic controllers, *ASME Trans.,* 64, 1942: 759–768.

Higher-order sliding modes for an electropneumatic system: differentiation and output-feedback control

L. Sidhom, M. Smaoui, M.D.Loreto, X. Brun, E.Bideaux, D.Thomasset

Laboratoire Ampère UMR 5005 - INSA Lyon, Bât Antoine de SAINT-EXUPERY, 25 avenue Jean Capelle 69621 Villeurbanne - France

lilia.sidhom@insa-lyon.fr, mohamed.smaoui@insa-lyon.fr, michael.di-oreto@insa-lyon.fr, xavier.brun@insa-lyon.fr , eric.bideaux@insa-lyon.fr, daniel.thomasset@insa-lyon.fr

ABSTRACT

This paper develops and uses a robust differentiator via sliding modes applied to velocity and acceleration measurements. From the only measure of the position, we are being able to accurately estimate the velocity and the acceleration of a servo drive system. Initially developed by Levant, this differentiator is based on high-order sliding modes. The goal of this work is to show the importance of the choice of the differentiator design in the control of an electropneumatic system. A comparative study is made between the 2nd-order robust differentiator and a classic digital differentiation algorithm, in order to show the influence of the structure differentiation algorithm on the control of the electropneumatic system.

Keywords: high order sliding modes, robust differentiator, electropneumatic system.

1. INTRODUCTION

Pneumatic cylinder systems have the potential to provide high output power to weight and size ratios at a relatively low cost. Adding to their simple structure, easy maintenance and low component cost, pneumatic actuators are one of the most common types of industry actuators (1). However, the complexity of the electropneumatic systems and the important range of control laws are a real industrial problem where the target is to choose the best control strategy for a given application. In recent years, research efforts have been directed toward meeting this requirement. Most of them have been in the field of feedback linearization (2) (3). However, reasonably accurate mathematical models for the pneumatic system are required by the feedback linearization. A number of investigations have been conducted on fuzzy control algorithms (4), adaptive control (5), backstepping control (6), classical sliding mode control (7) (8) and high order sliding mode control (HOSM) (9) (10). All of the previous mentioned feedback controllers require generally measurements of acceleration for feedback. However, accelerometers are seldom used in practical drive systems. Indeed, the use of accelerometers adds cost, energy consumption, increases the complexity of the overall system (the accelerometer is mounted to the load in displacement), and reduces its reliability. Many schemes for the estimation of states

Fluid Power and Motion Control 2008 Edited by Dr D N Johnston and Professor A R Plummer

variables have been proposed in recent years. Some of these methods are based on nonlinear observer theory such as high gain observer (11), sliding mode observer (12) and backstepping observer (13). However, nonlinear state observers are difficult to implement when poor knowledge on the system dynamics is available. Moreover, in some of these cases the exact differentiation is provided only when some differentiator parameters tend to inadmissible value, like high values. With the same idea of constructing differentiator based on an observer, a recurrent proposition found in the literature is to use an extended Kalman filter (14). This is a reason that the construction of a differentiator is inevitable. Indeed, differentiators are very useful tools to determine and estimate signals. For instance, using differentiators, the velocity and acceleration can be computed from the position measurements. However, the design of an ideal differentiator is a hard and challenging task. In (15) the author has presented a comparative study among some differentiation algorithms in real time. In (16) some discussion has been done on the properties and the limitations of two different structures of linear differentiation system. Other works (17) are reposed on the arbitrary-order robust exact differentiators with finite-time convergence based on a high-order sliding modes. This high-order sliding algorithm presents a simple form and easy design, so it may be use in real-time control system.

In order to avoid measurements velocity and acceleration from sensors which aims to minimize the number of sensors implemented on the system, the comparative study of a two order differentiator allows obtaining the first and the second derivatives of a measured position. The importance choice of the differentiator design in the control of an electropneumatic system is the main subject of this article. In this work, velocity and acceleration of the actuator will be made via the 2nd-order robust differentiator. In the first section of this paper, we recall some basic concepts of higher order sliding mode. In the second part, a 2nd-order robust differentiator via a third sliding mode is presented. Section 3 describes the model of the electropneumatic actuator and equations governing the motion of this plant have been put in a nonlinear affine form. Then the design of a 2nd-order sliding mode controller is presented. Part 5, will be devoted to the experimental result. Last section is consecrated to conclusions.

2. HIGH-ORDER SLIDING MODES

Sliding Mode Control (SMC) is a robust control scheme based on the concept of changing the structure of the controller in response to the alteration state of the system in order to obtain a desired response.
The aim of a SMC device is asymptotically to bring the state of the system starting from an unspecified initial condition $x(0) = x0$ towards the origin. The sliding mode technique rests on the use of a discontinuous feedback signal having for goal to maintain the evolution of the system on a judiciously selected switching function s. A high speed switching control action is used to force the trajectory of the system to move along a chosen switching manifold in the state space. The dynamic of the closed loop system is thus fixed by the sliding surface $s = 0$. So the system motion on the surface $s = 0$ is called the sliding mode. The main feature of this approach is its insensitivity to variation in system parameters, external disturbances and modelling errors. A specific problem associated with implementation of SMC is the chattering phenomenon, which is essentially a high frequency switching of the control. Firstly, chattering was reduced by smoothing out the control discontinuity in a thin boundary layer neighbouring the switching surface (18), (19).

This kind of solution allows reducing the chattering, but it remains sensitive to input signal. To avoid this drawback some approaches were proposed. The most important approach is a high order sliding mode control (HOSM). In effect the technique of a higher order sliding mode control constitutes a generalization of the concept of standard SMC. Such a technique preserves the main properties of the standard sliding mode and removes the above restriction. They are characterized by discontinuous control acting on the higher order time derivatives of the sliding variable, instead of influencing the first time derivative as happens in standard SMC. Hence the rth order sliding mode is determined by the equalities $s = \dot{s} = \ddot{s} = s^{(r-1)} = 0$. Knowing that the order of the sliding mode is the order of the first discontinuous total time derivative of the sliding variable. Thus by moving the switching to the higher derivatives of the control, chattering in the control is totally eliminated. The HOSM is applicable to control uncertain systems with arbitrary relative degree p. The r-sliding controllers require actually only the knowledge of the system relative degree (18).

3. 2ND-ORDER ROBUST DIFFERENTIATOR

Let the input signal $f(t)$ be a function defined on $[0,\infty[$ consisting of a bounded Lebesgue-measurable noise with unknown features and an unknown base signal $f_0(t)$ with the 2th derivative having a known Lipschitz constant $C > 0$.
The diagram recursive of differentiator proposed by (17) aims to obtain a robust estimate in real time of $\dot{f}_0(t), \ddot{f}_0(t), ..., f_0^{(n)}(t)$ and to be exact in absence of the noise. The 2nd-order differentiator is represented by the following equations:

$$\begin{cases} \dot{z}_0 = v_0, \\ v_0 = -\lambda_0 |z_0 - f|^{\frac{2}{3}} sign(z_0 - f) + z_1, \\ \dot{z}_1 = v_1, \\ v_1 = -\lambda_1 |z_1 - v_0|^{\frac{1}{2}} sign(z_1 - v_0) + z_2, \\ z_2 = -\lambda_2 sign(z_2 - v_1) = -\lambda_2 sign(z_1 - v_0), \end{cases}$$

Where $\lambda_0, \lambda_1, \lambda_2$ are positive gains depending on the constant Lipschitz C , as $|\ddot{f}| < C$.
Here v_0 , v_1 are the outputs of the differentiator. This differentiator bases himself on the three order sliding mode.
At time $t = 0$, the initial values $z_0(0) = f(0)$ $z_1(0) = z_2(0) = 0$ were taken.
Let us define the sliding surface by: $s = z_0 - f$
After a finite time, we obtain
$s = z_0 - f = 0$

$$\dot{s} = \dot{z}_0 - \dot{f} = -\lambda_0 |z_0 - f|^{\frac{2}{3}} sign(z_0 - f) + z_1 - \dot{f} = 0,$$

$$\ddot{s}_0 = \ddot{z}_0 - \ddot{f} = v_1 - \ddot{f} = 0,$$

Then

$$-\lambda_1 |z_1 - v_0|^{\frac{1}{2}} sign(z_1 - v_0) + z_2 - \ddot{f} = 0,$$

So after a finite time, the following relations can be written: $z_1 = v_0$ is the estimation of $\dot{f}(t)$, while $z_2 = v_1$ is the estimation of $\ddot{f}(t)$ .The accuracy of the reconstruction depends on the choice of the parameters $\lambda_0, \lambda_1, \lambda_2$ in the differentiator.

4. ELECTROPNEUMATIC SYSTEM MODEL

The considered system in figure 1 is a linear inline double acting electropneumatic servo-drive using a single rod controlled by two three-way servodistributors, with a stroke equal to 500 mm. The actuator rod is connected to one side of the carriage and drives an inertial load on guiding rails. The total mass (piston, rod and carriage) is equal to 17 kg.

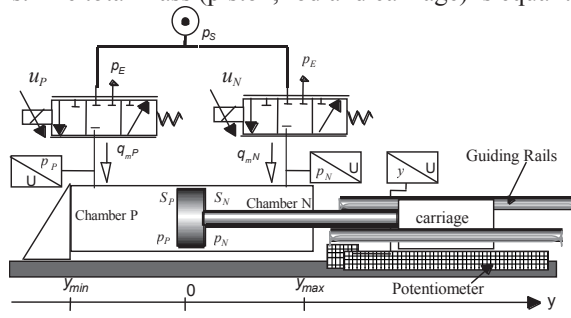

Figure 1: The electropneumatic system.

The electropneumatic system model can be obtained using three physical laws, says the mass flow rate through a restriction, the pressure behaviour in a chamber with variable volume and the fundamental mechanical equation. The pressure evolution law in a chamber with variable volume is obtained via the following assumptions: i) air is a perfect gas and its kinetic energy is negligible; ii) the pressure and the temperature are supposed to be homogeneous in each chamber; iii) the process is polytropic and characterized by coefficient k. The electropneumatic system model is obtained by combining all the previous relations and assuming that the temperature variation is negligible with respect to average and equal to the supply temperature. Moreover, we neglect the dynamics of the servodistributors. In such case, the servodistributors model can be reduced to two static relations between the mass flow rates $q_m^P(u_P, p_P)$ and $q_m^N(u_N, p_N)$, where u_P , u_N are the input voltages and p_P , p_N are the output pressures. The mechanical equation includes pressure force, friction and an external constant force due to atmospheric pressure. The following equation gives the model of the above system:

$$\begin{cases} \dfrac{dy}{dt} = v \\ \dfrac{dv}{dt} = \dfrac{1}{M}\left[S_P p_P - S_N p_N - bv - F_{ext}\right] \\ \dfrac{dp_P}{dt} = \dfrac{krT}{V_P(y)}\left[q_m^P(u_P, p_P) - \dfrac{S_P}{rT} p_P v\right] \\ \dfrac{dp_N}{dt} = \dfrac{krT}{V_N(y)}\left[q_m^N(u_N, p_N) + \dfrac{S_N}{rT} p_N v\right] \end{cases} \qquad [1]$$

where: $\begin{cases} V_P(y) = V_P(0) + S_P y \\ V_N(y) = V_N(0) - S_N y \end{cases}$ with: $\begin{cases} V_p(0) = V_{DP} + S_P \dfrac{l}{2} \\ V_N(0) = V_{DN} + S_N \dfrac{l}{2} \end{cases}$

are the effective volumes of the chambers for the zero position and are dead volumes present at each extremities of the cylinder.

The main difficulty for the following model [1] is related to the knowledge of the mass flow rates q_m^P and q_m^N. In this paper, the results of the global experimental method giving the static characteristics of the flow stage (20) have been used. The global characterization has the advantage of obtaining simply, by projection of the characteristic series $q_m(u,p)$ on three planes: (p,q_m), (u,q_m) and (u,p). The flow stage characteristics were approximated characteristics by polynomial functions affine in control such that: $q_m(u,p) = \varphi(p) + \psi(p, sign(u))$, [2]
where $\psi(.) > 0$ over the physical domain. In the case of monocriteria, it seems more interesting to choose a system with one five-way servo-valve. In fact this structure is more attractive in terms of cost, regarding the equipment. However, in our work, we use the two three-way servo-valves which seem equivalent to one five-way when they are controlled with input of opposite signs $(u_P = u)$ and $(u_N = -u)$. So we assumed that the two servovalves are identical and symmetrical.

5. SECOND ORDER SLIDING MODE CONTROLLER

The fixed goal in our work is synthesized a control law respecting an excellent accuracy in term of position tracking for a desired position. The relative degree of the position is three. This means that the electropneumatic system can only track position trajectory at least three times differentiable.
The desired trajectory has been carefully chosen in order to respect the differentiability required (see Figure 2).

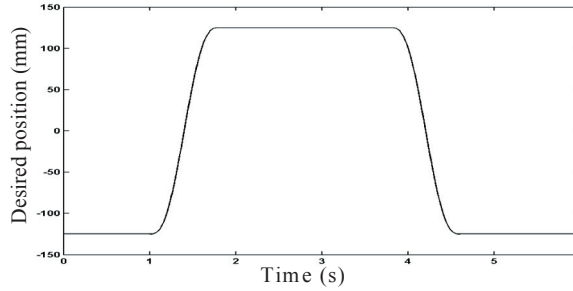

Figure2: Desired position (mm).

The choice of the order sliding mode control depends on the choice of the sliding surface and the relative degree compared to the sliding function.
Let define the sliding surface by:

$$s = \eta(y - y_d) + (v - v_d) = \eta.e_y + e_v.$$

Where η is a positive parameter, e_y and e_v are respectively a position error and velocity error. The relative degree of the position is equal two compared to the chosen variable sliding. So the order of the control law is be equal two, this mean that it should explicitly appear at least the command in the second derivative of the variable sliding s.
By using the model [1], the successive time derivatives of s are given by the expressions below:

$$\dot{s} = \eta.e_v + e_a,$$

$$\ddot{s} = \Delta\alpha(x) + \alpha(x) + \beta(x) \times u,$$

with

$$\alpha(x) = \eta.e_a - \frac{kv}{M}[\frac{S_N^2 p_N}{V_N(y)} + \frac{S_P^2 p_P}{V_P(y)}] - \frac{b}{M} \times \frac{dv}{dt} - j^d;$$

$$\beta(x) = \frac{krT}{M}[\frac{S_P}{V_P(y)}\psi(p_P, \mathrm{sgn}(u)) + \frac{S_N}{V_N(y)}\psi(p_N, \mathrm{sgn}(-u))];$$

$$\Delta\alpha(x) = \frac{krT}{M}[\frac{S_P}{V_P(y)}\varphi(p_P) - \frac{S_N}{V_N(y)}\varphi(p_N)].$$

$\Delta\alpha(x)$ is an uncertain and a bounded function.
The control input u is the sum of a continuous and discontinuous component, which means that u can be defined by the following feedback:

$$u = \beta^{-1}(x)[-\alpha(x) + u_d];$$

With u_d is the new discontinuous input whose role is to ensure the appearance of the sliding mode, despite the presence of uncertainties $\Delta\alpha(x)$.
In (18), a family of r-order sliding mode control with finite-time convergence is presented in (17). In this paper, an 2^{rd} order sliding mode controller from this family is used.
Indeed, the new input is defined by:

$$u_d = -\gamma_1 \,\mathrm{sgn}(\dot{s} + \gamma_2 |s|^{\frac{1}{2}} \,\mathrm{sgn}(s)). \quad [3]$$

In this case, two scalar parameters γ_1, γ_2 are to be adjusted.

6. EXPERIMENTAL RESULTS

Control law [3] is implemented using a Dspace 1104 controller board with the dedicated digital signal processor. The sensed signals, all analog were run through the signal conditioning unit before being read by the A/D converter. The position is given by an analog potentiometer. In our case, the control law is implemented by using just one sensor. Indeed, the position sensor is a NovoTECHNIK model TLH500, which have a precision and repeatability equal to 10 μm and present linearity equal to 0.05%. The gain controller γ_1 and γ_2 have been respectively tuned as $\gamma_1 = 310$ and $\gamma_2 = 15$.

Experiment results are provided here to demonstrate the effectiveness and the influence of the two different design differentiators on the control strategy. As indicated previously, a comparative study between the robust (R.D) differentiator defined above and the classic numerical derivation algorithm (C.A), studied in (15), is presented below. This classic algorithm is given by the following expression:

$$a(k) = \frac{v(k) - v(k-2)}{2T_e}, \quad [4]$$

With Te is a sampling period. We numerically build velocity from the measured position by the sensor of the electropneumatic bench, and the same thing for estimated acceleration a. Firstly, the classic algorithm [4] is used to recover the velocity and the acceleration.

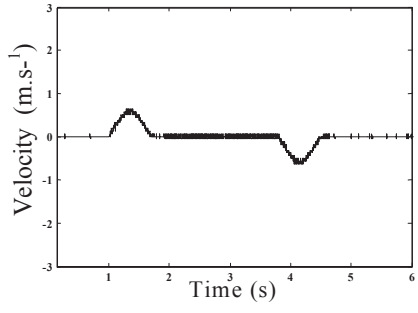

Figure 3: Velocity ($m.s^{-1}$): C.A

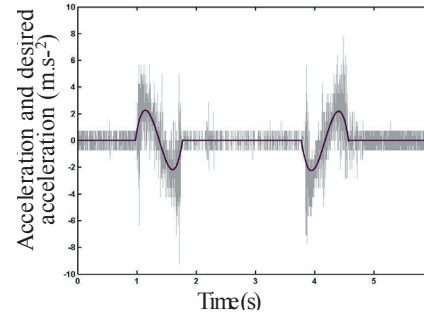

Figure 4: Acceleration and desired acceleration ($m.s^{-2}$):C.A

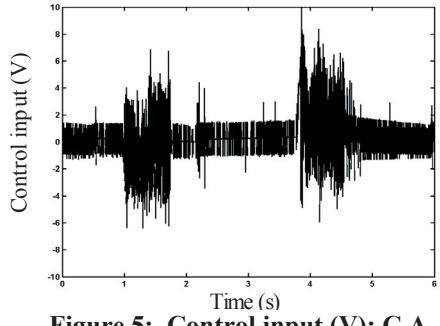

Figure 5: Control input (V): C.A

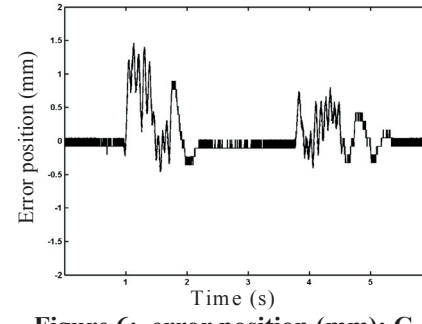

Figure 6: error position (mm): C.A

Figures 3, 4, 5 and 6 show the velocity, the estimated acceleration and the desired acceleration, the control input and the position error. The maximum position error is about 1.5mm, which is about 0.6% of the total displacement magnitude (see figure 6), when we used the classic differentiator. In additionally, it is important to note that the control law behaves well.

However, the control input (see figure 5) is affected by the chattering phenomenon, what is due to the velocity and mostly the acceleration signal. Effectively, the noise level is significant (see figure 3 and figure 4), so the control input which depends on velocity and

acceleration is affected.

It is clear that if the value of controller parameter γ_1 is decreased or the function sign is replaced by a smooth function, the control input is not affected by the chattering phenomena. But in this case, the position error becomes larger.

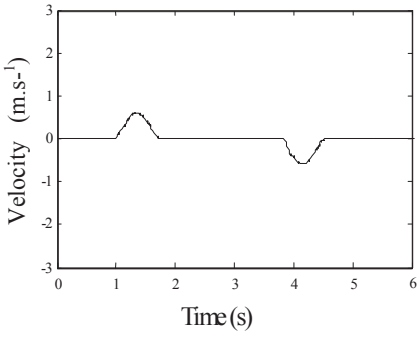

Figure 7: Velocity ($m.s^{-1}$): R.D

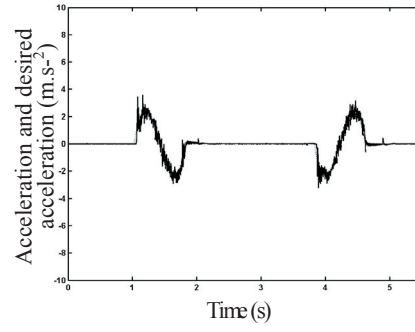

Figure 8: Acceleration and desired acceleration ($m.s^{-2}$):R.D

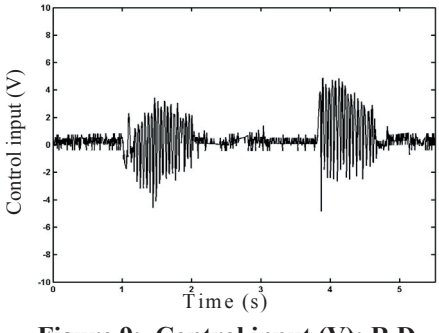

Figure 9: Control input (V): R.D

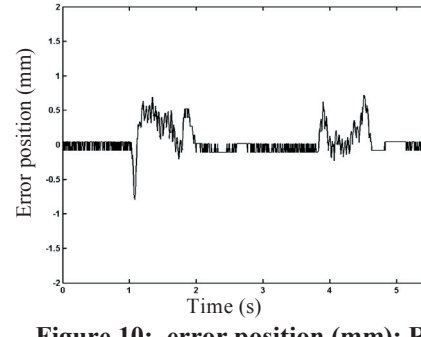

Figure 10: error position (mm): R.D

In the second part, differentiator based on third sliding order is used to recover the velocity and the acceleration signal. From figure 10, the maximum position error is about 0.8mm, so is about 0.32% of the total displacement magnitude. Remark that this value is smaller than the error value determinate with the classic differentiator. Considering figure 9, the control signal is less affected by the chattering phenomenon compared with the figure 5. Therefore the smooth control seems more satisfactory lifetime of components.

This combined controller/differentiator seems more interesting. It is normal that the control input obtained is more good than the controller combined with the classic differentiator, seen that the velocity and acceleration are also more filtered signal (see figure 7 and figure 8). However, the parameters of this robust algorithm depend on the input signal, through the Lipschitz constant of its 2nd order derivative. The Lipschitz constant is usually not known accurately beforehand and also contaminated by the noise. Consequently, the choice of these parameters for this differentiator is a difficult task.

7. CONCLUSION

In this paper, the 2nd order robust differentiator via high order sliding modes has been synthesized. We study, in this work the influence of the design differentiator in the control of an electropneumatic system and the important combination controller/differentiator in the control input. The robust algorithm shows a satisfactory result compared the classic one. The high order siding differentiator attenuates the noise related to differentiation velocity and acceleration signal. This improvement permit jointly to reduce the noise in the control input and cancelled the use of two sensors.
The results founded in this work, encourage testing experimentally the effectiveness of this algorithm design in the other linear or non linear control strategy.

NOTATION

b	viscous friction coefficient	N/m/s
k	polytropic constant	m/s
M	total load mass	kg
p	pressure in the cylinder chamber	Pa
q_m	mass flow rate provided from servodistributor to cylinder chamber	kg/s
r	perfect gas constant related to unit mass	J/kg/K
S	area of the piston cylinder	m^2
V	volume	m^3
y, v, a, j	Position, velocity, acceleration, jerk	m, m/s, m/s^2, m/s^3
$\varphi(.)$	leakage polynomial function	kg/s
$\psi(.)$	polynomial function	kg/s/V
l	length of stroke	m

Subscript

D	dead volume
S	supply
N	chamber N
P	chamber P
d	desired
C.A	classic algorithm
R.D	robust differentiator

REFERENCES

(1) K.A. Edge, "The control of fluid power systems responding to the challenge," Journal of Systems and Control Engineering, vol. 211, no. 12, 1997, pp. 91-110.
(2) X. Brun, S. Sesmat, D. Thomasset and S. Scavarda, "A comparative study between two control laws of an electropneumatic actuator," In European Control Conference ECC'99, Karlsruhe, [CD Rom], reference F1000-5, 1999, 6p.
(3) T. Kimura, S. Hara, T. Fujita and T. Kagawa, "Feedback linearization for pneumatic actuator systems with static fiction," Control engineering practice, vol. 5, no. 10, 1997,1385-1394.

(4) M. Parnichkun, and C. Ngaecharoenkul, "Kinematics control of a pneumatic system by hybrid fuzzy PID," Mechatronics, vol. 11, 2001, pp. 1001-1023.
(5) B. Li, Z. Li, and Y. Xu, "Study on adaptive control for a pneumatic position servo system," Advances in Modelling and Analysis,vol.49, no. 2,1997, pp. 21-28.
(6) M. Smaoui, X. Brun and D. Thomasset, "A study on tracking position control of an electropneumatic system using backstepping design" Control Engineering Practice, vol. 14, no 8, 2006, Pages 923-933.
(7) M. Bouri and D. Thomasset, "Sliding Control of an Electropneumatic Actuator Using an Integral switching Surface," IEEE Trans. on control syst. technology, vol. 9, no. 2, 2001, pp. 368-375.
(8) M. Smaoui, X. Brun and D. Thomasset, "Systematic Control of an Electropneumatic System: Integrator Backstepping And Sliding Mode Control" IEEE Trans. on control syst. Technology, vol. 14, no 5, 2006, pp.905-913.
(9) M. Smaoui, X. Brun and D. Thomasset, "A Combined First and Second Order Sliding Mode Approach for Position and Pressure Control of an Electropneumatic System," In American Control Conference, ACC'05, Portland, Oregon, USA, 2005, pp. 3007-3012.
(10) S. Laghrouche, M. Smaoui, F. Plestan and X. Brun "Higher order sliding mode control based on optimal approach of an electropneumatic actuator" Int. J. of Control, Vol. 79, no. 2, 2006, pp. 119–131.
(11) J.P Gauthier, H. Hammouri and S. Othman, "A simple observer for nonlinear systems applications to bioreactors," IEEE Trans. on Automatic Control , vol. 37, no 6, 1992, 875–880.
(12*) J.E. Slotine and W. Li*, Applied Nonlinear Control, Prentice-Hall 461p. 1991.
(13) *A.J. Krener and W. Kang* "Locally convergent nonlinear observers," Siam J. Control Optim, vol. 42, No. 1, 2003, pp. 155–177.
(14) S. Ibrir, New differentiators for control and observation applications. Proceedings of the American Control Conference, Arlington , 2001.
(15) E. Richard, De la commande linaire et non linaire en position des systèmes électropneumatiques. *PhD thesis* [in french], INSA of Lyon, 1990, 291p.
(16) S. Ibrir, Linear time-derivative trackers. Automatica ,vol.40, 2004, pp.397-405.
(17) A. Levant, Higher order sliding modes, differentiation and output feedback control. *Int.J.of Control*, vol. 76, 2003, pp. 924-941.
(18) A. Levant, Sliding order and sliding accuracy in sliding mode control. *Int.J.of Control* vol.58, 1993, pp. 1247-1263.
(19) A. Levant, Robust exact differentiation via sliding mode technique. *Automatica,* vol. 34, 1998, pp. 379-384.
(20) S. Sesmat, and S. Scavarda, Static characteristics of a three way servovalve. Proceeding scientific of the 12th Aachen Conference on Fluid Power Technology, Aachen, Germany, 1996, pp. 643-652.

Comparison of Digital Hydraulic and Traditional Servo System in Demanding Water Hydraulic Tracking Control

Matti Linjama[*], Juho Seppälä[+], Jouni Mattila[*], Matti Vilenius[*]
[*]Tampere University of Technology, Department of Intelligent Hydraulics and Automation
[+]Sandvik Mining and Construction

ABSTRACT

The remote maintenance of the ITER fusion reactor will be based on pure water hydraulics. Reliability and accuracy requirements are high because of narrow space, high radiation and extreme costs. Digital hydraulics is a potential solution because it uses robust on/off valves and is fault tolerant. In this paper, the performance of the traditional and digital hydraulic servo system is compared in a 1-DOF mockup. The traditional servo system consists of a servo valve and state feedback controller. The digital hydraulic servo system has 4x5 on/off valves and model based feedforward controller together with P-controller. Experimental results show similar tracking performance in both systems.

Keywords: Water Hydraulics, Digital Hydraulics, Tracking Control, ITER

1. INTRODUCTION

Remote maintenance is one important research topic of ITER fusion reactor programme (1). Main requirements of the remote handling system are reliability, good controllability, radiation tolerance, compact size and cleanliness. Water hydraulics is the only actuation technology, which can satisfy all the requirements. Radiation tolerance and cleanliness can be satisfied by proper material selections and by using demineralized water as fluid medium. The remaining problems are reliability and controllability. Water hydraulic servo valves have been studied a lot and good results can be achieved (2, 3). Reliability of servo valves – especially with demineralized water – is still a problem.

Digital hydraulics is based on parallel connected on/off valves series, so called Digital Flow Control Units (DFCU). Each DFCU controls one flow path and typical four-way valve configuration requires four DFCUs, see Fig. 1. The approach is similar to distributed valve systems (4) but control valves are discrete-valued DFCUs instead of proportional ones. An important benefit of digital hydraulics in this application is its fault tolerance (5). Flow capacities of individual valves are usually set according to some coding scheme, e.g. binary

Fluid Power and Motion Control 2008 Edited by Dr D N Johnston and Professor A R Plummer

(1:2:4:8 etc.), Fibonacci (1:1:2:3:5 etc.) or pulse number modulation (1:1:1:1 etc.). The coding scheme has strong effect on controllability, fault tolerance and pressure peaks (6). Binary coding is the most popular one because it gives the best controllability, and it is used in this paper also.

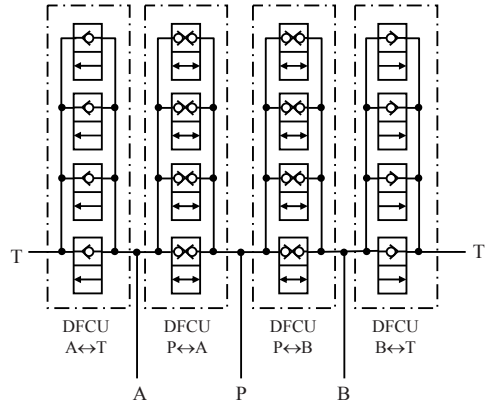

Figure 1. An example of digital hydraulic four way valve with 4×4 valves.

The objective of this paper is to study applicability of digital hydraulics on demanding trajectory tracking control of the ITER maintenance system. The application is cassette multifunctional mover and a mockup of the lift actuator is studied. Control performance is compared to a traditional servo system.

2. TEST SYSTEM

2.1 Mechanism

The test system is shown in Figure 2. It emulates dynamics of the lift joint of the cassette multifunctional mover. Load masses are 500 kg at cylinder side and 0 kg at the other end. The inertia of the system together with the hydraulic spring constant of the cylinder gives natural frequency of 7 Hz at the horizontal orientation. Details of the mechanical design are given in (7).

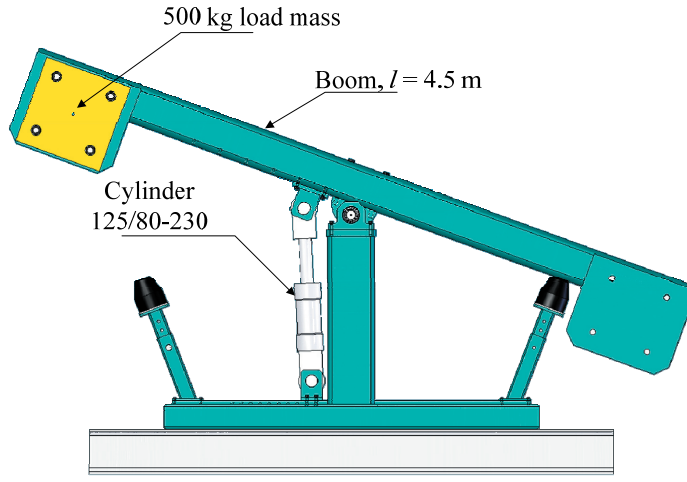

Figure 2. Single axis mockup of the lift joint of the cassette multifunctional mover (7).

2.2 Hydraulics

The hydraulic circuit diagram of the system is shown in Figure 3. The system consists of a row piston pump with three pistons, servo valve, 4×5 digital hydraulic valve system and cylinder. The target supply pressure is 21 MPa.

2.2.1 Servo Valve

The servo valve is Moog 30-417 nozzle-flapper type valve. The flow capacity is 6.8 l/min at 3.5 MPa pressure differential per notch and small-amplitude bandwidth is about 200 Hz. Hysteresis is below 3 percent and null bias below 2 percent, which are relatively big values. The valve can be used with water because of corrosion resistant materials.

2.2.2 Digital Valve System

The availability of high pressure water hydraulic on/off valves is poor. The on/off valves used are FloControl Q90366.000.671 valves with PTFE seals. Valves are directly operated with 24 VDC / 10 W coils and 0.8 mm internal orifices. The maximum operation pressure of on/off valves is 6 MPa only. An additional design constraint is that valve manifold is designed for 4×5 valves. The design is based on flow capacity of the servo valve. The flow rate of the single on/off valve is about 2 l/min at 3.5 MPa pressure differential. The standard binary coded DFCU (i.e. 2, 1, 0.5, 0.25 and 0.125 l/min @ 3.5 MPa) would give flow capacity of 4 l/min, which is considered as too small. Therefore, two largest valves are without orifices and three smallest valves are approximately according to the binary sequence. This “four and a half” bit design gives theoretical flow resolution of 23:1. The orifice sizes are fine tuned according to measured flow capacities and resulting orifices are shown in Figure 3.

2.3 Measurement and Control System

Pressures are measured by Druck PTX1400 pressure sensors and joint angle is measured by Heidenhein ROD 486 5000 pulse encoder and IBV 102 multiplier. The effective resolution

is 694 pulses/°. The control and measurement system is implemented by Matlab/Simulink and dSPACE DS1006 controller board. The control electronics of on/off valves has been implemented by low-side SmartFETs (International Rectifier IPS0151), which are controlled directly by TTL outputs of the dSPACE system.

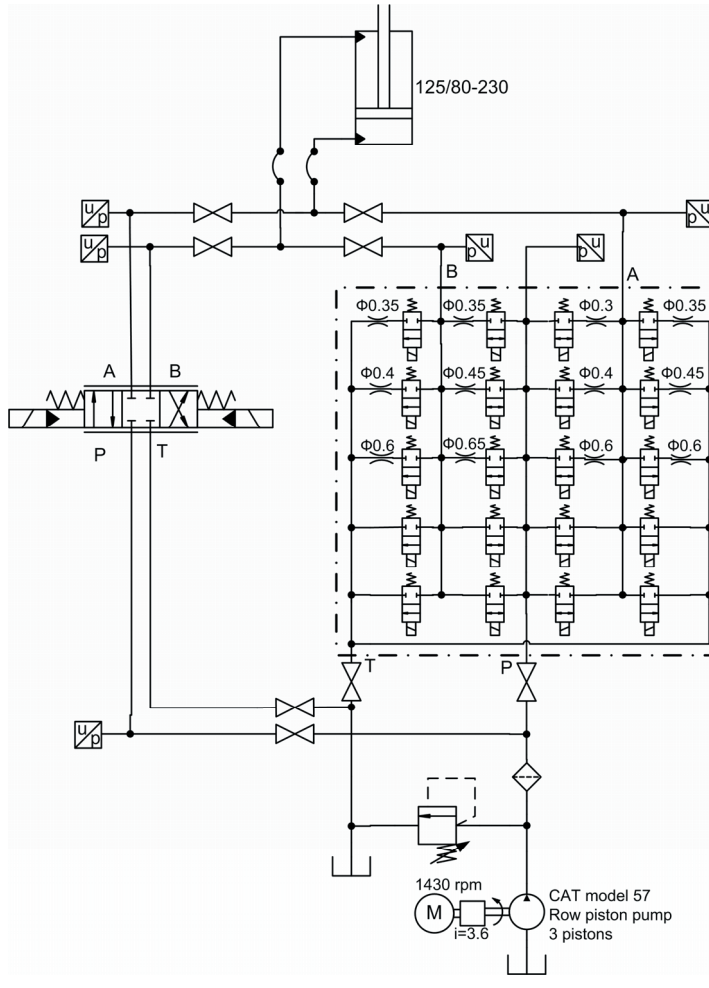

Figure 3. Hydraulic circuit diagram of the system.

3 TRAJECTORY TRACKING CONTROLLERS

3.1 Controller for Servo Valve

The state feedback controller is used together with servo valve as a reference controller. The controller controls directly the joint angle and consists of joint angle, angular velocity and acceleration feedbacks, velocity feedforward and compensation for valve offset. The angle feedback gain depends on the direction of movement. The velocity gain of the valve

cylinder combination is about 0.14 °/(s V) with load and supply pressure used. The block diagram of the controller is show in Figure 4. Backward differentiation is used to obtain derivatives required. Controller gains are tuned such that maximum tracking performance is achieved and that there are no hints of instability (8). The values used are given in Table 1.

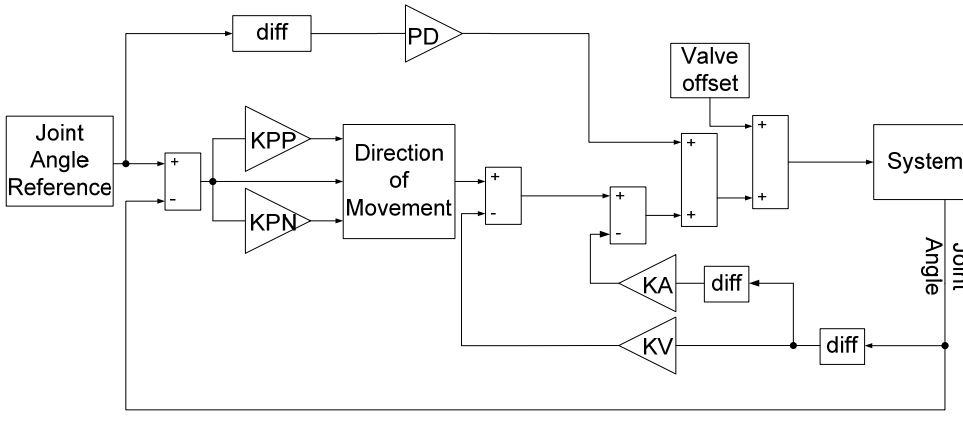

Figure 4. Block diagram of the state feedback controller.

Table 1. Parameter values of the state feedback controller.

KPP [V/°]	*KPN* [V/°]	*KV* [Vs/°]	*KA* [Vs^2/°]	Valve offset [V]	*PD* [Vs/°]	Sampling time [ms]
70	50	0,8	0,04	0,2	7,0	2

3.2 Controller for Digital Valve System

The controller for digital valve system is simplified version of that presented in (9). The most important simplification is that energy saving differential control modes are not used. The controller controls piston position and the measured joint angle is transformed into corresponding piston position according to system geometry. The core of the controller is model based controller, which utilizes the steady-state model of the system. The steady-state equations are

$$\begin{aligned} Q_{PA} - Q_{AT} &= A_A \cdot v \\ Q_{PB} - Q_{BT} &= -A_B \cdot v \\ F &= A_A \cdot p_A - A_B \cdot p_B \end{aligned} \tag{1}$$

where A_A and A_B are piston areas, p_A and p_B chamber pressures, F piston force, and v is piston velocity. The flow rates are modeled by equation of turbulent flow with cavitation choking

$$Q_{PA} = \begin{cases} Kv_{PA}\sqrt{p_P - p_A} & , b\,p_P < p_A \le p_P \\ Kv_{PA}\sqrt{(1-b)p_P} & , p_A \le b\,p_P \\ -Kv_{PA}\sqrt{p_A - p_P} & , b\,p_A < p_P < p_A \\ -Kv_{PA}\sqrt{(1-b)p_A} & , p_P \le b\,p_A \end{cases}$$

$$Q_{AT} = \begin{cases} Kv_{AT}\sqrt{p_A - p_T} & , b\,p_A < p_T \le p_A \\ Kv_{AT}\sqrt{(1-b)p_A} & , p_T \le b\,p_A \\ -Kv_{AT}\sqrt{p_T - p_A} & , b\,p_T < p_A < p_T \\ -Kv_{AT}\sqrt{(1-b)p_T} & , p_A \le b\,p_T \end{cases} \tag{2}$$

where p_P and p_T are pressures at P and T ports of the valve system, b is critical pressure ratio, and Kv_{PA} and Kv_{AT} are effective flow coefficients of DFCUs P↔A and A↔T. The effective flow coefficient of a DFCU is sum of flow coefficients of open valves. Each DFCU has 2^N different opening combinations where N is the number of parallel connected valves. The flow rates Q_{PB} and Q_{BT} are modeled similarly.

The operation principle of the model based controller is to solve steady-state velocity and pressures from Eq. 1 for different opening combinations of DFCUs and to select the opening combination that minimizes the given cost function. Although the principle is simple, the implementation is not. Firstly, Eq. 1 does not have useful analytical solution but it must be solved numerically. Secondly, typical system has $2^{20} \approx 10^6$ different opening combinations and it is impossible to solve all of them in real time. An essential step is to pre-select some small subset of opening combinations, i.e. the search space. The search space is determined by analyzing A- and B-side flow balance of the system. It is assumed that piston velocity and chamber pressures are at target values and following cost functions are determined

$$\begin{aligned} J_A &= \left(\frac{Q_{PA} - Q_{AT}}{A_A} - v_{ref} \right)^2 + \\ &\quad W_{pow} \cdot |v_{ref}| \cdot \left\{ \left[(1-z) \cdot (p_P - p_{Aref}) \cdot Q_{PA} \right]^2 + \left[z \cdot (p_{Aref} - p_T) \cdot Q_{AT} \right]^2 \right\} \\ J_B &= \left(\frac{Q_{PB} - Q_{BT}}{A_B} - v_{ref} \right)^2 + \\ &\quad W_{pow} \cdot |v_{ref}| \cdot \left\{ \left[z \cdot (p_P - p_{Bref}) \cdot Q_{PB} \right]^2 + \left[(1-z) \cdot (p_{Bref} - p_T) \cdot Q_{BT} \right]^2 \right\} \\ z &= \begin{cases} 1, v_{ref} \ge 0 \\ 0, v_{ref} < 0 \end{cases} \end{aligned} \tag{3}$$

Cost functions have quadratic term for velocity error and power losses. The power loss term set penalty for short-circuit flow through the valve system. Short-circuit flow occurs if DFCUs PA & AT or PB & BT are simultaneously open and it is needed to improve controllability at small velocities. Thus, the power loss term is multiplied by velocity

reference, which causes that short-circuit flow decreases with increasing velocity. The search space is determined by calculating J_A for all A-side opening combinations and J_B for all B-side opening combinations. After that, n best opening combinations are selected for both sides and their n^2 permutations form the search space. It is important to note that J_A and J_B have 2^{2N} different values only.

The optimal opening combination is determined by solving steady-state pressures (p_{Ass} and p_{Bss}) and velocity (v_{ss}) from Eq. 1 for all elements of the search space and by finding the minimum of following cost function

$$
\begin{aligned}
J &= J_v + J_{pres} + J_{pow} + J_{sw} \\
J_v &= \left(v_{ref} - v_{ss}\right)^2 \\
J_{pres} &= W_{pres} \cdot \left|v_{ref}\right| \cdot \left[\left(p_{Aref} - p_{Ass}\right)^2 + \left(p_{Bref} - p_{Bss}\right)^2\right] \\
J_{pow} &= W_{pow} \cdot \left|v_{ref}\right| \cdot \{[(1-z)\cdot(p_P - p_{Ass})\cdot Q_{PA}] + [z\cdot(p_{Ass} - p_T)\cdot Q_{AT}] + \\
&\quad [z\cdot(p_P - p_{Bss})\cdot Q_{PB}] + [(1-z)\cdot(p_{Bss} - p_T)\cdot Q_{BT}]\}^2 \\
J_{sw} &= W_{sw} \cdot \sum_{i=1}^{N} \left(Q_{N,PAi}\left|\Delta u_{PAi}\right| + Q_{N,ATi}\left|\Delta u_{ATi}\right| + Q_{N,PBi}\left|\Delta u_{PBi}\right| + Q_{N,BTi}\left|\Delta u_{BTi}\right|\right)
\end{aligned}
\tag{4}
$$

Where $Q_{N,XYi}$ is the flow rate of ith valve of DFCU XY with 1.5 MPa pressure differential and u_{XYi} is the change in control signal of the valve. Term J_v set penalty for velocity error, J_{pres} for pressure error, J_{pow} for power losses and J_{sw} for activity of valves. Weight factors W_{pres}, W_{pow} and W_{sw} determine the importance of each unwanted phenomena.

The pressure references are selected such that pressure differential over both control edges is the same, which yields

$$
\begin{aligned}
p_{Aref} &= \frac{(p_P + p_T)A_B + F}{A_A + A_B} \\
p_{Bref} &= \frac{p_{Aref}A_A - F}{A_B}
\end{aligned}
\tag{5}
$$

The load force F is calculated from low-pass filtered chamber pressures. The break frequency of low-pass pressure filters is 3 rad/s. All valves are closed if velocity reference is smaller than velocity threshold v_{tol2} and the model based controller is activated again if velocity reference becomes bigger than another velocity threshold v_{tol1}. The threshold values are selected as small as possible but such that no limit cycles occur. The closed-loop position controller is implemented by using P-controller together with velocity feedforward. The block diagram of the complete system is shown in Figure 5 and numerical values of the controller parameters are given in Table 2.

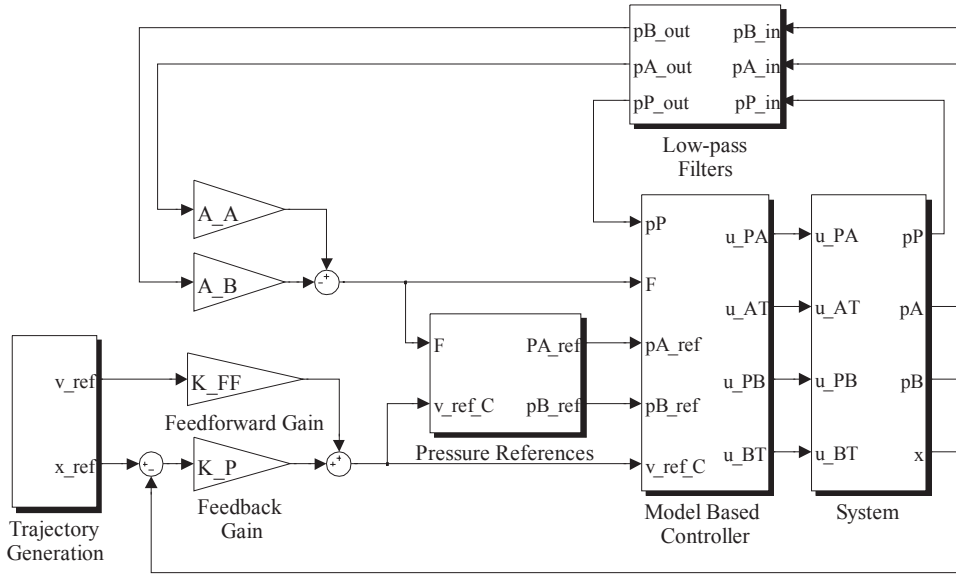

Figure 5. Block diagram of the control system of the digital hydraulic valve system.

Table 2. Parameter values of the controller of the digital hydraulic valve system.

K_P [s^{-1}]	K_{FF}	W_{pres} [$m\,s^{-1}Pa^{-2}$]	W_{sw} [$m^{-1}s^{-1}$]	W_{pow} [$m\,s^{-1}W^{-2}$]	Sampling time [ms]	v_{tol1} [$m\,s^{-1}$]	v_{tol2} [$m\,s^{-1}$]
4	1	1×10^{-14}	0.4	0.002	24	0.0003	0.0002

4 EXPERIMENTAL RESULTS

4.1 Flow Coefficients and Critical Pressure Ratios of On/Off valves

Flow coefficients and critical pressure ratios are determined from measured *p-Q* curves of each valve. The measurements are made with 7 MPa inlet pressure by gradually decreasing outlet pressure. Critical pressure ratio is the point where the flow rate saturates even if outlet pressure is decreased. The results of measurements are shown in Table 3.

Table 3. Flow coefficients and critical pressure ratios.

Valve	Flow coefficient $\times10^{-9}$ [$m^3s^{-1}Pa^{-0.5}$]				Critical pressure ratio			
	PA	AT	PB	BT	PA	AT	PB	BT
1	2.75	3.65	3.56	3.72	0.29	0.28	0.25	0.32
2	5.52	6.46	6.61	5.33	0.40	0.27	0.26	0.22
3	9.96	10.5	11.2	10.2	0.28	0.25	0.26	0.27
4	16.5	18.4	18.5	16.8	0.48	0.48	0.48	0.46
5	20.9	16.0	19.6	18.3	0.48	0.42	0.48	0.48

4.2 Measured responses

Experimental results are presented as joint angles even if the controller of digital valve system works in actuator space. Measured responses consist of 0.1 Hz sinusoidal trajectories with different amplitudes and offsets. Low frequency is selected because slow movements are typical in the application. Offset has hardly any effect on results and measurements around horizontal orientation are presented.

Figures 6 and 7 show measured responses with amplitude of ±1.2 degrees. Both systems have maximum tracking error about 0.01°. The operation principle of the digital hydraulic system causes some oscillations in velocity. The opening combinations of DFCUs are shown as states between 0 and 31, and control signals of individual valves can be obtained by converting state number into five-bit binary number. State plots show that short-circuit flow is used at small velocities only. One difference between responses is that pressure level is independent of direction of movement in the digital hydraulic system. Control signal of the servo valve is noisy because of quantized position signal and backward differentiation used. The valve dynamics filters out the noise and system output is smooth.

Figures 8 and 9 depict measured responses with ±0.3 degrees amplitude. Maximum tracking error is about 0.008° in both systems. The offset compensation of the servo valve seems to be slightly incorrect. Velocity tracking is relatively poor in the digital hydraulic valve system because velocity is close to the smallest possible value.

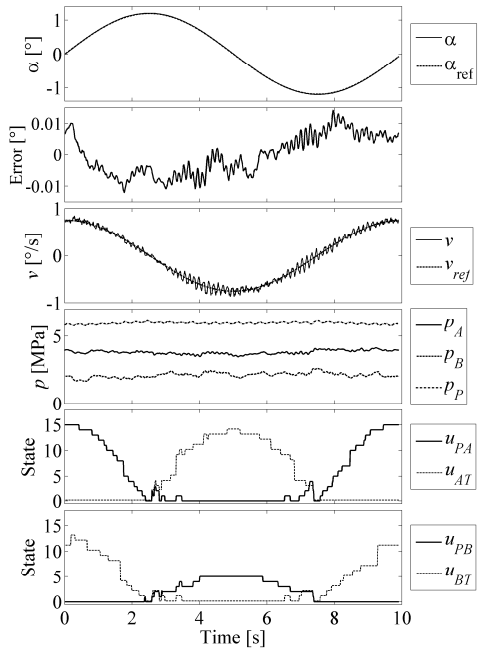

Figure 6. Measured ±1.2 degrees response with digital hydraulic valve system.

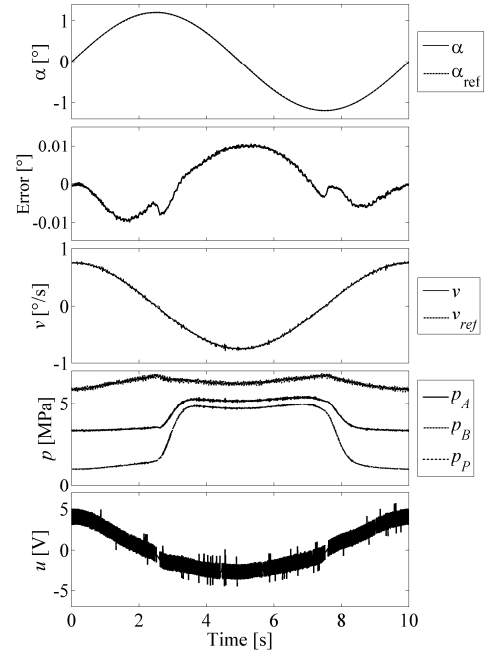

Figure 7. Measured ±1.2 degrees response with servo valve.

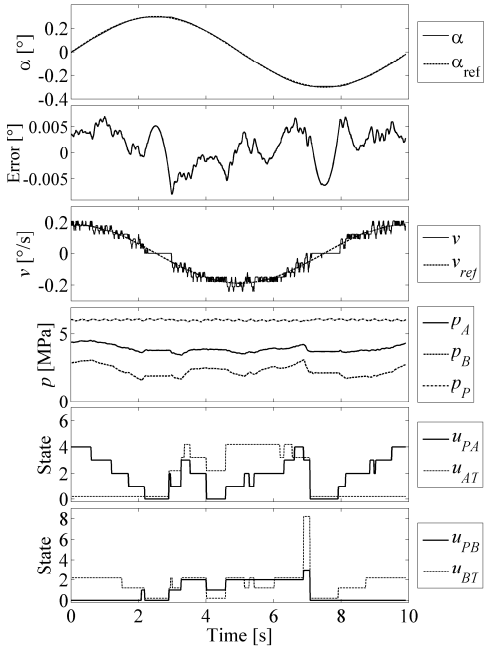

Figure 8. Measured ±0.3 degrees response with digital hydraulic valve system.

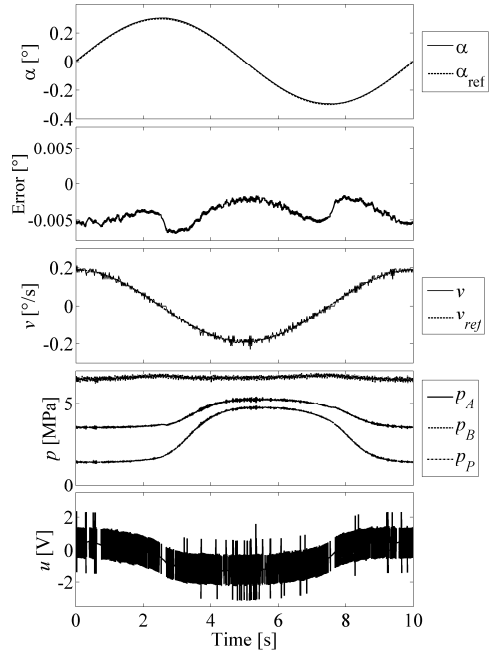

Figure 9. Measured ±0.3 degrees response with servo valve.

5 CONCLUSIONS

Results show that digital hydraulic valve system is a potential solution for implementation of ITER remote maintenance actuation system. Experimental results show similar position tracking performance with traditional servo system. However, the response of the traditional servo system is smoother and the digital system has difficulties at low velocities. Control performance can be improved by increasing the number of on/off valves or by introducing damping elements. Unique benefit of digital solution is its fault tolerance. The binary coding used is not the best from the fault tolerance point of view and other coding methods should be studied. Also, on/off valves for higher pressures should be developed.

REFERENCE LIST

1 Mattila, J., Poutanen, J., Saarinen, H., Kekäläinen, T., Siuko, M., Palmer, J., Irving, M. & Timperi, A. The design and development of ITER divertor RH equipment @ DTP2 facility. Proceedings of the Tenth Scandinavian International Conference on Fluid Power, May 21-23, 2007, Tampere, Finland, pp. 277–291 (Vol. 3).

2 Mäkinen, E.; Virvalo, T., Improving the accuracy of a water hydraulic position servo by compensating servo valve nonlinearities. In: Burrows, C.R. & Edge, K.A. (eds.) Bath Workshop on Power Transmission & Motion Control, September 13-15, 2000, Bath, UK, pp. 283-295.

3 Cho, S.-H., Linjama. M., Sairiala, H., Koskinen, K. T. & Vilenius, M. 2001. Sliding mode tracking control of a low-pressure water hydraulic cylinder under non-linear friction. Proceedings of the Institutions of Mechanical Engineers, Part I: Journal of Systems and Control Engineering, Vol. 216, No. I5, pp. 383–392.

4 Pfaff, J. 2005. Distributed Electro-Hydraulic Systems for Telehandlers. The 50th National Conference on Fluid Power, March 16-18, 2005, Las Vegas, USA. pp. 779–784.

5 Siivonen, L., Linjama, M. & Vilenius, M. Analysis of Fault Tolerance of Digital Hydraulic Valve System. In: Johnston, D.N., Burrows, C.R. & Edge, K.A. (eds.). Bath Workshop on Power Transmission and Motion Control (PTMC 2005), Sept. 7–9, 2005, Bath, UK, pp. 133–146.

6 Laamanen, A., Linjama, M. and Vilenius, M. On the pressure peak minimization in digital hydraulics. Proceedings of the Tenth Scandinavian International Conference on Fluid Power, SICFP'07, May 21-23 ,2007, Tampere, Finland, pp. 107-122 (Vol 2).

7 Mäkinen, H. 2006. Fuusioreaktorin huoltorobotin testausjärjestelmän suunnittelu. M.Sc. Thesis, Tampere university of Technology, Department of Automation, 72 p. (In Finnish).

8 Virvalo, T. & Linjama, M. Experimental study of robustness of some controllers in a hydraulic position servo drive. Hydraulica a pneumatica 2001, June 5–7, 2001, Ostrava, Czech Republic, pp. 199–208.

9 Linjama, M., Huova, M., Boström, P., Laamanen, A., Siivonen, L., Morel, L., Waldén, M. & Vilenius, M. Design and implementation of energy saving digital hydraulic control system. Proceedings of the Tenth Scandinavian International Conference on Fluid Power, May 21–23, 2007, Tampere, Finland, pp. 341–359 (Vol. 2).

Session 9
Systems, modelling and design

Study on the opening characteristics of high voltage circuit breaker with hydraulic operating mechanism

Wei Liu,Bing Xu, Huayong Yang, Zhongyu Wu
The State Key Laboratory of Fluid Power Transmission and Control, Zhejiang University,Zhejiang Province, Hangzhou City 310027, People's Republic of China
lw2002cn2000@163.com

ABSTRACT

High voltage circuit breaker is the most important protection and control apparatus in power system. The action of hydraulic operating mechanism in circuit breaker is different from general hydraulic mechanism for its high speed, short operating time and high pressure. In this paper, the working principle of hydraulic operating mechanism of 550kv high voltage circuit breaker is introduced. The high response speed and great rate of flow control valve is analyzed. Mathematical models of the system have been developed. Simulations are carried out with AMESIM, considering factor that influence on moving properties of hydraulic operating mechanism such as force in arc quenching chamber. Pressure loss in pipe is discussed detailed. Experiments are also carried out for opening operation of circuit breaker hydraulic mechanism. The simulation results show to be in accordance with the experiment results; and it is also shown models are correct.

Keywords: Hydraulic operating mechanism, Circuit breaker, Opening characteristics
Control valve

1. Introduction

High voltage circuit breaker have been extensively used in electrical power systems in order to make(close) and break (open) an electrical circuit under normal circuit conditions and also make for a specific time and break currents under specified abnormal circuit conditions such as those of short circuit [1]. Circuit breakers play an important role in power system transmission,

Fluid Power and Motion Control 2008 Edited by Dr D N Johnston and Professor A R Plummer

distribution and protection. They must clear faults and isolate faulted sections rapidly and reliably. The operating mechanism is a crucial part of circuit breaker. A hydraulic mechanism is a kind of all operating mechanisms, such as spring mechanism, magnetic mechanism, pneumatic mechanism, motor drive mechanism.

After its advent in circuit breaker at the beginning of 1960s，hydraulic operating mechanism drew great attention from countries all over the world. Compared working principle with other mechanisms，hydraulic operating mechanism has the advantages of less part numbers, higher reliability, stable output performance and larger power[2]. The action of hydraulic operating mechanism in circuit breaker is different from general hydraulic mechanism for its high speed, short operating time and high pressure. The reliability and high speed performance are the key characteristics of the circuit breaker's hydraulic operating mechanism. According to the second survey by CIGRE (International Council on Large Electric Systems) about the reliability and failure mode of high voltage circuit breakers, shown that over 40% of all circuit breaker failures can be traced to the operating mechanism [3]. The opening time and opening velocity are also circuit breaker's important opening characteristics. Thus, it is of great practical significance for improving reliability and opening performance of circuit breaker hydraulic operating mechanism.

In this paper，based on the development of hydraulic operating mechanism of 550KV high voltage circuit breaker，the operating principle and main characteristics of the operating mechanism have been analyzed. Mathematical models of the hydraulic system have been developed. Simulations are carried out with AMESIM. Experiments are also carried out for opening operation of circuit breaker hydraulic mechanism to verify the results of opening characteristics. The simulation results are shown to be in accordance with the experiment results.

2. The working principle of hydraulic operating mechanism

The 550KV high voltage circuit breaker (Figure 1) is taken as the investigation subject. Figure 2 illustrates the basic oil flow diagram. The system is less pipes connected and highly integrated. The mechanism is always held in high pressure, which is different from common hydraulic systems. The principle of this hydraulic mechanism is very simple because operations are done by controlling the pressurized oil in one side of the cylinder only. The moving piston of cylinder is connected with arc quenching chamber (interrupter) of circuit breaker. The control valve is a two-position three-way direction valve. It is composed of the solenoid, the pilot valve, the two- level valve and the main valve.

Before opening and closing operations, the accumulator should be filled with rated pressurized oil. When the hydraulic mechanism performs opening and closing operations, the accumulator is working instead of pump and motor. When the open coil in energized, the pilot valve (1-2 or 1-3) piston for opening moves downwards. The pressurized oil in the control chamber of the

two- level valve and the main control valve (3) is discharged to the oil tank through pilot valve (1-2 or 1-3) and two-level valve (2-2) respectively. The main control valve moves leftwards and the pressurized oil in the left of cylinder cavity are discharged to the oil tank through main valve. So cylinder‘s piston is driven rightwards and opens the breaker’s main contacts. When cushion stroke moves towards the end buffer room, opposing force in the back area of the piston is created, and the opening velocity decreased gradually. Both closing and opening operations are done by hydraulic force. The process of closing operation is similar to opening. The 1-1 pilot valve, 2-1 two-level valve and 3, main valve is at work when closing operation, as shown in figure 2.

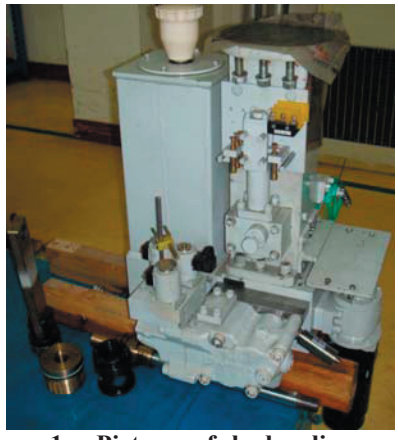

Figure 1 Picture of hydraulic operating hydraulic mechanism of circuit breaker

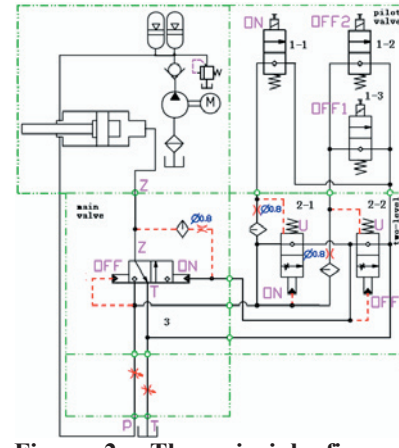

Figure 2 The principle figure of operating mechanism

Opening time and opening velocity are important parameters to evaluate performance of circuit breaker hydraulic mechanism. It is very beneficial to prolong circuit breaker's life time and enforce performance of breaking abnormal currents that Shortening opening time and increasing opening velocity [4] [5]. When the piston of cylinder moves to the position of 26 millimeter, 550KV high voltage circuit breaker’s contact breaks. The time is opening time and the average velocity in10ms after opening time is opening velocity.

3. The models of hydraulic system

Because of high speed action and short operating time, the direction control valve used in hydraulic operating mechanism of high voltage circuit breaker should have high work pressure，great flow rate and high response speed to meet the system requirement. The performance of control valve plays an important role in hydraulic operating mechanism [6]. The whole valve configuration is shown in figure 3. The work pressure and the rated flow are 32.6Mpa and 800L/min separately.

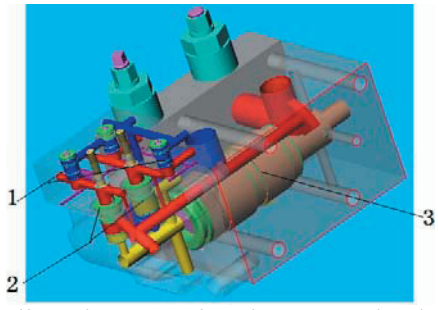

1. pilot valve 2. main valve 3.two-level valve

Figure 3 Sketch of direction control valve

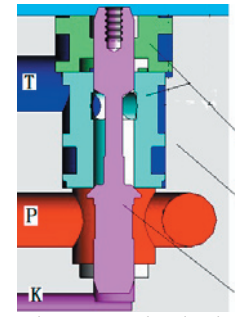

1. pocket 2. valve body 3. spool

Figure 4 Sectional view of pilot valve

3.1 Model of pilot valve

The sectional view is shown in figure 4. The pilot valve has two states. One is work state, the other is rest state. When solenoid is generated, it is at work. The solenoid force exerts on the spool. Then, it makes the entrance from port P to port T open. The pressurized oil in the port P which is connected with control cavity of the two-level valve is discharged to the oil tank through the entrance. The max solenoid force is up to 300N,which is far greater than $F_{tl.}$

Force balance equation of spool is modeled as follow:

$$F_e - F_{f1} - F_{s1} - F_{t1} - F_{v1} = m_{x_1} \frac{d^2 x_1}{dt^2} \tag{1}$$

In which, $F_{s1} = -C_q \pi d_1 x_1 \Delta P_1 \sin 2\theta$ (2)

$$F_{t1} = C_q \pi d_1 l_1 \sin\theta \sqrt{2\rho \Delta P_1} \frac{dx_1}{dt} \tag{3}$$

$$F_{v1} = \frac{\pi d_1 L dx_1 \mu}{dt \Delta r_1} \tag{4}$$

The flow equation [7] as follows:

$$Q_1 = C_q A_{00} \frac{\sqrt{2\Delta P_1}}{\sqrt{\rho}} = C_q A_{00} \frac{\sqrt{2(P_0 - P_D)}}{\sqrt{\rho}} \tag{5}$$

The throttle area as follows:

$$A_{00} = \pi d_1 x_1 \sin\theta (1 - \frac{x_1}{2d_1} \sin 2\theta) \tag{6}$$

From (5), (6) there's

$$Q_1 = C_q \pi d_1 x_1 \sin(1 - \frac{x_1}{2d_1} \sin 2\theta) \frac{\sqrt{2\Delta P_1}}{\sqrt{\rho}} \tag{7}$$

3.2 Model of two-level valve

The sectional view the two-level valve is shown in figure 5. It is controlled by pilot thought control cavity *P1* connected with the pilot valve correspondingly. When the pilot valve is at work, it makes the entrance from port *P2* to port *p3* open. The two-level valve spool correspondingly turns on because of hydraulic force.

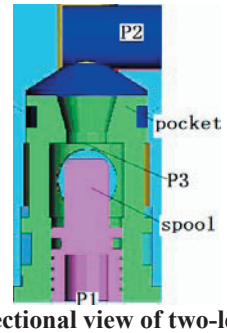

Figure 5 Sectional view of two-level valve

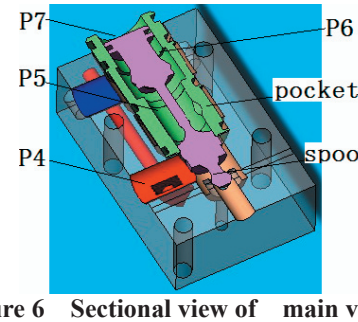

Figure 6 Sectional view of main valve

The moving equation of open operation of spool will be

$$P_2 A_2 - P_1 A_1 - F_{f2} - F_{s2} - F_{t2} - F_{v2} = m_{x_2} \frac{d^2 x_2}{dt^2} \tag{8}$$

In which, $F_{s2} = -C_q \pi d_2 x_1 \Delta P_2 \sin 2\alpha$ (9)

$$F_{t2} = C_q \pi d_2 l_2 \sin\theta \sqrt{2\rho \Delta P_2} \frac{dx_2}{dt} \tag{10}$$

$$F_{v2} = \frac{\pi d_2 L dx_2 \mu}{dt \Delta r_2} \tag{11}$$

The flow equation：

$$Q_2 = C_q \pi d_2 x_2 \sin(1 - \frac{x_2}{2d_2} \sin 2\alpha) \frac{\sqrt{2\Delta P_2}}{\sqrt{\rho}} \tag{12}$$

3.3 Model of main valve

The sectional view of the main valve configuration is shown in figure 6. It is a two-position, three-way direction valve. When performing opening operation, the pressurized oil in the control cavity of the main valve is discharged to the oil tank. Thus, it makes the entrance from port *P5* to port *P6* open and the pressurized oil is also discharged to the oil tank. As closing operation, the motion of spool is similar. Port *p4* is always filled with pressurized oil from accumulator. Port *p5* is connected with hydraulic cylinder. Port *p6* is connected with oil tank.

Port *P7* is the control cavity of the main valve, which is controlled by the two-level valve. The drive force on the spool is up to about 25000N when opening operation, which is far greater than transient flow force $F_{t3.}$ Transient flow force can be neglected.

The dynamic equation of the spool motion is given by the following equation:

$$P_7A_a + P_6A_b + P_4A_c - P_5A_d - F_{s3} - F_{t3} = m_{x_3}\frac{dx_3^{\ 2}}{dt^2} \tag{13}$$

In which, $F_{s3} = 2C_q\pi d_3 x_3 \cos\beta\Delta P_3$ (14)

$$F_{t3} = C_q\pi d_3 l_3\sqrt{2\rho\Delta P_3}\frac{dx_3}{dt} \tag{15}$$

The flow continuity equations for opening and closing of the control chamber are given respectively:

$$Q_3 = A_a\frac{dx_3}{dt} - \frac{V_A}{\beta}\frac{dP_B}{dt} \tag{16}$$

$$Q_3 = A_a\frac{dx_3}{dt} + \frac{V_A}{\beta}\frac{dP_B}{dt} \tag{17}$$

The flow equation for opening and closing are given respectively:

$$Q_4 = C_q A_{01}\frac{\sqrt{2(P_4 - P_5)}}{\sqrt{\rho}} \tag{18}$$

$$Q_4 = C_q A_{02}\frac{\sqrt{2(P_5 - P_6)}}{\sqrt{\rho}} \tag{19}$$

3.4 Pressure Loss in Hydraulic mechanism

Because of the characteristics of high-speed and great rate of flow of the hydraulic operating mechanism，pressure losses that composed of local pressure loss and pressure loss along the pipelines in hydraulic system at work can't be neglected in the process of design and simulation, besides the loss of internal pressure of valve, which is different from normal hydraulic system. The liquid flows through pipelines with changes in the section or shape, and elbow pipe, the local pressure loss and pressure loss along the pipelines [7] will be

$$\Delta p_m = \varepsilon\frac{\gamma}{2g}v^2 \tag{20}$$

$$\Delta p_d = \lambda\frac{l_0}{d}\frac{\gamma}{2g}v^2 \tag{21}$$

3.5 Model of cylinder and load

The piston rod cavity of hydraulic cylinder is always connected with accumulator. Thus, hydraulic mechanism is always held in high pressure. The dynamic equation of the cylinder motion is modeled as follows:

$$A_P P_B - A_z P_z - B_P \frac{dx_0}{dt} - F = m_g \frac{d^2 x_0}{dt^2} \tag{22}$$

The flow continuity equations for opening and closing of the control chamber are given respectively:

$$Q_5 = A_P \frac{dx_0}{dt} - \frac{V_B}{\beta}\frac{dP_B}{dt} \tag{23}$$

$$Q_5 = A_P \frac{dx_0}{dt} + \frac{V_B}{\beta}\frac{dP_B}{dt} \tag{24}$$

When cylinder moving with arcing contacts, the pressure difference that the main load is occurred because of the expansion and compression of the chamber [8]. The output force equation is modeled as follows:：

$$F = (\frac{P_l}{P_p} - 1)P_p A_p = P_p A_p [(\frac{V_0}{m_0}\frac{m_t}{V})^k - 1] \tag{25}$$

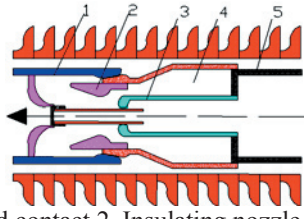

1. Fixed contact 2. Insulating nozzle 3. Arcing contacts 4. Compression chamber 5.fixed piston

Figure 7 Sketch of arc-quenching chamber

Figure 8 Experiment set-up

4. Simulation and experiment

According to the mathematic models, simulation is carried out by AMESIM, hydraulic simulation software. The AMESIM model is given in figure 9. To validate the simulation results of opening characteristics, the practical test is carried out on the experiment set-up of the circuit breaker hydraulic operating mechanism, which is shown in figure 8. The work pressure is 32.6Mpa. The fluid medium is 10# aviation hydraulic oil. The hydraulic operating mechanism motion time is very short, about 50-100ms. Thus, the sampling rate of data acquisition system should be high, which is set 80 KHz/ channel. The simulation and experiment were conducted by inputting 220V DC voltage to the on-off solenoid in the form of step.

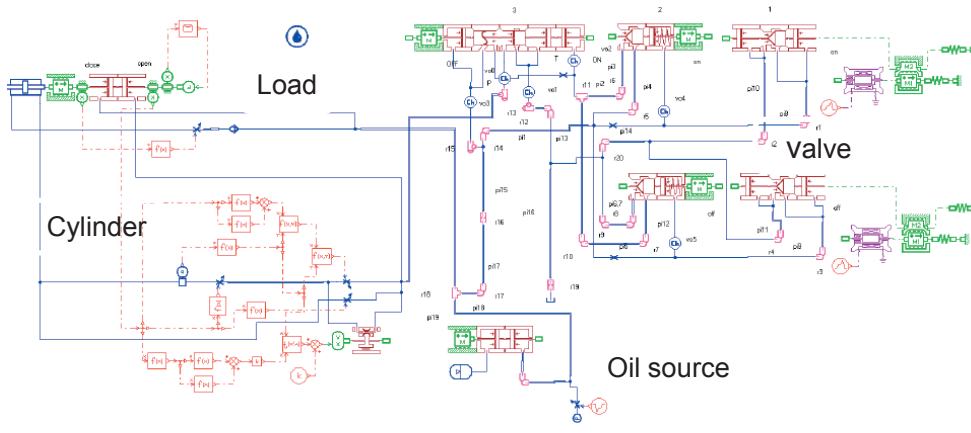

Figure 8 Sketch of the AMESIM modle of hydraulic system

4.1 response time of control valve

The simulation results of output displacement response of each stage valve are given in figure 10. S1, S2 and S3 are the displacement of the pilot, two-level and main valve respectively. The switch time of the control valve is about 10.6ms. The whole motion time after receiving opening command of the pilot valve, two-level, main valve is very short, about 8.8ms, 7.6ms, 10.6ms respectively.

The comparison of simulation and experiment result are given in figure11. The simulation result is shown to be in accordance with the experiment results nearly. The control chamber pressure change of the main valve shows the movement characteristic of main valve. With the two-level valve turning on, the control chamber pressure decrease rapidly. Then, the spool of main valve begins motion. With flow rate increasing, the pressure of the control chamber increases. When the valve stops motion, the pressure decreases sharply. The experiment and simulation motion time of main valve spool is 3.63ms and 3.95ms respectively. The movement time reaction in the pressure of control chamber is in agreement with the simulation in figure10.

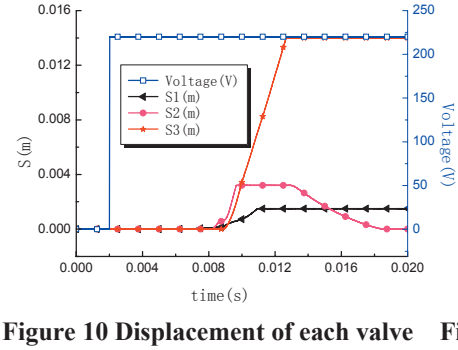

Figure 10 Displacement of each valve

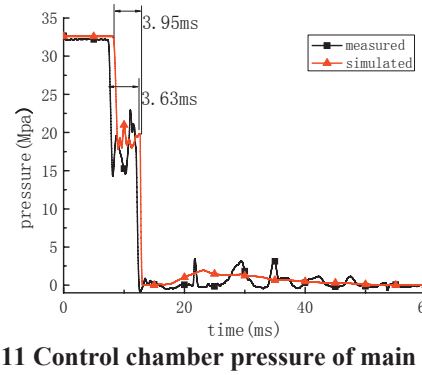

Figure 11 Control chamber pressure of main valve

4.2 opening characteristics

Opening time and opening velocity are the important characteristic of the circuit break, which are different with circuit breaker type. After the solenoid given 220V DC opening signal, the hydraulic cylinder begins motion with about 11ms delay. The hydraulic system stops about 50ms after opening operation command, as shown in figure13. The experiment velocity of hydraulic cylinder is derivation from experiment displacement data. Because of disturbing errors in experiment displacement data, the velocity indirectly calculated is not precise as displacement. But the error between experiment and simulation is acceptable for this high speed system.

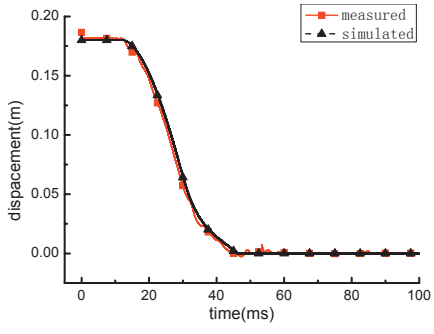

Figure 12 The displacement of cylinder

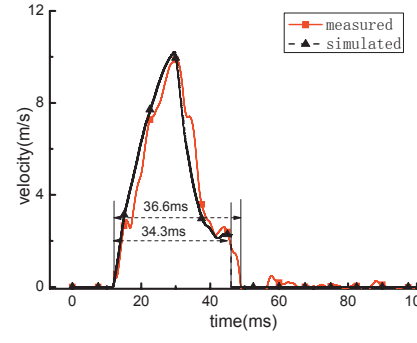

Figure 13 The velocity of cylinder

The opening time and opening velocity is about 21ms and 8.6m/s separately when the contact of arc quenching chamber breaks off at the 0.155m displacement of the hydraulic cylinder. The max velocity of the cylinder is about 10.2m/s. Then, the cylinder begins moving to the cushion room, the velocity decreases gradually.

4.3 analysis of pressure loss in pipe

The local pressure loss of 90 degree pipe elbow and the pressure loss in main valve can be calculated as follows:

$$\Delta P_{valve} = \frac{Q^2\rho}{2C_q{}^2A^2} = \frac{Q^2\rho}{2C_q{}^2(\pi d_3 x)^2} = \frac{Q^2\rho}{2C_q{}^2(\pi\times 0.0345\times 0.007)^2} \tag{26}$$

$$\Delta P_m = \xi\frac{\rho v^2}{2} = \xi(\frac{4Q}{\pi d^2})^2\frac{\rho}{2} = \xi(\frac{4Q}{\pi\times 0.016^2})^2\frac{\rho}{2} \tag{27}$$

$$\frac{\Delta P_{valve}}{\Delta P_m} = 1.77 \tag{28}$$

From the results, it can be seen that pressure loss in two 90 degree pipe elbows is more than in main valve. Thus pressure loss in pipe can't be neglected in circuit breaker hydraulic mechanism. The comparisons of simulation and experiment results (opening operation) about pressure losses in valve and pipe are given in figure 14. The simulation result is shown to be in accordance with the experiment results nearly. The pressure difference between 1 and 2 is

pressure loss in valve including elbow in valve. The pressure difference between 2 and 3 is pressured loss in pipe between valve outlet and tank. Pressure loss in pipe is the main part of the whole pressure loss.

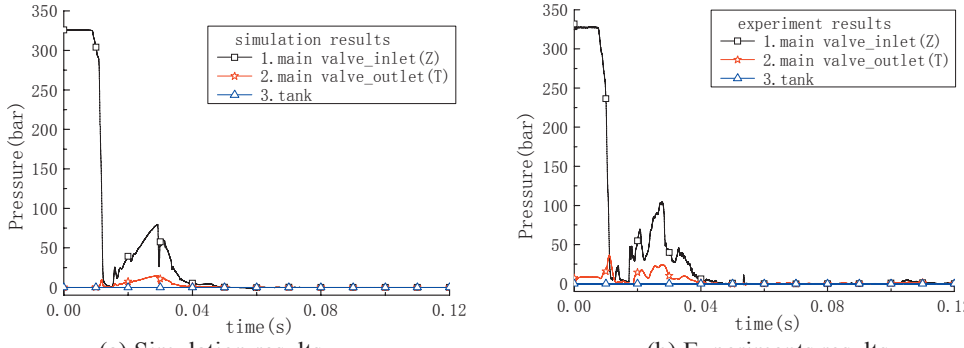

(a) Simulation results (b) Experiments results

Figure 14 Comparison of pressure loss in valve and pipe (opening operation)

Figure15 is shown that pipeline effect has an effect on opening characteristics of circuit breaker. With the length of main pipe and number of pipe elbow increasing, the pressure loss gain. Thus, the opening velocity descends. Fewer pipelines are the important improvement orientation. Else, fewer pipelines connected and highly integrated can reduce the probability of leak and enhance reliability of hydraulic system.

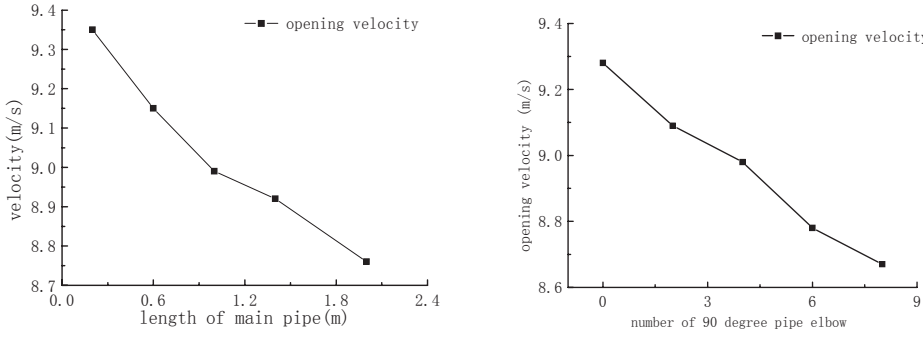

(a) Simulation results (b) Simulation results

Figure 15 Influence by pipe parameters of opening velocity

The comparisons of simulation and experiment results (closing operation) about pressure losses in valve and pipe are given in figure16. The pressure difference between 5 and 6 is pressure loss in valve including elbows in valve. The pressure difference between 4 and 5 is pressured loss in pipe between valve outlet and tank. It can be seen that pressure loss in pipe is the main part of press loss in circuit breaker system. In closing operation, because the length of main pipe is longer and the number of pipe elbow is more than that of in opening operation. The pressure loss in closing operation is more serious than that of in opening operation.

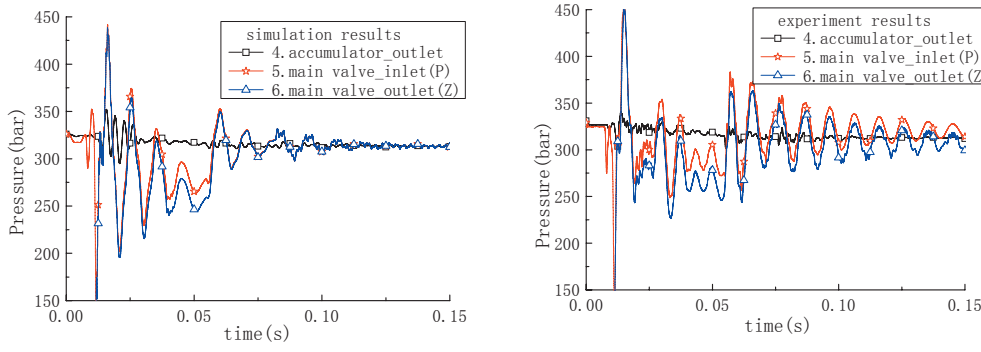

(a) Simulation results (b) Experiments results

Figure 16 Comparison of pressure loss in valve and pipe (closing operation)

5. Conclusions

The hydraulic operating mechanism of 550KV high voltage circuit breaker is introduced and analyzed. The simulation models of hydraulic operating mechanism are precisely established. Computation simulations coincide with experimental results in general, and these results show that the simulation models are correct. The results of simulations and experiments show that the opening time and opening velocity is about 21 ms and 8.9 m/s separately, and the switch time of control valve is about 10.6ms. Pressure loss in pipes is discussed, which has an important effect on opening characteristics of circuit breaker. They can't be neglected in the process of design and simulation in circuit breaker. Fewer pipes connected and pipe elbows can improve circuit breaker's characteristics effectively, which is the important development orientation of circuit breaker. The simulation model of the hydraulic operating mechanism is researched for effectively providing theoretical guidance for the design and optimization of hydraulic operating mechanism.

Nomenclature

C_q	Coefficient of discharge	F_e	Solenoid force
F_{f1} , F_{f21}	Spring force	F_{s1} , F_{s2} , F_{s3}	Steady flow force
m_{x3}	Mass of load	F_{t1} , F_{t2} , F_{t3}	Transient flow force
ρ	Density of oil	F_{v1} , F_{v2}	Viscosity friction
x_0	Displacement of cylinder	m_{x1} , m_{x2}, m_{x3}	Mass of spool
d_1,d_2 , d_3	Diameter of valve seat hole	Δr_1 , Δr_2	Constructional clearance;
L	Length of contact	x_1 ,x_2 ,x_3	Displacement of each stage valve
Q_1...Q_5	Flow rate	A_{00}, A_{01}, A_{02}	Throttle area
P_0	Pressure of the port P	P_B	Pressure of the piston rod cavity

P_D	Pressure of the port T	V_0, V_t	Volume of Gas in compression chamber
A_1	Effect acting area of P_1	m_0, m_t	Mass of Gas in compression chamber
A_2	Effect acting area of P_2	ΔP_m	Local pressure loss
ΔP_{valve}	Pressure in valve	ΔP_d	Pressure loss along the pipelines
ε	Damp coefficient	X_0	Displacement of cylinder
v	Velocity of fluid	B_p	Damp coefficient of cylinder
L_0	Length of pipe	P_1	Pressure of in compression chamber
d	Internal diameter of pipe	P_Z	Pressure of the piston pole cavity
V_B	Volume of the piston rod cavity	P_c	Pressure of outside compression chamber
F	Resistance force of load	λ	Friction damp coefficient along the pipelines
A_p	Acting area of compression chamber pressure		

Acknowledgements

This work is sponsored by the 11th-Five-Year National Science and Technology Planning Project (number:2006BAF01B12－02).

References

[1] IEEE Standard Definitions for Power Switchgear, ANSI/IEEE C37.100b-1986, 1981.
[2] Jiu Delin, Development of hydraulic operating devices LW-252 SF6 circuit breaker calculation and analysis of dynamic behavior, Dissertation of master degree, Shenyang Industry University, Shenyang,Liaoning,China,2002. (In Chinese)
[3] Janssen A.L.J at al, "A Summary of the Final Results and Conclusions of the Second International Enquiry of High Voltage Circuit Breakers" in CIGRE 1994 session, 1994, paper no. 13-202.
[4] Ken-ichi Natsui Ichiro Nakamura, Experimental Approach to One-Cycle Puffer Type SF6 Gas Circuit Breaker, IEEE Transactions on Power Apparatus and Systems, Vol.99,No.3,1980,833-840.
[5] TAKAGI HIROKAZU. Improvement in the Response of Hydraulic Systems for Circuit Breakers. Journal of Nihon Yukuatsu Gakkai Ronbunshu[C]. 2001(32), 124-130.
[6] Shi Wenyao, The Hydraulic Mechanism Of Switchgear, Beijing, China: Press of Mechanical Industry, 1990. (In Chinese)
[7] Li Zhuangyun, Hydraulic Components and system, Beijing, China: The press of engineering industry, 2005. (In Chinese)
[8] Thanapong Suwanasri, Investigation on No-load Mechanical Endurance and Electrical Degradation of a Circuit Breaker Model under Short Circuit Current Interruption. Dissertation of doctor degree. Rheinisch-Westfälischen Technischen Hochschule University, 2006.

Compositional Modeling of Fluid Power Systems using Predictive Tradeoff Models

Richard J. Malak Jr. (rmalak@gatech.edu)
Lina Tucker (lina@gatech.edu)
Christiaan J.J. Paredis (chris.paredis@me.gatech.edu)
Systems Realization Laboratory
G.W. Woodruff School of Mechanical Engineering
Georgia Institute of Technology
Atlanta, GA, USA

ABSTRACT

System-level decisions can have a large impact on the success of any design project, including those in the fluid power domain. Regardless of efforts by designers to optimize individual fluid power components, poor decisions at the systems level can lead to poor system performance and unsatisfied design requirements. In this paper, we apply the principles of system-level decision making to the design of fluid power systems. We describe a methodology for modeling fluid power component technology using predictive modeling and data mining techniques in a way that facilitates system-level modeling and decision making. We demonstrate the approach on the design of a hydraulic log splitter.

1. A SYSTEMS PERSPECTIVE ON FLUID POWER SYSTEMS DESIGN

The success of a design project involving fluid power technology depends on how well designers manage tradeoffs from a system-level perspective. Poor choices about circuit topology can limit efficiency and system performance regardless of how well designers optimize individual components. Even for a good topology choice, failure to relate system-level requirements to component specifications appropriately can limit system performance.

According to the principles of systems engineering, designers should approach systems design problems using a top-down hierarchical approach, with high-level decisions between alternative architectures and technologies preceding decisions about implementation details (1-5). The systems engineering approach can be effective for designing fluid power systems because such systems are comprised of well-defined functional components—e.g., pumps, valves, and accumulators—to which designers can allocate system-level requirements (also called requirements flowdown or requirements derivation). To decide between alternative configurations (e.g., load-sensing versus constant-displacement) or technologies (e.g., vane pumps versus gear pumps), designers can compare the "sized" system alternatives in light of their decision-making preferences.

Many of the requirements allocation procedures in common practice are effective within a limited scope, but are deficient from the perspective of system-level decision making. Designers usually are willing to make sacrifices in one system attribute in order to achieve

Fluid Power and Motion Control 2008 Edited by Dr D N Johnston and Professor A R Plummer

gains in another (e.g., giving up technical performance to save cost, paying extra for increased reliability). However, many requirements allocation procedures force designers to assume fixed values for certain attributes in order to compute others and to neglect attributes beyond a fairly narrow scope (for examples from the fluid power industry, see (6, 7)). Although such procedures are useful for verifying that a system meets its minimum technical requirements, they are insufficient for system-level decision making.

In this paper, we demonstrate a methodology for making requirements allocation and system configuration decisions for fluid power systems. It is based on predictive tradeoff modeling, which is an approach to abstracting the capabilities of a system or technology in a way that is useful for system-level decision making (8, 9). One generates a tradeoff model for a type of component (e.g., pumps, cylinders, engines) based on data about existing implementations of it, which allows designers to capture relationships between attributes for which a precise causal relationship may be unknown or difficult to derive analytically (e.g., ram force and cost, mass and maximum flow rate). Given a library of such models, designers can compose a model for a system-level design alternative using standard modeling practices and evaluate the alternative using optimization methods.

We have established a mathematical basis for this approach in prior work, and focus here on defining a methodology suitable for fluid power systems and demonstrating it on the design of a hydraulic log splitter. Section 2 is an overview of tradeoff modeling and a description of the proposed modeling methodology. Section 3 is a discussion of our efforts to generate a library of tradeoff models corresponding to common hydraulics components. In Section 4, we use the tradeoff model library to model the hydraulics system of a log splitter. Section 5 is a comparison of the decision we reach to the results of an exhaustive search of the database of components we use to generate the tradeoff models.

2. OVERVIEW OF COMPOSITIONAL TRADEOFF MODELING

2.1 Tradeoff modeling

Tradeoff modeling is an approach to abstracting the capabilities of a system or technology in a manner that is useful for system-level decision making. A tradeoff is a compromise designers must make when a decision involves conflicting objectives (e.g., to maximize efficiency while also minimizing cost). Tradeoff models capture relationships between attributes at one level of abstraction that occur due to the structure of the system at lower levels of abstraction (e.g., a relationship between efficiency and cost due to manufacturing, materials, or other constraints). Designers identify these relationships using data about existing design implementations, which enables them to generate models without knowing the underlying causal mechanism and helps ensure that predictions correspond to physically feasible designs. This is in contrast with the engineering analysis models designers typically use, which relate attributes at different levels of abstraction and often are physics-based. For example, a traditional model for a hydraulic piston pump might compute pump displacement as a function of piston dimensions, whereas a tradeoff model might relate pump displacement to cost or efficiency. Figure 1 is an illustration of this distinction.

Using predictions from a tradeoff model, designers can compare alternative system concepts and establish requirements for the detailed design of their components. As a simple example, designers could predict whether a load-sensing or constant-displacement circuit is

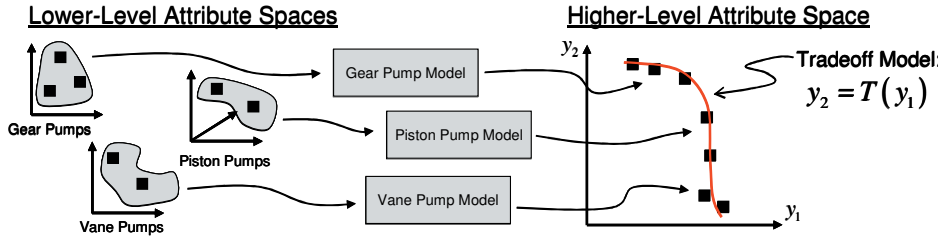

Figure 1: Visualization of the distinction between tradeoff models and the models typically used for evaluating designs.

preferable for their problem and, in the process, identify requirements (in terms of target attribute values) for designing the pump, valves and other components. Predictions depend on the preferences of a particular designer, so multiple designers can use the same tradeoff model and produce predictions appropriate for their respective problems.

Previously, we have investigated tradeoff models both for decisions in which risk is negligible (8, 9) and decisions under uncertainty (10). In this paper, we focus on decisions in which one can assume risk is negligible, which we formulate using multi-attribute value theory (MAVT) (11, 12). In MAVT, one formalizes preferences for different attributes (e.g., cost, mass, settling time) of a system and tradeoffs between these attributes. The formal representation of these preferences is called a value function.

Mathematically, a tradeoff model computes one or more of the attributes for a type of component as a function its other attributes. For example, to model hydraulic cylinders one could relate cost to mass, stroke, bore and maximum pressure. Designers obtain a tradeoff prediction by searching the input space of the tradeoff model using optimization methods with a search objective of maximizing the value function. Figure 2 is an illustration of this procedure for two hypothetical decision alternatives represented by the two tradeoff models, $T_1(\cdot)$ and $T_2(\cdot)$ ($V(\cdot)$ is a value function). A conventional approach to solving this decision problem would be to formulate an optimization problem in terms of the lower-level attribute spaces of the alternatives. In contrast, tradeoff models allow designers to abstract such lower-level details. Their role in the optimization problem is to constrain the search to

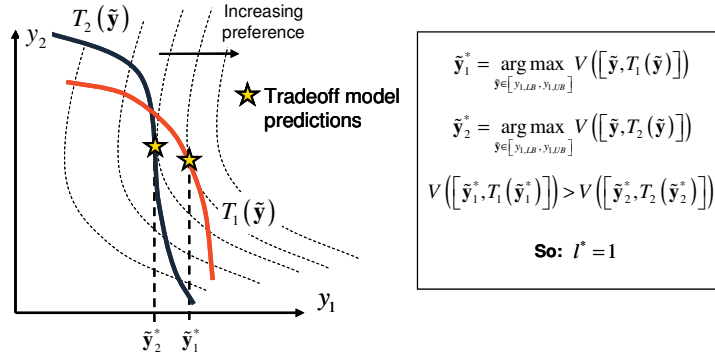

Figure 2: Visualization of prediction and selection procedure using tradeoff models. The dashed curves are iso-preference curves.

solutions that are both feasible and desirable—i.e., ones that rational designers can and would implement—without designers having to model explicitly what constitutes feasibility or rationality. This is because they are based on data about actual design implementations.

2.2 Tradeoff modeling methodology for fluid power systems

The tradeoff modeling methodology consists of two phases: (1) tradeoff model generation and (2) system composition and decision making. Designers can carry out the two phases independent of each other. For example, model generation can be an ongoing process in which one updates models as new data becomes available.

2.2.1 Tradeoff model generation phase

Figure 3 is a summary of the tradeoff model generation phase. With the exception of the dominance analysis step, this phase is similar to common data-driven modeling procedures (e.g., see (13-15)). The main concerns are defining what data to collect, how to validate the data prior to generalization and how best to generalize it into a valid continuous model.

Dominance analysis (Step 4) improves the accuracy of tradeoff predictions and is a key distinction between tradeoff modeling and other uses of predictive modeling in design (e.g., modeling cost (17-19) or environmental impact (20)). Domination is a decision-theoretic concept that is useful for eliminating alternatives a rational decision maker never would choose. In prior work, we extended a classical dominance rule to the case of eliminating

Step	*Description*
1. Model planning and scope definition	Decide what to model and how to model it. For fluid power systems, identify a type of component to model and the attributes designers typically associate with it in a decision-making context. Define clearly what constitutes a component of a given type.
2. Data collection	Gather data about components that fall within tradeoff model scope. Possible data sources: published datasheets and catalogs, manufacturers and vendors, experimental test data, and mathematical models of a component.
3. Data validation and data mining analysis	Verify that data fits tradeoff model scope. Data should appear plausible upon inspection by an expert. Examine for outliers. If necessary, use clustering analysis to re-scope into multiple tradeoff models. Many texts cover the required data analysis methods (e.g., (13-15)).
4. Dominance analysis	Eliminate data points that are dominated by the parameterized Pareto dominance criterion (8, 9).
5. Model fitting	Fit a tradeoff model to the non-dominated data using function approximation (e.g., regression, artificial neural network) or interpolation (e.g., Kriging). Model computes one or more attributes as a function of the others. Choice of inputs and outputs is arbitrary.
6. Model validation	Validate the model fit and estimate prediction error. For regression models, standard statistical analyses are reasonable. For other function approximation methods (e.g., artificial neural networks) and interpolation methods (e.g., Kriging), the hold-out or cross-validation approaches are more appropriate.
7. Domain characterization	Identify valid domain for model inputs to prevent automated search routines from extrapolating too far beyond the data. Often more complex than upper and lower bounds. If data set is convex, convex hull algorithms (e.g., qhull (16)) are useful.

Figure 3: Summary of tradeoff model generation phase of the compositional tradeoff modeling methodology.

component-level data and showed that this rule—called *parameterized Pareto dominance*—is sound with respect to MAVT. To apply the rule, designers must divide the attributes into two groups: those for which designer preferences always have the same orientation (e.g., all other factors being equal, designers would maximize reliability, minimize cost), called *monotone attributes*, and those for which designer preferences are problem-dependent (e.g., gear ratio) or conflicting (e.g., objectives to increase cylinder speed and ram force yield conflicting preferences for cylinder bore diameter), called *parameter attributes*. Designers can test whether one component dominates another by comparing their monotone attributes provided their parameter attributes are equivalent. For a formal definition and justification of this rule, see (9).

Formal domain characterization of a tradeoff model (Step 7) is of greater importance for tradeoff modeling than for other data-driven modeling problems. This is because one uses a tradeoff model in concert with optimization methods that rely on a formal domain definition to remain in a region of valid predictions. It often will be insufficient to simply identify upper and lower for the attributes, as we illustrate in Figure 4 using engine data from our example study (2D projection of 6D data). Note that this is not necessarily an indication of poor data collection, as such associations can occur due to marketing concerns (there may be no demand for certain combinations of attribute values) or physical constraints (it may be impossible to produce a component with certain properties).

2.2.2 System modeling and decision making phase

The system modeling and decision making phase is similar to other approaches for solving decision problems using optimization methods, but with the exception that designers use tradeoff models at the lowest level of abstraction. One creates a system-level model in the same way as if no tradeoff models were involved and then uses tradeoff models to constrain the search of the system model input space. This ensures that the resulting requirements correspond to components that are physically possible to implement (i.e., not beyond the barrier of current technology) and the predictions of overall system value are accurate.

Figure 5 (next page) is a summary of the procedure for this phase of the methodology. One repeats steps 3 through 5 for each system-level alternative or skips Step 6 if there is only one system-level alternative. Informational dependencies mean these steps should proceed more-or-less in sequence, but some iteration may be required. For example, a designer could change his or her decision objectives or preferences, or could identify a new alternative.

Figure 6 (next page) is a diagram of how the system composition model, tradeoff models, value function and optimization method relate to one another. The value function is the

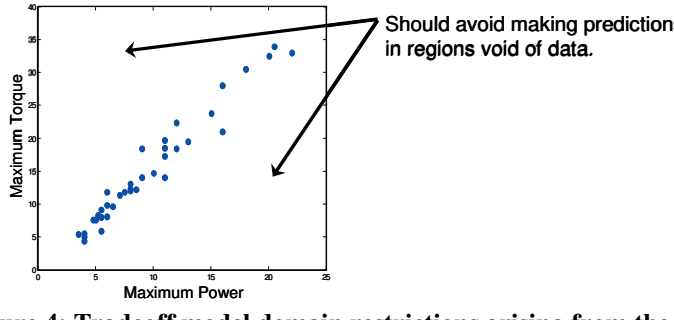

Figure 4: Tradeoff model domain restrictions arising from the data.

Step	*Description*
1. Formulate decision problem	Identify objectives and associated attributes for system-level decision (see (21) for how to identify objectives and attributes). Formalize preferences for tradeoffs between attributes using multi-attribute value theory (MAVT) (11, 12). The formalized preferences are called a *value function*.
2. Identify system-level alternatives	Creative process. Identify alternative system configurations and component technologies that might solve the design problem.
3. Model system-level alternatives	For each system-level alternative: Model the relationship between component-level and system-level attributes mathematically. This is called the *system composition model*, and may consist of multiple independent models.
4. Identify relevant tradeoff models	For each system-level alternative: Retrieve a tradeoff model from the library for each component in the system or create new tradeoff models as needed. Tradeoff model attributes must match attributes of component in system.
5. Search for most preferred tradeoff (requirements allocation)	For each system-level alternative: Use optimization methods to search tradeoff model input space for solution that maximizes decision preferences (value function from Step 1). Use tradeoff model domains to bound search space. Inputs at maximum are specifications for the components.
6. Final selection	Select system-level alternative that achieves largest value in Step 5 search.

Figure 5: Summary of model composition and decision making phase of compositional tradeoff modeling methodology.

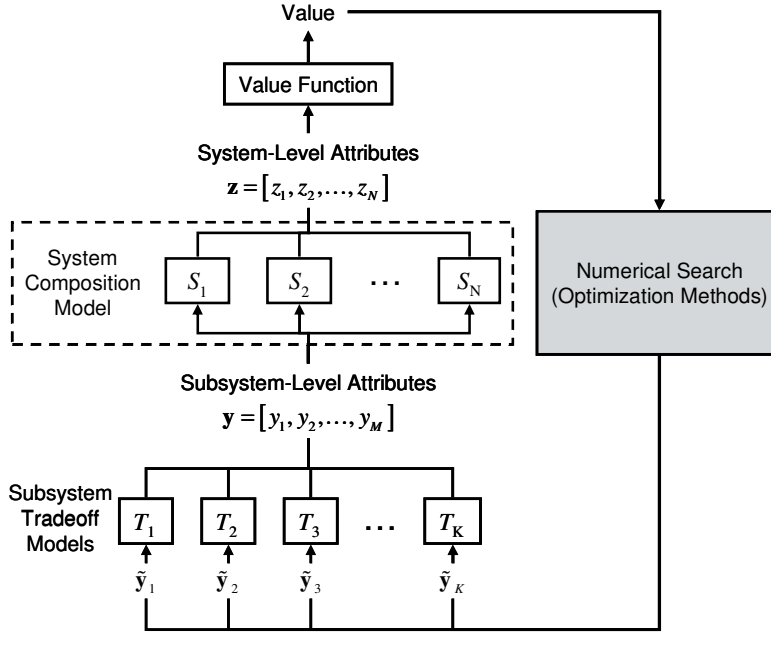

Figure 6: Compositional modeling framework. Component attributes are mapped to system-level attributes via the system composition model.

objective function for the optimization routine (value is to be maximized). The value function computes a scalar as a function of the system-level attributes. These attributes are a function of the component-level attributes. The system composition model consists of several individual models, $S_i(\cdot)$, that effect this mapping. Any $S_i(\cdot)$ may use only a subset of the component-level attributes, but every component-level attribute is an input to some $S_i(\cdot)$. The optimization routine controls the tradeoff model inputs and the tradeoff models compute the remaining component-level attributes.

3. GENERATING TRADEOFF MODELS FOR HYDRAULICS COMPONENTS

To demonstrate the tradeoff modeling methodology, we generate a library of tradeoff models for hydraulics components and use them to model a simple system. In this section, we address the first methodology phase: tradeoff model generation.

Our library consists of tradeoff models for gear pumps, directional control valves, cylinders and engines. We generate the models using data primarily from publicly-available data sheets and catalogs, with the remainder obtained from corporate partner companies or their venders. All of the pricing data is for similar purchase quantities and, whenever necessary, the data has been "anonymized" to protect proprietary interests.

Table 1 (next page) is a summary of the scope of the components in the database and Table 2 (next page) is a summary of the results from data analysis and model fitting. We removed a number of points prior to fitting based on our data analysis results. We found a vast majority of the data we collected had nearly the same maximum operating pressure, which rendered that attribute uninformative from a prediction standpoint. Accordingly, we eliminated any components with a maximum pressure below this level—about 172 bar (2500 psi)—and removed that attribute from the tradeoff models. A similar observation applies to the engine speed data: the speed at maximum power was the same for most engines in our database (3600 rpm), and the same was true for speed at maximum torque (2500 rpm). Consequently, we eliminated any engine data deviating from these marks by more than 100 rpm and did not use these attributes in the tradeoff models. We also eliminated a small percentage of components on the basis of being outliers or appearing suspect in some way (e.g., unusually high or low price for the stated performance attributes). After making these changes we performed the parameterized Pareto domination test, which also accounts for a large number of eliminations (see Table 2).

For each component, we formulate its tradeoff model to predict cost as a function of its other attributes. We use Kriging methods and the DACE Matlab Kriging Toolbox (22) to fit the tradeoff models and we perform validation using leave-one-out cross validation (15).

Initially, the fit of our engine tradeoff model was poor, and so we reexamined the data using clustering methods. We split the data into two disjoint clusters using the *k*-means algorithm (13) and fit two independent tradeoff models. The partitioning groups the engines into ones with higher maximum torque (those above 30 N-m (22 ft-lb)) and ones with lower torques. This improves prediction accuracy significantly, but at the expense of requiring two independent optimization searches to allocate requirements for the system (one using each engine tradeoff model).

Table 1: Summary of hydraulic component database.

Component	*Description*	*Attribute*	*Symbol*	*Min*	*Max*	*Units*
Pump	Single-stage gear pump with relief valve	Cost	c_{pump}	213	859	$
		Weight	w_{pump}	4.98 (2.26)	45.2 (20.5)	kg (lb)
		Displacement	V_g	1.18 (0.072)	48 (2.93)	cm^3/rev (in^3/rev)
		Max. op. pressure	$\Delta p_{\text{max,pump}}$	120 (1740)	250 (3625)	bar (psi)
		Max. op. speed	$n_{\text{max,pump}}$	3000	4000	rpm
		Efficiency (total)	η	0.44	0.92	-
Cylinder	Dual-acting medium- or heavy-duty.	Cost	c_{cyl}	57	404	$
		Weight	w_{cyl}	25.3 (11.47)	390 (177)	kg (lb)
		Stroke length	L_{cyl}	0.2 (8)	1.52 (60)	m (in)
		Bore diameter	b_{cyl}	0.038 (1.5)	0.127 (5)	m (in)
		Max. op. pressure	$\Delta p_{\text{max,cyl}}$	172 (2500)	207 (3000)	bar (psi)
Directional Control Valve (DCV)	Manual, spool-type, three-way closed center or four-way closed center (w/ open position) w/ load-side relief valve or detent	Cost	c_{dcv}	70	168	$
		Weight	w_{dcv}	15.4 (7)	35.3 (16)	kg (lb)
		Max. op. flow rate	Q	60.6 (16)	113.6 (30)	l/min (gal/min)
		Max. op. pressure	$\Delta p_{\text{max,dcv}}$	138 (2000)	310 (4500)	bar (psi)
Engine	Internal combustion engine (gasoline-powered)	Cost	c_{eng}	180	1907	$
		Weight	w_{eng}	3.4 (7.5)	58.5 (129)	kg (lb)
		Max. power output	$P_{\text{max,eng}}$	0.75 (1.0)	18.6 (25.0)	kW (hp)
		Speed at max. power output	$n_{\text{eng,maxP}}$	3600	7500	rpm
		Max. torque output	$\tau_{\text{max,eng}}$	1.08 (0.8)	55 (40.6)	Nm (lb-ft)
		Speed at max. torque output	$n_{\text{eng,maxT}}$	2200	5500	rpm

Table 2: Summary of data eliminations and tradeoff model generation.

Component	Engine (A)	Engine (B)	Pump	Cylinder	DCV
Total # in DB	59		61	188	36
# after outlier analysis	49		43	158	32
# after dom. analysis	14	5	24	137	8
Validation results: $\sqrt{MSE}$ *(% of mean)*	45.8 (15%)	33.2 (2%)	3.63 (1%)	14 (9%)	14.2 (13%)

Notes:
- Kriging interpolation used for all tradeoff models
- All tradeoff models predict cost as a function of the other attributes
- Engine split into two models after clustering analysis

4. SYSTEM COMPOSITION AND REQUIREMENTS ALLOCATION FOR A HYDRAULIC LOG SPLITTER

In this section, we demonstrate the system composition and decision making phase of the methodology (Figure 5). This phase relies on the modeling expertise of a designer to formalize the relationships between component-level attributes and system-level attributes for each system alternative. They use these system models together with their value function (i.e., formalized preferences for system-level attributes), tradeoff models and optimization methods to allocate requirements to each component and compare system alternatives.

We use a hydraulic log splitter as an example primarily for its simplicity. A log splitter is a system that divides a roughly cylindrical log into two or more pieces, typically in association with the harvesting of firewood. Several physical configurations are possible, but we limit the example to a horizontal-acting type (Figure 7). An operator loads a log into the system and then operates a control to drive a wedge into the log. The wedge action is aligned with the grain of the wood, so minimal effort is required after initiating the split. Critical requirements include portability (typically light weight, has wheels for transport, etc.), cost and splitting capabilities (maximum size of log it can handle, maximum force it can apply at wedge, etc.).

As a first step in formulating the decision problem, we identify the objectives hierarchy of Figure 8 (next page). Each leaf of the tree associates with an attribute the system model must compute:

- Cost: Sum of the purchase prices of the hydraulic components and the engine. We do not consider assembly or other cost factors in this example.
- Weight: Sum of the weights of the hydraulic components and the engine. We do not consider the weight of the structure.
- Ram Force: Maximum force the system can apply to the log.
- Log Length: The maximum length of log that will fit into the system.
- Cycle Time: An index for how long it takes to split a log. Defined as the time for the wedge to extend 0.15 meters (6 inches) at maximum engine torque (i.e., maximum ram force) plus the time to retract it with the engine running at maximum power (a conservative approximation of maximum ram speed).

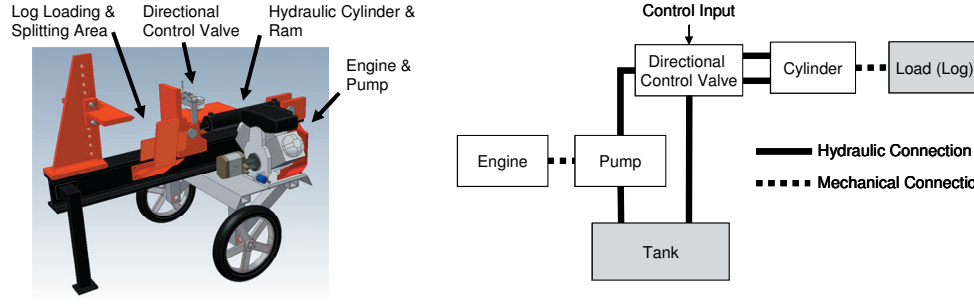

(a) (b)

Figure 7: Hydraulic log splitter: (a) physical layout, (b) functional configuration, where white boxes correspond to tradeoff models.

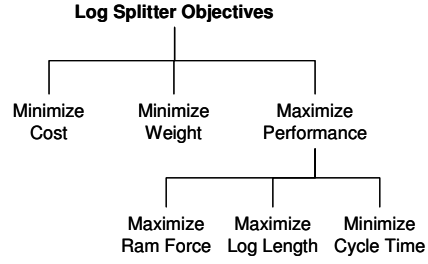

Figure 8: Objectives hierarchy for the log splitter problem.

Figure 9 contains graphs of the individual value functions corresponding to the system attributes. We elicit preferences for tradeoffs in a hierarchical fashion, first eliciting a value function for the three performance attributes and then combining this result with weight and cost for the top-level elicitation (for a discussion on eliciting preferences, see (12)). The performance attribute is a tradeoff among its constituent objectives:

$$v_{\mathrm{P}} = 0.0936v_{\mathrm{T}} + 0.0936v_{\mathrm{F}} - 0.1925v_{\mathrm{L}} + 0.163v_{\mathrm{T}}v_{\mathrm{F}} + 0.2946v_{\mathrm{T}}v_{\mathrm{L}} + 0.2946v_{\mathrm{F}}v_{\mathrm{L}} + 0.2530v_{\mathrm{T}}v_{\mathrm{F}}v_{\mathrm{L}}$$

where $v_T = V_{\mathrm{T}}(z_{\mathrm{T}})$ is the value function result for the cycle time attribute at z_{T}, $v_F = V_{\mathrm{F}}(z_{\mathrm{F}})$ is for the ram force attribute and $v_L = V_{\mathrm{L}}(z_{\mathrm{L}})$ is for the log length attribute. The top-level value function is

$$V(\mathbf{z}) = 1.03v_{\mathrm{C}} + 1.05v_{\mathrm{P}} + 0.95v_{\mathrm{W}} - 1.29v_{\mathrm{C}}v_{\mathrm{P}} - 1.18v_{\mathrm{C}}v_{\mathrm{W}} - 1.18v_{\mathrm{P}}v_{\mathrm{W}} + 1.62v_{\mathrm{C}}v_{\mathrm{P}}v_{\mathrm{W}} \quad (1)$$

where the $v_{\mathrm{C}} = V_{\mathrm{C}}(z_{\mathrm{C}})$ is the value function for the cost evaluated at z_C, $v_{\mathrm{W}} = V_{\mathrm{W}}(z_{\mathrm{W}})$ is for the weight attribute, v_{P} is the performance attribute defined above and $\mathbf{z}$ is the system-level attribute vector. Thus, the system-level decision problem is to maximize Equation 1, and the requirements allocation objective is to find the component-level attributes at this maximum. Let $\mathbf{S}$ represent the vector-valued system composition model (comprised of the $S_i(\cdot)$ from Figure 6), $\tilde{\mathbf{y}}$ denote the vector of component-level attributes controlled by the

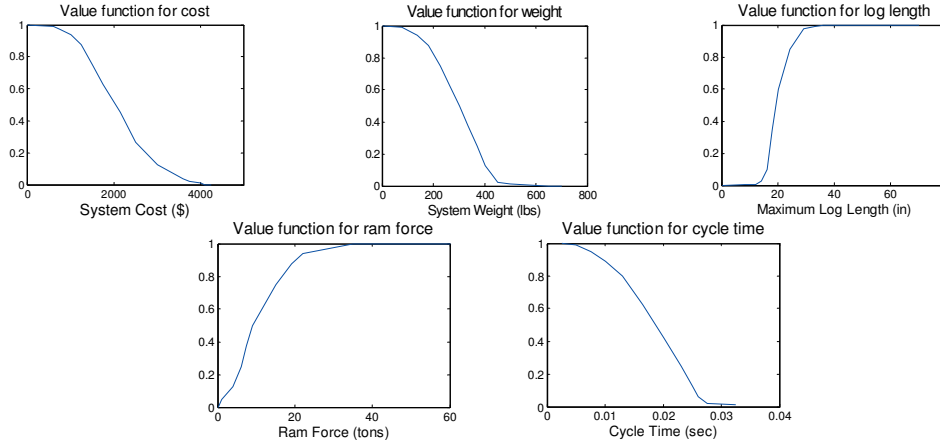

Figure 9: Graphs of the individual value functions for the five system-level attributes of the log splitter design problem.

Cost	$z_{\mathrm{C}} = S_{\mathrm{C}}(\mathbf{y}) = c_{\mathrm{pump}} + c_{\mathrm{cyl}} + c_{\mathrm{dcv}} + c_{\mathrm{eng}}$
Weight	$z_{\mathrm{W}} = S_{\mathrm{W}}(\mathbf{y}) = w_{\mathrm{pump}} + w_{\mathrm{cyl}} + w_{\mathrm{dcv}} + w_{\mathrm{eng}}$
Ram Force	$z_{\mathrm{F}} = S_{\mathrm{F}}(\mathbf{y}) = \left(\Delta p_{\mathrm{max,sys}}\right)\left(b_{\mathrm{cyl}}^2 \frac{\pi}{4}\right)$ where $\Delta p_{\mathrm{max,sys}}$ is the maximum operating pressure of the system as dictated by the rating limitations of components or the pressure that can be generated by the engine-pump combination.
Log Length	$z_{\mathrm{L}} = S_{\mathrm{L}}(\mathbf{y}) = L_{\mathrm{cyl}}$
Cycle Time	$z_{\mathrm{T}} = S_{\mathrm{T}}(\mathbf{y}) = 1.56\left(b_{\mathrm{cyl}}^2 \frac{\pi}{4}\right)\left(\frac{1}{Q_\tau} + \frac{1}{Q_{\mathrm{PWR}}}\right)$ where Q_τ is the maximum flow rate the system can achieve at $\tau_{\mathrm{max,eng}}$ and Q_{PWR} is the maximum flow rate (in gal/min) at $P_{\mathrm{max,eng}}$. Both are non-decreasing functions of pump displacement, the engine speeds at the respective operating points and component rating limitations.

Figure 10: Summary of system composition model for log splitter design problem.

optimization routine, and $\mathbf{T}(\tilde{\mathbf{y}})$ denote the vector of all the component-level tradeoff model predictions. Thus, one can state the requirements allocation problem formally as

$$\tilde{\mathbf{y}}^* = \arg\max_{\tilde{\mathbf{y}} \in \mathcal{Y}} V\left(\mathbf{z} = \mathbf{S}\left(\left[\tilde{\mathbf{y}}, \mathbf{T}(\tilde{\mathbf{y}})\right]\right)\right),$$

where $\mathcal{Y}$ is the domain in which the tradeoff model predictions are valid and $\left[\tilde{\mathbf{y}}^*, \mathbf{T}(\tilde{\mathbf{y}}^*)\right]$ are the most preferred component requirements for the system.

To solve the decision problem, it is necessary to relate the component-level attributes to those used in Equation 1. Figure 10 is a summary of the system composition model we use for the log splitter example. The models are the same as what system designers would use if they were not using tradeoff models, which matter mainly in the optimization search step of the process. It is important that one use every attribute of a tradeoff model in the system model or assign them constant value; passing unused variables to the optimization method can reduce solver efficiency significantly. We use all the component-level attributes in the log splitter system model.

To solve the decision problem, we integrate the various models according to the diagram in Figure 6. We are considering only one system configuration, but there are two engine tradeoff models. Thus, we execute this structure once for each engine tradeoff model and choose the best result from the two runs.

5. COMPARISON TO EXHAUSTIVE SEARCH OF COMPONENTS DATABASE

To demonstrate that the tradeoff modeling approach yields a reasonable requirements allocation solution for the log splitter, we compare the results of the optimization search defined in Section 4 to an exhaustive search of our components database. One typically would not do an exhaustive search in practice due to the large number of combinations that

can exist. Even after removing outliers, our modestly-sized database yields nearly 13 million possible combinations for the log splitter system. We do not necessarily expect the two approaches to yield equivalent solutions, since the tradeoff models are able to generalize beyond the database contents. However, the exhaustive solution does provide a meaningful baseline for comparison. We expect the tradeoff modeling approach to do no worse than the exhaustive search on the basis that the tradeoff models are representations of the database contents.

Table 3 contains results from the exhaustive search and the two tradeoff modeling optimization runs (one with each engine tradeoff model). The Engine A tradeoff model corresponds to the tradeoff model for lower-torque engines. According to the tradeoff modeling approach, a system that includes an engine from the Engine A domain is preferred to a system with an engine from the Engine B domain (preference value of 0.958 compared to 0.933). The exhaustive search corroborates this result, with its engine being virtually identical to the engine predicted using the Engine A tradeoff model.

Overall, the tradeoff modeling approach yields results similar to the exhaustive search solution. The tradeoff modeling approach identifies targets for the pump and engine that are virtually identical to those of the exhaustive search solution. However, the tradeoff modeling approach does generalize beyond the database contents for the cylinder and DCV requirements. Upon examining the system attribute valuations, one can see that the tradeoff

Table 3: Comparison of log splitter requirements allocation results from tradeoff modeling approach and exhaustive search.

Component	*Attribute*	*Composed Tradeoff Models (Engine A)*	*Composed Tradeoff Models (Engine B)*	*Exhaustive Search of DB*
Pump	Cost	$ 223	$ 221	$ 223
	Weight	11.7 kg (5.3 lb)	7.9 kg (3.6 lb)	11.7 kg (5.3 lb)
	Displacement	6.1 cc/rev (0.37 in^3/rev)	5.7 cc/rev (0.35 in^3/rev)	6.1 cc/rev (0.37 in^3/rev)
	Max. op. speed	4000 rpm	4000 rpm	40000 rpm
	Efficiency	0.88	0.63	0.88
Cylinder	Cost	$ 233	$ 213	$ 260
	Weight	181 kg (82.3 lb)	155 kg (70 lb)	253.75 kg (115.1 lb)
	Stroke length	0.68 m (27 in)	0.88 m (34.5 in)	0.71 m (28 in)
	Bore diameter	0.114 m (4.5 in)	0.102 m (4 in)	0.127 m (5 in)
Directional Control Valve	Cost	$ 83	$ 75	$ 90
	Weight	18.7 kg (8.5 lb)	25.9 kg (11.8 lb)	15.4 kg (7 lb)
	Max. op. flow rate	68.1 l/min (17 gal/min)	73.8 l/min (19.5 gal/min)	68 l/min (18 gal/min)
Engine	Cost	$ 330	$ 800	$ 300
	Weight	105 kg (47 lb)	192 kg (87 lb)	121 kg (55 lb)
	Maximum Power	6.7 kW (8.9 hp)	11.2 kW (15 hp)	6.7 kW (9 hp)
	Maximum Torque	18.8 N-m (13.8 ft-lb)	32.3 N-m (23.8 ft-lb)	19 N-m (14 ft-lb)
Value Components	Ram Force (v_F)	0.897	0.775	0.958
	Log Length (v_L)	0.944	0.996	0.963
	Cycle Time (v_T)	0.987	0.993	0.967
	Performance (v_P)	0.874	0.812	0.918
	Weight (v_W)	0.928	0.887	0.87
	Cost (v_C)	0.955	0.850	0.955
System Value (v)		**0.958**	**0.933**	**0.956**

modeling solution sacrifices small amounts in terms of the performance attributes in order to improve in the weight attribute. That this particular solution is not in the database, underscores a strength of the tradeoff modeling approach over discrete searches.

6. CONCLUSIONS

In this paper, we describe and demonstrate a methodology for modeling fluid power systems for system-level decision making. This approach is rooted in systems engineering principles and represents an improvement beyond common practice within the fluid power industry. A major advantage of the tradeoff modeling approach is that it provides designers with a means to capture and reason about associations among attributes that otherwise would be difficult to relate. Another advantage is that by virtue of being fit to data about existing design implementations, tradeoff models provide predictions that correspond to feasible design solutions. This is important for minimizing redesign and iteration in a systems design project. Also noteworthy is that designers can reuse tradeoff models on different design problems. A company could maintain a library of tradeoff models for common types of components that its designers could reuse frequently, thereby maximizing return on modeling investment. One limitation of tradeoff modeling is that the models are only as good as the data upon which they are based. This can be problematic if data about a particular attribute is hard to come by (e.g., for many types of components, reliability data can be hard to find) or if only few examples of a particular type of component exist (e.g., we had ample data about cylinders, but significantly less for the DCV). However, in such cases it is possible for designers to account explicitly for the risk introduced by inaccurate models by formulating decisions under uncertainty. We already have made a preliminary investigation into tradeoff modeling for decision under uncertainty (10) and plan to expand upon it in the future.

ACKNOWLEDGEMENT

This material is based in part upon work performed within the ERC for Compact and Efficient Fluid Power, supported by the National Science Foundation under Grant No. EEC-0540834. Additional support is provided by the National Science Foundation under grant CMMI-0522116.

REFERENCES

(1) Royce, W. W. (1970). "Managing the Development of Large Systems: Concepts and Techniques." 9th International Conference on Software Engineering. ACM, 328-38.

(2) Boehm, B. W. (1988). "A Spiral Model of Software Development and Enhancement." *IEEE Computer*, 21(5), 61-72.

(3) Forsberg, K. and Mooz, H. (1992). The Relationship of Systems Engineering to the Project Cycle. *Engineering Management Journal*, 4(3), 36-43.

(4) Buede, D. M. (2000). *The Engineering Design of Systems*. New York: John Wiley & Sons.

(5) Sage, A. P. and Armstrong Jr., J. E. (2000). *Introduction to Systems Engineering*. Wiley and Sons.

(6) (1997). "Selection of Driveline Components." Sauer-Sundstrand Company, Ames, IA.
(7) (1998). "Pump and Motor Sizing Guide." Eaton Corporation Hydraulics Division, Eden Prarie, MN.
(8) Malak, R. J. and Paredis, C. J. J. (2007). "Using Parameterized Pareto Sets to Model Design Concepts." ASME International Mechanical Engineering Congress and Exposition (IMECE2007), Seattle, WA, USA. Paper No. IMECE2007-43226.
(9) Malak, R. J., Tucker, L. and Paredis, C. J. J. (2008). "Composing Tradeoff Models for Multi-Attribute System-Level Decision Making." ASME 2008 International Design Engineering Technical Conferences and Computers and Information in Engineering Conference (IDETC/CIE 2008), New York, NY. Paper No. DETC2008-49970.
(10) Malak, R. J. and Paredis, C. J. J. (2008). "Modeling Design Concepts under Risk and Uncertainty using Parameterized Efficient Sets." SAE World Congress, Detriot, MI. Paper No. SAE2008-01-0709.
(11) Fishburn, P. C. (1965). *Decision and Value Theory*. New York: Wiley.
(12) Keeney, R. L. and Raiffa, H. (1993). *Decisions with Multiple Objectives* (2 ed.). Cambridge, UK: Cambridge University Press. (Original work published in 1976).
(13) Hand, D. J., Mannila, H. and Smyth, P. (2001). *Principles of Data Mining*. Cambridge, MA: MIT Press.
(14) Kutner, M. H., Nachtsheim, C. J., Neter, J. and Li, W. (2005). *Applied Linear Statistical Models* (5th ed.). New York: McGraw-Hill/Irwin.
(15) Witten, I. H. and Frank, E. (2005). *Data Mining: Practical Machine Learning Tools and Techniques*. Academic Press.
(16) Barber, C. B., Dobkin, D. P. and Huhdanpaa, H. T. (1996). The Quickhull Algorithm for Convex Hulls. *ACM Transactions on Mathematical Software*, 22(4), 469-83.
(17) Dean, J. (1976). *Statistical Cost Estimation*. Bloomington, IN: Indiana University Press.
(18) Daschbach, J. M. and Apgar, H. (1988). Design Analysis through Techniques of Parametric Cost Estimation. *Engineering Costs and Production Economics*, 14(2), 87-93.
(19) Farineau, T., Rabenasolo, B., Castelain, J. M., Meyer, Y. and Duverlie, P. (2001). Use of Parametric Models in an Economic Evaluation Step During the Design Phase. *International Journal of Advanced Manufacturing Technology*, 17(2), 79-86.
(20) Dewulf, W. (2003). *A Pro-Active Approach to Ecodesign: Framework and Tools*. Ph.D. thesis, Katholieke Universiteit Leuven.
(21) Clemen, R. T. (1996). *Making Hard Decisions: An Introduction to Decision Analysis* (2nd ed.). Pacific Grove, CA: Duxbury Press.
(22) Lophaven, S. N., Nielsen, H. B. and Sondergaard, J. (2002). "DACE: A Matlab Kriging Toolbox." Technical Report IMM-TR-2002-12. Technical University of Denmark.

A novel high efficiency electrohydrostatic flight simulator motion system

K G Cleasby
Thales Training and Simulation Ltd.

A R Plummer
Centre for Power Transmission and Motion Control
University of Bath

Abstract
Modern flight training simulators must be equipped with long stroke six degree-of-freedom motion systems that have high dynamic response. For many years electro-hydraulic actuators in a Stewart platform configuration have been found to best meet the performance requirements. However, valve-controlled actuators are very inefficient leading to a large power consumption, and also the need for a substantial cooling system to remove waste energy (heat) from the hydraulic oil. This paper describes a new design of motion system that uses a controlled brushless motor for each actuator, with power transmission via directly driven pumps to conventional simulator hydraulic cylinders. Accumulators are used to store and later recycle high pressure oil when actuators retract. In this way, power consumption has been dramatically reduced (for example from 45kW to 5kW during one representative motion waveform), while retaining the proven characteristics of the cylinder drive. Power consumption is lower, by a factor of between 2 and 4, than an equivalent all-electric solution. The motion system will be supplied for the first time with Boeing 787 simulators to be delivered in 2008. Design details are given in this paper, together with predicted and measured power consumption during a variety of representative cyclic motions.

1 INTRODUCTION

Flight training simulators, such as that shown in Figure 1, save the airlines significant amounts of money as pilots can be trained throughout the day, in safety and without risk of damage to the real aircraft. At most major airports the demand for take-off slots exceeds supply, but using simulators allows pilots to practice taking off and landing at a virtual re-creation of the airport without causing associated environmental damage and nuisance.

Pilot training involves creating the feel of how an aircraft will respond during each manoeuvre so that adjustments to the controls produce the correct feedback to the pilot. The best quality feel is achieved when such training simulators include a motion system that can reproduce the required motion cues produced by the aircraft in flight.

Fluid Power and Motion Control 2008 Edited by Dr D N Johnston and Professor A R Plummer

Fig. 1 Full flight training simulator

Motion systems require a good dynamic performance, large range of movement, and they need to be exceptionally smooth. As described in the next section, valve-controlled electro-hydraulic actuation has become accepted as the best way of meeting these challenging requirements. However valve-controlled systems consume a large amount of power, which then needs to be removed in the form of waste heat. This paper describes an alternative design which exhibits significant power saving. The new system is being supplied with the first Boeing 787 Dreamliner simulators.

2. CONVENTIONAL MOTION SYSTEM TECHNOLOGY

Stewart first proposed the use of a triangulated hexapod design for flight simulation in 1965 [1]. In this mechanism (Figure 2) each of the six legs can be extended or retracted to provide simultaneous movement in any of the 3 translational or 3 rotational degrees-of-freedom (DOF). The Stewart platform was first used for commercial flight simulators in the 1970's, replacing other designs with more limited DOF [2].

In the majority of commercial systems, long stroke hydraulic jacks are each driven by their own servovalve, supplied by oil at a fixed pressure from a large hydraulic power unit (HPU) – see Figure 3. This HPU is housed in its own substantially built acoustic room to prevent noise from interfering with training, and incorporates a sizeable water cooling unit. As an example, the Thales simulator HPU includes two 55kW electric motors each driving a variable displacement pump. The pump for circulating chilled water requires an additional 10kW.

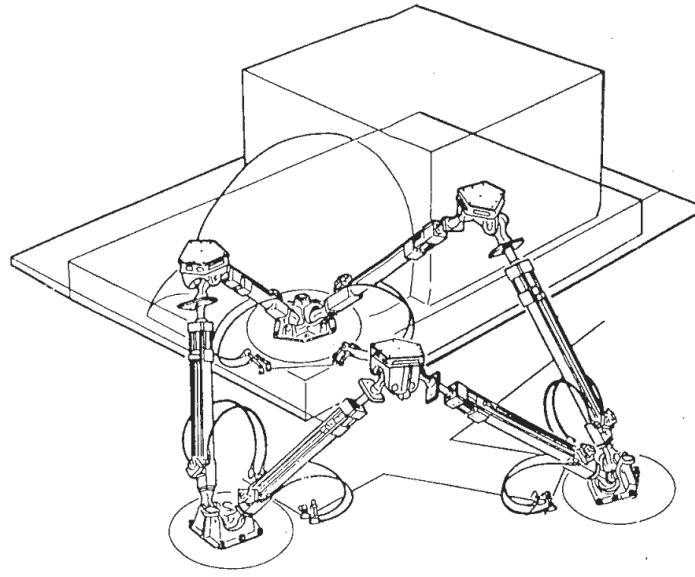

Fig. 2 Stewart platform motion system

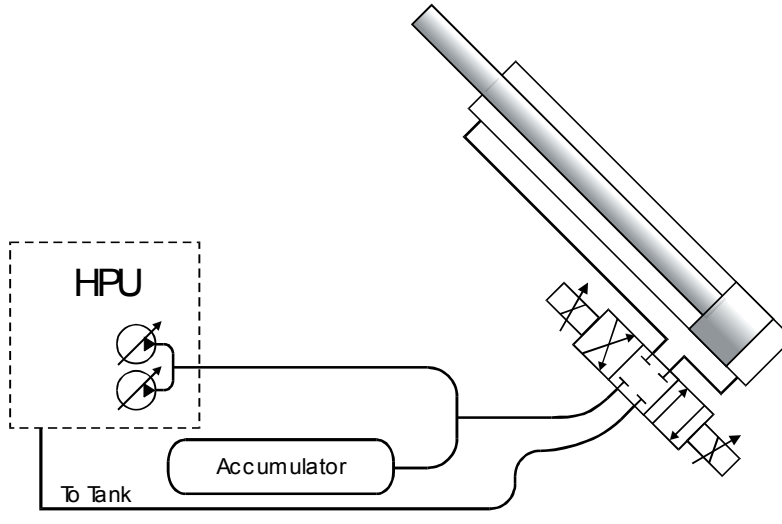

Fig. 3 A conventional valve-controlled hydraulic jack

3. NEW ELECTROHYDROSTATIC MOTION SYSTEM DESIGN

To reduce power consumption a new concept for driving the motion system jacks has been developed. The concept uses a coupled pair of fixed displacement pumps as shown in Figure 4. The pumps are driven by a 3-phase synchronous brushless servomotor. The servomotor is controlled in closed-loop using jack position feedback. By using two identical pumps on one shaft the flow pumped into the bottom of the jack is double the flow taken from the top of the jack. As the jack has been designed with a 2:1 area ratio the net flow

into the top (rod side) accumulator is theoretically zero, and its pressure remains constant. Sufficient pressure must be available on the rod side to generate the tensile loads required to support the platform in certain extreme positions.

The lower accumulator shown in Figure 4 provides a static pressure that counterbalances the weight of the simulator. It must also oppose the additional force resulting from the pressure in the rod side of the jack. With the correct choice of pressures to suit the weight of the simulator the net static torque on the electric motor can be very low. As the platform descends half of the flow from the head side of the jack is pumped into the lower accumulator. This causes the pressure in the lower accumulator to increase, but also the jack angle to the vertical will increase so that a greater load is placed on each jack, maintaining a better counterbalance throughout the vertical platform travel.

When the simulator is pitched or rolled to a static position there will be a larger unbalanced pressure drop across the pump. In this state the drive motor will have to provide a torque to oppose the pump torque and prevent rotation. Thus the motor needs to provide a static torque without using significant electrical power.

The extra efficiency compared to the conventional hydraulic system is obtained from two main factors:

1. Firstly the hydraulic counterbalance keeps the motor torque to a minimum when operating around mid stroke so that motor current is low and the associated copper losses are also low. The counterbalancing accumulators store and release energy associated which height changes, rather than this energy being dissipated.
2. Secondly the hydraulic part of the system does not restrict or meter the flow to provide control of velocity. Instead this comes from accurately controlling the speed of the electric motors that drive the hydraulic pumps.

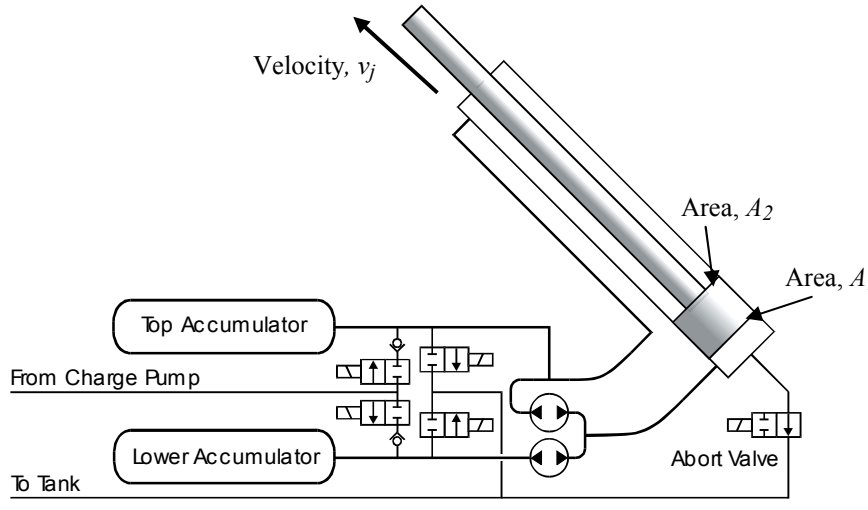

Fig. 4 New hydrostatic design

The concept of the electrohydrostatic actuator (EHA), i.e. linear motion control using a variable speed electrical drive via hydraulic transmission, is by no means new in other fields. EHA's are becoming commonplace for primary flight controls in aircraft (see e.g. [3]). Good performance is reported for an experimental gear-pump driven system in [4]. The design variant with a single-ended cylinder with accumulator energy storage is more unusual, but has been previously suggested as a way to save energy in mobile machines, in this case with the pump driven off the engine [5].

4. PREDICTION OF POWER CONSUMPTION IN A CONVENTIONAL VALVE-CONTROLLED MOTION SYSTEM

For the purposes of comparing power consumption, only sinusoidal motion in the heave (vertical) direction will be considered. For a valve-controlled system, the power consumption can be calculated using the supply pressure and the average rate at which fluid volume is consumed. Most flow is used in moving the piston, but some is continually lost via leakage, and when the flow requirement is less than that delivered by the minimum displacement of the pumps then there is an appreciable flow through the system relief valve.

Let the heave velocity be given by:

$$v_p = V_p \sin \omega t \tag{1}$$

A linearised conversion between platform heave and jack motion is given by using a simple scaling factor R:

$$v_j = RV_p \sin \omega t \tag{2}$$

To raise the platform the six servovalves connect the supply pressure to the head side of the jacks and connect the rod side to tank. They then reverse this connection to retract the jacks. The flow from the high pressure supply is given by the product of piston area and velocity, hence:

$$q = 6A_1 RV_p \sin \omega t \quad \text{for} \quad \sin \omega t \geqslant 0 \tag{3}$$

$$q = 6A_2 RV_p \sin \omega t \quad \text{for} \quad \sin \omega t < 0 \tag{4}$$

The average flow for all jacks is given by:

$$Q_{av} = \frac{1}{\mathrm{T}} \int_0^T q \; dt \tag{5}$$

$$Q_{av} = \frac{1}{\mathrm{T}} \int_0^{T/2} 6(A_1 + A_2) RV_p \left|\sin \omega t\right| \; dt \tag{6}$$

$$Q_{av} = \frac{6(A_1 + A_2) RV_p}{\pi} \tag{7}$$

where $T = 2\pi/\omega$. The total average power consumption is then:

$$\Psi_v = \frac{1}{\eta_v} \left(\frac{6(A_1 + A_2) RV_p P_s}{\pi} + \Psi_r \right) + \Psi_l \tag{8}$$

where P_s is the supply pressure, Ψ_l is a constant term representing water pump and leakage-related power loss, and Ψ_r is power loss through the relief valve (which is only significant when the jack flow requirement is below the minimum pump displacement), and η_v is the electric motor/pump efficiency. Thus for all but low velocities, the first term in equation (8) dominates and the power consumed is approximately proportional to the velocity amplitude.

5. PREDICTION OF POWER CONSUMPTION FOR NEW ELECTROHYDROSTATIC MOTION SYSTEM

5.1 Electrical drive considerations

In this application the motor and drive amplifier must accelerate and decelerate the platform. The actions required in this four-quadrant operation are shown in Figure 5. To operate in all four quadrants the drive amplifier must be able to force the motor current in either direction regardless of the direction of rotation. The electronic configuration required to perform this is shown in simplified form in Figure 6. In Figure 6(a) the direction of the output torque and hence current is the same as the direction of rotation and hence the back EMF (electro-motive force) opposes the DC supply voltage. This corresponds to the situation in quadrants 1 and 3, where there is electrical power input via the motor to the motion system. In Figure 6(b) the direction of the output torque and hence the current are in the opposite direction to the direction of rotation. This corresponds to the situation in quadrants 2 and 4 in which the platform mass is losing its kinetic energy. Hence the current must be reversed compared to quadrants 1 and 3 but the back EMF due to rotational speed has not reversed. Under these conditions the motor is acting as a generator and the kinetic energy is put back into the drive amplifier supply. However, in this application it is not feasible for the drive amplifier capacitors to store all the large amount of power generated during braking and the excess power is dissipated using large resistors.

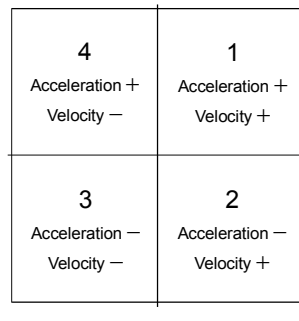

Fig 5. Four Quadrant Operation

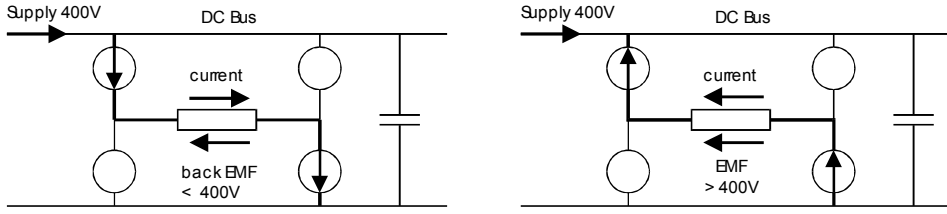

(a) Electrical power to motor (b) Electrical power from motor (regeneration)

Fig 6. Full bridge motor drive

In the following calculations it will be assumed that the power generated in quadrants 2 and 4 cannot be recovered. In practice there is some power generated by the motor in these quadrants but this approximately balances other losses which are not considered. Thus only the power taken from the supply in quadrants 1 and 3 will be included in the calculations.

5.2 Power consumed for platform acceleration

As previously stated the weight of the simulator is counterbalanced by the charge in the hydraulic accumulators and there is no static load on the electric motors. The power consumed is that required to accelerate the platform, and the net power during deceleration (braking) is assumed to be zero. Hence the instantaneous power consumption given by the product of inertial force and velocity is:

$$\psi = M\dot{v}_p v_p \quad \text{for} \quad \dot{v}_p v_p \geqslant 0 \tag{9}$$

$$\psi = 0 \quad \text{for} \quad \dot{v}_p v_p \geqslant 0 \tag{10}$$

where M is the platform mass. Note that:

$$\dot{v}_p v_p = V_p{}^2 \omega \sin \omega t \cos \omega t \tag{11}$$

$$\dot{v}_p v_p = \frac{V_p{}^2 \omega}{2} \sin 2\omega t \tag{12}$$

Thus the average acceleration power is:

$$\Psi_a = \frac{1}{\mathrm{T}} \int_0^T \psi \, dt \tag{13}$$

$$\Psi_a = \frac{M V_p{}^2 \omega}{2\pi} \tag{14}$$

Note that the inertia of motors and pumps will also be significant, and this should be determined as an effective mass referred to the platform and included in M.

5.3 Power consumption resulting from pressure losses

The main power losses in the hydraulic part of the system are the result of pressure losses in manifolds and pipework. The pressure loss is assumed to be proportional to the square of the flow rate. The losses on the head and rod side respectively are:

$$\left|\Delta p_1\right| = K_1\left(A_1 v_j\right)^2 \tag{15}$$

$$\left|\Delta p_2\right| = K_2\left(A_2 v_j\right)^2 \tag{16}$$

The instantaneous power loss for each jack is:

$$\psi_j = \left|\Delta p_1 A_1 v_j\right| + \left|\Delta p_2 A_2 v_j\right| \tag{17}$$

or

$$\psi_j = K\left|v_j\right|^3 \tag{18}$$

where

$$K = K_1 {A_1}^3 + K_2 {A_2}^3 \tag{19}$$

Using equations (2) and (18), the average power associated with pressure losses for all six jacks is:

$$\Psi_p = \frac{6}{\mathrm{T}}\int_0^T KR^3 {V_p}^3 \left|\sin \omega t\right|^3 dt \tag{20}$$

$$\Psi_p = \frac{8KR^3}{\pi} {V_p}^3 \tag{21}$$

5.4 Total Power Consumption

In addition to the acceleration and pressure loss powers, due to inexact counterbalancing of platform weight there is another power demand which is still present when the platform is stationary. This quiescent power (Ψ_q) is assumed to be constant. Thus the total power requirement is:

$$\Psi_e = \frac{1}{\eta}\left(\Psi_a + \Psi_p\right) + \Psi_q \tag{22}$$

$$\Psi_e = \frac{1}{\eta_e}\left(\frac{M\omega}{2\pi} {V_p}^2 + \frac{8KR^3}{\pi} {V_p}^3\right) + \Psi_q \tag{23}$$

where η_e is the motor drive / pump efficiency.

6 THEORETICAL AND EXPERIMENTAL POWER COMPARISON

6.1 Motion specification and predicted power consumption

To be approved for pilot training a flight simulator must have a motion performance in accordance with specifications provided by the regulatory authorities. Some requirements

relating to vertical motion are given in Table 1. Sinusoidal motion is assumed for this study. In normal training the simulator motion will rarely reach these amplitudes and consequently half the amplitudes specified will be used for comparing the power consumption (shown in the final column in Table 1, and Figure 7).

The parameters of the conventional and new motion systems which are compared in this paper are given in Table 2. Using these parameters, and equations (8) and (23), the power consumption of the two systems is compared in Figure 8.

Vertical Performance	Federal Aviation Authority (FAA) proposed requirements	Half amplitude requirements used for power calculations
Acceleration	+/- 0.80 g	+/- 0.4 g
Velocity	+/- 0.610 m/s	+/- 0.305 m/s
Amplitude	+/- 0.864 m	+/- 0.432 m

Table 1. Motion specification

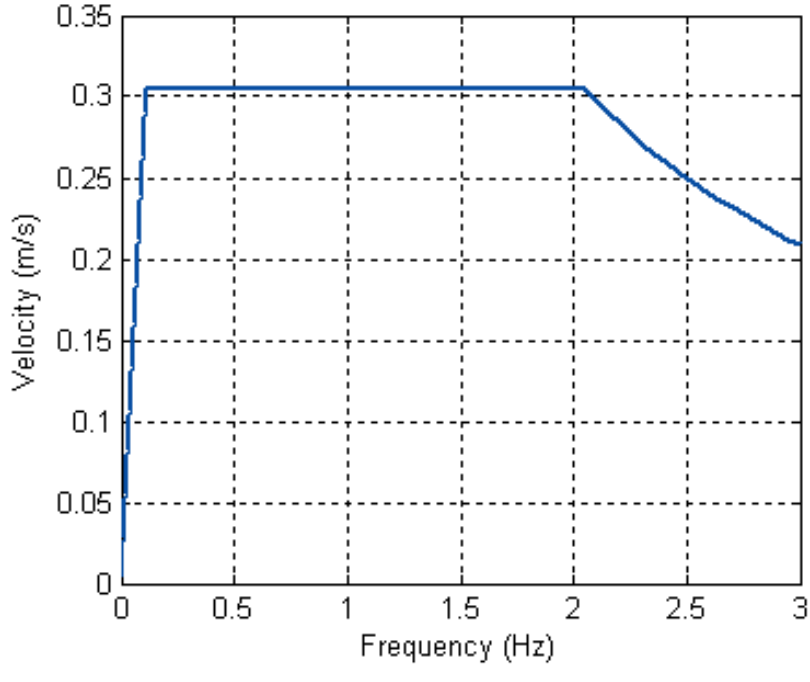

Fig 7. Half FAA vertical performance envelope

Platform / jack parameters		**Comments**
Piston head area, A_1	86.6 cm^2	
Piston rod-side area, A_2	42.4 cm^2	
Jack over vertical motion ratio, R	0.787	
Conventional valve-controlled jack		
Supply pressure, P_s	117 bar	
Water pump / leakage power, Ψ_l	10 kW	
Relief valve power loss, Ψ_r	≤ 8.5 kW	Maximum when static, rapidly becoming small with rising velocity
Drive/pump efficiency, η_v	0.85	
New electrohydrostatic system		
Quiescent power loss, Ψ_q	4 kW	
Head side pressure loss coefficient, K_1	6.19×10^{10} $m^5/(s^2N)$	Gives 22bar loss at 0.48m/s jack velocity
Rod side pressure loss coefficient, K_2	2.66×10^{11} $m^5/(s^2N)$	Gives 22bar loss at 0.48m/s jack velocity
Effective platform Mass, M	27 400 kg	Includes 11 400kg drive/pump inertia referred to platform
Drive/pump efficiency, η_e	0.85	

Table 2. System parameters

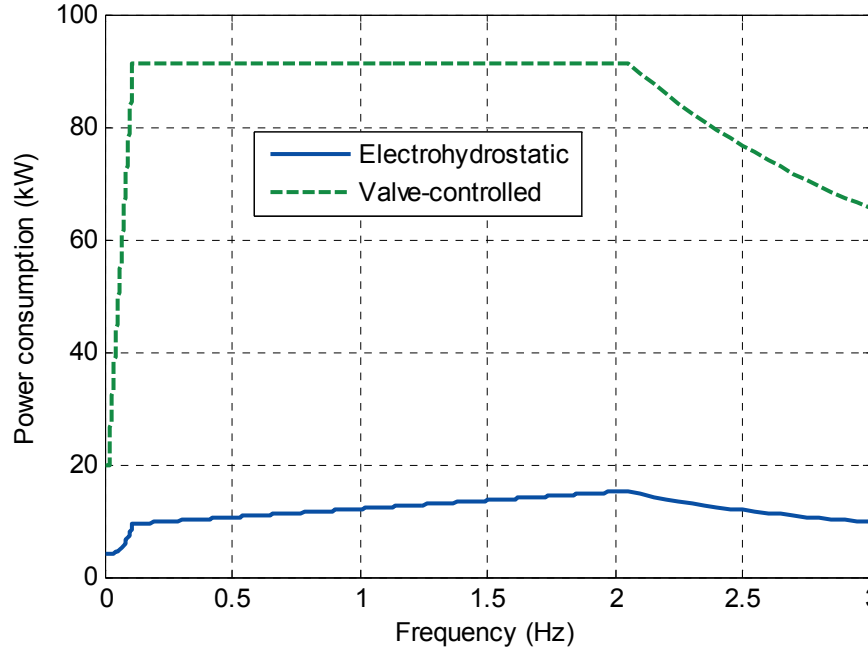

Fig 8. Comparison of Predicted Power Consumption (half FAA amplitude)

Note that the minimum power consumption for the valve-controlled system is 20kW, which is the measured consumption when the platform is not moving. This power is a combination of leakage losses and power required to drive the water circulation pump (together assumed to be a constant 10kW), and the minimum displacement of the variable displacement pumps meaning that flow is driven through the relief valve in this condition.

6.2 Measured power consumption for electrohydrostatic motion system

To confirm the calculation method power consumption tests were performed on both systems and the results compared to the predicted values. To perform the tests a 3-phase wattmeter was connected to the mains supplying the drive amplifiers of the electrohydrostatic system and to the HPU supply for the hydraulic system.

Averages over time were taken while static and while moving at a single frequency using a sinusoidal waveform. The results for the electrohydrostatic system are given in Table 3. The predictions are reasonably consistent with the measured values. Note that at higher frequencies there may be more flow through the hydraulic system components than predicted due to compressibility of the working fluid.

6.3 Measured power consumption for valve-controlled system

Two tests were made on a conventional valve-controlled motion system. The results were for the static case and for motion at 0.2 Hz as shown in Table 4.

7. CONCLUSIONS AND DISCUSSION

It has been shown that the new electrohydrostatic drive system gives significant power savings with a variety of motion amplitudes and frequencies. It is difficult to predict an overall power saving when in general use as the type of training will change the duty cycle and magnitude of any motion. For example the magnitude of turbulence selected by the instructor will change the power consumption.

If a comparison were to be made at a single test frequency and amplitude then 0.2 Hz at 0.1016 m (4 inch) vertical amplitude as used in Tables 3 and 4 could be a good choice. In acceleration this equates to 0.16g and would be equivalent to a continuous gentle manoeuvre. Under this condition the servovalve-controlled motion platform requires 45 kW while the electrohydrostatic system requires 4.7 kW. It should be remembered that a typical flight training school may have around 10 simulators and hence if all simulators were running the electrical power saving could be around 0.4 MW.

Calculation of energy consumption in a valve-controlled hydraulic system with a fixed supply pressure can be computed with good accuracy provided the swept volume of fluid consumed is known. However the minimum power consumption of the variable displacement pumps and other HPU equipment must be included in any calculation.

Cyclic Frequency Hz	Platform Amplitude m	Calculated Acceleration Power kW	Calculated Pressure loss Power kW	Total Calc Power inc Quiescent kW	Measured Power kW
0.050	0.55372	0.049	0.947	5.00	5.34
0.126	0.18910	0.091	0.604	4.69	5.27
0.200	0.1016	0.105	0.374	4.48	4.70
0.200	0.18910	0.364	2.414	6.78	8.48
0.600	0.08255	1.870	5.422	11.3	12.6
1.000	0.06309	5.058	11.205	20.3	22.3
2.048	0.02660	7.723	7.214	18.9	17.3
3.000	0.01958	13.15	9.043	26.2	24.6
4.100	0.00658	3.792	0.876	8.67	8.55
6.000	0.00270	2.000	0.190	6.20	4.9
10.00	0.00060	0.458	0.010	4.47	4.6
30.00	0.00003	0.031	0.000m’	4.03	4.1

Table 3 Predicted and measured power consumption – electrohydrostatic system

Cyclic Frequency Hz	Platform Amplitude m	Calculated Motion Power kW	Water pump / leakage power kW	Total Predicted Power kW	Measured Power kW
0	0	0	10	20	19.4
0.2	0.1016	34.1	10	44.1	44.64

Table 4 Predicted and measured power consumption – valve-controlled system

The power consumption in the electrohydrostatic system can be predicted with good accuracy by the consideration of three elements: the acceleration forces, the pressure loss and the quiescent consumption. When considering the acceleration forces the extent to which the amplifier DC bus system might be able to recover power during braking should be determined. Note that in this case, the DC bus for each drive has 1500μF of capacitance and can rise by 155V before power is dumped across resistors, giving a total (for all six) energy storage of 108J; thus a theoretical maximum regeneration of only 108W is possible for a 1Hz motion. There may be some future savings to be made by increasing the size of the capacitors on the DC bus or adding an inverter to put power back into the mains supply while the simulator is braking.

Further savings in power consumption may be possible by reducing the pressure loss within the hydraulic parts of the system. However as can be seen in Table 3 the 0.2 Hz 0.1016 m case absorbs very little pressure loss power and the cost of reducing this may not be justified by the savings during normal training.

It is highly likely that traditional valve-controlled hydraulic flight simulator motion systems will not be produced by the main manufacturers for much longer. As an alternative to the system described in this paper, an all-electric solution could be adopted in which each leg is driven by a brushless motor through a ball or roller screw. Power consumption for such a solution has been predicted at 10kW, compared with 40kW for a valve-controlled system under the same conditions, and in practice power consumption has been found to be between 25% and 50% of the traditional system [6]. The fact that the electrohydrostatic system consumes less power, by a factor of between 2 and 4, than the all-electric system is due to the energy storage capability of the former.

REFERENCES

1. Stewart, D. *A platform with six degrees of freedom.* Proc Instn Mech Engrs, Vol 180 Pt 1, No. 15, p371-378, 1965.
2. Rolfe J.M., Staples K.J. *Flight simulation.* Cambridge University Press, 1986.
3. Crowder, R., Maxwell, C. *Simulation of a prototype electrically powered integrated actuator for civil aircraft.* Proc Instn Mech Engrs Vol 211 Part G. p381-394, 1997.
4. Habibi, S., Goldberg, A. *Design of a New High Performance ElectroHydraulic Actuator*, IEEE/ASME Transactions on Mechatronics, Vol. 5, No. 2, pp 158-164, June 2000.
5. Rahmfeld, R., Ivantysynova, M. *Displacement Controlled Linear Actuator with Differential Cylinder - A way to save primary energy in Mobile Machines*. In: Proc. of the 5th Int. Conf. on Fluid Power Transmission and Control, Hangzhou, China, pp. 316-322, 2001.
6. Bartel, C, Foster, D *Life Cycle Motion Base Cost Comparison: Electric vs. Hydraulic.* Moog Inc Technical Paper.

Session 10
High performance valves II

Oil stiction in hydraulic valves – an experimental investigation

Markus Resch, Rudolf Scheidl
Institute of Machine Design and Hydraulic Drives
Johannes Kepler University, Altenbergerstr. 69, 4040-Linz, Austria

ABSTRACT

Oil stiction arises whenever two surfaces form a narrow gap filled with oil. For fast switching hydraulic valves with flat anchor solenoids this stiction force may degrade the valve opening response significantly.

In spite of a vast literature on oil sticking - about 100 papers from different engineering fields have been studied - an adequate model of the stiction process in hydraulic valves is missing. Some research work has been done in the area of compressor valves where oil stiction often reduces reliability. Most of the literature found concerns basic research addressing adhesion, surface tension, fingering, etc.. The authors' research intends to combine and extend the existing knowledge to get an appropriate model of the stiction process in hydraulic valves. The calculation of the maximum stiction force and some design rules to avoid the stiction force are the main final objectives.

To understand the fundamentals and to check theories a test rig has been built. This test rig can generate the very fast separation of two parallel plates by a servo-valve controlled short stroke hydraulic cylinder and is equipped with sensors for the gap size, the separation speed, and the stiction force. First stiction measurements between parallel plates were done. For small gaps the measured stiction force curves correspond to those computed from the Reynold's equation, known as Stefan's force in literature. For larger gaps, however, additional effects, like fluid inertia, become significant and need a refined computational model.

1. INTRODUCTION

Practical experience shows that a force is needed to separate two plates connected by a thin fluid film (see Figure 1). Such a separation force is called stiction force (especially oil stiction force if the fluid is oil) in the established literature. This phenomenon often causes problems in fluid power applications. Around 30 years ago, engineers became aware of this phenomenon in the area of automatic compressor valves (1). Because of the stiction force in compressor poppet valves pressure peaks appear, which are responsible for fatigue breaks

Fluid Power and Motion Control 2008 Edited by Dr D N Johnston and Professor A R Plummer

and increased noise (2). Also in the field of hydraulic valves the stiction effect is often a reason of performance problems.

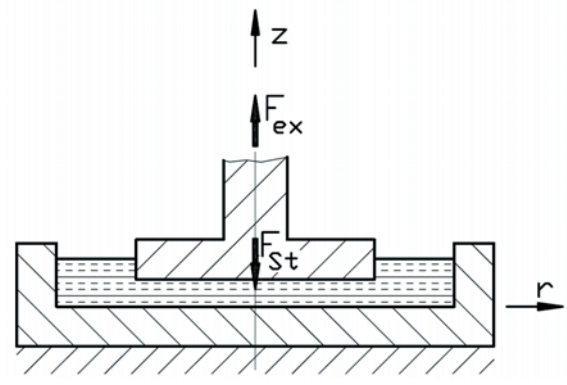

Figure 1 Principle of the stiction effect

Especially in the area of fast switching hydraulic valves with flat anchor solenoids the stiction force acting on the flat anchor (respectively on the valve spool) is able to degrade the opening dynamics of the valve because of the reverse effective direction of the stiction and the spring force (see Figure 2). For further designs of fast switching valves a detailed understanding and mathematical model of the stiction effect would be a big benefit to avoid such performance losses. Unfortunately, an adequate model of the sticking process is missing in the literature.

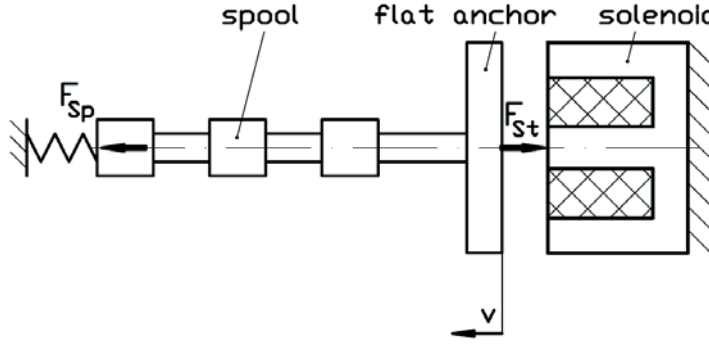

Figure 2 Principle of a flat anchor solenoid spool valve

2. LITERATURE SURVEY

The following chapter gives a short overview about the present knowledge addressing stiction effects in the literature. The most relevant results dealing with oil stiction, adhesion, surface tension, etc. are pointed out and discussed.

2.1 The very first investigations

In the year 1874 M. J. Stefan built up a first experiment dealing with the stiction force between two plates (3). Figure 3 shows the principle of the Stefan experiment.

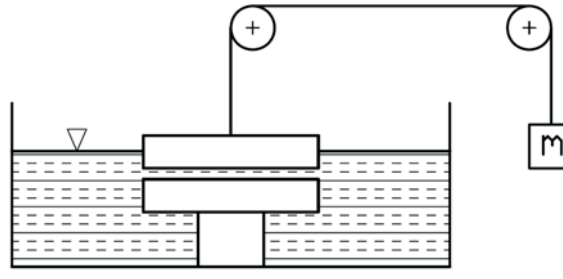

Figure 3 Stefan experiment

Stefan placed two plates with an initial gap in a fluid to analyze the separation force - separation time – relation. The aim was to measure the time to reach a desired gap size depending on the pulling force. By the help of this experiment Stefan postulated the following laws:

a) The mass, needed to start the separation process, is higher for smaller initial gap sizes, higher for lager plates and also depending on the fluid

b) The separation time is inverse proportional to the acting mass

c) The separation time is higher for smaller initial gap sizes

d) The separation time is proportional to the fourth power of the plate radius

In spite of those conclusions Stefan was not able to formulate a mathematical stiction force - gap size - relation.

2.2 Publications in the field of oil stiction in compressor valves

As mentioned in the first chapter, stiction phenomena also occur in compressor valves. Due to this problem some publications can be found in this research area too. In (5) Böswirth does a calculation of the oil stiction force for specific compressor valves. The calculation is based on the Reynold's equation (see chapter 3). Böswirth points out that as long as there is no cavitation the stiction force is proportional to the dynamic viscosity of the fluid and to the separation speed. Furthermore, the force is inverse proportional to the third power of the gap size. Bauer (6) and Stehr (7) derive the same relation. Aigner et. al. (8) developed the following formula:

$$F_{St} = f_1 \frac{\dot{h}}{h^3} \tag{1}$$

In this equation h denotes the gap distance and the factor f_1 depends on the valve geometry, the properties of the compressed gas and the lubrication oil. However no further information according the factor f_1 is provided.

2.3 Publications in the field of liquids under tension

Poivet et. al. (9) performed tension experiments on viscous fluids. Even though the tests were done with a relatively low separation speed (less than 1mm/s) cavitation occurred. In the non cavitation phase the following stiction force relation for circular test plates in essence is used in this publication:

$$F_{St} = \frac{3}{2}\pi\eta R^4 \frac{\dot{h}}{h^3} \tag{2}$$

R denotes the radius of the test plates and η the dynamic fluid viscosity. In chapter 3 the detailed computation of this equation is shown. Using this relation leads to a good accordance with measurements in the low speed - non cavitation case as pointed out in (10). In (11) Poivet et. al. refine the model taking the surface tension into account. This enhancement is based on the Laplace equation (see chapter 3). The same approach is used in (12) and (13) by Derks, Lindner et. al.. In (12) it is strongly pointed out that the amount of the force, resulting from surface tension, is less than 4% of the complete stiction force in the parameter setting they used.

2.4 Publications in special fields dealing with fluid stiction

In the dissertation of Rößler (14) the adhesive force of removable dental prosthesis is analyzed. Even though this problem looks completely different to the applications mentioned till now, the computations lead to similar results as mentioned in chapter 2.3. Especially the very low amount of surface tension is highlighted again (less than 1% in this case). The dissertations (15), (16) and (17) treat the tint disruption process in a rotary printing press. The problem of fluid stiction is faced in this area also. (15), (16) and (17) derive a stiction force relation based on the Reynold's and Laplace equation too.

Summarizing the literature survey a force relation predicated on the Reynold's theory seems to be a promising first approach.

3. THEORETICAL ANYLYSIS

3.1 Force relation based on the Reynold's equation

The Reynold's equation for parallel separating circular plates (as shown in Figure 1) in cylindrical coordinates reads

$$\left(\frac{\partial^2 p}{\partial r^2}\right)\frac{h^3}{\eta} + \frac{1}{r}\left(\frac{\partial p}{\partial r}\right)\frac{h^3}{\eta} = 12\dot{h} \tag{3}$$

with the boundary conditions

$$p(R) = 0, \quad \frac{\partial p}{\partial r}(R) = 0. \tag{4}$$

R denotes the plate radius. $p(r)$ is the gauge pressure, $p = 0$ refers to the surrounding pressure. The solution of (3) and (4) are the well known parabolic pressure distribution (5) and the stiction force (6) respectively.

$$p(r) = \frac{3\dot{h}\eta}{h^3}\left(r^2 - R^2\right) \tag{5}$$

$$F_{St} = \int p(r)dA = \frac{3}{2}\pi\eta R^4 \frac{\dot{h}}{h^3} \tag{6}$$

Equation (6) is known as Stefan's equation in the literature even though M.J. Stefan never postulated a force relation in this form.

3.2 Stiction force resulting from the surface tension

The pressure in a liquid bridge can be calculated from the Laplace equation:

$$\Delta p_{Bridge} = \gamma \cdot \kappa. \tag{7}$$

γ denotes the surface tension and κ the curvature of the free surface. The curvature also can be written as a function of the contact angle α (see Figure 4):

$$\kappa = \left(\frac{1}{R_1} + \frac{1}{R_2}\right) = \left(\frac{1}{R_1} - \frac{2\cos(\alpha)}{h}\right). \tag{8}$$

Assuming $R_1 >> h$ leads to simple stiction force relation resulting form the surface tension:

$$F_{Bridge} = R^2 \cdot \pi \cdot \gamma \cdot \left(\frac{2\cos(\alpha)}{h}\right). \tag{9}$$

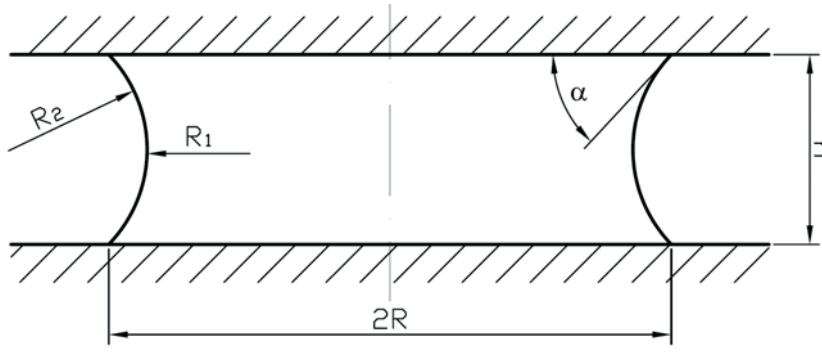

Figure 4 Liquid bridge

3.3 Comparison Reynold's force – Laplace force

The ratio

$$\frac{F_{Bridge}}{F_{ST}} = \frac{4}{3} \cdot \frac{\gamma}{\eta} \cdot \frac{h^2}{R^2} \cdot \frac{1}{\dot{h}} \cdot \cos(\alpha) \tag{10}$$

shows (especially for common hydraulic oils) that $F_{ST} >> F_{Bridge}$ because of $R >> h$ and the high desired separation velocities $\dot{h}$. That's why the authors focus on the Reynolds based stiction force relation first.

4. TEST RIG

For analyzing the stiction process in more detail and for the evaluation of the different theories it is absolutely necessary to verify the theoretical aspects by experiments. Because of this a stiction force test rig was built up in the laboratory. The basic structure of the experiment is shown in Figure 5. The hydraulically actuated test rig is able to create a fast separation of two plates by the use of a short stroke cylinder. The needed separation force (= stiction force) is identified by measuring the retention force of the second plate via a quartz force link. An exact measurement of the plate distance is also required. It is difficult to realize a direct gap distance measurement due to the oily surrounding. This problem is the main reason why a synchronizing cylinder is used and the gap distance is measured indirectly via an eddy current position sensor on the opposite piston rod side. A simple derivation of the position signal gives the separation velocity. Because of the relatively high separation velocities and the low noise of the position sensor this elementary method leads to an adequate velocity signal.

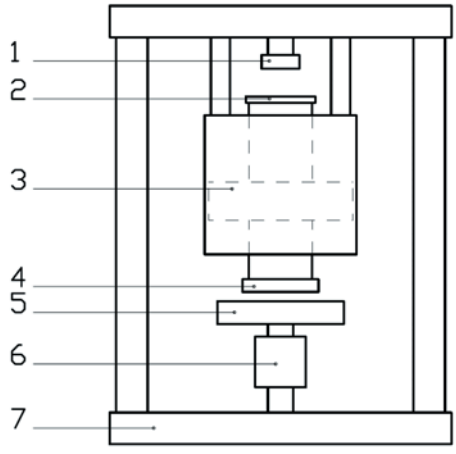

1	contact less position sensor
2	reference flag - pos. sensor
3	synchronizing cylinder
4+5	test plate pair
6	force sensor
7	frame

Figure 5 Basic structure of the test rig

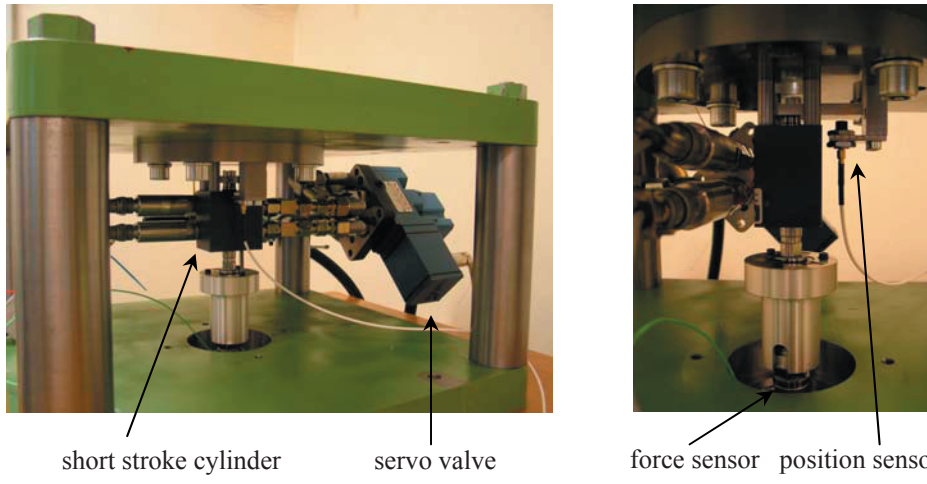

Figure 6 Test rig photos

5. FIRST EXPERIMENTAL RESULTS

The experimental results presented in this chapter are based on the following constants:

Tested hydraulic oil: Shell Tellus S32 @ 30°C $\eta = 43{,}2mPas$

Test – plate (# 4 in Figure 5): plate radius $R = 12.5mm$

Assuming a surrounding pressure of $1bar$ and total cavitation between the two stiction plates leads to a maximum theoretical stiction force of $F_{St\max} = 49N$.

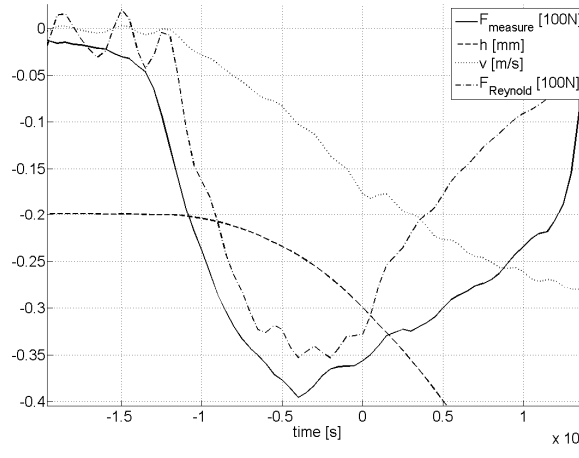

Figure 7 Initial gap 0.2mm, low separation speed

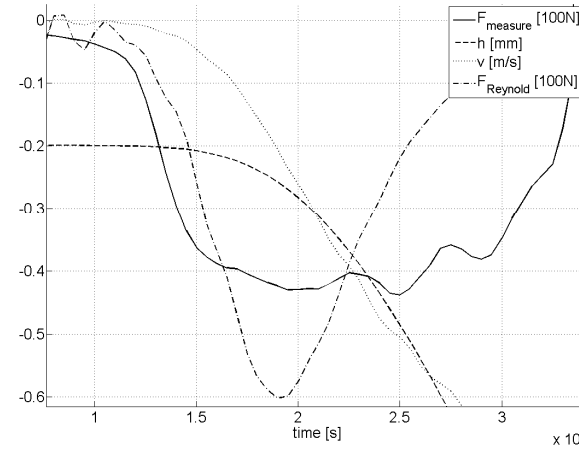

Figure 8 Initial gap 0.2mm, high separation speed

As shown in Figure 7 the measured stiction force $F_{measure}$ is quite similar to the calculated Reynold's force $F_{\mathrm{Re}ynold}$ (eq. 6) for a relatively low separation speed. For higher separation speeds (see Figure 8) an overshoot in the calculated force can be seen. The measured force saturates at around 45N according to the maximum stiction force $F_{St\max}$.

This deviation indicates cavitation between the plates. At the end of the stiction process always force oscillations of a high magnitude occur (see figure 9).

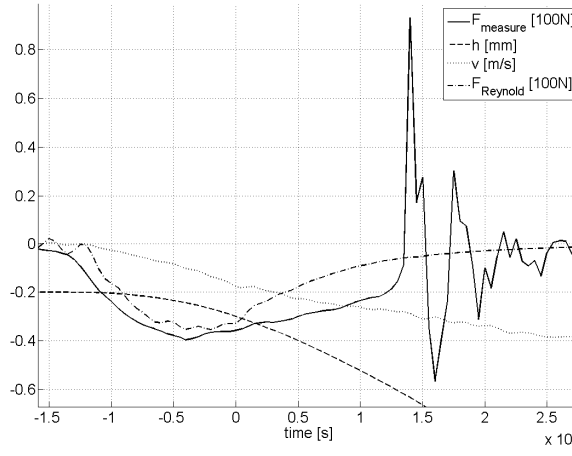

Figure 9 Initial gap 0.2mm, low separation speed, force oscillation

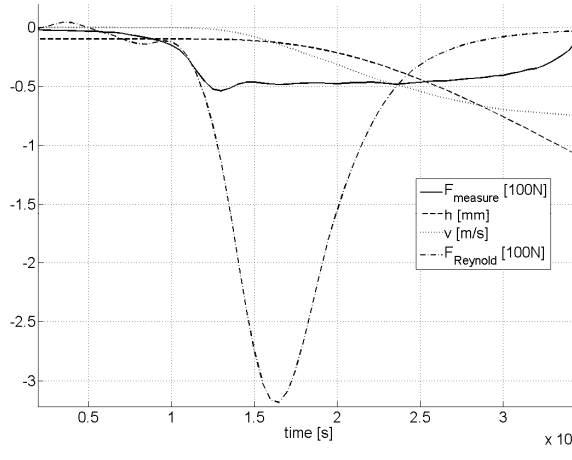

Figure 10 Initial gap 0.1mm, high separation speed

These force oscillations show a significant positive force pulse, corresponding to a positive pressure, which tends to separate the stiction plates. A finer resolution of the force signal with a digital oscilloscope showed that this pulse is the first point of a damped oscillation with a frequency of about 25kHz. Currently the authors have two conjectures about the physical reasons of this phenomenon:

a) radial hydraulic wave propagation excited by the fast plate separation (see Figure 1) and / or

b) dynamic process of the cavitation bubbles between the plates

The saturation of the stiction force due to the cavitation limit is also visible in Figure 10. Because of the small gap and the high separation speed the Reynold's force exceeds the cavitation limit which is not taken into account.

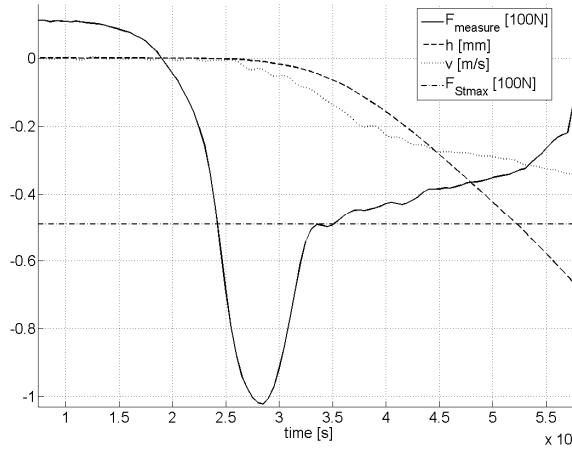

Figure 11 Initial gap 0mm, slow separation speed

In case of zero initial gap it is useless to calculate the stiction force out of the Reynold's equation, but the measurement shows an interesting effect. The measured force is not limited by the cavitation barrier (see Figure 11). This experiment clarifies that the Reynold's approach fails in the contact case. Other effects and mechanisms (tackiness, adhesion,…) have to be considered. In (18) and (19) a sticking force curve of synthetic adhesives is published which is similar to the measured stiction force behavior shown in Figure 11. This fact suggests including adhesion in an advanced theory of oil stiction that would be able to explain the extreme stiction force according to Figure 11.

The experiments were also done with different sizes of the stiction plates and the results are basically the same. All experiments are repeatable with a very low variance.

6. CONCLUSIONS AND OUTLOOK

A simple stiction force model based on the Reynold's theory is useful to describe the fluid stiction process as long as there is a small initial gap and no cavitation. For high separation speeds and moderate initial gaps the stiction force does not exceed the cavitation limit. At the end of the stiction process force oscillations always occur. This phenomenon is not yet explained coherently. The authors plan to clarify this problem first by adapting the test rig

to avoid wave propagation and secondly by studying the cavitation process in more detail. For extremely small initial gaps, due to the contact of the stiction plates, the stiction force can exceed the cavitation limit for a very short time. An explanation of this process is open and will be subject of further work.

REFERENCES

(1) Brown J., Pringle S., Lough A.; Oil Stiction in automatic compressor valves, Proc. Int. Congress of Refrigeration Moscow (1975), pp. 1049-1059.

(2) Vetter G., Grau U.; Öffnungsdruckspitzen bei Pumpenventilen oszillierender Verdrängerpumpen, Industriepumpen + Kompressoren, 4 (1997), pp. 216-221.

(3) Stefan M. J.; Versuche über die scheinbare Adhäsion, Sitzungsberichte der Mathematisch-Naturwissenschaftlichen Classe der Kaiserlichen Akademie der Wissenschaften Wien, Band LXIX (1874), pp 713-735.

(4) Böswirth L.; Zur Berechnung des Quetsch- und Klebeeffektes bei dünnen flüssigkeitsgefüllten Spalten; Fortschrittsbericht der VDI Zeitschriften, 7 Nr.47.(1979).

(5) Böswirth L.; Strömung und Ventilplattenbewegung in Kolbenverdichterventilen, Eigenverlag, erweiterter und verbesserter Nachdruck (2002).

(6) Bauer F.; The influence of Liquids on compressor valves, Proc. Int. Compressor Conference Purdue (1992).

(7) Stehr H.; Oil Stiction – investigations to optimize reliability of compressor valves, IMechE 2001, pp 477-486.

(8) Aigner R., Meyer G., Steinrück H.; Valve Dynamics and Internal Waves in a Reciprocating Compressor, 4th Conference of the EFRC, Antwerp, (2005).

(9) Poivet S., Nallet F.,Gay C., Fabre P.; Cavitation – induced force transition in confined viscous liquids under traction, Europhys. Lett. 62 (2), pp.244-250, (2003).

(10) Tirumkudulu M., Russel W.B., Huang T.J., On the measurement of “tack” for adhesives; Physics of Fluids 15 (6), pp.1588-1605, (2003).

(11) Poivet S., Nallet F., Gay C., Fabre P.; Force response of a viscous liquid in a probe – tack geometry: Fingering versus cavitation, Eur. Phys. Journal E 97, pp. 97-116, (2004).

(12) Derks D., Lindner A., Creton C., Bonn D.; Cohesive failure of thin layers of soft model adhesives under tension, Journal of Applied Physics 93 (3), pp. 1557-1566, (2003).

(13) Lindner A., Derks D., Shelley M.J.; Stretch flow of thin layers of Newtonian liquids: Fingering patterns and lifting forces, Physics of Fluids 17 (072107-1), (2005).

(14) Rößler J.; Der Haftmechanismus von Galvano – Doppelkronen – Systemen und seine Beeinflussbarkeit durch Zwischenflüssigkeiten, Dissertation, Friedrich Schiller Universität Jena, (2005).

(15) Voß C.; Analytische Modellierung, experimentelle Untersuchung und dreidimensionale Gitter – Boltzmann Simulation der quasistatischen und instabilen Farbspaltung, Dissertation, Universität Wuppertal, (2002).

(16) Hübner G.; Ein Beitrag zum Problem der Flüssigkeitsspaltung in der Drucktechnik, Technische Hochschule Darmstadt, (1991).

(17) Behler H.; Die Randstruktur von Druckpunkten – eine experimentelle Untersuchung der Farbspaltungsströmung, Technische Hochschule Darmstadt, (1993).

(18) Gay C., Leiber L.; Theory of Tackiness, Physical Review Letters 82 (5), pp. 936-939, (1999)

(19) Gay C.; Stickiness – Some Fundamentals of Adhesion, Integr. Comp. Biol. 42, pp. 1123-1126, (2002)

Influencing Parameters on Tightness of Hydraulic Seat Valves

Matthias Schmidt
Hubertus Murrenhoff
Institute for Fluid Power Drives and Controls, RWTH Aachen University, Germany

Henrik Lohrberg
Franz-Josef Körber
ABB AG – High Voltage Products, Hanau-Großauheim, Germany

ABSTRACT

Seat valves provide – compared to spool valves – the advantage of being able to isolate a hydraulic pressure nearly without leakage. However, in certain applications any leakage whatsoever is prohibited. Therefore, efforts are carried out to increase the tightness of the metallic sealing.

For this purpose, a test rig was designed and built to investigate different seat geometries in combination with varying hydraulic and mechanical parameters. To exclude the influence on the leakage of other seals, the flow is measured at the low pressure side of the seat. A revision after the first set of measurements could clearly improve the test rig's performance.

By means of a structured approach, the influences of factors on leakage as well as their interdependencies are being investigated. Within this paper measurement results of the leakage's dependency on time, contact force and geometry are presented.

1. INTRODUCTION

Hydraulic seat valves, as opposed to spool valves, offer the advantage of nearly leakage-free sealing. Any leakage still occurring is negligibly low for most applications. Still, for some applications a high tightness is crucial for proper functioning, for example in hydro-mechanical spring drives for high-voltage circuit breakers. Here, high pressures have to be sealed over longer periods with as little leakage as possible. Current seat valves cannot always provide the required performance. Therefore, the need for a structured investigation of the sealing effect arises.

It is known from experience that there are many possible influences on the tendency to leak of metallic seal seats. Geometry, for instance, plays an important role in the macroscopic

Fluid Power and Motion Control 2008 Edited by Dr D N Johnston and Professor A R Plummer

field as well as in the microscopic. But also hydraulic edge conditions, like the pressure-to-be-sealed and the force with which the sealing element is pressed into the seal seats, influence leakage. A final important aspect is the medium in question with its viscosity and its particle load.

In the frame of this project the connection between the mentioned parameters and leakage of metallic seal seats are to be determined empirically.

For this purpose, a test bench was constructed and set up, which enables the simultaneous examination of several test valves. Furthermore, diverse test valves were built, with which geometry variations could be conducted. After initiation of the test bench the dependencies of the different parameters on the leakage of metallic seal seats were determined experimentally.

2. STATE OF THE ART

Seat valves are valves in which the ports are joined or separated by attaching or taking off a sealing element. They are distinguished – following the style of their sealing element – into cone, ball, and disc seat valves. Cone seat valves have a ground, guided cone as a sealing element. Ball seat valves use a non-conducted ball as a seat element. This leads to a simple design for small nominal widths. Disc seat valves have a disc-shaped sealing element and are mainly used in water hydraulics and pneumatics (1).

Seat valves are often assumed to be hermetically tight, but in practice they always show a little leakage. This leakage is due to the fact that the surfaces of sealing elements always exhibit certain roughness. When closing the valve, the surface asperities come to rest on each other. Through the sealing element's contact pressure elastic and plastic deformations of the asperities occur. However, there still remain microscopic gaps between the asperities, where micro flows could be built up, leading to leakage (2).

High tightness can therefore be obtained through high surface quality and good accuracy with regard to form and position tolerances. This means that for high tightness high production expenditure is needed, which in turn leads to high costs in the production of seat valves.

Besides characteristics based on in manufacturing aspects there are other influences on a seat valve's tightness. For instance, leakage increases linearly with rising differential pressure (2). The lower the viscosity of the fluid, the higher is the leakage at the valve. The viscosity of oil, then again, strongly depends on temperature; it decreases with rising temperatures (3). A higher tightness can be expected with higher contact force when fitting the sealing element into the valve seat, as thereby the microscopic gaps get smaller. However, the exact correlations between force and leakage are not yet known.

A further influence is exerted by dirt particles in the oil. These can time-dependently clog up the microscopic gaps found in the valve seat after closing (4). Dirt particles which are too large, though, can prevent a closing of the valve or even damage the valve seat.

It is to be assumed that geometry also has an influence on leakage. We have to distinguish between macroscopic and microscopic geometry. Microscopic geometry describes the condition of a surface. Here the fabrication and surface treatment present a decisive influence. To what extent geometry influences leakage is unknown so far.

3. DEVELOPMENT OF TEST RIG

Deriving from the task and the application, different requirements were determined for the design of the test rig. High pressure of 500 bar–600 bar has to be sealed by the test valves without influencing the force in the contact. A separate hydraulic circuit was intended for supplying the contact force. To avoid influences of pulsation from the hydraulic pump on the leakage and increasing temperature during the measurements, the pressure has to be stored within accumulators. Further requirements like adequate flushing of the seat between two measurements and the possibility of testing three different valves at the same time were realized as well.

The most important and most challenging task is measuring the leakage. As the flow is expected to be much lower than measurable with a common positive displacement flow sensor, a different principle was in demand. The use of precision scales for determination of leakage provides the following advantages: Through the high resolution of 0,001 g very small volume flows can be determined. At the same time, it is also possible to reliably detect conceivably larger flows. These are only restrained by the overall weighing range of 0–160 g. The measurement pipes conduct the leakage to the beakers positioned on the scales. In order to prevent an abrupt rise in leakage through singular drops, the pipes end up underneath the beaker's oil surface. This ensures that a constant volume flow can be measured by the scales. By differentiating the time-dependant signal of the scales and dividing it by the density of the fluid, the flow can be calculated.

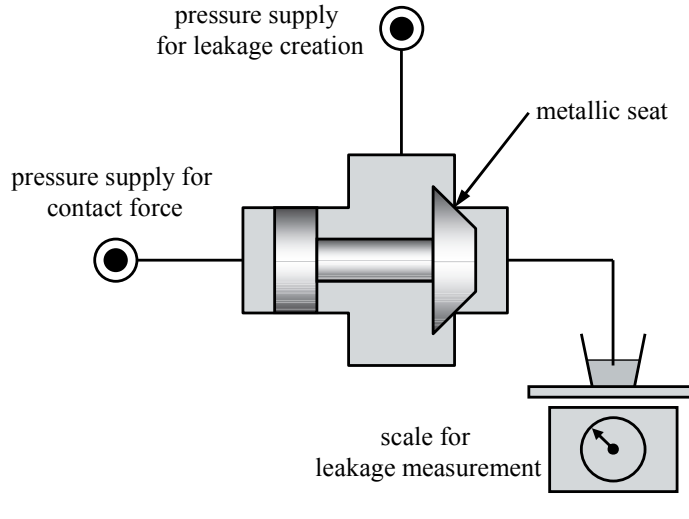

Figure 1 Simplified layout of the test rig's hydraulic circuit

The design of the test rig offers the possibility to measure the leakage of three custom-made test valves at the same time. The simplified hydraulic circuit and the measuring principle are presented in figure 1 exemplary for one test valve. The piston is pushed into a seat by an adjustable pressure. A second adjustable high pressure supply, which can provide pressures of up to 600 bar, is used to create leakage. To exclude the influence on the leakage of other seals, the flow is measured at the low pressure side of the seat.

A measurement made with the test setup is shown in figure 2. The total amount of leakage is plotted against the time. The declining curve reveals the continuous decrease of the flow. The fact that the square-like curve is not steady during the whole run, is caused by the behaviour of the pressure for leakage creation. Due to the leakage occurring at the test valves and other valves used for the test rig, the pressure drops despite the usage of an accumulator. When charging it with a pump, the test procedure is disturbed. This behaviour gave the occasion to improve the test rig in order to provide steady edge conditions.

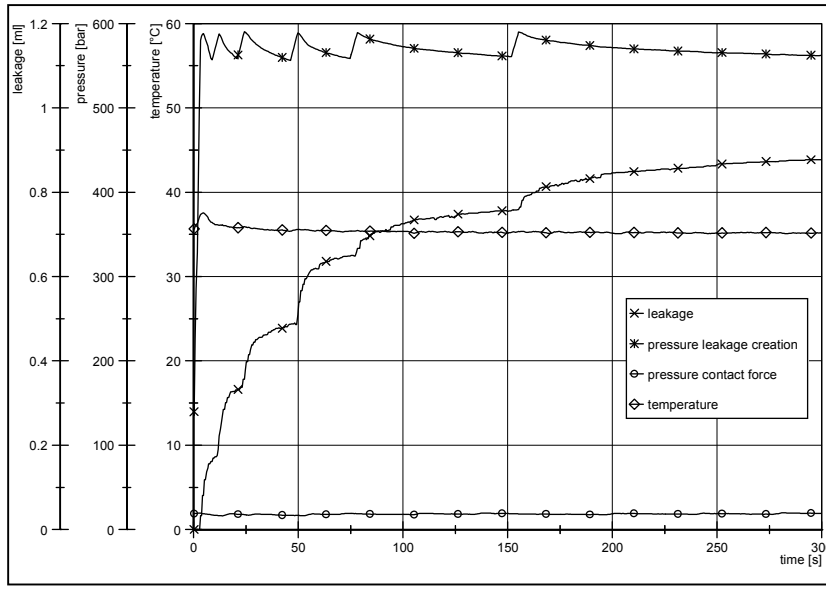

Figure 2 Sample measurement with first test set-up

For this reason two pumps are used working together continuously with pressure relief valves instead of using hydraulic accumulators. Thus a pulsation from the pumps is accepted for the benefit of constant and reliable pressure. The oil temperature is not exceeding 50 °C (122 °F) which means a common temperature for hydraulic systems. In figure 3 a measurement displays the improvement of the test rig. The leakage is not disturbed by recharging operations and the temperature remains on a constant level. Due to the new test set-up, the pressure for leakage creation can not exceed 400 bar. Consequently the leakage in figure 2 can not be compared quantitatively with the leakage in figure 3.

The revised test rig is shown in figure 4. The central component is the steel manifold in the background of the picture. It houses the test valves as well as switching and pressure relief

valves. Furthermore different pressure and temperature sensors are integrated and the possibility to feed oil to a particle counter. In the foreground the three laboratory scales are revealed with the beakers and the leakage pipes. They are connected directly to the test valves, which are placed behind the rings on the front side of the block.

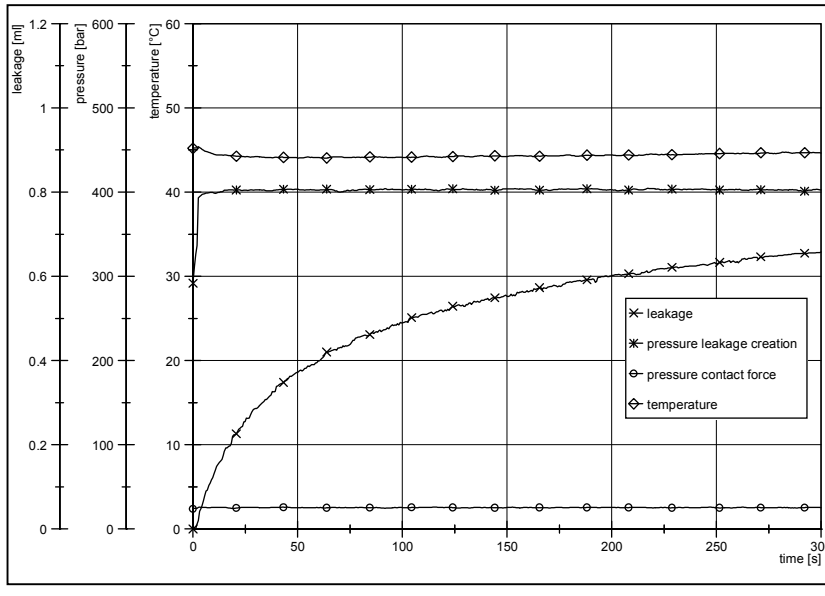

Figure 3 Sample measurement with second test set-up

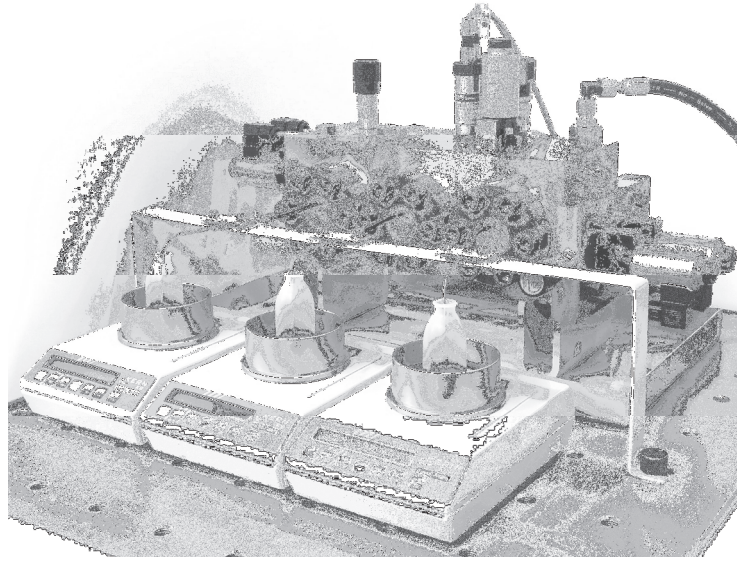

Figure 4 Leakage test rig at the IFAS' laboratory

4. DEVELOPMENT OF TEST ITEMS

Common seat valves are often characterized by the usage of ball-cone or cone-cone seat constructions. For special applications other designs can be found as well. The geometry of the valves is usually based on the manufacturer's long-time experience and has normally not only been investigated regarding the leakage. Within this project a structured approach was chosen to investigate the macroscopic geometry's influence on the leakage.

First of all, the geometry is determined by the resulting seal angle, as shown in figure 5. This seal angle indicates the effective direction between the contact force between sealing element and seal seat opposite the centre-line. There, a seal angle of 0° would characterise a disc seat valve, and an angle of 90° a spool valve. With very small angles, a self-centring of the sealing element in the seal seat is not given and the resulting contact forces are barely increased. With very large seal angles a good self-centring and a high increase of contact forces is provided. However, with large angles close to 90° it is possible for the sealing element to lock within the seal seat. Therefore, a seal angle of 45° is chosen for all test valves during experiments. This is also an established angle for common valves. It is assumed that with an increasing seal angle only the resulting contact force is increased as well.

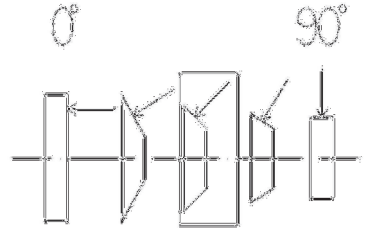

Figure 5 Variation of the resulting seal angle

For the development of a structured geometry variation, it is further assumed that the form of sealing element and seal seat always accords to a radius. This radius can be varied within a wide limit, as figure 6 shows. There, a radius with a value of 0 mm characterises an edge. At a positive radius one reaches a convex curvature of the sealing edge. An infinite radius produces a cone and a negative radius results in a concave curvature.

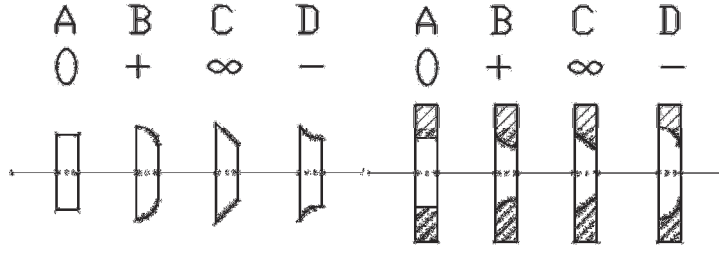

Figure 6 Variation of sealing radius

Based on these radii for seal seat and sealing element, combinations can be created. Every combination that is theoretically possible is depicted in figure 7. The crossed-out combinations are not reasonable. A sealing line contact is not possible, for instance, by pressing two concavely curved elements together, as is shown in example DD. Furthermore, with some combinations only the effective direction is reversed. In combinations BA and AB, for example, only the radii between sealing element and seal seat are interchanged. For the experiments made in the course of this work, the following combinations were chosen: BA, BB, CA, CB, DA, and DB. Here, the first letter always represents the sealing element's radius; the second represents the seal seat's radius. Furthermore the size of the radii is varied for each of these basic combinations.

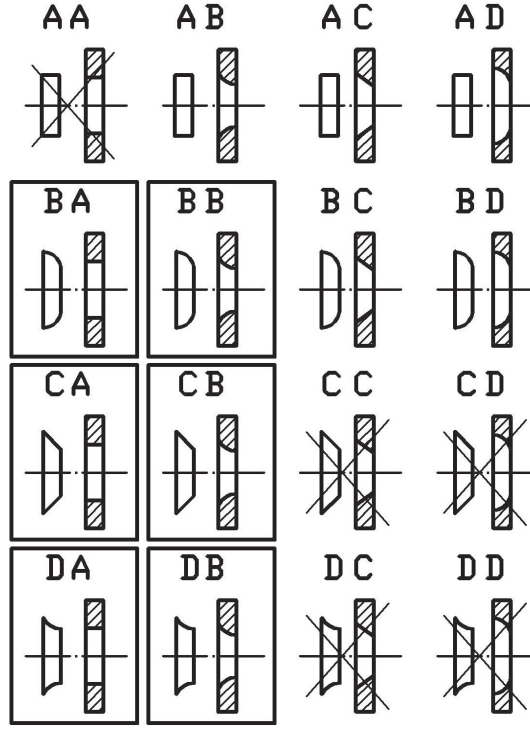

Figure 7 Possible combinations of sealing radii

As an example, figure 8 shows a combination of test valves consisting of a sealing element and a seal seat in built-in condition. The test valves are installed into the central block and can be easily exchanged. The strong forces put on the seal seat during operation are absorbed by a retaining ring. The sealing elements are pressed into the seat by oil pressure during operation. The oil pressure for leakage creation is thus sealed. Emerging leakage is collected in the leakage space and, via a bore and a gauge tube, conducted to the scales, which measure the amount of leakage. Between individual tightness checks, the test valves are to be rinsed by flush-bores. Therefore, a return spring is installed which opens the test valves under pressure-less condition.

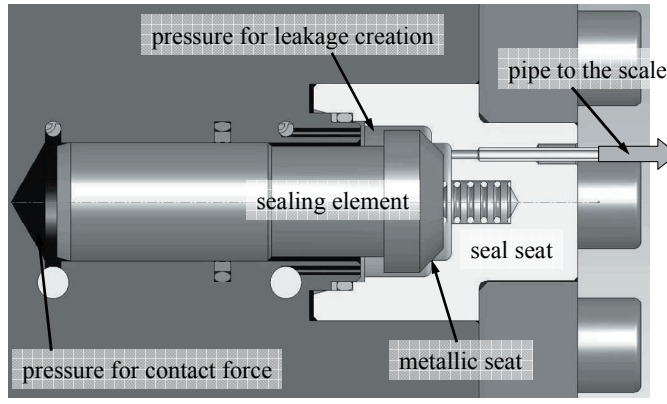

Figure 8 Cross section of test valve in the leakage test rig

Some test valves are presented in figure 9, consisting of the seal seats on the left side and the sealing element on the right side.

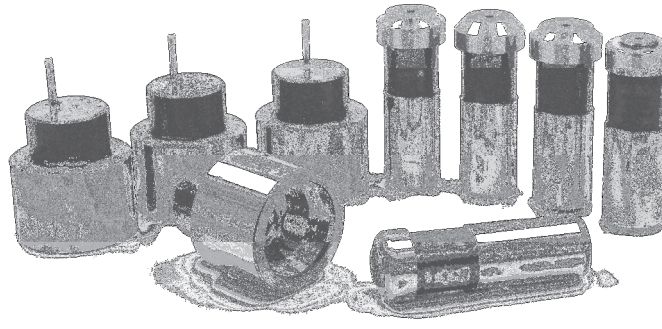

Figure 9 Test valves: seal seats (left) and sealing elements (right)

5. RESULTS OF FIRST MEASUREMENTS

5.1 Time and contact force dependant leakage

The above presented pictures show that leakage through this valve combination decreases with time. This behaviour can be noticed with most of the test valves and in current market valves. It can be explained by a slow clogging up of the sealing gap with particles from the hydraulic oil. After closing the valves it can be assumed that there are still a lot of microscopic gaps at the sealing contact, due to the surface's roughness. Through these little gaps a relatively large amount of leakage accumulates at first. As the hydraulic oil used is no pure fluid but laden with particles, it can be assumed that the remaining gaps slowly clog up with these particles. In this case, the sealing gap works like a filter for the leaking oil. Larger particles get stuck in the gap and thus decrease the flow of leaking oil.

This explanation for time-dependent leakage has still to be verified in further experiments in dependency on the purity of oil, as so far only experiments with a constant purity have been conducted. The particle load there was measured at ISO Code (2μ/5μ/15μ) 17/13/07.

The curve in figure 10 is derived from the results of several such individual measurements. It depicts the average leakage within the first 5 min measurement time in ml/min, above the contact force for valve combination BA (ball on edge). The pressure to be sealed was set to 590 bar. The curve consists of individual points, whereat each point represents an individual measurement. The contact force is calculated as an average value from the five minutes measurement time. The fluctuations in the pressure to be sealed, however, were not considered when calculating the contact force; only the set-up pressure taken into consideration. The average leakage is determined from the entire leakage after 5 min measurement time.

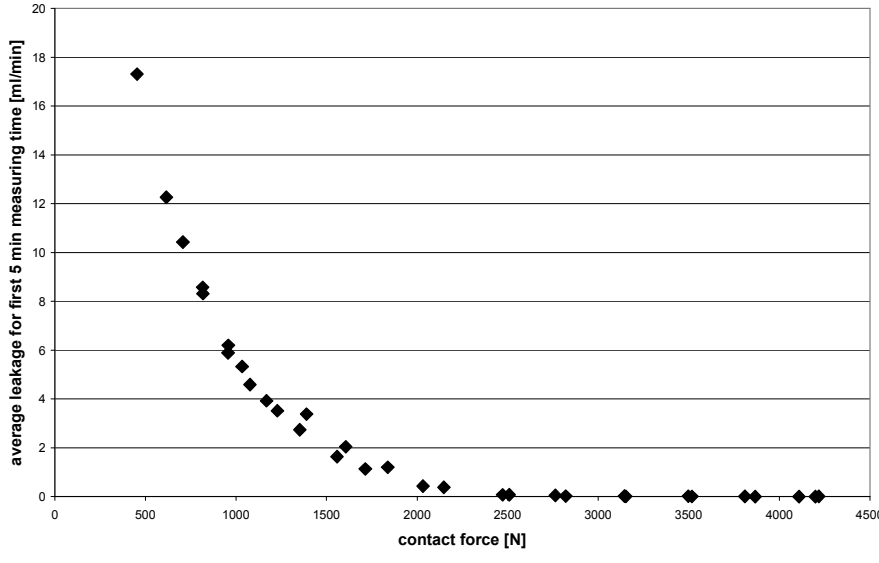

Figure 10 Leakage in dependency on contact force

It can be seen in figure 10 that with little contact force a relatively large amount of leakage occurs. This decreases with rising contact force and asymptotically approaches a leakage of zero. The resulting curve resembles an exponential developing.

Through the sealing element's contact force into the seal seat, these two elements are pressed together at the sealing edge. Due to the surface's roughness both elements at first only touch at the asperities**,** so that microscopically small gaps are left. Leakage can escape through these gaps. By raising the contact force, these asperities are further deformed and flattened. Thus, the microscopic gaps are diminished and the flow rate is lessened.

5.2 Influence of macroscopic geometry on leakage

In order to be able to examine the influence of macroscopic geometry on leakage, experiments with several different valve geometries were conducted. Here, leakage – as in chapter 5.1 – is in each case considered in dependence on contact force. Figure 11 shows the average leakage within the first 5 min of measurement time above the contact force of all examined valve geometries. The pressure to be sealed is set to 590 bar for every test run. The pressure for generating contact force is varied in each case. It gets clear that the individual gradients strongly differ. However, they all show a line of progress similar to that of an exponential function. All curves thereby asymptotically approach a leakage of zero.

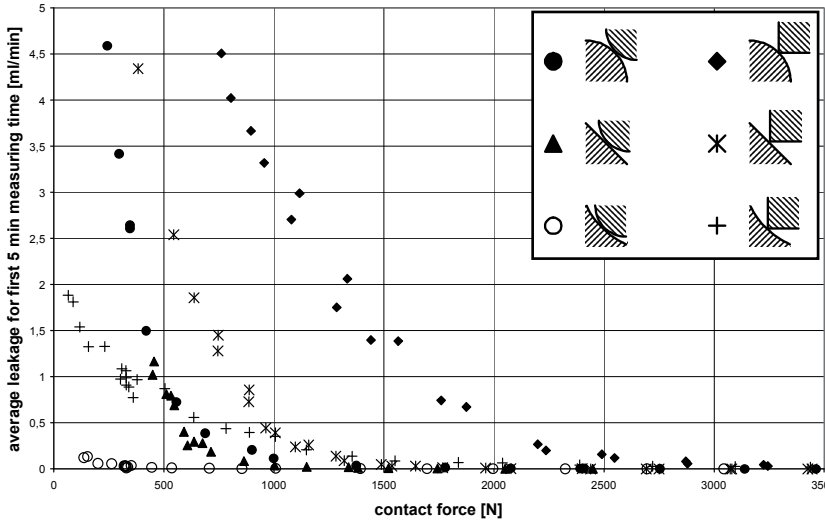

Figure 11 Leakage in dependency of macroscopic geometry

The measurements in figure 11 reveal a tightness dependency of the macroscopic geometry. The performance of the test valves improves in the topology from the top to the bottom and from the right side to the left. One can show, that the width b of the sealing contact increases in the same direction. This value can be calculated according to the formula of Hertz (eq. 1), which depends mainly on the radii r_1 and r_2 on the contact partners. Further values are the contact force F_{an}, Poisson's ratio ν, elastic modulus E and the diameter of the contact D_d. A large contact area seems to improve the tightness of a hydraulic seat valve clearly. To confirm this theory, more measurements have to be carried out.

$$b = \sqrt{\frac{32F_{an}\left(1-\nu^2\right)}{\pi^2 \cdot E \cdot D_d\left(\frac{1}{r_1}+\frac{1}{r_2}\right)}} \qquad \text{eq. 1}$$

6. CONCLUSION AND OUTLOOK

The aim of this project is experimentally investigate influences on leakage at metallic seal seats. For this purpose, first a test bench was constructed which allowed for the simultaneous investigation of three test valves. The test bench is laid out such that the test valves to be examined can be exchanged easily and quickly. This allows for variations of the test valves' geometries. Furthermore, the essential hydraulic factors on leakage can be varied and measured within the test bench. Thus, the pressure to be sealed can be set up variably up to 600 bar. The force for pressing the sealing element into the seal seat can be applied hydraulically and varied independently from the pressures to be sealed. It is further possible to change and measure the purity of oil. After carrying out measurements and gaining experience with the behaviour of the test rig, a revision clearly improved the performance.

Through a structured conduction of measurements the examined factors have been determined. It was thus shown that leakage at metallic seal seats is time-dependent and reduces with ongoing measurement time. Furthermore, the influence of contact force on leakage was determined. It turned out that leakage decreases similar to an exponential curve with rising contact force. It has also been shown that the test valves' macroscopic geometry has an influence on the tightness.

The experiences gained within this project show the complexity of metallic sealing and the problems of measuring leakage. To understand the interrelations of the different parameters of influence better, more measurements have to be carried out. Due to the test rig build up and the multitude of custom made valves, a foundation was created to successfully proceed with this project.

REFERENCES

(1)	H. Ebertshäuser S. Helduser	"Fluidtechnik von A bis Z", O+P Ölhydraulik und Pneumatik, Vereinigte Fachverlage Mainz, 1995
(2)	C. Marie	"Fuite monophasique au travers d´un contact rugueux: Contribution a l´etude de l´etancheite statique", Dissertation, L'Université Bordeaux I, 2002
(3)	H. Murrenhoff	"Grundlagen der Fluidtechnik", Hydraulik, Shaker Verlag, 2005
(4)	A. Stammer	"Gestaltung, Dichtigkeit und Prüfung von Hydraulikventilen mit Sperrelementen in Sitzausführung", VEB Kombinat Orsta-Hydraulik, Leipzig, 1981

Application of proportional seat valves to a Self-energising Electro-Hydraulic Brake

Julian Ewald, Matthias Liermann, Christian Stammen, Hubertus Murrenhoff

RWTH Aachen University, Germany
Institute for Fluid Power Drives and Controls
Steinbachstr. 53, 52074 Aachen, Germany
Julian.Ewald@ifas.rwth-aachen.de

ABSTRACT

A new hydraulic brake utilising a self-energising effect has been developed at the Institute for Fluid Power Drives and Controls (IFAS). The Self-energising Electro-Hydraulic Brake (SEHB) generates the brake pressure by supporting the brake torque via a hydraulic cylinder and hence doesn't need an external power supply. Until now, the SEHB has been used with seat-type switching valves for control of its brake torque only. Spool type valves cannot be used for SEHB because of leakage in the closed position due to radial clearance.

For high requirements concerning comfort and dynamics this paper presents a valve concept using 2/2 way proportional seat valves. The major advantage over previous concepts using switching valves is the adjustable closed loop gain. As the result of a simulation study regarding the requirements of the target application, a configuration of eight 2/2 way valves is set up. Measurements of the valve tappet's position with a laser vibrometer show the dynamics of the used valve-types. A map of the flow is measured to regard the pressure dependency in the SEHB controller. The valves are integrated in a compact unit for the SEHB prototype. The paper finishes with first results of closed loop brake force control.

1. Introduction

The brake concept of Self-energising Electro-Hydraulic Brake (SEHB) combines high dynamics and high force to weight ratio of closed-loop controlled hydraulic actuation with high efficiency by using the principle of self-energisation. It has been developed at the Institute for Fluid Power and Controls (IFAS, RWTH Aachen University) within a research project funded by the DFG (German Research Foundation). Its concept has been introduced in (1), (2). The brake calliper is mounted pivoting around the wheelset to use the brake torque as the source of power to supply hydraulic pressure for braking. Only low electric power for the operation of hydraulic valves, pressure sensors and controller electronics is required to operate the brake.

Fluid Power and Motion Control 2008 Edited by Dr D N Johnston and Professor A R Plummer

The design of the prototype has been published in (4). In first tests the brake force control has been realised using seat-type switching valves from an anti-lock brake system. For applications with higher requirements like electronic stability systems (ESP) or the electro-hydraulic brake (EHB) proportional seat valves have been developed (5). They allow a more continuous control of the flow and pressures.

1.1 SEHB concept using single-acting supporting cylinders

The idea of SEHB is that the pressure needed for actuation of a hydraulic disc brake is gained from the hydraulic support of the friction force. Unlike conventional brakes, where the brake calliper is fixed, in the SEHB concept it is movable tangential to the friction contact. In the case of braking, the friction force acts on the supporting cylinder causing a pressure build-up. In previous publications (4) a brake concept has been presented where the brake calliper is supported by a synchronising supporting cylinder, where the two pressure chambers are mechanically connected. Another option, presented in **Figure 1,** is to use two single-acting cylinders mounted on both sides of the brake calliper. Both of them are fully extended in the middle position. The brake in Figure 1 is shown for the case of braking, indicated by the pushed-in single acting supporting cylinder on the left.

Beginning with the open brake set up to a defined clearance between brake pads and brake disk, valves PV 2 and PV 3 are opened. This enables the preloaded spring to press the brake linings against the brake disk. As soon as the brake has moved beyond the clearance, the brake pads are pressed with the spring force towards the brake disk.

Dependent on the direction of rotation, one of the single-acting supporting cylinders is pressurised. The other supporting cylinder remains extended at its full stroke due to a mechanical stroke limitation and releases from the frame. The high pressure check valve conducts the fluid to the high pressure accumulator.

For increasing the brake force, valves PV 1 and PV 3 are opened. High pressure is applied on the piston face side of the brake actuator, while the ring side is connected to low pressure. The increased compression of the actuator increases the force acting on the supporting cylinder. This process is self-energising dependent on the ratio of piston areas of supporting cylinder and brake actuator.

Decreasing the brake force is done by opening valves PV 2 and PV 4. The piston face chamber is released, while the piston ring side is charged, reducing the actuator force and yielding a negative feedback of the supporting pressure on the braking pressure. By this mode of operation the brake force cannot be reduced completely and the brake pads cannot be lifted off from the brake disk. The preloaded spring in the brake actuator has to be pushed back. However, the pressure in the supporting cylinder is now too low. Therefore the high pressure check valve disconnects the supporting cylinder from the high pressure accumulator. With the oil supplied by the high pressure accumulator a defined clearance is set between brake pads and brake disk.

The advantage of this supporting cylinder configuration is that some components of the system presented in (4) are no longer required. Through the direct connection between both

supporting cylinders there is only one hydraulic capacity which provides the pressurised oil to the valves in both driving directions. Two of the original four check valves can be saved. Only a high pressure check valve for separation of supporting pressure and high pressure accumulator and a suction check valve for separation of supporting pressure and low pressure reservoir are needed. This suction valve is needed during the retraction of the supporting cylinders. It connects the supporting cylinder with the low pressure part after braking. The pushed in single acting supporting cylinder is retarded into its end position by a spring, while being filled with oil from the low pressure reservoir.

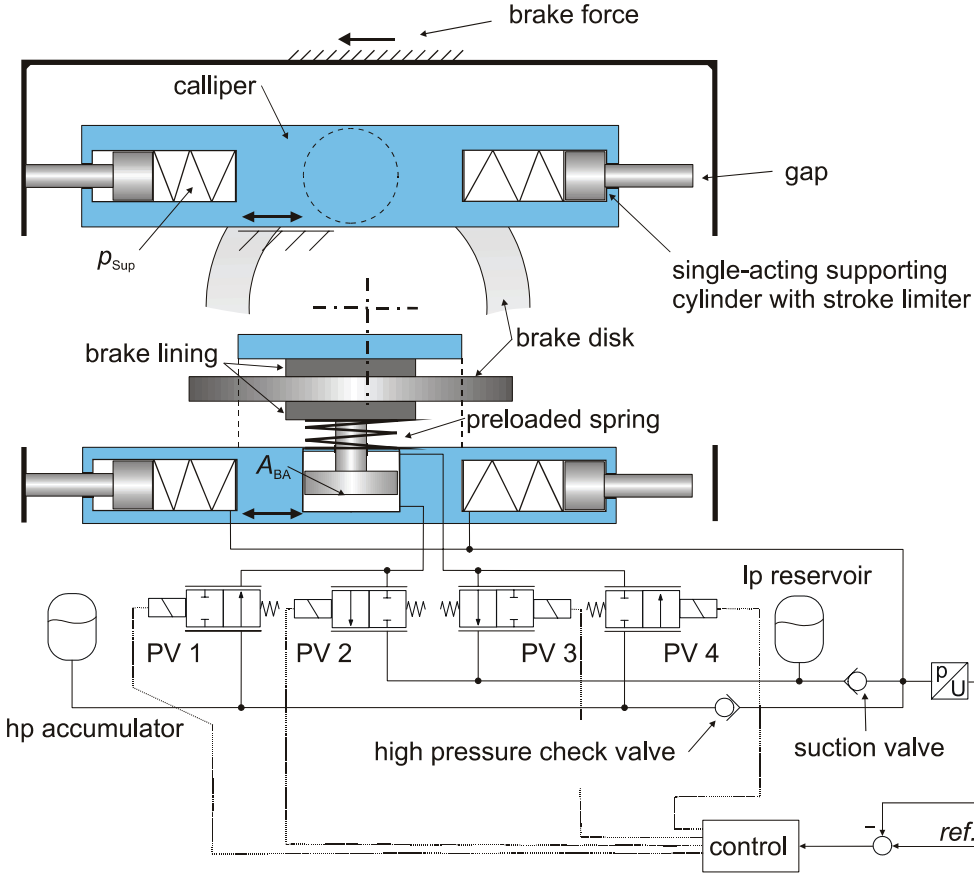

Figure 1: Principle of Self-energising Electro-Hydraulic Brake (SEHB), using four proportional seat-type valves

The SEHB, which so far has been developed for a train application, is designed with a fail-closed concept. This means, that in case of a failure like the loss of electric power, the brakes apply and the vehicle is stopped safely. This is realised hydraulically by a configuration of normally open and normally closed valves depicted in (3). Without electric power the seat valves are either opened or closed by an integrated spring. The power-off state is shown in Figure 1.

2 Proportional valves from automotive applications

The normally opened (NO) and normally closed (NC) types of the seat-type 2/2 way proportional valves used for this study were provided by Continental Teves. They are originally used for automotive brake applications. The NC valve is used for the electro hydraulic brake (EHB). The NO valve has been designed for a traction control system (ASR), where the wheel slip is controlled by braking the wheel in case of loss of traction. The valves are made as cartridges for being press-fitted into a valve block.

Three forces are applied to the valve tappet. For the normally closed valve, shown in **Figure 2** on the left side, the spring force F_{Spring} closes the valve, while the force generated by the pressure difference acts opening the valve as well as the magnetic actuation force $F_{magnetic}$. The valves has a pressure-dependent characteristic due to the pressure drop at the seat. In comparison to seat-type switching valves the force between armature and solenoid is constant over the tappet movement. By this, partially open positions of the valve tappet are achieved.

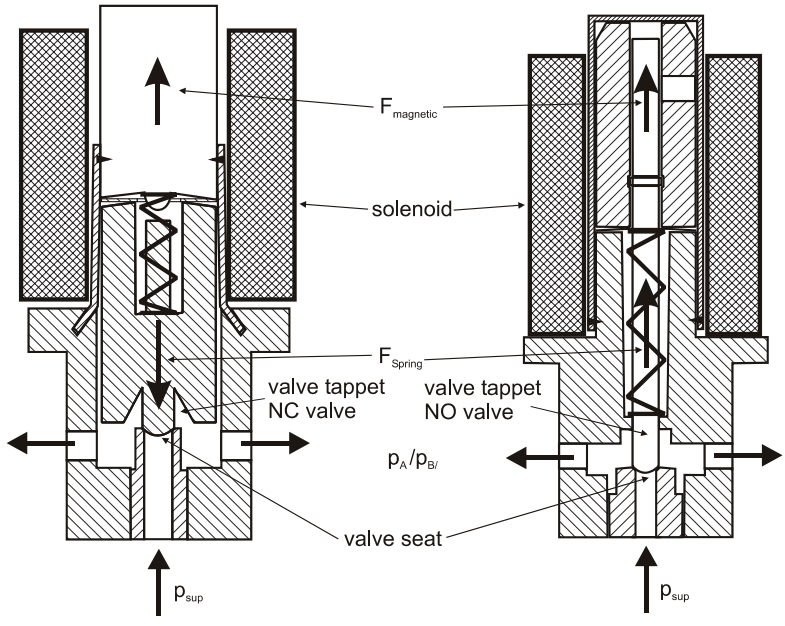

Figure 2: Normally open and normally closed seat-type valve

The NC valve has a rated flow of 40 cm³/s, the NO valve has 52 cm³/s at a pressure drop of 100 bar using DOT 4 brake fluid. However, the SEHB prototype is using HLP46 hydraulic fluid instead. The different specific weights result in a different rated flow, which can be calculated by Eq. 1.

$$Q_{HLP} = \sqrt{\frac{\Delta p_{HLP} \cdot \rho_{DOT\,4}}{\Delta p_{DOT\,4} \cdot \rho_{HLP}}} \cdot Q_{DOT\,4} \qquad \text{Eq. 1}$$

Table 1: Rated flow for a normally open and a normally closed valve

Valve type	flow rate forDOT 4 @ 1 00bar ($\rho_{\text{DOT-4}} = 1060\,\text{kg/m}^3$)		flow rate for HLP 46 @ 35 bar ($\rho_{\text{HLP}} = 870\,\text{kg/m}^3$)	
	[ml/s]	[l/min]	[ml/s]	[l/min]
NC EHB	40	2.4	26	1.56
NO ASR	52	3.12	34	2.04

Concerning the needed flow, two main requirements can be identified. A high rated flow is needed at low brake forces or in case when the brake is not engaged yet. In this operating point the pressure difference at the valve is low, thus the valve has to provide a wide flow section. On the other hand, at high brake force, the applied pressure difference at the valve is high. The bulk modulus at high pressure is high hence the quotient dp/dQ describing the pressure build-up is high as well. Therefore a high resolution of the valve is needed.

The valve has to combine the two characteristics composed of a high rated flow and a good resolution at small openings. To be able to make use of the valve resolution, the pressure dependent behaviour must be known very well.

The first step is the determination of the required rated flow. A high rated flow can be achieved by using more than one valve in parallel. The number of valves needed can be derived by requirements given form the desired railway application. The time from an open brake calliper to a defined brake force is limited. Based on the requirements given from the EABM framework a limit of half a second is set. With the rated flows given by the above described valves a simulation model in DSHplus is build up to get a measure for the closing time using one or two valves.

Table 2: Tested valve configurations

Configuration	PV 1	PV 2	PV 3	PV 4
No. 1	1 NO	1 NC	1 NC	1 NO
No. 2	2 NO	2 NC	2 NC	2 NO
No. 3	2 NO	2 NC	1 NC	1 NO
No. 4	2 NO	1 NC	1 NC	1 NO

The possible valve configurations with a number of valves between four and eight are shown in **Table 2**. In configuration No. 2 all valves are doubled. In configuration No. 3 and No. 4 the valves connected to the piston rod side are not doubled. For benchmarking these configurations, the simulation is run with a reference signal curve of the demanded brake force as shown in **Figure 3**.

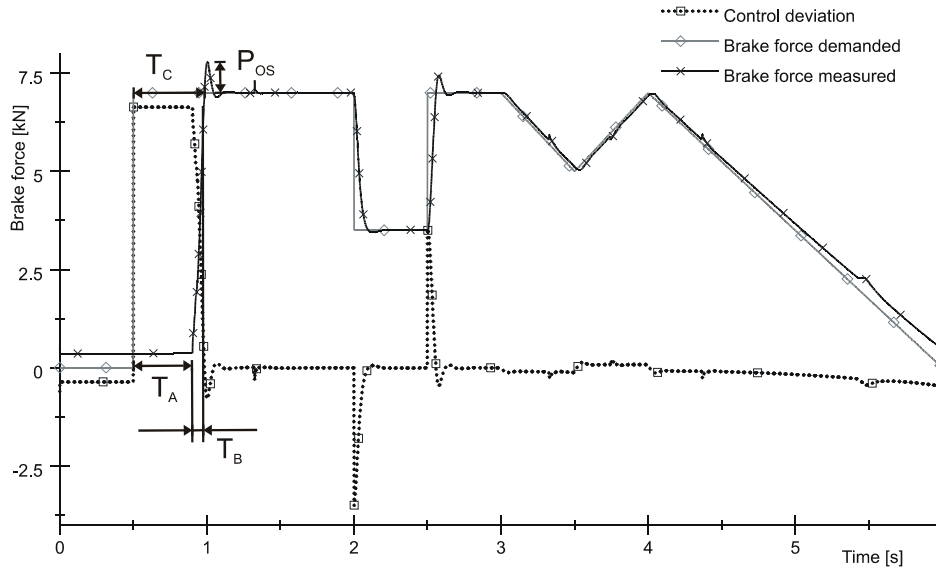

Figure 3: Simulation to verify valve configuration (Configuration No. 2)

From the simulation results five characteristic parameters are extracted, these are:

T_A: Time to get over a clearance of 1 mm between brake pad and disk
T_B: Time for step response from 0% to 90% of the maximum brake force
T_C: $T_A + T_B$
P_{OS}: Overshooting at step response from 0% to 90% of the maximum brake force

Table 3: Simulation results

	T_A	T_B	$T_C = T_A + T_B$	P_{OS}
No.1	0,662s	0,142s	0,804s	1,4%
No.2	0,402s	0,074s	0,476s	11,2%
No.3	0,675s	0,084s	0,759s	8,7%
No.4	0,662s	0,085s	0,747s	9,2%

With a configuration of four singular valves (No. 1) the dynamics at low brake forces are too slow. The configurations where only one or two valves are doubled (No. 3 and No. 4) cannot offer the short time to get other over the clearance between brake pad and brake force (T_A), although they do well in reaching 90% of the maximum brake force after the brake has travelled over the clearance (T_B). Configuration No. 2 is chosen to be used with the SEHB prototype because it has the lowest values for T_A, T_B and T_C. The overshooting with this configuration can be reduced to the valve of configuration Nr. 1 by using the parallel valve only to get over the clearance and at low brake forces. By this a fast response of the brake with a very small overshoot can be realised.

4. Valve measurement

In this chapter a measurement of the valve tappet position and a measurement of the flow are presented. With a laser vibrometer the valve tappet's position of a NC valve is measured. Due to the design of the cartridge valves only the NC valve could be opened in such a way that the laser could be focused onto the tappet. The NO valve has a filter element above the valve tappet which could not be removed without damaging it. The optical principle allows a measurement up to a very high dynamic which the flow sensor cannot achieve. However, the laser vibrometer needs an optical access to the valve tappet hence the measurement cannot be used for the pressurised valve.

The test bench with the laser vibrometer is depicted in **Figure 4**. The reference signal generated by the measuring computer is given to the current driver. The current driver supplies a closed loop controlled current to the valve's solenoid. By the laser vibrometer and its amplifier the tappet position is given back to the measuring computer.

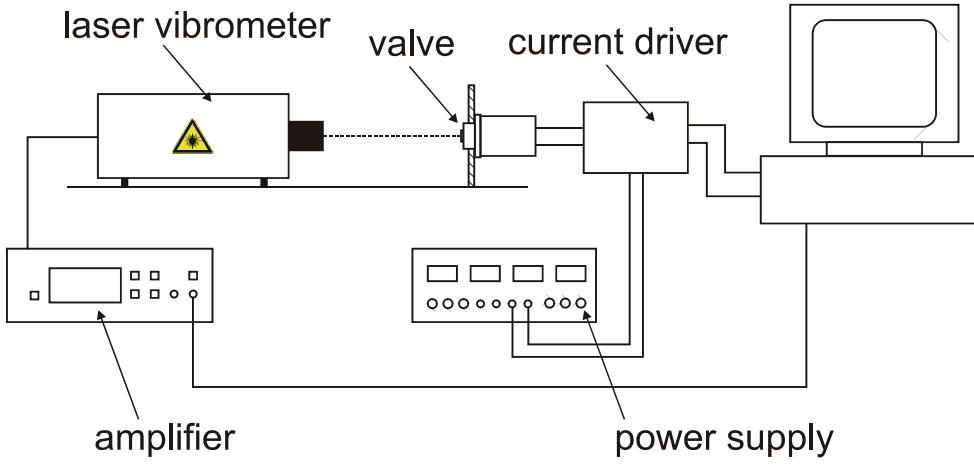

Figure 4: Test bench with laser vibrometer

At first, a static measurement is done to determine the current where the valve starts to open. As shown in **Figure 5**, without pressure, the valve is beginning to open at about 0.9 A and is reaching its maximum opening of 125 µm at about 1.1 A. The upper graph shows the measured position of the valve tappet over time. The lower plot shows the displacement of the tappet as a function of the current for both directions of actuation, opening and closing the valve. The measured step which occurs in the tappet position at 0.92 A and 0.86 A could not be settled conclusively. There are three theories: One is that due to high friction, for the nearly closed valve, the tappet stops. Another explanation is that the tappet is tilting in its seat. The third possibility is that another part of the valve is moving prior the tappet starts moving out of its seat.

There is a hysteresis between the opening and closing of the valve. Due to the friction force, which is always directed against the direction of movement, the force for pulling the tappet out of the seat against the spring is higher than the force for closing it. The valve is

designed such that the valve is closed by a spring pressing the tappet into the seat, see Figure 2. The magnetic force pulls the tappet against the spring out of its seat. While the valve is opened, the friction force is directed against the magnetic force. When closing the valve, due to reducing the force from the solenoid, the friction force is aligned to the same direction as the magnetic force.

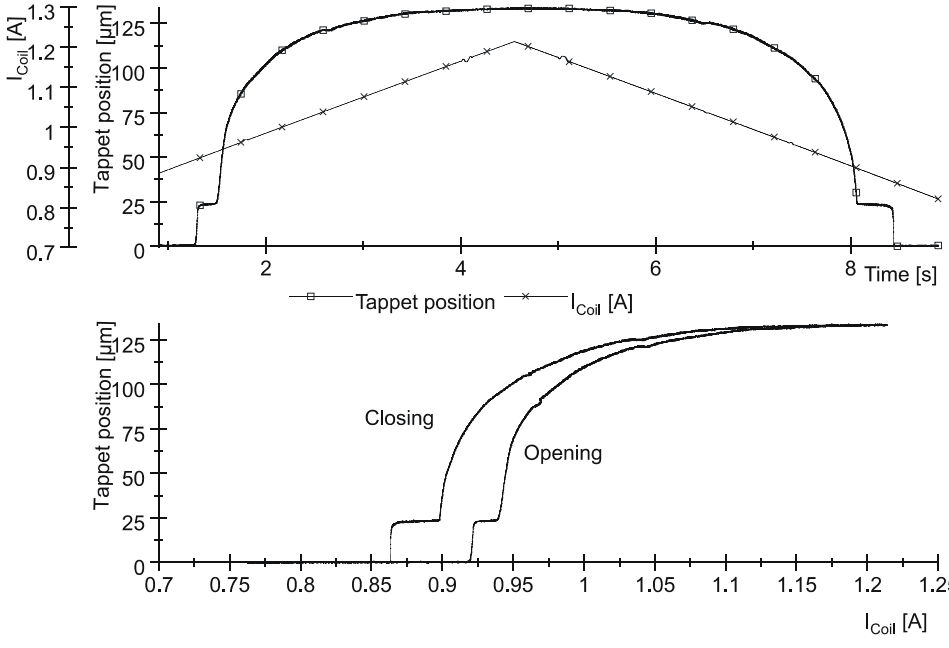

Figure 5: Static measurement of tappet position

4.1 Tappet dynamics

For an evaluation of the tappet dynamics, the solenoid is actuated with a sinusoidal signal and the response is measured. The sinusoidal signal increases its frequency exponentially to provide equal number of oscillations through the frequency bandwidth.

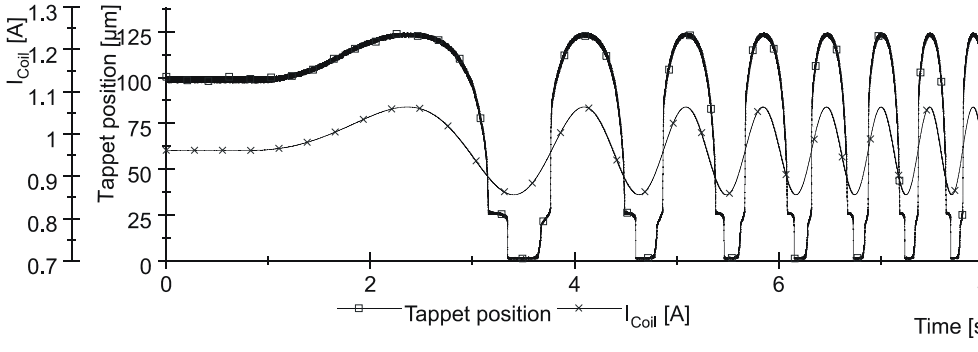

Figure 6: Sinusoidal signal for the bode diagram

Beginning with the half open valve, the reference signal is applied as shown in **Figure 6**. The position of the tappet is measured. The data acquisition is done with a dSPACE rapid control prototyping board where the data is logged at a rate of 40 kHz. By Fast Fourier Transformations (FFT) the measured data is transformed to a bode diagram. The measurement is done for 10%, 25%, 50% and 100% of the possible tappet movement. **Figure 7** shows the bode diagram for 10% of the possible tappet movement. The bode plot shows increasing noise for amplitude and phase values above 200 Hz. This is caused by different dynamics of the valve in closing and opening direction, as can be seen from Figure 6. The difference between closing and opening dynamics results in two values for phase lag and amplitude for each excited frequency. This effect becomes more dominant for higher frequencies as Figure 7 shows.

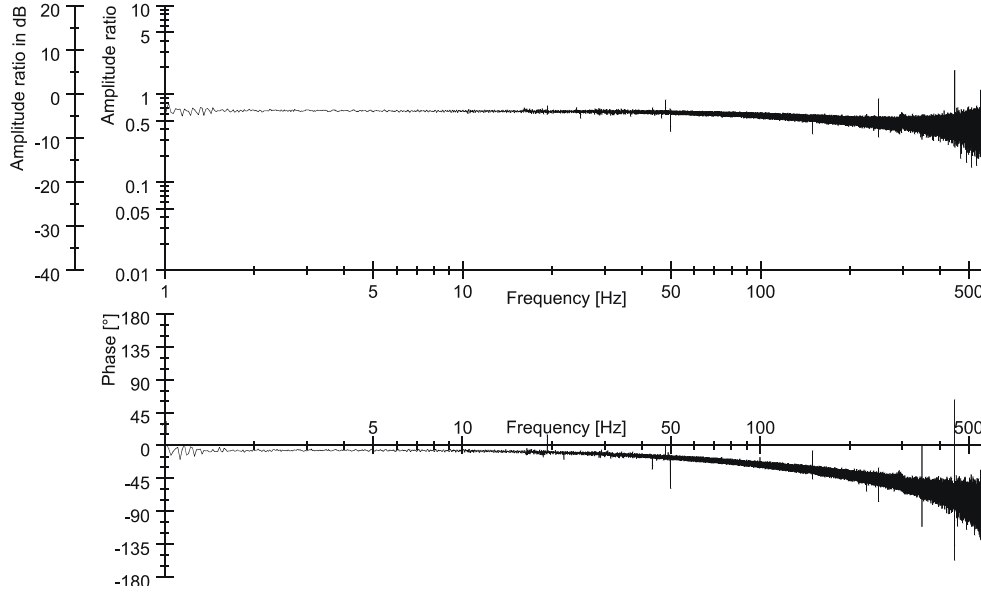

Figure 7: Frequency response to sinusoidal signal for 10% tappet movement

From the whole measurements a characteristic of a PT_1T_t can be identified. The first-order time-delay element is identified from the falling amplitude at increasing frequency. The dead time element results from the phase response with a steady rising gradient. A PT_1 would reach the maximum gradient in its phase response at -45° and then would tend to -90° phase delay. The measurements, however, show a rising gradient far beyond this value of the phase delay. Measurements of the step response for closing and opening valve show that the valve is faster in closing than in opening.

4.2 Flow rate measurement

In addition to the dry measurement, the flow rate through both types of the used valves is measured against pressure drop and solenoid current. The valve unit is connected between two pressure controlled servo valves. The pressures at both sides of the valve unit can be adjusted to the demanded pressure with a high accuracy by these two servo valves. The oil for this measurement is supplied by a pump and not from the supporting cylinder.

Basically three variables can be set individually: The pressures before and after the valve and the solenoid current. Changing every parameter individually leads to a four-dimensional map. Comparing the flow at the same pressure drop but different absolute values, the flow is not significantly different, neither for the normally open valve nor for the normally closed valve. Therefore the degree of freedom can be reduced to two; the flow is now depended on the current and the pressure drop only.

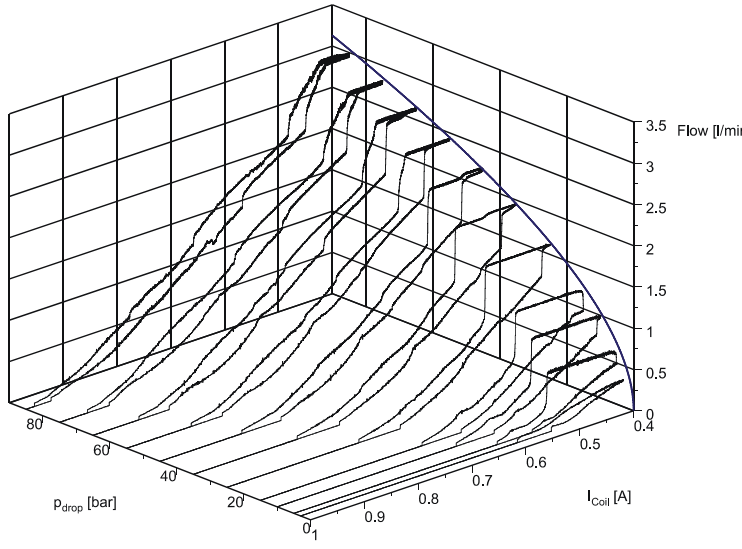

Figure 8: valve flow maps for NO valve

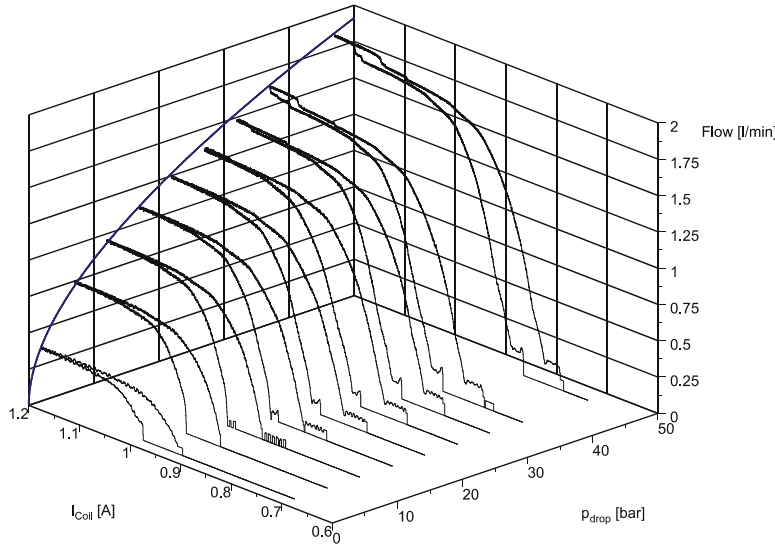

Figure 9: valve flow maps for NC valve

The flow rate is displayed in **Figure 8** and **Figure 9** for various pressure drops over the current. A characteristic parameter for the valve is the flow at a pressure drop of 35 bar. The NO valve has a nominal flow of 1.95 lpm and the NC valve a flow of 1.6 lpm. This data complies with the data from the manufacturer. The flow rate for a fully open valve at 1.2 A is shown in Figure 8 and Figure 9 calculated by the basic equation of an orifice. A distinctive hysteresis between opening and closing is shown especially for the normally open valve.

4 Mechanical design and current driver

The eight valves are pressed as cartridges into a valve block made from aluminium as shown in **Figure 10**. The valves are mounted as closely together as possible for a low weight of the valve unit and a good package of the complete brake calliper where the hydraulics are mounted onto. Like at a common 4/3 way valve, the four hydraulic connections are lead out at one side. On this side the valve is put on a mounting plate with integrated check valves.

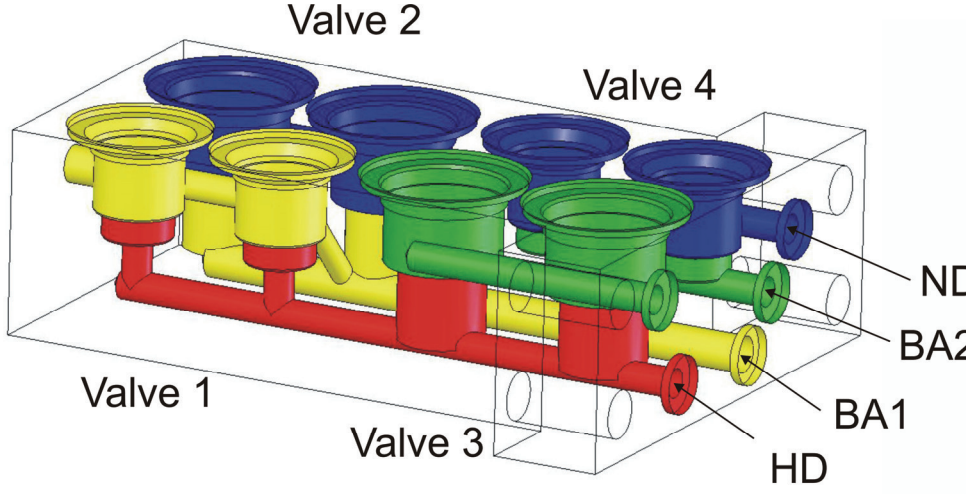

Figure 10: valve unit

3.4 Electronic control

Each valve is driven by a current controller. The current driver is based on an asymmetric half bridge built up from two transistors and a comparator. The circuit diagram is depicted in **Figure 11** consisting of a transistor between the solenoid and the power source and the second transistor between the solenoid and ground. Three states are realised. For rising current both transistors are switched on and current is conducted from source over the solenoid to ground. If the measured current is higher than a dead band around the desired current, the transistor S_1 between source and coil is opened. By the inductance of the solenoid the current is falling slowly while the circuit is closed by the free wheeling diode D_1 and a shunt. For cutting down the current quickly, the energy stored in the inductance is moved to the capacitor. Therefore both transistors are turned off and the solenoid is

"pushing" its current over the diode D_2 to the capacitor with the other port connected to ground by diode D_1. The magnetic force applied from the solenoid to the valve tapped is cut off fast.

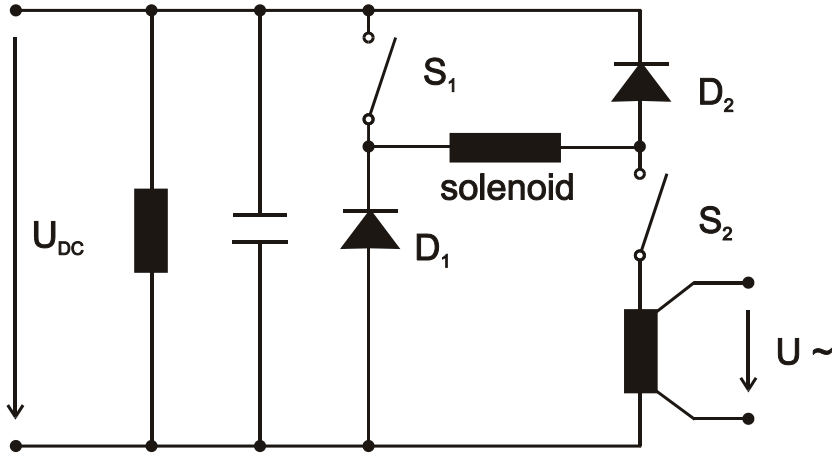

Figure 11: wiring scheme of current driver

4. Brake force control

The flow maps depicted in Figure 8 and Figure 9 are implemented to a brake force control software using a rapid control prototyping board. The closed loop controller is set up with a PI controller. From simulations a P controller has been considered to work well with the SEHB (4). The hysteresis shown in the flow maps can be compensated in a first step with a switched integral controller.

Figure 12 shows he measurement of three values, the brake force, the pressure in the piston side of the brake actuator and the stroke of the supporting cylinder. The reference signal is a ramp rising from 1000 N to 3000 N tangential brake force. The measured brake force is following the reference signal well. Only at 16 s, when the falling ramp begins, a greater control deviation occurs. This should be eliminated with some optimisation on the controller setup.

The pressure signal shows a ripple. By closing all valves manually the ripple is still present hence the ripple can be considered to be caused by the friction contact between brake disk and brake lining. Future research will attend to the question of decreasing this effect with a high dynamic brake force control.

The supporting cylinder stroke, shown in the plot at the bottom of Figure 12, points out the low needed oil supply from the supporting cylinder. For the shown ramp rising from 1000 N to 3000 N only 5.5 mm (11%) of the maximum stroke of 50 mm are needed.

Included in these 5.5 mm are about 3 mm for charging the high pressure accumulator, which is only needed once during a brake operation.

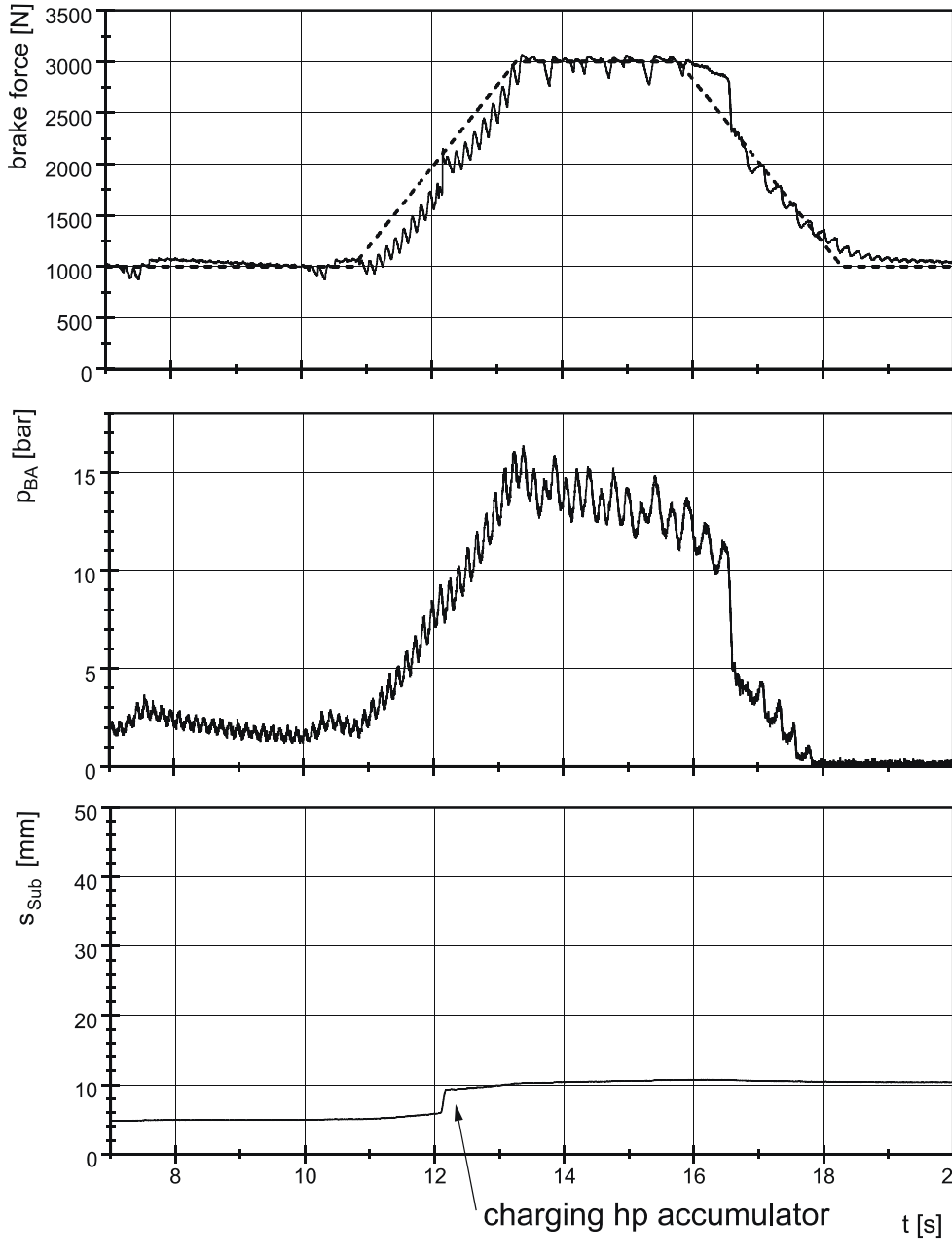

Figure 12: brake force measurement

5. Conclusion and Outlook

This article presents the development of a valve unit for the SEHB prototype. Four doubled 2/2 way seat valves take over the functionality of a 4/3 way valve. The advantage in comparison to spool type 4/3 way valves is the leakage free seat and the higher degree of freedom in control.

By simulation the needed nominal flow is evaluated and the valve configuration is determined. Without the exact knowledge of the valve characteristic the controller cannot be set up to offer the desired smooth characteristic and the exact brake force control which is needed by comfort and safety demands. Therefore, the tappet dynamics of the used seat-type 2/2 way valve is measured. Additionally the flow is measured at different pressure drops over the solenoid current. The data from the measurement is considered in the SEHB controller and depicted in a flow map for the used normally open and normally closed valve.

The valves are fitted to a valve block and used for a closed loop brake force control with the SEHB prototype. The valve measurements are the basis for a fitted controller design enabling a good performance. Future work is concerned with a controller design compensating the hysteresis of the valve between closing and opening current in a better way.

The authors thank the German Research Foundation (DFG) for funding this project and Continental Teves for supply of the valves.

6. References

(1) Matthias Liermann, Christian Stammen Self-Energizing Hydraulik Brake for Vehicles Selbstverstärkende hydraulische Bremse für Schienenfahrzeuge - Intelligentes, Integriertes Einzelrad-Antriebs-Brems-Modul, Ölhydraulik und Pneumatik O+P 10/2006, 500-507

(2) Matthias Liermann, Christian Stammen, Hubertus Murrenhoff Development of Selfenergizing Electro-Hydraulic Brake (SEHB) for Rail Vehicles, The Tenth Scandinavian International Conference on Fluid Power, SICFP'07, May 21-23, 2007, Tampere, Finland

(3) Dipl.-Ing. M. Liermann; Dr.-Ing. C. Stammen; Prof. Dr.-Ing. H. Murrenhoff, Development and experimental results of a self-energizing Electro-Hydraulic Brake using switching valves, IFK 2008, Dresden, Germany

(4) Liermann, M.; Stammen, C.; Murrenhoff, H. Pressure tracking control for a self-energizing hydraulic brake, Proceedings to the 20th Bath Symposium on Power Transmission and Motion Control (PTMC) 2007, Bath, England

(5) Bert Breuer, Karlheinz H. Bill (Publisher) Bremsenhandbuch - Grundlagen, Komponenten, Systeme, Fahrdynamik [Brake Handbook - basic principles, components, systems, dynamic of vehicle movement], (2nd Edition), Vieweg Verlag, 2004, Wiesbaden

Experimental Evaluation of a Metering Poppet Valve

Roger Fales (falser@missouri.edu)
Chang Li (clbk6@mizzou.edu)
Mechanical and Aerospace Engineering Department
University of Missouri
Columbia, Missouri
USA

ABSTRACT

In this work, a model with experimental validation is developed for a unique electro hydraulic flow control valve. The model is intended to be used for control design and simulation of hydraulic systems. The valve is a unique design developed at the University of Missouri with two stages: a pilot stage and a main stage. Both stages employ poppet valves rather than more common spool valves. The dynamic response is analyzed through the use of experiments. The experimental dynamic response is compared to that of a nonlinear and a linear simulation. A linear model is developed to agree with the experimental responses. Since the performance is found to vary based on changes in operating conditions, a model of the error is also determined using frequency domain techniques. The error model can be used in robust stability analysis for future control system designs.

1. INTRODUCTION

In this work a metering poppet valve design model and experimental validation are presented. Also, model uncertainty and valve performance are considered. The valve was designed and built at the University of Missouri. The valve design was based largely on linearized model root locus techniques and the use of nonlinear simulations (Muller, 2008). The design techniques used were similar to those used by Li for a spool valve application (Li, 2002). The prototype was only recently completed with initial test results appearing for the first time in this paper.

Recently, there has been an interest in developing poppet valves for flow metering applications in place of the typically used spool valves (Ardema, 1997), (Schexnayder, 1995), and (Yang, 2005). The poppet valve offers certain advantages over the spool valve. Mainly, poppet valves have extremely low leakage when closed, they require less precise machining, they are capable of adjusting themselves with wear, and they are self-flushing and therefore less sensitive to contamination (Manring, 2005). Key disadvantages to using the poppet valve for flow metering are centered on dynamic stability issues of poppets

Fluid Power and Motion Control 2008 Edited by Dr D N Johnston and Professor A R Plummer

which have been studied by Hayashi (1995) and Funk (1964) for example. The performance of metering poppet valves in feedback control systems have been found to be limited by various factors such as the location of an open loop pole in a valve studied by Zhang et al (2002) and possibly model uncertainty studied by Fales (2006).

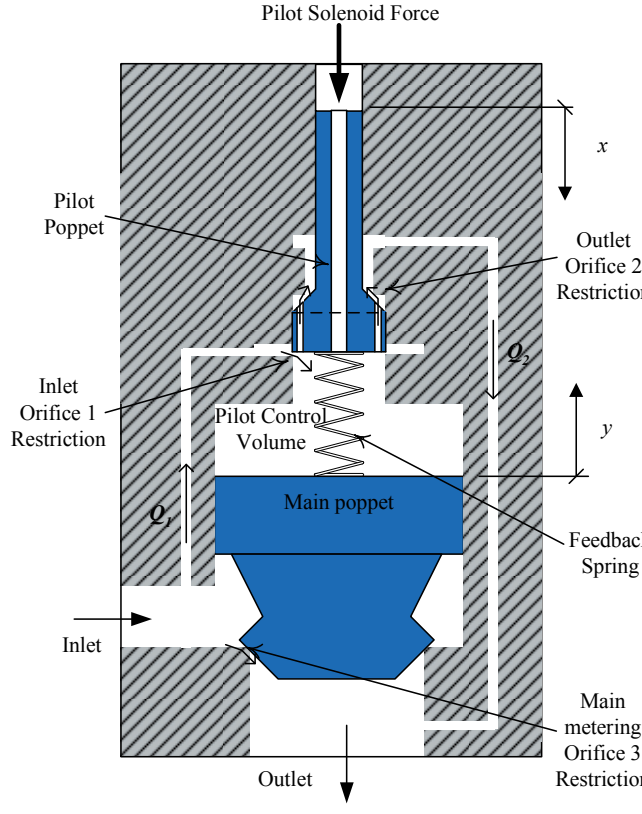

Figure 1 Diagram of the metering poppet valve

The following paragraph gives a brief description of the operation of the metering poppet valve design presented in this work. With respect to Figure 1, the valve is in the closed position with high pressure connected to the inlet port while low pressure is connected to the outlet port. The only two pathways from high to low pressure are sealed by poppet seats and therefore the valve maintains a very low leakage flow when closed. It is assumed that the pilot poppet is pressure balanced by the passage shown within the pilot poppet while being subjected to the pilot solenoid force, the feedback spring's force, viscous damping, and flow forces. In order to raise the main poppet off its seat, a pulse width modulated signal (PWM) signal supplies current to the pilot actuator solenoid which pushes the pilot poppet off its seat and allows fluid to exit the pilot control volume through its outlet orifice (2) restriction. Once the pilot poppet opens, the control volume inlet orifice 1 is effectively smaller than its outlet orifice creating a net outflow which allows the main poppet to lift off its seat. This opens the main metering orifice (3) restriction directly between supply and

load, allowing flow to be metered. The upward movement of the main poppet will push the feedback spring and in turn push the pilot poppet back towards its seat until an equilibrium position is reached where the main poppet is open yet no longer moving. In order to close the main poppet, the actuator current is turned off allowing the feedback spring to push the pilot poppet back to its seat. The control volume outlet orifice is now closed while high pressure fluid from the inlet orifice fills the control volume and pushes the main poppet closed.

The remainder of the paper is organized into the following sections. The modeling section presents the valve model equations. In the next section, the experimental verification of the model is presented including a comparison of simulation and experimental step responses. An uncertainty model is presented next where the uncertainty in the linearized model due to changing operating conditions is analyzed. Performance analysis follows, with analysis of the open loop performance of the valve along with a discussion of possible closed loop performance as well. Finally, the conclusions of the paper about model validation, uncertainty, and valve performance are presented.

2. MODEL

In this section, the model is briefly discussed. More detail can be found in previous works by the authors (Muller and Fales, 2008). The general model can be broken into four basic systems or governing equations: two spring mass damper systems with flow and pressure forces for each poppet, a pressure rise rate equation for the control volume, and a pressure rise rate equation for the load volume. The forces acting on the main poppet are represented by

$$M\ddot{y} = -b_y\dot{y} - k(y+x) - P_cA_c + P_sA_s + P_LA_L - 2\cos(\theta)C_d{}^2h_3y(P_s - P_L)\,. \tag{1}$$

The force balance on the main poppet includes flow force, viscous friction, feedback spring, and, hydrostatic forces due to pressure at the inlet, outlet and pilot pressure. The pilot poppet has similar forces except for the hydrostatic forces since the pilot poppet is pressure balanced. Also, the solenoid force is present which actuates the valve. The pilot poppet dynamic equation is given as follows:

$$m\ddot{x} = -b_x\dot{x} - k(y+x) + f - 2\cos(\theta)C_d{}^2h_2x(P_c - P_L) + 2\cos(\theta)C_d{}^2h_1x(P_s - P_c) \tag{2}$$

The pressure in the pilot control volume is affected by main poppet movement, flow entering and exiting the control volume as follows:

$$\dot{P}_c = \frac{\beta}{V_{CO}}(Q_1 - Q_2 + A_c\dot{y}) \tag{3}$$

The load pressure (pressure at the outlet of the valve) can be given as,

$$\dot{P}_L = \frac{\beta}{V_L}(Q_2 + Q_3 - Q_4)\,, \tag{4}$$

assuming that there is some load flow, Q_4, due to a load orifice for example. Later in this work, when experimental results are compared with simulations, P_L is simply an input to the model rather than a simulated state. The flow terms, Q_1-Q_4, in Eq. 3 and Eq. 4 are modeled using the classic orifice equation.

$$Q = aC_d\sqrt{\tfrac{2}{\rho}\Delta P} \tag{6}$$

The orifice areas are functions of the position of the pilot poppet position for areas one and two and the main poppet for area three. The slopes for these area functions with respect to poppet displacement are h_1, h_2, and h_3.

The linearization of the model is discussed in previous work by the authors (Muller and Fales, 2008). The linearized model equations are given as follows:

$$M\ddot{y} = -b_y\dot{y} - k(y_n + x_n) - kfq_3 y_n - kfc_3(P_s - P_L) - P_c A_c + P_s A_s + P_L A_L \qquad (7\text{-}10)$$

$$\dot{P}_c = \frac{\beta}{V_{CO}}\left\{A_C\dot{y} + kq_1 x_n - kq_2 x_n - kc_1 P_C - kc_2(P_C - P_L) + kc_1 P_s\right\}$$

$$m\ddot{x} = -B_x\dot{x} - k(y_n + x_n) - kfq_2 x_n + kfq_1 x_n - kfc_1 P_C - kfc_2(P_C - P_L) + f + kfc_1 P_s$$

$$\dot{P}_L = \frac{\beta}{V_L}\left\{kq_2 x_n + kc_2(P_c - P_L) + kq_3 y_n + kc_3(P_s - P_L) - kc_4(P_L - P_T)\right\}$$

3. EXPERIMENTL VERIFICATION

Experiments were carried out to correct the model parameters based on the actual construction of the valve. Prior to completing the test results presented here, it was decided to apply a dither signal to the valve solenoid current commands to reduce nonlinear friction effects. The dither signal frequency and amplitude are 100 Hz and 820 mA. The dither signal has a small influence on the position of the main poppet (other than eliminating static friction effects). In particular, it can be seen from experimental results that a low amplitude 100 Hz component is superimposed on the position response. The experimental results in this section were compared to model simulations. The parameters in the simulation were adjusted to match experimental results since there were some characteristics of the model such as friction that require experimental data to determine.

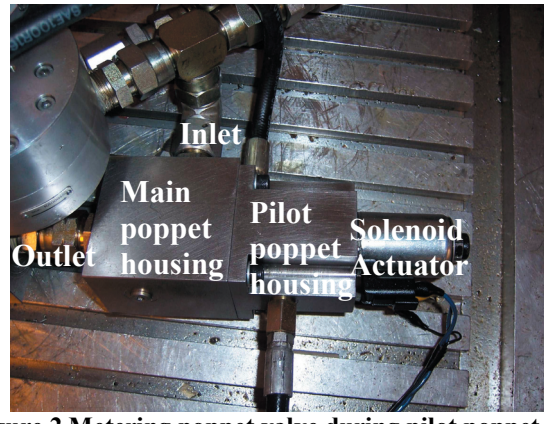

Figure 2 Metering poppet valve during pilot poppet tests

The testing of the valve includes separate tests of the pilot poppet with the main poppet disabled and main and pilot poppets working together. Slow modulation of current was used to determine steady state relationships between poppet position, current, flow and pressure. Dynamic tests were used to determine the performance and dynamic parameters

of the model such as friction. In all tests, a pressure supply was connected to the inlet port of the valve and the outlet port was connected to a line leading to the hydraulic reservoir. Pressure sensors were placed near the inlet and outlet ports to measure P_S and P_L. Flow was measured using a positive displacement flow meter placed at the outlet of the valve. The outlet flow is equal to the sum of the flow passing through the pilot orifices and the main poppet orifice, $Q_L = Q_2+Q_3$.

First, the static tests of the pilot poppet are discussed. In this test, the main poppet is disabled so that no flow passes through the main orifice since the main poppet is not allowed to move off of its seat. An LVDT (Linear Variable Differential Transformer) sensor is attached to the pilot poppet during the pilot poppet tests. A specially modified main poppet is used to allow for the temporary installation of the LVDT which is attached to the pilot poppet. In Figure 3 test results are shown that were obtained by supplying a current sweep to the solenoid while no pressure is supplied to the pilot inlet. It can be seen that there is a nonlinear "sticking" friction effect especially at the upper limit of motion as the valve begins to descend as current is decreased (near 7 seconds in the test). A simulation is compared to the test data which is given the same input supply pressure (zero) and downstream pressure (also zero). The simulated current is maintained above zero to avoid simulating zero poppet opening. In further pilot poppet tests (Figure 4), pressure is supplied to the system at various levels. In Figure 4, a supply pressure of 4 MPa is used. The effects of the nonlinear "sticking" friction can be seen in the pilot poppet position response. The simulated flow matches the experiment well. Note that there is a high amount of noise in the flow measurement.

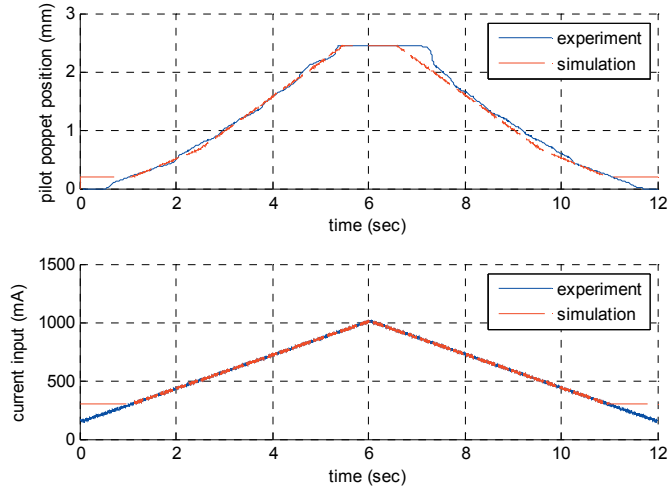

Figure 3 Pilot poppet position response under zero supply pressure and zero flow conditions

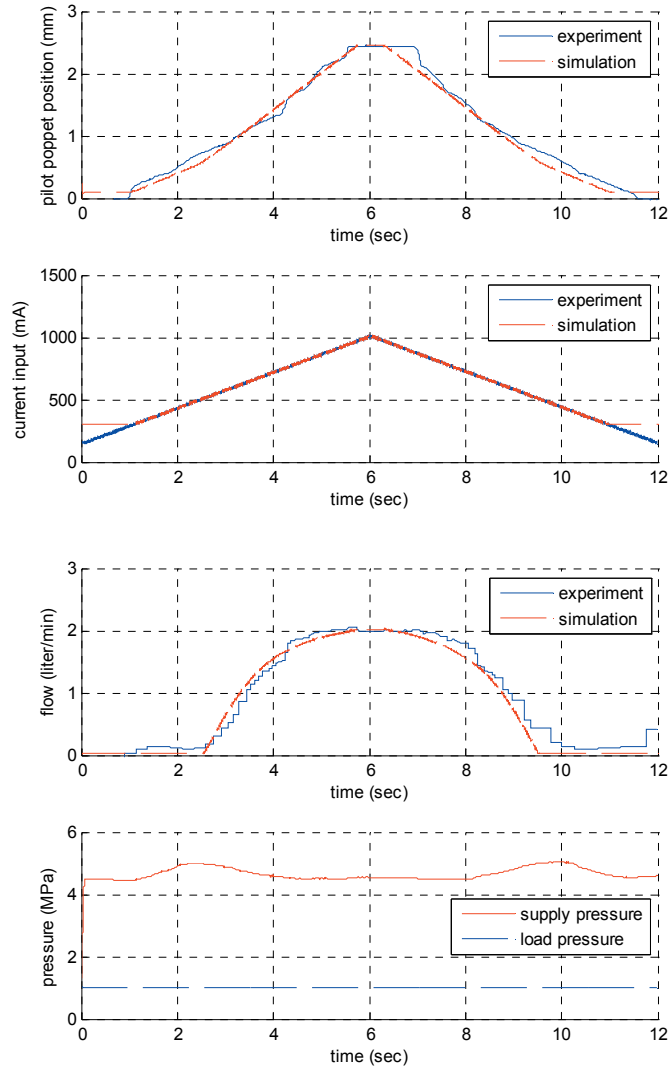

Figure 4 Steady state test for pilot poppet only with supply pressure above 4 MPa

Steady state tests with both the main poppet and pilot poppet in operation are discussed next. Only the main poppet position can be measured when the functioning main poppet is installed in the prototype valve. Again supply and load pressure are measured. Supply and load pressure dynamics are not modeled in the simulation. Therefore, the experimentally measured supply and load pressures are given as inputs to the simulation. Ideally, the supply pressure would have been held constant during the test. However, during the tests, the supply pressure varied a great amount. This condition was also accounted for by supplying the measured pressures as inputs to the valve model. The results indicate that the model accurately represents the actual system as can be seen from the comparison of

experimental and simulated responses in Figure 5. Notice that there is some oscillation in the supply pressure which is likely due to the performance of the hydraulic power supply used for the valve test.

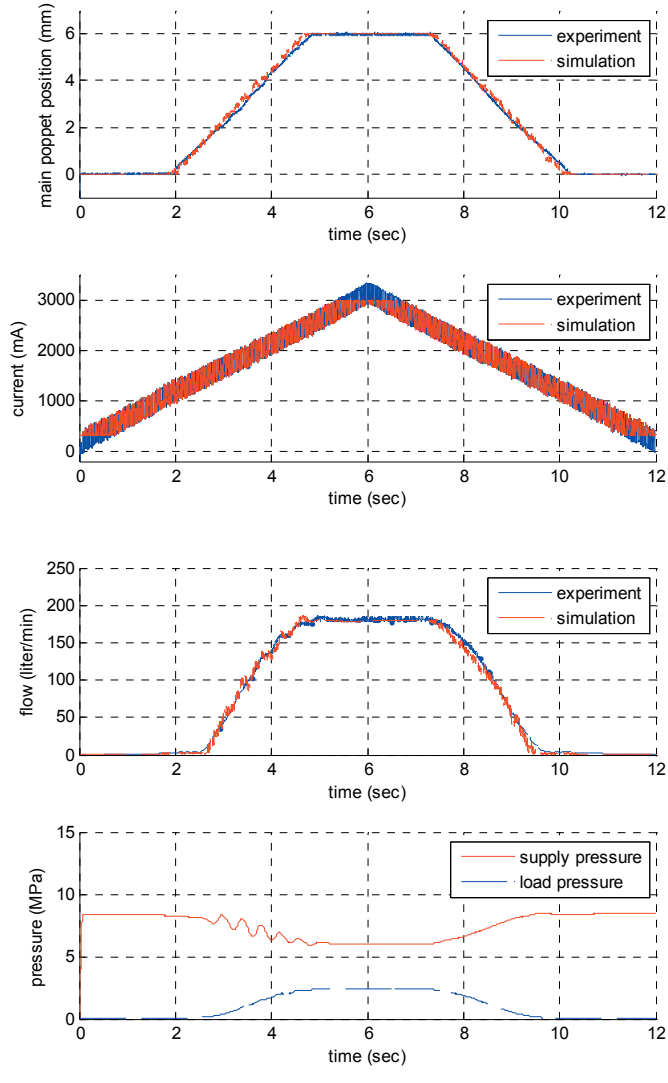

Figure 5 Steady state test results with both main poppet and pilot poppet in operation

4. LINEARIZATION AND UNCERTIANTY MODEL

The nonlinear model was linearized using Equations 7-10 about an operating point to study the dynamics of the system. A step response of the linearized model is given in Figure 6. The supply (valve inlet) pressure is approximately 3.2 MPa. The step increase in force is 8

Newtons (The solenoid actuator range is 60 Newtons). Even with the nonlinearities of the system the linear model simulation follows the experimental data well. For this small step input, the linear and nonlinear models are nearly identical so the nonlinear simulation is not shown in Figure 6.

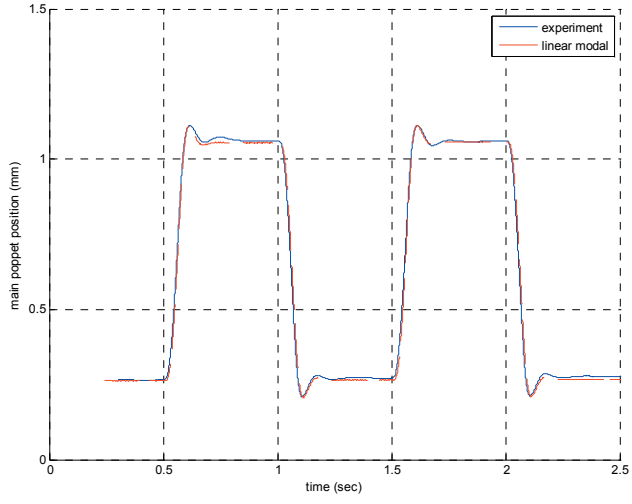

Figure 6 Experimental step response compared to a linear model

An uncertainty model can be used to predict stability and performance of a valve control system with consideration of uncertain parameters within the model. In this work, model uncertainty will refer to variations in the linear model used to create the simulation plot in Figure 6. Generally the higher the plant model uncertainty, the lower performance of a feedback control system must be. In classical control terms, more plant model uncertainty means that a controller applied to create a closed loop system must have a greater gain margin. Greater gain margin typically is obtained by reducing performance. Therefore it is important to design components with the least amount of model uncertainty possible. Frequency domain uncertainty model can be used to analyze the robust stability of closed loop control systems (Skogestad, 1996).

There are several sources of uncertainty in the metering poppet valve model. Parameters can vary from valve to valve if the valve were to be mass produced or as the valve wears over time causing model uncertainty. Also, the complexity of the geometry make the determination of a physics based flow force model difficult. The model linearization changes depending on operating conditions which can be treated as uncertain. This study will focus on two causes of uncertainty: varying operating conditions and unknown flow force model.

In the uncertainty study, the supply pressure was allowed to vary from 20 MPa to 35 MPa. The system was linearized at steady state conditions with five evenly spaced supply pressures in the range indicated. The five frequency response plots are given in Figure 7. The model error can be thought of in terms of the maximum distance from the frequency response of the nominal model to any of the perturbed models. The errors are captured as a

multiplicative plant uncertainty as follows (Skogestad, 1996). A nominal plant is chosen as the plant linearized with a supply pressure of 20 MPa with the pilot poppet solenoid force input of 10 N. Plots are made of relative error in magnitude response between the nominal plant, *G,* and other linearizations (perturbed plants) at other supply pressures, G_p. an element of all possible perturbations Π. The error for each is given by $\frac{G_p(j\omega)-G(j\omega)}{G(j\omega)}$. The relative error in the plant model is the maximum error associated with all perturbation plants and is given as $w_i(\omega) \geq \max_{G_p \in \Pi} \left| \frac{G_p(j\omega)-G(j\omega)}{G(j\omega)} \right|$. The error, $w_i(\omega)$, is shown graphically in Figure 8 as a solid line which is the upper boundary for the model error for all cases of supply pressure.

It can be seen from Figure 8 that the multiplicative uncertainty due to varying supply pressure is greater than 60 percent at frequencies near 100 rad/sec. This means that the overall gain of the poppet valve changes greatly depending on the supply pressure. It would be important for the stability of the system for a control system designed using this valve to have robustness to this level of model error given in Figure 8. At low frequencies, it can be seen from both Figure 7 and Figure 8 that the model error is low at low frequencies. This low error at low frequencies is fortunate because a control system involving this valve would typically have performance requirements that are most stringent at the low frequencies.

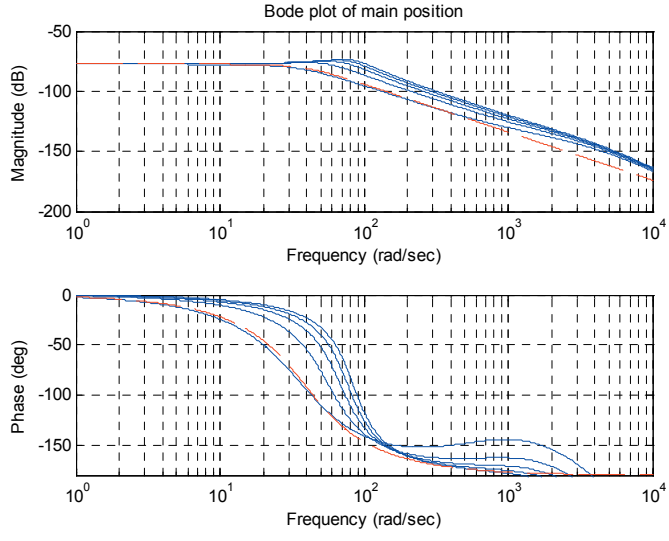

Figure 7 Family of Bode diagrams for linearizations of the model at various operating conditions – nominal plant response given as a dashed line

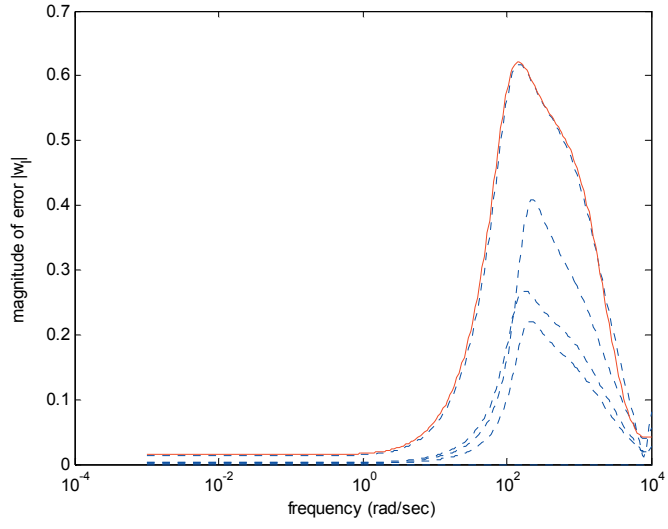

Figure 8 Uncertainty in the model linearization in the form of frequency response due to changing operating conditions – dashed lines are the perturbed plant errors, solid line is the uncertainty model

Next, the linear model is further analyzed to evaluate uncertainty due to the unknowns associated with modeling the flow forces. For this study, the jet angle, θ, was chosen as an unknown parameter which can be used to scale the flow forces up and down. A range of 50 to 70 degrees was chosen. Similar to Figure 8 calculations were carried out to determine a model bounding the uncertainty due to varying the jet angle. It can be seen in Figure 9 that the uncertainty (less than 8 percent) due to unknown flow forces is much less than that of varying supply pressure.

If all of the plant perturbations are combined for both supply pressure variations and flow force variations, one uncertainty model can be found. The combined uncertainty is given in Figure 10. Combining the uncertainties results in a maximum uncertainty of about 70 percent. Again, it can be seen that the characteristic of low uncertainty at low frequencies is preserved making it more likely than control system performance can be achieved at low frequencies.

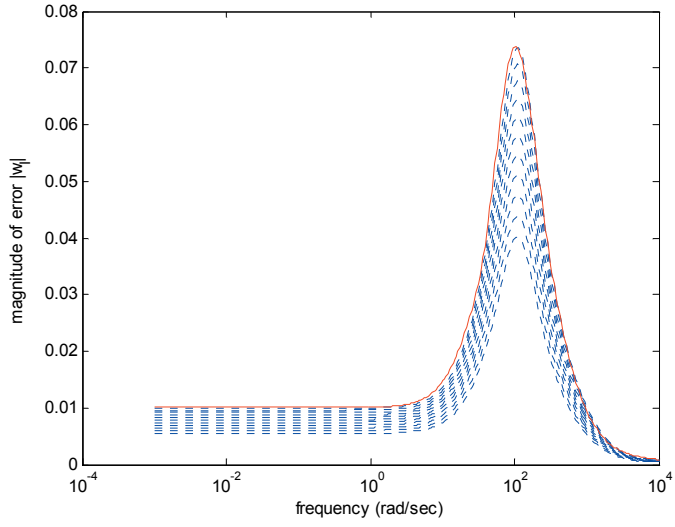

Figure 9 Uncertainty in the frequency response due to varying jet angle

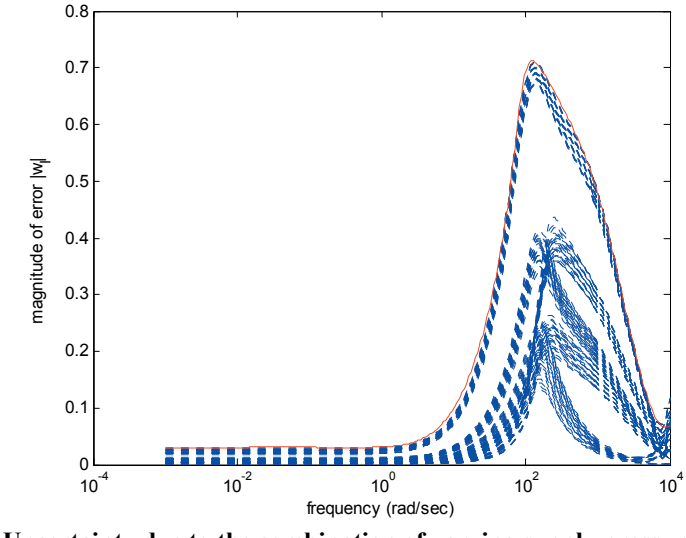

Figure 10 Uncertainty due to the combination of varying supply pressure and jet angle

5. PERFORMANCE

In this section, the open loop performance is analyzed based on test data. From the test results in Figure 6, second order underdamped system response specifications can be determined. The natural frequency and damping ratio were found to be 8.5 Hz and 0.6 respectively. Percent overshoot corresponding to the damping ratio is about 10%. The rise time and settling time were fund to be 0.034 seconds and 0.14 seconds respectively.

Figure 7 indicates that the natural frequency shifts as the supply pressure changes. In this case, the peak of the magnitude response increases in frequency as the pressure increases. This indicates the speed of response will become faster and faster as the pressure increases. As pressure increases the peak of the frequency response also increases, indicating that the damping ratio is reduced and percent overshoot is increased at higher pressures.

6. CONCLUSIONS

The model was found to agree with experimental results to a great degree. The model results presented in this work show that even linearizations represent the system well. The uncertainty of the system model was found over a range of frequencies. The model uncertainty due to the unknown flow forces was much less than model uncertainty due to varying supply pressure. Uncertainty in the model is as much as 70 percent at high frequencies. At low frequencies the model exhibits much less uncertainty than at higher frequencies. This will allow good control performance at low frequencies .

Performance of the valve is adequate for many applications in mobile hydraulic systems. The bandwidth is near 8.5 Hz which would eliminate the possibility of using the valve for industrial or servo hydraulic purposes. Feedback control may be employed to improve the speed of the valve response.

Future work includes further model verification and performance tests as well as the development of an observer based control system. Future work will include an analysis of the experimentally determine frequency responses for a range of different valve openings and other operating conditions to help understand the effects of nonlinearities on the system dynamics. Implementation of feedback control will be used to improve the performance of the valve response.

NOMENCLATURE

A_C	Area of main poppet exposed to control pressure	[m^2]
A_L	Area of main poppet exposed to load pressure	[m^2]
A_S	Area of main poppet exposed to supply pressure	[m^2]
a_1	Area of the orifice from supply to control volume	[m^2]
a_2	Area of the orifice between control and load volumes	[m^2]
a_3	Area of the orifice from supply to load volume	[m^2]
a_4	Area of the orifice from the load volume to tank	[m^2]
b_X	Damping coefficient for the pilot poppet	[N/m/s]
b_Y	Damping coefficient for the main poppet	[N/m/s]
C_d	Orifice discharge coefficient	
f	Actuator input force	[N]
h_2	Slope of orifice 1 area vs. position curve	[m^2/m]
h_2	Slope of orifice 2 area vs. position curve	[m^2/m]
h_3	Slope of orifice 3 area vs. position curve	[m^2/m]
k	Feedback spring coefficient	[N/m]
$kc_{(1-4)}$	Pressure flow coefficient for orifices 1 – 4	[m^3/s/Pa]

$kfc_{(1-3)}$	Pressure flow force coefficient for orifices 1 - 3	[N/Pa]
$kq_{(1-3)}$	Flow gain for orifices 1 – 3	[m^3/s/m]
M	Mass of the main poppet	[kg]
m	Mass of the pilot poppet	[kg]
$_O$	All *o* subscripts represent nominal conditions	
P_C	Control volume pressure	[Pa]
P_L	Load volume pressure	[Pa]
P_S	Fixed supply pressure	[Pa]
P_T	Fixed tank pressure	[Pa]
$Q_{(1-4)}$	Flow rate across orifices 1 - 4	[m^3/s]
θ	Jet angle for flow force	[rad]
V_C	Volume of the control volume above the main poppet	[m^3]
V_L	Load volume	[m^3]
x	Position of the pilot poppet referenced from closed position (positive is down in Fig. 1)	[m]
x_n	Pilot poppet position referenced from the nominal opening	[m]
y	Position of the main poppet referenced from closed position (positive is up in Fig. 1)	[m]
y_n	Main poppet position referenced from the nominal opening	[m]
β	Fluid bulk modulus	[Pa]
ρ	Fluid density	[kg/m^3]

REFERENCES

Aardema, J. A., 1997, "Pilot Valve for a Flow Amplifying Poppet Valve," U.S. Patent 5 645 263, Jul. 8, 1997.

Fales, R., 2006. "Stability and Performance Analysis of a Metering Poppet Valve." International Journal of Fluid Power. Vol. 7, No. 6, Pages 11-18.

Muller, M., and R. Fales. 2008. "Design and Analysis of a Two-Stage Poppet Valve For Flow Control." International Journal of Fluid Power. Vol. 9, No. 1, Pages 17-26. Mar. 2008.

Funk, J. E., 1964. "Poppet Valve Stability," Journal of Basic Engineering, June 1964, pp. 207-212

Hayashi, S., 1995. "Instability of Poppet Valve Circuit," JSME International Journal Series C, Vol. 38, No. (3), pp. 357-366

Li, P. Y., 2002, "Dynamic Redesign of a Flow Control Servovalve Using a Pressure Control Pilot," Journal of Dynamic Systems, Measurement, and Control, Vol. 124, pp 428-434.

Manring, N. D., 2005. Hydraulic Control Systems, Hoboken, NJ: John Wiley & Sons, pp. 224-228

Opdenbosch, P., Sadegh, N., Book, W., 2004. "Modeling and Control of an Electo-hydraulic Poppet Valve." ASME International Mechanical Engineering Congress and Exposition, Anaheim, CA.

Schexnayder, L. F., 1995. "Poppet Valve with Force Feedback Control," U.S. Patent 5 421 545, Jun. 6, 1995.

Skogestad, S., I. Postlethwaite. 1996. "Multivariable Feedback Control." Wiley. New York.

Yang, X., Stephenson, D. B., Paik, M. J., 2005. "Hydraulic Poppet Valve with Force Feedback," U.S. Patent 6 869 060, Mar. 22, 2005.

Zhang, R., Alleyne, A. G., Prasetiawan, E. A., 2002. "Performance Limitations of a Class of Two-Stage Electro-Hydraulic Flow Valves," International Journal of Fluid Power, Vol. 3, 2002, No. (1).

Session 11
Control III

Force control of a roller-screw electro-mechanical actuator for dynamic loading of aerospace actuators

Wissam KARAM, Jean-Charles MARE
Université de Toulouse; INSA, UPS;
LGMT (Laboratoire de Génie Mécanique de Toulouse)
135 Avenue de Rangueil, F-31077 Toulouse, France
wissam.karam@insa-toulouse.fr Jean-charles.mare@insa-toulouse.fr

ABSTRACT

The research work reported in this communication aims to provide key information on the performance of force controlled roller screw electromechanical actuators (EMA). The first part introduces the dominant parasitic effects (friction, rotor inertia and test-bench compliance) that alter both steady state and dynamic open loop performances. The second part proposes a practical methodology to identify the natural dynamics and to get both simulation and control models of the EMA without intrusive measurements. The third part presents the force control of the EMA that is performed through a RST controller, using a practical step-by-step approach. The controller design is finally validated through multiple experiments, covering the whole operation domain and proving the control robustness. As a conclusion, the force control is assessed for a typical requirement corresponding to the certification of a flight control actuator.

Keywords: Force control, Dynamic loading, EMA, Electromechanical actuator, Friction model

1. INTRODUCTION

Thanks to the development of high performance power electronics, motors and mechanical transmission, EMAs are now suitable for low power position control applications and cover different domains, consisting of high speed and/or high accuracy applications. Consequently, when price, easiness of control and environment are considered, it is often thought best to switch to electromechanical actuation that is more attractive for low power applications that require typically less than 5 kW. Opposite to that, it appears that there is a lack of experience feedback concerning the use of EMAs as dynamic force generators acting on moving loads.

Fluid Power and Motion Control 2008 Edited by Dr D N Johnston and Professor A R Plummer

The present work has been initiated by flight control actuators and test-bench suppliers. Until now, qualification, certification and endurance tests of such actuators are performed using servovalve controlled electro-hydraulic dynamic force generators [1]. In order to provide realistic order of magnitudes, Table 1 summarizes the common load generator requirements for low speed applications (e.g. aileron of single aisle commercial aircraft).

Low speed application *Representative of single aisle commercial aircraft*			
Stall force	50 kN	Nominal force	25 kN
No load speed	30 mm/s	Nominal speed	26 mm/s
Requirements	**# 1:** 2000 Cycles at 12 kN, full stroke, low frequency **# 2:** 6,5 Mcycles at 4 mm/s, ± 0.5 to ± 5 mm, 20 kN static + 2 kN/mm **# 3:** 2 Mcycles at 11 mm/s, ± 2 mm to ± 8 mm, 9 kN static + 0.5 kN/mm **# 4:** 3 Mcycles at 0.6 mm/s, 9 kN static + 0.5 kN/mm		

Table 1: Typical flight control dynamic test requirements

Unfortunately, until now, there were no reported real attempts to perform such tests with force controlled EMAs. This situation generates a real need to develop engineering methodologies enabling power sizing, performance prediction and control synthesis. Some proposals of EMA architectures, power sizing, modelling and guidelines for the test-bench design have already been presented in [2] and [3].

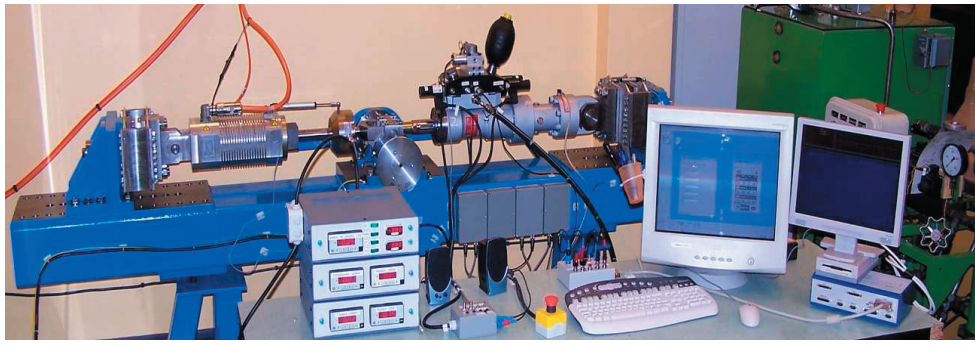

Figure 1: Global view of the test-bench, designed and implemented at LGMT / INSA

The test-bench, presented in Figure 1, that has been designed to assess the EMA prototype, is representative of development or production ones that are used by flight control actuator (FCA) suppliers and aircrafts makers. Furthermore, it reproduces the effective operation environment of the flight control actuator to be tested, according to:

- the equivalent load inertia effect m_e, with a mean value of 600 Kg,
- the equivalent anchorage and transmission stiffness k_e of 1.4 10^7 N/m.

This communication introduces the dominant parasitic effects and a control model of the EMA that enables the structure selection and the parameters tuning of the EMA force control. Moreover, intrusive measurements have been avoided to allow direct integration of off-the-shelf EMAs. In the present study, the EMA has been supplied by *SKF linearmotion* [4]. It combines an industrial, hollow shaft, brushless DC motor with its power drive and an inverted roller screw. The power drive controls the motor with respect to the user

electromagnetic torque demand. Therefore, the force controller to be designed in the present work must generate the torque setpoint as a function of the force demand and the sensors signals.

2. PARASITIC EFFECTS

Parasitic effects alter both steady state and dynamic open loop behaviour. Consequently, special attention must be paid to the dominant effects like friction, rotor inertia and test-bench compliance that set the efficiencies of the EMA and the natural dynamics of the system.

2.1 Friction

The EMA suppliers [4] usually declare that the efficiencies of such actuators are around 70% neglecting the presence of differences between the driving and the braking quadrants of operations. The quantification of the mechanical losses is of prime importance for the virtual modelling of the EMA and the force control synthesis. It was performed as described hereafter in such a way to operate the EMA in both driving and braking quadrants:

- the EMA is controlled at constant velocity (cyclically switching between positive and negative),
- a servo-controlled hydraulic actuator (SHA), simulating the aircraft actuator to be certified, is force controlled so as to create a constant external force F_{ext} on the rod of the EMA.

By varying the EMA rotor velocity ω_m between 2 and 105 rd/s (corresponding to a rod velocity of 1 and 50 mm/s) and the SHA force from 0 to 20 kN, most of the EMA operating domain was covered (200% nominal required speed, 80% nominal required force).

On the other hand, since the individual identification of the several friction forces acting inside the EMA (roller-screw, bearings, rod …) is difficult without any intrusion, they have been merged into an overall friction force F_{frict} at rod level. Thus, the EMA is modelled as a perfect power transformer associated with a lumped frictional dissipation. Consequently, at constant velocity, the motor torque T_m is the sum of the friction torque T_{frict} and the load driving torque T_{load}:

$$T_m = T_{frict} + T_{load} \quad \text{with} \quad T_{load} = F_{ext}\frac{l}{2\pi} \quad \text{and} \quad T_{frict} = F_{frict}\frac{l}{2\pi} \tag{1}$$

where:

- l [m] lead of the roller screw (3 mm in the present application)

In practice, non intrusive measurement of the motor torque is performed by using its estimation provided by the motor power drive. The EMA overall friction forces are plotted in Figure 2 as a function of the external force and the rotor velocity.

As it can be noticed, the friction force increases in function of F_{ext} and ω_m and changes significantly between the driving and the braking quadrants. This arises from the difference between the direct and the indirect efficiencies of the roller screw. To reproduce these complex dependencies, it is suggested to model the friction loss by eq. 2 [5]. According to the numerous experimental data, partly displayed on Figure 2, this representation model is proposed with reference to basic physical effects:

- the roller screw preload generates Coulomb and Stribeck friction (tending to a constant value as speed increases),
- the friction changes with the transmitted force that modifies directly the normal force applied to the surfaces in contact,
- the friction also depends on the operating quadrant as it results of the combination of normal force and relative nut-screw velocity.

It is emphasised that the proposed model includes the force transmitted to the load, this significant effect being generally ignored in the modelling of mechanical transmission devices.

$$F_{frict} = \left[F_c + F_s \; e^{(-|\omega_m|/\omega_s)} + |F_{ext}| \; (c + d \;\; \mathrm{sgn}(\omega_m F_{ext})) \right] \; \mathrm{sgn}(\omega_m) \qquad (2)$$

where:

- F_c [N] Coulomb friction force
- F_s [N] Stribeck friction force
- ω_s [rd/s] Reference speed for the Stribeck friction force
- c [-] Mean coefficient of external applied force
- d [-] Quadrant coefficient

The best fitting model (mean relative error less than 10 %) is found with F_c = 7590 N, F_s = -4702 N, ω_s = 70.55 rd/s, c = 0.218 and d = -0.13.

It is here interesting to notice that:

- the Stribeck friction force is negative. Further investigations show that, in this application, the Stribeck friction is representative of a regular viscous friction that diminishes with the speed increasing due to the lubricant temperature rise.
- this above phenomenon is also observed in the case of compact gearboxes [6].
- no positive Stribeck effect has been detected even if the minimum measured speed represents only 1 % of the required nominal range.

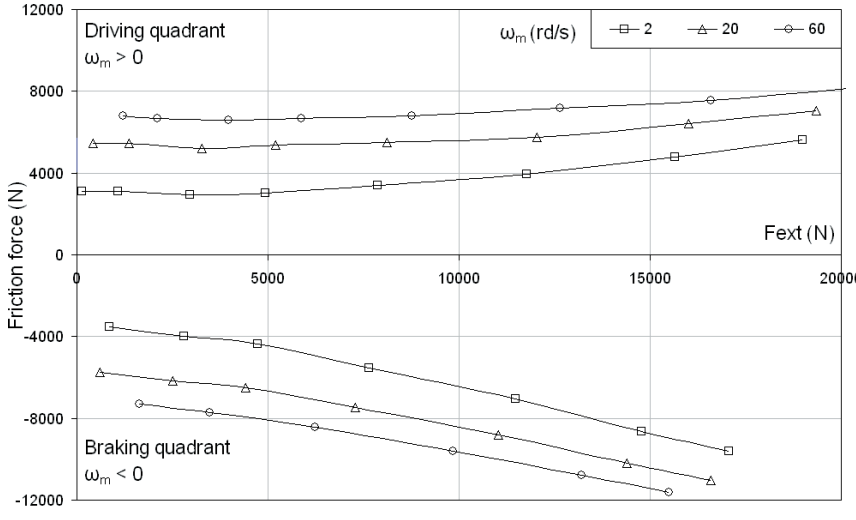

Figure 2: Friction force as a function of external applied force and rotor velocity ω_m

On the other hand, knowing the external force and the motor torque enables the computation of the EMA efficiency with respect to the motor operating quadrant defined by $\mathrm{sgn}(\omega_m T_m)$:

$$\eta_g = \left| T_{load} / T_m \right|^{\mathrm{sgn}(\omega_m T_m)} \tag{3}$$

Figure 3 shows the EMA efficiency with its three distinct parts: direct (power flows from motor to load), indirect (power flows from load to motor) and pseudo (both motor and load input power to the transmission).
As it can be noticed, the rotor velocity has a real influence on the efficiency that decreases nearly 10 points when the EMA speeds. Another interesting sighting is the poor performance of the EMA under small external forces (less than 5 kN), since the direct efficiency is lower than 50%. The EMA becoming irreversible leads to the introduction of the pseudo-efficiency. According to the identified friction model, this mainly results from the very high value of the Coulomb friction force.

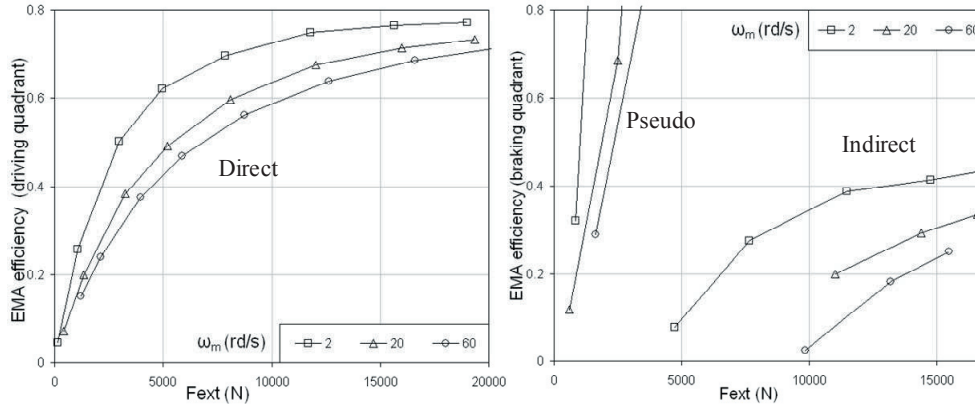

Figure 3: EMA efficiencies

2.2 Rotor inertia

A direct-drive compact EMA consists of a hollow shaft synchronous motor and an inlaid inverted roller screw [7]. Consequently, this architecture increases the rotor diameter leading to a high rotational inertia J_r. When combined with the high roller-screw reduction ratio, it reflects a huge equivalent mass at the rod level ($J_r 4\pi^2/l^2$). This results in significant shocks during the trespassing of backlash and causes severe damages to end-stops. In addition, considering the reflected mass is of prime importance to study the system natural frequencies.

An identification procedure with a customer view rather than an EMA designer approach was performed and presented in an earlier article [3]. By this mean the identified inertia takes into account all the extra rotating parts such as the rollers, the nut and the ball bearings. A numerical value of 0.00846 kgm^2 has been therefore obtained corresponding to a reflected mass m_e of 37000 kg.

2.2 Overall test-bench compliance and backlash

The test-bench structure has been designed, using the same rules as for hydraulic loading systems, to be 10 times stiffer than the anchorage device simulating the airframe

compliance. The multiple rod-clevis and eye-ball joints contribute in decreasing this stiffness, especially around the null transmitted force due to the presence of backlash.

Some experiments were performed to evaluate the importance of these parasitic effects. First, the SHA has been replaced by a rigid bar and the anchorage device has been disabled so that their compliances do not alter the tests being conducted. Second, the EMA is used to load the structure, producing a force F, while its rod relative displacement x_r is measured in order to get the test-bench deformation as seen by the EMA. The results are plotted on Figure 4.

As Figure 4 reveals, the test-bench deformation is quite linear and presents a large amount of backlash (0.36 mm) around null force. On the other hand, even though the stiffness, felt by each of the two actuators, is the double of the overall stiffness k_b ($2k_b$= 5.4 10^7 N/m), its value is well below the structure stiffness (15 10^7 N/m). This highlights the importance of considering the links compliances' during the early stages of the test-bench design.

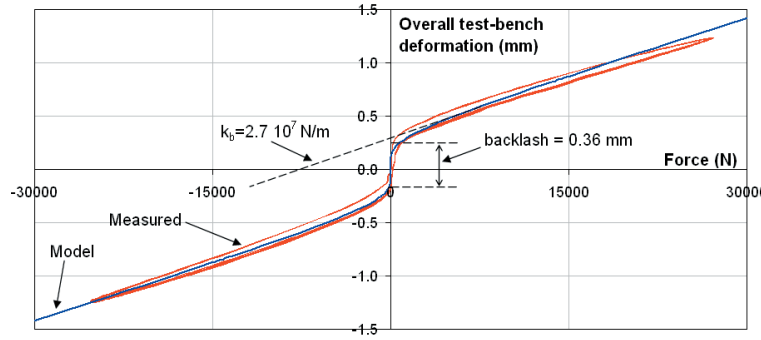

Figure 4: Overall test-bench deformation as seen from the EMA

As for now, a simple mathematical model is proposed in order to reproduce the real test-bench behaviour in the virtual prototype:

$$F = (k_0 - k_1 \tanh\frac{x_0}{|x_r|})x_r \tag{4}$$

The best fitting model is found with: x_0 = 0.36 10^{-3} m, k_0 = 2.804 10^7 N/m and k_1 = 2.798 10^7 N/m.

3. EMA MODELLING

EMA accurate modelling is a pre-requisite for model based design of the EMA force control. So, a close attention has been paid to this part that starts by the elaboration and the validation of a virtual prototype then shows a practical methodology to identify the control model.

3.1 Virtual prototype

Several key information (inertia, stiffness, mechanical losses) were gathered during the study of the parasitic effects in the precedent paragraph. The technical data concerning the electrical part (current loop dynamics and equivalent DC motor parameters) have been

provided by the EMA suppliers [4]. By combining these informations, a virtual prototype of the EMA and the test-bench has been developed within the AMESim environment [8].

The current loop has been tuned in such a way that it gives the same second order dynamics (600 Hz, 0.6 damping ratio) as the ones specified by the supplier. The voltage saturation value is related to the power-dive bus voltage. The synchronous motor is replaced by an equivalent DC motor. In addition, data acquisition filters are placed to simulate the measurement devices and processes (signal conditioning, filtering and sampling).

On the mechanical side, the overall rotating inertia and the EMA stiffness model were identified in a precedent work [3]. As for the mechanical losses, the model presented in eq. 2 has been used in combination with frictionless movement transformation. The test-bench stiffness is divided into two identical parts acting in series, with respect to the model of eq. 4, each placed on an actuator side.

It is important to add that, since this communication focuses on the EMA modelling, the SHA and load models will not be detailed.

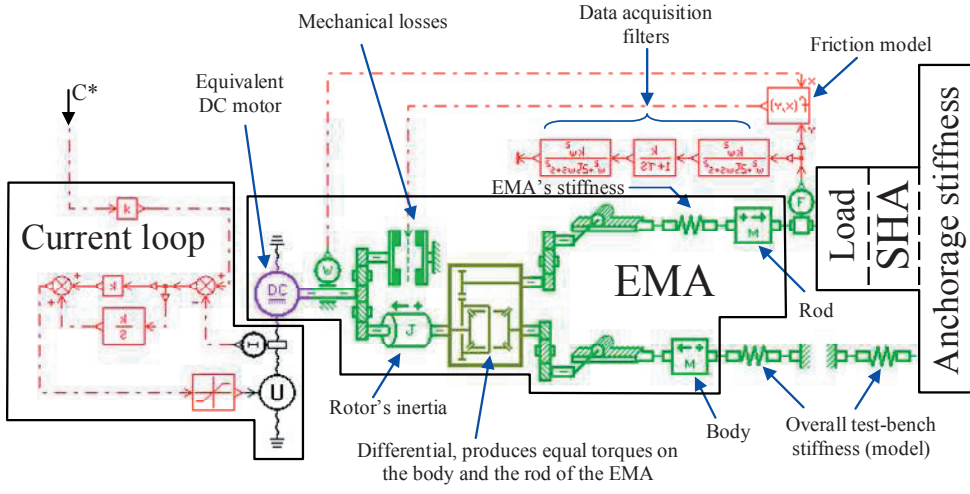

Figure 5: Virtual model of the EMA in the AMESim environment

In order to validate the above EMA virtual model, several experiments were conducted and the acquired data were compared with the simulated responses. At the test-bench level, the EMA was run in open loop by fixing the electromagnetic torque set-point and measuring the external force. The load, SHA and anchorage stiffness were omitted and replaced by a rigid bar so as to avoid introducing unknown dynamics into the loop.

Two types of torque signals were used so that the tests cover as much as possible the test-bench operational domain. A pulse signal excites the natural dynamics that can be identified by studying the force produced by the EMA. A sine signal enables identifying the breakaway force needed to overcome the static friction and enables detecting the stick-slip phenomenon usually present at low velocity.

Figure 6 presents a comparison between the measured and simulated responses of the EMA. First of all, it points out the backlash at null force and the slight phase lead (3 ms) of the simulated response. In addition, the pulse diagrams show the influence of the side to

side backlash trespassing on the forces overshoot: within the backlash, the rotor accelerates and stores a great amount of kinetic energy. Figure 6 also displays the poor reversibility of the EMA when it has to balance high external forces.

A good agreement is found between the simulated and measured pulse responses, especially if it is considered that sticking position is very sensitive to friction and control signal. As to the sine torque signal, the curves shapes in the driving quadrant are very similar while their slopes are a bit different in the braking quadrant.

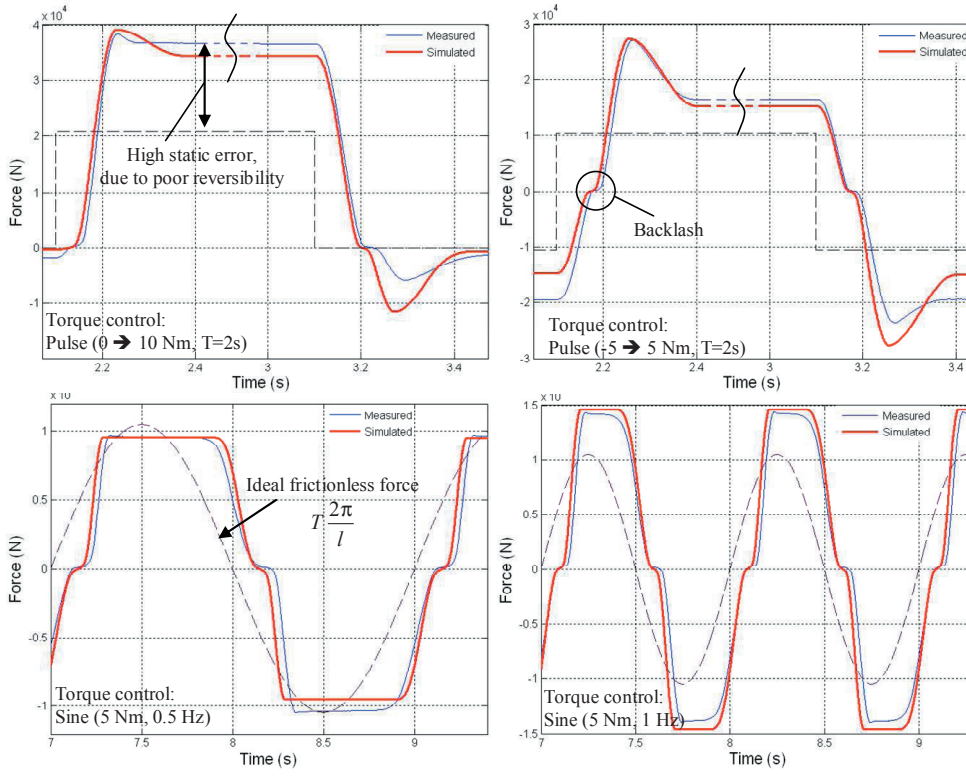

Figure 6: Comparison between the measured and the simulated responses of the EMA

Nevertheless, even with the presence of these several non-linearities, the virtual EMA model showed a good representation of the real functioning. This remark is particularly important as for these tests the EMA was operated in open loop and its response does not benefit from the loop linearising effect.

3.2 Natural dynamics

The natural dynamics of a system provides good means to study its bandwidth and performance limits. The theoretical natural frequency $f_{n\text{-}th}$ of the system (EMA + test-bench, anchorage device disabled), computed using eq. 5 with the measured rotor inertia and the test-bench overall stiffness, is 4.14 Hz.

$$f_{n\text{-}th} = \frac{1}{2\pi}\sqrt{\frac{k_b}{J_r\left(2\pi/l\right)^2}} \tag{5}$$

In the present case, the effective natural frequency could be highly affected by complex friction at nut-screw level, therefore it must be measured in order to validate or correct the calculated one. The oscillations of the step response usually enable the computation of the natural frequency and the damping. They are nearly inexistent, for the EMA under study, because of its poor reversibility. This means that it is difficult to obtain experimentally the natural frequency with open loop control. The proposed alternative solution consists in measuring the closed loop natural frequency ω_n' and damping ξ' with a proportional control P (loop gain $P2\pi/l$). In this way, the closed loop operation reduces the damping which results in more visible oscillations. The open loop characteristics (frequency ω_n and damping ξ) are then deduced analytically using eq. 6.

$$\xi' = \frac{\xi}{\sqrt{1+P2\pi/l}} \quad \text{and} \quad \omega_n' = \omega_n\sqrt{1+P2\pi/l} \tag{6}$$

Figure 7 presents the closed loop step responses of the EMA for different force set-points and proportional gains. As it can be noticed, the selected set-points avoid any backlash trespassing so that the system remains in the high and constant stiffness area. In this condition, the closed loop natural frequencies are independent from the steps magnitude and vary only with the proportional gain. The overshoots are quite representative of a second order system.

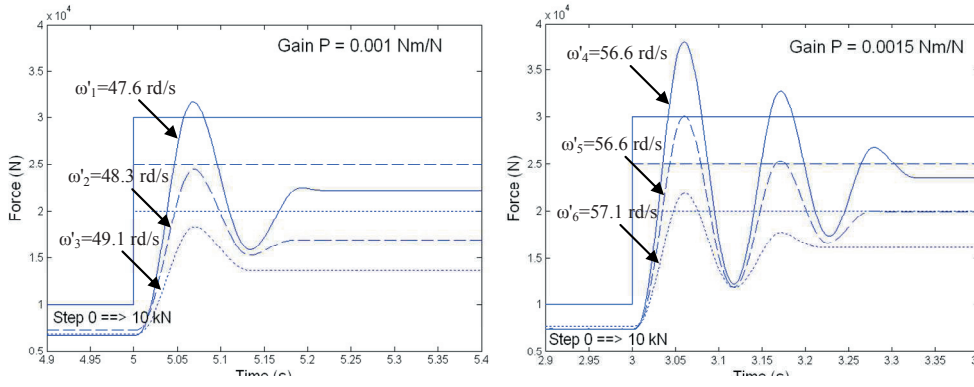

Figure 7: Step responses of the EMA for different force set-points and proportional gains

Measuring the first overshoot and pseudo-period allows to identify the closed loop frequency and damping and then deduce the open loop ones. The measured natural frequencies are therefore 4.16 Hz from the tests performed with a gain P=0.001 Nm/N and 4.33 Hz from the tests performed with a gain P=0.005 Nm/N. These two frequencies are quite close and match with the estimated theoretical natural frequency (4.14 Hz).

3.3 Simplified control model

In the proposed approach, the control synthesis starts from the linear equivalent model of the EMA. Thus the process to be controlled is a combination of a second order system (dynamics of the motor power drive), the roller-screw gain of $2\pi/l$ and parasitic effects: acquisition filters, EMA friction and motor inertia. The simplified control model of the EMA is consequently presented in Figure 8.

Nevertheless, it must be kept in mind that this model is not representative of the EMA behaviour when it operates around the null effort (near the backlash zone).

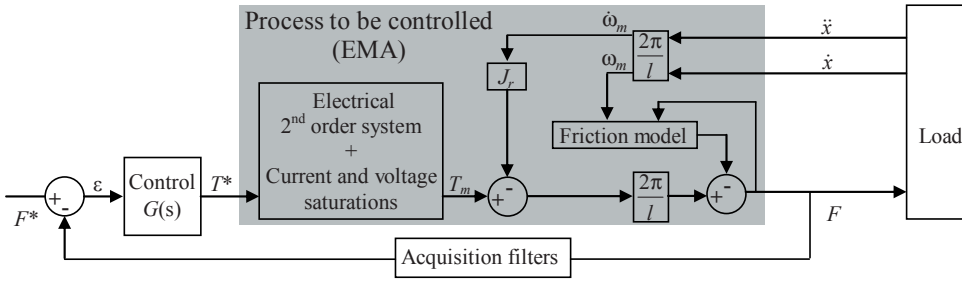

Figure 8: Simplified control model of the EMA

4. FORCE CONTROL

The development of the force control debuted with the study of the blocked-load case. Even if this mode of operation is not included in the requirements, it enables to create a performance reference by getting rid of the load speed influence.

As for the normal-load condition, a conventional RST controller has been selected for the EMA force control. The succeeding paragraph will detail the controller design and then present the more relevant validation tests.

4.1 RST controller

The RST controller, presented in Figure 9, combines three actions. The [R] feedback correction draws from the sensors' signals (e.g.: F) or the partial state variables vector $\boldsymbol{X}$. It has a linearizing effect.

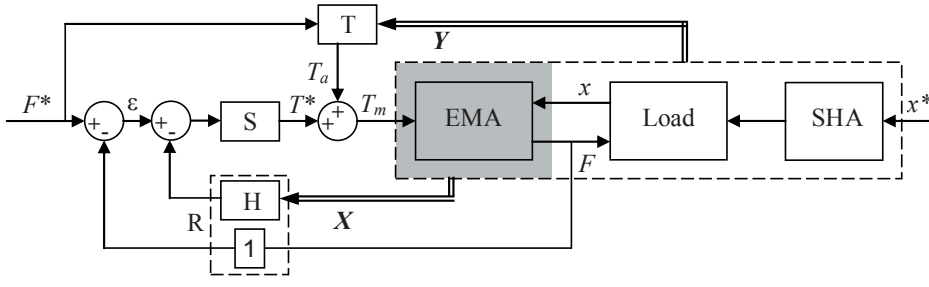

Figure 9: Simplified scheme of the RST controller

The [S] correction, placed in series, is simple to install since it does not need any additional sensor or state observer. Finally, the [T] feed-forward correction anticipates the effect of the functional or perturbation inputs. The main strength of the anticipation is its position outside of the control loop which prevents harming the system stability.

- **Force derivative feedback**

The study of the blocked-load case showed that the use of a proportional gain P with a force derivative feedback D_f offers a satisfactory solution. Thus the measured force and its first derivative compose the [R] correction. According to the authors' experience, the use of an integral action to cancel static error is avoided as far as possible because it generates

non-linear limit cycles in the presence of strong non linearities like dry friction. Therefore, the required static accuracy is ensured by mean of the feed-forward action.

- **Feed-forward**

The validation of the EMA virtual model, presented in 3.1 proves the predictive character of the friction model, which can be used for anticipation [9] [10]. Moreover, the torque required to accelerate the rotor also acts as a perturbation on the force control as explained by the next two equations (eq. 7 and eq. 8):

$$(T_m - J_r\dot{\omega}_m)\frac{2\pi}{l} = F + F_{frict} \tag{7}$$

$$\varepsilon = F^* - F, \quad T_m = T^* + T_a \quad \text{and} \quad T^* = S(\varepsilon - HX) \tag{8}$$

The feed-forward action is calculated at torque demand level (anticipation torque T_a) so as to cancel the error ε:

$$T_a = F^*\frac{l}{2\pi} + J_r\dot{\omega}_m + F_{frict}\frac{l}{2\pi} + SHX \tag{9}$$

Since the force control is of class zero in open loop (no integration), the static error generated by the force demand is compensated by the first term of eq.9. On its side, the second term anticipates the rotor inertia effect. As the EMA is very stiff, it can be assumed that the rotor angle is proportional to the load position, which acceleration can be measured thanks to an accelerometer. If not available, it can be replaced by double derivation that is generally noisy or phased by the unavoidable filtering. In the present case, it has been decided to estimate the load acceleration $\hat{\dot{\omega}}_m$ from the SHA dynamic model. The third term of eq.9 is in charge of compensating the friction force. It is estimated using eq. 2 that involves the output force and the load velocity. The velocity is estimated in the same way as the acceleration while the output force is supposed to be equal to the demanded force F^*. Conisdering that the feed-forward action should anticipate without altering the control loop, the last right-hand side term is not considered. The anticipation torque then becomes:

$$T_a = (F^* + \hat{F}_{frict})\frac{l}{2\pi} + J_r\hat{\dot{\omega}} \tag{10}$$

- **Notch filter**

The vibratory analysis of the whole test-bench revealed the presence of two poorly damped dynamics:

- the first mode (4.14 Hz) results from the oscillation of the rotor equivalent mass on test-bench overall stiffness,
- the second mode (33 Hz) results from the oscillation of the load equivalent mass (600 Kg) on the test-bench overall stiffness.

As the first mode is within the EMA bandwidth (5.3 Hz), it can be actively damped by the force derivative feedback. On the contrary, the EMA does not have the dynamic capacity to reject the 33 Hz force perturbation. An interesting solution consists on using a notch filter to avoid exciting this mode by the controller. As a result, the notch filter, when combined with the proportional gain, constitutes the [S] correction. Finally, the full scheme of the EMA RST force control is presented in Figure 10.

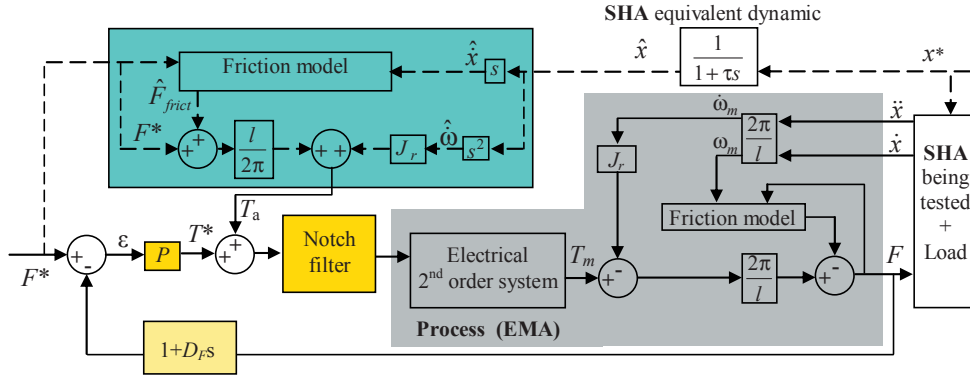

Figure 10: Full scheme of the EMA RST force control

4.2 Controller validation

The analytically studied RST controller requires validation tests in order to be firmly adopted. Thus, an experimental process has been designed to point out the usefulness and the efficiency of each component of the controller.

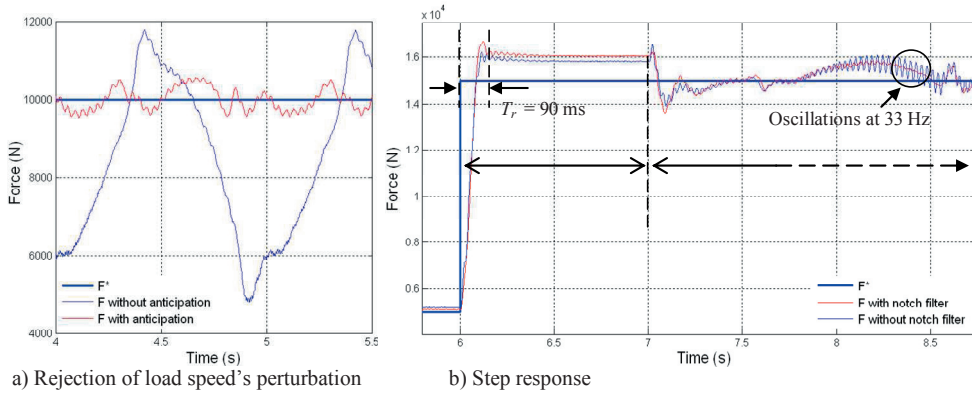

a) Rejection of load speed's perturbation
- 10 kN constant force demand
- 5 mm @ 1 Hz sine load position demand

b) Step response
- 10 kN step force demand starting at 6 s from 5 kN
- 10 mm @ 0.5 Hz sine load position demand starting at 7 s

Figure 11: Usefulness of the anticipation and the notch filter

The first part of Figure 11 (Figure 11-a) shows the effect of the anticipation which is based on the force demand F^* and load position setpoint x^*. This feed-forward enabled reducing the static error, resulting from the load motion, from nearly 5 kN to less than 500 N (corresponding to 2% of the required nominal force) in both driving and braking quadrants. The second part of Figure 11 (Figure 11-b) displays, in its first half, the step response in the high stiffness area (far from the backlash zone). The PD_F loop enables getting a 95 % time response T_r of 90 ms which corresponds to a bandwidth of 5.3 Hz at -3dB (first order equivalent model). In addition, the second half of Figure 11-b validates the notch filter that eliminates efficiently the 33 Hz oscillations that occur when a speed perturbation is generated by the SHA.

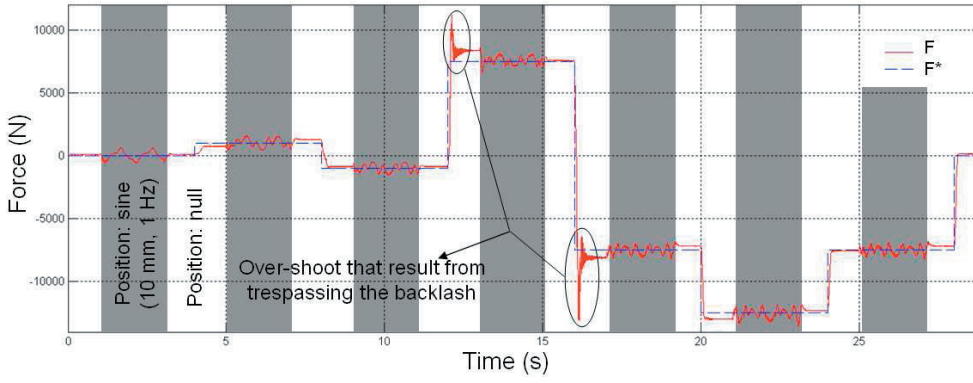

Figure 12: Robustness of the control method

The test shown on Figure 12 presents a sweep of the EMA functioning domain so as to prove the robustness of the proposed controller. Alternated null and sine position command signals overlay several steps and constant forces ones. The aim of this complex profile is to study the pursuit of the force demand and the elimination of the load velocity perturbation in practically every part of the operating domain.

A satisfactory performance is observed in and around the backlash area as well as in the high stiffness zone. On the other hand, the overshoots that occur during the high speed backlash trespassing do not exceed 30 % of the step signals and are quickly damped.

4.3 Requirements fulfilment

A fair example of the EMA response to a mid range force demand is displayed on Figure 13. The test case corresponds to requirement #3 in which the load is driven in sine motion so as to achieve a maximum speed of 11 mm/s. The 9 kN + 0.5 kN/mm force setpoint is function of the load position in order to create a spring effect that is representative of the aerodynamic load applied to the flight control surface. In the left side experiment, the SHA forces a sine load displacement with a magnitude of 8 mm @ 0.22 Hz.

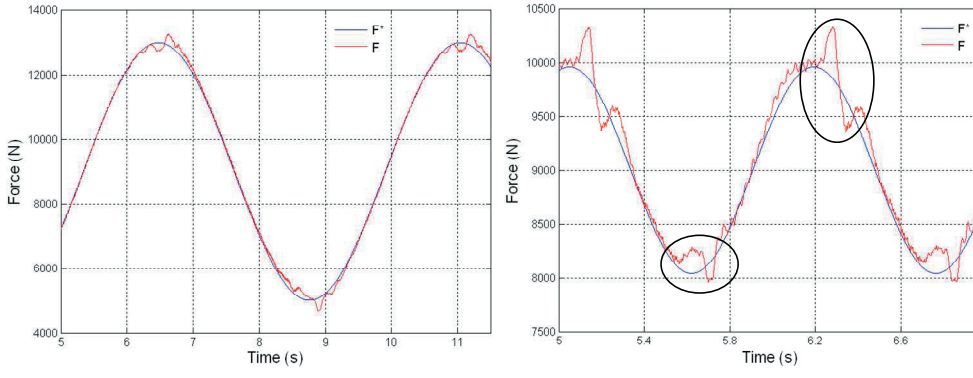

Figure 13: Test of requirement #3 using the two extreme amplitudes

A good correlation is found between the measured and the demanded forces. In the right side experiment the load is moved with a magnitude of 2 mm @ 0.88 Hz. The perturbation generated by the load displacement on the force control is clearly observed, especially at

the load speed reversals. The force scale makes this fault less visible on the first graph. Even if in this test the dynamic error reaches 350 N (17.5 % of the needed force amplitude), it only corresponds to 1.4 % of the rated force of the SHA actuator to be tested.

5. CONCLUSION

The roller-screw EMA has been studied and force controlled in order to be used later on as a dynamic load generator. The dominant parasitic effects, not encountered in electro-hydraulic loading systems, have been identified, modelled and compensated by an appropriate RST controller design. The required force control bandwidth has been achieved by using a proportional and force derivative feedback. The significant friction of the roller-screw has been modelled as a function of the transmitted force and the load velocity including Coulomb, Stribeck, force-dependant and quadrant-dependant effects. This model has been used successfully in a feed-forward force compensation that was combined with the anticipation of the inertial torque required by the rotor during the load acceleration. A serial notch filter has been implemented to avoid any excitation of the high frequency dynamics resulting from the load inertia and the test-bench compliance. In the particular case of EMA based force control, the present study has clearly pointed out that the closed loop performance is significantly driven by the amount of reflected inertia and the linkages backlash. Opposite to electro-hydraulic force control, these effects must be considered as key design drivers for the design of test bench involving EMA for dynamic loading.

REFERENCES

[1] **Maré J-C.**, Dynamic loading systems for ground testing of high speed aerospace actuators, *Aircraft engineering and aerospace technology (international journal)*, Vol. 78 No 4, 2006, Emerald ltd

[2] **Karam W., Maré J-C.**, Comparison of EMA and HA performance for dynamic load simulators, *Power Transmission and Motion Control (PTMC 2006)*, pp 211-224, Hadleys Ltd, 2006

[3] **Karam W., Maré J-C.**, Modelling and measure of the compliance and friction losses of screwjack electromechanical actuators, *Power Transmission and Motion Control (PTMC 2007)*, pp 145-157, Hadleys Ltd, 2007

[4] SKF, http://www.linearmotion.skf.com, contact: pascal.hude@skf.com

[5] **Karam W.,** Investigation into the electromechanical actuator when used for high performance force control, *PhD thesis, INSA Toulouse, 2007*

[6] **J.-P. Hauschild, G. R. Heppler and J. J. McPhee**, Friction Compensation of Harmonic Drive Actuators

[7] Exlar, http://exlar.com/TI_ref_catalog_oview.html (GSX series)

[8] AMESim, *Advanced Modelling Environment for Simulation*, Imagine SA, Roanne, France

[9] **Armstrong-Lehouvry B.**, Control of machines with friction, *Kluwer Academic Publishers*, Dordrecht, 1991, ISBN 0-7923-9133-060

[10] **Olson H., Astrom K.J., Canudas de Wit C.,** Friction Models and Friction Compensation, November 28, 1997, www.control.lth.se/~kja/friction.pdf

Controlling a Conventional LS-pump based on Electrically Measured LS-pressure

Torben O. Andersen
Professor, Ph.D.
Energy Technology
Aalborg University
DK-9220 Aalborg East
+45 9940 9269
toa@iet.aau.dk

Henrik C. Pedersen
Ass. Professor, Ph.D.
Energy Technology
Aalborg University
DK-9220 Aalborg East
+45 9940 9275
hcp@iet.aau.dk

Michael R. Hansen
Asc. Professor, Ph.D.
Mechanical Engineering
Aalborg University
DK-9220 Aalborg East
+45 9940 9321
mrh@ime.aau.dk

ABSTRACT

As a result of the increasing use of sensors in mobile hydraulic equipment, the need for hydraulic pilot lines is decreasing, being replaced by electrical wiring and electrically controllable components. For controlling some of the existing hydraulic components there are, however, still a need for being able to generate a hydraulic pilot pressure. In this paper controlling a hydraulic variable pump is considered. The LS-pressure is measured electrically and the hydraulic pilot pressure is generated using a small spool valve. From a control point of view there are two approaches for controlling this system, by either generating a copy of the LS-pressure, the LS-pressure being the output, or letting the output be the pump pressure. The focus of the current paper is on the controller design based on the first approach. Specifically a controlled leakage flow is used to avoid the need for a switching control structure.

1 INTRODUCTION

The development of hydraulic systems shows a clear tendency towards electrically controlled components, as pointed out by e.g. [1]. This also means that the need for hydraulic pilot lines is decreasing, as load pressures are starting to be measured and distributed electronically instead of hydraulically. However, in the transition phase between traditionally hydraulically controlled components and fully electrically controlled systems, some components may still need a hydraulic LS pressure to operate, and there is a need for being able to generate this hydraulic LS pressure based on an electrical reference. One such example is e.g. where a hydraulic LS-pump is connected to an otherwise electronically controlled system, where there is no hydraulic LS-pressure available. This problem is the objective of the current paper, where focus is on generating a hydraulic LS-pressure for a conventional variable displacement pump.

To the knowledge of the authors, no other such solution has been made; although the problem has some resemblance to controlling the pump pressure in an electronic load sensing

Fluid Power and Motion Control 2008 Edited by Dr D N Johnston and Professor A R Plummer

system, which has been the subject of several studies, see e.g. [2, 3, 4, 5, 6, 7]. Common for these studies are that they have used a sufficiently fast servo valve/proportional valve directly controlling the flow to the displacement piston of the pump. Hence removing the original hydro-mechanical LS-regulator in the pump and in effect replacing the dynamics of the hydro-mechanical LS-regulator and pilot line. The idea of using an artificially generated LS-pressure has also indirectly been presented by [8] as part of a pump regulator, where the LS-pressure was generated based on the pump pressure using a series connection consisting of a fixed orifice and electrically controlled relief valve, hereby obtaining the effect of a pressure divider. Apart from the idea of generating the LS-pressure based on the pump pressure, the two solutions do however pose different problems, not only due to different topologies and control problems, but also as the presented solution is intended to be mounted a distance away from the pump and should be applicable in combination with a large variation of pumps.

The paper first presents the considered system and an experimentally verified model. For stability analysis a linearized model is derived and sensitivity of the system to varying operating conditions discussed. Based on the results of this analysis the controller design is presented and robustness evaluated. Finally, experimental results are presented, and the performance of the electro-hydraulic pressure regulator is compared to that of the hydraulic reference system.

2 SYSTEM MODELLING

The system considered consists of the pump, spool valve, hoses and the load system, as shown in figure 1. From the figure it is seen that the set-up may also be used as a classical LS-system (parallel circuit), making it possible to test the two systems individually.

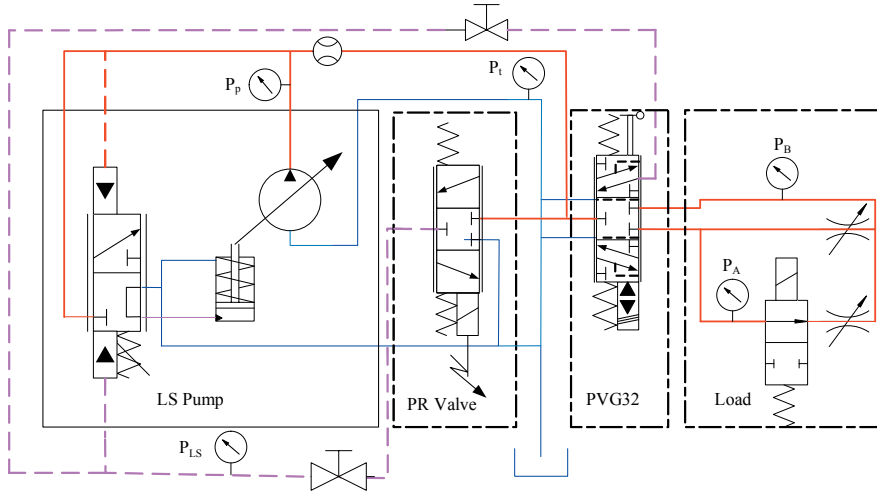

Figure 1: Diagram of the experimental set-up with indication of the various components.

The system consists of a $57[cm^3]$ Sauer-Danfoss series 45 H-frame pump, a load system consisting of a PVG 32 pressure compensated proportional valve, two variable orifices connected

in parallel and an on-off valve. The spool valve (Pressure Regulating-valve) used is a 3/3-NC under lap valve. The PR-valve is actuated with a voice coil connected to a DC/DC inverter, by which the voice coil may be current controlled.

2.1 Pressure regulating valve

The purpose of PR-valve is to control the flow to/from the pilot line, hereby generating the hydraulic LS-pressure. The reference is a measured electrical LS pressure signal. A schematic drawing of the valve is shown in figure 2 with indication of the used notation.

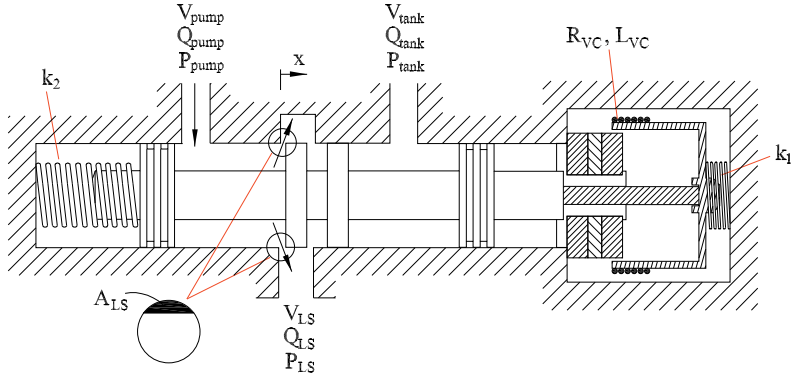

Figure 2: Model view of the spool valve with used notation.

The flow through the valve is described by the orifice equation and a laminar term describing the flow from a notch in the spool

$$Q_{LS} = \begin{cases} C_d \cdot A_{LS}(x) \cdot \sqrt{\frac{2}{\rho} \cdot (P_P - P_{LS})} - K_{lam} \cdot P_{LS} & , \quad 0 \leq x < x_l \\ C_d \cdot A_{LS}(x) \cdot \sqrt{\frac{2}{\rho} \cdot (P_P - P_{LS})} & , \quad x \geq x_l \\ -C_d \cdot A_{LS}(x) \cdot \sqrt{\frac{2}{\rho} \cdot (P_{LS} - P_T)} & , \quad x < 0 \end{cases} \tag{1}$$

Where x_l is the length of a notch made in the spool, and K_{lam} is a laminar flow coefficient. To determine the spool dynamics and hence position, the free-body diagram shown in figure 3 is considered.

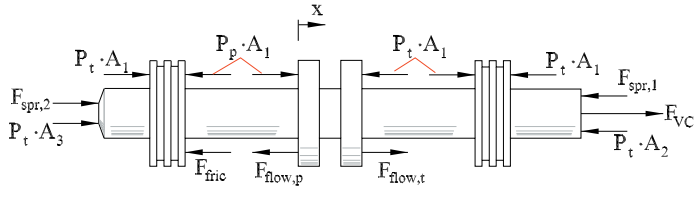

Figure 3: Forces acting on the spool.

From the figure it may be seen that the spool is pressure balanced. The force equilibrium for the spool may therefore be written as:

$$m_{spool} \cdot \ddot{x} = F_{VC} + F_{spr} - F_{flow,p} + F_{flow,t} - F_{fric} \tag{2}$$

where m_{spool} is the movable mass (including voice coil etc.). $F_{spr} = x_{spool} \cdot (k_1 - k_2) + F_{spr,0}$ is the spring force, $F_{flow,p}$ and $F_{flow,t}$ are the flow forces for the pump side and tank side valve openings respectively and F_{fric} is the friction force. F_{VC} is the voice coil force, which is proportional to the current in the voice coil, which again may be found from the voltage equation, i.e.

$$u_{VC} = R_{VC} i_{VC} + L_{VC} \frac{di}{dt} + K_m \dot{x} \tag{3}$$

$$F_{VC} = K_m \cdot i_{VC} \tag{4}$$

where $K_m \dot{x}$ is the back emf and K_m is the voice coil force constant.

The friction force is modelled as a combination of stiction, Coulomb and viscous friction as

$$F_{fric} = \begin{cases} F_{VC} + F_{spr} - F_{flow,p} + F_{flow,t} & , \dot{x} = 0 \wedge F_{VC} + F_{spr} - F_{flow,p} + F_{flow,t} < F_s \\ F_c \cdot sign(\dot{x}) + B \cdot \dot{x} & , |\dot{x}| > 0 \end{cases} \tag{5}$$

Where F_c is the Coulomb friction, F_s the stiction force and B the viscous friction coefficient. Finally, the flow forces are modelled as purely stationary flow forces, i.e. for the pump side

$$F_{flow,p} = 2 \cdot C_d \cdot A_{LS}(s) \cdot (P_P - P_{LS}) \cdot cos(\theta) \tag{6}$$

and similarly for the tank side opening.

2.2 Pump, Volumes and Load Models

The other components in the system considered include the pump, volumes (hoses) and the load model. Considering first the different volumes in the system, these are generally described using the continuity equation, which for the LS-hose volume yields:

$$\frac{V_{LS}}{\beta} \frac{dp}{dt} + \frac{dV_{LS}}{dt} = Q_{in} - Q_{out} \tag{7}$$

With Q_{in} and Q_{out} being the flows in and out of the volume and β the effective oil bulk modulus. The latter is modelled as being pressure dependent as described in e.g. [9]. The load consists of the two variable orifices, which are simply described by the orifice equation, whereas the on-off valve is simply modelled as a switch. The load is here only used to generate a load pressure for a given pump flow. As described earlier the pump is a Sauer-Danfoss series 45 H-frame pump. The model is quite comprehensive and is presented in [10].

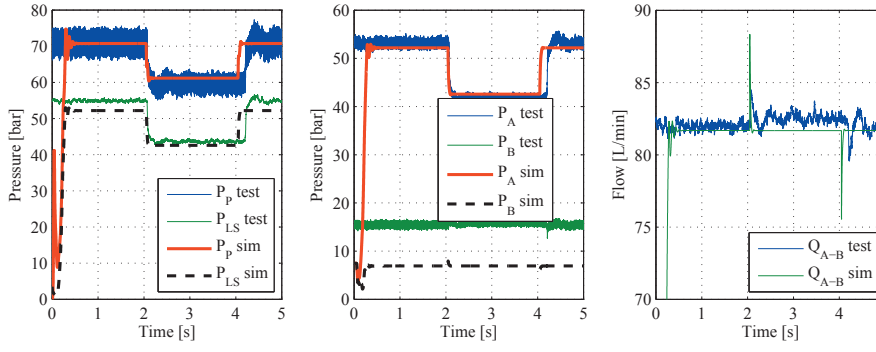

Figure 4: System response when applying load pressure steps.

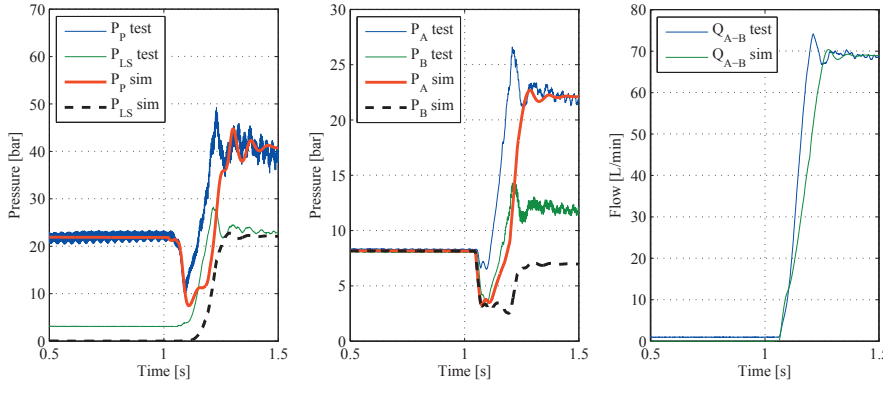

Figure 5: Step at the flow from 0 to 70 $[L/min]$ and constant load.

2.3 Verification of Model

To verify the non-linear model and obtain performance data for the benchmark system, results from the simulation model are compared to experimental data for three different operating situations. The results of these tests are shown in figures 4- 6 on the following page below.

From the different results it may be seen that there generally is a good agreement between the measured and the simulated data. There are minor deviations, which are due to simplifications in the modelling, but the model shows the correct tendencies capturing the dominant dynamics. The model is therefore considered valid as basis for the controller design and testing.

3 LINEARISED MODEL

Based on the above described non-linear model a linearized model may be derived. This is done under the approximation that bulk modulus, discharge angle and discharge coefficients are constant. Linearising and Laplace transforming then yield the following system

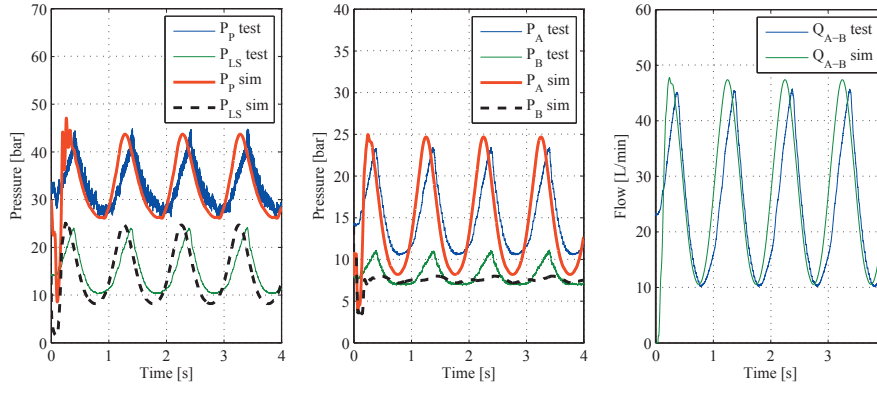

Figure 6: Sinusoidal input with frequency of 1 $[Hz]$.

equations:

$$m_{spool} \cdot s^2 \cdot x = K_f \cdot i_{VC} - K_{spr,fq} \cdot x + K_{fqp_{pt}} \cdot P_{LS} + K_{fqp_p} \cdot P_p - B \cdot s \cdot x \quad (8)$$

$$q_{LS} = K_{q_{pt}} \cdot x - (K_{qp_{pt}} + K_{lam}) \cdot p_{LS} + K_{qp_p} \cdot p_p \quad (9)$$

$$p_{LS} = \frac{\beta}{s \cdot V_{LS}} \cdot q_{LS} \quad (10)$$

$$u_{VC} = R_{VC} \cdot i_{VC} + L_{VC} \cdot s \cdot i_{VC} + K_{g,VC} \cdot s \cdot x \quad (11)$$

The first expression here describe the linearised spool force equilibrium, the second the flow to the LS-hose, the third the pressure build up in the LS-hose and the fourth the voice coil dynamics. Combining these equations in block diagram form, the block diagram shown in figure 7 may be obtained.

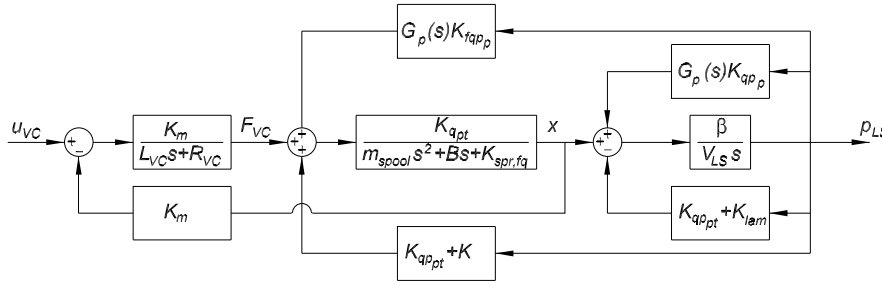

Figure 7: Block diagram relating valve voltage input $(u_{p,LS})$ to pressure in the LS-line (p_{LS}).

In the block diagram the term, $G_p(s)$, represents the pump and pump volume dynamics. As a rough approximation this is modelled by a first order filter:

$$G_p(s) = \frac{p_p}{p_{LS}} = \frac{1}{\tau_p \cdot s + 1} \quad (12)$$

To simplify the following analysis, the system may be considered in two different situations, where in the first the valve opens for connection between pump volume and the LS-hose (pump side connection), whereas in the second situation the valve opens to tank. As the system is current controlled the analysis is further simplified. For the case where the valve opens to the pump side the transfer function for the system may then be found to be

$$G_{LS,p}(s) = \frac{p_{LS}}{i_{VC}} = \frac{\beta K_{q,pt} K_f \left(\tau_p s + 1\right)}{G_d(s)\left(m_{spool}s^2 + Bs + K_{spr,fq}\right) - \left(\tau_p s + 1\right)\beta K_{qp,t} K_{fqp,pt} - \beta K_{q,pt} k_{fqp,p}} \tag{13}$$

where $G_d(s) = \left(\left(V_{LS}s + \beta K_{qp,t} + \beta K_{leak}\right)\left(\tau_p s + 1\right) - \beta K_{qp,p}\right)$. For the tank side connection case the system transfer function reduces to:

$$G_{LS,t}(s) = \frac{\beta K_{q,pt} K_f}{\left(V_{LS}s + \beta K_{qp,t} + \beta K_{leak}\right)\left(m_{spool}s^2 + Bs + K_{spr,fq}\right) - \beta K_{q,pt} K_{fqp,pt}} \tag{14}$$

4 STABILITY AND SENSITIVITY ANALYSIS

In order to determine a control strategy for the system, it must be determined under which operating conditions the system is likely to become unstable. The main influence is due to the pressure drop over the spool valve, Δp, the spool position, x, and the pump time constant, τ_p (dependent on pump volume and pump type). In order to investigate this influence the poles variations for varying operating conditions are investigated by looking at pole variations.

4.1 Pump side

The open loop pump side transfer function given in eq. (13) has four poles and one zero. The zero originates from the pump dynamics, always being in the left half plane and hence being of no interest at this point. Therefore, only the movement of the four poles is considered. The results of varying the pressure drop over the spool and the spool travel are shown in the figures (8) and (9).

From these results it may be seen that increasing the pressure drop[1] over the spool does not have a major influence on the dominating poles, but does mean that the damping is decreased. Increasing the spool position does however have major influence on the dominant dynamics, where large spool movements may actually lead to an unstable system in combination with the highest pressure drops. In reality it is, however, very unlikely that these worst case operating points may ever be reached, as a full spool travel in combination with the highest possible pressure drop of $18\ [bar]$ will yield unrealistic operation conditions. From simulations with the non-linear model described in section 2, it has been found that realistic flow requirements are around $1.35[l/min]$. Plotting the pole locations for varying pressure drop and spool displacement yields the plot shown in figure 10 when ensuring a flow of $1.35[l/min]$. Based on this plot, the worst case working point for the pump side is therefore found to be for a pressure drop of $\Delta p = 18[Bar]$ and a spool displacement $x = 0.277[mm]$.

[1] The pressure drop cannot exceed the pressure margin of the pump, which is $18[bar]$.

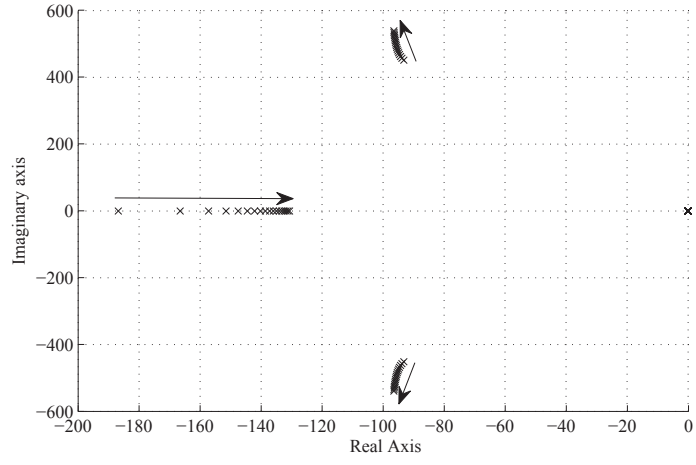

Figure 8: ***Pole movement for pressure drop*** $\Delta p = p_p - p_{LS} \in [1 - 18]\ [bar]$**.**

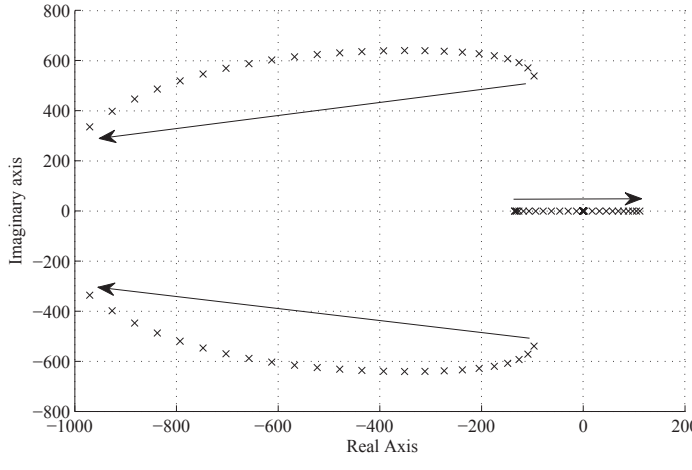

Figure 9: ***Pole movement at*** $\Delta p = p_p - p_{LS} = 18[bar]$ ***and spool position from*** $x \in [0.01 - 2.5]\ [mm]$**.**

4.2 Tank side

For the tank side the transfer function defined in eq. (14) has three poles and no zeros. As oppose to the pump side, the pump and pump volume dynamics is not influencing the tank side dynamics and hence the linearisation point will only be dependent on the pressure drop over spool ($\Delta p = p_{LS} - p_T$) and the spool position. The pressure drop over the spool is, on the other hand, only bounded by the maximum pressure in the system, why the pressure drop in opening situation may be very large. The stability and damping of the system for varying

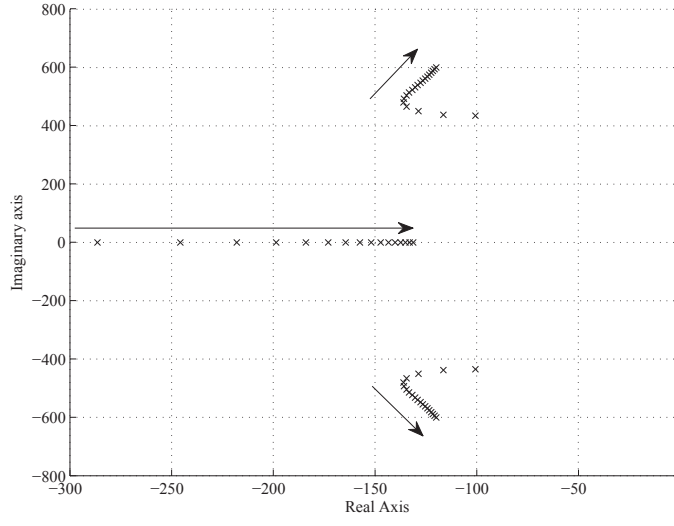

Figure 10: ***Pole movement at*** $1.35\ [l/min]$ ***for rising pressure and hence decreasing spool displacement.***

pressure drop and spool opening may be seen in figures 11 and 12.

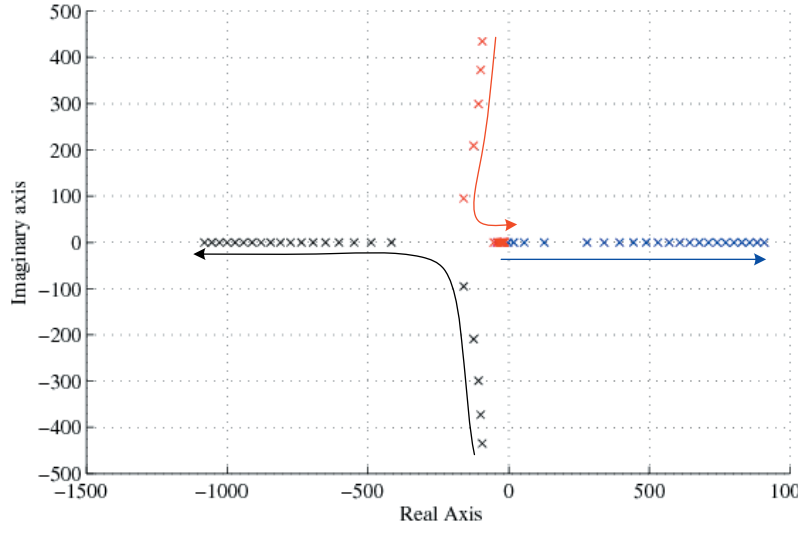

Figure 11: ***Pole movement for pressure drop 1-250 [bar].***

For the higher pressure drops ($> 30[bar]$) the system has one of the poles in the right half plane and is therefore unstable. As for the pump side the worst case operating point is for the

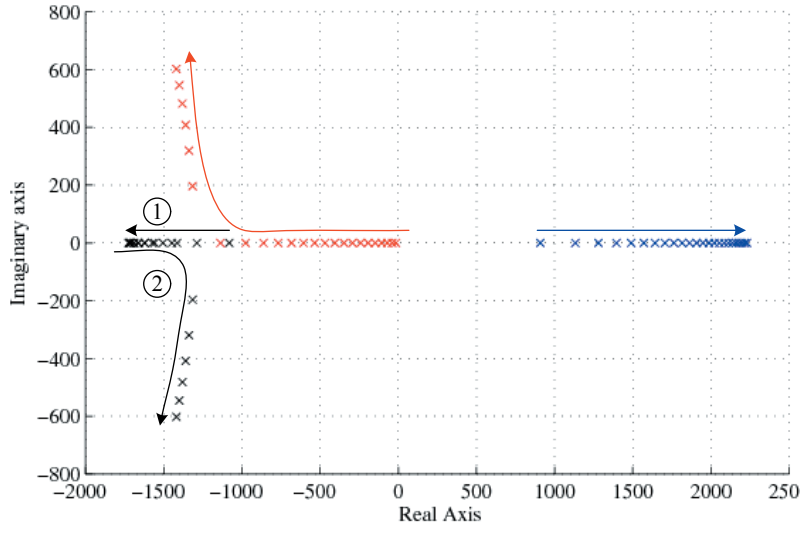

Figure 12: ***Pole movement at 250 [bar] and spool position from 0.01-2.5 [mm].***

highest possible pressure drop and the flow requirement of $1.35[l/min]$. This correspond to $\Delta p = 250[bar]$ and $x = 0.114[mm]$.

4.3 Sensitivity to varying LS-Hose Volume

The LS-hose volume directly influences the (open loop) system gain, i.e. the larger the volume, the lower the system gain. To illustrate this influence on the stability, the pole location as a function of the LS-hose volume is shown in figure 13 for the pump side case and figure 14 for the tank side case. The variations are made for $V_{LS} \in [20[ml], 320[ml]]$.

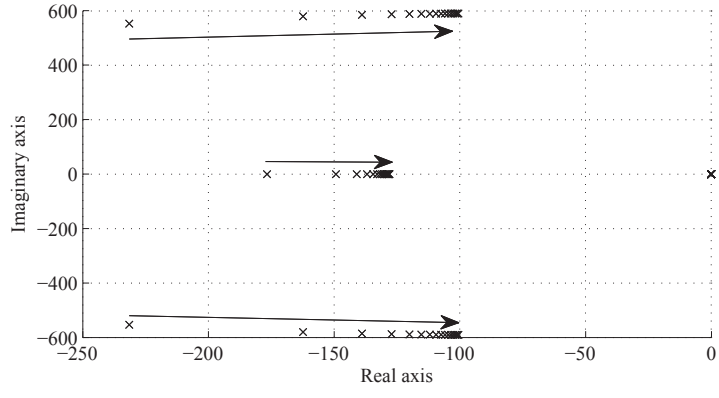

Figure 13: Open-loop poles location on pump side when considering LS-hose volume variations.

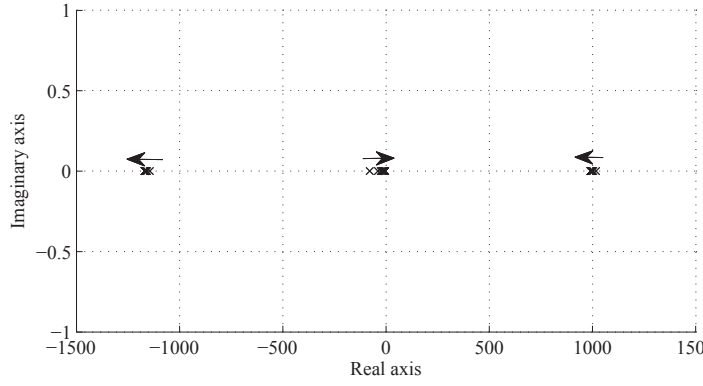

Figure 14: Open-loop poles location on tank side when considering LS-hose volume variations.

As expected the dominant system eigen frequency is lowered and the damping increased for the pump side when the volume is increased, and hence the system becomes slower. For the tank side the variation of the LS-volume is of minor influence.

5 CONTROLLER DESIGN

The basic demands of the system are that the performance must be comparable to that of the benchmark system, and that the control system is robust to changes in the system layout, i.e. hose volumes and pump type. Basically, as the system structure changes dependent on the spool position (i.e. open between pump side and LS-hose or between LS-hose and tank side), two controllers should be considered - one for each opening situation. Utilising this type of control structure, however, requires correct handling of the transition situation, where the spool crosses the zero position and the system structure changes. The situation is further complicated by the fact that the tank side dynamics is very sensitive to the pressure in the LS hose, and even becomes unstable for a pressure drop above approximately 30 bars, as shown in the previous sections. One way to overcome the switching problems is to use a kind of pressure dividing, by making a notch in the spool, allowing flow to pass from the LS hose to tank. By proper design of the area characteristic of the notch, crossing the zero position will only take place when the LS pressure is small (less than approximately 30 bars), i.e. we need to dump a relatively large amount of flow. In this situation the tank side dynamics will be stable and we can handle both situations with the same controller. Also, by allowing the spool to cross the zero position will decrease the loss inevitable arising from the ”leakage” flow.

The system dynamics can now in both cases approximately be described by a relatively well damped third order system. However, the flow from the notch will change the system type from being a type 1 to being a type 0 system. Based on these considerations a standard PI-controller is utilised.

$$G_{cp}(s) = 0.69 \cdot \left(1 + \frac{1}{1.5 \cdot s}\right) \tag{15}$$

The open-loop bode plot of the system with applied PI-controller is shown in figure 15.

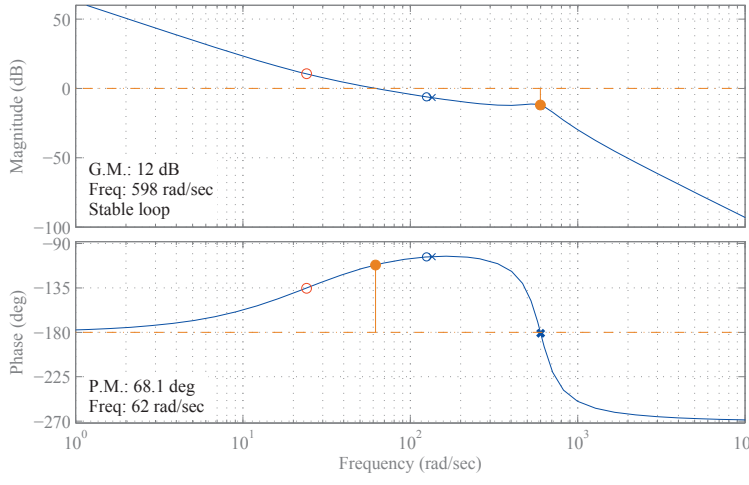

Figure 15: Open-loop bode plot of the pump side with the PI-controller. The circles and crosses representing respectively the zeros and the poles of the system, with the the first circle (red) resulting from the zero added by the PI-controller.

Based on the above analysis the designed controller has been implemented and tested experimentally. The results are shown in figures 16-18.

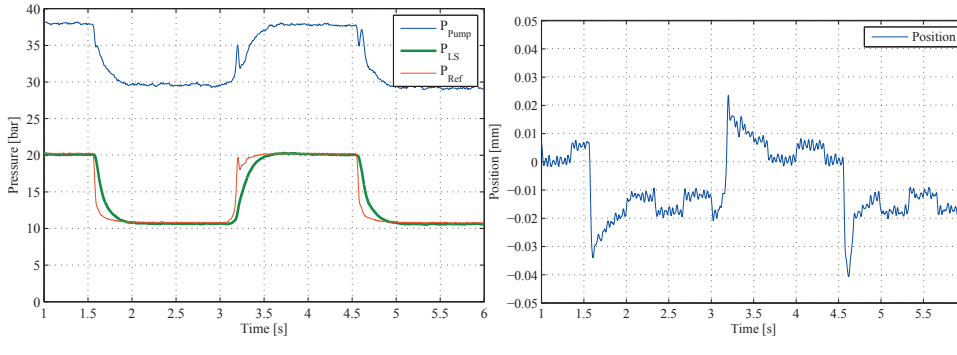

Figure 16: Measured pressure and spool position when operating at low pressures and applying pressure steps.

From the results it may be seen that the system is operating as expected. For small pressure steps the system is continuously operating with a positive spool position, as seen in Fig. 17, meaning that the system is continuously controlling the leakage flow to tank. For the larger

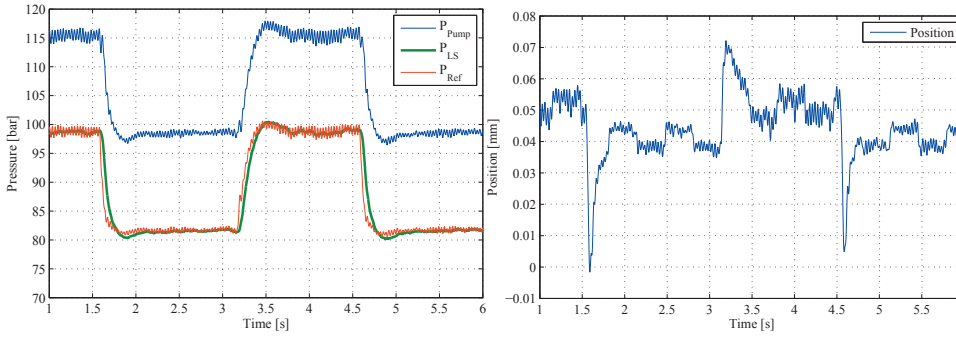

Figure 17: Measured pressure and spool position when operating at high load pressure and applying minor pressure steps.

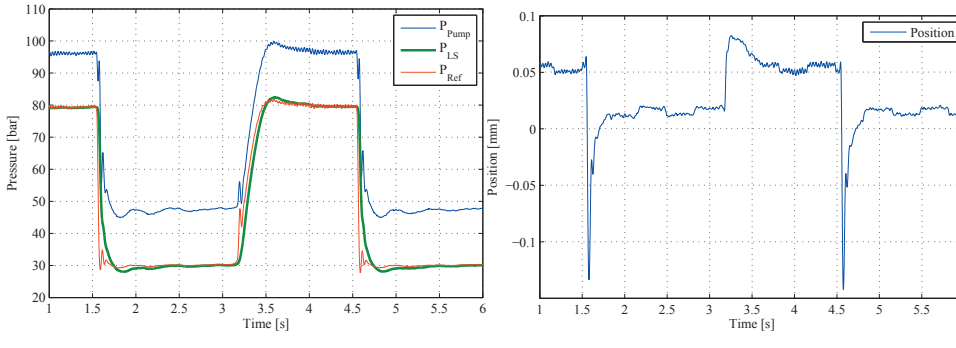

Figure 18: Measured data for high load pressure and large pressure steps.

downwards pressure steps and when operating at low system pressure (Fig. 18 and 16 respectively), the leakage flow is however not large enough, to swash out the pump sufficiently fast, why the valve switches over and operates with a negative spool position. In this case the pressure drop over the spool have, however been lowered (due to the initial leakage flow), to a level where the system is not unstable, cf. the above analysis.

6 CONCLUSION

The focus of this paper has been on generating a hydraulic (LS) pilot pressure based on an electric reference for use in systems without hydraulic feedback of the load pressure. This was done using a small spool valve, where a model of the valve and the considered system was first presented. A linear analysis of the system yielded the worst case operating conditions of the system, and based on this analysis an approach using a controlled leakage flow was utilised, hereby enabling the system to be operated with a simple PI-controller and still be stable and robust towards transitions between pump and tank side operation. Finally experimental results were presented showing the validity of the approach.

References

[1] H.H. Harms. Hydraulic fluid technology: Current problems and future challenges. In *International Exposition for Power Transmission and Technical Conference*, Apr. 2000.

[2] A. Langen. *Experimentelle und analytische Untersuchungen an vergesteuerten hydraulisch-mechanischen und elektro-hydraulischen pumpenregulungen.* PhD thesis, Rheinisch-Westfälischen Technishen Hochshule Aachen, 1986.

[3] H. Esders. *Elektrohydraulisches Load Sensing für mobile Anwendungen*. PhD thesis, Technischen Universität Carolo Wilhelmina zu Braunschweig, 1995.

[4] B. Lantto. *On Fluid Power Control - with Special Reference to Load-Sensing Systems and Sliding Mode Control*. PhD thesis, Linköping, 1994.

[5] G. Tewes and H.H. Harms. Fuzzy control for an electrohydraulic load-sensing system. In *Fluid Power Systems, Ninth Bath International Fluid Power Workshop*, Sep. 1996.

[6] B. Zähe. *Energiesparende Schaltungen hydraulischer Antrieb mit verändelichem Versorgungsdruck und ihre Regelung*. PhD thesis, Rheinisch-Westfälischen Technischen Hochschule Aachen, 1993.

[7] W. Backé and B. Zähe. Electrohydraulic load-sensing. *SAE Technical Paper Series*, 1991.

[8] P. Krus, T. Persson, and J.-O. Palmberg. Complementary control of pressure control pumps. In *Proceedings of the IASTED International Symposium, MIC'88*, 1988.

[9] B. Nielsen, H.C. Pedersen, T.O. Andersen, and M.R. Hansen. Modelling and simulation of mobile hydraulic crane with telescopic arm. In J.S. Stecki, editor, *1st International Conference on Computational Methods in Fluid Power Technology*, pages 145–154, Melbourne, Australia, Nov. 2003.

[10] H.C. Pedersen, T.O. Andersen, and M.R. Hansen. Designing an electro-hydraulic control module for an open-circuit variable displacement pump. In *Proc. of The Ninth Scandinavian International Conference on Fluid Power, SICFP05*, Linköping, Sweden, June 2005. SICFP05.

Equalization Techniques for Dual Redundant Electrohydraulic Servoactuators for Flight Control Systems

Giovanni Jacazio Laura Gastaldi
Department of Mechanics - Politecnico di Torino – Italy

ABSTRACT

Electrohydraulic servovalves have been the most common device used to control the flow to hydraulic actuators in aircraft fly-by-wire flight control systems. Though servovalves offer several advantages, they present a few drawbacks, among which an unpredictably variable offset between hydraulic null and electrical null. In flight control systems at least two actuators supplied by two independent power sources and independently controlled are connected to the same flight control surface to provide the necessary redundancy; when the flows to the actuators are simultaneously and directly controlled by two servovalves, an unfavourable combination of servovalves offsets can originate a force-fighting condition with negative effects on the overall system stiffness, resolution and frequency response. This paper presents an optimal equalization control strategy capable of minimizing the force fighting between two redundant electrohydraulic servoactuators.

1 ELECTROHYDRAULIC SERVOACTUATORS FOR FLY-BY-WIRE FLIGHT CONTROL SYSTEMS

As it is well known, digital fly-by-wire flight control systems use flight control computers (FCCs) to issue the commands to the flight control actuators and accept from them the electrical feedback signals. In order to ensure the necessary redundancy, two actuators are normally used in primary flight controls to drive the same aerodynamic control surface, with each actuator interfacing with one or more FCCs. When two hydraulic actuators are connected to the same aerodynamic control surface, a very important design issue is to guarantee that no conflict originates between the two actuators such to impair the flight control system performance. This is particularly critical when the servoactuators hold the flight control surface at a certain fixed position under rapidly varying loads, such as those occurring when the flying aircraft is subjected to gusts or turbulence.

Over the years different design solutions have been worked out for redundant electrohydraulic servoactuators and have been implemented into operational aircraft. The main critical issues to be addressed have been: input signal mismatch, control valve offset, difference between supply pressures of the two hydraulic systems interfacing with the actuators, system robustness following failures and, of course, overall system complexity. Though generalization is often a risky business, still it is possible to state that the different

Fluid Power and Motion Control 2008 Edited by Dr D N Johnston and Professor A R Plummer

configurations of redundant electrohydraulic servoactuators for flight control systems can be grouped in the following four categories.

Active/standby systems. In these systems one of the two actuators connected to the same flight control surface is active while the second one is in standby. In case the operating actuator fails, the other one is activated and ensures an unabated operation.

Single flow control valve. In these systems the flows to the two hydraulic actuators are simultaneously controlled by two sections of a single control valve.

Reduction of the sensitivity to the control valve offsets. In these systems appropriate actions are taken to reduce the effects of the offsets of the control valve and hence the associated mismatch between the actuator forces.

Equalization between the two electrohydraulic servoactuators. In these systems sensors are introduced to measure the differences between the two servoactuators parameters and appropriate control laws are defined to correct those differences.

These four types of architectures will be discussed in the following and the results of a research activity aimed at defining an optimal and robust equalization technique will be presented.

2 LOAD SHARING BETWEEN REDUNDANT SERVOACTUATORS

When two electrohydraulic servoactuators are connected to the same flight control surface, the forces developed by the two actuators are summed and the problem of ensuring an even load sharing between the two actuators arises (1). The force developed by an actuator is a function of the pressures acting on the two sides of the actuator piston, and when the actuator is stationary, the pressure differential across the two control valve ports, and thus across the two actuator sides, changes very rapidly with the change of the input signal of the control valve. The valves used to control the pressurized fluid flow to flight control actuators typically consist of closed-center spool valves with very high pressure gains around null so that a large pressure differential, and therefore a large actuator force, is created as a result of small spool displacements. In general, close-center spool valves have a pressure gain that brings about the full pressure differential for a spool displacement equal to 3-5% of maximum.

The flow control valves commonly used in electrohydraulic servoactuators for flight control systems are two-stage electrohydraulic servovalves (EHSVs) which use an internal hydraulic amplifier to convert the electrical input signal into valve spool displacement. A problem associated with servovalves is their offset, that can greatly differ from one servovalve to another and that can change with life and with the operating conditions in a non-deterministic manner; two nominally equal servovalves may exhibit different offsets, and also in the opposite directions, with the same operating and environmental conditions. As a worst case the maximum total servovalve offset can reach 15% of the rated input current.

This particular behaviour of the servovalves has always been a critical issue and to counter that effect high performance light-weight proportional valves, known as direct drive valves (DDVs) within the aerospace community, have also been applied as flow control devices for electrohydraulic servoactuators. DDVs use the force developed by a proportional solenoid to drive the valve spool and do not rely on an internal hydraulic amplifier. DDVs minimize the problem of valve offset, but they require much greater electrical input power, have greater weight, reduced chip shear capability and higher cost. Moreover, DDVs

require an internal spool position feedback loop and often also a spool velocity loop nested within the spool position loop to ensure a high dynamic response with adequate stability. Although DDVs have been used in recent applications, EHSVs are still the preferred choice as flow control valves in electrohydraulic flight control systems, especially considering their low electrical power consumption.

Let us now consider two electrohydraulic servoactuators driving a flight control surface as shown in the concept block diagram of figure 1. Each servoactuator consists of a linear hydraulic actuator, a flow control valve, a solenoid valve, a shutoff/bypass valve and a control electronics; a position transducer inside the hydraulic actuator provides the feedback signal to the control electronics to close the position control loop. The actuator control electronics receives the position command from the flight control computer and generates the control signal to the EHSV according to a proper control law, thereby modulating the flow and pressures to the hydraulic actuator as required to respond to the pilot inputs and to the variable loads on the aerodynamic surface. The actuator control electronics also generates an on/off electrical signal to a solenoid valve to either arm the hydraulic system or set the actuator into a bypass mode.

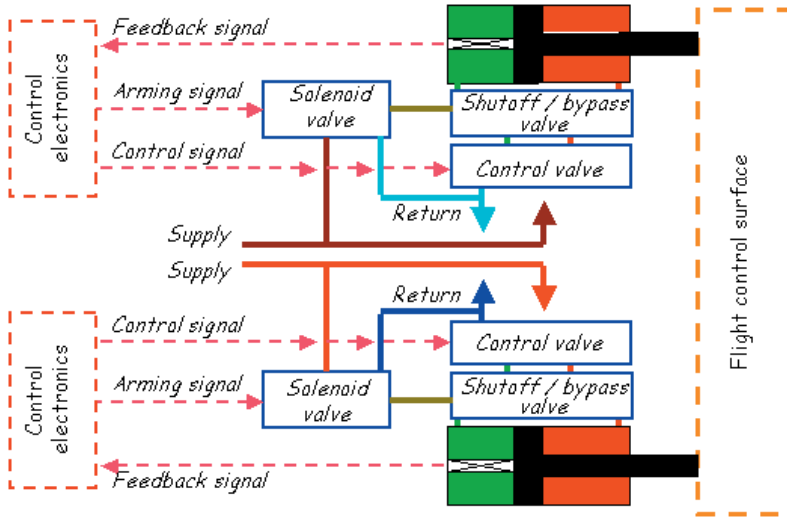

Figure1 Concept schematic of dual redundant eletcrohydraulic servoactuator

Each of the two identical electrohydraulic servoactuators is supplied by a different aircraft hydraulic system and it is often controlled by two different control lanes, thereby leading to a dual hydraulic / quadruplex electrical architecture. With this architecture, each of the electrical components of the servoactuator (solenoid valve, control valve, position transducer) is dual electrical and accepts/transmits two electrical signals; moreover, the four position signals provided by the position transducers of the two servoactuators (two electrical signal per transducer) are exchanged among the four flight control computers (FCCs) via optoisolated links. Each FCC has thus available all position transducers signals, performs a signal consolidation according to a common logic, and perfectly identical control signals are thus issued by the FCCs to the electrical lanes of the two control valves.

We now consider the case of the two control valves consisting of EHSVs. When a servovalve receives a control signal to move away from null, a pressure differential is created between the control ports that is proportional to the magnitude of the control signal

and dependent on the servovalve pressure gain; this pressure differential is acting upon the actuator that develops a load drive force.
If only one servoactuator were driving the flight control surface, or if the two EHSVs of the two servoactuators had exactly the same offset, the presence of an offset would non originate any problem to the system operation. As it is shown in figure 2a, if a certain load drive force F must be developed by the sum of the two actuators controlled by two EHSVs with equal offsets, a control signal *i* must be created by each of the control electronics, such to create a pressure differential across the two sides of each actuator to develop a total force equal to F. The control signal i is equal to:

$$i = i_0 + \frac{F}{2AG_P} \tag{1}$$

where:

i_0 = servovalve offset
F = load drive force on the flight control surface (total of the two actuators)
A = active area of each actuator (assuming balanced area actuators)
G_P = servovalve pressure gain

For the simple case of a servoactuator controlled with a proportional control law, the position error is equal to the control signal divided by the proportional gain, and since this gain can normally be set sufficiently large while still maintaining the system stability, the resulting position error is low and generally acceptable. Should it be required to further reduce this error, that can be achieved by adding an integrator with a suitable gain in the control law. If the two servoactuators driving the same flight control surface are controlled by two servovalves with offsets in opposite directions, a total load drive force is obtained as shown in the diagram of figure 2b. The total load drive force diagram shows a region of zero force gradient in which the overall system does not respond to the control signals issued by the electronic controllers. This behaviour is totally unacceptable in flight control systems because of the resolution, frequency response and dynamic stiffness requirements.
The resolution requirements depend upon the aircraft category, but are most often in the range from 0.006° to 0.025° of angular deflection of the flight control surface.

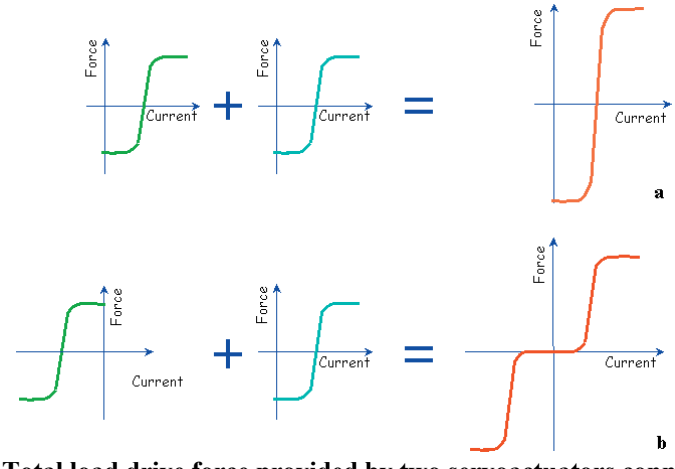

Figure 2 Total load drive force provided by two servoactuators connected to the same flight control surface for servoactuators controlled by servovalves with identical offsets (a), and of servoactuators controlled by servovalves with opposite offsets (b)

For the case of 60° maximum angular travel a servoactuator resolution between 0.01% and 0.04% of full actuator travel is thus required. Consider now the unlucky case of a dead band (figure 2b) equal to 20% of maximum servovalve control signal; the electronic controller gain is typically set such that the maximum servovalve control signal is obtained for a position error equal to 4-5% of the full actuator travel, and this stems from the need to provide a suitable frequency response while maintaining an adequate stability margin. As a result, a 20% dead band for the control signal is reflected into a dead band of 0.8% to 1% of full actuator travel, which is about two orders of magnitude greater than the specified resolution. The dead band around the null condition also negatively affects the system frequency response to small amplitude commands introducing excessive phase lag and gain attenuation.

A second critical condition created by the dead band of the actuator's load drive force is that the system stiffness is practically reduced to zero in that area. As a consequence, when the aircraft flight control surface is subjected to fluctuating loads created by the atmospheric turbulence, large oscillations of the flight control surface are originated which in turn give rise to a bumpy aircraft flight.

It is therefore clear that a flight control actuation system architecture in which two servovalve controlled electrohydraulic servoactuators driving the same flight control surface are both active is not acceptable for aircraft primary flight control systems.

3 EXISTING TECHNIQUES FOR IMPROVING LOAD SHARING OF REDUNDANT SERVOACTUATORS

A solution often used to avoid the dead band in the signal versus load drive force diagram is to always operate one servoactuator at a time (2): one of the two servoactuators is operating while the second one is in a bypass mode (active / standby architecture). This solution is simple and eliminates the root cause of the dead band and has for instance been used by Airbus in the fly-by-wire primary flight control actuators of their aircraft. Two main drawbacks are however associated with this architecture. First, the actuators must be overdesigned since under normal operating conditions the active actuator must be capable of driving the maximum aerodynamic load plus the load created by the standby actuator. Second, in case of a failure of the hydraulic system providing the pressure supply to the active actuator, a time delay occurs between the onset of hydraulic system failure and the instant in which the standby servoactuator is activated and takes up the control of the aerodynamic surface. During this time delay there is a temporary loss of control of the aerodynamic surface, which does not lead to a flight critical condition since it lasts relatively little time (0.1 to 0.2 s), but can anyhow create an unpleasant sudden disturbance during the aircraft flight.

Another approach to minimize the effect of the servovalve offsets and improving the load sharing between two actuators driving a common flight control surface is that to reduce the sensitivity to the offsets by softening the pressure gain characteristics of the servovalves. A reduction of the pressure gain can be obtained by overcutting the spool lands in order to achieve an open-center valve configuration. This solution is effective in eliminating the dead band of the load drive force diagram, but it brings about two main disadvantages: an average low stiffness due to the low pressure gain and large internal leakages due to the open-center configuration. For these reasons, this solution had very limited applications.

A different way for obtaining an even load sharing between two hydraulic actuators driving

a common aerodynamic surface consists of controlling the pressurized fluid flows to the two hydraulic actuators with a single control valve made up by a long spool sliding inside a sleeve interfacing with the two hydraulic systems and the two actuators (3), (4), (5). A very careful and accurate machining of the spool lands allows an excellent matching between the two hydraulic sections, so that equal pressure differentials are created for the two actuators as a result of a spool displacement away from null, providing that the supply pressures of the two hydraulic systems are equal. With this solution, the movement of the spool is obtained by applying appropriately controlled pressures at its two ends by two small EHSVs with low pressure gain. The position of the main control valve spool is measured by a position transducer that provides a feedback signal used to close a main control valve position loop. Although this architecture is more complex, it has been widely used in fly-by-wire primary flight control systems due its undisputable performance advantages. The primary flight control systems of the Tornado and of the F-18 are examples of application of this architecture.

The same design concept of using a single valve for modulating the flows to two hydraulic actuators can be pursued by using a direct drive valve whose spool is driven by multiple force motors. Primary flight control actuation systems based on this architecture have been used in the primary flight control systems of some military aircraft such as the Eurofighter. A DDV based architecture has the merits of an overall greater reliability and of lower internal leakages, but the much greater electrical power draw and cost may thwart their use in several applications. Moreover, the lower axial force developed on the spool by the force motors when compared to that developed by hydraulic pressure raises concerns about their ability of shearing off large debris that could remain stuck between spool and sleeve and create a spool lock.

A fourth way to improve the load sharing between two electrohydraulic servoactuators while simply using two servovalves, with each valve controlling the flow to its own actuator, is to sense the pressure differentials across the two actuators (6), compare the two pressure differentials and inject compensation signals into the servovalves currents such to equalize the actuators pressure differentials (figure 3). This technique is simple in principle, but its implementation is not an easy task since both the equalization algorithm and the strategy to deal with failures of the hydraulic systems must be properly addressed. Concerns about these design issues have been the main reason for a very limited application of this type of architecture to fly-by-wire flight control systems (7). A partial application of this architecture is found in the primary flight controls of the B2, which uses the signals of two differential pressure sensors to create compensation signals to two DDVs to reach a better load sharing between the actuators. DDVs, however, exhibit a much lower offset than EHSVs, therefore, the equalization issue is much less critical than with EHSVs.

4 SETTING THE CONTROL STRATEGY FOR EQUALIZING EHSV CONTROLLED REDUNDANT SERVOACTUATORS

As emphasized before, the purpose of the research activity presented in this paper was to define an optimized solution for achieving an even load sharing between two hydraulic actuators separately controlled by individual electrohydraulic servovalves. The merits of the solution that was eventually developed are: simple system architecture, lower cost, limited transient disturbance following a failure, possibility of operation following a seizure of a valve spool. Though the probability of a seizure of valve spool is considered very low, still

the system architectures based on a single flow control valve for the two actuators present a common link made up by the single main control valve; a failure of this valve leads to the loss of operation of the relevant flight control surface. Controlling the actuator flows with two different control valves offers a greater survivability to the flight control system. The concept schematic for the system under study is therefore the one shown in figure 3.
In order to define the general architecture of a control law aimed at equalizing the forces developed by two actuators controlled by electrohydraulic servovalves it is convenient to refer to a linear model of the system; the actual values of the control parameters will then be fine tuned with the use of a detailed non-linear model.

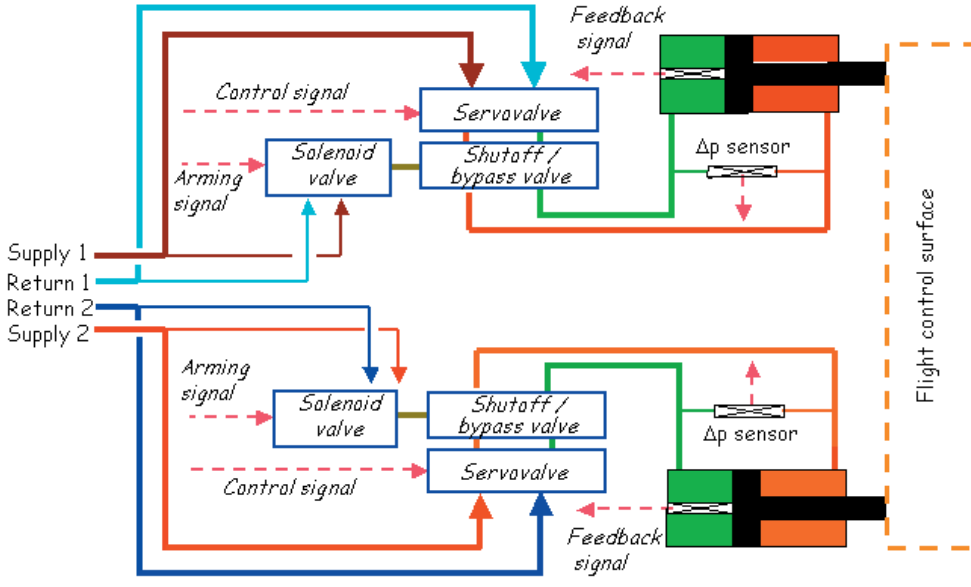

Figure 3 Concept schematic of two electrohydraulic servoactuators with individual servovalves and differential pressure equalization

The block diagram of the linearized mathematical model of the system is illustrated in figure 4. The input command xc is compared to the position feedback z to generate the position error e which is processed by a control law with a transfer function $G_1(s)$ to provide the control signals to the two servoactuators. The control signals (equal for both servoactuators) are modified by the equalization signal h, which is subtracted from the control signal of servoactuator 1 and added to the control signal of servoactuator 2; the modified control signals are then fed to digital-to-analogue converters to generate the input signals to the servoamplifiers with a gain G_A generating the controlled currents i_1 and i_2 to the servovalves. The offsets of the two servovalves are represented in the block diagram by disturbance currents id1 and i_{d2}, which are added to the actual currents i_1 and i_2. Therefore, the two servovalves will behave in response to equivalent currents $i_{v1} = i_1 + i_{d1}$ and $i_{v2} = i_2+i_{d2}$. The remaining portion of the forward path of the control loop is the usual block diagram of a hydraulic servoactuator; $G_V(s)$ is the transfer function defining the servovalve dynamics, G_Q and G_P the servovalves flow and pressure gains, C the hydraulic capacitance of each actuator chamber with the actuator assumed at mid position, k_L the internal leakage coefficient, A the actuator area, k the stiffness of the actuator attachment point to the

underlying structure, c_V the external damping coefficient, m the total mass of the moving parts reflected to the actuators linear output. In the same block diagram δ_{p1} and δ_{p2} are the pressure differentials across the two sides of actuators 1 and 2, F_1 and F_2 the corresponding actuator forces, R the load force, y the actuator's linear displacement.

The transfer function H(s) of the feedback path is that of the demodulator filtering the electrical signal provided by the actuator's position transducer. Fly-by-wire flight control systems typically use LVDT type position transducers because of their robustness and capability of operating in harsh environments; these transducers are supplied with a high frequency ac input voltage and require low-pass second-order filters to attenuate significantly the alternating component of the output signal.

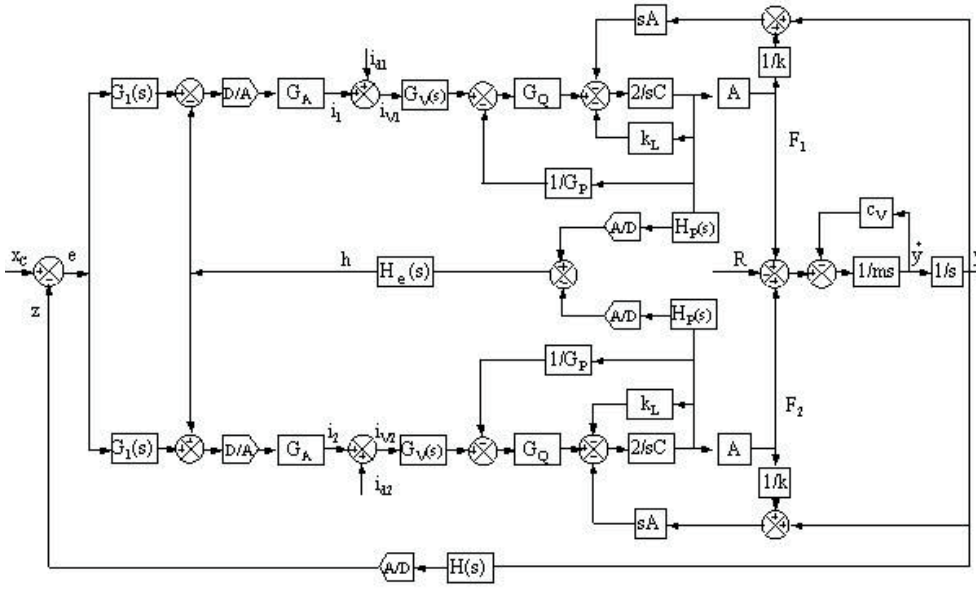

Figure 4 System block diagram

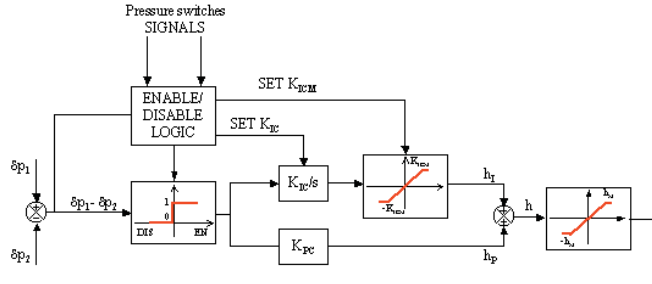

Figure 5 Block diagram of the equalization control law

The two pressure differentials δp_1 and δp_2 are measured by differential pressure transducers also consisting of LVDTs measuring the displacement of a spring centered cylinder subjected to the pressure differential. The output signal of each of these transducers is therefore demodulated by a filter with a transfer function $H_P(s)$. The difference between the two pressure differential signals is then fed to the equalization control law that is indicated

in the block diagram of figure 4 with the transfer function $H_e(s)$, which is actually a complex function as shown in the diagram of figure 5.
The difference $\delta p_{1\text{-}2} = \delta p_1 - \delta p_2$ between the two pressure differential signals first passes through an activation block that is commanded by the enable/disable control logic. In order for the equalization function to be activated, both servoactuators must operate correctly and be pressurized, which condition is signalled by pressure switches of the two servoactuators. If both pressure switches signals are "on", an enable signal is sent to the activation block that transfers the $\delta p_{1\text{-}2}$ signal to the following blocks;otherwise, the output of the activation block is equal to zero. The $\delta p_{1\text{-}2}$ signal is processed by a modified PI controller in which the gain K_{IC} of the integral part of the controller is varied with time when the equalization logic is activated, starting from an initial large value at switch-on to a smaller one after the initial equalization transient has settled. The integrator output signal is saturated to maximum / minimum values; the saturation limits are enabled if both pressure switches signals are "on"; otherwise they are set to zero. The output signals h_I and h_P from the integral and proportional controllers are summed up, the resulting equalization signal h is saturated to a maximum/minimum limit and injected with the appropriate sign into the summing points of the forward paths of the two servoactuators control loops.
In order to better understand the rationale behind the selection of the equalization control law outlined above, it is convenient to consider a simplified case of a system with a null load force R and in which the control transfer function $G_I(s)$ is a pure gain K_I, the equalization transfer functions $H_e(s)$and $H_P(s)$ are replaced by a proportional gain K_{PC}, and the system is in a stationary condition. For this simplified condition, the two pressure differentials δp_1 and δp_2 are given by the following expressions, where e is the servoactuator's position error.

$$\delta p_1 = \frac{K_I G_Q G_A}{k_L + G_Q/G_P} e + \frac{G_Q\left(\dfrac{k_L + G_Q/G_P}{G_A G_Q K_{PC}} + 1\right) i_{d1} + G_Q i_{d2}}{\left(k_L + G_Q/G_P\right)\left(\dfrac{k_L + G_Q/G_P}{G_A G_Q K_{PC}} + 2\right)} \tag{2}$$

$$\delta p_2 = \frac{K_I G_Q G_A}{k_L + G_Q/G_P} e + \frac{G_Q i_{d1} + G_Q\left(\dfrac{k_L + G_Q/G_P}{G_A G_Q K_{PC}} + 1\right) i_{d2}}{\left(k_L + G_Q/G_P\right)\left(\dfrac{k_L + G_Q/G_P}{G_A G_Q K_{PC}} + 2\right)} \tag{3}$$

For the worst case of servovalves with opposite offsets, $i_{d1} = -i_{d2} = i_{d0}$, equations (2) and (3) become:

$$\delta p_1 = \frac{K_I G_Q G_A}{k_L + G_Q/G_P} e + \frac{i_{d0}}{\dfrac{1}{G_Q}\left(k_L + G_Q/G_P\right) + 2G_A K_{PC}} \tag{4}$$

$$\delta p_2 = \frac{K_I G_Q G_A}{k_L + G_Q/G_P} e - \frac{i_{d0}}{\dfrac{1}{G_Q}\left(k_L + G_Q/G_P\right) + 2G_A K_{PC}} \tag{5}$$

The flow gain G_Q is a parameter that is selected as a function of the actuation speed to be developed by the actuator, therefore, should no equalization be present ($K_{PC} = 0$), the only possible way for reducing the difference between δp_1 and δp_2 is to increase the internal leakage (greater k_L) or reduce the pressure gain G_P. However, both these ways lead to a reduction of the value of the coefficient multiplying the servoloop error e, which implies a reduction of the servoactuator stiffness, since a greater error is necessary to obtain the same pressure differential. Introducing the pressure equalization ($K_{PC} > 0$) brings about a reduction of the effect of the offset current i_{d0} on the pressure differentials. The difference between δp_1 and δp_2 thus decreases with increasing the value of K_{PC}, but this process cannot continue above a certain limit for it would lead to an instability of the pressure equalization loop. However, it must be considered that the servovalve offsets are the result of different contributions. Some contributions (null bias and null shift with temperature) are steady-state or quasi-steady-state factors and their effect can thus be recovered by introducing a low gain integrator (K_{IC} in the block diagram of figure 5), that eventually develops a signal such to compensate these contributions to the servovalve offsets. Since the maximum null bias is about 4% of the rated servovalve current, and the maximum null shift with temperature can take another 4% of rated servovalve current, the saturation limit K_{ICM} of the block diagram of figure 4 can be set such to correspond to 8% of the rated servovalve current. However, in case the signal of one of the two pressure switches is "off", the saturation limit K_{ICM} is set to zero to fully disable the equalization logic. At the same time, the saturation limit h_M of the entire equalization control law can be set to 15% of the rated servovalve current, which is the maximum possible offset under normal servovalve operation.

The rationale for this control law is to use the integral control for compensating the steady-state offsets, while leaving to the proportional control for the task of compensating rapid variations of servovalve offsets that can be originated during system operation. A common case is for instance a different temporary null shift of the two servovalves resulting from variations of the return pressure, that can be different for the two hydraulic systems to which the two servovalves are hooked. Since the proportional control has to compensate only a fraction of the servovalve offset, its gain can be kept lower than it would be required for entire offset compensation, and the equalization loop stability can be maintained while minimizing the residual difference between the two pressure differentials.

The integrator gain K_{IC} must be kept low to prevent an adverse effect on the stability of the equalization loop, but this may be a negative factor at the start-up when the equalization logic is activated, since it would lead to a long settling time. The value of the integrator gain is thus initially set high and equal to 10 times its normal value and is reduced to its normal value as the difference $\delta p_1 - \delta p_2$ is reduced to a value equal to 20% of the supply pressure. From then on, the integrator gain remains constant at that value, no matter of the variations of $\delta p_1 - \delta p_2$. This technique allows an acceleration of the initial settling time without affecting the equalization loop stability.

5 REFERENCE SERVOACTUATORS

The merits of the equalization control technique described in the previous paragraph have been assessed with reference to a typical fly-by-wire system for the control and actuation of a primary flight control surface of a medium-size aircraft. The system consists of two microprocessor controlled electrohydraulic servoactuators with the main characteristics

reported in table I.
The design characteristics of the actuators and their components, and the system control law were defined to meet the requirements listed above. Extensive simulations were run for the ideal case of two servoactuators supplied with identical pressures and controlled by zero offset servovalves; the results of these simulations were used as a benchmark for the performance of servoactuators with serovalves exhibiting different offsets and for assessing the merit of the equalization control technique. The system response to different conditions was taken as representative of the system dynamic behaviour; these conditions were:

- No-load - frequency response for input commands of ±0.1 mm (autopilot adjustments) and ±2 mm (small amplitude pilot commands)
- No actuator command - dynamic stiffness for a load fluctuations of ±500 N (level flight under turbulence) and ±3000 N (level flight under gusts)
- No actuator command - half sine variation of load from 0 to 10000 N to 0 in 0.5 s (windshear).

Table I: Characteristics of the reference servoactuators

Supply pressure	*28 MPa*
Return pressure	*0.5 MPa*
Hydraulic fluid	*conforming to MIL-PRF-5606*
Actuator stroke	*100 mm*
Maximum external load	*25000 N*
No-load speed	*100 mm/s*
Total system mass reflected to actuator output	*90 kg*
External damping coefficient	*10000 Ns/m*
Stiffness of the actuator attachment point	*$4x10^7$ N/m*
LVDTs excitation frequency	*3 kHz*
Microprocessor recursion rate	*400 Hz*
Microprocessor computation time	*1 ms*
Analogue/digital converters resolution	*12 bit*

6 SIMULATED BEHAVIOUR OF SERVOACTUATORS

Starting from the reference system with ideal servoactuators, a system consisting of actuators controlled by servovalves with different offsets was analyzed. In particular, servovalves with two opposite offsets corresponding to 10% of the rated current were considered, which case could well occur within the normal range of operating conditions. The dynamic behaviour of the system was assessed in response to the same input conditions considered for the ideal servoactuator. A system **without equalization** was first analyzed which showed as expected a large worsening of its dynamic characteristics, as clearly seen in figures 6 through 9. When a small input command of ±0.1 mm amplitude is given at a very low frequency of 0.1 Hz (figure 6a), a system with opposite servovalve offsets can respond to the command, though with a relatively large phase lag; however, if the command frequency is increased to 0.2 Hz (figure 6b), the same system is practically not responding any longer to the small amplitude command. If the amplitude command is increased to ±2 mm, the differences between systems with and without servovalve offsets become marginal, since the dead band in the combined pressure gain curve is negligible with respect to the command amplitude, and some differences show up only at high

frequencies as it can be seen in figure 7.
A very large difference in the system performance between the two conditions of zero servovalve offsets or maximum opposite offsets occurs for the dynamic stiffness. Since the typical frequency range for the loads fluctuations on the primary flight control surfaces is between 5 and 20 Hz, it can be seen from the diagrams of figure 8 that a dramatic reduction of the dynamic stiffness up to 30 dB can be originated by the opposite servovalves offsets, which is clearly unacceptable. This loss of dynamic stiffness is reflected into the system response to a strong gust, as shown in figure 9. A system without offsets reacts with a minimum transient error, while a system with opposite servovalves offsets shows a large compliance and a transient disturbance up to 0.7 mm of actuators stroke.

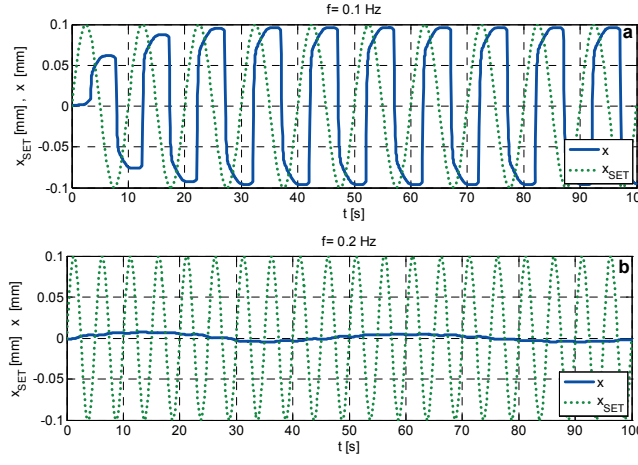

Figure 6 Servosystem without equalization: time response with no-load and input displacement of ±0.1 mm (a) f=0.1 Hz and (b) f=0.2Hz

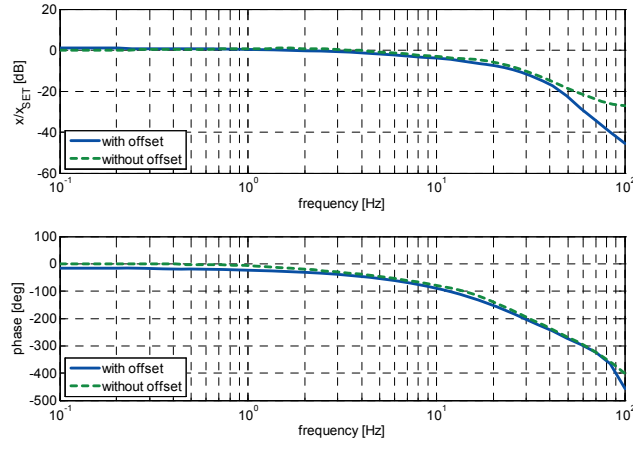

Figure 7 Servosystem without equalization: frequency response with no-load and input displacement of ±2 mm

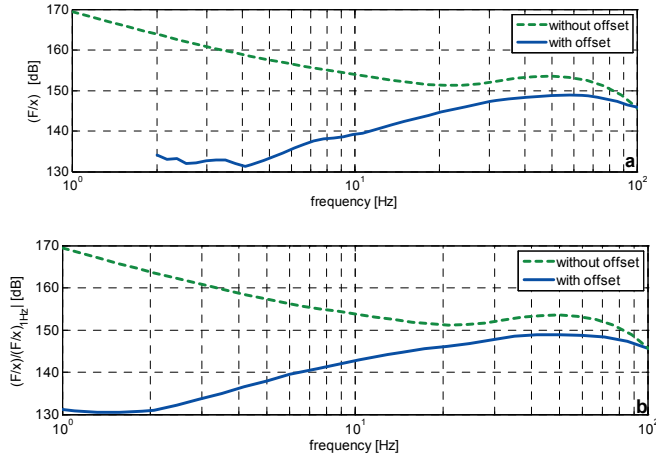

Figure 8 Servosystem without equalization: dynamic stiffness with eternal force (a) R=±500 N and (b) R=±3000 N. (Stiffness units are N/m)

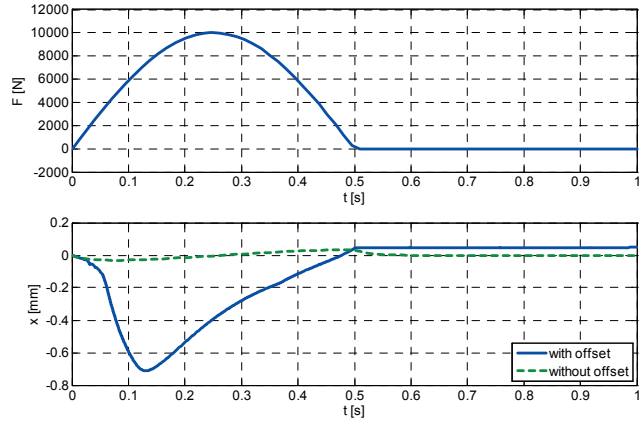

Figure 9 Servosystem without equalization: response to a half sine variation of load

A system **with pressure differential equalization** according to the strategy outlined at the end of paragraph 4 was then analyzed, and the system response to the different input conditions is illustrated in figures 10 through 13. In particular, figure 10 shows that no practical difference exists between the ideal system (no servovalve offset) and a system with maximum opposite servovalves offsets and differential pressure equalization; the curves for these two conditions are actually superimposed in the diagrams of figures 10 and 11. Some minor difference exists in the response to a large gust (figure 13), and the maximum transient position error is equal to 0.052 mm compared to 0.03 mm of the ideal system. However, this error is one order of magnitude lower than the error of a system with servovalve offset without differential pressure equalization, which is equal to 0.7 mm as it can be seen in figure 9.

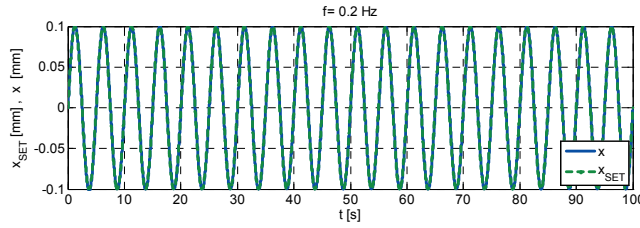

Figure 10 Servosystem with equalization: time response with no-load and input displacement of ±0.1 mm at f=0.2Hz

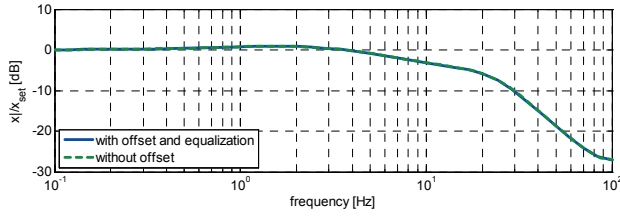

Figure 11 Servosystem with equalization: frequency response with no-load and input displacement of ±2 mm

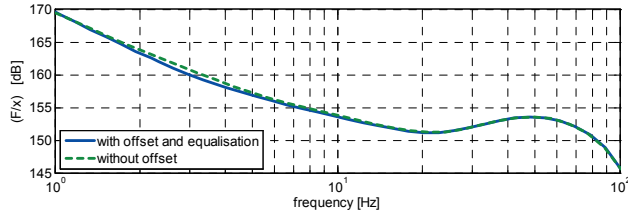

Figure 12 Servosystem with equalization: dynamic stiffness with external force R=±3000 N. (Stiffness units are N/m)

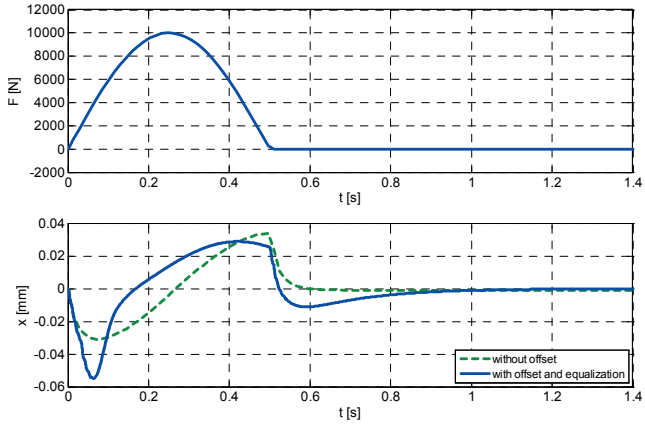

Figure 13 Servosystem with equalization: response to a half sine variation of load

7 CONCLUSIONS

The research activity performed on the equalization techniques for dual redundant electrohydraulic servoactuators for aircraft flight controls showed that the implementation of a suitable control strategy permits the attainement of a good load sharing between two electrohydraulic servoactuators of the aerodynamic force acting on a flight control surface. By using in an appropriate way the signals provided by two pressure differential transducers it is possible to perform an effective compensation of variable servovalves offsets and to minimize the transient disturbances following a failure, which enables the use of servoactuators with a simple and less expensive architecture. An accurate analytical model was prepared that clearly showed the merits of implementing the pressure differential equalization control algorithm.

REFERENCES

(1) Thayer, W.J.: Redundant Electrohydraulic Servoactuators Moog Technical Bulletin 127, May 1976

(2) Van den Bossche, D.: A380 Primary Flight Control Actuation System Proceedings of the Int. Conference on Recent Advances in Aerospace Actuation Systems and Components; Toulouse, France, June 2001

(3) Harschburger, H.E.: Development of Redundant Flight Control Actuation Systems for the F/A-18 Strike Fighter SAE paper 831484, 1983

(4) Straub, H.H.; Creswell, R.: The Boeing 747-400 Upper Rudder Control System with Triple Tandem Valve SAE paper 912133, 1991

(5) Raymond, E.T.; Chenoweth, C.C.: Aircraft Flight Control Actuation System Design SAE, 1993

(6) Shaefer, W.S.; Inderhees, L.J.; Moynes, J.F.: Flight Control Actuation System for the B-2 Advanced Technology Bomber SAE paper 91112, 1991

(7) Schmitt, V.R.; Morris, J.W.; Jenney, G.D.: Fly-by-Wire SAE, 1998

Authors' Index

Fluid Power and Motion Control 2008 Edited by Dr D N Johnston and Professor A R Plummer